IntechOpen

Microwave Systems and Applications

Edited by Sotirios K. Goudos

WEB OF SCIENCE™

MICROWAVE SYSTEMS AND APPLICATIONS

Edited by **Sotirios K. Goudos**

Microwave Systems and Applications
http://dx.doi.org/10.5772/62931
Edited by Sotirios K. Goudos

Contributors

Vincenzo Stornelli, Leonardo Pantoli, Giorgio Leuzzi, Dalia Elsheakh, Young Chul Lee, Mohammad Alibakhshikenari, Bal Singh Virdee, Mohammad Naser-Moghadasi, Ramazan Ali Sadeghzadeh, Ernesto Limiti, Alireza Sadrossadat, Farnaz Mohammadi, Milka Potrebic, Snezana Stefanovski Pajovic, Dejan Tosic, Kok Yeow You, Hatem El Matbouly, Xi Sung Loo, Kiat Seng Yeo, Kok Wai, Johnny Chew, Modar Shbat, Francisco Ordaz-Salazar, Javier Salvador González-Salas, Ramesh Pokharel, Adel Barakat, Hala Elsadek, Jian Wang, Yun Long, Dusan Kocur, Daniel Novák, Mária Švecová, Mustafa Murat Bilgiç, Korkut Yeğin, Imran Mohsin

Notice

First published in Croatia, 2017 by INTECH d.o.o.
eBook (PDF) Published by IN TECH d.o.o.
Place and year of publication of eBook (PDF): Rijeka, 2019.
IntechOpen is the global imprint of IN TECH d.o.o.
Printed in Croatia

Legal deposit, Croatia: National and University Library in Zagreb

Additional hard and PDF copies can be obtained from orders@intechopen.com

Microwave Systems and Applications
Edited by Sotirios K. Goudos
p. cm.
Print ISBN 978-953-51-2867-0
Online ISBN 978-953-51-2868-7
eBook (PDF) ISBN 978-953-51-4125-9

Meet the editor

Sotirios K. Goudos received his BSc degree in Physics in 1991 and his MSc in Electronics in 1994, both from the Aristotle University of Thessaloniki, Greece. In 2001, he received his PhD degree in Physics from the Aristotle University of Thessaloniki and in 2005 his master's degree in Information Systems from the University of Macedonia, Greece. In 2011, he obtained his diploma degree in Electrical and Computer Engineering from the Aristotle University of Thessaloniki. He joined the Department of Physics, Aristotle University of Thessaloniki, in 2013, where he is currently an assistant professor. His research interests include antenna and microwave structure design, electromagnetic compatibility of communication systems, evolutionary computation algorithms, mobile communications, and semantic web technologies. He is a member of the editorial board of the International Journal of Antennas and Propagation (IJAP), the International Scholarly Research Notices (ISRN) under the Computer Engineering subject, the International Journal of Energy Optimization and Engineering, and the International Journal on Advances in Intelligent Systems. Dr. Goudos is a member of the IEEE (senior member), the IEICE, the Greek Physics Society, the Technical Chamber of Greece, and the Greek Computer Society.

Contents

Preface

Microwave systems are an important technology for several aspects of our everyday life. They are key components of every modern wireless communication system. Wireless local area networks (WLANs) and cellular communications use microwave components, microwave integrated circuits (ICs), and antennas operating in microwave frequency bands. Additional emerging applications of microwave systems include wireless power transfer and energy harvesting, as well as applications to medicine like wireless body area networks (WBANs). Antenna design for microwave systems is another challenging task that needs to be addressed for all the abovementioned applications.

The main objective of this book was to collect as many different state-of-the-art studies as possible in order to cover in a single volume the main aspects of microwave systems and applications. This book contains 17 chapters written by acknowledged experts, researchers, academics, and microwave engineers, providing comprehensive information on all aspects of microwave systems and applications. This book is divided into four parts. The first part is devoted to microwave components. The second part deals with microwave ICs and innovative techniques for on-chip antenna design. The third part presents antenna design cases for microwave systems. Finally, the last part covers different applications of microwave systems.

The authors of each book part cover a wide range of topics. The chapters that follow in the next pages demonstrate a range of approaches to a diverse set of microwave systems and application areas using different novel design techniques and with usage scenarios from material characterization to multiple person localization. They represent only a small fraction of the current research, the emerging trends, and applications of microwave systems. I hope that this book will help researchers and students all over the world to attain new and interesting results in all the aspects of microwave systems and applications.

I would like to thank all the authors, who submitted their work for consideration to this book, for their valuable and interesting contributions in all areas of microwave systems and applications.

Sotirios K. Goudos
Assistant Professor
Department of Physics
Aristotle University of Thessaloniki
Thessaloniki, Greece

Section 1

Microwave Components

Chapter 1

Microwave Active Filter Design

Vincenzo Stornelli, Leonardo Pantoli and Giorgio Leuzzi

Additional information is available at the end of the chapter

http://dx.doi.org/10.5772/65917

Abstract

A simplified method for the project and design of microwave active filters is presented here. The presented design is based on the use of an active inductor that emulates an inductor behavior by implementing a passive variable phase- and amplitude-compensating network and amplifiers, forming a gyrator-C architecture. This method can be applied with success for the design of bandpass filters with very high performances in terms of integration and application from a few hundreds of MHz to tens of GHs with filter high dynamic range and frequency tuning capability.

Keywords: filters, active filter, active inductor, high dynamic range, gyrator

1. Introduction

Nowadays advancements in communications systems, in conjunction with the great increasing request for miniaturization and size reduction of wireless systems and devices, have led to an increase of performances and space reduction of modern communications systems and devices. Several RF building blocks have consequently been successfully implemented as integrated circuits (ICs) with different technologies. In this scenario, analog tunable filters working, in general, at RF and microwave frequencies still remain the most difficult part to be integrated in a single chip [1–18] due to requirements in input and output impedance matching, stability, and dynamic range. In fact, most commercial wireless receivers only use off-chip filters that are typically implemented with discrete components. This scenario leads to the occupation of a large area at the front-end. Even though the integrated version of filters has been presented in several papers, it must be noticed that in monolithic integrated microwave circuits (MMIC) most of the semiconductor area is occupied by passive elements, while active devices play a marginal role in area occupation. It is in fact generally known that passive inductors are largely responsible for the area occupation in IC. Classical spiral induc-

tors, in fact, require large amounts of substrate area or air bridges and present a very limited bandwidth, a general high series resistance, and crosstalk problems. For this reason, it can really be important to replace spiral inductors with active circuits behaving like inductors, but characterized by a very reduced semiconductor area occupation. It is well known that an inductor can be simulated by a gyrator loaded by a capacitance; in the literature and in the commercial market, a lot of solutions have been proposed that use the gyrator principle to simulate an inductive behavior at microwave frequency range [15, 16, 18–32]. Analog filters using Active Inductors (AIs) are good candidates for high-frequency operation; therefore, considerable interest has been shown in their use in active filters. In this perspective, in particular, band-pass filters designed by means of active inductor, usually suffer from a very low dynamic range due to the combination of a high noise level introduced by the AI and the relatively low compression power level of the AI itself. For all these reasons, there are only a few commercial solutions available on the market based on active inductors. Moreover, complex arrangements with many transistors tend to degrade the stability, preventing their use in practical applications. All these considerations show how the availability of simple, stable AIs with relatively high-power handling is therefore a critical issue, for their use as a replacement for spiral inductors in integrated filters especially when high-order filters with tunable characteristics are required. In the following paragraph, we will see how filters using active inductors have good potential to operate at high frequency, with high dynamic range, maintaining a constant quality factor (Q) in tunable applications when coupled with varactors diode, so considerable amount of interest has been shown in their use. A very simple approach for the design of tunable, high-quality factor, stable active inductors by means of an active inductor is presented here.

2. The active inductor design

Generally, active filters suffer from a very low dynamic range (see **Figure 1**) [33–53] due to the combination of a high noise level introduced by the AI and the relatively low compression power level of the AI itself. An interesting way to design active filters, in order to overcome this problem, is through the use of AI. The first high-Q AIs were reported over two decades ago, and the use of these inductors for the implementation of inductor-capacitor (L-C) resonator-type active filters was presented both in several papers and conferences.

However, as already mentioned, high-frequency active bandpass filters designed by means of AI usually suffer from a low dynamic range due to the combination of high noise level introduced by the AI and of low compression point of the AI itself, which limits the maximum handled power. Several kinds of AI have been proposed in the past [1–52], especially grounded inductors that are usually based on gyrator scheme loaded with a capacitor (**Figure 2**). With reference to **Figure 2**, the input voltage through the inverting amplifier (that can be based on a common-source stage) drives the loaded capacitor, producing a 90° delayed voltage; this in turn drives the output current through a noninverting transconductance, typically a source follower.

http://dx.doi.org/10.5772/65917

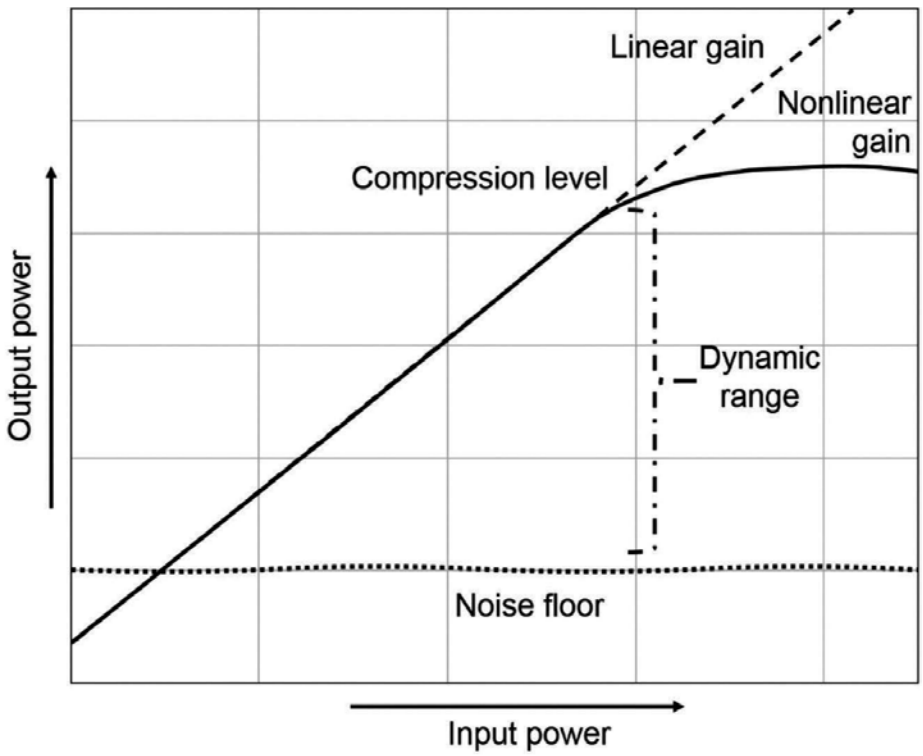

Figure 1. Dynamic range for an active filter.

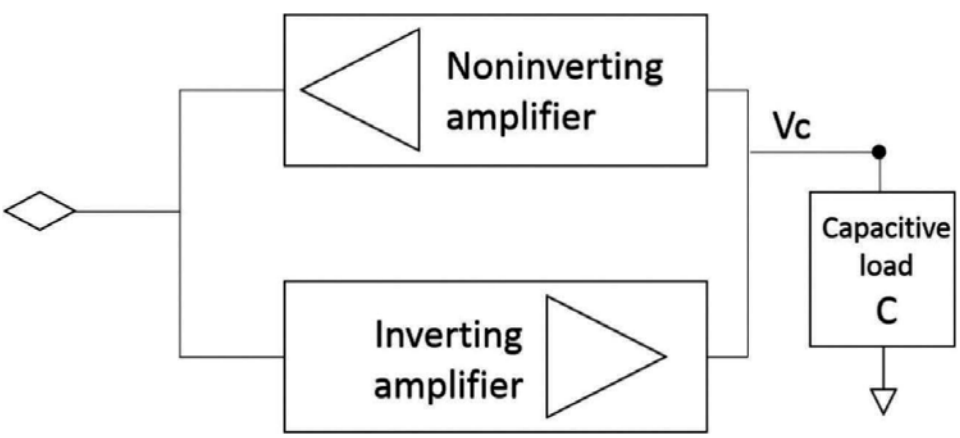

Figure 2. A gyrator-based active inductor scheme.

From **Figure 2** circuit, if we assume ideal amplifiers, the following equations can be derived [tcas]:

$$V_C = -\frac{g_{m1}}{j\omega C} \cdot V_{in} \tag{1}$$

$$I_{in} = -g_{m2} \cdot V_C = \frac{g_{m1} \cdot g_{m2}}{j\omega C} \cdot V_{in} = \frac{1}{j\omega L_{eq}} \cdot V_{in} \tag{2}$$

Finally, the equivalent inductance of the gyrator-based active inductor can be expressed as:

$$L_{eq} = \frac{C}{g_{m1} g_{m2}} \tag{3}$$

Eq. (3), of course, is valid only if the two amplifiers are ideal and zero phase delays and zero losses are present in the architecture. It is important to notice that if nonidealities in the amplifiers are considered, two unwanted effects appear: (1) a parasitic resistance (positive or negative) arises in series to the equivalent inductance; (2) the bandwidth of the inductive impedance becomes finite. **Figure 3a** shows that a phase relation between input less than 90° gives positive resistance, while a phase relation in excess of 90° causes a negative resistance: the AI can now be considered as in **Figure 3b**

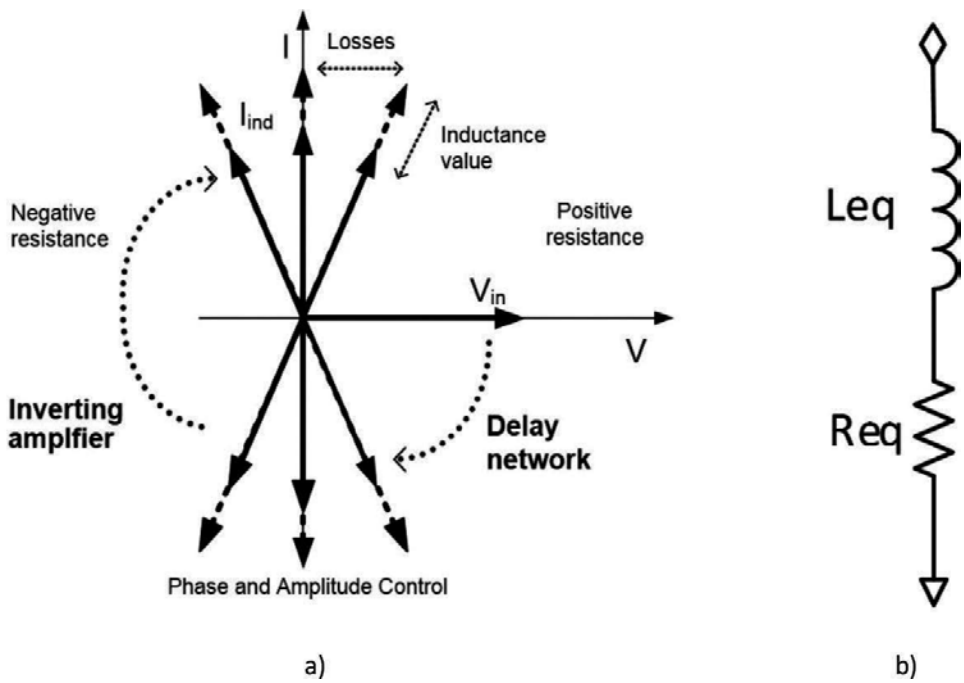

Figure 3. (a) AI voltage and current relations and (b) AI with series resistance.

If we were able to control both these phase relations, without acting on the bias condition of the amplifiers, the linearity of the active component of the gyrator will not be affected. This condition can be reached by the insertion of a suitable variable passive compensation network [35] (**Figure 4**).

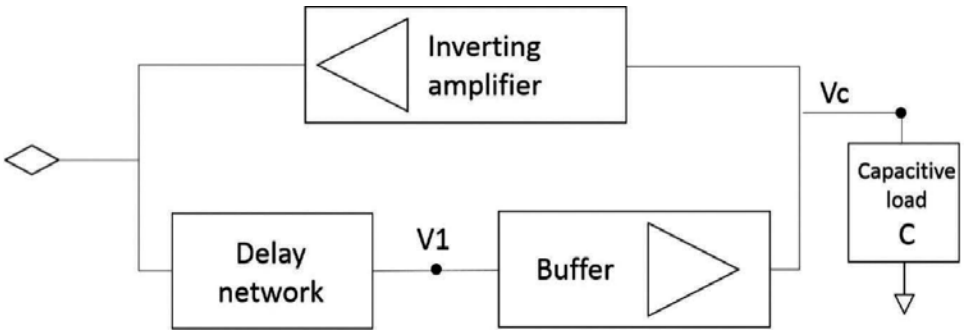

Figure 4. Block scheme of the active inductor with high dynamic range.

It has already been demonstrated in reference [35] that

$$R_{eq} = \frac{1}{g_m A_{\text{var}}}\cos(\varphi_{\text{var}}) + \frac{\omega R_{par} C_{tot}}{g_m A_{\text{var}}}\sin(\varphi_{\text{var}}) \tag{4}$$

$$L_{eq} = -\frac{1}{g_m A_{\text{var}}}\sin(\varphi_{\text{var}}) + \frac{\omega R_{par} C_{tot}}{g_m A_{\text{var}}}\cos(\varphi_{\text{var}})$$

From Eq. (4), it can be noticed that the phase of the compensating network must be such that the two addends cancel in the expression of the equivalent resistance, in the band of interest. This leads to a complex scenario. In order to simplify the design, a single active block AI and a compensation network can be also adopted as shown in **Figure 5**. In **Figure 6**, an equivalent circuit of the single active block AI [38] is shown. In this case, a simplified model of the capacitance gyrator with a single active block is shown.

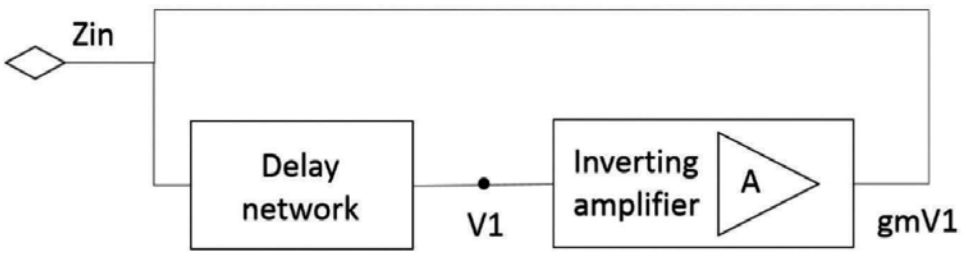

Figure 5. Block scheme of the proposed single active block active inductor.

An exact set of values of the resistor-capacitor (R-C) network gives a correct phase delay between input and output (voltage and current), minimizing the real part of the equivalent impedance. In the ideal case [38], the circuit input impedance is given by the following relation:

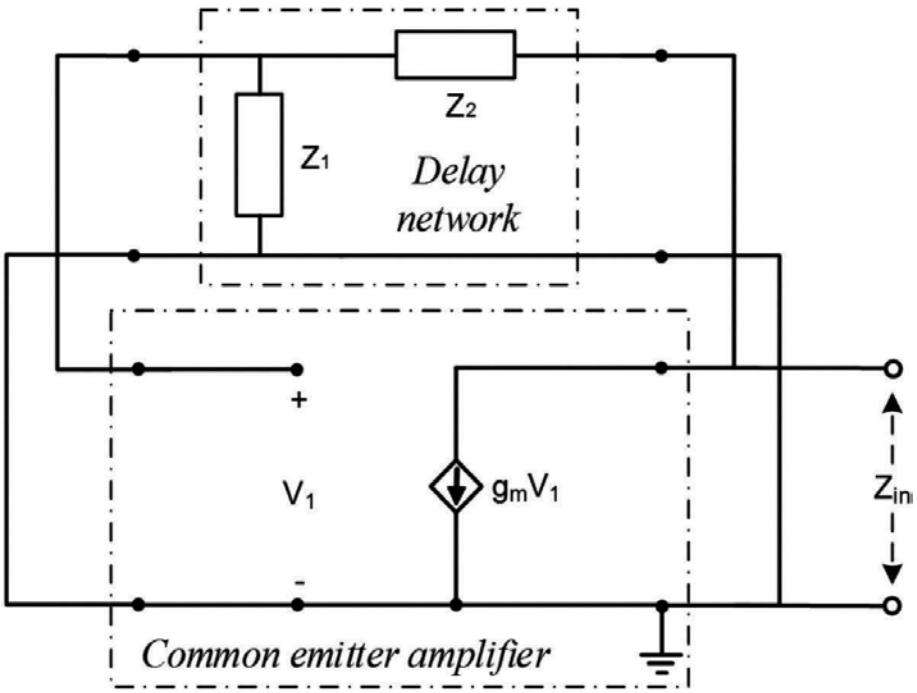

Figure 6. Simplified schematic model of the single-transistor AI.

$$Z_{in} = \frac{1 + j\omega RC}{g_m + j\omega C} \tag{5}$$

Eq. (5) can be also written in a more simple way as real and imaginary parts as in the following:

$$\mathrm{Re}\{Z_{in}\} = \frac{g_m + \omega^2 RC^2}{g_m^2 + \omega^2 C^2} \tag{6}$$

$$\mathrm{Im}\{Z_{in}\} = \frac{\omega g_m RC - \omega C}{g_m^2 + \omega^2 C^2} \tag{7}$$

Now it can be seen that the input impedance of the network is not always inductive [38]. By analyzing the imaginary part, we notice that the imaginary part of the AI impedance has a zero in $\omega = 0$, and it is always positive only if:

$$g_m R > 1 \tag{8}$$

The last is a very important condition if we want to obtain an inductive behavior. By considering also the amplifier block parasitic, we obtain the real and imaginary part of the input impedance of the single transistor (common emitter stage as the transconductance amplifier) gyrator as shown in **Figures 7** and **8**.

http://dx.doi.org/10.5772/65917

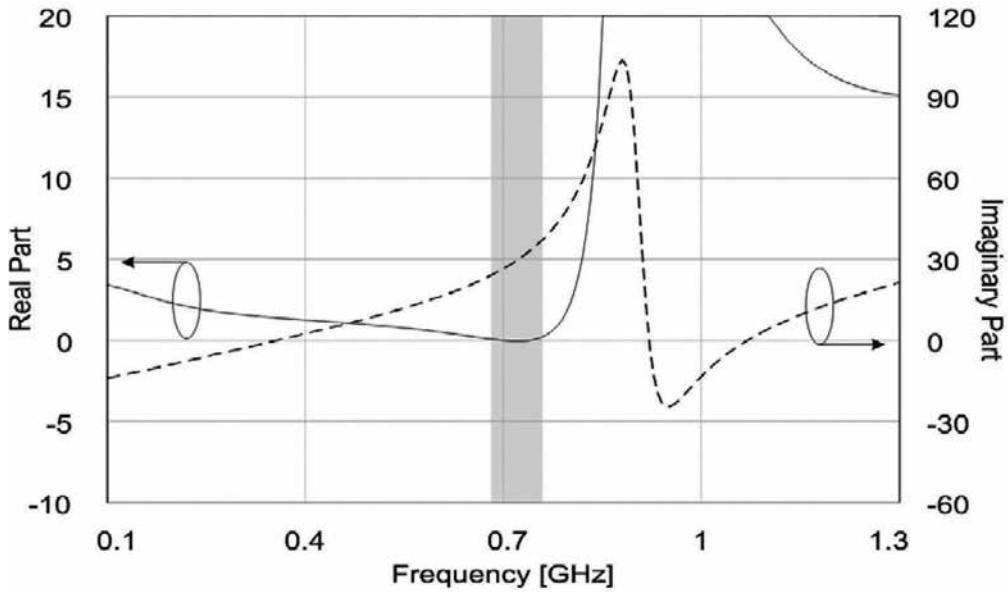

Figure 7. Real and imaginary part of the input impedance of the single transistor gyrator.

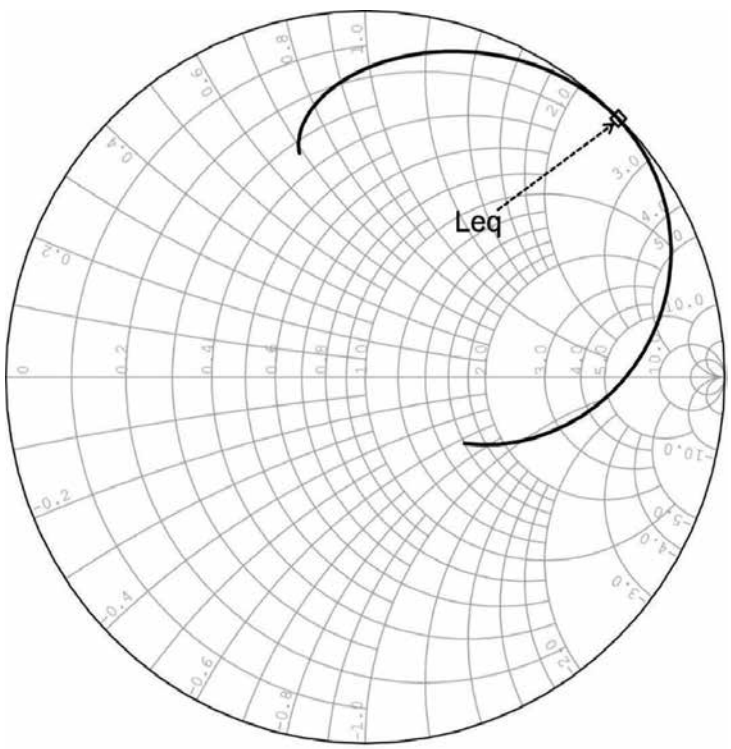

Figure 8. Complex input impedance of the AI.

3. Tunable microwave active filter example application

Thanks to the aforementioned approach, it is now possible to design an AI using, for example, medium-power bipolar transistor. The topology of the compensating network can be designed by means of an optimizer numerical software and the exact values of the network elements can be found by optimization, in order to take into account microstrip discontinuities and lines [38]. The ideal AI application is, of course, in monolithic integrated circuits, but as an example, a preliminary discrete design can be made on microstrip with discrete components. First, the AI design has to be performed, and consequently, a first-order (or greater) passband filter can be optimized (see **Figure 9**). As mentioned, the internal AI transconductance amplifier can be implemented by a bipolar transistor (e.g., the BFP420 bipolar junction transistor by Infineon in common-emitter configuration). **Figure 10** shows a simulated standalone AI real and imaginary part, while in **Figure 11**, the Smith chart complex input impedance is shown. In this case, the topology of the compensating network, and its components value, has been chosen in order to have an inductive behavior with minimum nonnegative series resistance around 2500 MHz. The standalone AI Q is shown in **Figure 12**. The implemented filter response in terms of S-parameters is shown in **Figure 13** showing the design success of microwave active filters by means of AI.

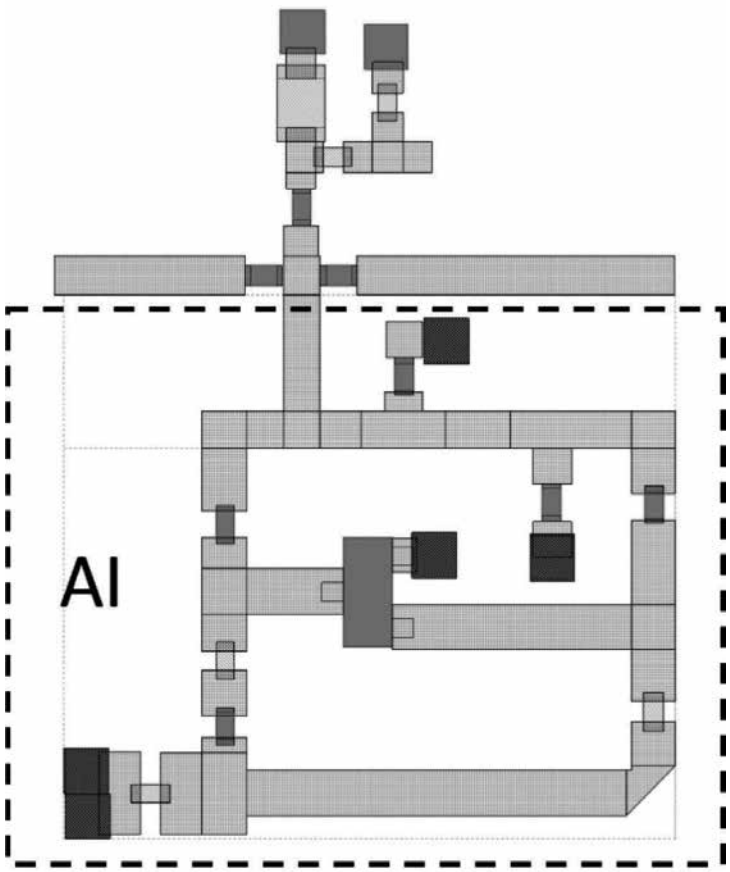

Figure 9. AI-based LC filter.

http://dx.doi.org/10.5772/65917

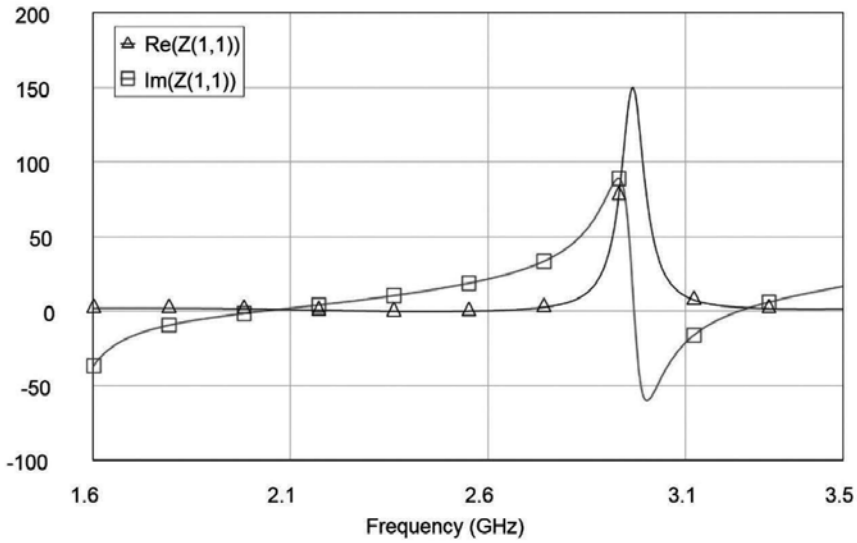

Figure 10. AI real and imaginary part.

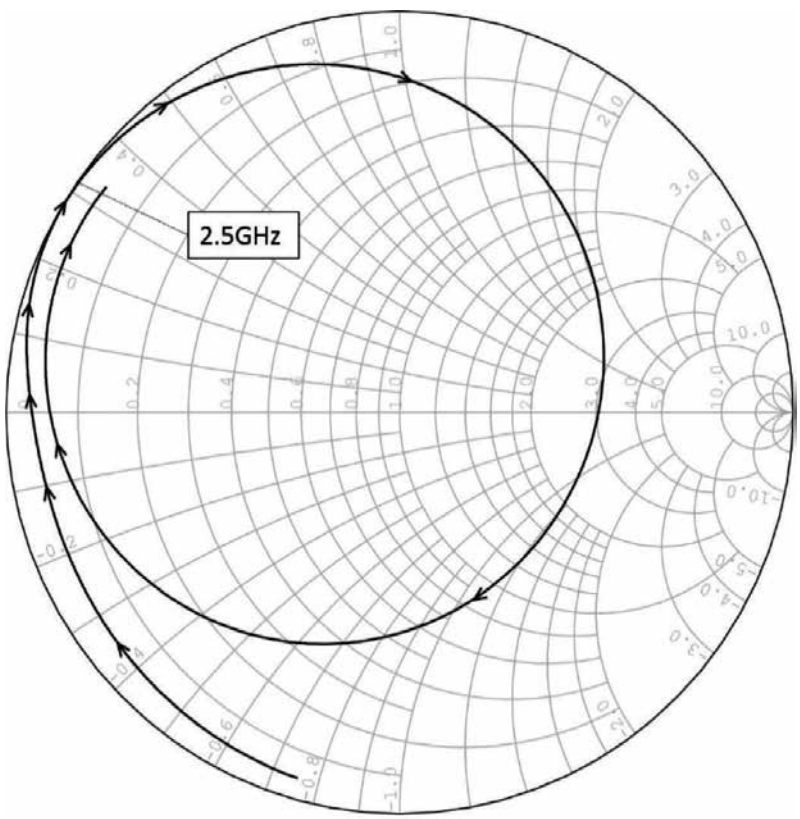

Figure 11. Complex input impedance of the active inductor.

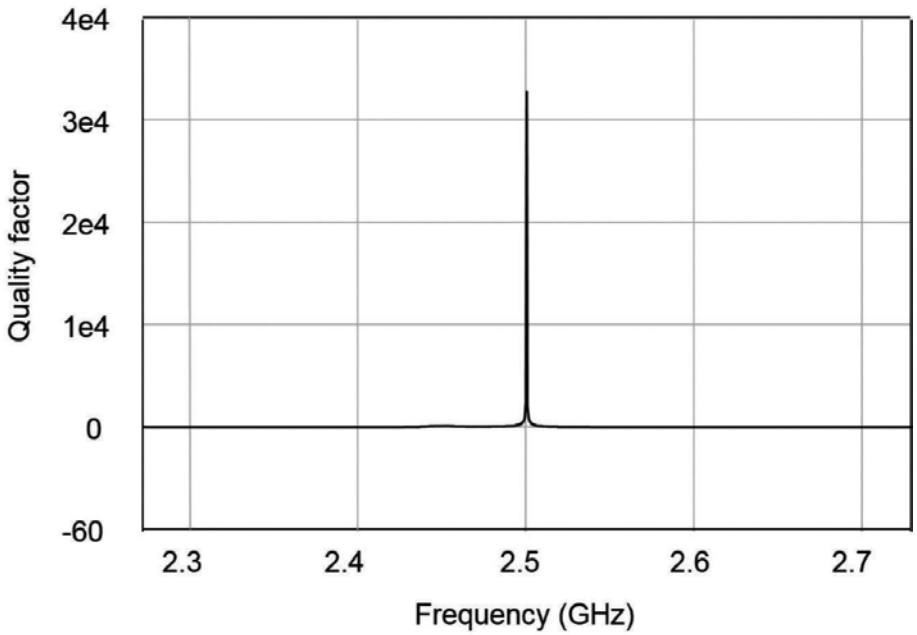

Figure 12. Quality factor of the active inductor.

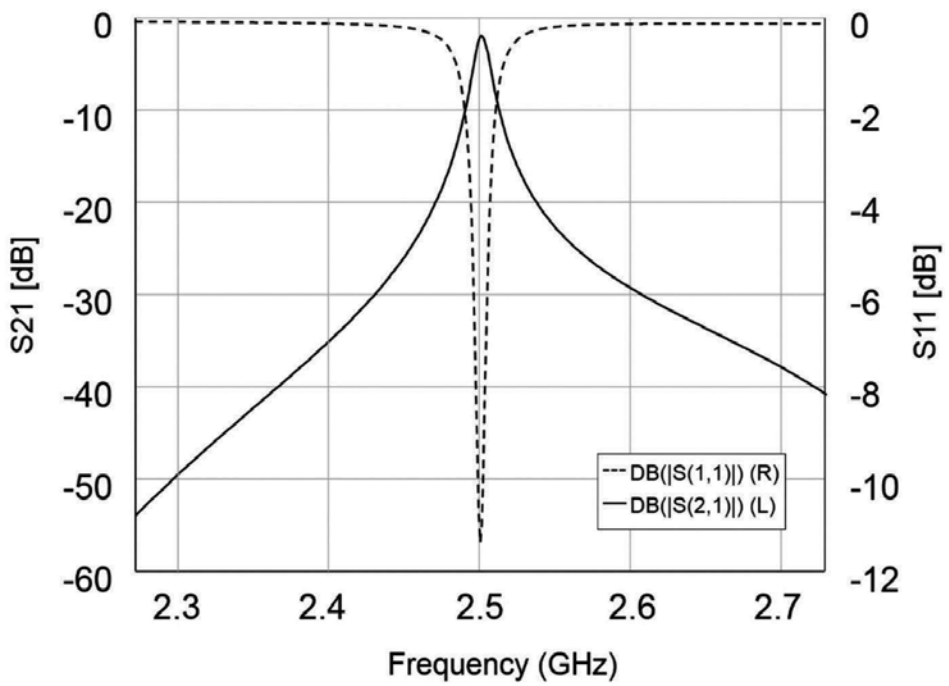

Figure 13. S-parameters of the designed active filter.

Author details

Vincenzo Stornelli*, Leonardo Pantoli and Giorgio Leuzzi

*Address all correspondence to: vincenzo.stornelli@univaq.it

Department of Industrial and Information Engineering and Economics, University of L'Aquila, L'Aquila, Italy

References

[1] Hara, S., Tokumitsu, T., Aikawa, M. "Lossless broad band monolithic microwave active inductor," IEEE Transactions on Microwave Theory and Techniques vol. 37, no. 12, pp: 1979–1984, December 1989.

[2] Wu, Y., Ding, X., Ismail, M., Olsson, H. "RF bandpass filter design based on CMOS active inductors" IEEE Transactions on Circuits and Systems-II: Analog and Digital Signal Processing vol. 50, no. 12, pp: 942–949, December 2003.

[3] Hara, S., Tokumitsu, T., Tanaka, T., Aikawa, M. "Broad band monolithic microwave active inductor and its application to miniaturized wide band amplifiers," IEEE Transactions on Microwave Theory and Techniques, vol. 36, no. 12, pp: 1920–1924, December 1988.

[4] Mukhopadhyay, R., Nuttinck, S., Woo, S. H., Kim, J. H, Lee, S. S., Lee, C. H., Laskar, J. Tunable active inductor, United States Patent Application Publication, no. US 2006/0170523 A1, appl. no. 60/649/221, Int. Cl. H03H 11/00, August 3, 2006.

[5] Kaunisto, R., Alinikula, P., Stadius, K., Porra, V. "A Low-Power HBT MMIC filter based on tunable active inductors," IEEE Microwave and Guided Wave Letters, vol. 7, no. 8, pp: 209–211, 1997.

[6] Wu, Y., Ding, X., Ismail, M., Olsson, H. "CMOS active inductor and its application in RF bandpass filter," IEEE Radio Frequency Integrated Circuits Symposium, pp: 655–658, 2004 .

[7] Campbell, C. F., Weber, R. J. "Design of a broadband microwave BJT active inductor circuit," Proceedings of the 34th Midwest Symposium on Circuits and Systems, vol. 1, pp: 407–409, 1991.

[8] He, X., Kuhn, W. B. "A 2.5-GHz low-power, high dynamic range self-tuned Q-enhanced LC ¯ filter in SOI," IEEE Journal of Solid-State Circuits, vol. 40, no. 8, 1618–1628, 2005.

[9] Kaunisto, R., Alinikula, P., Stadius, K. "Q-enhancing technique for high speed active inductors," IEEE International Symposium on Circuit and Systems ISCAS 1994, vol. 5, pp: 735–738, 1994.

[10] Hsiao, C., Kuo, C., Ho, C., Chan, Y. "Improved quality-factor of 0.18-μm CMOS active inductor by a feedback resistance design," IEEE Microwave and Wireless Components

Letters, vol. 12, no. 12. pp: 467–469, 2002.

[11] Lucyszyn, S., Robertson, I.D. "Monolithic narrow-band filter using ultrahigh-Q tuneable active inductors," IEEE Transactions on Microwave Theory and Techniques, vol. 42, no. 12, pp. 2617–2622, 1994.

[12] Thanachayanont, A. "Low-voltage Low-power high-Q CMOS RF bandpass filter" Electronics Letters, vol. 38, no. 13, pp. 615–616, 2002.

[13] Cho, Y., Hong, S., Kwon, Y. "A novel active inductor and its application to inductance-controlled oscillator," IEEE Transactions on Microwave Theory and Techniques, vol. 45, no. 8, pp. 1208–1213, 1997.

[14] Sharman, R., A'ain, A. K., Azmi, M., Huang, M. Z. "Design approach for tuneable CMOS active inductor," IEEE International Conference on Semiconductor Electronics ICSE 2004.

[15] Lu, L. H., Hsieh, H. H., Liao, Y. T., "A wide tuning-range CMOS VCO with a differential tunable active inductor," IEEE Transactions on Microwave Theory and Techniques, vol. 54, no. 9, pp. 3462 - 3468, 2006.

[16] Mukhopadhyay, R., Park, Y., Yoon, S. W., Lee, C. H., Nuttinck, N., Cressler, J. D., Laskar, J. "Active-inductor-based low-power broadband harmonic VCO in SiGe technology for wideband and multi-standard applications," IEEE MTT-S International Microwave Symposium Digest, Long Beach, CA. June 2005.

[17] van Vliet, F. E., van der Bogaart, F. L. M., Tauritz, J. L., Baets, R. G. F. "Systematic analysis, synthesis and realization of monolithic microwave active inductors," IEEE MTT-S International Microwave Symposium Digest, vol. 3, pp. 1659–1662, 1996.

[18] Thanachayanont, A., A. Payne, "VHF CMOS integrated active inductor," Electronics Letters, vol. 32, no. 11, pp. 999–1000, 1996.

[19] Georgescu, B., Finvers, I. G., Ghannouchi, F. "2 GHz Q-enhanced active filter with low passband distortion and high dynamic range," IEEE Journal of Solid-State Circuits, vol. 41, no. 9, pp. 2029 - 2039, 2006.

[20] Soorapanth, T., Wong, S. S., "A 0-dB IL 2140 § 30 MHz bandpass filter utilizing Q-enhanced spiral inductors in standard CMOS," IEEE Journal of Solid-State Circuits, vol. 37, no. 5, pp. 579 - 586, 2002.

[21] Gao, Z., Yu, M., Ma, J. "Wide tuning range of a CMOS RF bandpass filter for wireless application," IEEE Conference on Electron Devices and Solid-State Circuits, pp. 53–56, 2005.

[22] Allidina, K., Mirabbasi, S. "A widely tunable active RF filter topology," 2006 IEEE International Symposium on Circuits and Systems, pp. 879–882, 2006.

[23] Sae-Ngow, S., Thanachayanont, A. "A low-voltage, wide dynamic range CMOS floating active inductor," TENCON 2003. Conference on Convergent Technologies for Asia-Pacific Region, vol. 4, pp. 1460–1463, 2003.

[24] Mukhopadhyay, R., Yoon, S. W., Park, Y, Lee, C. H., Nuttinck, S., Laskar, J. "Investigation of inductors for digital Si-CMOS technologies," 2006 IEEE International Symposium on Circuits and Systems, pp. 3750–3753, 2006.

[25] Sussman-Fort, S.E. "Design concepts for microwave GaAs FET active filters," IEEE Transactions on Microwave Theory and Techniques, vol. 37, no. 9, pp. 1418–1424, 1989.

[26] Sujin, S., Namsik, R., Heungjae, C., Yongchae, J. "Novel high-Q inductor using active inductor structure and feedback parallel resonance circuit," IEEE Symposium on Radio Frequency Integrated Circuits (RFIC), vol. 1, pp. 467–470, 2007.

[27] Andriesei, C., Goras, L., Temcamani, F., Delacressoniere, B. "CMOS RF active inductor with improved tuning capability," International Semiconductor Conference, vol. 2, pp. 397–400, 2009.

[28] Chun-Lee, L., A'ain, A., Kordesch, A. V. "CMOS active inductor linearity improvement using feed-forward current source technique," IEEE Transactions on Microwave Theory and Techniques, vol. 57, no. 8, pp. 1915–1924, 2009.

[29] Yongho, C., Songcheol, H., Youngse, K. "Monolithic VCO using a novel active inductor," IEEE Microwave and Millimeter-Wave Monolithic Circuits Symposium, DOI: 10.1109/MCS.1996.506325, pp. 155–158, 1996.

[30] Rohde, U. L., Poddar, A.K. "Active inductor oscillator and noise dynamics," IEEE MTT-S International Microwave Symposium Digest (MTT), DOI: 10.1109/MWSYM.2011.5972933, pp. 1–4, 2011.

[31] Yushi, Z., Fei, Y. "Subthreshold CMOS active inductors with applications to low-power injection-locked oscillators for passive wireless microsystems," Circuits and Systems (MWSCAS), 2010 53rd IEEE International Midwest Symposium on, Aug. 2010.

[32] Gamm, G. U. "Low power wake-up receiver for wireless sensor nodes," IEEE Conference on Intelligent Sensors, Sensor Networks and Information Processing, vol. 1, pp. 121–126, 2010.

[33] Pantoli, L., Stornelli, V., Leuzzi, G. "A low-voltage low-power 0.25 μm integrated single transistor active inductor-based filter," Analog Integrated Circuits and Signal Processing, vol. 87, no. 3, pp. 463–469, 2016.

[34] Pantoli, L., Stornelli, V., Leuzzi, G. "Low-noise tunable filter design by means of active components," Electronics Letters, vol. 52, no. 1, pp. 86–88, 2016.

[35] Leuzzi, G., Stornelli, V., Del Re, S. "A tuneable active inductor with high dynamic range for band-pass filter applications," IEEE Transactions on Circuits and Systems II: Express Briefs, vol. 58, no. 10, pp. 647–651, 2011.

[36] Pantoli, L., Stornelli, V., Leuzzi, G. "Class AB tunable active inductor," Electronics Letters, vol. 51, pp. 65–67, 2015, ISSN: 0013-5194.

[37] Branchi, P., Pantoli L., Stornelli, V., Leuzzi, G. "RF and microwave high-Q floating active

inductor design and implementation," International Journal of Circuit Theory and Applications, vol. 43, no. 8, pp. 1095–1104, Aug. 2015. ISSN: 0098-9886.

[38] Leuzzi, G., Stornelli, V., Pantoli, L., Del Re, S. "Single transistor high linearity and wide dynamic range active inductor," International Journal of Circuit Theory and Applications, vol. 43, no. 3, pp. 277–285, March 2015. ISSN: 0098-9886.

[39] Pantoli, L., Stornelli, V., Leuzzi, G. "Tunable active filters for RF and microwave applications," Journal of Circuits, Systems, and Computers, vol. 23, pp. 1450088, 2014. ISSN: 0218-1266.

[40] Stornelli, V., Pantoli, L., Leuzzi, G. "High quality factor L-band AI-based band-pass filters," Journal of Circuits, Systems, and Computers, vol. 22, 3, 2013. ISSN: 0218-1266.

[41] Colucci, P., Leuzzi, G., Pantoli, L., Stornelli, V. "A third order integrable UHF bandpass filter using active inductors," Microwave and Optical Technology Letters, Microwave and Optical Technology Letters, vol. 54, no. 6, pp. 1426–1429, June 2012.

[42] Stornelli, V., Pantoli, L., Leuzzi, G. "An assessment on low voltage low power integrable single transistor active inductor design for RF filter applications" (Invited Paper), IEEE International Conference on Integrated Circuit Design and Technology (ICICDT), June 27–29, 2016.

[43] Pantoli, L., Stornelli, V., Leuzzi, G. "Class AB gyrator-based active inductor." In: IEEE Integrated Nonlinear Microwave and Millimetre-wave Circuits (INMMiC), 2015 International Workshop, Taormina, 29–30 September, 2015.

[44] Pantoli, L., Stornelli, V., Leuzzi, G. "RF active circuit simulating a floating inductance." In: IEEE, Integrated Nonlinear Microwave and Millimetre-wave Circuits (INMMiC), 2015 International Workshop, Taormina, 29–30 September, 2015.

[45] Pantoli, L., Stornelli, V., Leuzzi, G. "A wideband class-AB tunable active filter." In: IEEE, European Microwave Week 2015. EuMW 2015—Conference Proceedings; EuMIC 2015: European Microwave Integrated Circuits Conference, Parigi, 7–8 September, 2015.

[46] Pantoli, L., Stornelli, V., Leuzzi, G. "A wideband class-AB tunable active filter." In: IEEE, European Microwave Week 2015. EuMW 2015—Conference Proceedings; EuMC 2015: European Microwave Conference, Parigi, 7–8 September, 2015.

[47] Pantoli, L., Stornelli, V., Leuzzi, G., Di Carlofelice, A. "A single transistor post selector active tunable filter for radio receivers applications." In: IEEE Integrated Nonlinear Microwave and Millimetre-wave Circuits (INMMiC), 2014 International Workshop on. DOI: 10.1109/INMMIC.2014.6815106, 2014.

[48] Pantoli, L., Stornelli, V., Leuzzi, G. "Low voltage high-order agile active filter for microwave applications." In: IEEE. EuMC 2013: 43rd European Microwave Conference, pp. 1203–1206, 2013.

[49] Pantoli, L., Stornelli, V., Leuzzi, G. "A single-transistor tunable filter for bluetooth applications." In: EuMW 2012, Conference Proceedings—7th European Microwave Integrated

Circuits Conference, EuMIC 2012, Amsterdam, October 29–30, 2012.

[50] Pantoli, L., Stornelli, V., Leuzzi, G. "A single-transistor tunable filter for bluetooth applications." In: Conference Proceedings—42nd European Microwave Conference, EuMC 2012. pp. 1269–1272, ISBN: 978-287487027-9.

[51] Stornelli, V., Leuzzi, G., Pantoli, L., Del Re, S. "High dynamic range bandpass filters design based on active inductor." In: Microwave Integrated Circuits Conference (EuMIC), 2011 European, Manchester, October 10–11, pp. 168–171.

[52] Leuzzi, G., Stornelli, V., Del Re, S., Pantoli, L. "High quality factor integrable bandpass filter by using tunable active inductor." In: Integrated Nonlinear Microwave and Millimetre-Wave Circuits (INMMIC), 2011 Workshop on, Vienna, April 18–19, 2011.

[53] Leuzzi, G., Stornelli, V., Colucci, P., Pantoli, L. "Low-noise electronic circuit simulating the behavior of an inductance. 2014, US201414301526 20140611.

Chapter 2

Modeling and Simulation Techniques for Microwave Components

Sayed Alireza Sadrossadat and Farnaz Mohammadi

Additional information is available at the end of the chapter

http://dx.doi.org/10.5772/66356

Abstract

This chapter discusses about methods used in simulation and modeling of radio frequency (RF)/microwave circuits and components. The main topic that is discussed here is about one of the most powerful methods, that is, artificial neural networks. In this chapter, different types of neural network such as dynamic and recurrent neural networks will be discussed. Other techniques that are popular in the area of microwave components simulation and modeling are numerical techniques such as vector fitting, Krylov method, and Pade approximation. At the end of the chapter, vector fitting as an example of numerical methods will be discussed.

Keywords: artificial neural networks, circuit simulation and modeling, transient analysis, function approximation, RF/microwave circuits

1. Introduction

In recent years, ascending development of wireless communication products and huge trend for commercial market in this ground caused significant improvement in modeling and simulation approaches of radio frequency (RF) and microwave circuits. Such high-frequency circuits are leading to the development of a large variety of microwave models for passive and active devices and circuit components [1]. Modeling and computer-aided design (CAD) methods have an essential role in microwave designs and simulations [2]. The older approaches were mainly based on slow trial-and-error processes and an emphasis on performance at any price, but today seems to be a new era in high-frequency circuit design and modeling, since development in this ground has enabled microwave engineers to design larger, more efficient, and more complicated circuits than before [1, 3]. This complexity requires new materials and technologies that require not only new models but also new

algorithms in computer-aided design [4] for RF/microwave circuits, antennas, and systems to keep up with the advancement of technology with emphasis on time-to-market and low-cost approaches [1, 3]. In addition to accurate parametric-modeling techniques to describe the behavior of the microwave device, a reliable description that explains the changes of its behavior against geometrical or physical parameters is also needed [5].

Also, since circuit models at high frequencies often lack fidelity, detailed electromagnetic (EM) simulation techniques are needed to improve design accuracy. Although EM simulation techniques are heavily used yet, they are computationally expensive, so there is a demand for design methodologies to be not only accurate but also fast. Another concerning problem today is optimization. To meet this purpose, computer-based algorithms that work with iterative circuit evaluation are needed; this process also needs a highly repetitive computational process. Another concerning issue according to Ref. [6] is the possibility of employing knowledge-based tools for initial design, that is, one of the steps toward designing and modeling process. It is hard to satisfy all these problems with the traditional CAD technologies [1, 3]. In conclusion, obviously there is a serious need for a powerful accurate and fast processing and modeling tool.

Neural networks (NNs), or artificial neural networks, are information-processing systems that can imitate the ability of human brain to learn from observation and generalize by abstraction to create complex models [7]. Neural network gives a great approximation of system regardless of linear or nonlinear correlation between the input data and can be used as knowledge-based tool (to be employed for initial design in RF/microwave applications) [1]. The ability of NN to be trained resulted in their use in many diverse fields such as pattern recognition, system identification, control, telecommunications, biomedical instrumentation, and many other grounds. Recently, many researchers in communication area are focusing on using neural network in their modeling and simulation, and NN has been recognized as a useful alternative to conventional approaches in microwave modeling [1, 3]. Neural network models are simple and fast, and they can enhance the accuracy of existing models. The basis of neural network is on the universal approximation theorem, which says that a neural network with at least one hidden layer can give an approximation of nonlinear multidimensional function to any intended accuracy [8]. This property makes neural network a favorite modeling tool for microwave engineers. Neural network approach is generic, that is, the same modeling technique that can be reused for passive/active devices/circuits. Another advantage of NN is the ease of updating neural models regarding changes in technology [2]. Neural network is now used in various microwave modeling and simulation applications, such as vertical interconnect accesses (Vias) and interconnects [9], parasitic modeling [10], coplanar waveguide (CWG) components [11], antenna applications, nonlinear microwave circuit optimization [12], power amplifier modeling, nonlinear device modeling, wave-guide filter, enhanced elemental method (EM) computation, and so on [2].

Artificial neural networks are classified into two main categories: static neural networks and dynamic neural networks. In this chapter, the first neural network structures will be presented, and then a general overview of static and dynamic neural networks and different types of them and their applications in microwave modeling will be discussed. The last part is devoted to another method called vector fitting (VF) that is a numerical technique used for system identification and macromodeling [13].

http://dx.doi.org/10.5772/66356

2. Training neural network

2.1. Basic structure of neural network

The idea behind neural network is similar to the function of human brain. A typical neural network structure has two types of basic components: the processing elements and interconnection between them. The processing elements are known as neurons, and the interconnections are called links. Each link is recognized with a corresponding weight parameter. Every neuron receives stimuli from neighbor neurons connected to it [3]. Input neurons receive stimuli from the outside of the network and the neurons that produce the output result are called output neurons, and neurons that not only send but also receive stimuli are called hidden neurons [1]. There are different ways to connect neurons to each other, so there are different neural network structures. A neural network structure defines how information is processed inside a neuron, and how the neurons are connected. In this chapter, we discuss the models that are more common in microwave simulations and modeling.

Generally, artificial neural networks have an input data vector, an output data vector, a vector including all the weight parameters, and a function that mathematically presents the neural network [14].

Assume N_i and N_o to represent the number of input and output neurons of the neural network, respectively, w to be the vector of weight parameters, and $y = y(x,w)$ to define the function that represents the neural network. A simple scheme of artificial neural network is shown in **Figure 1**.

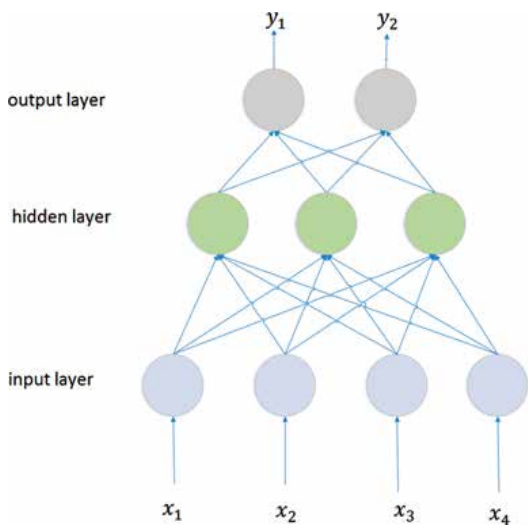

Figure 1. A general scheme of a neural network with four input neurons, two output neuron, and one hidden layer. Also, the links between the neurons are the weights.

Given a set of input and output data, a neural network can be constructed and trained. The network tries to estimate a function, so that it is able to give the closest result to the intended output. Commonly, a large percentage of input and corresponding output data are used as

training data and the network will be trained by means of them. The act of training means identifying the weights, so that they reach the optimum values. The remaining percentage of data is used as validation and testing. Validation set is used to determine an approximation of generalized error and is a factor for determining when to stop the process to prohibit over-learning and under-learning [7]. Testing data obviously is used for checking the accuracy and correctness of the network after training is completed.

In each level of information processing, the output of each neuron is received by the next neuron, from input neurons to output neurons. An overview of information processing in layers is shown in **Figure 2**. The inputs of a neuron are first multiplied by the corresponding weight parameters individually, then the results are added to produce a weighted sum of γ, which then will pass through a neuron activation function $\sigma(.)$ to produce the final output of the neuron. This output is the input of the neuron in the next layer, and this process is repeated for all the neurons, until it reaches the output layer.

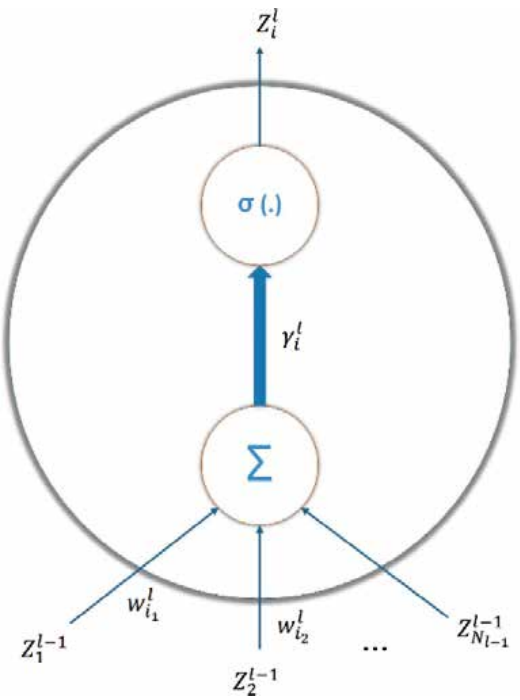

Figure 2. Information processing inside a neuron.

Let $w_{i0}{}^l$ to be the bias for i^{th} neuron of l^{th} layer. So the vector of weights is $w = [w_{10}^2 w_{11}^2 w_{12}^2 \ldots w_{2N_1}^2 w_{10}^3 \ldots w_{N_L N_{L-1}}^L]^T$ and the output of the neuron is $z_i^l = \sigma(\gamma_i^l)$.

There are different types of training in neural network [1], here we explain each of them shortly:

1. Sample-by-sample (or online) training: each time a training sample is presented, the weights (w) are updated based on training error.
2. Batch-mode (or offline) training: after each epoch weights are updated based on training error from all the samples in training data set.
3. Supervised training: using x and y data for training process, where x is the input of the neural network and y is the output of the neural network.
4. Un-supervised training: using just x data for training process.

2.2. Activation functions

Activation function, also known as transfer function, is one of the most important units in a neural network structure, that is, a scalar-to-scalar function transforms a set of input signals into an output signal. Common types of activation functions are arctangent as shown in **Figure 3**, hyperbolic tangent shown in **Figure 4**, and sigmoid functions which are shown in **Figure 5** [15].

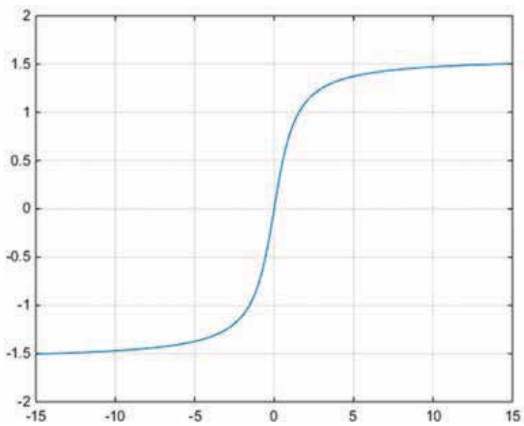

Figure 3. Mathematical graph of arctangent function $z = \sigma(\gamma) = \frac{2}{\pi} \arctan(\gamma)$.

Sigmoid function:

$$z = \sigma(\gamma) = \frac{1}{1 + e^{-\gamma}} \tag{1}$$

Arctangent function:

$$z = \sigma(\gamma) = \frac{2}{\pi} \arctan(\gamma) \tag{2}$$

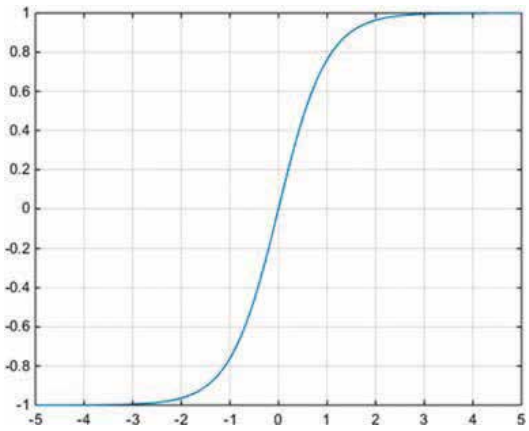

Figure 4. Mathematical graph of hyperbolic tangent function $z = \sigma(\gamma) = \frac{e^{\gamma}-e^{-\gamma}}{e^{\gamma}+e^{-\gamma}}$.

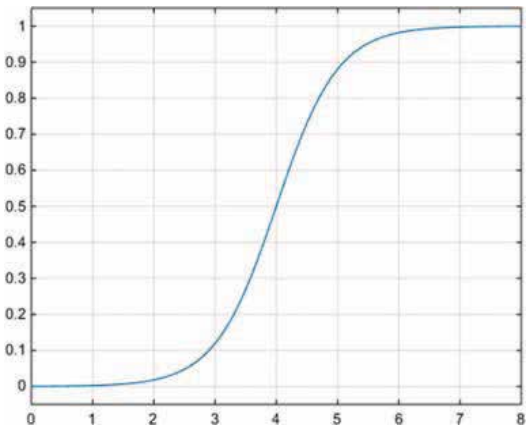

Figure 5. Mathematical diagram of sigmoid function $z = \sigma(\gamma) = \frac{1}{1+e^{-\gamma}}$.

Hyperbolic tangent function:

$$z = \sigma(\gamma) = \frac{e^{\gamma}-e^{-\gamma}}{e^{\gamma}+e^{-\gamma}} \tag{3}$$

3. Static neural networks

In the past few years, artificial neural networks have gained attention as a valuable computer-aided design tool for modeling high-frequency circuits. They can mainly be categorized as techniques for modeling frequency-domain response of components and time-domain response of them. For frequency-domain modeling, static neural networks are employed. Their

http://dx.doi.org/10.5772/66356

main architectures are multilayer perceptron (MLP) and radial-basis function (RBF), which will be discussed in this section.

3.1. Multilayer perceptron (MLP)

Multilayer perceptron structure is the most frequently used structure in many areas including microwave modeling and optimization problems. This technique belongs to a subcategory of neural network called feed-forward neural network, which is able to approximate continuous and integrable functions [1], and their connectivity consists of layer groups that are only linked to adjacent layers, meaning that there is not a cycle or a recursive path [16].

3.1.1. MLP structure

In MLP structure, neurons are classified into different layers. A typical MLP neural network consists of one input layer, one or more hidden layers, and one output layer, as shown in **Figure 6**. Consider L as the total number of layers, layer 1 is the input layer, layer 2 to layer (L-1) are hidden layers, and layer L is the output layer. Also, suppose the number of neurons in l^{th} layer is N_l, $l = 2, 3, \ldots, L$.

Here, consider x_i as the i^{th} input of the MLP, and z_i^l as the output of i^{th} neuron of l^{th} layer. Also, w_{ij}^l is the weight of the link between j^{th} neuron of $(l - 1)^{\text{th}}$ layer, and i^{th} neuron of l^{th} layer $1 \le j \le N_{l-1}, 1 \le i \le N_l$.

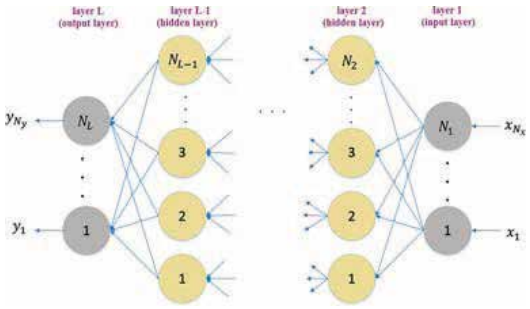

Figure 6. MLP structure with one input layer, several hidden layers, and one output layer.

One of the most commonly used activation functions in MLP structure is sigmoid function [1], which is shown in **Figure 5**.

In summary, if we suppose $x = [x_1\ x_2 \ldots\ x_n]^T$ is the input vector, and $y = [y_1\ y_2 \ldots\ y_m]^T$ is the output vector,

For

$$l = 1: \ z_i^l = x_i, \ i = 1, 2, \ldots, \ n = N_1 \tag{4}$$

For

$$l = 2,3,\ldots,L : \gamma_i^l = \sum_{j=0}^{N_{l-1}} w_{ij}^{l-1} z_j^{l-1}, z_i^l = \sigma(\gamma_i^l) \tag{5}$$

And

$$y_i = z_i^L, i = 1,2,\ldots,m, m = N_L \tag{6}$$

3.2. Radial-basis function (RBF) networks

Radial-basis function neural network, like MLP, is a subset of feed-forward neural network. It is used in a wide range of applications related to microwave transistors and high-speed integrated circuits, and modeling of intermodulation distortion behavior of MESFETs and HEMTs [1, 17].

3.2.1. RBF structure

A radial-basis function is a real-valued function whose value depends only on the distance from the origin, so that $\varphi(x) = \varphi(\|x\|)$, or alternatively on the distance from some other point c, called a *center*, so that $\varphi(x,c) = \varphi(\|x-c\|)$. Any function that satisfies the property $\varphi(x) = \varphi(\|x\|)$ is a radial function.

The main approach in this structure is based on approximation of a curve that best fits to the training data set in high-dimensional space by determining λ and c that are standard deviation and center of the activation functions, respectively, and are parameters of the function [7, 15]. The dimension of the hidden space is related directly to the accuracy of the approximated model [14]. In this structure, we have

$$y(x) = \sum_{i=1}^{N} w_i \varphi(\|x-x_i\|), \tag{7}$$

where *y(x)* is the approximating function that is the weighted sum of radial-basis functions [1].

In RBF structure, there is just one hidden layer, and the function of input and output layers stays the same like MLP structure. RBF uses the radial basis as activation function [7]. **Figure 7** shows a typical RBF neural network.

Radial-basis activation functions include Gaussian and multiquadratic functions.

Gaussian function:

$$\sigma(\gamma) = \exp\left(-\left(\frac{\gamma}{\lambda}\right)^2\right) \tag{8}$$

Multiquadratic function:

http://dx.doi.org/10.5772/66356

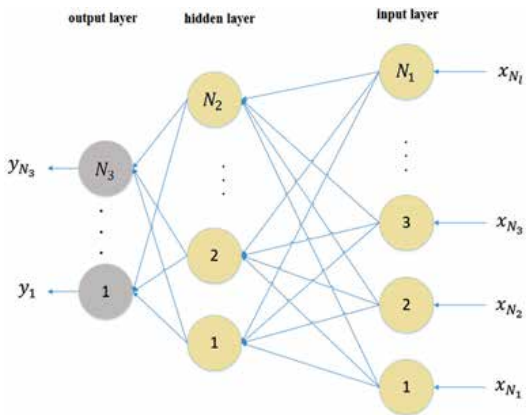

Figure 7. Structure of RBF neural network.

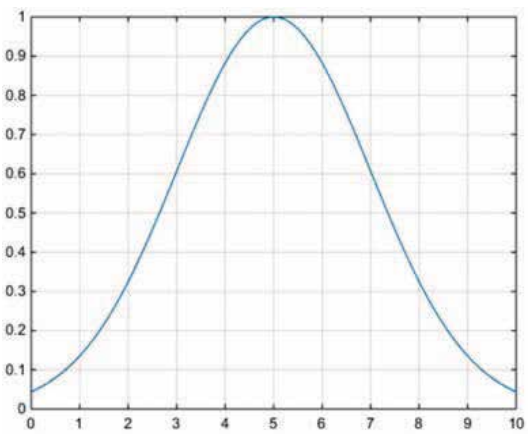

Figure 8. The Gaussian function.

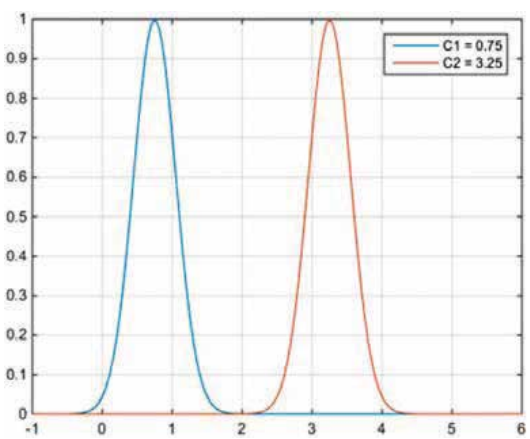

Figure 9. The multiquadratic function. *C* represents the value of centers.

$$\sigma(\gamma) = \frac{1}{(c^2 + \gamma^2)^{\alpha}}, \alpha > 0 \tag{9}$$

The Gaussian and multiquadratic functions are shown in **Figure 8** and **Figure 9**, respectively.

4. Time-domain neural networks

For time-domain modeling of components and systems, time-domain artificial neural network structures are usually employed in the literature. The main time-domain architectures are dynamic neural networks (DNNs) and recurrent neural networks (RNNs), which will be discussed in this section.

Most neural network structures used by engineers are feed-forward neural networks that are suitable for time-independent static input-output mapping [18]. In feed-forward neural networks, the flow of information is straight forward from the first neuron of the first layer to the last neuron of the output layer, and the procedure is not recursive, so the output of neurons does not have any effect on the input of the last neurons, although the stability of a neural network is the result of the absence of feedback in the network. In spite of static NNs, a dynamic neural network uses feedback between neurons in the same layer, or even neurons in different layers, also it provides more computational advantages [19]. Feedback-based neural networks are good approaches for modeling, identification, and control of systems, since most of systems in real world such as airplanes, rockets, and so forth are nonlinear dynamical systems [18, 20].

4.1. Recurrent neural networks (RNNs)

Recurrent neural network is a discrete time-domain neural network that allows time-domain behaviors of a dynamic system to be modeled [1]. Its structure is suitable for modeling tasks such as dynamic system control and finite-difference time-domain (FDTD) solutions in electromagnetic modeling [21]. The output of the neural network is a function of its present inputs and a history of its inputs and outputs [22]. The delayed outputs are fed back to the inputs and the feed-forward network along with the feedback delay constructs the recurrent neural network structure. In this architecture, we suppose the inputs and outputs to be a function of time, representing this functionality with parameter t, also τ which is the delay representing the effect of history of the neural network inputs and outputs.

Suppose the external single input of the neural network to be $x(t)$ so the history of it would be $x(t\text{-}\tau)$, $x(t\text{-}2\tau)$, $x(t\text{-}3\tau)$, …, $x(t\text{-}\alpha\tau)$ where α is the maximum number of delay steps for x, and suppose the single output of the RNN to be $y(t)$ with history of it demonstrating as $y(t\text{-}\tau)$, $y(t\text{-}2\tau)$, $y(t\text{-}3\tau)$, …, $y(t\text{-}\beta\tau)$ that β is the maximum number of delay steps for y. The architecture of the RNN is shown in **Figure 10**. The corresponding formulation is

$$y(t) = f\left(y(t-\tau), y(t-2\tau), ..., y(t-\beta\tau), x(t), x(t-\tau), x(t-2\tau), \ldots, x(t-\alpha\tau)\right) \tag{10}$$

Suppose a three-layer discrete-time MLP neural network as above, with activation function $z = \sigma(\gamma)$. Applying the delays to the process, the output of the i^{th} neuron at t is

$$y_i(t) = \sigma\left(\gamma_i(t-\tau)\right) \tag{11}$$

in which,

$$\gamma_i(t) = x_i(t) + \sum_{j=1}^{T} w_{ij} y_j(t) \tag{12}$$

where T is the total number of neurons, x_i is the external input, $i = 1, 2, 3, \ldots, T$, y_i is the output of neuron itself, also y_j is the output of other neurons, $j = 1, 2, 3, \ldots, T$, $i \neq j$.

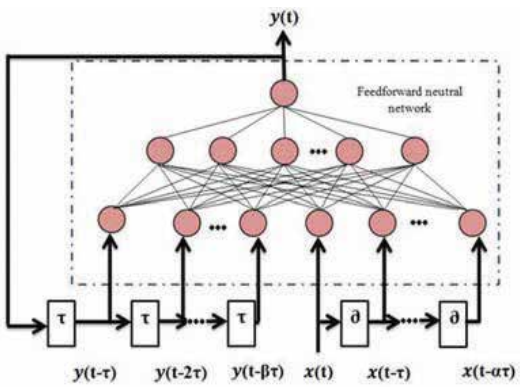

Figure 10. Recurrent neural network.

5. Dynamic neural networks (DNNs)

Dynamic neural network is a continuous time-domain neural network that is one of the best formulations for modeling nonlinear microwave circuits [9]. DNN is highly efficient in theory and practice. It is suitable for a wide range of needs in nonlinear microwave simulations, for example, it is suitable for both time- and frequency-domain applications, multitone simulations, and so on [12]. In comparison with other neural network methods, DNN provides a faster and more accurate network modeling that is significantly required in today's efficient CAD algorithms in high-level and large-scale nonlinear microwave designs. DNN also can be

developed directly from input-output data without a need to depend on internal details of the circuit [12]. In DNN, the outputs are a function of inputs and their derivatives, and also a function of derivatives of outputs. **Figure 11** shows the architecture of dynamic neural network and the process occurring at each level.

In **Figure 11**, $y^{(n)}(t)$ is the n^{th} derivative of $y(t)$ and is integrated and fed back as an input to the system along with the inputs $x(t)$ and their derivatives, $x^{(i)}(t)$. $y^{(n)}(t) = f\left(y^{(n-1)}(t), y^{(n-2)}(t), \ldots, y(t), x^{(n)}(t), x^{(n-1)}(t), \ldots, x(t)\right)$, in which f (.) represents the MLP nonlinear function and $y^{(i)}(t)$ represents i^{th} derivative of $y(t)$.

The DNN model can represent a nonlinear circuit when trained and tested with an appropriate data set, measured or obtained from the original circuit.

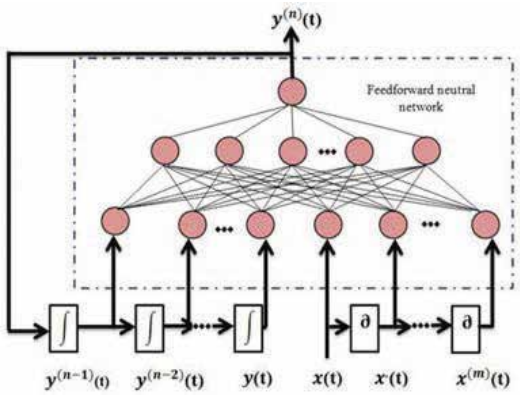

Figure 11. Dynamic neural network.

5.1. State-space dynamic neural network (SSDNN)

State-space dynamic neural network (SSDNN) is a technique for modeling nonlinear transient behaviors especially in high-speed IC and nonlinear circuits. The SSDNN-modeling technique is based on DNN structure and is a combination of DNN and state-space concept, which expands continuous DNN into a more general and flexible approach for nonlinear transient modeling and design with good accuracy [23].

Let $v \in \mathbb{R}^N$ be the transient input signal of a nonlinear circuit, and let $y \in \mathbb{R}^M$ be the transient output signal of a nonlinear circuit, where N and M are the number of inputs and outputs of the circuit, respectively, w also is the weight parameter matrix that is divided into three matrixes: w_v, w_s, w_o, which are weights connecting to the inputs (v), weights connecting to the state variables, and weights connecting the hidden neurons of the hidden layer to the outputs, respectively. Also, η is a constant scaling parameter. SSDNN model formulation can be represented by the equations as follows:

http://dx.doi.org/10.5772/66356

$$\left\{ \begin{array}{c} \dot{x}(t) = -x(t) + \eta g_{\text{ANN}}\left(v(t), x(t), w\right) \\ y(t) = Bx(t) \end{array} \right\} \tag{13}$$

where $x = [x_1, \ldots, x_L]^T \in \mathbb{R}^L$ and is a vector of state variables, with initial condition $x(0) = x_0$ and L is the dimension of the state space, that is, the order of the model, $g_{\text{ANN}} = [g_{\text{ANN-1}}, \ldots, g_{\text{ANN-}L}]^T$ is a representation of feed-forward MLP neural network, which has $N + L$ input neurons and L output neurons, also $B = [b_{ij}] \in \mathbb{R}^{LM}$ is the matrix which maps state space into output space [23]. A simple structure of SSDNN is shown in **Figure 12**.

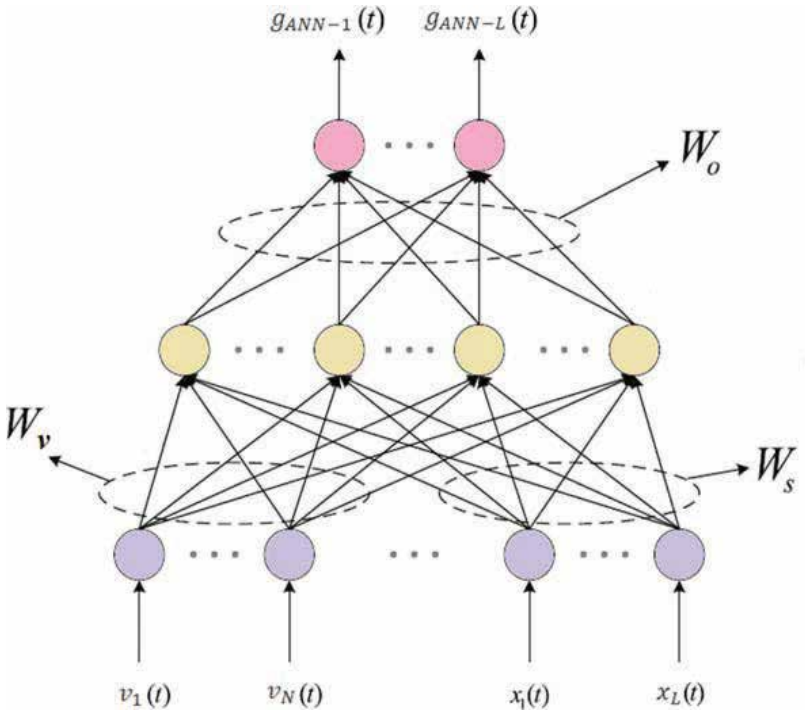

Figure 12. Structure of SSDNN model.

5.1.1. Adjoint state-space dynamic neural network (ASSDNN)

Adjoint state-space dynamic neural network (ASDNN) method, like SSDNN method, is used for modeling the transient behavior of nonlinear electronic and photonic components. It is an extension of SSDNN technique that is capable of adding the derivative information of the output to the training patterns of nonlinear components simultaneously, so that the training process can be done more efficient requiring less data without sacrificing model accuracy and efficiency [23, 24]. It has been shown in Ref. [24] that testing error from the model trained by ASSDNN method is much less than that obtained from SSDNN. Here is the formulation of ASSDNN using notation similar to SSDNN mentioned already, and an overview of structure of ASSDNN is shown in **Figure 13**.

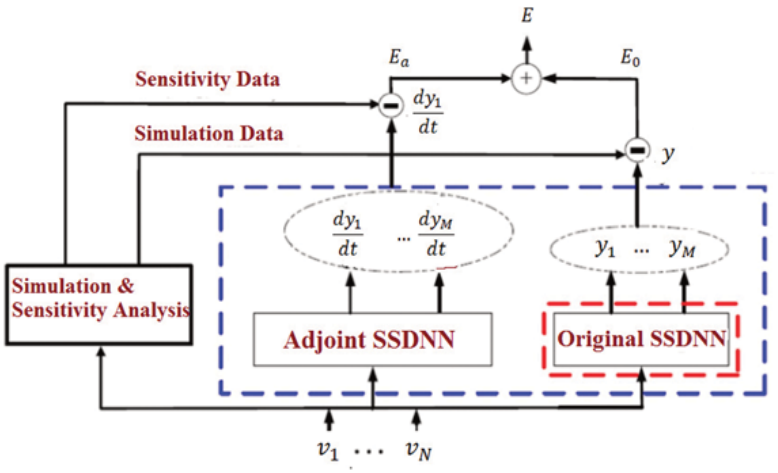

Figure 13. Structure of ASSDNN-based model.

$$\left\{\begin{array}{c} \dot{x}(t) = -x(t) + \eta g_{\text{ANN}}\left(v(t), x(t), w\right) \\ y(t) = Bx(t) \\ \dot{y}(t) = B\dot{x}(t) \end{array}\right\} \tag{14}$$

6. Other methods in microwave modeling

There are other methods which are not based on neural networks for modeling microwave components such as Krylov method [25], finite element [26], mode-matching method [27], vector-fitting method, and so forth [28]. In the preceding section, we present vector-fitting method. This technique has been used in many microwave simulations and modeling researches [29–31].

6.1. Vector-fitting method

Vector fitting (VF) is a robust numerical technique for rational approximation of transfer functions and *s*-parameter in the frequency domain, especially in microwave devices using poles and residues [32]. It allows calculating multiport models directly from measured or computed frequency responses. The resulting approximation has guaranteed stable poles that are real or come in complex conjugate pairs, and the model can be converted directly into a state-space model [13].

Basically, vector fitting is a pole relocation method where the poles are improved in an iterative manner. This is achieved by repeatedly solving a linear problem until convergence is achieved [13]. The VF formulation avoids the ill-conditioning problems encountered with some alternative approaches, as the formulation is given in the form of simple fractions instead of polynomials. Unstable poles are flipped into the left-half plane to enforce stable poles. This makes VF applicable to high-order systems and wide frequency bands [33].

http://dx.doi.org/10.5772/66356

Mathematical representation of vector-fitting method is presented briefly in this section.

Let $\{p_n\}$ be a set of unknown poles, and $\{r_n\}$ be residues, $H(s)$ is the given rational function:

$$H(s) = \left(\sum_{n=1}^{M} \frac{r_n}{s - p_n} \right) \tag{15}$$

in which M is the order of the macromodel. The poles are identified by solving the linear problem shown in Eq. (16) for i^{th} iteration,

$$\sum_{n=1}^{M} \frac{r_n^i}{s - p_n^i} \approx \left(\left(\sum_{n=1}^{M} \frac{\gamma_n^i}{s - p_n^i} \right) + 1 \right) H(s) \tag{16}$$

in which ${r_n}^i$ is r_n for i^{th} iteration, the same is ${p_n}^i$, and ${\gamma_n}^i$ is found in matrix x. In Eq. (6), we call $\left(\left(\sum_{n=1}^{M} \frac{r_n^i}{s - p_n^i} \right) + 1 \right)$ as $\sigma^i(s)$, and $\sum_{n=1}^{M} \frac{r_n^i}{s - p_n^i}$ as $\sigma H^i(s)$ which are unknown rational functions with given poles. By writing Eq. (16) for several frequency points, we have an overdetermined linear problem with a frequency-sampled data point f_t:

$$A_t x = H_t(f_t), \tag{17}$$

in which t = 1, 2, …, N_f, $A_t = \left[\frac{1}{s + p_1^i} \ldots \frac{1}{s + p_n^i} 1 \frac{-H(f_t)}{s + p_1^i} \ldots \frac{-H(f_t)}{s + p_n^i} \right]$, and $x = [r_1^i \ldots r_N^i 0 \gamma_1^i \ldots \gamma_N^i]$ that can become a linear equation problem that is,

$$[A_1^T A_2^T \ldots A_{N_s}^T]^T x = [H_1 H_2 \ldots H_{N_f}]^T \tag{18}$$

It can be proven that the poles of *H(s)* are equal to the zeroes of $\sigma^i(s)$, also the zeroes of $\sigma^i(s)$ can be calculated by solving an eigenvalue problem as shown in Eq. (19) [33]

$$\varphi = \begin{bmatrix} p_1^i & & & & \\ & p_2^i & & & \\ & & p_3^i & & \\ & & & \ddots & \\ & & & & p_N^i \end{bmatrix} - \begin{bmatrix} 1 \\ 1 \\ 1 \\ \vdots \\ 1 \end{bmatrix} \cdot \begin{bmatrix} \gamma_1^i \\ \gamma_2^i \\ \gamma_3^i \\ \vdots \\ \gamma_N^i \end{bmatrix}^T \tag{19}$$

Also for initialization there are different approaches. Basically, initial poles should be complex with weak attenuation and can be obtained by a simple calculation such as Prony method [13] or simply can be spaced within the desired range of frequency, for example, between 50 Hz and 1 MHz [17], and the advantage here is even if the starting poles were selected poorly, the result does not change significantly [32]. By solving Eq. (19), new set of poles are identified. After identifying all the poles, residues are calculated by solving Eq. (16) which is again a linear problem. As a conclusion, VF method samples the given function with an appropriate sample rate, and in this way a summation of partial fractions can be found, that is, the discrete-function approximation of the original transfer function.

7. Related work

This part of the chapter briefly discusses about the application of computer-aided design (CAD) techniques in modeling and simulation of RF and microwave-passive components. Neural network-based modeling approaches have been widely used for modeling variety of RF and microwave-passive components such as coupled-line filters, coplanar waveguides, Vias and multilayer interconnects, and some other passive components.

7.1. General procedure of modeling

Here, we provide a brief review of procedure used in neural network-based modeling of RF and microwave-passive components.

For modeling microwave components in frequency domain [1], first input and output parameters of the components should be selected in a wide range of frequencies. In most ANN models, it is desired to represent the parameters in terms of scattering parameters (*S*-parameters). The next step is data generation. For passive component models, electromagnetic simulation approach is widely used for generating data. EM simulators, which are used in the process of developing ANN models, produce *S*-parameter for the components. After data training, there should be a criterion for deliberation of the accuracy of the model, so error of the model in different formulations is measured. In most EM-ANN models, the absolute average and standard deviation of error is measured for each output.

After training and verification of the EM-ANN model, based on the usage they can be used either in stand-alone mode or in integrated mode along with microwave circuit simulators. In integrated mode, there is a linear model subroutine that connects models to the simulator. This subroutine returns *S*-parameter of a component back for further simulation. When the simulation is running, the simulator passes parameters such as frequency of a component. For computation of *S*-parameter, there is a feed-forward ANN subroutine that receives input variables and also it holds the algorithm for finding the output of the ANN model. Besides, models can be connected to the circuit simulator as a group, where these collections of models are called libraries [34].

7.2. Parametric modeling of a coupled-line filter

In this example, we demonstrate the use of ANN techniques to develop a model for a family of coupled-line filters [35]. Here, S_1 and S_2 are the spacing between lines and D_1, D_2, D_3 are offset distances from the ends of each coupled lines to the corresponding fringes. This model has six inputs that are $x = \{S_1, S_2, D_1, D_2, D_3, \omega\}$ and four outputs as *S*-parameters RS_{11}, IS_{11}, RS_{12}, IS_{12} which are real and imaginary parts of *S*-parameters S_{11} and S_{12}. The testing and training data were obtained from CST microwave studio [36]. **Table 1** shows the final testing and training results after developing the ANN model for coupled-line filter. In the table, 6-40-4 as neural network structure means a neural network with four inputs, 40 hidden neurons, and four outputs that was used to develop the model for this component. As it can be seen from the table, the ANN model matches the desired data obtained from the simulation tool with very good accuracy, which validates the usage of this method for model creation.

Model type	Neural network structure	Average training error (%)	Average testing error (%)
ANN model using 120 sets of training data	6-40-4	0.897	0.989
ANN model using 40 sets of training data	6-35-4	1.073	4.357

Table 1. Final testing and training results of ANN model (from Ref. [35]).

7.3. EM-ANN models for CPW components

The use of coplanar waveguides (CPWs) in RF and microwave-integrated circuits has brought many advantages. Accurate modeling of these components is necessary for accurate simulation of circuits. One of the fields that experts recently have been working on is toward the development of accurate and efficient methods for EM simulation of CPW discontinuities, but the challenge of using these tools for iterative CAD and circuit optimization [37] is the time-consuming nature of EM simulation. To overcome this problem, EM-ANN models have been suggested [38]. The models include CPW transmission line, short- and open-circuit stubs, step-in width discontinuities, and T-junctions. These EM-ANN models are linked to microwave circuit simulators and allow for the accurate and very fast EM circuit optimization in the framework of circuit simulator [1]. A general schematic of a coplanar waveguide is shown in **Figure 14**. In this figure, *W* is the center conductor width, *G* is the spacing between conductor and ground plane, and *L* is the center conductor length.

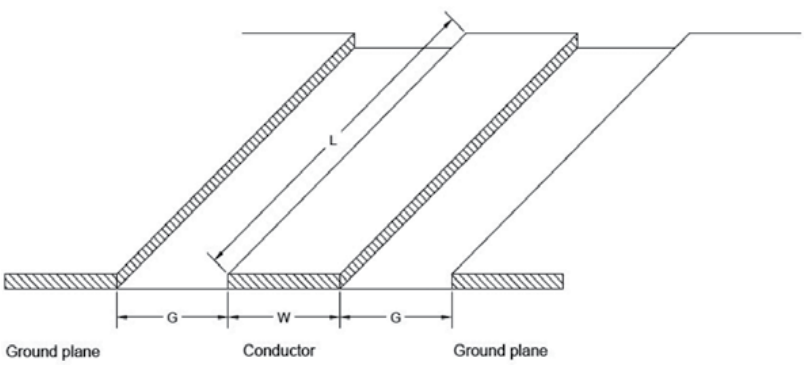

Figure 14. Simple coplanar waveguide.

7.4. Vias elements in microstrip circuits and multilayer Vias connectors

Progress in technology caused merging large number of microwave circuits and creating multilayer complexities that leads to investing much effort on optimizing and lowering the cost and weight of these circuits. Besides, accuracy and efficiency are important factors that should be satisfied in designs to have desirable simulation results. EM-ANN-based methodology despite other solutions that have been suggested was enormously successful in modeling Vias elements in microstrip circuits and multilayer Vias connectors [39]. Some other suggestions had limitations such as heavily computational expenses or limited range of frequency. As

an example, microstrip transmission line model is one of the implemented ANN-based models in this case. In this model, input parameters are frequency which is in the range, $\log\left(\frac{W_I}{H_{\text{sub}}}\right)$ in which W_I is the microstrip width and H_{sub} is the substrate height which varies between -1 and 1, and ε_r relative dielectric constant of the substrate in the range of 2–13. A simple schematic of microstrip transmission line is shown in **Figure 15**.

Output parameter is Z_0 which is the characteristic impedance, and ε_{eff} is the effective dielectric constant. A total of 155 data were used as training, 100 for validation, and 10 hidden neurons to create the model. To test the model, standard deviation and average error criteria were used. Error results for microstrip transmission line are shown in **Table 2**.

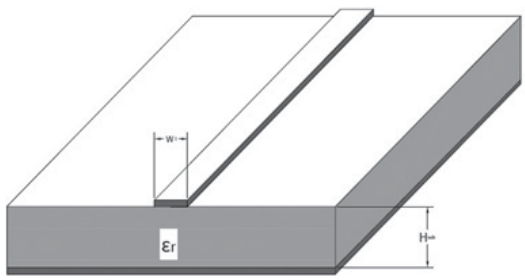

Figure 15. Simple schematic of microstrip transmission line.

	Z_0(%)	τ_{eff}(%)
Training data average error	1.161	0.377
Training data SD	1.157	0.376
Validation data average error	0.774	0.293
Validation data SD	0.875	0.223

Table 2. Average and standard deviation (SD), for absolute error training (from Ref. [1]).

8. Conclusion

In this chapter, a review of some tools commonly used in RF/microwave simulation and modeling has been presented. In the last few decades, high-frequency effects have become an important factor in RF/microwave area. These effects can be found in all levels of design from tiny chips to packaging structures. In order to capture these effects, it is common to use physics-based models or electrical models which lead to large equations and large computational efforts for solving and simulating them, which is extremely time-consuming and expensive. Artificial neural networks recently have become popular among computer-aided design tools. The main topic in this chapter was a discussion on neural network which was mentioned as a powerful tool in modeling and simulation areas, also two main types of neural network structures including static and dynamic neural networks and their different types has been

presented. In static neural network section, we talked about multilayer perceptron (MLP) and radial-basis function (RBF) structure, and in time-domain part we discussed recurrent neural network (RNN), dynamic neural network (DNN), state-space dynamic neural network (SSDNN), and adjoint state-space dynamic neural network (ASSDNN) methods. Other than neural network, as mentioned already, there are several numerical methods that are being used in the procedure of simulation and modeling microwave components such as Krylov method, finite-difference time-domain (FDTD), finite-element time-domain (FEDT), and vector fitting (VF). Here, we presented vector-fitting method that is widely used for modeling microwave and electromagnetic components with good performance. VF despite other system identification methods avoids ill-conditioning calculation, and because of this, it works more efficiently. Also, this method is very robust; it performs well even for high-order fitting and does not disturb by poorly selected starting poles. VF technique is very easy to implement in a computer program, since it is constructed upon matrices from simple fractions, and the problems in this case are easy to solve.

As a conclusion, the ANN-based methodologies and other mentioned methods are capable of applying to RF/microwave modeling and components simulation and are shown to have both speed and accuracy advantage for modeling nonlinear functions, despite many other conventional techniques.

Author details

Sayed Alireza Sadrossadat* and Farnaz Mohammadi

*Address all correspondence to: Alireza.sadr@ece.ut.ac.ir

Department of Electrical and Computer Engineering, University of Tehran, Tehran, Iran

References

[1] Zhang Q. J., Gupta K. C. Neural Networks for RF and Microwave Design. Boston: Artech House; 2000. 369 p.

[2] Zhang Q. J., Gupta K. C., Devabhaktuni V. K. Artificial Neural Networks for RF and Microwave Design – From Theory to Practice. IEEE Trans. Microwave Theory Tech. 2003; 51(4): 1339–1350.

[3] Kabir H., Zhang L., Yu M., Aaen P. H., Wood J., Zhang Q. J. Smart Modeling of Microwave Devices. IEEE Microwave Mag. 2010; 11(3): 105–118.

[4] Burrascano P., Fiori S., Mongiardo M. A Review of Artificial Neural Networks Applications in Microwave Computer-Aided Design. Int. J. RF Microwave CAE. 1999; 9: 158–174.

[5] Steer M. B., Bandler J. W., Snowden C. M. Computer-Aided Design of RF and Microwave Circuits and Systems. IEEE Trans. Microwave Theory Tech. 2002; 50(3): 996–1005.

[6] Gupta K. C. ANN and Knowledge-Based Approaches for Microwave Design. In Directions for the Next Generation of MIMIC Devices and Systems, N. K. Das and H. L. Bertoni, Eds. NY: Plenum. 1996; 389–396.

[7] Engelbrecht A. P. Computational Intelligence: An Introduction. John Wiley & Sons, New York; 2007[23]. 581 p.

[8] Hornik K., Stinchcombe M., White H. Multilayer Feed-Forward Networks Are Universal Approximators. Neural Netw. 1989; 2: 359–366.

[9] Watson P. M., Gupta K. C. EM-ANN Models for Microstrip Vias and Interconnects in Dataset Circuits. IEEE Trans. Microwave Theory Tech. 1996; 44(12): 2495–2503.

[10] Sen P., Woods W. H., Sarkar S., Pratap R. J., Dufrene B. M., Mukhopadhyay R., Lee C., Mina E. F., Laskar J. Neural-Network-Based Parasitic Modeling and Extraction Verification for RF/Millimeter-Wave Integrated Circuit Design. IEEE Trans. Microwave Theory Tech. 2006; 54(6): 2604–2614.

[11] Nihad D., Jehad A., Amjad O. CAD Modeling of Coplanar Waveguide Interdigital Capacitor. Int. J. RF Microwave Computer-Aided Eng. 2005; 15(6): 551–558.

[12] Xu J. J., Yagoub M. C. E., Ding R., Zhang Q. J. Neural-Based Dynamic Modeling of Nonlinear Microwave Circuits. IEEE Trans. Microw. Theory Tech. 2002; 50(12): 2769–2780.

[13] Lei C., Wang Y., Chen Q., Wong N. On Vector Fitting Methods in Signal/Power Integrity Applications. Proc. Int. Multi-Conf. Eng. Comp. Scient. 2010; 2: 1407–1412.

[14] Haykin S., Lippmann R. Neural Networks, a Comprehensive Foundation. International Journal of Neural Systems; 1994. 823 p.

[15] Karlik B., Vehbi O. A. Performance Analysis of Various Activation Functions in Generalized MLP Architectures of Neural Networks. Int. J. Artificial Intellig. Expert Syst. 2011; 1 (4): 111–122.

[16] Dorffner G. Unified Frameworks for MLP and RBFNs: Introducing Conic Section Function Networks. Cybern. Syst. 1994; 25: 511–554.

[17] Gustavsen B. Improving the Pole Relocating Properties of Vector Fitting. IEEE Trans. Power Deliv. 2006; 21(3): 1587–1592.

[18] Sinha N. K., Gupta M. M., Rao D. H. Dynamic Neural Networks: An Overview. Proc. IEEE Int. Conf. Industr. Technol. 2000; 2: 491–496.

[19] Bertsekas D. P., John N. T. Neuro-Dynamic Programming: An Overview. Proc. 34th IEEE Conf. 1995; 1: 560–564.

[20] Narendra K. S., Parthasarthy K. Identification and Control of Dynamical Systems Using Neural Networks. IEEE Trans. Neural Netw. 1990; 1(1): 4–27.

[21] Wu C., Nguyen M., Lima J. On Incorporating Finite Impulse Response Neural Network with Finite Difference Time Domain Method for Simulating Electromagnetic Problems. IEEE AP-S Antennas Propag. Int. Symp. 1996; 3: 1678–1681.

[22] Aweya J., Zhang Q. J., Montuno D. A Direct Adaptive Neural Controller for Flow Control in Computer Networks. IEEE Int. Conf. Neural Netw. (Anchorage, Alaska). 1998; 1: 140–145.

[23] Cao Y., Ding R., Zhang Q. J. State-Space Dynamic Neural Network Technique for High-Speed IC Applications: Modeling and Stability Analysis. IEEE Trans. Microwave Theory Techn. 2006; 54(6): 2398–2409.

[24] Sadrossadat S. A., Gunupudi P., Zhang Q. J. Nonlinear Electronic/Photonic Component Modeling Using Adjoint State-Space Dynamic Neural Network Technique. IEEE Trans. Comp. Packaging Manufact. Technol. 2015; 5(11): 1679–1693.

[25] Chaniotis D., Pai M. A. Model Reduction in Power System Using Krylov Subspace Methods. IEEE Trans. Power Syst. 2005; 20: 888–894.

[26] Singh T. Design and Finite Element Modeling of Series-Shunt Configuration Based RF MEMS Switch for High Isolation Operation in K-Ka Band. J. Comput. Electr. 2015; 14(1): 167–179.

[27] Kordiboroujeni Z., Bornemann J., Sieverding T. Mode-Matching Design of Substrate-Integrated Waveguide Couplers. Asia-Pacific Symp. Electromag. Compatib. Singapore. 2012; 1: 701–704.

[28] Bai Z. Krylov Subspace Techniques for Reduced-Order Modeling of Large-Scale Dynamical Systems. Appl. Numer. Math. 2002; 43(1): 9–44.

[29] Li E. P., Liu E. X., Li L. W., Leong M. S. A Coupled Efficient and Systematic Full-Wave Time-Domain Macromodeling and Circuit Simulation Method for Signal Integrity Analysis of High-Speed Interconnects. IEEE Trans. Adv. Packag. 2004; 27(1): 213–223.

[30] Antonini G. SPICE Equivalent Circuits of Frequency-Domain Responses. IEEE Trans. Electromagn. Compat. 2003; 45(3): 502–512.

[31] Cai Y., Mias C. Faster 3D Finite Element Time Domain-Floquet Absorbing Boundary Condition Modeling Using Recursive Convolution and Vector Fitting. IET Microwaves Antennas Propag. 2009; 3(2): 310–324.

[32] Gustavsen B., Semlyen A. Rational Approximation of Frequency Domain Responses by Vector Fitting. IEEE Trans. Power Deliv. 1999; 14(3): 1052–1061.

[33] Semlyen A., Gustavsen B. Vector Fitting by Pole Relocation for the State Equation Approximation of Nonlinear Transfer Matrices. Circuits Syst. Signal Process. 2000; 19(6): 549–566.

[34] Cao Y., Wang G., Gunupudi P., Zhang Q. J. Parametric Modeling of Microwave Passive Components Using Combined Neural Networks and Transfer Functions in the Time and Frequency. Int. J. RF Microwave Comp. Aid. Eng. 2013; 23: 20–33.

[35] Sadrossadat S. A., Cao Y., Zhang Q. J. Parametric Modeling of Microwave Passive Components Using Sensitivity-Analysis-Based Adjoint Neural-Network Technique. IEEE Trans. Microwave Theory Techn. 2013; 61(5): 1733–1747.

[36] CST Microwave Studio. CST AG, Darmstadt, Germany, 2010 [Online]. Available at: http://www.cst.com.

[37] Doerner R., et al. Modelling of Passive Elements for Coplanar SiGe MMIC's. Microwave Symp. Digest IEEE MTT-S Int. Orlando, FL, USA. 1995; 3: 1187–1190.

[38] Watson P. M., Kuldip C. G. Design and Optimization of CPW Circuits Using EM-ANN Models for CPW Components. IEEE Trans. Microwave Theory Techn. 1997; 45(12): 2515–2523.

[39] Cao Y., Zhang Q. J. Neural Network Techniques for Fast Parametric Modeling of Vias on Multilayered Circuit Packages. IEEE Electr. Design Adv. Pack. Syst. Symp. 2010; 1: 1–4.

Chapter 3

Advanced Filtering Waveguide Components for Microwave Systems

Snežana Stefanovski Pajović, Milka Potrebić and Dejan V. Tošić

Additional information is available at the end of the chapter

http://dx.doi.org/10.5772/66228

Abstract

Microwave filter design is a popular topic in the area of modern microwave engineering. Novel technologies, novel applications and more demanding component miniaturization are some of the key drivers for the development of novel microwave filters. For the systems operating with high power and low losses, waveguide filters represent sustainable solutions, in spite of their size. Herein, a method for the advanced bandpass and bandstop waveguide filter design is presented. Properly designed printed-circuit inserts, with simple resonators, are used as resonating elements inside a standard rectangular waveguide. In this manner, multi-band bandpass or bandstop waveguide filters are developed. Multiple resonant frequencies can be obtained using single insert, with properly positioned resonators. Filter design is exemplified by numerous three-dimensional electromagnetic models of the considered structures, equivalent microwave circuits and fabricated devices. Some of the advantages of the proposed design are simplicity, ease of implementation, possibility of miniaturization and experimental verification. The waveguide filters considered here are designed to operate in the X frequency band, so their application is recognized with the radar and satellite systems. Further improvement of the proposed method is possible, according to the future use of the presented devices.

Keywords: bandpass filter, bandstop filter, multi-band filter, waveguide technology, planar inserts, 3D EM modeling and simulation

1. Introduction

Microwave filters are essential components of every modern communication system operating at microwave frequencies. In general, filters are used to pass the signals at chosen frequencies and to block or weaken the undesired signals. Microwave filter design represents an important topic in the area of modern microwave engineering. The researchers are developing novel microwave filters using various technologies, keeping their focus on the novel applications and more demanding device miniaturization, but also bearing in mind the basic filter requirement —to meet a given specification [1].

This chapter focuses on the waveguide filter design. As high quality-factor devices [2], waveguide filters still represent sustainable solutions for the systems where high power and low losses are required (e.g., satellite systems and radar systems).

Waveguide filters can be implemented in different ways. Various solutions based on the waveguide structure modification, by adding branches, are known for decades and are widely implemented. Furthermore, numerous implementations using substrate integrated waveguide (SIW) technology can be found. Herein, waveguide filters using discontinuities inside the waveguide structure are of interest. These discontinuities can have various shapes and positions [3]. Numerous examples, along with the equivalent circuits and closed-form expressions to calculate the parameters of discontinuities, are given in [4].

In this chapter, waveguide filters using printed-circuit discontinuities are considered. These inserts can be differently positioned inside the waveguide, and some classification can be made accordingly. In the available literature, various solutions can be found for the filters using inserts placed in the E-plane of a rectangular waveguide. Actually, this is a widespread approach, and an example of such design applied to the bandpass filter is presented in [5]. Split-ring resonators (SRRs) are often used as resonating elements for the bandstop filter design. Implementations of bandstop filters using E-plane inserts with SRRs can be found in [6], with a single rejection band, and in [7], with multiple rejection bands. Another approach is based on the use of H-plane inserts. Similarly as for the E-plane insert, various types of resonators can be implemented on the H-plane insert, as well. For the bandpass filters, complementary split-ring resonators (CSRRs) are widely used, as presented in [8, 9], for the filter with a single pass band. Dual-band filter with SRRs is proposed in [10], while compact filter solutions can be found in [11].

The main advantage of the implementations based on the concept of using inserts in the waveguide, compared to the solutions with modified waveguide structure, is simpler design and ease of fabrication.

A method for the advanced bandpass and bandstop waveguide filter design has been developed and reported. It is based on the use of printed-circuit discontinuities, with relatively simple resonators, acting as resonating elements. Multiple resonant frequencies can be obtained using single insert, with properly positioned resonators. The goal is to implement multi-band bandpass or bandstop waveguide filters using printed-circuit inserts, having better characteristics (e.g., bandwidth, return loss, insertion loss and structure size), compared to the

ones published in the available literature. The method considers three-dimensional electromagnetic (3D EM) modeling of the structures, generating equivalent microwave circuits, optimization and device miniaturization. Relatively simple design, ease of implementation and experimental verification are important aspects of the proposed design guidelines.

The waveguide filters considered here are designed to operate in the X frequency band (8.2–12.4 GHz), so they can be used as components of radar and satellite systems of various purposes. Proposed design method allows their further improvement in accordance with their potential future use. We have been investigated various planar structures, as well, which might be suitable for miniaturization, see for example [12–15].

The chapter is organized as follows. Section 2 will briefly cover waveguide fundamentals, while Section 3 will provide basic concepts of microwave filter design. Section 4 will elaborate on the method for the waveguide filter design, explaining 3D EM modeling and simulation, equivalent microwave circuits and experimental verification of the considered waveguide filters. Sections 5 and 6 will introduce bandpass and bandstop waveguide filters using the presented method for an advanced waveguide filter design, respectively. Section 7 will focus on the multi-band filter design. Finally, the obtained results and findings will be outlined in conclusion.

2. Brief review of waveguide fundamentals

Hollow waveguides represent structures for transmission of electromagnetic waves, consisting of a single transmission line [16]. Depending on the shape of their cross-section, they can be classified as rectangular or circular. Actually, rectangular waveguide is the most commonly used waveguide component [17]. Hollow metal waveguide is a shielded structure, so there is practically no electromagnetic coupling with the surrounding devices. In spite of their size at lower frequencies, they still represent sustainable solution for the systems operating with high power (e.g., transmitters and radars) and low losses (e.g., satellite systems). Also, they can be used for the implementation of high quality-factor resonators.

Rectangular waveguide is used for the transmission of transverse electric (TE) and transverse magnetic (TM) waves. **Figure 1** depicts the rectangular waveguide for the wave propagating along the z-axis. We can assume that the conductor is perfect, while the waveguide is filled by the homogeneous and lossless dielectric. The analysis of the wave propagation assumes solving the wave equation, taking into account the boundary conditions on the waveguide walls.

For the TE wave propagation, with axial electric field $E_z = 0$, it is required to solve the wave equation as a function of H_z, $\Delta_t H_z + K^2 H_z = 0$, or in Cartesian coordinates $\left(\partial^2 H_z / \partial x^2\right) + \left(\partial^2 H_z / \partial y^2\right) + K^2 H_z = 0$, where $K^2 = \gamma^2 + k^2$, $\gamma = j\beta$ is propagation coefficient (β is phase coefficient), $k = \omega\sqrt{\varepsilon\mu}$. Scalar function H_z, given in Cartesian coordinates, $H_z(x, y, z) = H_z(x, y, 0)e^{-\gamma z}$, represents the solution of the given wave equation, and each non-

zero field component can be expressed as a function of H_z. By solving the wave equation, the following expression is obtained for H_z: $H_z(x,y,z) = H_0\cos(m\pi x/a)\cos(n\pi y/b)e^{-j\beta z}$, $m = 0,1,2,\ldots$, $n = 0,1,2,\ldots$, where H_0 is a complex constant. Starting from this solution, the other field components of the TE_{mn} mode can be derived [17].

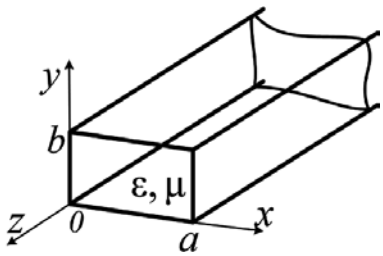

Figure 1. Rectangular waveguide (wave propagation is along *z*-axis).

Similarly, for the TM wave propagation, with axial magnetic field $H_z = 0$, it is required to solve the wave equation as a function of E_z, $\Delta_t E_z + K^2 E_z = 0$, or in Cartesian coordinates $\left(\partial^2 E_z/\partial x^2\right) + \left(\partial^2 E_z/\partial y^2\right) + K^2 E_z = 0$. Scalar function E_z, given in Cartesian coordinates, $E_z(x,y,z) = E_z(x,y,0)e^{-\gamma z}$, represents the solution of the given wave equation, and each non-zero field component can be expressed as a function of E_z. The following expression is obtained for E_z, by solving the wave equation: $E_z(x,y,z) = E_0\sin(m\pi x/a)\sin(n\pi y/b)e^{-j\beta z}$, $m = 1,2,\ldots$, $n = 1,2,\ldots$, where E_0 is complex constant. Starting from this solution, the other field components of the TM_{mn} mode can be obtained, as in [17].

For each TE_{mn} or TM_{mn} mode, the frequency from which that mode starts to propagate, called a cut-off frequency, can be defined as: $f_c = (c/2)\sqrt{(m/a)^2 + (n/b)^2}$ $c = 1/\sqrt{\varepsilon\mu}$.

The wavelength of the guided wave in the waveguide is calculated as: $\lambda_g = \lambda_0/\sqrt{1 - \left(f_c/f\right)^2}$,where λ_0 is the wavelength in the vacuum at frequency *f*. The following equations are used to determine the wave impedance for the TE_{mn} and TM_{mn} mode: $Z_{TE} = \sqrt{\mu/\varepsilon}/\sqrt{1 - \left(f_c/f\right)^2}$, $Z_{TM} = \sqrt{\mu/\varepsilon}\sqrt{1 - \left(f_c/f\right)^2}$.

The dominant mode of propagation is the one with the lowest cut-off frequency. In case $a > b$, the dominant mode is TE_{10}. The propagation of the dominant mode is of interest, and it will be considered throughout the chapter. Its cut-off frequency is $f_{cTE_{10}} = c/2a = 1/(2a\sqrt{\varepsilon\mu})$, and a set of field equations for this mode is: $E_x(x,y,z) = 0$, $E_y(x,y,z) = -j\omega\mu H_0(a/\pi)\sin(\pi x/a)e^{-j\beta z}$, $H_x(x,y,z) = j\beta H_0(a/\pi)\sin(\pi x/a)e^{-j\beta z}$, $H_y(x,y,z) = 0$, $H_z(x,y,z) = H_0\cos(\pi x/a)e^{-j\beta z}$, where $\beta = \sqrt{\omega^2\varepsilon\mu - (m\pi/a)^2 - (n\pi/b)^2}$ denotes the phase coefficient.

http://dx.doi.org/10.5772/66228

Maximum power in the waveguide is limited by the dielectric breakdown, that is, by the critical field in the waveguide. Furthermore, in case the waveguide is not matched to its ports, so there is a reflected wave beside the incident one, the maximum power will be decreased by the value of the reflected power.

For the waveguide filters considered in this chapter, standard WR-90 rectangular waveguide is used. According to **Figure 1**, dimensions of its cross-section are a = 22.86 mm and b = 10.16 mm. The frequency range for this waveguide is 8.2–12.4 GHz. The cut-off frequency for the dominant mode of propagation TE_{10} is 6.56 GHz. Next, higher mode, TE_{20}, starts propagating from 13.12 GHz, which is in accordance with the observed frequency range for this waveguide.

3. Basic concepts of microwave waveguide filter design

This section briefly covers resonators, as building blocks of the filters, and filter design principles, with the focus on the waveguide filters.

3.1. Resonators

The resonators can be characterized as fundamental passive microwave components and basic elements of the frequency selective circuits, such as filters. They are capable to store frequency-dependent electric and magnetic energy [2]. Under ideal circumstances, resonator is electromagnetically isolated part of the space, without losses, so once excited electromagnetic field can be indefinitely retained [16]. However, in real situations, every resonator loses its energy due to various losses (e.g., losses in conductors and dielectric) and the coupling with the surrounding components, which is usually weak. This means that the energy must be continuously added to the resonator, in order to compensate for the losses and maintain the excited field.

The main parameters which qualify a resonator are its resonant frequency and the quality factor (Q-factor). In general, Q-factor reflects the resonator performance [17].

Resonators can be implemented in different ways: for the frequencies up to 1 GHz as *LC* circuits and for the frequency range 1 MHz–10 GHz as transmission line sections, while for the frequency range 1–100 GHz as waveguide resonators.

Planar resonators can be classified as resonators implemented in planar technologies, such as the microstrip technology. Quarter-wave and half-wave planar resonators are widely used for the filter design, either as short-circuited or opened lossless transmission-line section of electrical length $\theta = \pi/2$ or $\theta = \pi$ (at resonant frequency $\omega_0 = 2\pi f_0$), respectively. Besides the short-circuited quarter-wave resonators (QWRs), we have developed various models of the waveguide filters using SRRs (for bandstop filters) and CSRRs (for bandpass filters). Filters using these resonators can have one or more pass bands or rejection bands [18–24].

3.2. Basic filter design principles

Filters can be defined as frequency selective networks, with two or more ports, used to pass signals at chosen frequencies and weaken other signals (mostly by reflecting them) [16]. Depending on their use, they can be implemented in different ways. However, the filter design procedure is pretty much determined; it consists of several steps which can be classified as follows [1, 16, 25]: specification, approximation, synthesis, simulation model, implementation, study of imperfections and optimization.

Specification represents a set of criteria that a filter should meet [1, 16]. Approximation is a mathematical representation of the frequency response, so the filter specification can be met and the filter itself can be implemented. It is usually given as an attenuation, in dB, for the low-pass filter, and based on that, approximations for the other types of filters can be derived. Some of the most commonly used approximations are Butterworth, Chebyshev, elliptic (Cauer), Bessel and Gaussian function.

Synthesis assumes generating the filter schematic, using ideal elements, which fulfills transfer function given by approximation. Filter simulation model is a filter schematic with real components instead of ideal ones. Filter implementation is actually a laboratory prototype—fabricated device; it is used to experimentally validate the filter response by measurements, in order to evaluate the simulation model and modify it, if necessary. Study of imperfections investigates various parasitic effects caused by the use of real components. Optimization assumes systematic variation of the filter parameters, using some numerical method, in order to meet the specification.

The filter transfer function is the ratio of the Laplace transforms of the output signal and the input signal assuming zero initial conditions, and the filter is treated as a linear time-invariant two-port network. The frequency response is the transfer function on the imaginary axis. Microwave filter response is typically represented by scattering parameters (*S*-parameters) [16].

Generic representation of the filter as a two-port network is depicted in **Figure 2a**. At the first port, filter is excited by a real generator, with internal resistance, and the second port is terminated by a resistor.

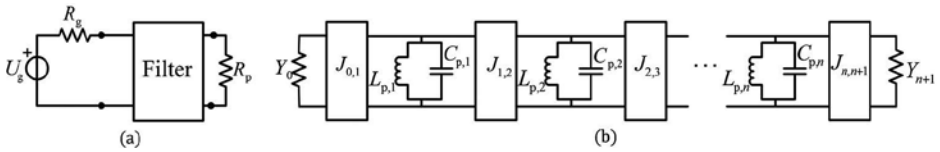

Figure 2. (a) Generic representation of the filter as a two-port network, (b) bandpass filter schematic with parallel *LC* circuits and admittance inverters.

A filter prototype is a ladder *LC* network of the low-pass filter with ideal elements. Starting from the prototype, the parameters of the real filter elements can be obtained, by using frequency and impedance transformations [2, 26, 27]. In this manner, bandpass and bandstop filters, consisting of parallel and series *LC* circuits, can be obtained. Often, it is convenient to

have a network with *LC* circuits only in parallel branches or only in series branches. This can be achieved by adding inverters.

Immittance inverter (a common name for the impedance and admittance inverter) is a two-port, frequency independent, network without losses. Impedance inverter can be used to transform parallel admittance into series impedance, and admittance inverter can be used to transform series impedance into parallel admittance. **Figure 2b** depicts the band-pass filter schematic, with admittance inverters and parallel *LC* circuits. The following equations are used to calculate the characteristic inverter admittance (*J*): $J_{0,1} = \sqrt{Y_0 BC_{p,1}/\Omega_{p,\text{proto}} g_0 g_1}$, $J_{i,i+1} = \left(B/\Omega_{p,\text{proto}}\right)\sqrt{C_{p,i} C_{p,i+1}/g_i g_{i+1}} (i = 1, ..., n-1)$, $J_{n,n+1} = \sqrt{Y_{n+1} BC_{p,n}/\Omega_{p,\text{proto}} g_n g_{n+1}}$, $L_{p,i} = 1/\omega_0^2 C_{p,i}$ $(i = 1, ..., n)$. Parameters g_i are those used for the prototype filter, as well as $\Omega_{p,\text{proto}}$, while B denotes the bandwidth. The values of the elements Y_0, Y_{n+1}, C_i can be arbitrarily adopted, and the filter response will be identical to the prototype response if the parameters $J_{i,i+1}$ are calculated using aforementioned equations.

Immittance inverters can be implemented in different ways. In this chapter, inverters as quarter-wave transmission line sections are of interest. To be more precise, since waveguide filters are considered, inverters are implemented as waveguide sections.

4. Method for advanced waveguide filter design using printed-circuit discontinuities

Advanced waveguide filter design method assumes the development of resonating elements employed as printed-circuit inserts, placed inside a rectangular waveguide [28]. The goal is to obtain one or more resonant frequencies using a single resonating insert, which can be achieved by optimal layout of the resonators on the plate. Desired solution might assume uncoupled resonators, in order to be able to tune each resonator independently for each frequency band. In this manner, multi-band filter can be implemented. Herein, SRRs, CSRRs, QWRs and similar types of simple resonators are used on the printed-circuit inserts as resonating elements.

Waveguide filters can be implemented using H-plane or E-plane inserts. For the higher-order multi-band filters with H-plane inserts, it is necessary to properly implement inverters between the resonators, for each center frequency. For the considered filters, waveguide section of length equal to $\lambda_g/4$ (λ_g – guided wavelength in the waveguide) is used as an inverter. Furthermore, for the higher-order bandpass filter, folded H-plane inserts are used in order to meet requirement regarding quarter-wave inverter implementation for each center frequency. For the compact filter design, miniaturized inverters are considered, by introducing properly designed additional plates between H-plane resonating inserts. The other solution for the waveguide filter design is based on the E-plane insert implementation, with properly coupled resonators on the plate. Along with the waveguide filter design, structures for precise positioning of inserts are developed and used for the measurement of the frequency responses.

Based on the presented filter design method, an algorithm has been developed, that assumes-following steps: making 3D EM models, optimizing resonator and filter parameters, investigating frequency responses, (optionally) generating microwave circuits and, finally, experimental verification by measuring the response of the fabricated prototype. In order to complete these steps, software tools supporting full-wave simulations have been used, as well as the tools for microwave circuit simulations. Experimental verification is performed to validate simulation results and verify the filter design method.

Various bandpass and bandstop waveguide filters have been developed using proposed method [28, 29]. The same standard rectangular waveguide (WR-90) is used for each implementation in the chosen frequency band, since there is no modification of the waveguide structure. The dominant mode of propagation (TE_{10}) is of interest. Filters are designed to operate in the X frequency band (8.2–12.4 GHz).

For precise modeling of the waveguide filters, WIPL-D software (http://www.wipl-d.com) is used, as powerful software capable to perform EM simulations of the complex 3D structures. It allows us to work with a large number of elements (nodes, plates, generators, etc.) and variables. In terms of numerical calculations, the software is based on the method of moments (MoM), and theoretical background is elaborated in detail in [30]. Besides the network parameters (*S*/*Z*/*Y*), it can efficiently calculate near field, far field (radiation) and current distribution.

WIPL-D software provides the possibility of precise geometrical modeling of the structure, meaning it can be completely defined using various elements and parameters available in the software. Virtually, every structure can be modeled in this manner. For example, structures can be modeled as pure metallic, pure dielectric or composite (metallic and dielectric). Every structure primarily consists of nodes, as essential elements, and they are further used to create wires, plates, junctions and generators. As an excitation, an ideal delta-function generator is used. Graphical interface allows us to visually track the modeling procedure.

WIPL-D software provides the possibility to take into account conductor and dielectric losses. The losses due to the surface roughness and the skin effect in conductors are taken into account, so the conductivity of the metal plates, for the X frequency band, is set to $\sigma = 20$ MS/m. Dielectric losses are given as parameters of the domain used to model the considered dielectric.

There are several features in WIPL-D software which can be used to increase the accuracy of the obtained results (edge manipulation) or simplify the modeling procedure (symbols, grids, imaging, symmetry, etc.). All these features are thoroughly explained in the software documentation (http://www.wipl-d.com).

Besides the modeling of the waveguide filter itself, it is important to properly model its excitation, that is, its ports. Each waveguide port (one port on each waveguide end) can be represented as a short-circuited waveguide section with a monopole, fed by an ideal delta-function generator [28]. This section should be long enough so each evanescent mode ceases toward the port end, thus only desired mode propagates in the considered structure. In order to obtain required filter response, that is, to determine its *S*-parameters, de-embedding

technique is applied, so the influence of the ports on the amplitude response is eliminated. This technique is explained in detail at http://www.wipl-d.com.

In order to generate microwave circuits of the considered filters, the following software tools have been used: WIPL-D Microwave Pro (http://www.wipl-d.com) and NI AWR Microwave Office (http://www.awrcorp.com). The equivalent microwave circuits have been generated using lumped elements (for the resonant circuits) and waveguide sections (for the inverters). The goal is to develop an equivalent circuit as simple as possible, starting from the known equivalent circuits of the corresponding elements, thus allowing for a relatively simple filter optimization.

The printed-circuit inserts are fabricated on the machine MITS Electronics FP-21TP (http://www.mitspcb.com). Experimental verification is performed by measuring the frequency characteristics of the fabricated filters using network analyzer Agilent N5227A (http://www.keysight.com), as shown in **Figure 3**.

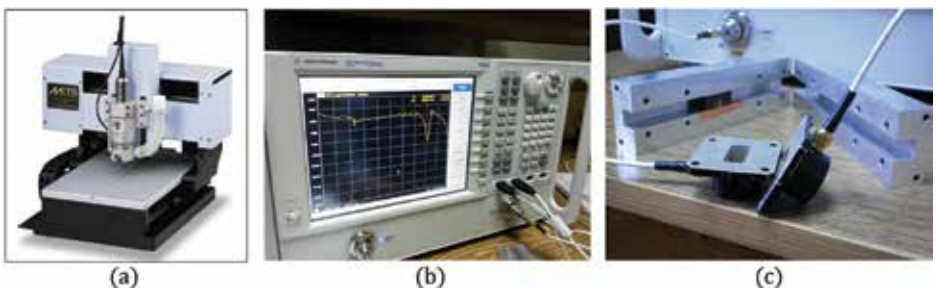

Figure 3. (a) MITS Electronics FP-21TP machine, (b) Agilent N5227A network analyzer, (c) ports used for the measurements.

5. Bandpass filters

Bandpass waveguide filter design is based on the use of CSRRs. Starting from the models given in [9], various types of waveguide resonators and filters have been developed and proposed. The inserts are placed in the H-plane of the standard rectangular waveguide. The 3D EM models and equivalent microwave circuit of the CSRR on the multi-layer planar insert can be found in [31, 32]. Such CSRR can be further upgraded by adding a central section on the inner side, providing for resonant frequency fine-tuning, as proposed in [32].

Third-order bandpass waveguide filter has been developed using aforementioned printed-circuit inserts with CSRRs [31]. For the printed circuits, RT/Duroid 5880 substrate (http://www.rogerscorp.com) is used, and its parameters are relative permittivity $\varepsilon_r = 2.2$, losses $\tan\delta = 0.0009$, substrate thickness $h = 0.8$ mm, metallization thickness $t = 0.018$ mm. The inserts are placed in the transverse planes of the waveguide (**Figure 4a**). Filter is designed to operate at center frequency of 11.95 GHz and 3-dB bandwidth of 500 MHz, so the parameters of the CSRRs

are tuned accordingly. In order to properly design higher-order filter, it is necessary to take into account the inverters between the resonating elements (waveguide sections of length equal to $\lambda_g/4$ at 11.95 GHz). The obtained amplitude response is shown in **Figure 4b**.

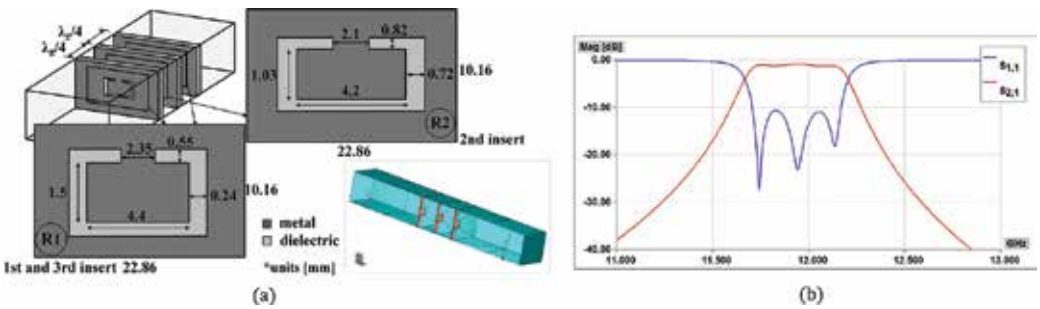

Figure 4. Third-order bandpass filter using CSRRs on the printed-circuit inserts: (a) 3D model, (b) amplitude response.

6. Bandstop filters

Bandstop filters presented here are implemented using SRRs and QWRs on the multilayer planar inserts. Depending on the filter design, the inserts can be placed in the H-plane or E-plane of the rectangular waveguide, as will be elaborated in this section.

The basic model of the waveguide resonator uses printed-circuit insert with dimensions equal to those of the waveguide cross-section (**Figure 5a**, type 1). SRR is used as a resonator. Such model can be found in the available literature [10, 11], and it is also investigated in detail in [33]. Another planar insert with SRR (type 2), introduced in [34, 35], is implemented as a small dielectric plate (it is significantly smaller than the waveguide cross-section), attached to the top and bottom waveguide walls by thin dielectric strips. The waveguide resonator using this type of resonating insert is also shown in **Figure 5a**. In both cases, inserts are designed using RT/Duroid 5880 substrate (its parameters are given in Section 5). Dimensions of the SRR in both cases are optimized to achieve f_0 = 9 GHz. The amplitude responses of the waveguide resonators using previously described inserts are compared in **Figure 5b**. Although resonant frequencies are slightly moved apart, it is notable that the return loss beyond the stop band has lower values for the type 2 insert. Therefore, better matching in the pass band can be obtained using smaller planar insert. This is an important result for the higher-order filter design.

For this model of the resonator, the equivalent circuit is proposed (**Figure 5c**). The parameters of the *RLC* circuit are calculated using following equations [28]: $R = \left(2\left|S_{11}\left(j\omega_0\right)\right|Z_0\right)/\left(1-\left|S_{11}\left(j\omega_0\right)\right|\right)$, $L = \left(2B_{3dB}Z_0\left|S_{11}\left(j\omega_0\right)\right|\right)/\omega_0^2$, $C = 1/\left(2B_{3dB}Z_0\left|S_{11}\left(j\omega_0\right)\right|\right)$, where R represents resistance, L inductance, C capacitance, ω_0 is the resonant frequency in [rad/s], $|S_{11}(j\omega_0)|$ is the amplitude characteristic of S_{11} at resonant frequency, B_{3dB} is a 3-dB

http://dx.doi.org/10.5772/66228

bandwidth, Z_0 represents the nominal impedance and it is calculated according to equations given in Section 2.

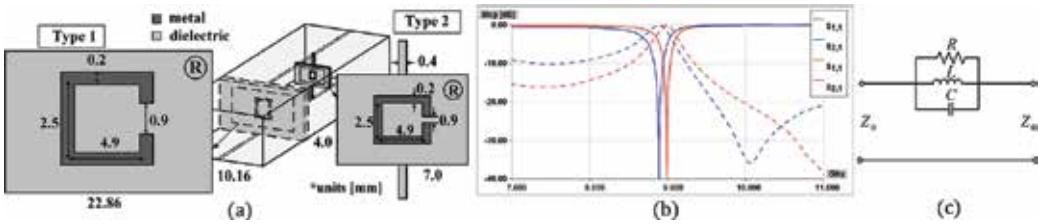

Figure 5. Waveguide resonator using printed-circuit insert with SRR: (a) type 1 and 2, (b) comparison of amplitude responses: blue—type 1 insert, red—type 2 insert, (c) equivalent circuit.

Besides SRRs, properly designed QWRs can be also used for the bandstop filter design. They are short-circuited to top or bottom waveguide wall, depending on the implementation. The insert with the QWRs can be placed in the H-plane [36] or E-plane [37] of the rectangular waveguide.

6.1. Third-order H-plane bandstop filter using printed-circuit insert with SRR

The third-order bandstop filter using aforementioned type 2 planar inserts is shown in **Figure 6a**. Small dielectric plates are centrally positioned in the waveguide. The filter is designed for the center frequency of 9 GHz and the 3-dB bandwidth of 320 MHz, so dimensions of the SRRs are optimized accordingly. The obtained amplitude response is given in **Figure 6b**.

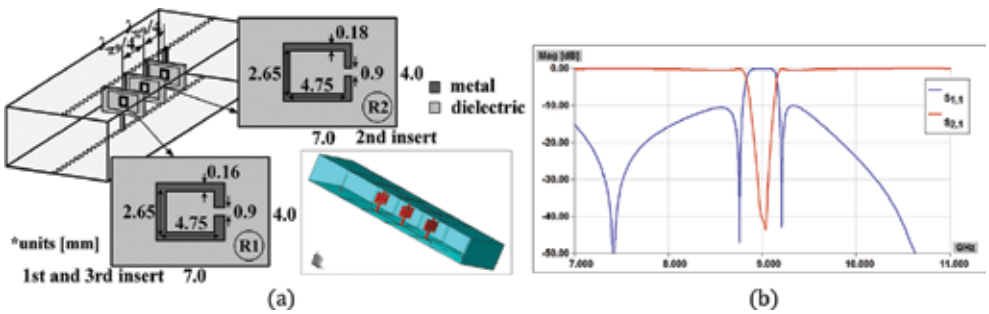

Figure 6. Third-order bandstop filter using printed-circuit insert with SRR (type 2): (a) 3D model, (b) amplitude response.

6.2. E-plane bandstop waveguide filter using QWRs

Herein, second-order bandstop filter using E-plane insert with QWRs is considered. Filter specification requires the center frequency of 10 GHz and 3-dB bandwidth of 680 MHz. Two QWRs, with identical dimensions, are used to achieve this, and they are positioned on the

insert as shown in **Figure 7a**. For the planar insert, copper clad PTFE/woven glass laminate (TLX-8) (http://www.taconic-add.com) is used as a substrate, and its parameters are $\varepsilon_r = 2.55$, $\tan\delta = 0.0019$, $h = 1.143$ mm, $t = 0.018$ mm.

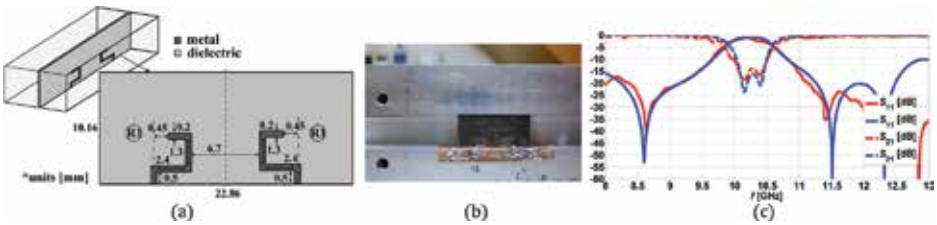

Figure 7. Bandstop filter using E-plane insert with QWRs: (a) 3D model, (b) fabricated insert, (c) comparison of amplitude responses: blue—simulation results, red—measurement results.

The amplitude response is analyzed for various values of the distance between the QWRs. It has been shown that this variation primarily influences the bandwidth; to be more precise, by increasing the distance, the bandwidth becomes narrower.

For the considered filter model, the coupling between two QWRs is investigated in terms of their mutual distance, as proposed in [26, 38]. By increasing the distance, the coupling gets weaker. Based on the obtained results for the 3-dB bandwidth and the coupling coefficient k, it can be concluded that these results are in accordance with the statements in the available literature [26], that is, B_{3dB} and k change in the same manner.

In order to validate the proposed design, the planar insert for the filter containing QWRs is fabricated (**Figure 7b**), and the obtained response is experimentally verified using the WR-90 waveguide. **Figure 7c** shows comparison of the simulation and measurement results, and their good matching confirms filter design.

Proposed filter can be further upgraded to achieve bandwidth fine-tuning, by adding a coupling element, realized as a SRR and positioned between the QWRs on the insert (**Figure 8a**). The positions of the QWRs and their mutual distance are the same as in the original model without coupling element. The amplitude response is shown in **Figure 8b**. The obtained results show that, by adding the coupling element between the QWRs, the bandwidth becomes narrower for 50 MHz (which is nearly 7.37% compared to the reference value of 678 MHz for the second-order filter).

In order to investigate the possibility for bandwidth fine-tuning, using the coupling element, its printed line width is varied, while the distance between the QWRs remains the same. In this case, the center frequency practically does not change, while the bandwidth is slightly changed. This is in accordance with the purpose of the coupling element to fine-tune the bandwidth, without modifying the filter response.

Similarly as for the filter with two QWRs, the coupling between the resonators is also analyzed for this case, for the chosen distance between the resonators and different values of the printed line width of the coupling element. The obtained results and conclusions regarding the

http://dx.doi.org/10.5772/66228

proposed filter design can be summarized as follows. By adding the coupling element between the QWRs: (1) the bandwidth is decreased, (2) the coupling is weakened, (3) the bandwidth can be tuned (decreased) without increasing the distance between the QWRs, thus providing for the device miniaturization.

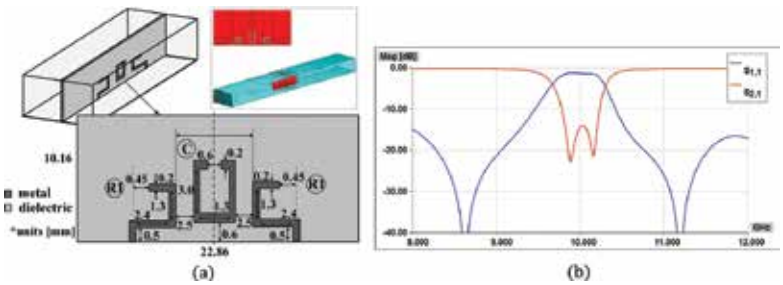

Figure 8. Waveguide filter using E-plane insert with QWRs and coupling element: (a) 3D model, (b) amplitude response.

7. Multi-band waveguide filter design

Multi-band filter design represents a significant research field, particularly for the modern communication systems. One of the advantages of the presented method for the waveguide filter design is that it can be used to relatively easy develop multi-band bandpass or bandstop filters. Namely, multiple resonant frequencies can be obtained using single insert with properly designed and positioned resonators. It is recommended to have uncoupled resonators on the insert, since in that case, each frequency band can be independently controlled by tuning only particular resonator [28]. Waveguide resonator with multiple resonant frequencies can be obtained in this manner. It can be designed using H-plane insert with multiple CSRRs or similar resonating elements for the bandpass characteristic, as in [32, 39–41], or with SRRs for the bandstop characteristic, as in [33, 34]. H-plane insert with QWRs, providing multiple resonant frequencies and having bandstop characteristic, is introduced in [36]. Herein, compact dual-band bandpass filter with CSRRs and dual-band bandstop filter are elaborated in detail. They both use H-plane inserts.

7.1. Compact dual-band bandpass filter with H-plane inserts

Design starts from the resonating insert with two CSRRs in order to obtain two resonant frequencies, 9 GHz and 11 GHz. Flat metal insert with two CSRRs can be placed in the H-plane of the rectangular waveguide, as explained in [40, 41].

Since it is necessary to properly implement inverters for each center frequency, for higher-order filters, folded insert is introduced as a suitable solution [40, 41]. The second-order filter using two identical folded metal inserts is shown in **Figure 9**. Dimensions of the CSRRs are the same for both inserts and optimized to obtain f_{01} = 9 GHz, $B_{3dB\text{-}1}$ = 450 MHz, f_{02} = 11 GHz, $B_{3dB\text{-}2}$ = 650

MHz. The length of the plate connecting parts of the folded insert with CSRRs is $l_{pl} = (\lambda_{g9GHz} - \lambda_{g11GHz})/8$. In this manner, quarter-wave inverters are implemented for both center frequencies, as shown in **Figure 9a**.

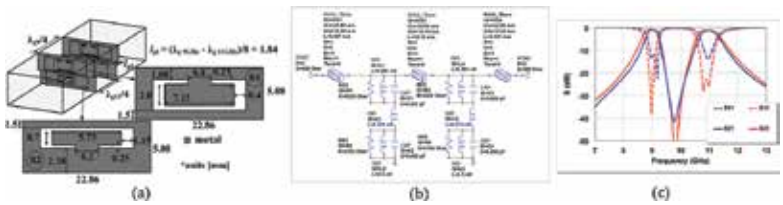

Figure 9. Second-order bandpass filter using folded metal inserts with CSRRs: (a) 3D model, (b) equivalent microwave circuit, (c) comparison of amplitude responses for the 3D EM model (blue) and equivalent circuit (red).

The equivalent microwave circuit is generated for the proposed second-order filter (**Figure 9b**). Two separate networks are used for each insert, and the waveguide section is added between them as a quarter-wave inverter. The short plate providing the fold is represented by an inductor. The following equations are derived [28] and used to calculate the parameters of the *RLC* circuits: $R = \left(Z_0\left|S_{21}\left(j\omega_0\right)\right|\right)/\left(2\left(1-\left|S_{21}\left(j\omega_0\right)\right|\right)\right)$, $L = \left(B_{3dB}Z_0\left|S_{21}\left(j\omega_0\right)\right|\right)/\left(2\omega_0^2\right)$, $C = 2/\left(B_{3dB}Z_0\left|S_{21}\left(j\omega_0\right)\right|\right)$, where R represents resistance, L inductance, C capacitance, ω_0 is the resonant frequency in [rad/s], $|S_{21}(j\omega_0)|$ is the amplitude characteristic of S_{21} at resonant frequency, B_{3dB} is a 3-dB bandwidth, Z_0 represents the nominal impedance and it is calculated according to equations given in Section 2. The inductances of the additional inductors between *RLC* circuits, for each insert, are tuned. The port impedance is set to Z_0 = 500 Ω, which is the wave impedance at 10 GHz (the frequency between the targeted ones, 9 GHz and 11 GHz). The amplitude responses obtained for the 3D EM model and circuit are compared in **Figure 9c**, and their good mutual agreement validates proposed equivalent representation.

The next step is to develop compact solution, based on the use of miniaturized inverters. Precisely, quarter-wave inverter between the resonating inserts, for each center frequency, is replaced by a shorter waveguide section and additional, properly designed, metal insert. In this manner, the length of the device decreases, by shortening the inverters, without degrading filter response. The realization details, including 3D EM models and the equivalent microwave circuit, of the filter with inverters of length equal to $\lambda_g/8$ for each center frequency, can be found in [40, 41]. The inverters are halved compared to the original model, and additional metal plate for miniaturization (with properly designed slots) is centrally positioned between the resonating inserts, to preserve the original filter response.

In order to simplify fabrication and experimental verification, presented filter can be further modified. Therefore, a compact filter with flat inserts is proposed. This means that the inserts with CSRRs, as well as the additional insert for miniaturization, are flat. However, the inverters for both center frequencies are not miniaturized in the same manner. The distance between the CSRRs with f_{01} = 9 GHz is set to $\lambda_{g9GHz}/8$, while the normalized length of the inverter between

http://dx.doi.org/10.5772/66228

the CSRRs with f_{02} = 11 GHz is equal to $0.18\lambda_{g11GHz}$ (**Figure 10a**). Dimensions of the slots on the additional metal insert are tuned to preserve the original filter response, without miniaturization. Comparison of amplitude responses of the second-order dual-band filter before and after applying inverter miniaturization, with the same and different normalized lengths of the inverters, is shown in **Figure 10b**. Since the obtained results match well, compact filter with flat inserts is confirmed as a solution more suitable for experimental verification.

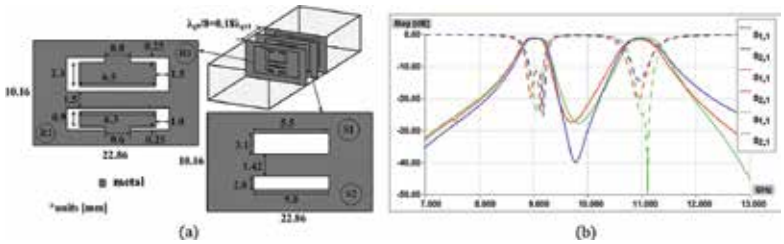

Figure 10. (a) Compact bandpass filter with unequal inverter miniaturization, (b) comparison of amplitude responses of the filter without inverter miniaturization (blue), with equal (red) and unequal (green) inverter miniaturization.

In order to confirm the proposed compact filter solution, the amplitude response of the second-order dual-band filter with flat metal inserts and unequal inverter miniaturization is experimentally verified. Resonating inserts and additional plate for miniaturization are fabricated using metal foil of thickness 100 μm. However, it is necessary to have stable inserts inside the waveguide to successfully measure the amplitude characteristics. Therefore, we propose fixtures for supporting metal inserts. They are fabricated using FR-4 epoxy substrate (ε_r = 4.5, h = 1.0 mm, tanδ = 0.02). Structures for precise positioning of inserts are depicted in **Figure 11a**, and the detailed description of their design can be found in [41]. The photographs of the fabricated inserts and the structures for precise positioning are given in **Figure 11b**. Comparison of the simulated and measured amplitude responses is shown in **Figure 11c**, confirming the compact filter solution by a good agreement of the obtained results.

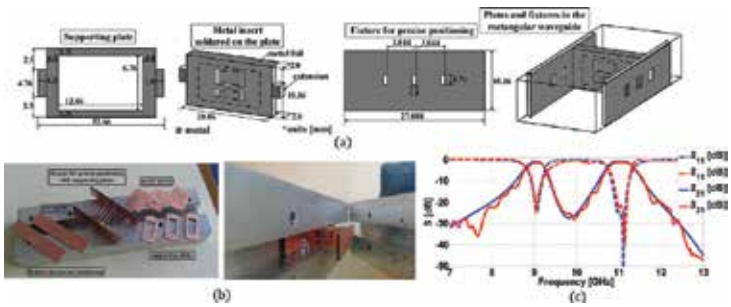

Figure 11. Experimental verification: (a) structures for precise positioning of inserts, (b) photographs of the fabricated components, (c) comparison of simulated (blue) and measured (red) amplitude responses for the compact filter.

7.2. Third-order dual-band bandstop filter using planar insert with SRR

Herein, third-order bandstop filters using printed-circuit inserts with SRRs, introduced in Section 6, are considered. In this manner, the use of such inserts for the higher-order multi-band filters is exemplified. First, third-order bandstop filters with f_0 = 9 GHz and f_0 = 11 GHz, each having a single rejection band, are designed. Based on that, by combining elements of these single-band filters, third-order dual-band filter is designed with f_{01} = 9 GHz and f_{02} = 11 GHz, and each rejection band has the same 3-dB bandwidth of 335 MHz [35].

For the bandstop filter, it is convenient to have *LC* circuits, representing resonators, connected in series; thus, the inverters are used and the parameters of the resonators are determined as explained in [26]. Microwave circuit of this filter is shown in **Figure 12a**.

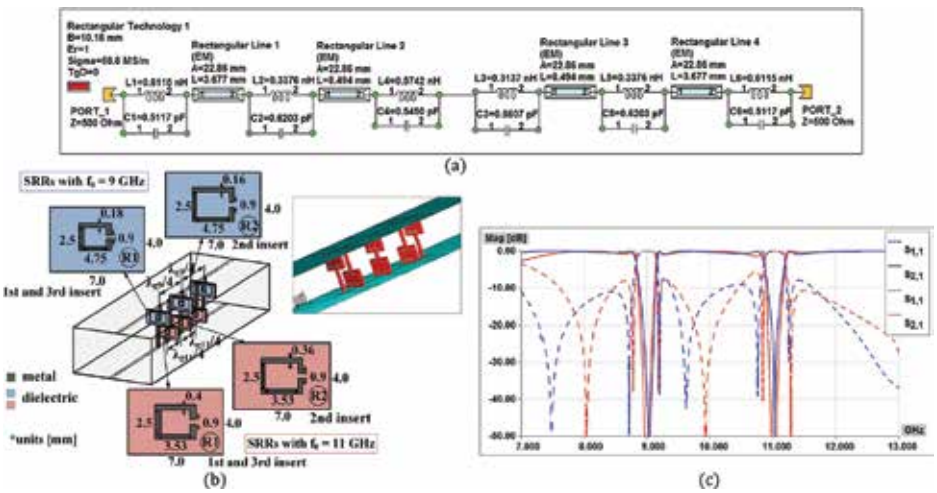

Figure 12. Third-order dual-band bandstop filter: (a) microwave circuit, (b) 3D model, (c) comparison of amplitude responses (blue—3D EM model, red—microwave circuit).

The 3D model of the filter is shown in **Figure 12b**. The inserts are optimally positioned so the inverters can be properly realized between the corresponding resonators, as explained in details in [35]. Comparison of the amplitude responses of the microwave circuit and 3D EM model is given in **Figure 12c**, showing good matching of the obtained results and confirming the proposed filter design.

The experimental measurements for the filter using the presented inserts cannot be easily performed without finding a way to have stable inserts in the waveguide. Therefore, a structure for precise positioning, in a form of ladder fixtures, is introduced in [42]. Since we use dielectric inserts, the fixtures are also designed using dielectric substrate although they can be made as multi-layer planar structures. These fixtures are attached to the top and bottom waveguide walls, and the inserts are attached to them. As shown in [42], the use of the fixtures does not degrade the filter response, so they can be used for precise positioning of inserts in the measurement procedure.

http://dx.doi.org/10.5772/66228

8. Conclusion

Starting from the microwave filter design principles, a method for the advanced waveguide filter design has been developed. It is based on the use of printed-circuit discontinuities as resonating elements. Relatively simple resonators, such as SRRs, CSRRs and QWRs, have been used for the printed-circuit insert design. In spite of their simple forms, these types of resonators provide a lot of possibilities to tune the amplitude response. Since multiple resonant frequencies can be obtained using single insert, these inserts can be employed for the multiband filter design. Therefore, various implementations of novel waveguide filters have been made using H-plane or E-plane inserts. For bandpass filters, metal or multilayer planar inserts with CSRRs have been used. Also, a compact filter solution has been proposed. Furthermore, bandstop filters have been designed using planar inserts with SRRs and QWRs. Besides 3D EM simulations and microwave circuits of the considered filters, prototypes have been fabricated so the amplitude responses can be measured. Also, structures for precise positioning of inserts, for bandpass and bandstop filters, have been designed and fabricated, since they are necessary to smoothly perform the measurements on the laboratory prototypes. The obtained experimental results have shown good agreement with the simulated ones, thus confirming the application of the proposed method for the advanced waveguide filter design.

Although considered waveguide filters are designed for radar and satellite systems, it is expected that the same design guidelines can be applied to the filters operating in other frequency bands by using the proper waveguide and scaling dimensions of the resonating components. Also, it can be further upgraded to keep up with the continuous technological development (e.g., tunable filter design). The most important advantage of the proposed method is a relatively simple design and implementation of structures which can be used in modern communication systems.

Acknowledgements

This work was supported by the Ministry of Education, Science and Technological Development of the Republic of Serbia under Grant TR32005.

Author details

Snežana Stefanovski Pajović*, Milka Potrebić* and Dejan V. Tošić

*Address all correspondence to: stefanovskisnezana@gmail.com and milka_potrebic@etf.rs

School of Electrical Engineering, University of Belgrade, Belgrade, Serbia

References

[1] Lutovac MD, Tošić DV, Evans BV. Filter Design for Signal Processing using MATLAB and Mathematica. Upper Saddle River, NJ: Prentice Hall; 2001 (Translated in Chinese. Beijing, P. R. China: Publishing House of Electronics Industry, PHEI; 2004).

[2] Cameron RJ, Kudsia CM, Mansour RR. Microwave Filters for Communication Systems: Fundamentals, Design, and Applications. New Jersey: John Wiley & Sons; 2007.

[3] Hunter I. Theory and Design of Microwave Filters. London: The Institution of Engineering and Technology; 2006.

[4] Marcuvitz N. Waveguide Handbook. Stevenage, UK: Peter Peregrinus Ltd., on behalf of the Institution of Electrical Engineers; 1986.

[5] Budimir D, Glubokov O, Potrebic M. Waveguide filters using T-shaped resonators. Electronics Letters. 2011;27(1):38–40. doi:10.1049/el.2010.2958

[6] Jitha B, Nimisha CS, Aanandan CK, Mohanan P, Vasudevan K. SRR loaded waveguide band rejection filter with adjustable bandwidth. Microwave and Optical Technology Letters. 2006;48(7):1427–1429. doi:10.1002/mop.21641

[7] Kehn MNM, Quevedo-Teruel O, Rajo-Iglesias E. Split-ring resonator loaded waveguides with multiple stopbands. Electronics Letters. 2008;44(12):714–716. doi: 10.1049/el:20081108

[8] Ortiz N, Baena JD, Beruete M, Falcone F, Laso MAG, Lopetegi T, Marques R, Martin F, Garcia-Garcia J, Sorolla M. Complementary split-ring resonator for compact waveguide filter design. Microwave and Optical Technology Letters. 2005;46(1):88–92. doi: 10.1002/mop.20909

[9] Bahrami H, Hakkak M, Pirhadi A. Analysis and design of highly compact bandpass waveguide filter utilizing complementary split ring resonators (CSRR). Progress in Electromagnetics Research. 2008;80:107–122. doi:10.2528/PIER07111203

[10] Fallahzadeh S, Bahrami H, Tayarani M. A novel dual-band bandstop waveguide filter using split ring resonators. Progress in Electromagnetics Research. 2009;12:133–139. doi:10.2528/PIERL09103103

[11] Fallahzadeh S, Bahrami H, Tayarani M. Very compact bandstop waveguide filters using split-ring resonators and perturbed quarter-wave transformers. Electromagnetics. 2010;30:482–490. doi:10.1080/02726343.2010.483942

[12] Miljanović D, Potrebić M, Tošić DV. Design of microwave multibandpass filters with quasilumped resonators. Mathematical Problems in Engineering. 2015;2015(Article ID 647302):1–14. doi:10.1155/2015/647302

[13] Miljanović D, Potrebić M, Tošić DV, Stamenković Z. Design of miniaturized bandpass filters using quasi-lumped multilayer resonators. Journal of Circuits, Systems and Computers. 2014;23(6):1450083. doi:10.1142/S0218126614500832

[14] Potrebić M, Tošić DV. A novel design of a compact multilayer resonator using double-sided microstrip. Optoelectronics and Advanced Materials-Rapid Communications. 2012;6(3–4):441–445. [online] http://oam-rc.inoe.ro/index.php?option= magazine&op=view&idu=1851&catid=71

[15] Potrebić M, Tošić DV. Selective bandpass filter with concentrated impulse response. Microwave and Optical Technology Letters. 2008;50(11):2772–2777. doi:10.1002/mop.23785

[16] Pozar DM. Microwave Engineering. New York: John Wiley; 2012.

[17] Collin RE. Foundations for Microwave Engineering. New York: McGraw-Hill; 1992 (Reprinted by John Wiley—IEEE Press; 2001).

[18] Bonache J, Martin F, Falcone F, Baena JD, Lopetegi T, Garcia-Garcia J, Laso MAG, Gil I, Marcotegui A, Marques R, Sorolla M. Application of complementary split-ring resonators to the design of compact narrow band-pass structures in microstrip technology. Microwave and Optical Technology Letters. 2005;46(5):508–512. doi: 10.1002/mop.21031

[19] Baena JD, Bonache J, Martin F, Marques Sillero R, Falcone F, Lopetegi T, Laso MAG, Garcia-Garcia J, Gil I, Portillo MF, Sorolla M. Equivalent-circuit models for split-ring resonators and complementary split-ring resonators coupled to planar transmission lines. IEEE Transactions on Microwave Theory and Techniques. 2005;53(4):1451–1461. doi:10.1109/TMTT.2005.845211

[20] Bonache J, Gil I, Garcia-Garcia J, Martin F. Complementary split rings resonators (CSRRs): towards the miniaturization of microwave device design. Journal of Computational Electronics. 2006;5(2–3):193–197. doi:10.1007/s10825-006-8843-0

[21] Kim SI, Jang MY, Kee CS, Park I, Lim H. Characteristics of microwave filters based on microstrip photonic bandgap ring structures. Current Applied Physics. 2005;5(6):619–624. doi:10.1016/j.cap.2004.08.008

[22] Fan JW, Liang CH, Dai XW. Design of cross-coupled dual-band filter with equal-length split-ring resonators. Progress in Electromagnetics Research. 2007;75:285–293. doi: 10.2528/PIER07060904

[23] Li D, Xie YJ, Wang P, Yang R. Applications of split-ring resonances on multi-band frequency selective surfaces. Journal of Electromagnetic Waves and Applications. 2007;21(11):1551–1563. doi:10.1163/156939307782000271

[24] Wu GL, Mu W, Dai XW, Jiao YC. Design of novel dual-band bandpass filter with microstrip meander-loop resonator and CSRR DGS. Progress in Electromagnetics Research. 2008;78:17–24. doi:10.2528/PIER07090301

[25] Matthaei GL, Young L, Jones EMT. Microwave Filters, Impedance Matching Networks, and Coupling Structures. New York: McGraw-Hill; 1964 (Reprinted by Norwood, MA: Artech House; 1980).

[26] Hong JS. Microstrip Filters for RF/Microwave Applications. New Jersey: John Wiley & Sons; 2011.

[27] Jarry P, Beneat J. Advanced Design Techniques and Realizations of Microwave and RF Filters. New Jersey: John Wiley & Sons; 2008.

[28] Stefanovski SLJ. Microwave waveguide filters using printed-circuit discontinuities [Ph.D. dissertation, advisor: prof. dr Milka Potrebić]. Belgrade: School of Electrical Engineering, University of Belgrade; 2015.

[29] Stefanovski Pajović S, Potrebić M, Tošić D. Microwave bandpass and bandstop waveguide filters using printed-circuit discontinuities. In: Proceedings of the 23rd Telecommunications Forum (TELFOR 2015); N/A, 24–26 November 2015; Belgrade, Serbia. pp.520–527.

[30] Kolundžija BM, Djordjević AR. Electromagnetic Modeling of Composite Metallic and Dielectric Structures. Norwood, MA: Artech House; 2002.

[31] Potrebić MM, Tošić DV, Cvetković ZŽ, Radosavljević N. WIPL-D modeling and results for waveguide filters with printed-circuit inserts. In: Proceedings of the 28th International Conference on Microelectronics N/A, (MIEL 2012); 13–16 May 2012; Niš, Serbia. pp. 309–312.

[32] Stefanovski S, Potrebić M, Tošić D. Design and analysis of bandpass waveguide filters using novel complementary split ring resonators. In: Proceedings of the 11th International Conference on Telecommunications in Modern Satellite, Cable and Broadcasting Services (TELSIKS 2013); N/A, 16–19 October 2013; Niš, Serbia. pp. 257–260.

[33] Stefanovski S, Potrebić M, Tošić D, Cvetković Z. Design and analysis of bandstop waveguide filters using split ring resonators. In: Proceedings of the 11th International Conference on Applied Electromagnetics (PES 2013); N/A, 1–4 September 2013; Niš, Serbia. pp.135–136.

[34] Stefanovski S, Potrebić M, Tošić D. Novel realization of bandstop waveguide filters. Technics. N/A., 2013; pp.69–76 (special edition). [online] http://www.sits.org.rs/include/data/ docs0485.pdf

[35] Stefanovski S, Potrebić M, Tošić D. A novel design of dual-band bandstop waveguide filter using split ring resonators. Journal of Optoelectronics and Advanced Materials. 2014;16(3–4):486–493. [online] http://joam.inoe.ro/index.php?option=magazine&op=view&idu=3461&catid=83.

[36] Stefanovski S, Potrebić M, Tošić D, Cvetković Z. Bandstop waveguide filters with two or three rejection bands. In: Proceedings of the 29th Conference on Microelectronics (MIEL 2014); N/A, 12–15 May 2014; Belgrade, Serbia. pp. 435–438.

[37] Stefanovski S, Potrebić M, Tošić D. A novel design of E-plane bandstop waveguide filter using quarter-wave resonators. Optoelectronics and Advanced Materials—Rapid

Communications. 2015;9(1–2):87–93. [online] http://oam-rc.inoe.ro/index.php? option=magazine&op=view&idu=2487&catid=88

[38] Villarroya RL. E-plane Parallel Coupled Resonators for Waveguide Bandpass Filter Applications [Ph.D. dissertation]. Edinburgh, Scotland, UK: Heriot-Watt University; 2012.

[39] Stefanovski S, Mirković Đ, Potrebić M, Tošić D. Novel design of H-plane bandpass waveguide filters using complementary split ring resonators. In: Proceedings of Progress in Electromagnetics Research Symposium (PIERS 2014); N/A, 25–28 August 2014; Guangzhou, China. pp. 1963–1968.

[40] Stefanovski S, Potrebić M, Tošić D, Stamenković Z. A novel compact dual-band bandpass waveguide filter. In: Proceedings of IEEE 18th International Symposium on Design and Diagnostics of Electronic Circuits and Systems (DDECS 2015); N/A, April 22–24 2015; Belgrade, Serbia, p. 51–56.

[41] Stefanovski S, Potrebić M, Tošić D, Stamenković Z. Compact dual-band bandpass waveguide filter with H-plane inserts. Journal of Circuits, Systems, and Computers. 2016;25(3):1640015 (18 pages). doi:10.1142/S0218126616400156

[42] Stefanovski S, Potrebić M, Tošić D. Structure for precise positioning of inserts in waveguide filters. In: Proceedings of the 21st Telecommunications Forum (TELFOR 2013); N/A, 26–28 November 2013; Belgrade, Serbia, pp. 689–692.

Chapter 4

Manifold Multiplexer

Imran Mohsin

Additional information is available at the end of the chapter

http://dx.doi.org/10.5772/66407

Abstract

In wireless communications, bandwidth is a valuable resource that can be smartly shared by multiple users simultaneously utilizing multiplexers. This chapter offers a short review and brief impression of the working principle and the design methodology of the multiplexers in RF and microwave systems. Predominantly used different multiplexer design patterns are discussed here, however the compact manifold multiplexer is discussed in details with an example. It is designed by using advanced design system (ADS) software and implemented utilizing Microstrip technology for its low cost and simplicity.

Keywords: manifold multiplexer, diplexer, microwave filters, advanced design system, microstrip technology

1. Introduction

The idea of multiplexing has been used in different areas. In telegraph systems, it was used for the first time in 1870s, after few decades it was employed in telephony [1]. Multiplexing is a useful process applied in different wireless communication systems where signals from different users (channels) can be multiplexed or demultiplexed by utilizing the multiplexers in order to use the primary recourse (frequency spectrum) intelligently and to increase the speed of the data transmission. **Figure 1** shows the basic block diagram of the transmitter-receiver pair in the wireless communication system. It consists of antenna, RF front-end and baseband system. Usually, the RF front-end is the set of circuit component after antenna which down converts the RF frequency into the intermediate frequency for further processing in the baseband [2]. The well-known components in the front-end are low noise amplifier (LNA), band pass filter (BPF), power amplifier (PA), local oscillator (LO) and mixers. Microwave multiplexers can also be found in front-end [3–5].

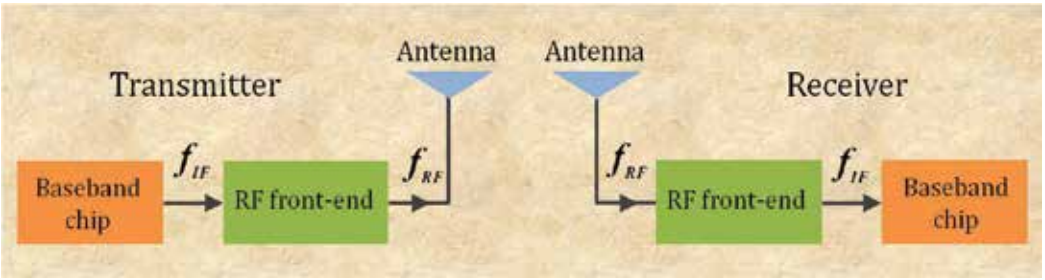

Figure 1. Basic block diagram of wireless communication system.

Frequencies more than 1 GHz are typically known as microwave frequencies in which most of the systems operate [3]. High-frequency circuit designs are different compared to the low-frequency circuit design because at high frequency, wave nature of current is needed to be considered (it will be further discussed in microstrip transmission line technology). After the announcement of a wide range of ultra-wide band (UWB) for public use in 2002 by Federal Communication Commission (FCC), many designs dealing with high frequency and wide bandwidth became centre of attraction [4]. With the evolution of the technology, design and implementation of multiplexing networks become more sophisticated. **Figure 2** shows the scheme of sharing the bandwidth among N channels using multiplexing.

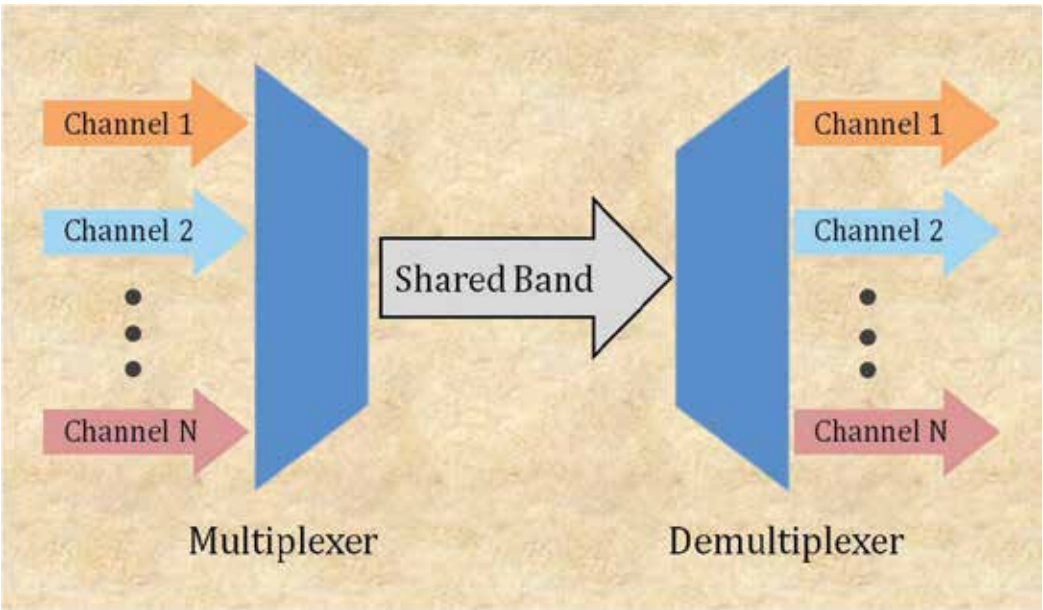

Figure 2. N channels multiplexing to share the bandwidth.

http://dx.doi.org/10.5772/66407

2. Literature review

In RF and microwave systems, different multiplexer design patterns have been adopted [3–24]. Most of the designs have been implemented by utilizing various technologies such as waveguide and microstrip, and high-temperature superconducting (HTS) materials. Various existing multiplexers are able to deal with the multiple sub-bands with a short guard band. Due to the future generation system, amenable front-end design requirement has become more challenging. Some well-known design patterns of the multiplexer are hybrid-coupled multiplexer, directional filter multiplexer, circulator coupled multiplexer and manifold multiplexer [5–7].

The hybrid-coupled multiplexer design pattern has been adopted by many researchers [8–10]. This design approach is easy to tune and there is no interaction between channel filters, so it can accommodate any change in channel frequencies or addition of new channel. Hybrid multiplexers are comparatively large due to the presence of two hybrid and two filters for each channel. Jonathan et al. [8], designed hybrid coupled multiplexer using microstrip technology. Mansour et al. [9] studied the possibility of building HTS using hybrid-coupled multiplexers. Rubin [10] represented the frequency multiplexer with the hybrid-coupled configuration by two-port analysis.

In another design pattern of multiplexer, four port directional filters are used [6, 11, 12]. By keeping one port terminated the other three ports are used for incident input, filtered output and reflected signals. Unlike hybrid-coupled multiplexers, it uses one filter per channel which can be designed separately and can be easily modified without changing the whole design [6]. Despite all these benefits, its use is constrained due to narrow bandwidth. Volker et al. [11], in their study, presented a microwave design based on directional filters. This paper shows the measured and simulated results for the triplexer with centre frequencies of 1.472, 2.944 and 4.416 GHz. Ref. [12] shows the design and implementation of the miniaturized coupled-line directional filter multiplexer in a multilayer microstrip technology.

The circulator-coupled multiplexer is another design which is used in different applications [6, 7, 13, 14]. This multiplexer consists of channel dropping circulators along with one filter per channel. It provides no interaction between channel filters but have comparatively high insertion loss in later channel circulator. Raafat [7] presents experimental results for a three-channel circulator-coupled multiplexer using HTS materials for microwave. Chen et al. [13] used an optical multiplexer employing multiport optical circulator (MOC) using optical fibre. Theoretical and experimental studies which were carried out upon a waveguide multiplexer that consists of two branches joined by a circulator are presented in Ref. [14].

The manifold multiplexer is a well-known design pattern used to realize multiplexers. This approach is the focus of this chapter. It provides better insertion loss and amplitude response. It has been used in HTS thin film integrated technology and it shows better loss performance but is sensitive to the material defects [15]. On the other hand, tuning this multiplexer is little complex because of its need to deal with all filters at the same time. So, it is not flexible to

frequency changes or additional channel frequency and in the case of any modification in frequency arrangement, the whole multiplexer need to be redesigned.

This topology has been presented in many research papers using waveguides and microstrip technology. Morinil et al. [15] presented an improvement in the dual manifold multiplexer to design the reconfigurable multiplexer. Ho and Battensby [16] discuss the application of microwave active filter manifold in multiplexing. Ten-channel manifold multiplexer by using waveguide is presented with contiguous and non-contiguous channels [17]. In Ref. [18], the theory of manifold multiplexer using helical filter is discussed. Although the reconfigurable filter technology still not fully developed, a theoretical study of tunable manifold multiplexer has been carried out with five channels [19].

Figure 3 illustrates the most adopted structural patterns of the manifold multiplexer with one filter for each channel and these are the most compact design approach patterns [6, 7]. Several manifold multiplexer designs with all filters on the same side are presented in **Figure 3(a)** [20]. An alternate filter design as shown in **Figure 3(b)** is presented in Refs. [21, 22]. Both this approaches have been adopted according to requirements. Cameron and Yu [6] classified the manifold multiplexer design patterns into three categories namely comb, herringbone and end-fed (can be applicable in both **Figure 3(a)** and **(b)**, where one filter feed the manifold design).

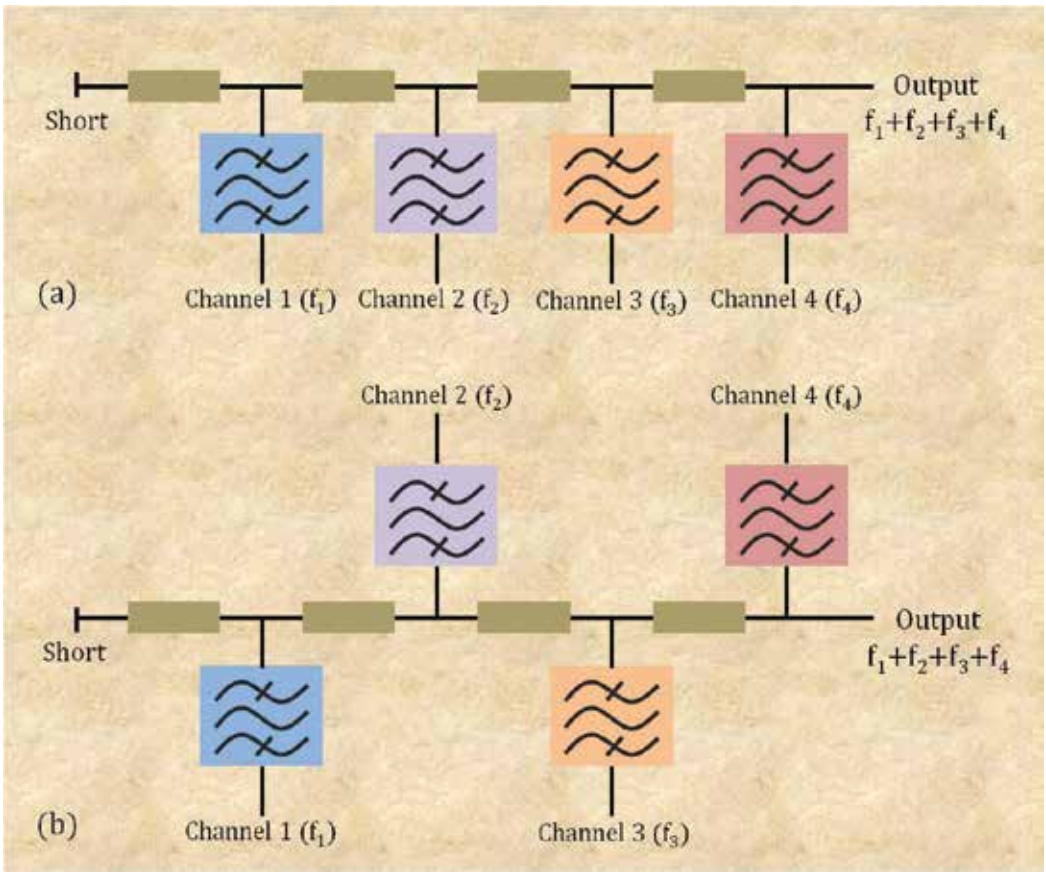

Figure 3. Manifold multiplexer design pattern, (a) all channels on one side, and (b) filters on alternate sides.

http://dx.doi.org/10.5772/66407

Compared to other multiplexer patterns, manifold has no isolation between channels, which make it act as a whole circuit but at the same time, which make it more complicated when the number of channels are increased. However, it gives small losses due to the absence of the lossy isolation. That is why manifold design is the preferred choice of the circuit designer aiming for small losses and miniaturized circuit. With the help of circuit design software, complexities in the design can be overcome.

3. Frequency multiplexing network

Figure 4 shows the working principle of the frequency multiplexing network (FMN) using manifold approach for *N* number of channels with one filter per channel. Filters are interconnected by using quarter wavelength transformer and horizontal transmission line. The

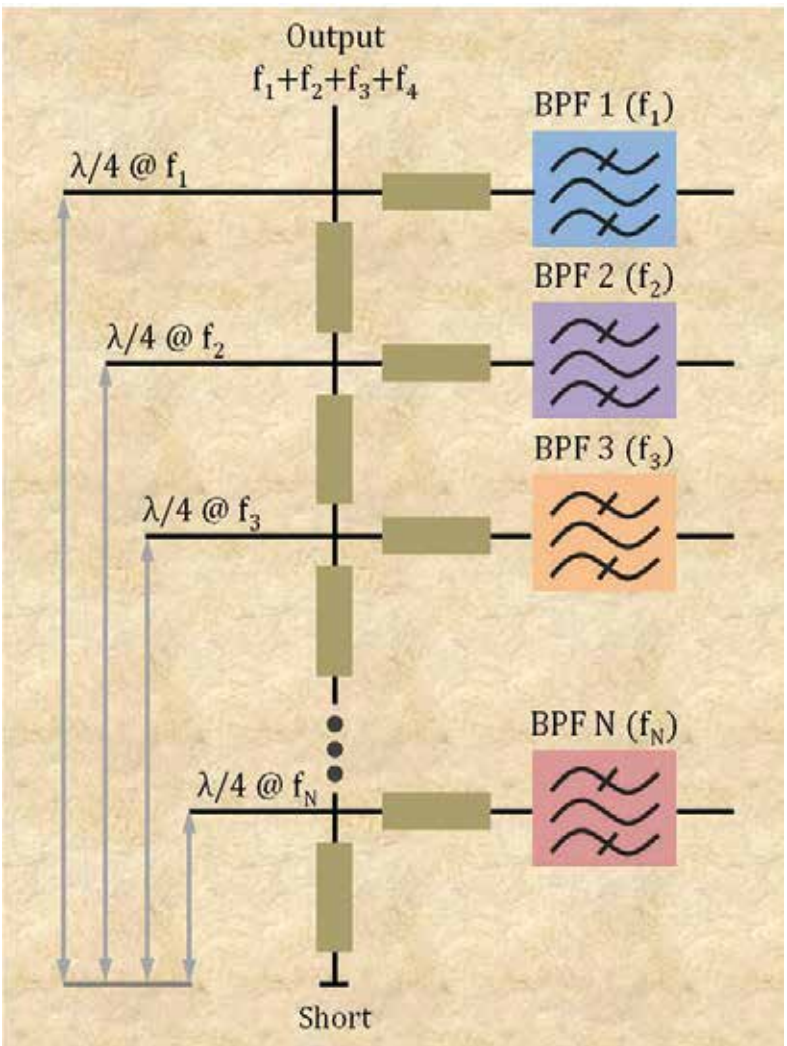

Figure 4. Frequency multiplexing network [23].

available frequency bandwidth is divided into N channels with frequencies f_1, $f_{2, \ldots,}$ f_N, where f_1 is lowest frequency band and f_N is the highest frequency band. Quarter wave transmission lines provide the high impedance to the corresponding frequency band, where as horizontal transmission lines help in tuning that band. FMN is a passive network that can be used as a multiplexer in the transmitter and demultiplexer in the receiver. The presence of a suitable guard band can prevent overlapping of the sub-bands. The minimum guard band is always preferred as this band will not be used in transmission. Normally the guard band of less than 10% relative bandwidth is used most of the time [4].

4. Microstrip transmission line technology

Transmission line is a special purpose medium intended to transmit high-frequency signals which have short wavelengths. According to the rule of thumb, signal carrying medium will be considered as the transmission line, if the wavelength of the signal is less than the ten times the circuit component [24]. **Figure 5** shows the microstrip transmission line, which has two conductors separated by the dielectric material of permittivity ε_r and substrate height h. Here L is the length, W is the width and t is the thickness of the microstrip. It can be manufactured utilizing a double-sided printed circuit board (PCB). Input impedance (Z_{in}) of a terminated transmission line can be represented as [24]:

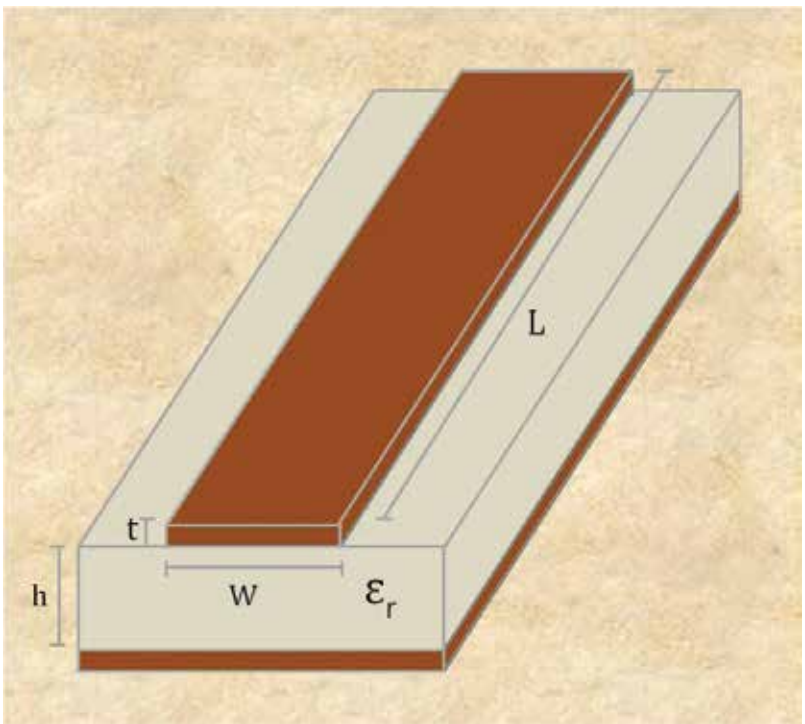

Figure 5. Microstrip transmission line.

http://dx.doi.org/10.5772/66407

$$Z_{in}(d) = Z_o \frac{Z_L + j Z_o \tan(\beta d)}{Z_L - j Z_o \tan(\beta d)} \quad (1)$$

where Z_L is load impedance, Z_o characteristic impedance, d is the length of transmission line and β is the wave number.

In order to achieve the maximum power transfer we need to match the source and load power, which can be done by using a passive network known as matching network. Many types of matching networks are using discrete components as a cheapest solution in circuit designing such as LC network, T network and Pi network in low-frequency applications. A combination of lumped and discrete component matching network can be used for comparatively high frequencies and purely discrete components have been used in high frequencies of the order GHz. Quarter wavelength transmission line, single and double stub are examples of discrete matching networks.

Quarter wavelength transmission line or transformer is a simple matching network. The impedance of the quarter wavelength transmission line can be calculated for matching load and source. **Figure 6** shows the quarter wavelength microstrip transmission line.

From Eq. (1) for (Z_S=Z_L)

$$Z_{\text{in}}\left(d = \frac{\lambda}{4}\right) = \frac{Z_o^2}{Z_L} \text{ or } Z = \sqrt{Z_{\text{in}} Z_L} \quad (2)$$

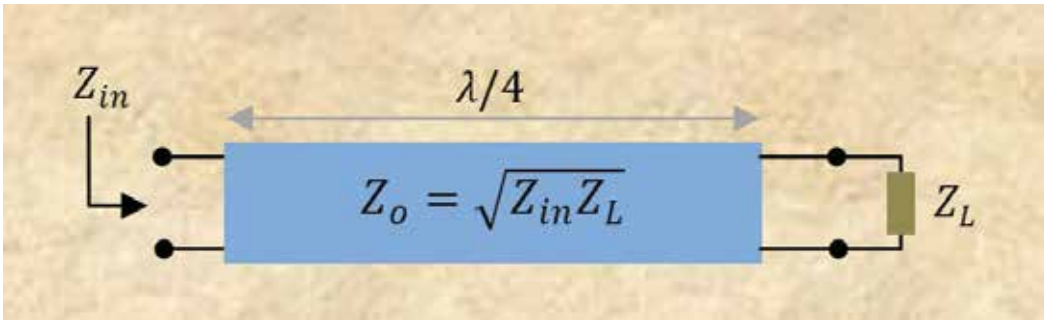

Figure 6. Quarter wavelength microstrip transmission line.

5. Frequency division multiplexing

When the available bandwidth of the medium is more than that of communicating devices, then it is better to share the medium. FDM can enhance the data rate of the transmission by parallel processing [4, 5]. Multiplexing can be done in various ways, which can depend on the target application. Some of these famous schemes for multiplexing are:

- Frequency division multiplexing (FDM)
- Time division multiplexing (TDM)
- Wavelength division multiplexing (WDM)

In wireless communications, different schemes are applied to efficiently use the valuable bandwidth. FDM is mostly used in the radio frequency band. It is the analog multiplexing schemes which divide the available bandwidth into two or more frequency bands (channels). **Figure 7** shows the schematic of frequency division for the multiple channels utilizing FDM. The guard band (narrow portion of the band spectrum which is not used in communication but used to protect sub-bands from interference) is present between each neighbouring channel. One antenna pair is sufficient for the communication of all the users of the sub-bands.

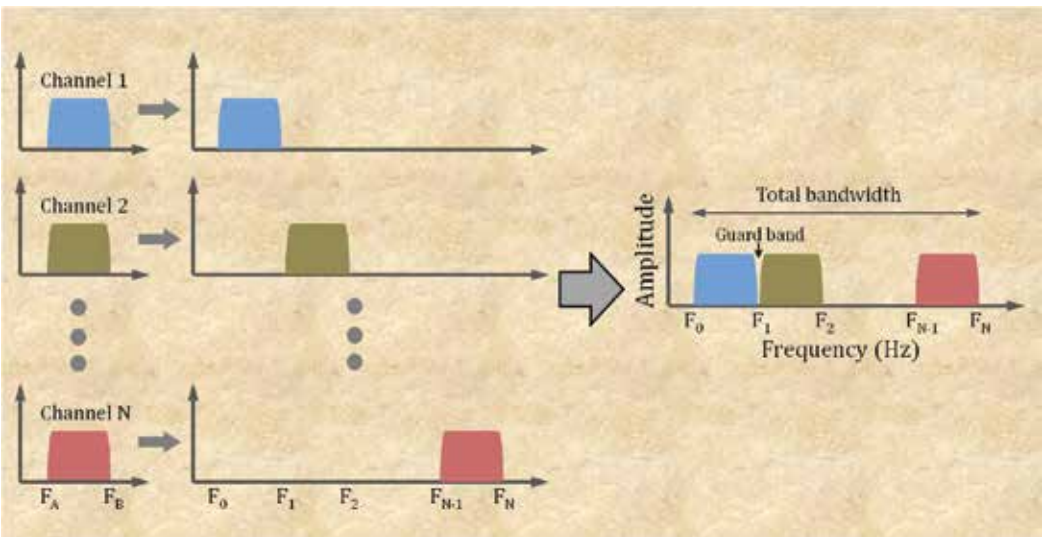

Figure 7. Multiple sub-bands (channels) in available bandwidth using FDM scheme.

6. Design and implementation of manifold multiplexer

This section will give the detailed designing process of the diplexer (an example of manifold multiplexer) using advanced design circuit (ADS) from Agilent's simulation software and implementation on a double-sided PCB. Finally, the prototype will be measured by a two-port vector network analyser.

6.1. Frequency diplexer network (manifold multiplexer)

By using the working principle of the FMN (discussed earlier), a diplexer is designed. **Figure 8** shows the block diagram of the frequency diplexer network (FDN). It has two channels in the UWB frequency range from 6 to 9 GHz. The guard band of 200 MHz is present between these two sub-bands (6–7.4 and 7.6–9 GHz). As discussed earlier all the filters in the manifold design are needed to be tuned at the same time. However, individual channel filters are optimized and then combined with a matching network which is a systematic approach to make the designing process simple.

http://dx.doi.org/10.5772/66407

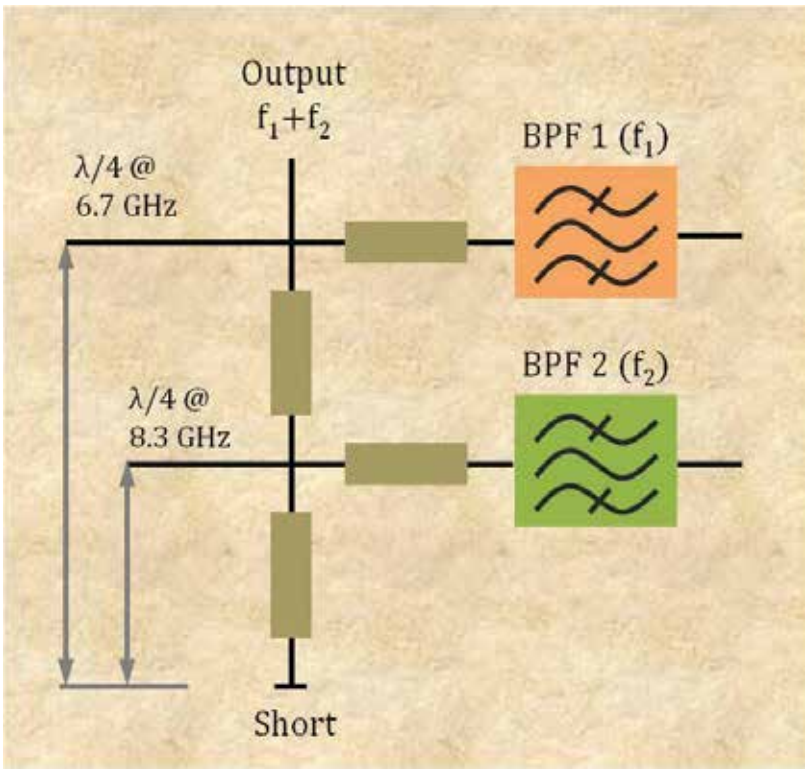

Figure 8. Frequency diplexer network [21].

6.2. Systematic processes

In order to understand the process of design and implementation it is categorised into the four following steps [4].

1. Schematic designing by using selected substrate properties of PCB to show the ideal behaviour.
2. Layout of the schematic design to see the real behaviour by running momentum tool.
3. Analysis of schematic and momentum results together by using layout in schematic for final simulation results.
4. Implementation of the approved design on to the PCB and comparison of the measured results with simulation results.

6.2.1. First step

Rogers 4350B is used in many high frequency electronic circuits. It is a double-sided PCB and selected here for the design implementation. **Table 1** shows the substrate properties of PCB.

Dielectric thickness	254 μm
Relative dielectric constant	3.48
Metal thickness	25 μm
Metal conductivity	58 MS/m

Table 1. Substrate properties of Rogers 4350B.

Diplexer can be divided in three blocks as first channel filter, second channel filter and matching network. **Figure 9** shows the schematic view of the first filter in ADS. MSub and S-parameters show the substrate properties and frequency plan, respectively.

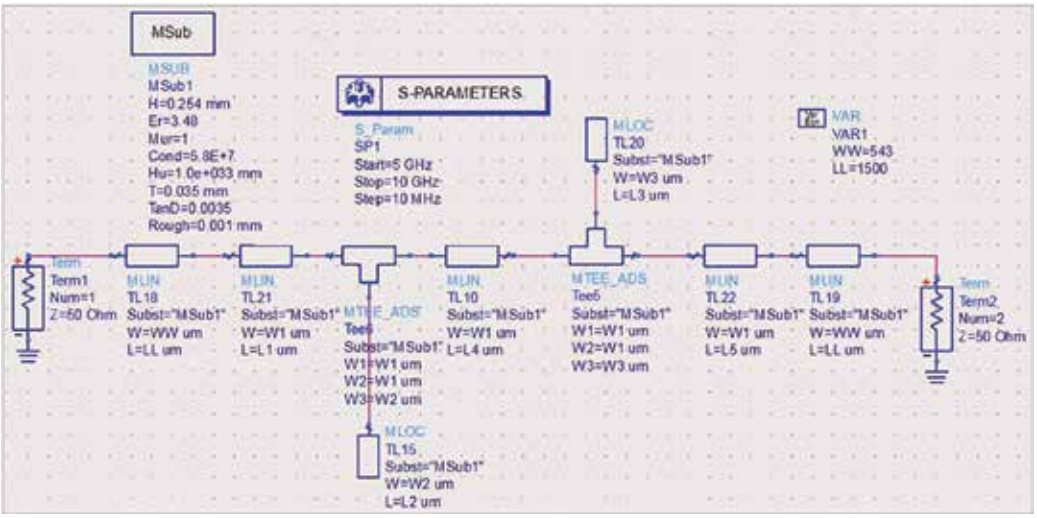

Figure 9. Schematic diagram of first filter for 6–7.4 GHz.

Figure 10 presents the simulated forward transmission and input reflection result for the first filter in S-parameter. In a similar way, schematic of the second filter can be designed. After the optimization of the filters, both can be combined by the transmission line network as shown in the FDN figure to form the diplexers. Now tune the whole circuit together to get the optimization. Different tuning tools are available in ADS which can be used to tune the circuit.

6.2.2. Second step

After getting the optimized diplexer's schematic, second step is to convert the whole schematic into a layout as shown in **Figure 11**. It has three inputs/outputs and one connected to ground, so four ports are assigned to this FDN. Now run momentum, to see the real behaviour of the design which is a simulation engine use for the layout. It has two modes, RF and microwave (microwave mode gives full electromagnetic simulation with radiation effect and RF mode is quick simulation for the designs which do not radiate).

http://dx.doi.org/10.5772/66407

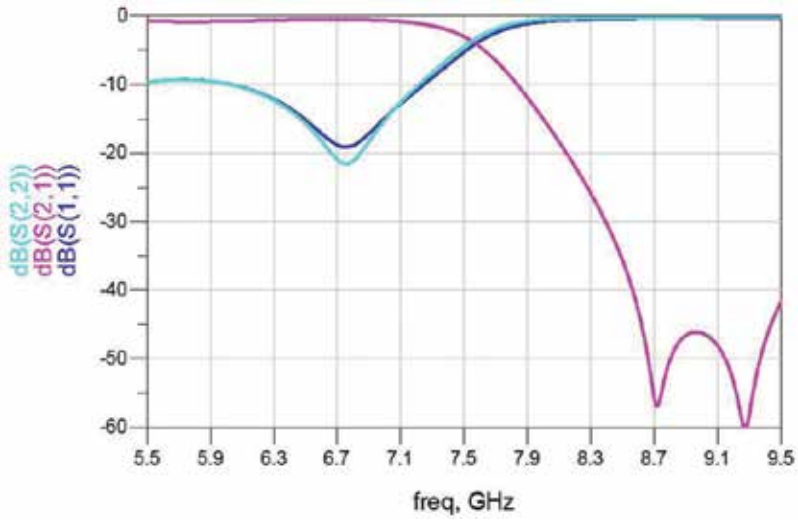

Figure 10. Forward transmission and input reflection for first filter for 6–7.4 GHz.

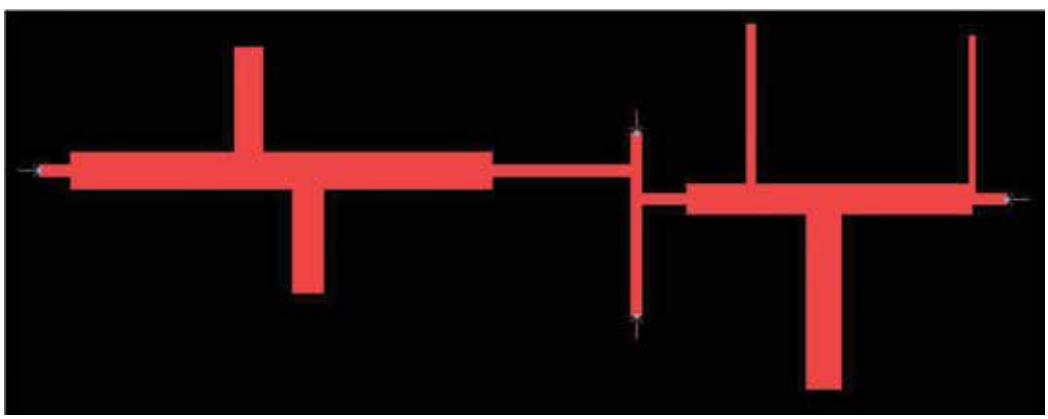

Figure 11. Layout of the FDN.

6.2.3. Third step

Third step is to convert the layout of the FDN into the component and call this component into the schematic as shown in **Figure 12**. Here schematic and layout simulate together and provide final simulation results in terms of ideal and real physical design.

Figure 13 shows the final simulated results of the FDN in terms of the S-parameters. Forward transmission (S21, S31) and input reflection (S11, S22, S33) show flat response in their respective bands jamming others. Appropriate values of group delay can be observed from the results that show small variations.

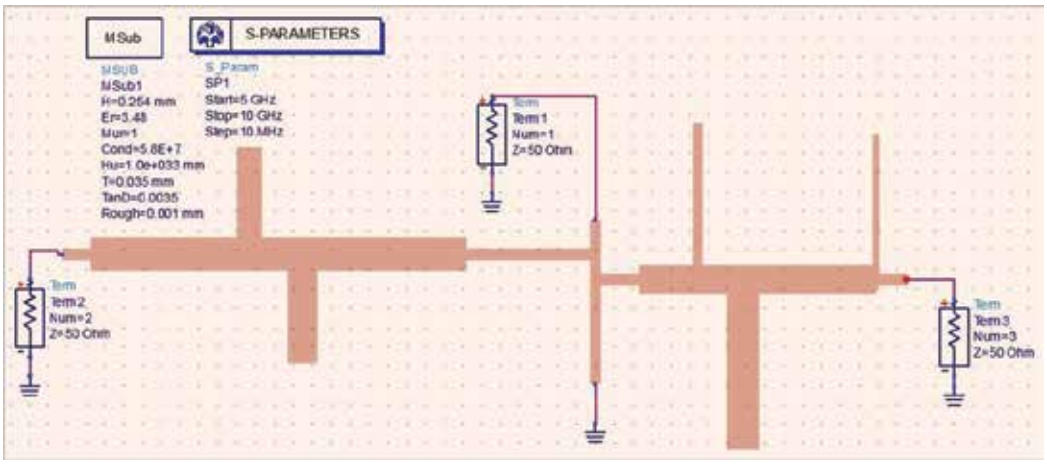

Figure 12. FDN as layout component in schematic representation.

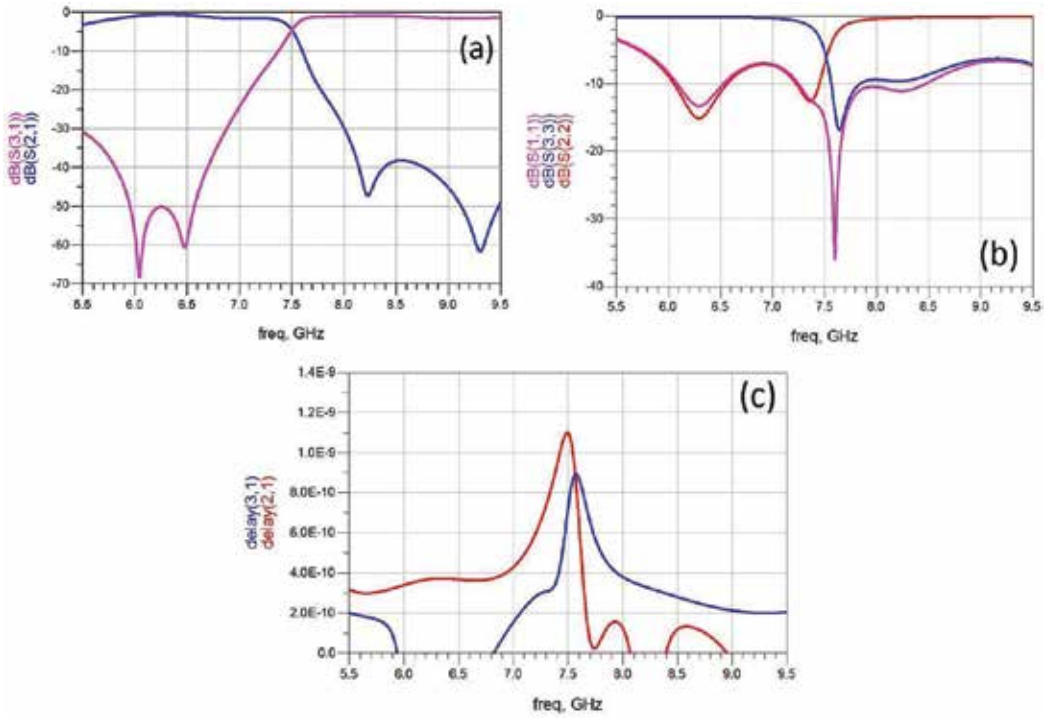

Figure 13. Simulated results for FDN, (a) forward transmission, (b) input reflection, and (c) group delay.

6.2.4. Fourth step

Finally, the layout of the PCB is prepared for the implementation on the double-sided PCB. **Figure 14** shows the top ground plane connected with the bottom ground plane through ground via hole. Small diameter circles are placed in already defined layer for holes. The

http://dx.doi.org/10.5772/66407

number of holes depend on the highest operating frequency by RF design rules. The ground plane on the top can reduces the possible crosstalk between transmission lines. Now the final design file is ready to be exported from ADS for the implementation on PCB.

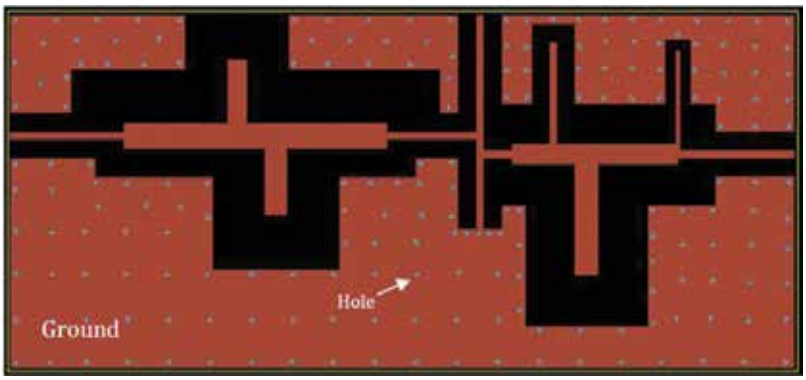

Figure 14. Layout of FDN for PCB.

PCB manufacturing has various steps, such as film processing, CNC drilling, brushing, plating, laminating photoresist on PCB, UV-exposure of photoresist, development of photoresist and etching. After etching, a visual inspection of PCB is needed in order to remove any possible copper remained during etching. **Figure 15** shows the final prototype of the diplexer with 50 Ω line at the input/output extended for connecting the big size SMA. Three SMA connectors have been soldered in the PCB in order to measure the results.

Figure 16 shows the measured results of the prototype which are measured using a Rhode and Schwartz ZVM vector network analyser. Any possible difference between measured and the simulated results can be due to the soldering and SMA [25].

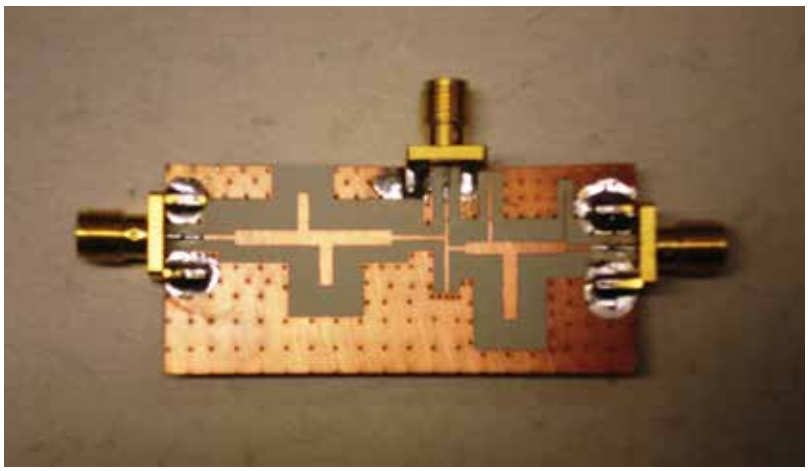

Figure 15. Prototype of FDN.

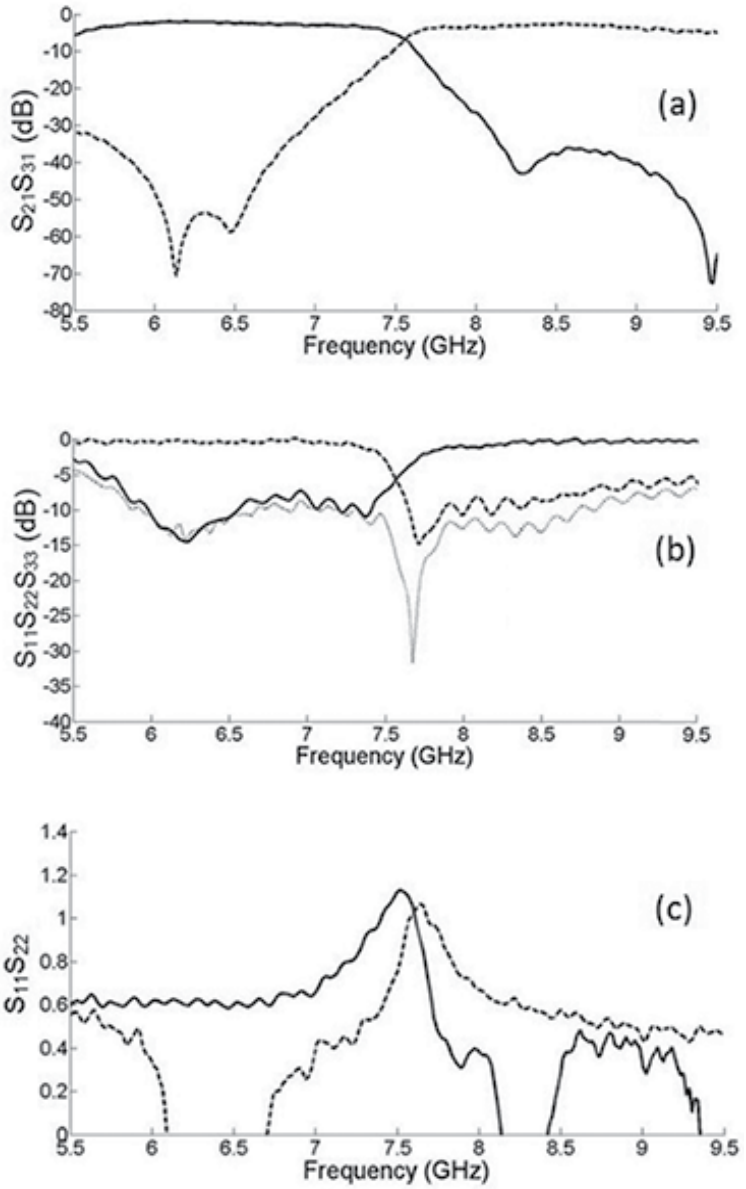

Figure 16. Measured results for FDN, (a) forward transmission, (b) input reflection, and (c) group delay.

Note: Here a diplexer is designed and implemented on the basis of FMN (**Figure 4**) and to see the design and implementation of the triplexer with a different BPF, see Ref. [22].

Acknowledgements

The author thanks Magnus Karlsson and Gustav Knutsson at the Department of Science and Technology Linköping University Sweden, for the assistance in PCB manufacturing.

http://dx.doi.org/10.5772/66407

Appendices and nomenclatures

ADS	Advanced Design System
BPF	Band Pass Filter
FCC	Federal Communications Commission
FDM	Frequency Division Multiplexing
FDN	Frequency Diplexer Network
FMN	Frequency Multiplexing Network
HTS	High-Temperature Superconductor
LO	Local Oscillator
LNA	Low Noise amplifier
MOC	Multiport Optical Circulator
PA	Power Amplifier
PCB	Printed Circuit Board
PPM	Pulse Position Modulation
PSM	Pulse Shape Modulation
SMA	Sub-Miniature version A
TDM	Time Division Multiplexing
UWB	Ultra-Wide Band
WDM	Wavelength Division Multiplexing

Author details

Imran Mohsin

Address all correspondence to: imranmoh27@gmail.com

1 Shenzhen Institutes of Advanced Technology (SIAT), Chinese Academy of Sciences, Shenzhen, China

2 Shenzhen College of Advanced Technology, University of Chinese Academy of Sciences, Shenzhen, China

References

[1] Angwin A S. The Alexander Graham Bell centenary lecture. Graham Bell-pioneer: An era of outstanding developments in world communication. Journal of the Institution of Electrical Engineers—Part I: General. 2010; 94(78): 269–274. DOI: 10.1049/ji-1.1947.0084

[2] Joseph Carr. The Technician's Radio Receiver Handbook: Wireless and Telecommunication Technology. 1st ed. Oxford: Newnes; 2000. 23 p. DOI: 9780080518596

[3] Karlsson M. Ultra-wideband antenna and radio front-end system. [thesis]. Sweden: Department of Science and Technology, Linkoping University; 2007.

[4] Mohsin I. Design of a smart six-port circuit and wireless parallel data transmission. [thesis]. Sweden: Department of Science and Technology, Linkoping University; 2010.

[5] Håkansson P. High speed wireless parallel transmission and six-port transmitters and receivers. [thesis]. Sweden: Department of Science and Technology, Linkoping University; 2008.

[6] Cameron R I, Yu M. Design of manifold-coupled multiplexers. IEEE Microwave Magazine. 2007; 8(5): 46–59. DOI: 10.1109/MMM.2007.904715

[7] Raafat R M. Design of superconductive multiplexers using single-mode and dual-mode filters. IEEE Transactions on Microwave Theory and Techniques, 1994; 42(7): 1411–1418. DOI: 10.1109/22.299738

[8] Jonathan C, Jerry F, Stephen B, Duane H. Microstrip hybrid coupled input multiplexer design for satellite communications. In: IEEE MTT-S International Microwave Symposium (IMS2014); 1—6 June 2014; FL.

[9] Mansour R, Rammo F, Dokas V. Design of Hybrid-Coupled Multiplexers and Diplexers using Asymmetrical Superconducting Filters. In: Microwave Symposium Digest, IEEE MTT-S International; 14–18 June 1993; IEEE; 2002. pp. 1281–1284.

[10] Rubin D. Millimeter-wave hybrid coupled reflection amplifiers and multiplexer. IEEE Transactions on Microwave Theory and Techniques. 1982; 30: 2156–2162. DOI: 10.1109/TMTT.1982.1131400.

[11] Volker N, Markus M, Gottfried M. A Novel Low Loss Microwave Multiplexer Design Based on Directional Filters. In: Radio and Wireless Conference, RAWCON; 11–14 August 2002; IEEE; 2002. pp. 257–260.

[12] Jakub S, Ilona P, Slawomir G, Krzysztof W. Miniaturized Directional Filter Multiplexer for Band Separation in UWB Antenna Systems. In: International Symposium on Antennas and Propagation (ISAP); 9–12 November 2015; IEEE; 2016. pp. 1–4.

[13] Chen K Y, Hu C J, Lee C C, Feng K M, Lu M K, Chang C H, Tu Y K, Tzeng S L. Low-crosstalk and compact optical add–drop multiplexer using a multiport circulator and fiber Bragg gratings. IEEE Photonics Technology Letters. 2000; 12(10): 1394–1396. DOI: 10.1109/68.883841.

[14] Andrzejewski N. K, Pietraszewy-ski E J. Waveguide Multiplexer with Eight Contiguous Channels X Band. In: Microwave Conference, 9th European; 17–20 Sept. 1979; IEEE; 1979. pp. 392–396.

[15] Morinil A, Baldellil M, Venanzonil G, Cifolal L, Farinal M, Iglesias P M, Emst C, Macchiarella G. Improvement of Dual-Manifold Architecture for the Design of

Reconfigurable Diplexers. In: IEEE MTT-S International Microwave Symposium; 17–22 May 2015; IEEE; 2015. pp. 1–4.

[16] Ho R Y C, Battensby B. Subminiature Microwave Active Filter Manifolds. In: Microwave Symposium, G-MTT 1970 International; 11–14 May 1970; IEEE; 2010. pp. 62–65.

[17] María B, Santiago C, Mónica M, Pablo S, Vicente E B, Marco G. Design of Waveguide Manifold Multiplexers with Dual-Mode Filters Using Distributed Models. In: IEEE MTT-S International Microwave Symposium (IMS2014); 1–6 June 2014; IEEE; 2014. pp. 1–4.

[18] Liang P L, Tao S, Zhi P R., Bian W. Design of Helical Filters Manifold Multiplexer Using A Novel Equivalent Circuit Model. In: International Symposium on Signals, Systems and Electronics; 17–20 Sept. 2010; IEEE; 2010. pp. 1–4.

[19] Uwe R, Dietmar R, Wolfgang R, Dieter W. Tunable Manifold Multiplexers - A New Possibility For Satellite Redundancy Philosophy. In: Microwave Conference, 18th European; 12–15 Sept. 1988; IEEE; 2007. pp. 870–875.

[20] Santiago C, Pablo S, Vicente E. B, Marco G, María B, Benito G, and David R. Efficient design of waveguide manifold multiplexers based on low-order EM distributed models. IEEE Transactions on Microwave Theory and Techniques. 2015; 63(8): 2540–2549. DOI: 10.1109/TMTT.2015.2442990

[21] Mohsin I, Karlsson M, Gong S. Frequency diplexer network for wireless parallel data transmission and ultra-wideband systems utilizing manifold technique. Microwave and Optical Letters. 2014; 56(8): 1869–1871. DOI: 10.1002/mop.28464

[22] Karlsson M, Håkansson P, Gong S. A frequency triplexer for the ultra-wideband systems utilizing combined broadside- and edge-coupled filters. IEEE Transactions on Advanced Packaging. 2008; 31(4): 794–801. DOI: 10.1109/TADVP.2008.2004415

[23] Håkansson P, Huynh A, Gong S. A Study of Wireless Parallel Data Transmission of Extremely High Data Rate up to 6.17 Gbps per Channel. In: Asia-Pacific Microwave Conference; 12–15 Dec. 2006; IEEE; 2008. pp. 975–978.

[24] Ludwig R, Bretchko P. RF Circuit Design, Theory and Application. 2nd ed. Upper Saddle River, NJ: Prentice Hall; 2000. ISBN:0-13-095323-7

[25] Mohsin I, Karlsson M, Owais O, Gong S. Design and implementation of a UWB six-port correlator for 6–9 GHz frequency band. Microwave and Optical Letters. 2012; 55(1): 190–193. DOI: 10.1002/mop.27235

Microwave ICs

Chapter 5

Innovative Techniques for 60-GHz On-Chip Antennas on CMOS Substrate

Adel T. Barakat, Ramesh K. Pokharel and
Hala A. Elsadek

Additional information is available at the end of the chapter

http://dx.doi.org/10.5772/66238

Abstract

The 60-GHz band has a 7-GHz of bandwidth enabling high data rate wireless communication. Also, it has a short wavelength allowing for passive devices integration into a chip, that is, fully integrated system-on-chip (SOC) is possible. This chapter features the design, implementation, and measurements of 60-GHz on-chip antennas (OCAs) on complementary-metal-oxide-semiconductor (CMOS) technology. OCAs are the primary barrier for the SOC solution due to their limited performance. This degraded performance comes from the low resistivity and the high permittivity of the CMOS substrate. We present here two innovative techniques to improve the CMOS OCAs' performance. The first method utilizes artificial magnetic conductors to shield the OCA electromagnetically from the CMOS substrate. The second methodology employs the PN-junction properties to create a high resistivity layer. Both approaches target the mitigation of the losses of the CMOS substrate; hence, the radiation performance characteristics of the OCAs are enhanced.

Keywords: CMOS, on-chip antenna (OCA), artificial magnetic conductor (AMC), distributed PN-junctions

1. Introduction

The millimeter wave band around the 60-GHz carrier has a broad bandwidth of 7 GHz and a short wavelength. This wide-ranging bandwidth allows for high data rate transmission of several gigabit-per-second (Gbps) suppressing the current low-frequency systems below 10 GHz. This excessive data rate opens the door for many applications such as high-speed video

and computer display streaming, Gbps networking, uncompressed high-definition media transfers, wireless personal area access, chip-to-chip communications, sensing applications, information showers, and virtually instantaneous admission to massive libraries of information. Moreover, an additional advantage of the 60-GHz carrier is the possibility of small-distance frequency reuse because of the high attenuation caused by oxygen molecules at the level of 10–15 dB/km. This frequency reuse attribute empowers the 60-GHz system to be an appropriate replacement for the contemporary short-range wireless communications systems. Additionally, the short free-space wavelength of 5 mm at 60 GHz enables small-size passive devices fabrication with integration capability into a chip. On-chip integration of passive devices leads to a wholly system-on-chip (SOC) realization. SOC is an individual and remarkable solution that can facilitate low-cost wireless communication devices. The SOC promotes the integration on the same chip of the antenna, front-end circuits, and back-end circuits. This SOC guarantees economical wireless communication devices thanks to the elimination of the costs associated with materials required for external antennas. Also, the antennas' matching circuits will be dismissed given that the 50-Ω boundary is no longer obligatory. Finally, SOC will guarantee a one-step foundry fabrication of the entire wireless system [1–16].

The cost-effective complementary-metal-oxide-semiconductor (CMOS) process, which is the mainstream digital circuits' technology, guarantees further cost reduction of the wireless system. Even though the CMOS substrate causes degradation of the radiation performance of the on-chip antennas (OCAs) due to its low resistivity and high permittivity [4–7], that is, the CMOS substrate is not optimized for the antennas operation. Many design methodologies have been utilized [4–12] to permit the improvement of the CMOS OCAs' performance. These OCAs' enhancement approaches have two main categories: (1) post-processing techniques [8–12] and (2) electromagnetic (EM) shielding [13–16].

Post-processing methods are techniques that utilize additional fabrication steps to the standard CMOS process to allow changing the characteristics of the CMOS substrate [8–12]. Micro-machining [8, 9] and proton implantation [10, 11] are two conventional CMOS post-processing methods. On the one hand, in the micro-machining approach, the OCA performance is enhanced by selectively removing parts of the CMOS substrate that lie directly below the OCA. Thus, the loss source is eliminated [8]. Wang et al. [8] had realized a peak measured gain and efficiency of 8 dBi and 60% by employing the selective etching technique together with array antenna at 130-GHz-operating frequency. Another micro-machining tactic uses post-supportive micro-machined walls to isolate the OCA far apart from the CMOS substrate [9]; hence, the coupling between the OCA and the substrate reduces and its radiation performance is enhanced. Kim et al. [9] had achieved a peak simulated gain and efficiency of 9.9 dBi and 94%, respectively by using this post-supportive walls method with patch antenna array at 60-GHz-operating frequency.

On the other hand, the proton implantation course implements high-energy ions into the CMOS substrate below the OCA such that the CMOS substrate's resistivity below the OCA becomes very high, the corresponding losses are reduced, and the OCA's performance is enhanced [10, 11]. In Ref. [10], proton implantation increased the CMOS substrate resistivity

http://dx.doi.org/10.5772/66238

from [22] 10 Ω.cm to 0.1 MΩ.cm. In return, the transmission gain is enriched by 20 dB. In Ref. [11], a helium-3 ion irradiation process is applied to reduce the substrate losses of the OCA. Therefore, the radiation efficiency of the OCA is doubled, and a measured peak gain of -4.1 dBi is possible at 60 GHz. However the possibility of high performance using the post-processing techniques, these techniques have two major disadvantages: (1) the extra costs associated with them due to the additional fabrication steps and (2) the repeatability of the fabrication process [12].

Alternatively, the EM shielding uses the standard CMOS technology without any further processing. The EM shielding employs artificial magnetic conductors (AMCs) to enhance OCA radiation performance such as gain and radiation efficiency [12–16]. In Ref. [13], Chu et al. implemented a wide band patch OCA with two parasitic patches and used a snowflake AMC as a shield. However the wide bandwidth, this design had shown low gain and low efficiency of -2.2 dBi and 15%, respectively. Barakat et al. [14, 15] designed a triangular patch OCA over Jerusalem-Cross (JC) [14] and square [15] AMC. A methodology to enhance gain and efficiency while maintaining small area is also proposed [14, 15]. In this methodology, gain and efficiency have been enhanced by increasing the number of AMC cells in the E-plane direction and reducing the number of AMC cells in the H-plane direction. A simulated gain and efficiency of 0 dBi and 39%, respectively, were observed for JC-AMC [14] and 0.7 dBi and 47%, respectively, for square-AMC [15]. Bao et al. [16] has proposed a double-loop OCA with modified star AMC. The double-loop OCA originally has circular polarization. When using full AMC layer below the double loop, the axial ratio bandwidth is reduced due to the coupling between the OCA and the AMC cells. To overcome this problem, Bao et al. [16] proposed selectively removing some cells from the AMC plan to maintain a wide axial-ratio bandwidth while efficiency is enhanced. An AR bandwidth (AR <3) was possible from 57 to 67 GHz with a peak measured gain of -4.4 dBi [16]. The AMC-based OCAs still have poor measured performance when compared to the post-processed OCAs [8–16].

This chapter presents the design, implementation, and measurements of the 60-GHz CMOS OCAs. We propose two innovative techniques to advance the CMOS OCAs' performance. The first method uses electromagnetic shielding employing asymmetric AMC. The OCAs based on the asymmetric AMC is superior in the gain-to-active-area ratio when compared to the OCAs making use of the traditional symmetric AMC as will be detailed in Section 2. The second scheme is the distributed N-well method. In this distributed N-well approach, the semiconductor physics characteristics of the PN-junction (PNJ) are utilized to consent the increase of the effective resistance of the CMOS substrate, hence, reducing the resulting losses and the OCA's performance enhances. This chapter describes the distributed N-well tactic and its application to OCA's performance boosting in Section 3.

2. OCA with asymmetric AMC

In this section, we report the use of asymmetric AMC to enhance the performance of the OCA. First, in Section 2.1, we detail the background of the AMCs showing their importance in

antenna engineering applications. Then, we discuss the development of the asymmetric AMC from the traditional symmetric AMC in Section 2.2. Furthermore, in Section 2.3, we manipulate the symmetric and the asymmetric AMC in the OCA's characteristics progression, comparing the resulting performances. Then, we detail the layout and fabrication consideration, the measurements technique used, and the measured data of the OCA with asymmetric AMC in Section 2.4.

2.1. History of AMC

An AMC layer consists of periodic metal patches over a dielectric substrate in one-, two-, or three-dimensional (3D) configurations. AMC surfaces have two important and exciting properties that do not occur naturally and benefit a variety of microwave circuit applications. These two AMC individualities are the high impedance and the in-phase reflection properties. First, an AMC surface acts as a high-impedance layer that is useful as an antenna ground plane regarding surface-wave suppression. AMC shields have very high-surface impedances within an explicitly narrow frequency band, where the tangential magnetic field intensity is small, even with a large electric field intensity along the surface [17, 18]. Second, an AMC has an unusual reflection phase (RP) features of 0° at its center frequency; hence, an antenna on AMC produces a smoother radiation profile than a similar antenna on a conventional metallic ground plane, with less power wasted in the backward direction. These AMC capabilities are useful to the diversity of antenna schemes, for example, patch antennas, that frequently suffer from the consequences of surface waves propagation. For phased arrays, the suppression of the surface waves can reduce the mutual coupling between the array elements; hence, it helps to eliminate the blind-scanning angles.

Furthermore, an AMC is particularly applicable to the field of portable hand-held communication devices, in which the interaction between the antenna and the user can have a significant impact on both the antenna's performance and the user's health. An AMC acting as a shield between the antenna and the user in portable communications equipment can lead to a higher antenna efficiency, a longer battery life, a lower specific absorption rate (SAR) of the human body, and a lighter device weight. Likewise, in the case of OCA, an AMC surface is placed between the antenna and the lossy CMOS substrate. Consequently, the AMC surface allows for better OCA's efficiency [13–18]. The reflection phase is the ratio between the phase of the reflected electric field and the phase of the incident electric field at the reflecting surface. In practice, the AMC plane exhibits a reflection coefficient of +1 at its center frequency and thus the reflected wave can constructively enhance the total electromagnetic field with the incident wave together at a low profile. On the contrary, the conventional perfect electrical conductor (PEC) plan delivers a reflection coefficient of -1 and therefore the reflected wave will destructively cancel the incident signal for low-profile operation.

The reflection phase on the AMC plane varies with the frequency continuously from -180° to 180° and become zero at the center-operating frequency. The operational band of an AMC layer is the range for which the reflection phase changes from +90° to -90°, as in this bandwidth, the reflection phase values would not cause destructive interference between the direct and the reflected waves. Following this definition of the reflection phase, the AMC percentage

http://dx.doi.org/10.5772/66238

bandwidth (BW_{AMC}) can be calculated as in Eq. (1) [13–18], where f_h is the frequency at which the reflection phase equals -90°, f_{lo} is the frequency at which the reflection phase equals 90°, and f_c is the center frequency at which the reflection phase equals 0°.

$$\mathrm{BW_{AMC}} = \frac{f_h - f_{lo}}{f_c} \times 100\% \tag{1}$$

2.2. Development of the asymmetric rectangular AMC-based OCA

2.2.1. Symmetric square AMC

Figure 1(a) shows two consecutive unit cells of the symmetric square AMC [15, 19]. We used the high-frequency-structure-simulator (HFSS) to optimize the reflection phase (RP) response of this AMC and for other simulations in this chapter. **Figure 1(b)** shows the simulation setup to determine the square AMC's RP response. Perfect-E and perfect-H boundary conditions are used to realize the periodic boundary conditions (PBCs). Excitation port is a wave port. We embed the reflection coefficient (S11) in the surface of the AMC unit cell and compute the RP response as the angle of the embedded S11. A percentage bandwidth of 16.5% is achieved for the dimensions d = 260 μm and g = 30 μm as shown in **Figure 1(c)**.

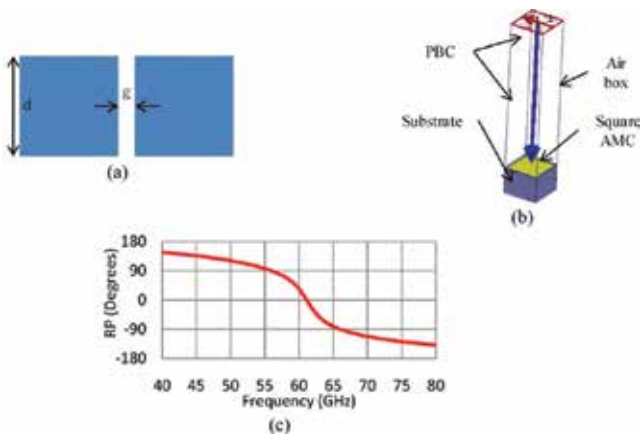

Figure 1. Two consecutive unit cells of square AMC. (b) HFSS simulation setup. (c) Reflection phase (RP) of the square AMC with d = 260 μm and g = 30 μm. "Reprinted with permission from Microwave Journal."

2.2.2. Asymmetric rectangular AMC

A transverse-magnetic (TM) wave with its electric field (E-field) directed in the YZ-plan and magnetic field (H-field) propagating in the x-direction incident on a "Cohn square" in free space [20] is shown in **Figure 2(a)**. For this TM wave, no detected E-field on the square AMC's plan appears in the space between the edges parallel to the y-direction. Thus, the square AMC reduces to a strip array of asymmetric rectangular AMC as shown in **Figure 2(b)** [21].

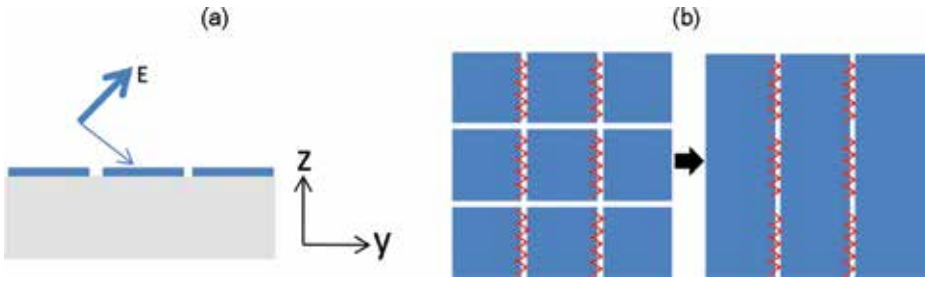

Figure 2. Square AMC with incident TM wave polarized in the *YZ*-plan. (b) Original and equivalent AMC structures at *XY*-plan. "Reprinted with permission from Microwave Journal."

2.2.3. Circular OCA over AMC

The AMCs presented in Sections 2.2.1, and 2.2.2 are utilized to enhance the radiation characteristics of a circular OCA. First, the methodology presented in [14, 15] is maintained to guarantee high gain-to-active-area ratio. According to this method, a high gain-to-active-area ratio is possible by increasing the number of AMC cells in the direction of the antenna polarization and decreasing them at the normal to this direction. **Figure 3(a)** and **(b)** shows a top view and three-dimensional (3D) view of the OCA employing square AMC, respectively. **Figure 3(c)** displays a top view of the circular OCA on rectangular AMC. We designed the two structures (OCA on square AMC and OCA on rectangular AMC) with the dimensions listed in **Table 1**, and they have the same chip area of 840 × 1710 μm^2.

Also, the two structures have a high agreement in the matching performance, gain and efficiency responses, and current distribution as can be interpreted from **Figure 3(d)** and **(f)**, respectively. The simulated gain and radiation efficiency are -0.8 dBi and 22.5%, respectively, at 60 GHz. These observations in **Figure 3** stand as an additional proof that the symmetric square AMC and asymmetric rectangular AMC are equivalent for TM mode antennas.

2.2.4. Circular OCA over modified asymmetric AMC

In the previous sections from 2.2.1 to 2.2.3, we have demonstrated that TM-mode circular OCA, which is exploiting the symmetric square AMC, and the asymmetric rectangular AMC undergo similar performances regarding impedance matching and radiation characteristics such as gain and efficiency. In this section, we detail how the asymmetric rectangular AMC can be modified such that the gain-to-active-area ratio can increase. **Figure 4(a)** shows the circular OCA over a modified asymmetric AMC. We applied the following adjustments to the asymmetric AMC:

Removing the two AMC cells that lay directly below the OCA in **Figure 3(c)**. Bao et al. [16] originally proposed this AMC cells removal for peak gain and axial ratio bandwidth boosting.

http://dx.doi.org/10.5772/66238

Limiting the length (L) of the modified AMC unit cell from 860 to 710 μm since in this direction the gain performance is negligibly affected as pointed in [14, 15]. Also, the gap "g" between each of the remaining consecutive cells is reduced to 5 μm.

Adding circular rounds to the AMC cells near to the OCA as shown in **Figure 4(a)** and then adjusting the separation between the OCA and the modified AMC cells with circular rounds "d1" and the separation between the modified AMC cells with circular rounds "d2."

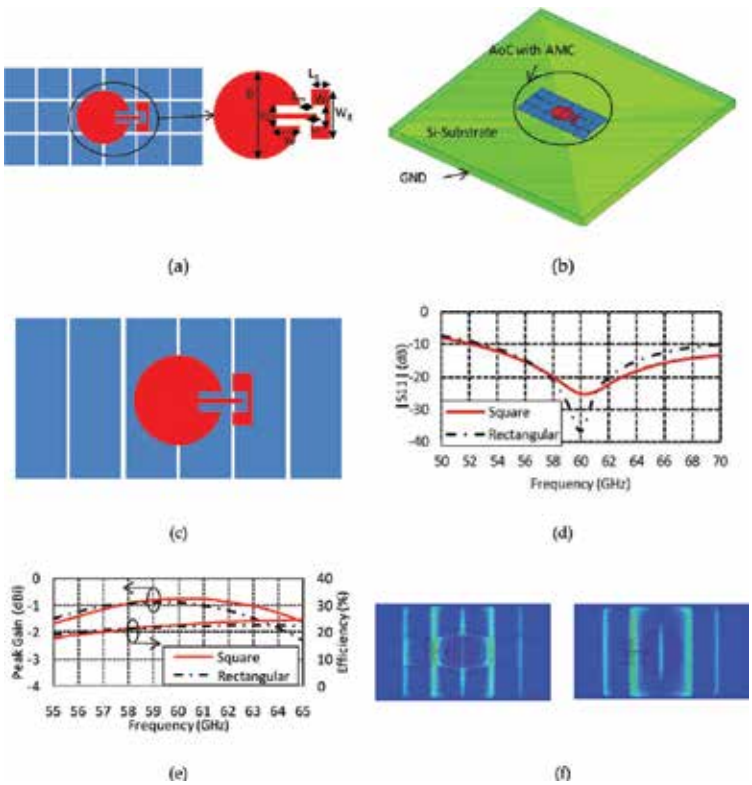

Figure 3. Top view of circular OCA over square AMC. (b) 3D view of circular OCA over square AMC. (c) Top view of circular OCA over rectangular AMC. (d) Simulated |S11| comparison. (e) Simulated peak gain and efficiency comparison. (f) Simulated current distribution comparison (left: square AMC; right: rectangular AMC) "Reprinted with permission from Microwave Journal."

D	x_0	y_0	L_m	W_m	L_f	W_f	L_g	W_g
450	64	85	60	14	50	54	100	254

Reprinted with permission from Microwave Journal.

Table 1. Optimized dimensions of circular OCA employing square AMC.

By applying the above modifications to the asymmetric rectangular AMC, the resulting OCA over modified asymmetric AMC establishes a gain of 0 dBi at 60 GHz within a chip area of 1.19 mm^2. The design dimensions are the same as in **Table 1** except x_0 = 44 μm and y_0 = 100 μm. The values of x_0 and y_0 are changed to adjust impedance matching. Besides, this OCA over modified asymmetric AMC has a 0.8-dB higher gain than that of the OCA over square/rectangular AMCs described in Section 2.2.3 while the chip area of this OCA reduces from 840 × 1710 to 710 × 1710 μm^2 (by more than 17%). **Figure 4(b)** presents the simulated |S11| and peak gain responses of the OCA over modified asymmetric AMC. Moreover, this OCA is matched (|S11|<-10 dB) from 52 GHz until above 70 GHz covering the bandwidth of interest around the 60-GHz carrier.

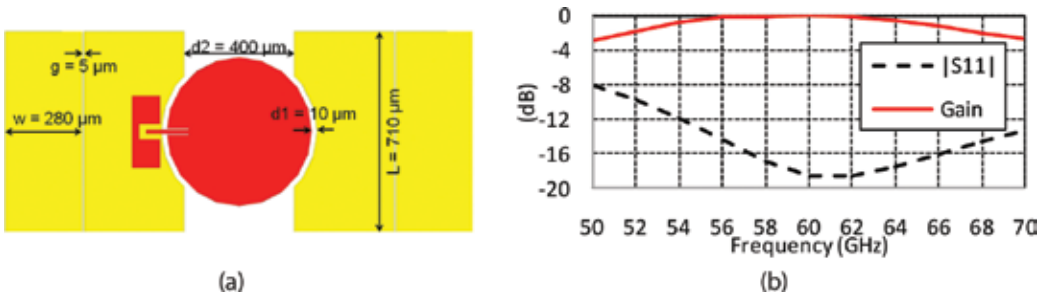

Figure 4. Circular OCA over modified asymmetric AMC: (a) top view and (b) simulated |S11| and peak gain. "Reprinted with permission from Microwave Journal."

3. OCA with distributed N-well grid

In Section 2, the chapter focused on enhancing the gain-to-active-area ratio by employing a modified asymmetric AMC EM shield. Otherwise, this section presents a different procedure based on the semiconductor properties of the PN-junction (PNJ) to improve this ratio. A PNJ creation results from the coexistence of the P and N semiconductor types. A depletion layer, which is carriers' free area, will appear between the two semiconductors' types [22, 23]. Subsequently, in this section, we employ this depletion layer concept in the OCA's gain-to-active-area ratio enrichment, as will be clarified in the following sections.

3.1. Large depletion layer formation

A PNJ is described by its built-in voltage (V_i) and depletion width (x_d) which can be computed by Eq. (2) and Eq. (3), respectively, where, K is Boltzmann constant, T is temperature, q is electron's charge, N_a and N_d are acceptors and donors doping concentrations in P-type and N-type, respectively, while n_i and ε_s are intrinsic doping and permittivity of the silicon, respectively, and V_a is bias voltage applied on the PNJ [22, 23]. The width of depletion on the P-type (x_P) and N-type (x_N) semiconductors can be computed as Eq. (4) [22, 23].

http://dx.doi.org/10.5772/66238

$$V_i = \frac{KT}{q}\ln\left(\frac{N_a N_d}{n_i^2}\right) \tag{2}$$

$$x_d = \sqrt{\frac{2\varepsilon_s}{q}\frac{N_a + N_d}{N_a N_d}\left(V_i - V_a\right)} \tag{3}$$

$$x_P = x_d\frac{N_d}{N_d + N_a} \qquad x_N = x_d\frac{N_a}{N_d + N_a} \tag{4}$$

Typically, a depletion area will be in the range of a few micrometers. However, we achieved a large depletion area by distributing N-type semiconductor within the P-type semiconductor in a manner for which all the targeted area has depleted. **Figure 5** reveals how this criterion is possible. In **Figure 5(a)**, rectangular-shaped N-type semiconductor cells are spread within the P-type with a cell width of $2x_N$ and each of the two sequential cells is separated by $2x_P$ [23]. These values are selected to deplete the formed two PNJs.

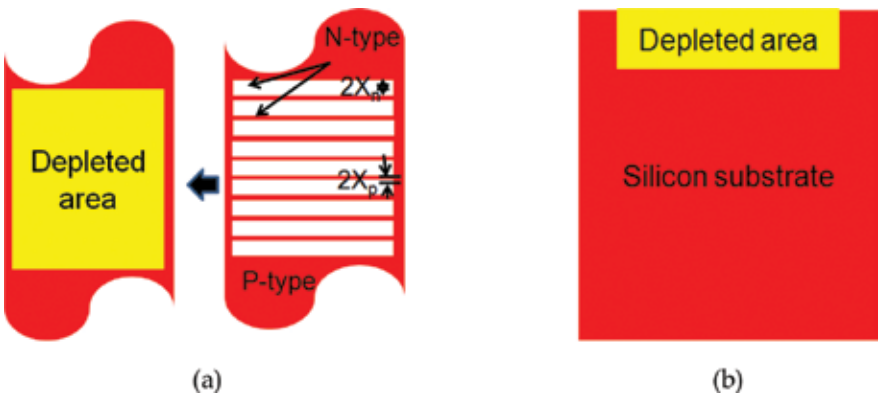

Figure 5. (a) Grid of rectangular-shaped N-type semiconductor on a P-type semiconductor with dimensions that satisfy full depletion condition and its equivalent depleted area. (b) Side view of the depleted region [23].

3.2. Gain-to-active-area ratio improvement using large depletion layer

As shown in **Figure 6(a)**, we have implemented the outsized depletion area below the OCA. This OCA is originally the OCA on modified asymmetric AMC shown in **Figure 4(a)**. The depletion layer has the same dielectric constant as silicon (ε_r = 12), and we modeled its conductivity as σ = 0.1 S/m, representing a very low loss. The depletion depth (t = 20 μm) is equal to the typical height of the N-type material (N-well) in the 0.18-μm CMOS process [23].

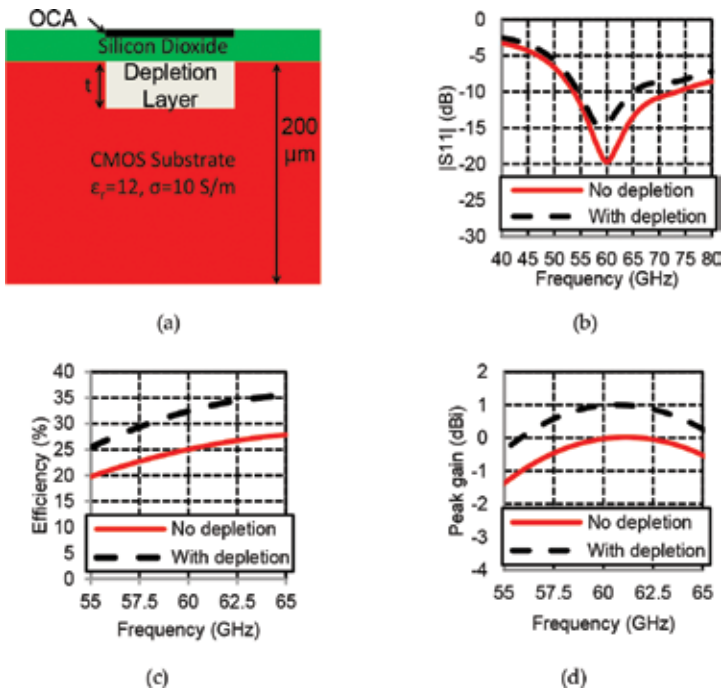

Figure 6. Simulation comparison of the OCA with/without depletion layer below (a) cross-sectional view of the OCA with the depletion zone, (b) |S11|, (c) efficiency, and (d) peak gain [23].

Hereafter, we compare the simulated performance of the OCA on modified AMC with/without depletion area in terms of |S11|, radiation efficiency, and peak gain as shown in **Figure 6(b)–(d)**, respectively. Both OCAs with/without depletion demonstrate a matched response (|S11|<-10 dB) at the bandwidth of interest around 60 GHz. Besides, the existence of the depletion layer leads to the improvement of the radiation efficiency and the peak gain of the OCA. The radiation efficiency is increased at 60 GHz from 25 to 32% as shown in **Figure 6(c)**. Moreover, the peak gain at 60 GHz is improved from 0 to 1 dBi as illustrated in **Figure 6(d)**. The optimized design dimensions of the OCA with depletion layer are similar to the one without depletion layer except x_0 = 44 μm [23].

4. Layout, fabrication, and measurements

4.1. Layout and fabrication

The 0.18-μm CMOS technology used is a TSMC six-metal process. These process six metals are denoted as M1–M6 from bottom to top. The top metal layer "M6" is selected for the circular OCA implementation and its feeding microstrip line for two reasons. First, it has the largest thickness and then it has lower conduction losses than the other metal layers (M1–M5). Second, M6 layer has the highest separation from the lossy CMOS substrate; hence, it should have the

http://dx.doi.org/10.5772/66238

least coupling with the CMOS substrate and the lowest power leakage to it [19, 23]. The other metal layers (M1–M5) are used for the construction of the modified asymmetric AMC. We illustrate the specific layout tips in the following paragraph.

The HFSS and Cadence Virtuoso layouts of the circular OCA on modified asymmetric AMC plan are shown in **Figure 7(a)** and **(b)**, respectively. Also, a photograph of the fabricated OCA is provided in **Figure 7(c)**. We performed a slight change in the feeding position. The modification in the feeding topology targeted the compensation of the measuring pads' low impedance and capacitive nature. The pads' coplanar waveguide (CPW) grounds at M6 are connected using via connections to M1 "the AMC unit cell." Moreover, to fulfill design rules of the TSMC 0.18-μm CMOS process, the design has the following alternations:

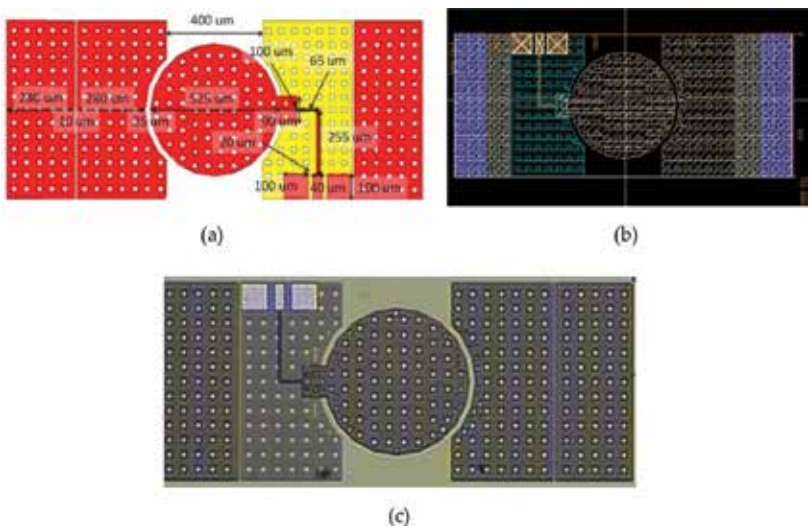

Figure 7. (a) OCA layout at HFSS with dimensions. (b) OCA layout at Cadence Virtuoso. (c) Fabricated OCA.

Minimum density design rule: The two AMC cells far from the circular radiator are redesigned to be composed of a stacked metal from layer 1 (M1) to layer 6 (M6). Also, a layer of polysilicon is included below these AMC cells to fulfill the same purpose. Then, the design is resimulated, and some dimensions are adjusted as shown in **Figure 7(a)** to confirm no/slight effect in performance.

Maximum metal width design rule: 20-μm × 20-μm rectangle slots are etched from all of the metals. These slots' sizes were selected considering that they resonate far beyond the 60-GHz band.

4.2. Measurements

The measurements are performed using a VNA (E8361C PNA 10 MHz to 67 GHz) and a Cascade Microtech manual probe station. A Cascade Microtech calibration kit with part

number "101-190" allowed the ground-signal-ground (GSG) short-open-load-through (SOLT) Calibration for the infinity probe used to measure the |S11| of the fabricated OCAs.

Figure 8 shows the measured matching and gain performance of the OCAs without depletion. This OCA exhibits a matched behavior (|S11|<-10 dB) at the bandwidth of interest with good agreement with the simulated |S11| as shown in **Figure 8(a)**. Also, it has a measured gain of -3 dB at 64 GHz as shown in **Figure 8(b)**. The OCA with depletion area below has the same layout as in **Figure 7** except that it has an additional grid of N-well (N-type material) with width of $2x_n$ = 0.86 μm and separated by $2xp$ = 1.4 μm on the P-type substrate to guarantee the depletion layer formation. The measured |S11| of this antenna is in fair agreement with the simulated performance as shown in **Figure 9**. This OCA underdoes a peak gain of -1.5 dB at 66 GHz. The discrepancy in the gain performances is due to nearby metals, probe pins, and probe body which are not considered in simulations [19, 23]. The OCA with depletion has a 1.5 dB higher gain than that without depletion layer.

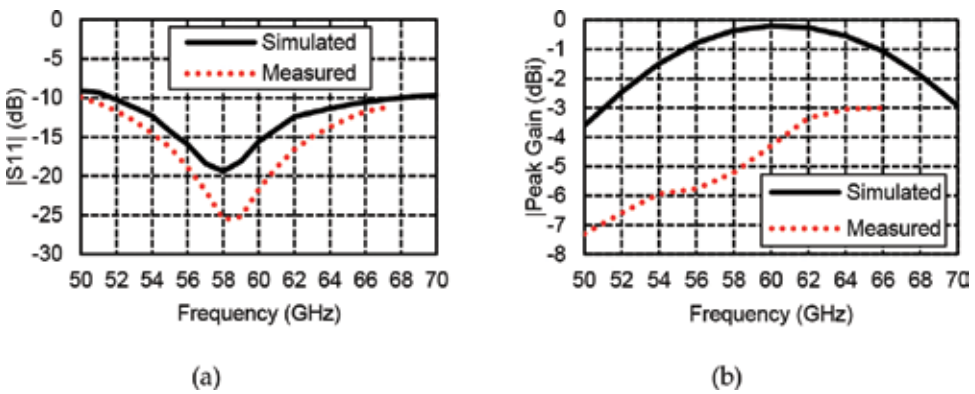

Figure 8. The simulated and measured performances of the OCA on modified AMC without depletion (a) |S11| and (b) peak gain.

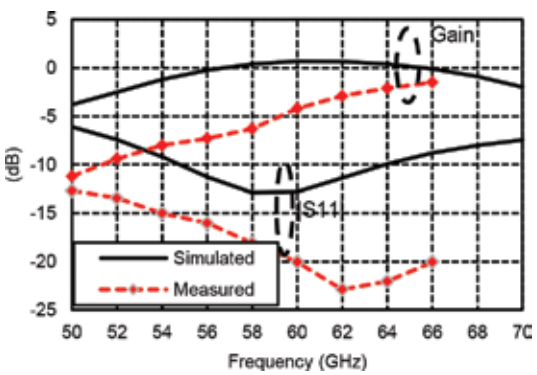

Figure 9. Simulated and measured performance of the OCA with depletion (t = 20 μm) [23].

http://dx.doi.org/10.5772/66238

We used a simple setup based on the reference antenna gain method [24] for the OCA peak gain measurements shown in **Figure 8(b)** and **Figure 9**. First, we performed a VNA insertion loss response calibration by placing a two V-band standard gain horn (SGH) antennas separated by 1 m to calibrate all losses caused by including cables and free-space path loss. Second, the target OCA replaced the receiving SGH while keeping the same measuring distance between the two antennas, and insertion loss ($S_{21_{calibrated}}$) is measured again. Finally, we calculate the OCA gain (G_{OCA}) using Eq. (5), where L_{probe} is losses of feeding infinity® GSG probe and G_{SGH} is receiving SGH antenna gain.

$$G_{OCA} = S_{21calibrated} + L_{probe} + G_{SGH} \tag{5}$$

To enable the measurement of the OCA efficiency and radiation pattern, we used the advanced setup described in [25]. A photograph of the measurement setup is shown in **Figure 10(a)**. For correct handling, the OCA is placed using supporting foam which is mostly invisible to the EM waves as shown in **Figure 10(b)**. A piece of metal is placed below the chip to realize the package ground. We used this setup to characterize the OCA without depletion shown in **Figure 7(c)**. The measured |S11| is in good agreement with the simulated |S11| and is identical to that in **Figure 8(a)** which was measured on probe station.

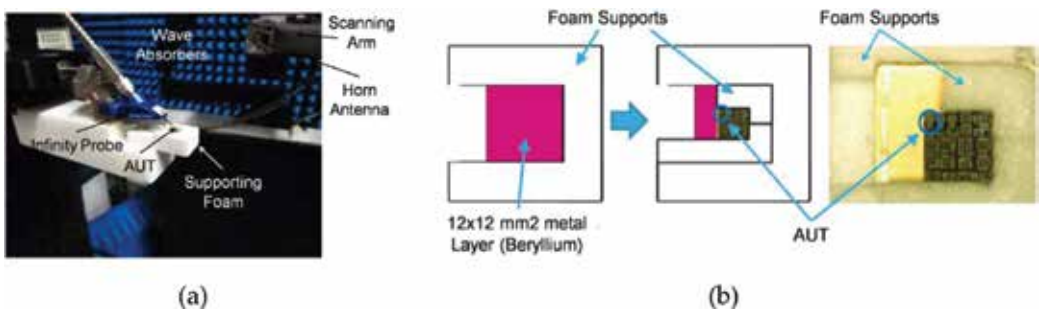

Figure 10. (a) Measurement setup. (b) Visualization of the measurements support structure. "Reprinted with permission from Microwave Journal."

The measured peak gain has a discrepancy of up to 4 dB when compared to the simulated one as shown in **Figure 11(a)**. This inconsistency resulted from the other fabricated structures surrounding the OCA, the probe pins, and the probe body which are not considered in simulations. So, we performed additional simulations to validate these gain measurements. In **Figure 11(b)**, we show another simulation model which we used in this validation. This model considers the nearest fabricated structures which may affect the OCA performance. Using this model, the simulated peak gain noted as "With metals" in **Figure 11(a)** is in fair agreement with the measured results especially for frequencies up to 58 GHz. Other discrepancies between measured and simulated gain may be due to other metals which are not modeled, and also due to the ±0.8-dB accuracy of the measurement setup [25].

Finally, we present the measured E-plane and H-plane radiation patterns at 56, 60, and 64 GHz in **Figure 12**. The E-plane and H-plane are located at XZ- and XY-cut planes, respectively. The radiation patterns are in fair agreements. However, these radiation patterns show some twist especially for the E-plane.

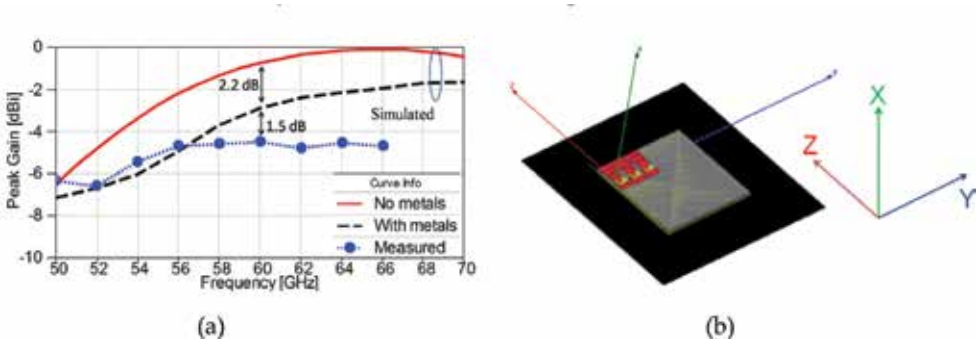

Figure 11. (a) Measurement results using the setup in Ref. [25]. (b) HFSS model for measurement validation. "Reprinted with permission from Microwave Journal."

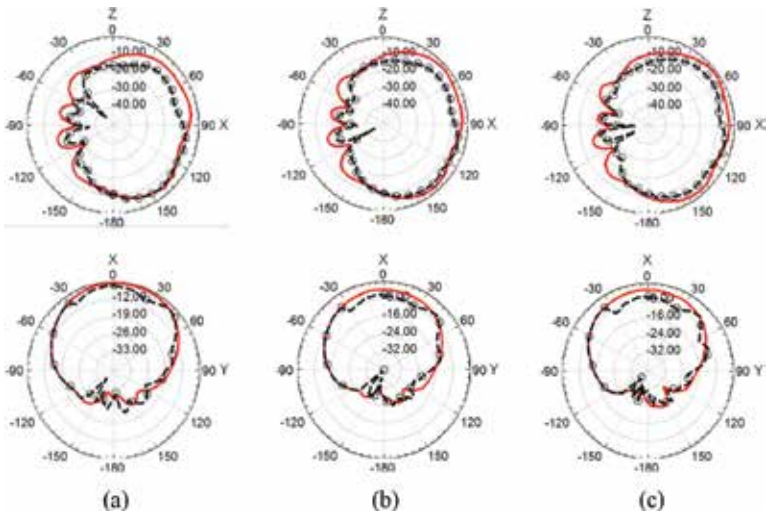

Figure 12. E-plane (top) and H-plane (down) radiation patterns at (a) 56GHz, (b) 60GHz, and (c) 64GHz. Measured (dashed) and simulated (solid). "Reprinted with permission from Microwave Journal."

5. Conclusions

We have presented in this chapter two unconventional distinct techniques to improve the OCAs' performance on CMOS technology regarding a high gain-to-active-area ratio. The first

http://dx.doi.org/10.5772/66238

technique extended the concept of EM shielding using asymmetric AMC, then modified asymmetric AMC. The OCA based on modified asymmetric AMC realized a peak gain of -4 dBi within a chip area of 1.21 mm^2. The second technique employed the PNJ depletion concept to form a large area of low loss. The OCA on modified asymmetric AMC and large depletion area showed a gain of -1.5 dBi on the same area of 1.21 mm^2. The measured gain performances were lower than that predicted by simulation due to the sensitivity of the OCAs to the surrounding chip environment.

Acknowledgements

The authors like to thank Prof. H. Kanaya of Kyushu University, Fukuoka, Japan, and Prof. R. Suga of Aoyama Gakuin University, Tokyo, Japan, for their support in the initial measurements. The authors are grateful for Prof. C. Luxey and Mr. A. Bisognin of the University of Nice Sophia-Antipolis, Nice, France, for performing the complete measurements of the OCA on modified asymmetric AMC. A part of this work is supported by a Grant-in-Aid for Scientific Research (C) (16K06301), and VLSI Design and Education Center partially (VDEC), the University of Tokyo in collaboration with CADENCE and Keysights Corporations.

Author details

Adel T. Barakat[1,2], Ramesh K. Pokharel[1*] and Hala A. Elsadek[2]

*Address all correspondence to: pokharel@ed.kyushu-u.ac.jp

1 Kyushu University, Fukuoka, Japan

2 Electronics Research Institute, Cairo, Egypt

References

[1] Hansen C. J., WIGIG: multi-gigabit wireless communications in the 60 GHz band. IEEE Wireless Communications Magazine. 2011;18(6):6–7. DOI: 10.1109/MWC.2011.6108325

[2] Singh H., Oh J., Kweon C., Qin X., Shao H-R, and Ngo C., A 60 GHz wireless network for enabling uncompressed video communication. IEEE Communications Magazine. 2008;47(12):71–78. DOI: 10.1109/MCOM.2008.4689210

[3] Rappaport T. S., Murdock J. N., and Gutierrez F., State of the art in 60-GHz integrated circuits and systems for wireless communications. Proceedings of the IEEE. 2011;99(8): 1390–1436. DOI: 10.1109/JPROC.2011.2143650

[4] Zhang Y. P., Sun M., and Guo L. H., On-chip antennas for 60-GHz radios in silicon technology. IEEE Transactions on Electron Devices. 2005;52(7):1664–1668. DOI: 10.1109/TED.2005.850628

[5] Hsu S. S., Wei K. C., Hsu C. Y., and Ru-Chuang H., A 60-GHz millimeter-wave CPW-fed yagi antenna fabricated by using 0.18-um CMOS technology. IEEE Electron Device Letters. 2008;29(6):625–627. DOI: 10.1109/LED.2008.920852

[6] Lin C. C., Hsu S. S., Hsu C. Y., and Chuang H. R., A 60-GHz millimeter-wave CMOS RFIC-on-chip triangular monopole antenna for WPAN applications. In: IEEE Antennas and Propagation Society International Symposium; 9–15 June 2007; Honolulu, HI, USA. USA: IEEE; 2007. p. 2522–2525. DOI: 10.1109/APS.2007.4396047

[7] Guo P. J. and Chuang H. R., A 60-GHz millimeter-wave CMOS RFIC-on-chip meander-line planar inverted-F antenna for WPAN applications. In: IEEE Antennas and Propagation Society International Symposium; 5–11 July 2008; San Diego, CA, USA. USA: IEEE; 2008. p. 1–4. DOI: 10.1109/APS.2008.4619464

[8] Wang R., Sun Y., Kaynak M., Beer S., Borngräber J., and Scheytt J. C., A micromachined double-dipole antenna for 122–140 GHz applications based on a SiGe BiCMOS technology. In: IEEE International Microwave Symposium Digest; 17–22 June 2012; Montreal, QC, Canada. USA: IEEE; 2012. p. 1–3. DOI: 10.1109/MWSYM.2012.6258421

[9] Kim J-G. , Lee H. S., Lee H-S., Yoon J-B., and Hong S., 60-GHz CPW-fed post-supported patch antenna using micromachining technology. IEEE Microwave and Wireless Components Letters. 2005;15(10):635–637. DOI: 10.1109/LMWC.2005.856690

[10] Rashid A. B. M. H., Watanabe S., and Kikkawa T., High transmission gain integrated antenna on extremely high resistivity Si for ULSI wireless interconnect. IEEE Electron Device Letters. 2002;23(12):731–733. DOI: 10.1109/LED.2002.805754

[11] Wu R. et al., A 60-GHz efficiency-enhanced on-chip dipole antenna using helium-3 ion implantation process. In: 44th European Microwave Conference; 6–9 October 2014; Rome, Italy. USA: IEEE; 2014. p. 108–111. DOI: 10.1109/EuMC.2014.6986381

[12] Cheema H. M. and Shamim A., The last barrier: on-chip antennas. IEEE Microwave Magazine. 2013;14(1):79–91. DOI: 10.1109/MMM.2012.2226542

[13] Chu H., Guo Y. X., Lin F., and Shi X. Q., Wideband 60GHz on-chip antenna with an artificial magnetic conductor. In: 2009 Radio-Frequency Integration Technology; 9–11 December 2009; Singapore. USA: IEEE; 2009. p. 307–310. DOI: 10.1109/RFIT.2009.5383667

[14] Barakat A., Allam A., Pokharel R. K., Elsadek H., El-Sayed M., and Yoshida K.,Performance optimization of a 60 GHz antenna-on-chip over an artificial magnetic conductor. In: 2012 Japan-Egypt Conference on Electronics, Communications, and Computers; 6–9 March 2012; Alexandria, Egypt. USA: IEEE; 2012. p. 118–121. DOI: 10.1109/JEC-ECC.2012.6186968

[15] Barakat A., Allam A., Pokharel R. K., Elsadek H., El-Sayed M., and Yoshida K., 60 GHz triangular monopole antenna-on-chip over an artificial magnetic conductor. In: 6th European Conference on Antennas and Propagation; 26–30 March 2012; Prague, Czech Republic. USA: IEEE; 2012. p. 972–976. DOI: 10.1109/EuCAP.2012.6206127

[16] Bao X. Y., Guo Y. X., and Xiong Y. Z., 60-GHz AMC-based circularly polarized on-chip antenna using standard 0.18-μm CMOS technology. IEEE Transactions on Antennas and Propagation. 2012;60(5):2234–2241. DOI: 10.1109/TAP.2012.2189725

[17] Yang F. and Rahmat-Samii Y., Electromagnetic band-gap structures in Antenna Engineering, 1st ed. The Cambridge RF and Microwave Engineering Series. Cambridge: Cambridge University Press; 2008. 282 p. DOI: 10.1017/CBO9780511754531

[18] Sohn J. R., Kim K. Y., Tae H.-S., and Lee H. J., Comparative study on various artificial magnetic conductors for low-profile antenna. Progress in Electromagnetics Research. 2006;61: 27–37. DOI: 10.2528/PIER06011701

[19] Barakat A., Allam A., Elsadek H., Abdel-Rahman A. B., Pokharel R. K., Bisognin A., and Luxey C., 60 GHz CMOS circular patch AoC on modified asymmetric AMC. Microwave Journal. Forthcoming.

[20] Cohn S. B., Electrolytic-tank measurements for microwave metallic delay-lens media. Journal of Applied Physics. 1950;21:674–680. DOI: 10.1063/1.1699730

[21] Clavijo S., Diaz R. E., and McKinzie W. E., Design methodology for Sievenpiper high-impedance surfaces: an artificial magnetic conductor for positive gain electrically small antennas. IEEE Transactions on Antennas and Propagation. 2003;51(10):2678–2690. DOI: 10.1109/TAP.2003.817575

[22] Zeghbroeck B. V., Principles of Semiconductor Devices and Heterojunctions. 1st ed. New Jersey: Prentice Hall; 2009. 450 p.

[23] Barakat A., Allam A., Elsadek H., Abdel-Rahman A. B., Pokharel R. K., and Kaho T., Improved gain 60 GHz CMOS antenna with N-well grid. IEICE Electronics Express. 2016; 13(5): 20151115. DOI: 10.1587/elex.13.20151115

[24] Park J., Mun G., Yu D., Lee B., and Kim W. N., Proposal of simple reference antenna method for EMI antenna calibration. In: IEEE International Symposium on Electromagnetic Compatibility (EMC); 14–19 August; Long Beach, CA, USA. USA: IEEE; 2011. p. 90–95. DOI: 10.1109/ISEMC.2011.6038290

[25] Titz D., Ferrero F., and Luxey C., Development of a millimeter-wave measurement setup and dedicated techniques to characterize the matching and radiation performance of probe-fed antennas. IEEE Antennas and Propagation Magazine. 2012; 54(4):188–203. DOI: 10.1109/MAP.2012.6309179

Chapter 6

On-Wafer Microwave De-Embedding Techniques

Xi Sung Loo, Kiat Seng Yeo and
Kok Wai Johnny Chew

Additional information is available at the end of the chapter

http://dx.doi.org/10.5772/66237

Abstract

Wireless communication technology has kept evolving into higher frequency regime to take advantage of wider data bandwidth and higher speed performance. Successful RF circuit design requires accurate characterization of on-chip devices. This greatly relies on robust de-embedding technique to completely remove surrounding parasitics of pad and interconnects that connect device to measurement probes. Complex interaction of fixture parasitic at high frequency has imposed extreme challenges to de-embedding particularly for lossy complementary metal oxide semiconductor (CMOS) device. A generalized network de-embedding technique that avoids any inaccurate lumped and transmission line assumptions on the pad and interconnects of the test structure is presented. The de-embedding strategy has been validated by producing negligible de-embedding error (<−50 dB) on the insertion loss of the zero-length THRU device. It demonstrates better accuracy than existing de-embedding techniques that are based on lumped pad assumption. For transistor characterization, the de-embedding reference plane could be further shifted to the metal fingers with additional Finger OPEN-SHORT structures. The resulted de-embedded RF parameters of CMOS transistor show good scalability across geometries and negligible frequency dependency of less than 3% for up to 100 GHz. The results reveal the importance of accounting for the parasitic effect of metal fingers for transistor characterization.

Keywords: CMOS, de-embedding, microwave frequencies, scattering parameters, test structure

1. Introduction

Aggressive scaling of complementary metal oxide semiconductor (CMOS) devices over the past decades has led to tremendous increase in speed, making it suitable to be employed in

radio frequency circuits. Current CMOS devices (28 nm) are able to deliver maximum ft (maximum cut-off frequency) of 340 GHz [1] with superior improvement in noise, power, and gain performance. **Table 1** shows the key comparisons of transistor performance characteristics at various technology nodes.

Technology node (nm)	180	130	90	40	28
Supply voltage (V)	1.8	1.5	1.2	1.1	1.05
Peak cut-off frequency, ft (GHz)	60	75	140	260	340
Peak transconductance, gm (μS/μm)	562	809	1030	1128	1377

Table 1. Performance-related characteristics of GLOBALFOUNDRIES' NFET (N-type field-effect transistor) at different technology nodes.

However, the growing complexity of radio frequency-integrated circuits requires highly accurate CMOS device model to predict the circuit behavior correctly for successful design. Therefore, accurate and precision RF measurement data are essential to ensure high quality of RF CMOS model developed. Nevertheless, raw measurement data itself does not represent the high-frequency behavior of intrinsic CMOS device as it includes parasitic effects of test structure. Therefore, additional data processing steps, known as de-embedding, are required to remove the impact of test structure parasitic effects from the raw noise measurement data. De-embedding is challenging for RF characterization of short channel device as parasitic effect of interconnects and lossy Si substrate would appear much larger than the device itself. The reason is that interconnects of test structure do not scale proportionally with CMOS device size as minimum distance between probes has to be maintained to avoid collision. Further, the parasitic effects of test structures (i.e. substrate interaction, distributed effect of interconnects, etc.) become more complex at higher measurement frequency and require more sophisticated de-embedding technique. The aim of this chapter is to present an insight of microwave de-embedding theory and knowledge on various techniques to overcome challenges at high frequencies.

Many de-embedding techniques have been reported up to date. They could be broadly classified as lumped circuit model-based technique [2–6] and network model-based technique [7–12]. As the name implies, the aforementioned techniques model the test fixture parasitics as a combination of parallel-series connections of discrete components. Nevertheless, such a de-embedding technique could not be used to address the distributed effect of metal interconnect. In order to overcome the deficiency mentioned, the network model-based de-embedding techniques [7–12] have been proposed. In particular, the technique proposed in Ref. [7] is renowned for its high generality as it models the surrounding fixture parasitic as a single four-port network without any assumptions made on the network topology. However, it requires five test structures and suffers accuracy degradation at very high frequencies due to ideality assumptions made on the intrinsic standards of dummy test structures. Instead, cascade network model-based de-embedding techniques [8–12] offer alternate way to address

http://dx.doi.org/10.5772/66237

the distributed effects of metal interconnects without any precision standards required. Nevertheless, techniques in Refs. [8–11] require lumped assumption on the pad parasitics.

A generalized cascade-based de-embedding technique [12] that addresses the distributed effects of pad and interconnect parasitics will be presented in this chapter. It utilizes unique combination of pad and line de-embedding structures that avoid any lumped assumptions. The description covers parasitic model adopted, de-embedding structures used, and corresponding mathematical de-embedding algorithm in separate subsections. Also, an extension of cascade-based de-embedding technique [13] to further remove the metal finger parasitics of CMOS transistor will be detailed in Section 5. Finally, the validation results of the de-embedding methodology will be presented and supplemented by comparison against existing de-embedding techniques.

2. Test structure

Direct probing on transistor device is impossible due to its minute size. Therefore, test structure is introduced to provide essential electrical interface in between the embedded device and measurement probes through its bond pads and metal interconnections. However, these test fixture components introduce undesirable parasitic effects that lead to error in the device measurements. Particularly, the CMOS test structure is fabricated on silicon substrate that is more lossy than alumina substrate in impedance standard substrate (ISS). One way to reduce the impact of these fixture parasitics is to optimize the design of test structure. **Figure 1(a)** and **(b)** shows the top and cross-sectional view of G-S-G test structure used for characterization of an Negative channel Metal-Oxide Semiconductor (NMOS) device. There are three bond pads with appropriate sizes (70 μm × 60 μm) and separation pitches (50 μm) on both side of test fixture for locating the ground and signal probes at each port. Signal interconnects are used to connect gate and drain lead of NMOS devices to bond pads at input and output ports, respectively. As shown in **Figure 1(b)**, it is actually a metal-via stack that consists of three metal layers, Metal 6 to Metal 8 (M6–M8). Sufficient length of interconnects (>50 μm) is required to avoid possible collision and interference between probes. Also, wide interconnects (10 μm) provide low-resistance paths to gate and drain terminals. The test structure is developed based on shielded design [14] where a wide Metal 1 (M1) ground conductor is included to mitigate the substrate coupling effect. It is connected to the ground bars (M1–M8 metal-via stacks) and is tied to silicon substrate through P+ implants. Since the Metal 1 metal shield is large in size, it provides low-resistive ground connections to all ports. Meanwhile, the NMOS device lies inside the fixture gap of Metal 1 shield where it is directly exposed to silicon substrate. **Figure 2** shows the enlarge view of NMOS transistor. The transistor possesses interdigitated layout whereby the source and drain regions are shared for the reduction of parasitic resistance and capacitance. Nevertheless, layout optimization could only partially suppress the fixture parasitic effect, and further de-embedding is required to remove effects of these fixture parasitics from measurements particularly when it gets worsened at high frequencies.

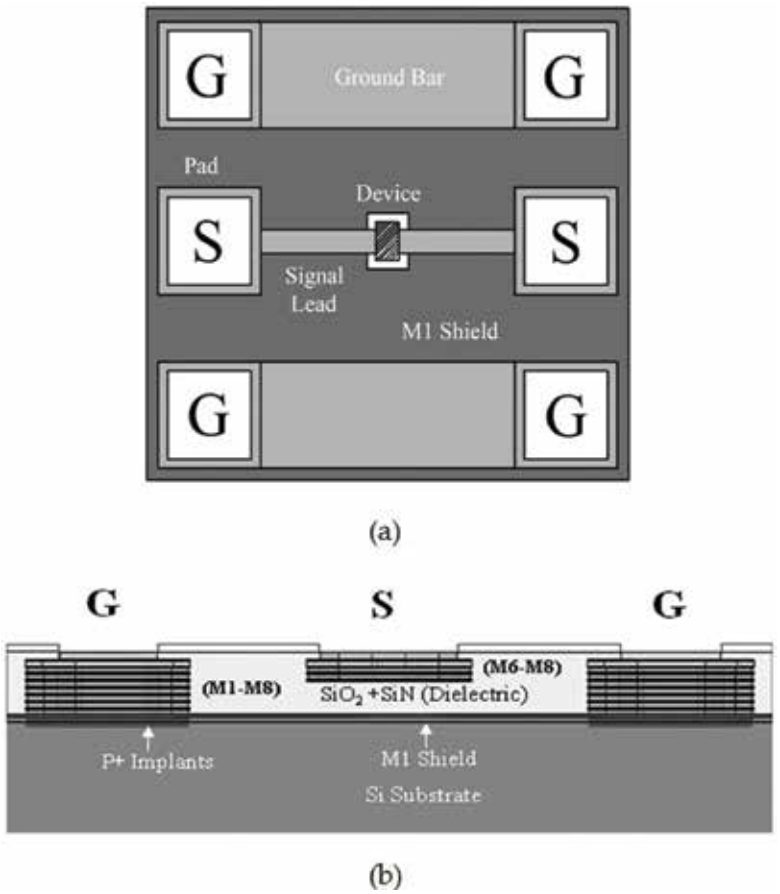

Figure 1. (a) Top schematic and (b) cross-sectional view of transistor test fixture for GHz probing.

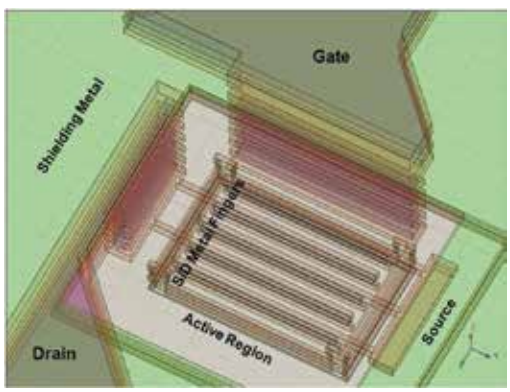

Figure 2. Enlarge view of transistor device embedded in test fixture.

http://dx.doi.org/10.5772/66237

3. Overview of de-embedding techniques

Two popular categories of de-embedding techniques are reviewed theoretically in this section. They are equivalent circuit model-based de-embedding and cascade network model-based de-embedding.

3.1. Equivalent circuit model-based de-embedding

In this method, device (transistor) test fixture is modeled by an equivalent circuit which is basically complex combinations of fixture parasitic components and intrinsic device itself. Network parameters of intrinsic device could be de-embedded from raw S-parameter measurements, provided that the network parameters of fixture parasitic are known. This could be determined through a set of S-parameter measurements on dummy test structures. The number of dummy test structures required typically increase with the complexity of parasitic circuit model. Specifically, open-short de-embedding methodology [2] has been widely adopted for transistor characterization due to its sufficient accurate prediction of fixture parasitic for conventional microwave frequencies of interest at below 30 GHz. As the name implies, it requires an OPEN dummy test structure which consists of only test fixture frame (without intrinsic device) and a SHORT dummy test structure that is associated with short-circuited interconnections for complete characterization of fixture parasitics. The equivalent circuit models of required test structures are shown in **Figure 3**.

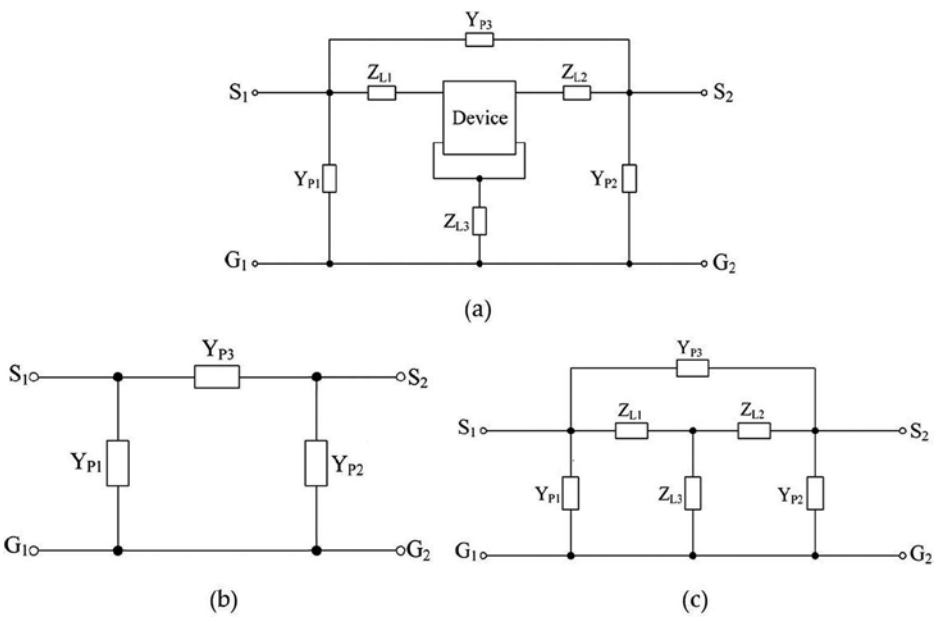

Figure 3. (a) Equivalent circuit model of DUT for open-short de-embedding [6]. (b) π-Circuit model of OPEN dummy test structure. (c) Equivalent circuit model of SHORT dummy test structure for Open-Short de-embedding.

In the device under test (DUT) model (**Figure 3(a)**), admittance component, Y_{p3}, is used to determine the amount of cross talk between port 1 and port 2 due to substrate coupling and fringing capacitances. On the other hand, admittance components, Y_{p1} and Y_{p2}, measure the parasitic capacitances that exist between bond pad and ground for left and right ports. Meanwhile, the metal parasitic components are modeled by a T-network which connected in series with the intrinsic device. Specifically, the series parasitic of metal lines that appear at left and right port is represented by Z_{L1} and Z_{L2}, respectively. Meanwhile, the dangling ground lead parasitic is denoted as Z_{L3}. By employing a two-port network theory for parallel-series network, intrinsic device admittance matrix, Y_{DEV}, could be easily extracted from raw measurements on test structures by Eq. (1).

$$Y_{DEV} = \left[\left(Y_{DUT} - Y_{OPEN} \right)^{-1} - \left(Y_{SHORT} - Y_{OPEN} \right)^{-1} \right]^{-1} \tag{1}$$

3.2. Cascade network model-based de-embedding

At much higher frequency where the length of metal interconnects approaches one-tenth of the frequency wavelength, fixture parasitic could no longer be described by lumped circuit model due to worsening of distributed effect. Fortunately, the problem could be overcome with a network model-based de-embedding technique, which is basically the extension of S-parameter probe-tip calibration techniques (SOLT, TRL, LRRM, etc). The cascade configuration model used to describe S-parameter measurement system is now applied on test fixture model instead. The pad and interconnect parasitics of test fixture are now modeled as error adapters connected in cascade with intrinsic device at left and right port. High generality is achieved with this method as interconnect parasitic is characterized by network parameters instead of inaccurate lumped circuit models. Unlike calibration, fixture parasitic is characterized via measurements of de-embedding structures due to unavailability of accurate on-wafer calibration standards. More recently, on-wafer TRL calibration has been reported [15] to directly remove on-wafer parasitics without extra de-embedding steps and known standards needed. However, it is not suitable for modeling since broadband accuracy is unachievable. Also, it is more recommended to be used with expensive gold pads, low substrate loss process, and high layout symmetry for improved accuracy [15].

In conventional cascade-based de-embedding approaches [8–11], probe pads and interconnects of test fixture are characterized by separate networks that are connected in cascade configuration (**Figure 4(a)**). Similarly, THRU structures are used to extract the two-port network parameters or transmission line parameters of interconnects directly. Specifically, the probe pad network is simplified to lumped circuit model which consists of only one parallel admittance element, Y_{PAD} [8, 9], or encompass additional series pad impedance, Z_{PAD} [10, 11]. PAD OPEN structure is commonly used for finding pad to ground admittance, Y_{PAD}, while PAD SHORT structure is used in [10] to determine the series pad impedance, Z_{PAD}. The major drawback of these techniques is that the pad-line discontinuity effect is not accounted, and extraction of series pad impedance is associated with obvious SHORT interconnection parasitic that span from top metal to bottom ground metal. Although no SHORT structure is used in

http://dx.doi.org/10.5772/66237

lumped cascade approach [16], it is unable to account for distributed effects of metallic parasitics. In effort to avoid the deficiencies mentioned, an alternate algorithm has been presented by the authors [11] whereby only THRU structures are used to extract both pad and interconnect parasitics directly. Two set of THRU structures (THRU LL', THRU LH and THRU R'R, THRU RH) are used for determining the network parameters of interconnect at left and right ports, respectively. With each fixture block being characterized using Ref. [11], network parameters of transistor could simply be extracted from raw measurements through chain matrix manipulations as shown in Eq. (2):

$$A_{DEV} = A_{IN}^{-1} A_{DUT} A_{OUT}^{-1} \tag{2}$$

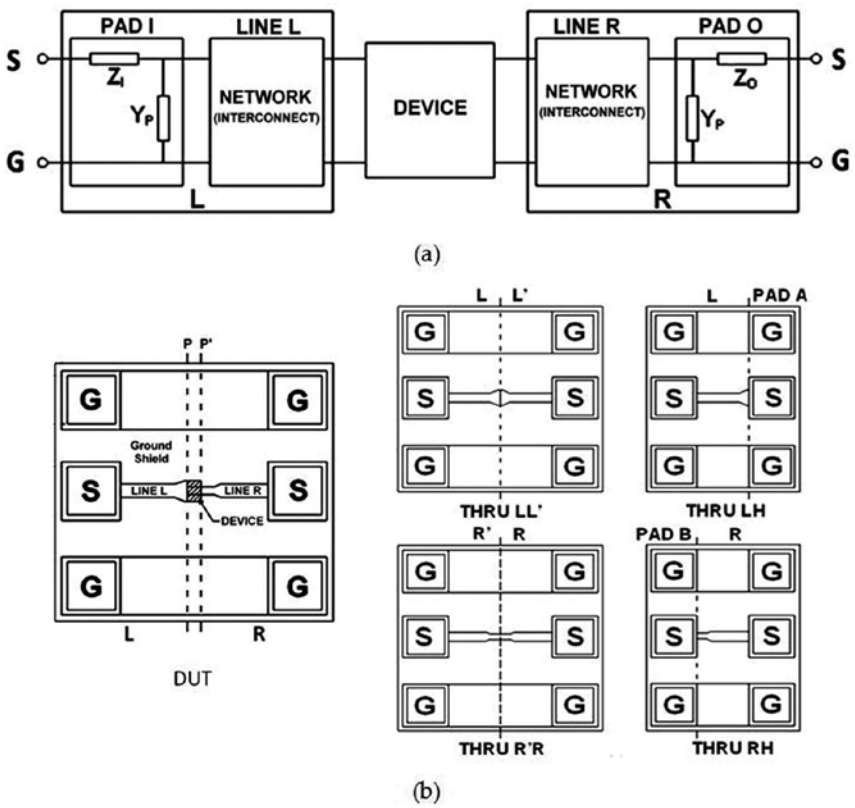

Figure 4. (a) DUT model for author's THRU-based cascade network-based de-embedding approach. (b) Schematic diagram of associated test structures used for author's THRU-based cascade network-based de-embedding technique [11].

For symmetrical DUT structure, the number of THRU structures required for cascade-based de-embedding approach could be reduced further from four to two. Also, the interaction between ports due to leaky substrate and fringing capacitances could be accounted with additional OPEN structure as described in Ref. [17].

4. Generalized cascade-based de-embedding technique

Despite improvement has been made by existing cascade-based de-embedding techniques to address the distributed effects of interconnects, still the pad counterpart is approximated by lumped circuit element. Such issue could potentially be resolved by four-port de-embedding technique in Ref. [7], which avoids any circuit assumption made on the pad and network topology of fixture parasitics. Nevertheless, it requires precision or ideal standards that are unable to be realized on practical CMOS technology. The size of the pad is normally fixed by the dimension of measurement probes and cannot be reduced for optimization of parasitics. As a results, the pad length could become comparable with interconnect length that is usually optimized to be short for parasitic reduction. In effort to overcome the drawback mentioned, a generalized cascade-based de-embedding technique [12] is presented in this section. It utilizes unique combinations of two THRU structures that enable efficient de-embedding of fixture parasitics without any inaccurate lumped pad approximation or requirement of known standards.

4.1. De-embedding concept

Similar to existing cascade de-embedding approaches describe in Section 4, the DUT structure is represented by interconnections of input (L) and output (R) network adapters that appear at both ports of the embedded device (**Figure 5(b)**). Shielded-based test structure is used here to mitigate the forward coupling effect between two ports [14] as described in Section 2. These fixture network adapters (L, R) include the parasitic contribution of probe pads and metal lines of arbitrary lengths (x1, x2). The main advantage of this de-embedding technique is that it does not require any lumped assumption on the pad parasitics since the network parameters of the fixture adapters could be computed directly from measurements on designated de-embedding structures described in the next subsection.

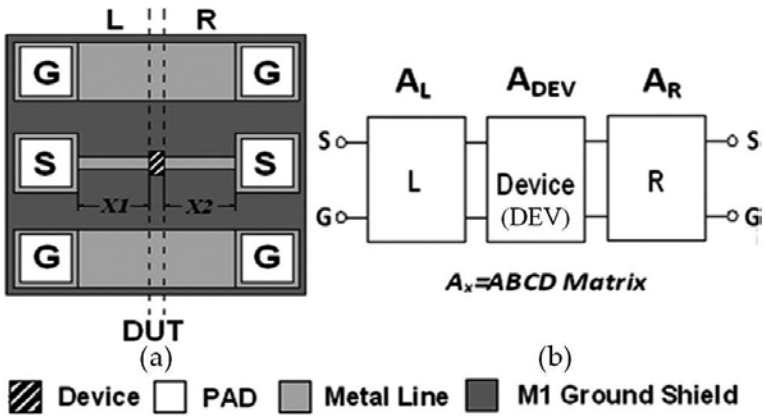

Figure 5. (a) Shielded DUT structure used in device measurement. (b) It is modeled as cascade connections of fixture parasitic networks (L, R) and device [12].

http://dx.doi.org/10.5772/66237

4.2. De-embedding structure

As illustrated in **Figure 6(a)**, two types of THRU de-embedding structures are adopted for extraction of fixture parasitics, namely, THRU LLR and THRU LR structures. The THRU LR structure is simply direct connections of left and right half of test fixture excluding embedded device. Thus, its bond pads and metal line have the same total length as those in DUT structure. Meanwhile, the THRU LLR structure is equivalent to direct connections of left half section of test fixture to the left port of THRU LR structure. Based on the physical layout of the de-embedding structures described, their two-port network models could be determined as illustrated in **Figure 6(b)**. Thus, their cascade matrix (A_{LR}, A_{LLR}) are related to those of fixture parasitic networks (A_L, A_R) by Eq. (3):

$$A_{LR} = A_L A_R \text{ and } A_{LLR} = A_L A_L A_R. \tag{3}$$

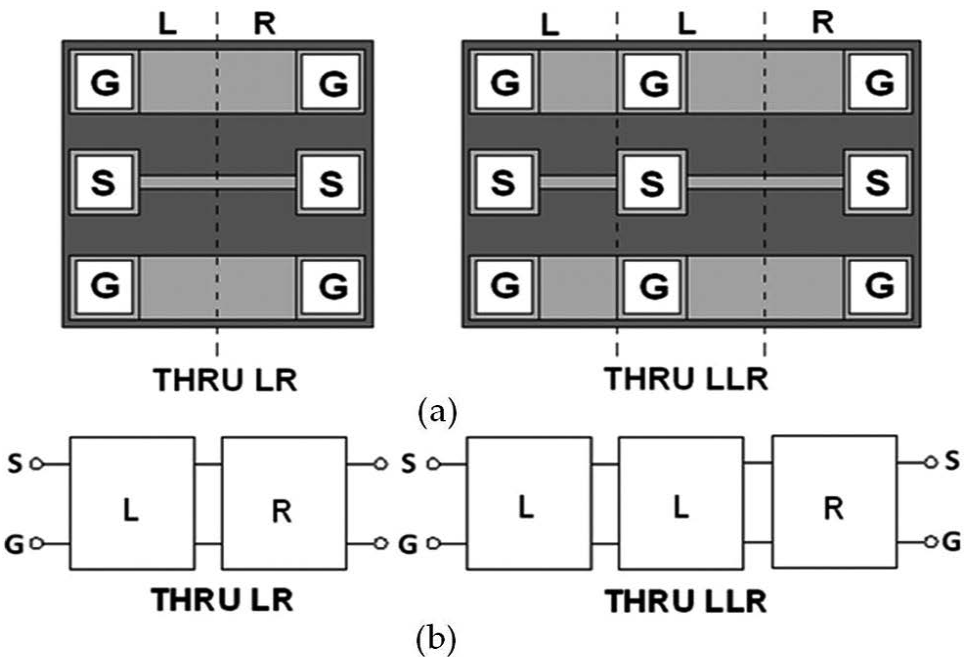

Figure 6. (a) De-embedding structures (THRU LR, THRU LLR) used. (b) They are equivalent to cascade connections of fixture network adapters (L, R) [12].

4.3. De-embedding procedures

The procedure for S-parameter de-embedding is listed as follows:

1. Measure S-parameters of all test structures and convert them into ABCD matrices (A_{DUT}, A_{LR}, and A_{LLR}).

2. Based on the ABCD matrix expression above, determine A_L by $A_{LLR}A_{LR}^{-1}$ and AR by $A_L^{-1}A_{LR}$ with A_L computed.

3. Finally, de-embed both A_L and A_R from measured ABCD matrix of DUT, A_{DUT}, by Eq. (4) to obtain A_{DEV}:

$$A_{DEV} = A_L^{-1} A_{DUT} A_R^{-1} \tag{4}$$

Further correction of forward coupling effect could be achieved with additional OPEN structure as detailed in Ref. [17]. Overall, the generality of the de-embedding technique is improved as the cascade network parameters determined (A_L, A_R) are valid regardless of their internal circuit configuration. Besides that, the de-embedding methodology is greatly simplified as no determination of pad parasitics or transmission line parameters are required.

4.4. De-embedding validation

In order to validate the de-embedding technique presented above, measurements are carried out on test structures using the E8361 PNA and calibrated to probe tips using LRRM technique [18]. The DUT used for validation has symmetrical layout (x1 = x2) whereby both halves of test fixture are mirrored copies of each other. For such condition, the ABCD matrices of L and R parasitic networks are related by $A_L = IA_R^{-1}I$ and vice versa $A_R = IA_L^{-1}I$ where $I = \begin{bmatrix} -1 & 0 \\ 0 & 1 \end{bmatrix}$ is the permutation matrix. Possible extraction errors due to process variations in between the test structures could be minimized by arithmetic averaging of AL (or AR) with $IA_R^{-1}I$ $\left(\text{or } IA_L^{-1}I\right)$. Here, the de-embedding validation is performed on 0.13 μm CMOS devices and compared with other techniques [2, 9].

4.4.1. Verification on zero-length THRU

The de-embedding accuracy of interconnect and pad parasitics is verified on THRU device of zero electrical length. Theoretically, it exhibits constant transmission coefficient S_{21} of 1 across frequencies since no parasitics associated with its intrinsic behavior. This could be done by applying de-embedding on the THRU LR structure where interconnects at both ports are connected. The deviations of de-embedded S_{21} from theoretical value are shown in **Figure 7**. Note that the de-embedding error by conventional OPEN-SHORT de-embedding technique [2] is relatively higher than the cascade-based methods in [9] and current work due to inaccurate lumped approximations of fixture parasitic. These results show that the proposed de-embedding method is more accurate than [9] at high frequencies (S_{21} error <0.01 at 50 GHz) since no lumped pad assumption is made in the fixture model.

http://dx.doi.org/10.5772/66237

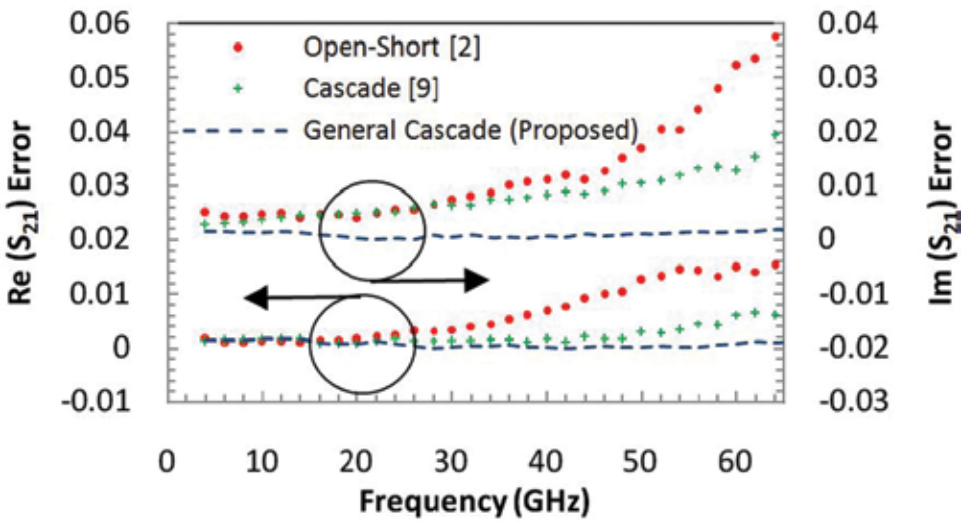

Figure 7. De-embedded S_{21} (real and imaginary) of THRU device versus frequency [12].

4.4.2. Frequency dependencies of transistor parameters

Next, the de-embedding techniques proposed in the current work are validated on frequency dependencies of transistor gate capacitances, C_{gg0}, C_{gd0}, and transconductance, gm. **Figure 8(a)** shows the de-embedded transistor gate capacitances (width = 32 μm, length = 0.13 μm) at zero DC biases where no quasi static effects occur. It could be calculated from $Im(Y_{11DEV})/\omega$ [19]). Under such circumstances, the transistor gate capacitance exhibits constant behavior across frequencies. The de-embedded C_{gg0} by the de-embedding technique in current work reflects physical behavior described since it is nearly independent of frequencies. It varies only by 2.3% for frequency span of 64 GHz when compared to 10% and 5% by Koolen et al. [2] and Cho et al. [9], respectively. Note that the study by Cho et al. [9] shows more physical results than the study by Koolen et al. [2] as the distributed effects of metal lead are taken into consideration. Still, it demonstrates less physical results than proposed de-embedding technique as the distributed effects of pad are ignored. Meanwhile, the transistor gate drain capacitance could be extracted by $(-Im(Y_{12DEV})/\omega)$. **Figure 8(a)** demonstrates the de-embedded transistor gate drain capacitances at zero bias. The comparison of de-embedding results shown is consistent with previous on the order of frequency dependency.

The de-embedding validation discussed is further extended to transconductance of transistor in active region (Vgs = Vds = 1.2 V). It could be extracted from real part of Y-parameters, Y_{21}. The comparison results in **Figure 8(b)** show that the de-embedded gm by Koolen et al. [2] and Cho et al. [9] unphysically enhanced over wide range of frequencies despite worsening impact of non-quasi static effects [19]. Meanwhile, the de-embedded gm by the proposed de-embedding technique is more physical as it demonstrates attenuation over 5% at 64 GHz.

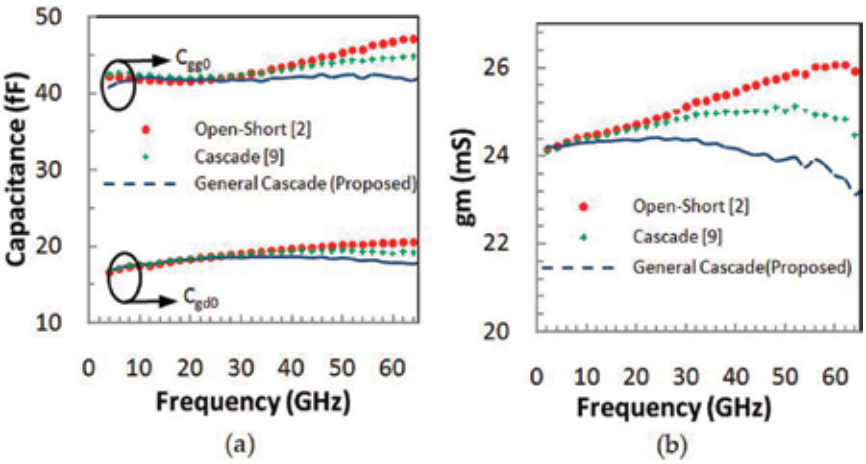

Figure 8. De-embedded parameters of 0.13 μm NMOS transistor versus frequency ((a) C_{gg0}, C_{gd0}, at Vgs = Vds = 0 V and (b) transconductance, gm at Vgs = Vds = 1.2 V) [12].

5. De-embedding metal finger parasitics with hybrid methodology

The de-embedding techniques discussed in previous section focus primarily on removal of pad and interconnect parasitic at top metal level. Nevertheless, it is desirable to establish de-embedding reference plane as close as possible to the device boundary through additional removal of metal fingers parasitic and interconnect via stack. Although several de-embedding techniques [5, 6] have been reported to remove the test fixture parasitics for up to metal fingers, it requires lumped assumptions on interconnects and pad parasitics. Meanwhile, cascade-based de-embedding techniques alone [8–12] are not suitable for removal of metal finger parasitics due to complex inter-couplings between two ports.

In effort to overcome the deficiencies of aforementioned techniques, a hybrid Pad-Line Finger de-embedding technique [13] is presented in this section for mm-wave characterization and modeling of two-port transistor devices. It could simultaneously account for distributed effects of metallic conductors and metal finger parasitics through mix combinations of cascade and lumped series-parallel de-embedding approaches.

5.1. De-embedding concept

Based on the nature of fixture parasitics mentioned, the DUT structure could be described by mix combinations of cascade series-parallel model as shown in **Figure 9**. Similar to de-embedding technique [12] presented in the previous section, metal lines and pads are modeled by generalized cascade network models (PAD, LINE1, 2) to address their transmission line effects. In addition to that, the resistive and coupling characteristics of interdigital fingers are described by series-parallel model (FP, FS).

http://dx.doi.org/10.5772/66237

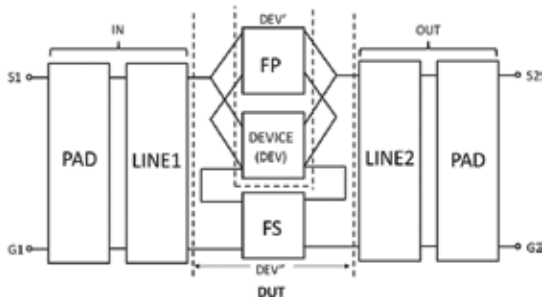

Figure 9. Device under test (DUT) structure modeled as hybrid cascade-series-parallel combinations of two-port device and parasitic networks [13].

5.2. De-embedding structures

Two types of THRU structures (LINE2, PAD-LINE2) are used to extract cascade network parameters of fixture adapters that consist of pad and interconnect parasitics. They consume around 50% less silicon area than those used in the previous section.

As shown in **Figure 10**, the LINE2 structure is equivalent to right half section of DUT structure with pad attached to its left port. On the other hand, the PAD-LINE2 structure differs from LINE2 structure that its left pad is associated with twice of pad length ($2 \times l_{PAD}$). Parasitic extraction for asymmetrical DUT requires additional LINE1 + 2 structure that has total line length of $l_1 + l_2$. It is equivalent to THRU LR structure presented in the previous section. Further extraction of metal finger parasitics is taken care by FINGER OPEN and FINGER SHORT structures. They differ from existing OPEN and SHORT structures that the metal fingers exist in their layouts. Specifically, the FINGER OPEN structure is the same copy of DUT structure but without active region lies underneath the metal fingers. Finally, the FINGER SHORT is similar to FINGER OPEN structure but with source-drain fingers extended and shorted to the gate metals at both ends. Based on the layout configurations, the equivalent network models of the de-embedding structures could be determined as illustrated in **Figure 11**.

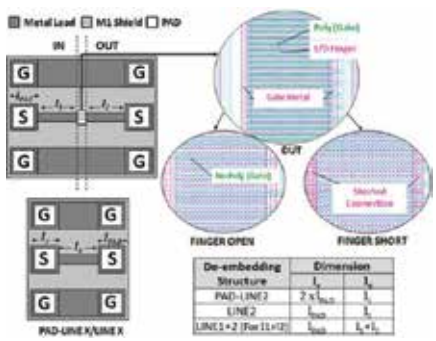

Figure 10. Schematic layout of DUT and de-embedding structures used [13].

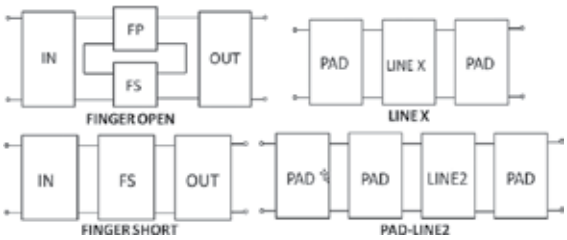

Figure 11. Equivalent parasitic network models of de-embedding structures [13].

5.3. De-embedding procedure

The de-embedding procedure is summarized as follows:

1. Measure S-parameters of all test structures and convert them into cascade ABCD matrices (A_{DUT}, A_{LINE2}, $A_{PAD\text{-}LINE2}$, $A_{FINGER\ OPEN}$, $A_{FINGER\ SHORT}$, and optional $A_{LINE1+2}$).

2. Compute ABCD matrix of input pad by Eq. (5):

$$A_{PAD} = A_{PAD\text{-}LINE2} A_{LINE2}^{-1}. \tag{5}$$

3. Compute ABCD matrix of output half fixture by Eq. (6):

$$A_{OUT} = A_{PAD}^{-1} A_{LINE2} \tag{6}$$

4. Compute ABCD matrix of input half fixture by Eq. (7):

$$A_{IN} = IA_{OUT}^{-1} I \; or A_{IN} = A_{LINE1+2} A_{OUT}^{-1} \text{ for the case of } l1 \neq l2 \text{ where, } I = \begin{bmatrix} -1 & 0 \\ 0 & 1 \end{bmatrix} \tag{7}$$

5. Calculate the resultant ABCD matrix, $A_{DEV''}$ after de-embed the cascade parasitic network components using Eq. (8):

$$A_{DEV''} = A_{IN}^{-1} A_{DUT} A_{OUT}^{-1} \tag{8}$$

Convert the de-embedded results into Z-matrix, $Z_{DEV''}$.

6. Compute ABCD matrix of series parasitic network by Eq. (9):

$$A_{FS} = A_{IN}^{-1} A_{FINGERSHORT} A_{OUT}^{-1} \tag{9}$$

and convert A_{FS} into equivalent Y-matrix, Y_{FS}.

7. Compute Z-matrix of parallel FP network by $Z_{FP} = Z'_{FP} - Z_{FS}$ where ABCD matrix of Z'_{FP}' is computed from $A_{IN}^{-1} A_{FINGEROPEN} A_{OUT}^{-1}$. Convert Z_{FP} into equivalent Y-matrix, Y_{FP}.

8. De-embed series metallic parasitic of routing fingers by Eq. (10):

$$Z_{DEV'} = Z_{DEV''} - Z_{FS} \tag{10}$$

9. Finally, de-embed parallel coupling parasitic of fingers by Eq. (11):

$$Y_{DEV} = Y_{DEV'} - Y_{FP} \tag{11}$$

5.4. De-embedding results and discussion

In this section, the de-embedding methodology presented is verified and demonstrated on various performance parameters of the 40 nm CMOS transistor. Specifically, the de-embedding results are supplemented by comparisons with [9] to investigate the impact of metal finger parasitic on transistor de-embedding. The experimental results discussed are based on the same measurement setup as previous with exception that the characterization frequency is further extended up to 100 GHz for benchmarking against [2] and previous work [6].

5.4.1. Verification against electromagnetic simulation

The extracted insertion loss of cascade parasitics at input (IN) and output (OUT) port is validated against electromagnetic simulation (EM) by Integrand's EMX tool. It generates electromagnetic simulations based on boundary element method. As shown in **Figure 12**, the extracted and simulation results agree well with each other. The deviation error of extracted results is within 2% for entire frequency span of 100 GHz.

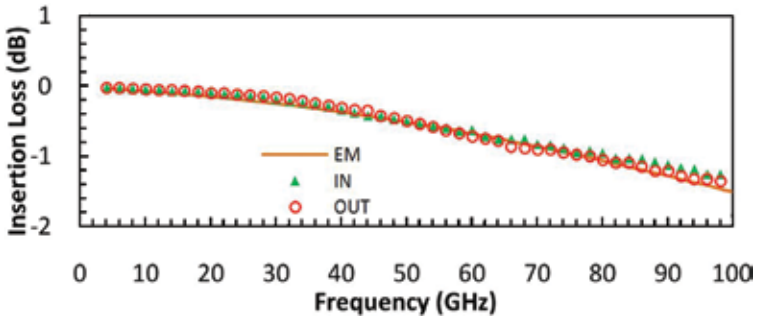

Figure 12. Simulated and extracted insertion loss of input (IN) and output (OUT) network [13].

5.4.2. Scalability of transistor gate capacitance

De-embedding verification on the scalability of transistor gate capacitance provides useful indication on whether the de-embedding technique is correctly applied for up to metal finger. It could be extracted directly from de-embedded Y-parameters ($Im(Y_{DEV,11})/\omega$) [20] as mentioned in previous section. Interestingly, it becomes frequency independent when the non-quasi static effect of the transistor is negligible. This occurs when the transistor is in cut-off mode since no transcapacitance exists in between its gate and drain terminals [21]. **Figure 13** shows the frequency characteristics of de-embedded gate capacitances across different width geometries of transistors at zero bias and frequency of 8 GHz. They are compared against simulation results by GLOBALFOUNDRIES' 40 nm CMOS model. The results clearly show that the de-embedded transistor gate capacitance by the proposed distributed hybrid de-embedding method is scalable and closely agrees with the simulation results. Meanwhile, the de-embedded results by existing cascade-based de-embedding [9] demonstrate larger gap and less scalability. This shows that exclusion of metal finger parasitics in de-embedding has clear impact even at low frequency.

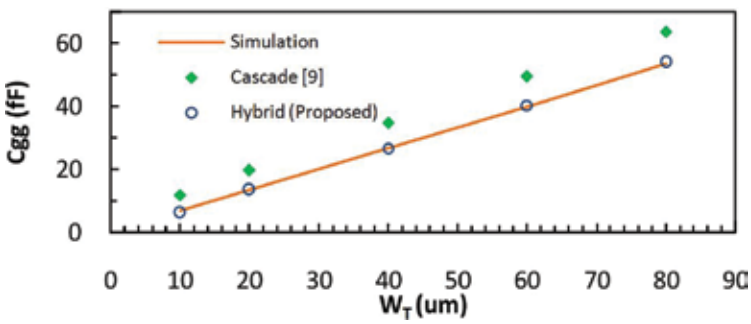

Figure 13. Simulated and de-embedded total gate capacitances of 40 nm NMOS transistor across width geometries at Vgs = 1.1 V, Vds = 1.1 V, and 8 GHz [13].

5.4.3. Frequency variability of de-embedded transistor parameters

In this section, the frequency variability of de-embedded transistor parameters is examined for up to 100 GHz. **Figure 14** shows the comparison of extracted transconductance (Real(Y21)) by different de-embedding techniques for reference plane established underneath metal fingers. As compared to Refs. [2, 6], the extracted transconductance by the proposed de-embedding technique is almost constant with variation of only 1 ms at 100 GHz. The result is physical as non-quasi static effect of 40 nm transistor is negligible for frequencies below 100 GHz and at strong inversion regime [22]. The frequency variability of de-embedded transistor gate capacitance is further examined for drain bias at 0 V. In such case, the characteristic of CMOS transistor could be described by a passive capacitor. As demonstrated in **Figure 15**, the proposed hybrid de-embedding technique has shown to be more robust than previous work by Loo et al. [6] and Koolen et al. [2] as the maximum variation of de-embedded C_{gg} is within 3% for frequency span of 100 GHz. Similar to previous verification

http://dx.doi.org/10.5772/66237

results, the larger de-embedding error exhibited by Koolen et al. [2] for frequencies beyond 30 GHz indicates that the behavior of test fixture parasitics could no longer be sufficiently described by single stage of parallel-series lumped equivalent circuit. Although greater improvement has been made by Loo et al. [6] with more comprehensive test fixture model, still it suffers larger error than the proposed de-embedding technique due to lumped approximation of metallic conductors. Finally, the frequency dependency of de-embedded maximum current gain bandwidth product ($H_{21}x\Delta f$) is examined. Theoretically, it is frequency invariant since the maximum current gain of CMOS transistor degrades at constant rate of 20 dB/decade. As illustrated in **Figure 16**, the extracted gain bandwidth product by the proposed hybrid de-embedding technique is more physical since it is almost frequency independent with only 2.1% variation from low frequency value at 100GHz. Comparatively, the de-embedded results by [2, 6] reveal more than 4% error at 100 GHz due to the aforementioned reasons. Note that the transistor gain parameter is more immune to de-embedding error in [2] as it is function of ratio in between transconductance and total gate capacitance.

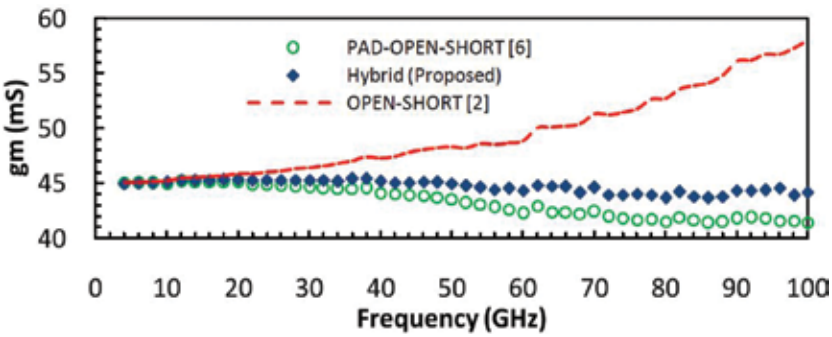

Figure 14. De-embedded transconductance, gm of 40 nm NMOS transistor (W_T = 40 μm) at Vgs = 1.1 V, Vds = 1.1 V [13].

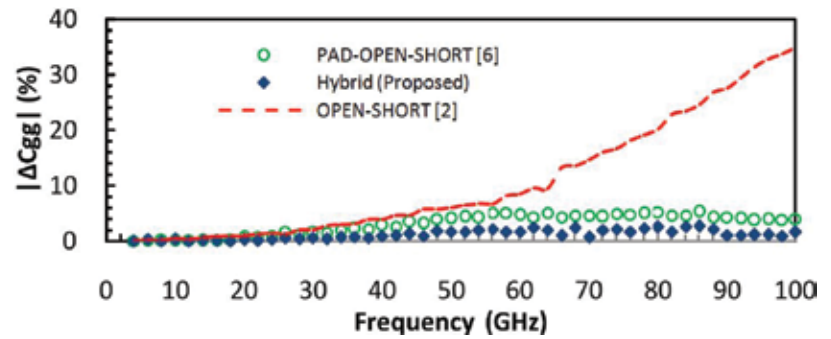

Figure 15. Frequency variability of de-embedded total gate capacitance C_{gg} of 40 nm NMOS transistor (W_T = 40 μm) at Vgs = 1.1 V, Vds = 0 V [13].

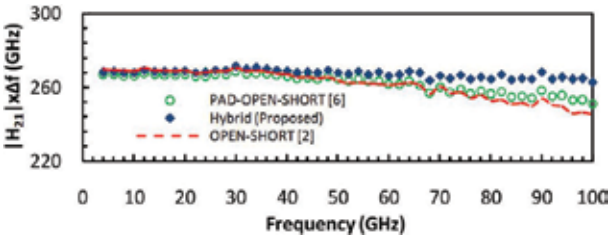

Figure 16. De-embedded maximum current gain bandwidth product, |H21|*Δf of 40 nm NMOS transistor (W_T = 40 μm) at Vds = 1.1 V.

6. Conclusion

This chapter presents a generalized network de-embedding technique that avoids any inaccurate lumped and transmission line assumptions on the pad and interconnects of the test structure. The de-embedding strategy has been validated by producing negligible de-embedding error (<−50 dB) on the insertion loss of the zero-length THRU device. It demonstrates better accuracy than existing de-embedding techniques that are based on lumped pad assumption. For transistor characterization, the de-embedding reference plane could be further shifted to the metal fingers with additional Finger OPEN-SHORT structures. The resulted de-embedded RF parameters of CMOS transistor show good scalability across geometries and negligible frequency dependency of less than 3% for up to 100 GHz. The de-embedding findings suggest that the parasitic effects of metal fingers could not be ignored in modeling of intrinsic transistors. Also, the distributed effect of metallic conductors has to be considered when the line length is comparable to 1/20 of frequency wavelength.

Acknowledgements

The authors like to thank GLOBALFOUNDRIES Singapore Pte Ltd for providing tape-out resources and measurement support.

Author details

Xi Sung Loo[1*], Kiat Seng Yeo[2] and Kok Wai Johnny Chew[1]

*Address all correspondence to: xisung.loo.phd@ieee.org

1 GLOBALFOUNDRIES Singapore Pte Ltd, Singapore

2 Singapore University of Technology & Design, Singapore

http://dx.doi.org/10.5772/66237

References

[1] Verma, P. R.; Shaoqiang, Z.; Wai, C. K.; Boon, T. J. and Nair, R. "Foundry RF technologies," Proceedings of Technical Program–2014 International Symposium on VLSI Technology, Systems and Application (VLSI-TSA), Hsinchu, 2014, pp. 1–2.

[2] M. C. A. M. Koolen, J. A. M. Geelen and M. P. J. G. Versleijen, "An improved de-embedding technique for on-wafer high-frequency characterization," Bipolar Circuits and Technology Meeting, 1991., Proceedings of the 1991, Minneapolis, MN, 1991, pp. 188–191.

[3] Cho, H.; Burk, D. E. "A three-step method for the de-embedding of high-frequency S-parameter measurements," IEEE Transactions on Electron Devices, vol. 38, no. 6, pp. 1371–1375, 1991.

[4] T. E. Kolding, O. K. Jensen and T. Larsen, "Ground-shielded measuring technique for accurate on-wafer characterization of RF CMOS devices," Microelectronic Test Structures, 2000. ICMTS 2000. Proceedings of the 2000 International Conference on, Monterey, CA, 2000, pp. 246–251.

[5] KangI. M. ; Jung, S. J.; Choi, T. H.; Jung, J. H.; Chung, C.; Kim, H. S.; Oh, H.; Lee, H. W.; Jo, G.; Kim, Y. K.; Kim, H. G.; Choi, K. M. "Five-step (Pad CPadShort CPadOpen CShort COpen) de-embedding method and its verification," IEEE Electron Device Letters, vol. 30, no. 4, pp. 398–400, 2009.

[6] Loo, X. S. et al."An accurate two-port de-embedding technique for RF/Millimeter-wave noise characterization and modeling of deep submicrometer transistors," in: IEEE Transactions on Microwave Theory and Techniques, vol. 59, no. 2, pp. 479–487, 2011.

[7] Liang, Q.; Cressler, J. D.; Niu, G.; Lu, Y.; Freeman, G.; Ahlgren, D. C.; Malladi, R. M.; Newton, K.; Harame, D. L. "A simple four-port parasitic deembedding methodology for high-frequency scattering parameter and noise characterization of SiGe HBTs," IEEE Transactions on Microwave Theory and Techniques, vol. 51, no. 11, pp. 2165–2174, 2003.

[8] Chen, C. H.; Deen, M. J. "A general noise and S-parameter deembedding procedure for on-wafer high-frequency noise measurements of MOSFETs," IEEE Transactions on Microwave Theory and Techniques, vol. 49, no. 5, pp. 1004–1005, 2001.

[9] Cho, M. H.; Huang, G. W.; Wang, Y. H.; Wu, L. K. "A scalable noise de-embedding technique for on-wafer microwave device characterization," IEEE Microwave and Wireless Components Letters, vol. 15, no. 10, pp. 649–651, 2005.

[10] Cho, M. H.; Chen, D.; Lee, R.; Peng, A. S.; Wu, L. K. and Yeh, C. S., "Geometry-scalable parasitic deembedding methodology for on-wafer microwave characterization of MOSFETs," IEEE Transactions on Electron Devices, vol. 56, no. 2, pp. 299–305, 2009.

[11] Loo, X. S.; Yeo, K. S. and Chew, K. W. J. "THRU-based cascade de-embedding technique for on-wafer characterization of RF CMOS devices," IEEE Transactions on Electron Devices, vol. 60, no. 9, pp. 2892–2899, 2013.

[12] Loo, X. S.; et al. "A new millimeter-wave fixture deembedding method based on generalized cascade network model," IEEE Electron Device Letters, vol. 34, no. 3, pp. 447–449, 2013.

[13] Loo, X. S.; Chew, K. W. J.; Yeo, K. S.; Win, M. Z. and Boon, C. C. "A hybrid pad-line-finger de-embedding technique for broadband modeling of CMOS transistor," IEEE Microwave and Wireless Components Letters, vol. 26, no. 7, pp. 507–509, 2016.

[14] Kolding, T. E. "Shield-based microwave on-wafer device measurements," IEEE Transactions on Microwave Theory and Techniques, vol. 49, no.6, pp. 1039–1044, 2001.

[15] Williams, D. F.; et al."Calibrations for millimeter-wave silicon transistor characterization," IEEE Transactions on Microwave Theory and Techniques, vol. 62, no. 3, pp. 658–668, 2014.

[16] Song, J.; Ling, F.; Flynn, G.; Blood, W. and Demircan, E. "A de-embedding technique for interconnects," Electrical Performance of Electronic Packaging, Cambridge, MA, pp. 129–132, 2001.

[17] Loo, X. S.; et al."A cascade-parallel based noise de-embedding technique for RF modeling of CMOS device. IEEE Microwave and Wireless Components Letters, vol. 21, no. 8, pp. 448–450, 2011.

[18] Davidson, A., Jones, K. and Strid, E. "LRM and LRRM calibrations with automatic determination of load inductance," ARFTG Conference Digest-Fall, 36th, Monterey, CA, USA, pp. 57–63, 1990.

[19] Cheng, Y. and Matloubian, M., "Frequency-dependent resistive and capacitive components in RF MOSFETs," IEEE Electron Device Letters, vol. 22, no. 7, pp. 333–335, 2001.

[20] Je, M.; Han, J.; Shin, H.; Lee, K. "A simple four-terminal small signal model of RF MOSFETs and its parameter extraction," Microelectronics Reliability., vol. 43, no. 4, pp. 601–609, 2003.

[21] Kwon, I.; Je, M.; Lee, Kwyro; Shin, H. "A simple and analytical parameter-extraction method of a microwave MOSFET," IEEE Transactions on Microwave Theory and Techniques, vol. 50, no. 6, pp. 1503–1509, 2002.

[22] H. Hassan, M. Anis and M. Elmasry, "Impact of technology scaling on RF CMOS," *SOC Conference, 2004. Proceedings. IEEE International*, Santa Clara, CA, 2004, pp. 97–101.

Chapter 7

Chip-Scale Microwave Photonic Signal Processing

Jian Wang and Yun Long

Additional information is available at the end of the chapter

http://dx.doi.org/10.5772/66322

Abstract

The use of optical technology can provide unprecedented performance to the generation, distribution, and processing of microwave. Recently, on-chip microwave photonics (MWP) has gained significant interests for its numerous advantages, such as robustness, reconfigurability as well as reduction of size, weight, cost, and power consumption. In this chapter, we review our recent progress in ultracompact microwave photonic signal processing using silicon nanophotonic devices. Using the fabricated silicon waveguide, silicon microring resonators (MRRs) and silicon photonic crystal nanocavities, we demonstrate on-chip analog signal transmission, optically controlled tunable MWP filter, and ultrahigh peak rejection notch MWP filter. The performance of analog links and the responses of MWP filters are evaluated in the experiment. In addition, microwave signal multiplication and modulation are also demonstrated based on a silicon Mach-Zehnder modulator in the experiment with favorable operation performance. The demonstrated on-chip analog links, MWP filters, microwave signal multiplication/modulation may help understand on-chip analog signaling and expand novel functionalities of MWP signal processing.

Keywords: optical signal processing, microwave photonics, analog transmission, silicon photonics, microring resonator, photonic crystal nanocavity, microwave photonic filter

1. Introduction

Silicon photonics has become one of the most promising photonic integration platforms owing to its small footprint, low power consumption, and availability of complementary metal-oxide-semiconductor (CMOS) fabrication technology for low-cost mass production [1–4]. Typical silicon nanophotonic devices include silicon waveguides, silicon microring resonators (MRRs), and silicon photonic crystal [5–10], showing unprecedented small size for potential large-scale integration [11–16]. The great success of silicon photonics benefits from the rapid growth of digital optical communications systems such as high capacity optical communications and optical interconnects [4, 17–34].

It has been proved that photonic systems can be also applied to deliver analog signals and process microwave radio frequency (RF) signals in the optical domain, deriving an emerging subject called microwave photonics (MWP) [35, 36]. The initial of MWP was for distributing microwave signal over long distances. However, the applications have evolved dramatically and now include photonic generation of microwave signal [37–40], photonic processing of microwave signal [41–50], frequency measurement of microwave signal [51, 52], and so on. MWP signal processing is of great importance among these applications. As shown in **Figure 1**, MWP signal processing functionalities include microwave signaling [53, 54], filtering [42, 43, 47], differential [48–50], integral [55, 56], pulse shaping [57, 58], Hilbert transformation [59], arbitrary waveform generation [60–63], frequency multiplication [64, 65], beamforming [66, 67], and more.

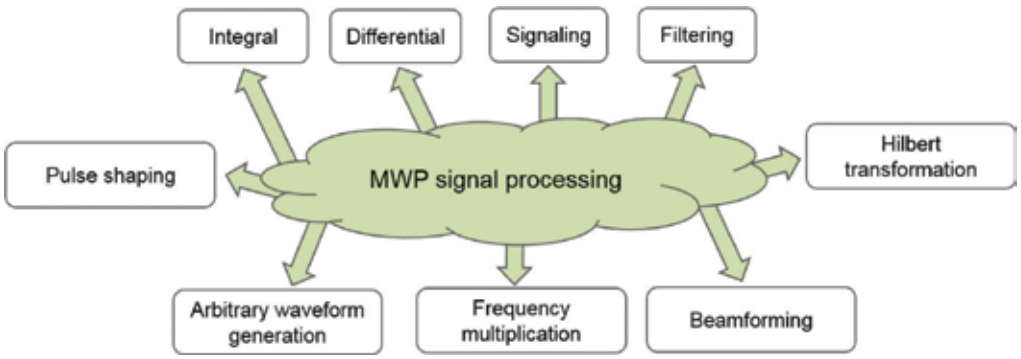

Figure 1. Functionalities classification of MWP signal processing.

Traditional MWP signal processing technologies are mainly based on fibered devices. Recently, there has been an increasing interest on developing integrated components to realize MWP signal processing functionalities. Adopting integrated photonics technologies in MWP signal processing will address the issues such as stability and compactness in traditional fiber-based devices. Very recently, owning to the advance on silicon photonics, some microwave photonic devices such as MWP filters [41, 43, 47, 68], on-chip pulse shapers [57, 58], differentiators [48–50], and Hilbert convertors [59], and ultra wide band (UWB) signal generators [69] have been implemented on silicon on insulator (SOI) platforms. **Figure 2** shows the basic schematic illustration of microwave photonic signal processing using a silicon chip. Usually, a laser source emits a continuous wave (CW) light. The RF signal is generated using a RF generator. After modulation, the RF signal carried by the light carrier is launched to a silicon chip for signal processing. After that, a photodiode is used to convert optical signal to RF signal for detection. The basic silicon photonic devices for MWP signal processing include silicon waveguide, microdisk, microring resonator (MRR), photonic crystal (PhC) nanocavity, Mach-Zehnder modulator (MZM), Bragg grating, and more, as shown in **Figure 3** [70]. Based on the combination of these elementary elements, many complicated MWP processing functionalities can be realized.

In this chapter, we review our recent works in chip-scale microwave photonic signal processing. First, we present the progress of on-chip analog signal transmission. We analyze the

performance of on-chip analog signal transmission using the fabricated silicon waveguide and resonators, that is, microring resonators and photonics crystal nanocavities. Second, we report the progress of MWP filters, various types of MWP filters are introduced, and the impact of optical nonlinearities on MWP filters is also discussed. Finally, we show the results of on-chip photonic-assisted microwave signal multiplication and modulation.

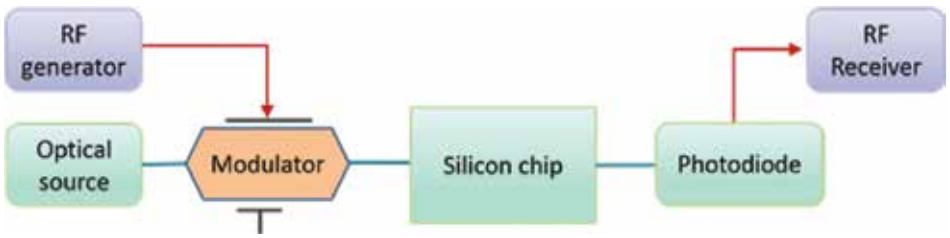

Figure 2. Schematic illustration of chip-scale microwave photonic signal processing.

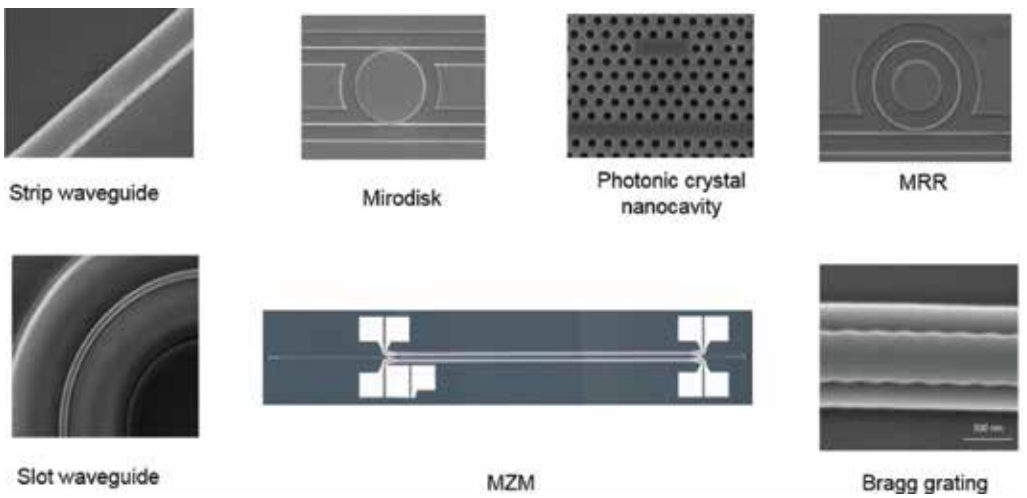

Figure 3. Some photographs of basic silicon photonic devices for MWP signal processing. (The photograph of Bragg grating is reprinted from Ref. [70]).

2. On-chip analog signal transmission

All the MWP systems are essentially analog links. For an analog optical link, linearity is one of the key performance metrics. Traditionally, there are mainly three methods to increase the linearity of analog signal transmission in various systems: (1) improving the driving/bias schemes or optical structures of the modulators to construct linear or quasi-linear modulators [71–74]; (2) using a tunable filter with proper center wavelength and bandwidth to remove the unwanted optical carrier and thus rise the linearity of analog links [75, 76]; (3) using

optical waveguides with extremely low nonlinearity, low-loss and high thermal stability for signal transmission [77]. Integrated silicon photonic devices such as silicon waveguides, MRR, microdisk resonators, and PhC cavities have promoted the evolution of on-chip MWP signal processing functions due to the high nonlinear effects of waveguides and diverse filtering properties of resonators. However, these characteristics may also degrade analog signal quality awfully, leading to extra nonlinear signal distortions, which may show different properties compared with traditional signal distortions. To investigate the impacts on analog optical links induced by the nonlinearity of integrated photonic devices, many interesting and meaningful works related to on-chip analog performance have been done recently [53, 54, 78–81]. In this section, we analyze the performance of on-chip analog signal transmission using silicon waveguide, MRR, and PhC nanocavity.

For an on-chip analog link, silicon waveguide is used for light routing. Compared to fiber-based links, the optical nonlinearities induced by the tight light confinement of the silicon waveguides may affect the performance of on-chip analog photonic links. So it is essential to experimentally exploit analog signal transmission distortions induced by the integrated silicon waveguide for future chip-scale analog systems. The experimental setup for analog signal transmission through the fabricated silicon strip waveguide is shown in **Figure 4**. At the transmitter side, the output of an external cavity laser (ECL) is injected to a MZM. Two microwave at frequencies f_1 = 1.98 GHz and f_2 = 2 GHz are combined at the input of MZM. The light source is modulated by the two RFs in the MZM. **Figure 4(a)** and **(b)**describes the typical RF signals at the input and output of MZM. A 1550-nm source emitted from the ECL is modulated by MZM, and then amplified by an erbium-doped fiber amplifier (EDFA). A variable optical attenuator (VOA) is employed to control the optical input power of the silicon strip waveguide. The analog signals are polarization controlled by using a polarization controller (PC), and then coupled into the silicon strip waveguide by vertical grating coupler from fiber. For the dimensions confinement of the SOI wafer, there is a bending region of the long waveguide and the scanning electron microscope (SEM) image of the waveguide bending region is shown in **Figure 4(c)**. **Figure 4(d)** depicts the field distribution of the fundamental mode in silicon strip waveguide calculated by using a full-vector finite-element-method software (COMSOL). After transmission through the silicon strip waveguide, the analog signal is coupled out from the silicon strip waveguide to fiber with the same vertical grating coupler. An electrical spectrum analyzer (ESA) is used to measure the fundamental, second-order harmonic distortion (SHD), third-order harmonic distortion (THD), second-order intermodulation (IM2), and third-order intermodulation (IM3) products.

Figure 5 shows the measured signal-to-noise ratios (SNRs) of IM2, IM3, SHD, and THD as a function of the silicon strip waveguide length. The waveguide length we fabricated is 1, 3.23, 5.25, and 7.38 mm, respectively. One can see that the SNRs of distortions have a negligible change with the increase of the waveguide length.

Figure 6 shows the measured SNRs of IM2, IM3, SHD, and THD as a function of optical input power fed into the silicon strip waveguide. One can see that the SNRs of IM2, IM3, and SHD have a negligible change when increasing the optical input power. The SNR of the THD gradually increases with the input optical power, which might be due to the relatively high sensitivity of THD to the nonlinearity-induced degradation of the silicon strip waveguide.

http://dx.doi.org/10.5772/66322

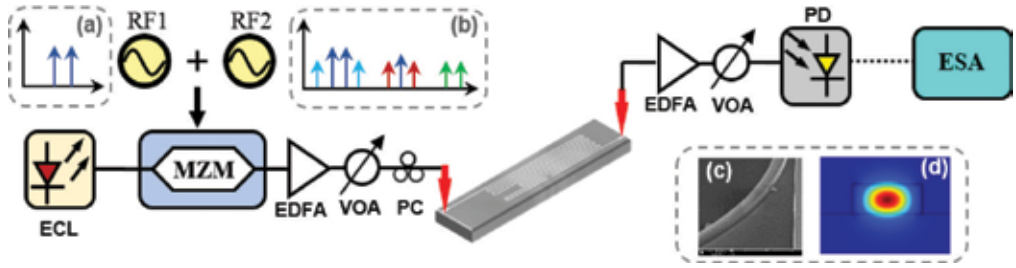

Figure 4. Experimental setup for analog signal transmission through the silicon strip waveguide. Insets: (a) and (b) describe the RF signal at the MZM input and output; (c) is the SEM image and (d) is the simulated mode distribution of silicon strip waveguide.

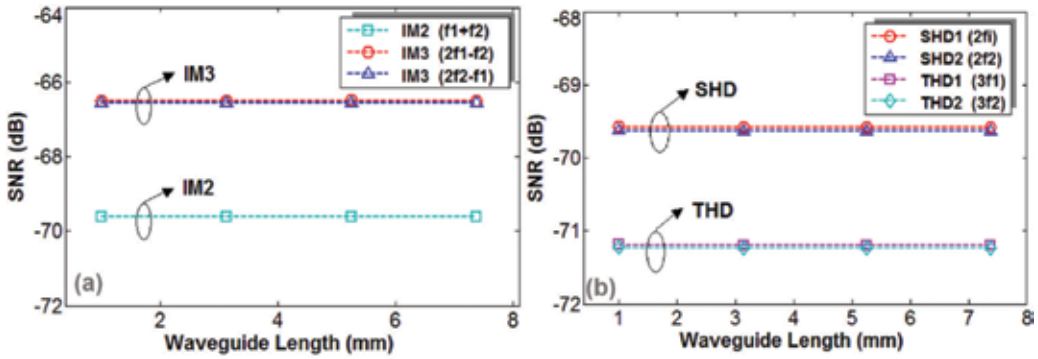

Figure 5. Measured SNRs of (a) IM2, IM3 and (b) SHD, THD versus waveguide length.

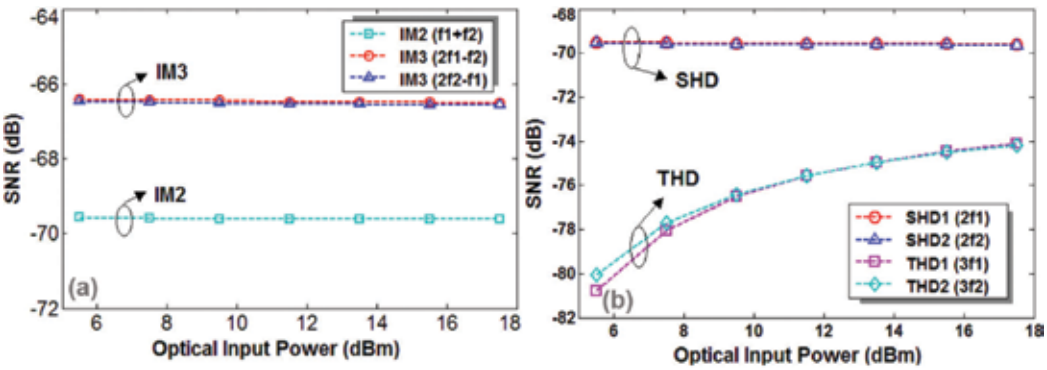

Figure 6. Measured SNRs of (a) IM2, IM3 and (b) SHD, THD versus optical input power.

We then evaluate the performance of on-chip analog signal transmission in a silicon MRR [53]. **Figure 7** shows the experimental setup. At the transmitter, the output of an ECL is sent to a MZM driven by a 6-GHz RF signal. The analog signal is amplified by an EDFA, polarization controlled by a PC, and then adjusted by a VOA. With a vertical grating coupler, the analog

signal is coupled from fiber to silicon microring resonator. After the transmission through a silicon microring resonator, at the receiver, the signal is coupled from the silicon microring resonator to fiber with a vertical grating coupler. After being amplified by EDFA and attenuated by VOA, the signal is sent to a photodetector (PD) and then measured by an ESA. The insets (a) and (b) in **Figure 7** depict the SEM images of the fabricated vertical grating coupler and silicon microring resonator. In the experiment, the silicon microring resonator has a resonance wavelength of ~1581.26 nm and a 3-dB bandwidth of ~0.12 nm.

Figure 8(a) and **(b)** shows the acquired output power of the RF carrier and distortions as a function of the RF input power at input signal wavelength of ~1581.07 and ~1581.21 nm, respectively.

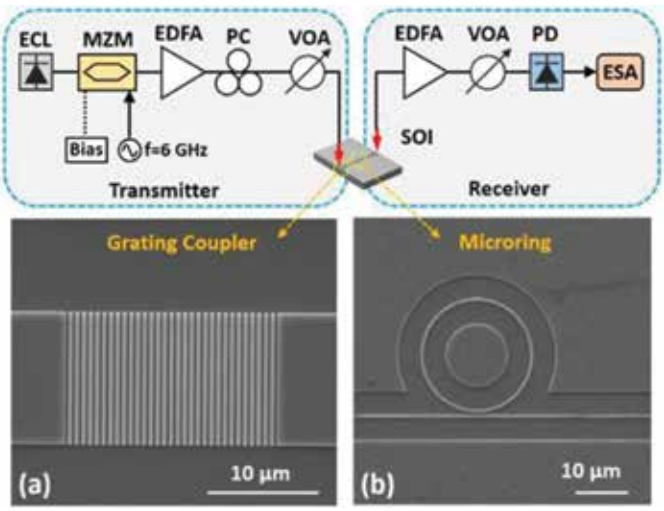

Figure 7. Experimental setup for analog signal transmission in a silicon microring resonator. (a) and (b) SEM images of the grating coupler and silicon microring resonator, respectively.

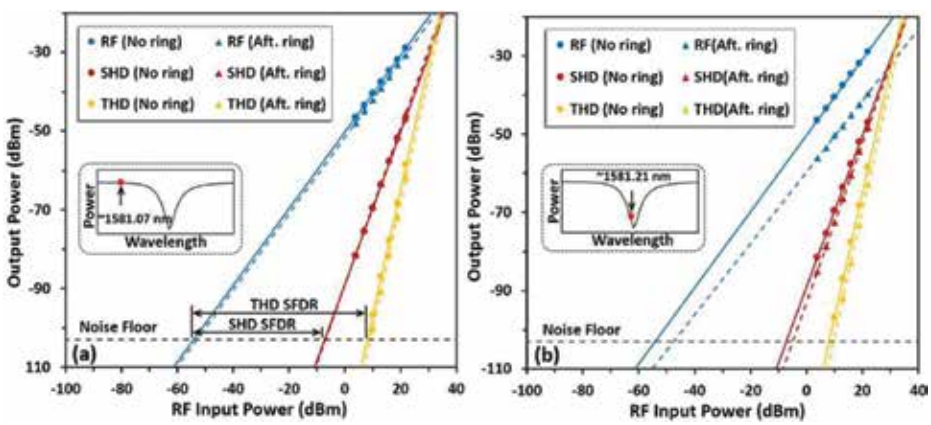

Figure 8. Measured output power of RF carrier and distortions as a function of the RF input power at input signal wavelength of (a) 1581.07 nm and (b) 1581.21 nm, respectively. The optical power of input signal is −17 dBm.

http://dx.doi.org/10.5772/66322

The spurious-free dynamic range (SFDR) of the SHD and THD are used to estimate the analog link performance. A higher SFDR system facilitates a more linear analog signal transmission. As shown in **Figure 8(a)**, for input signal wavelength of 1581.07 nm which is away from the dip resonance wavelength, the output power of RF carrier and distortions after microring change slightly compared with those without microring. The resultant SHD and THD SFDR after microring almost remain the same as those without microring. As shown in **Figure 8(b)**, for input signal wavelength of 1581.21 nm which is close to the dip resonance wavelength, the output power of RF carrier decreases while the distortions vary slightly after microring compared with those without microring. Hence, the SHD and THD SFDR decrease after the transmission, which is due to the notch filtering effect of the silicon microring resonator around the dip resonance wavelength.

To further investigate the analog signal transmission in the 3-dB bandwidth region near the resonance wavelength of 1581.26 nm, we change input signal wavelength from ~1581.07 to ~1581.26 nm with a 0.048-nm spacing. **Figure 9(a)** plots the relationship between SFDR and input signal wavelength at input signal power of 3.5 dBm. One can see two interesting phenomena from **Figure 9(a)**. First, although the minimum optical power transmission wavelength (i.e., notch resonance wavelength) is at ~1581.26nm, the worst SFDRs are obtained at ~1581.21 nm due to the notch filtering effect on the RF carrier sideband. Second, SFDRs at ~1581.12 nm achieve maximum values, which can be explained with the fact that the high-order harmonic sidebands (output SHD and THD) fall into the 3-dB bandwidth region (close to the notch resonance), while the fundamental frequency sideband (output RF carrier) is away from the notch resonance. For low-level input signal power, it is found that the analog signal transmission performance through microring resonator is mainly affected by the notch filtering effect. Input signal power is also taken into consideration to assess its role in the analog signal transmission, as shown in **Figure 9(b)**. For relatively high input signal power, it is interesting to note that the analog signal transmission might be affected by the nonlinearity-induced resonance wavelength shift of the microring with the increase of input signal power.

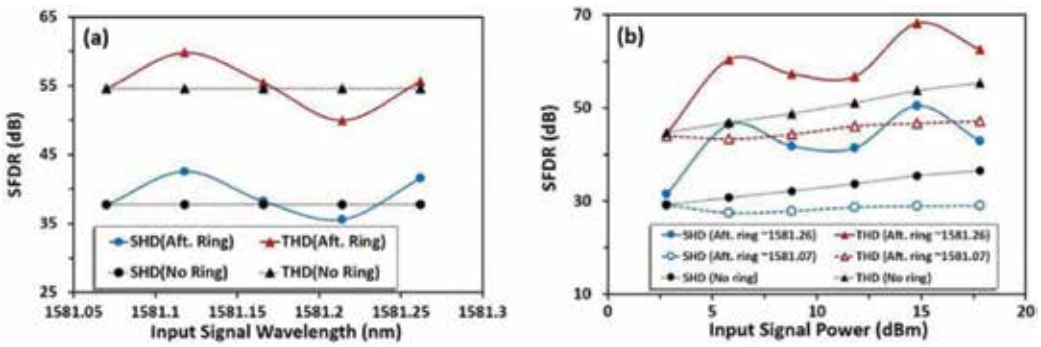

Figure 9. (a) Measured SHD and THD SFDR versus input signal wavelength at input signal power of 3.5 dBm. (b) Measured SHD and THD SFDR versus input signal power.

We further assess the performance of on-chip analog signal transmission using the fabricated silicon photonic crystal nanocavities [54]. The designed and fabricated silicon photonic crystal nanocavity is shown in **Figure 10**. The lattice constant (a) is 420 nm, the radius of air holes (r)

is 126 nm, and the three air holes adjacent to the cavity are laterally shifted by 0.175a, 0.025a, and 0.175a, respectively. In the experiment, the silicon photonic crystal nanocavity has a resonance wavelength of ~1552.99 nm, an extinction ratio of ~18.4 dB, and a 3-dB bandwidth of ~0.19 nm.

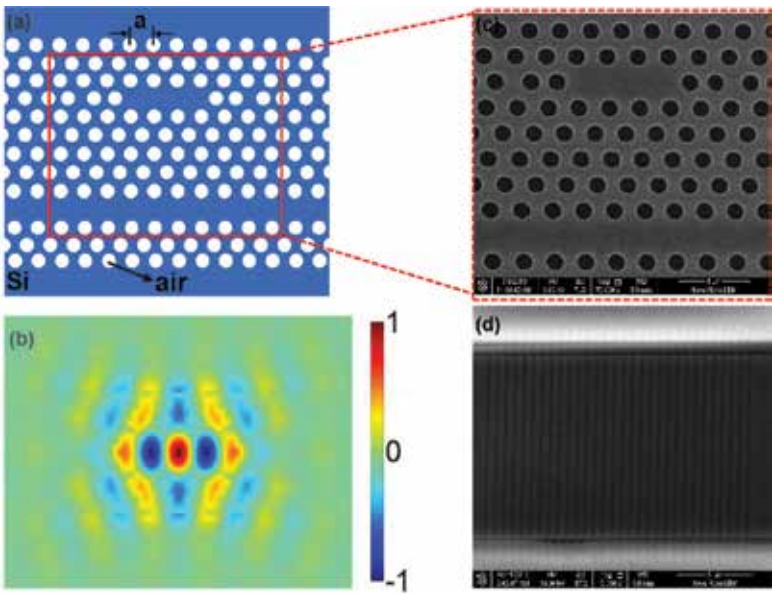

Figure 10. (a) Structure, (b) mode profile and (c) SEM image of silicon photonic crystal nanocavity. (d) SEM image of vertical grating coupler.

Figure 11(a) and **(b)**shows the measured output power of the RF carrier and distortions (SHD, THD) as a function of the RF input power at input optical carrier wavelength of 1552.83 and 1552.99 nm, respectively. As shown in **Figure 11(a)**, for input optical carrier wavelength of 1552.83 nm, the SHD SFDR (~29.8 dB) and THD SFDR (~50.0 dB) degrade slightly. As shown in **Figure 11(b)**, for input optical wavelength of 1552.99 nm (i.e., resonance wavelength), slight degradations of SHD SFDR (~34.6 dB) and THD SFDR (~52.2 dB) are observed. Actually, when the optical carrier is tuned at the resonance wavelength, the modulated optical sidebands after MZM (RF modulation), which are related to the RF carrier and distortions (SHD, THD), are offset from the dip resonance wavelength. As a result, it might not be the worst case for analog signal transmission with the optical carrier sitting at the resonance wavelength of the photonic crystal L3 resonator.

The influences of the optical carrier wavelength and input optical power on the SHD SFDR and THD SFDR are also studied in the experiment. **Figure 12(a)** shows the dependence of SHD SFDR and THD SFDR on the input optical carrier wavelength. **Figure 12(b)** shows the dependence of SHD SFDR and THD SFDR on the optical input power. The obtained results shown in **Figures 11** and **12** indicate favorable analog link performance using the designed and fabricated silicon photonic crystal L3 resonator.

http://dx.doi.org/10.5772/66322

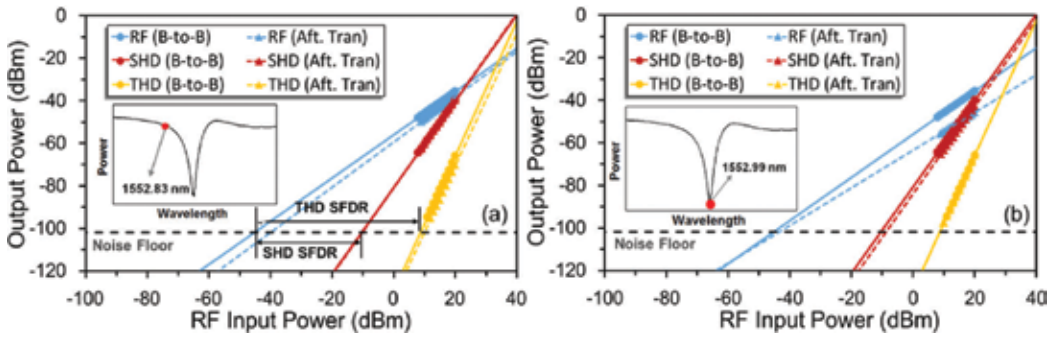

Figure 11. Measured output power of RF carrier and distortions (SHD, THD) as a function of RF input power at different optical carrier wavelengths of (a) 1552.83 and (b) 1552.99 nm.

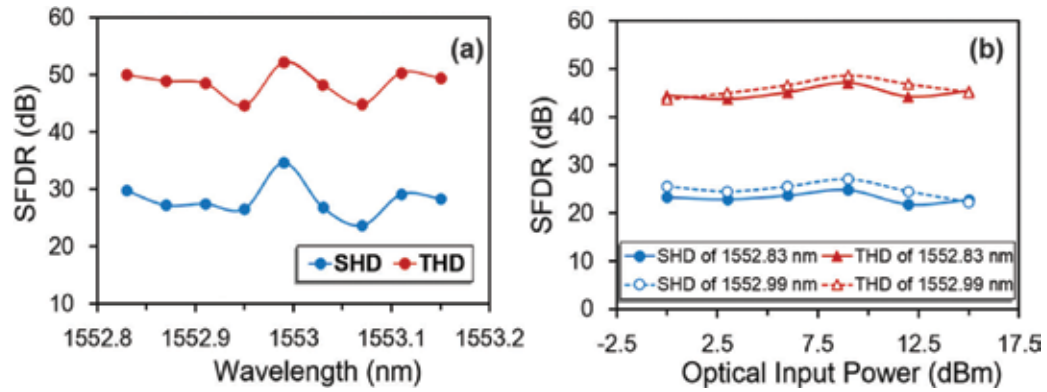

Figure 12. Measured output power of RF carrier and distortions (SHD, THD) as a function of RF input power at different optical carrier wavelengths of (a) 1552.83 and (b) 1552.99 nm.

3. Microwave photonics filters

A MWP filter is a photonic subsystem designed with the aim of carrying equivalent tasks to those of a traditional microwave filter within a RF system [35, 82–85]. Comparing to conventional microwave filters, MWP filters have attracted increasing interest for their advantages, such as huge bandwidth, electromagnetic immunity as well as reconfiguration and tunability. Now, MWP filters are used broadly ranging from radar, satellite to wireless communications. Many approaches to realizing MWP filters have been proposed and demonstrated based on fiber devices in the last decade [86–91]. To enhance the stability and reduce the cost and footprint of the MWP filters, integrated MWP filters have been widely concerned by several groups recently [41, 44, 47, 92–99]. Many of the preliminary approaches have been based mainly on single integrated cavity resonators. For instance, Ref. [96] reports the results for a single passband MWP filters based on a silicon MRR. A few works have also focused on more elaborated designs involving more than one cavity, such as cascaded MRRs [94], MZI-assisted MRRs [41], and more. In this section, we introduce various types of MWP filters.

Using a silicon MRR assisted by a phase modulator (PM) and a tunable optical filter (TBF) to prepare an optical single sideband (OSSB) modulation signal, we demonstrate a bandstop microwave photonic filter [42]. Moreover, using light (pump) to control light (signal optical carrier), we present an alternative approach to tuning the resonance of the bandpass microwave photonic filter, that is, all-optical tuning microwave photonic filter. **Figure 13(a)** illustrates the typical scheme of the all-optical tuning process of the MWP filter based on an SOI MRR. The microwave signal is modulated on a signal optical carrier, and then processed by an SOI MRR and detected by a PD. Since the optical response of the MRR can be adjusted by a pump light, the electrical response of the link can be tuned. The inset of **Figure 13(a)** depicts typical transmission spectrum of an SOI MRR, in which the microwave-modulated signal is located close to one notch resonance frequency and pump light positioned at another notch

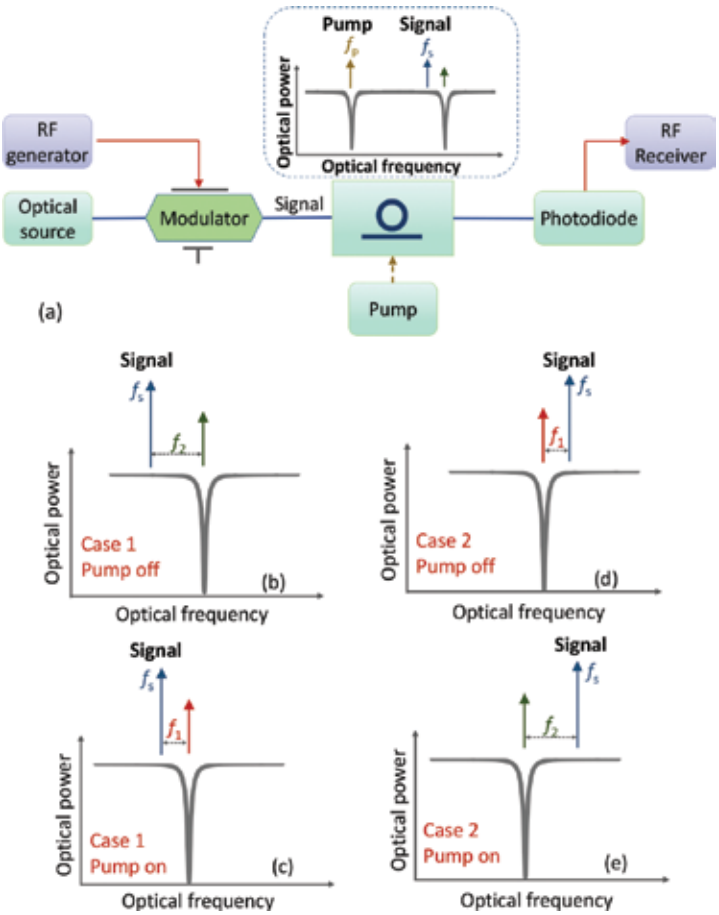

Figure 13. (a) Schematic illustration of the proposed all-optical tuning process of the MWP filter. (b)–(e) Operation principle of the all-optical tuning process of the MWP filter. (b) and (d) Pump off. (c) and (e) Pump on. Case 1: the frequency of the signal optical carrier (fs) is located at the left side of the notch resonance frequency of the MRR. Case 2: the frequency of the signal optical carrier (fs) is located at the right side of the notch resonance frequency of the MRR. The inset of (a) shows typical transmission spectrum of the MRR with relative positions of microwave modulated signal and pump light.

http://dx.doi.org/10.5772/66322

resonance frequency. **Figure 13(b)–(e)** summarizes the operation principle of the proposed all-optical tuning process of the MWP filter. An optical carrier is modulated by an RF signal with OSSB modulation. The output field after modulation is then applied to the MRR for microwave photonic signal processing. The frequency of the signal optical carrier is f_s. There are two cases depending on the relative position between the signal optical carrier and the notch resonance of the MRR. For the Case 1 with the signal optical carrier f_s located at the left side of the notch resonance of the MRR, when the frequency component ($f_s + f_2$) is just aligned to the notch frequency of the MRR spectrum as shown in **Figure 13(b)**, the output RF response in the absence of the pump vanishes at f_2. Hence, a notch MWP filter with a central frequency of f_2 is obtained. When the pump light is on, one would expect a red shift of the notch peak of the MRR owing to the combined nonlinear effects in the MRR, resulting in a notch MWP filter with a central frequency of f_1, as shown in **Figure 13(c)**. Hence, the central frequency of the notch MWP filter can be tuned from f_2 to f_1 by increasing the pump light power. For the Case 2 with the signal optical carrier f_s located at the right side of the notch resonance of the MRR, as shown in **Figure 13(d)** and **(e)** similar tunable notch MWP filter with its central frequency changed from f_1 to f_2 is also achievable by increasing the pump light power. Both Case 1 and Case 2 shown in **Figure 13(b)–(e)** indicate possible all-optical tunale MWP filter using nonlinear effects of MRR.

We first calculate the RF responses under different pump light power to show the all-optical tuning process of the MWP filter. The parameters used to calculate MRR field transmission are extracted from the measured MRR transmission spectrum. The MWP filter responses under different pump powers in Case 1 and Case 2 are shown in **Figure 14(a)** and **(b)**, respectively. As shown in **Figure 14(a)**, the central frequency of the MWP filter decreases from 15.5 to 9.5 GHz as the pump power increases in Case 1. The central frequency of the MWP filter increases from 9.5 to 15.5 GHz as the pump power increases in Case 2, as shown in **Figure 14(b)**.

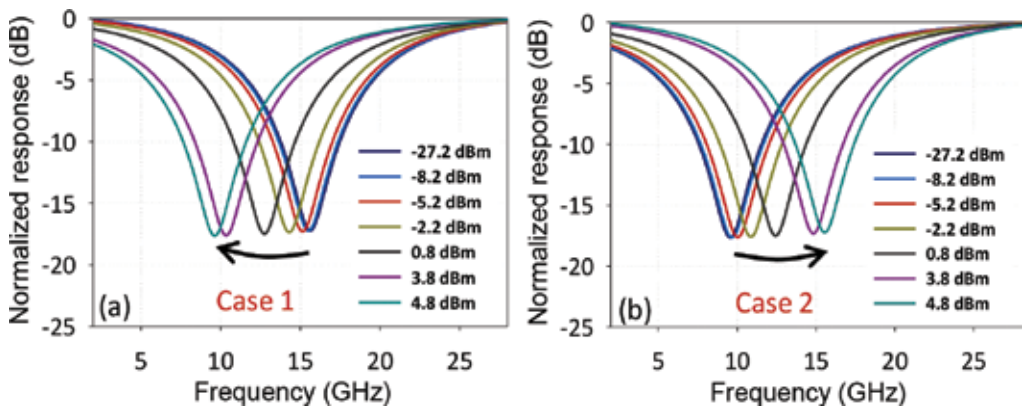

Figure 14. Calculated microwave responses under different pump power levels in (a) Case 1 and (b) Case 2, respectively. Case 1: the central frequency of the MWP filter decreases as the pump power increases. Case 2: the central frequency of the MWP filter increases as the pump power increases.

The measured microwave responses of MWP filter under different pump power levels are shown in **Figure 15**. The pump light wavelength is fixed at 1591.786 nm for all the configurations.

In Case 1, the optical carrier wavelength is 1581.730 nm in both forward and backward pumping configurations. As shown in **Figure 15(a)** and **(b)**, the central frequency of the notch MWP filter is tuned from 15.64 to 8.79 GHz in the forward pumping configuration while from 15.60 to 10.04 GHz in the backward pumping configuration by adjusting the pump light power from −27.2 to 4.8 dBm. In Case 2, the optical carrier wavelength is 1581.564 nm in the forward pumping configuration and 1581.534 nm in the backward pumping configurations. As shown in **Figure 15(c)** and **(d)**, the central frequency of the notch MWP filter is tuned from 5.27 to 12.47 GHz in the forward pumping configuration and from 8.84 to 15.04 GHz in the backward pumping configuration as increasing the pump light power from −27.2 to 4.8 dBm.

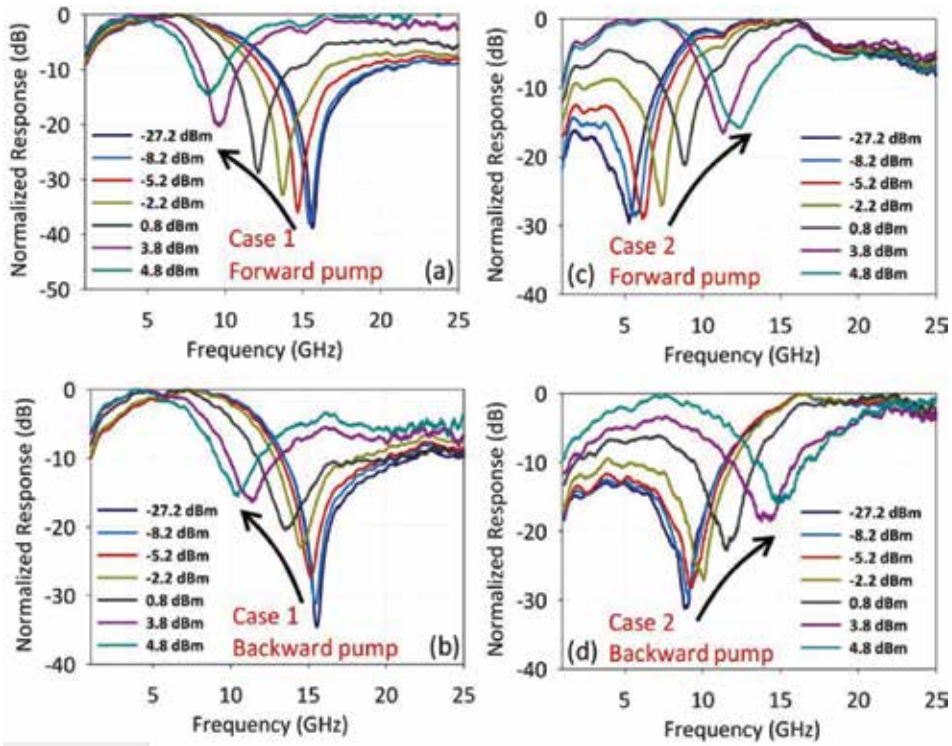

Figure 15. Measured microwave responses of all-optical tunable MWP filter under different pump power levels with (a) Case 1/Forward pump, (b) Case 1/Backward pump, (c) Case 2/Forward pump, and (d) Case 2/Backward pump, respectively.

We also propose a simple yet effective approach to realizing notch MWP filter with an ultra-high peak rejection [43]. We use the combination of a PM, TBF, and an SOI MRR to manipulate the phase and amplitude of optical sidebands for inducing a signal cancellation at the RF notch filter frequency. **Figure 16** shows the concept and operation principle of the proposed approach. A conventional PM driven by an RF signal generates out of phase lower sideband (LSB) and upper sideband (USB). A TBF is used to attenuate the USB signal followed by an SOI MRR. The resonant frequency of the SOI MRR is aligned to the frequency of LSB signal, thus the LSB signal will be filtered by the SOI MRR. Since the SOI MRR has a limited extinc-

http://dx.doi.org/10.5772/66322

tion ratio, the amplitude of the remaining LSB signal could be equal to the USB signal. Due to the equal amplitude and π phase difference of the attenuated USB and remained LSB, the signal power at the modulated RF frequency can be cancelled after detection by a photodetector, and a notch microwave photonic filter with infinite rejection in principle can be achieved.

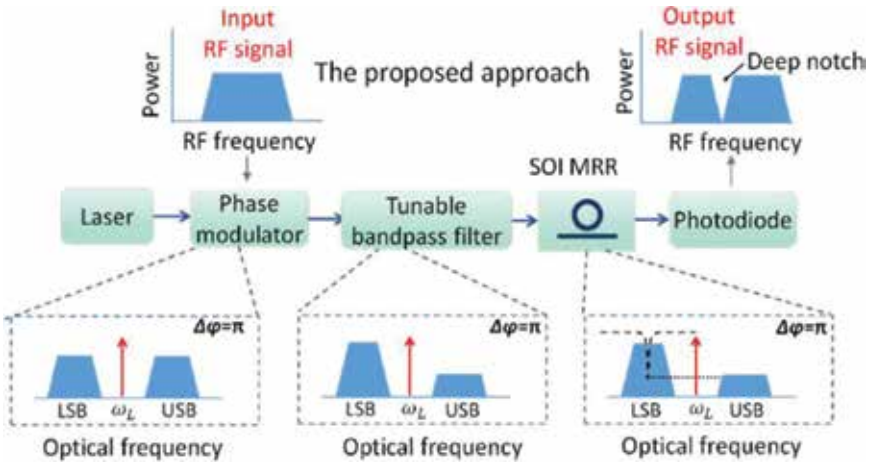

Figure 16. Schematic illustration of the proposed notch MWP filter with ultra-high peak rejection.

The measured optical spectra after the TBF and the corresponding MWP filter responses are shown in **Figure 17**. The optical carrier wavelength is 1581.576 nm. The optical spectra are measured by modulating a microwave signal to the optical carrier. The frequency of the microwave signal is 20 GHz, which is comparable with the central frequency of the MWP filter. **Figure 17(a)–(d)** depicts the optical spectra when the central wavelength of the TBF is 1581.746, 1581.776, 1581.806, and 1581.836 nm, respectively. The transmission spectra of the TBF in these four cases are also plotted in **Figure 17(a)–(d)** for reference. **Figure 17(e)–(h)** shows the corresponding MWP filter responses. As shown in **Figure 17(a)** and **(d)**, when the USB component is slightly attenuated by the TBF, after passing through the MRR, the amplitude difference of the LSB and USB is relatively large, resulting in a shallow RF notch of about 14.5 dB. When we shift the TBF, more power of the USB component is attenuated, and the peak rejection of the MWP filter remarkably increases. The peak rejection of the MWP filter is 29.1 dB when the central wavelength of the TBF is 1581.776 nm as shown in **Figure 17(b)** and **(f)**. A maximum peak rejection of about 61.5 dB is observed with balanced amplitude between LSB and USB components when the central wavelength of the TBF is 1581.806 nm as shown in **Figure 17(c)** and **(g)**. When we further increase the central wavelength of the TBF, the USB signal will be further attenuated, thus the peak rejection decreases again. For example, when the central wavelength of the TBF is 1581.836 nm, the USB almost disappears, and the peak rejection of the MWP filter decreases to 40.9 dB as shown in **Figure 17(d)** and **(h)**.

By changing the carrier light wavelength, the operating frequency of the ultra-high peak rejection MWP filter can be tuned. We measure the operating frequency tunability of the

MWP filter, as shown in **Figure 18**. When the wavelength of the carrier light is changed from 1581.476 to 1581.626 nm, the central frequency of the MWP filter is tuned from 12.4 to 30.6 GHz, maintaining an ultra-high peak rejection. The obtained results shown in **Figure 18** indicate that the proposed ultra-high peak rejection MWP filter can operate over a large tunable frequency range.

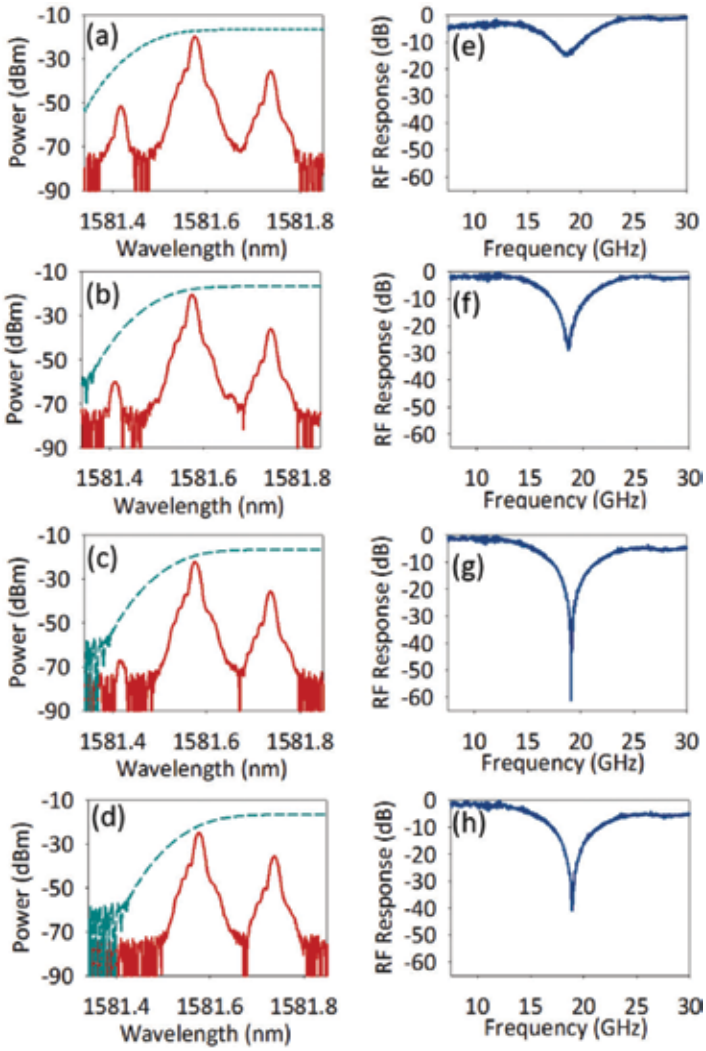

Figure 17. (a)-(d) Optical spectra after the TBF when the central wavelength of the TBF is 1581.746, 1581.776, 1581.806, and 1581.836 nm, respectively. The dashed lines are the corresponding transmission spectrum of TBF. (e)–(h) The corresponding MWP filter responses.

Based on a similar principle, we also demonstrate a rejection ratio tunable notch MWP filter based on a silicon PhC nanocavity. The resonant wavelength of the cavity is around 1554.313 nm. The measured optical spectra after the TBF and the corresponding MWP filter responses are shown

http://dx.doi.org/10.5772/66322

in **Figure 19**. The carrier light wavelength is 1554.153 nm. **Figure 19(a)–(d)** depicts the optical spectra when the central wavelength of the TBF is 1554.262, 1554.292, 1554.322, and 1554.352 nm, respectively. **Figure 19(e)–(h)** shows the corresponding MWP filter responses. The experimental results agree well with the simulation. As shown in **Figure 19(a)** and **(e)**, when the USB signal is slightly modified by the TBF, the peak rejection of the obtained MWP filter is very small (~11.8 dB). When we shift the TBF, the power of USB signal decreases, and the peak rejection of the MWP filter increases. A maximum peak rejection of about 62.1 dB is observed when the central wavelength of the TBF is 1551.315 nm (**Figure 19(b)** and **(f)**). When we further increase the central wavelength of the TBF, the USB signal will be further attenuated, thus the peak rejection will decrease again. For example, as shown in **Figure 19(d)** and **(h)**, the peak rejection of the MWP filter decreases to 15 dB when the central wavelength of the TBF is 1551.375 nm. **Figure 19(i)** plots the rejection ratio as a function of the central wavelength of the TBF. The red curve shows the simulation data, while the experimental results are marked by blue circles.

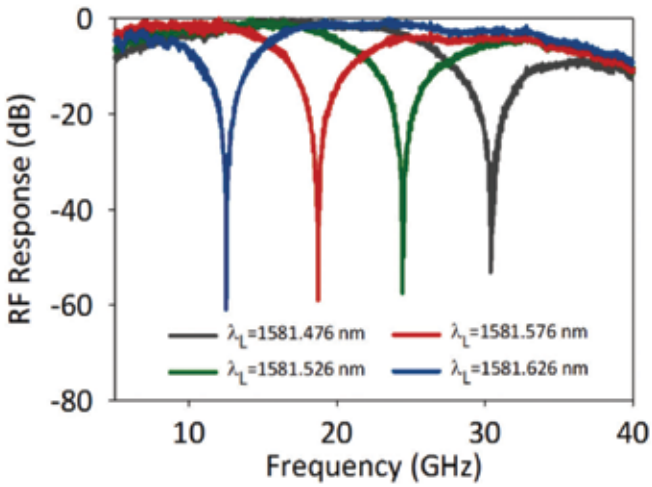

Figure 18. Measured tunable ultra-high peak rejection MWP filter responses with different optical carrier wavelengths.

To evaluate the effect of the filter shape of TBF, we study the performance of the rejection ratio tunable MWP filter with four types of super-gaussian filter shape. We calculate the MWP filter tunability response when the transmission of the TBF is $T_{TBF}(\omega) = e^{-\left(\frac{\omega-\omega_{center}}{2\pi\times 34.89\times 10^9}\right)^N}$ $(N = 2, 4, 6, 8)$. **Figure 20(a)** shows the rejection ratio of the MWP filter as a function of TBF central wavelength with different filter shapes of TBF. To show the operation stability in high rejection ratio region with different TBF filter shapes, we define the TBF central wavelength tolerance as operation span of TBF central wavelength when the rejection ratio is greater than 40 dB. **Figure 20(b)** plots the TBF tolerance of central wavelength with different filter shapes of TBF. It can be seen that higher-order super-gaussian function leads to worse stability of the system.

Since the high nonlinearities induced by the tight light confinement of silicon photonic devices, the influence of optical nonlinear effects should also be taken into consideration

when designing MWP devices. MWP devices such as MWP filters based on silicon waveguide devices might have strong nonlinear microwave responses, which are dependent on the optical carrier power level. Taking the PhC microcavity as an example, we study the nonlinear microwave responses of the MWP filters based on the SOI waveguide devices.

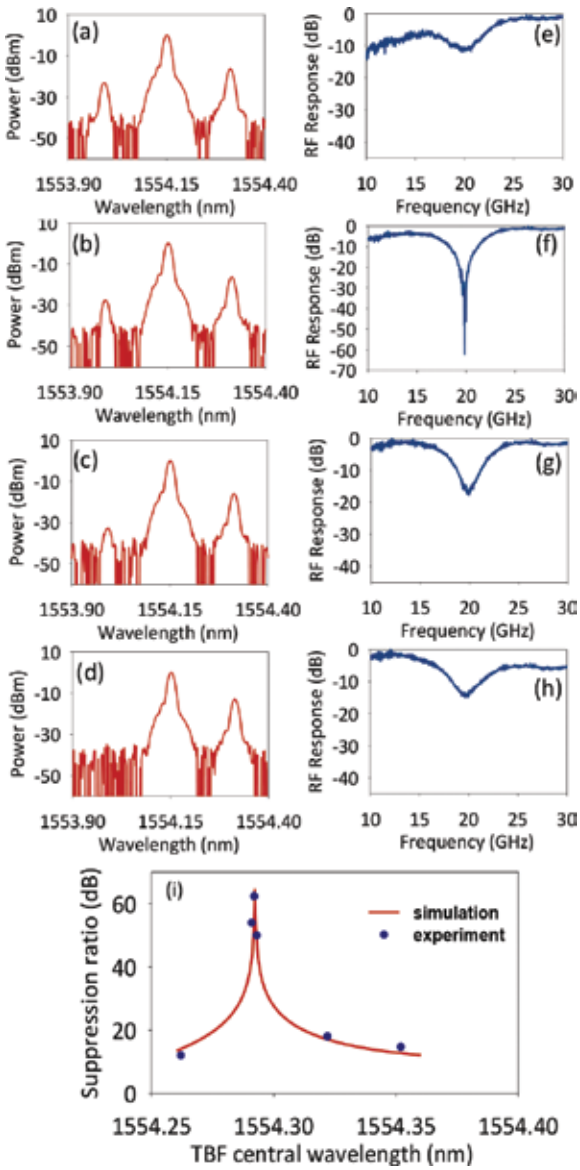

Figure 19. (a)–(d) Optical spectra after the TBF when the central wavelength of the TBF is 1554.262, 1554.292, 1554.322, and 1554.352 nm, respectively. (e)–(h) The corresponding MWP filter response. (i) Rejection ratio as a function of TBF central wavelength.

Figure 21(a) illustrates the typical scheme of an MWP filter based on a PhC microcavity. **Figure 21(b)** and **(c)** summarizes the operation principle of the device. After been phase

http://dx.doi.org/10.5772/66322

modulated, the output field is then sent to a PhC microcavity. Assuming that the wavelength of optical carrier is λ_c, locating on the left side of the linear notch resonant wavelength of the PhC microcavity (Case 1), as shown in **Figure 21(b)**, when the optical carrier power is very low and one of the sideband (f_1) is just aligned to the notch resonant wavelength of the PhC microcavity, a bandpass MWP filter with a central frequency of f_1 is obtained. When the optical carrier power is increased, considering the combined nonlinear effects in the PhC microcavity, the notch peak of the microcavity will red shift (e.g., shift by f_2-f_1), resulting in an bandpass MWP filter with a varied central frequency of f_2. When the wavelength of optical carrier is located on the right side of the linear notch resonant wavelength of the PhC microcavity, the situation is a little more complicated. For Case 2, as shown in **Figure 21(c)**, the initial notch peak of the PhC microcavity is aligned to the left sideband corresponding to f_2. When the optical carrier power is increased, the notch peak wavelength will red shift, leading to the decrease of the central frequency of the MWP filter. Remarkably, when we further increase the optical carrier power, the notch peak will go across the optical carrier wavelength. Hence, the central frequency of the MWP filter will first decrease and then increase when gradually increasing the optical carrier power from a very low level to a relatively high level.

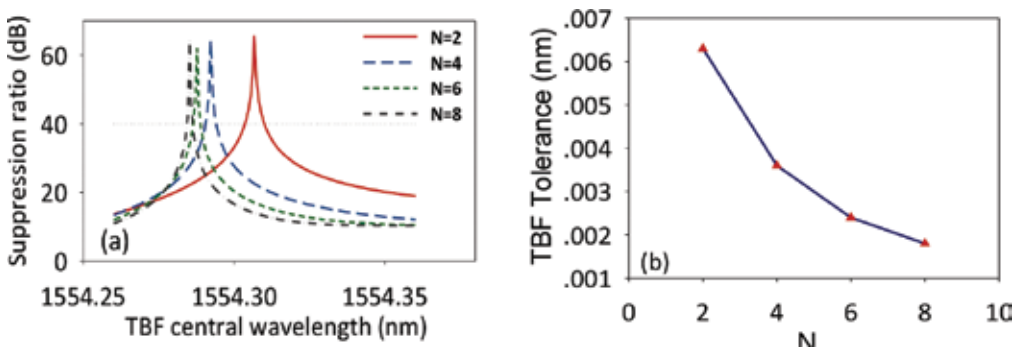

Figure 20. (a) Rejection ratio as functions of TBF central wavelength with different filter shape of TBF. (b) TBF tolerance of central wavelength with different filter shape of TBF.

The resonant wavelength of the cavity is around 1554.152 nm. **Figure 22** shows measured MWP filter responses under different optical carrier power levels for Case 1 and Case 2. The wavelengths of the carrier are 1554.056 and 1554.296 nm, respectively. For Case 1, since the notch resonant wavelength of the PhC microcavity red shifts as the optical carrier power increases, the central frequency of the MWP filter increases. When the optical carrier power increases from −13.5 to 5.5 dBm, the central frequency of the MWP filter is changed from 13.9 to 24 GHz. For Case 2, when the optical carrier is increased from −13.5 to −3.5 dBm, the central frequency of the MWP filter decreases, which indicates that the resonant wavelength of the PhC microcavity is still on the left side of the optical carrier in the process. When we increase the power from −3.5 to −1.5 dBm, the central frequency of the MWP filter suddenly jumps to another frequency at about −2 dBm. When we further increase the power of the carrier light, the central frequency of the MWP filter increases, in contrast with the decrease in low-power region. The obtained results here indicate that the resonance of the

PhC microcavity first jumps to the right side of the carrier, and then red shifts as the carrier further increases.

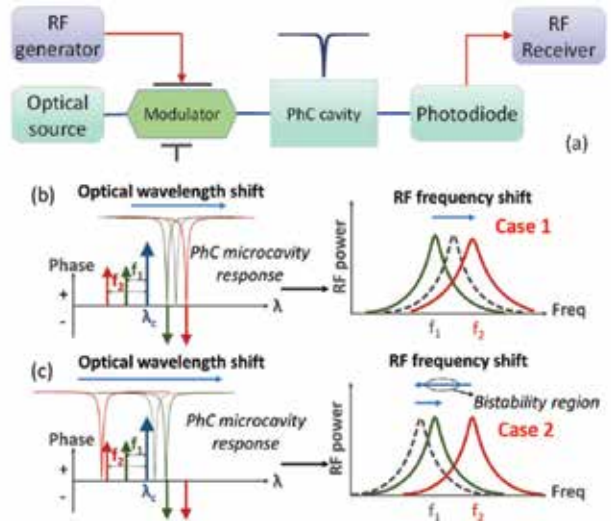

Figure 21. (a) Schematic illustration of the typical scheme of a MWP filter based on PhC cavity. (b) and (c) Working principle of the optical carrier power dependent MWP filter. Case 1: the wavelength of the optical carrier is located on the left side of the linear notch resonant wavelength of the PhC microcavity. Case 2: the wavelength of the optical carrier is located on the right side of the linear notch resonant wavelength of the PhC microcavity.

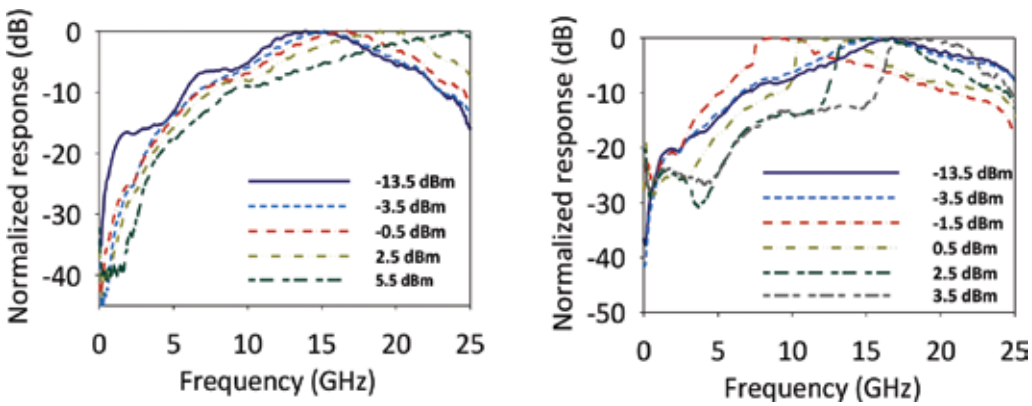

Figure 22. Measured MWP filter responses under different optical carrier power levels for (a) Case 1 and (b) Case 2.

4. Photonic-assisted microwave signal multiplication and ASK modulation

Photonic-assisted generation of microwave signals can find interesting applications in many microwave photonic systems, such as broad-band wireless access networks, software-defined radio, antenna remoting, phased-array antenna, and radar systems [65]. Usually,

http://dx.doi.org/10.5772/66322

optical microwave generation is based on heterodyne techniques. Several approaches to generating two phase-correlated optical waves have been proposed and demonstrated based on free space devices [100, 101] and fiber devices [64, 65, 102–111]. Among these approaches, microwave frequency multiplication based on external modulation using MZMs has been considered an effective solution for high frequency and tunable microwave signal generation. Photonic generation of RF binary digital modulation signals is another key technology in microwave photonics. Amplitude-shift keying (ASK), phase-shift keying (PSK), and frequency-shift keying (FSK) are basic modulation formats in wireless communications, which convey information by modulating the amplitude, phase or frequency of a continuous carrier wave. Traditionally, these modulation microwave signals are generated in electrical domain using digital electronic circuits [40]. Due to the electronic bottleneck, the major difficulty of this traditional technique is that the frequency of the generated signals is limited to a few gigahertz. An effective method to generate high frequency RF signals is to generate RF signals in the optical domain [38, 39, 112]. Similar to microwave frequency mulitiplication, the use of MZM is also considered to be a competitive approach to generating binary digital modulation signals. Microwave PSK and FSK signals have been proposed and realized based on commercial MZMs [38, 39, 112]. However, microwave ASK signal as a fundamental digital modulation format in wireless communication has rarely been realized using MZM. In this section, we introduce our recent work on microwave signal multiplication and ASK modulation based on an integrated silicon modulator.

We first propose a simple scheme to obtain frequency-multiplicated microwave signals [113]. **Figure 23** illustrates the schematic illustration of the proposed photonic frequency-multiplicated microwave signal generation system using an integrated silicon MZM. CW light from a tunable laser diode (TLD) is sent to the MZM. The driving signal and the DC-bias are combined by a bias-tee and applied to the MZM. The output light intensity of the MZM can be written as:

$$\begin{aligned} I &= \frac{1}{2} I_0 [\,1 + J_0(m)\cos\varphi_0] + I_0 \cos\varphi_0 \sum_{n=1}^{\infty} (-1)^n J_{2n}(m)\cos(2n\,\omega_{\mathrm{RF}}\,t) \\ &\quad + I_0 \sin\varphi_0 \sum_{n=1}^{\infty} (-1)^n J_{2n-1}(m)\cos[\,(2n-1)\,\omega_{RF}\,t] \end{aligned} \tag{1}$$

where $m = \pi V_{RF}/V_{\pi}$ is the modulation indice of the MZM. I_0 is the intensity of the input optical carrier. $\phi_0 = \pi V_b/V_{\pi}$ is the constant phase difference between the two arms determined by the constant DC-bias voltage V_b. V_{π} is the half-wave voltage of the MZM. V_{RF} and ω_{RF} are the amplitude and angular frequency of the applied electrical drive voltage, respectively. It can be seen from Eq. (1) that if the modulator is biased at V_{π}, the odd components will be suppressed. Ignoring the high-order harmonic wave, a frequency-doubled microwave signal is obtained. In addition, by adjusting the driving microwave signal amplitude to let $J_2(m) = 0$, the quadruple response will dominate the output, and a frequency-quadrupled signal can be obtained. Similarly, a frequency-tripled signal is generated by suppressing the even components and $J_1(m)$ term of the signal.

We investigate the generation of frequency-doubled microwave signal. **Figure 24(a)** and **(b)** shows the wave-forms of the original 500-MHz driving signal and the generated 1-GHz signal. **Figure 24(c)** and **(d)** shows the obtained 2-GHz signal when the driving signal frequency is 1 GHz.

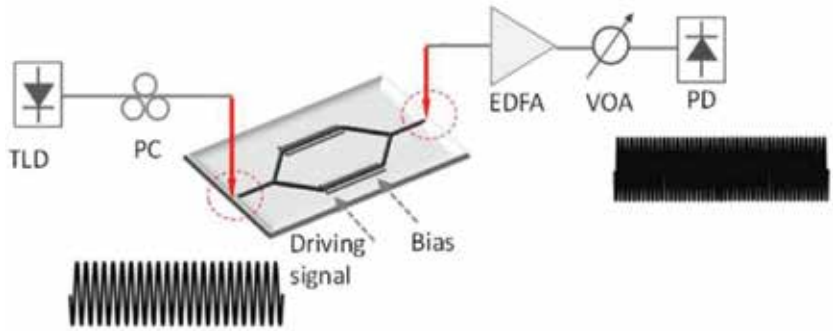

Figure 23. Schematic illustration of the proposed photonic-assisted microwave signal multiplication.

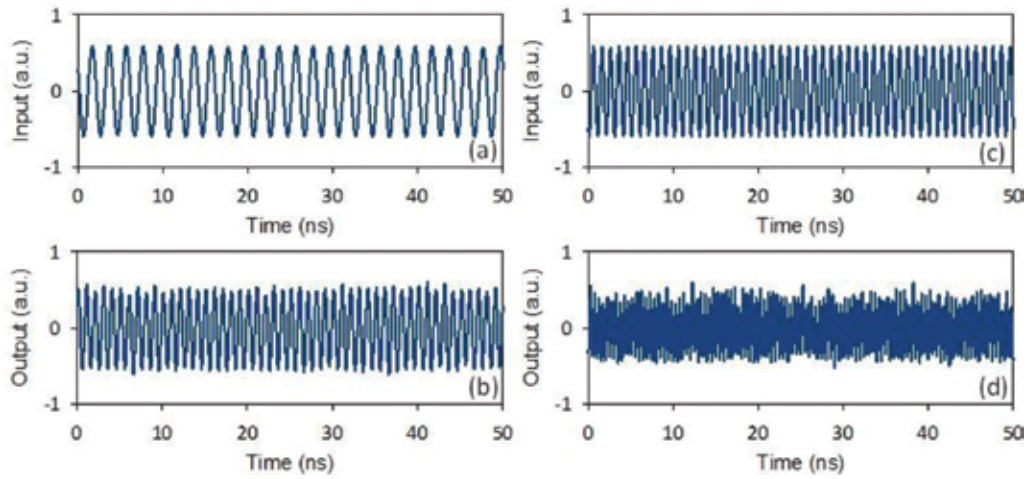

Figure 24. Waveforms of (a) the input 500-MHz driving signal, (b) the generated 1-GHz frequency-doubled signal, (c) the input 1-GHz driving signal, and (d) the generated 2-GHz frequency-doubled signal.

Using the fabricated integrated MZM, we also demonstrate the feasibility of microwave ASK modulation using an integrated photonic approach [113]. **Figure 25** illustrates the schematic illustration of the proposed photonic microwave ASK signal modulation system using an integrated silicon MZM. The microwave carrier signal and the binary coding signal s(t) are applied to the two RF ports of the MZM, respectively. The AC term of the detected signal at the output of the PD can be written as:

$$i_{AC} \propto 2J_1(m)\cos(\omega_{RF}t)\sin(\gamma s(t)-\varphi_0)+J_0(m)\cos(\gamma s(t)-\varphi_0) \quad (2)$$

where ω_{RF}, m, $V_{RF,}$ V_{π}, and ϕ_0 are defined as previously mentioned. $\gamma=\pi V_s/V_{\pi}$ is the modulation index in the arm where the binary coding signal is applied. Assuming $\phi_0 = 0$, Eq. (2) can be simplified as:

http://dx.doi.org/10.5772/66322

$$i_{AC} \propto 2J_1(m)\cos(\omega_{RF}t)\sin(\gamma s(t))+J_0(m)\cos(\gamma s(t)) \tag{3}$$

The second term in Eq. (3) is located in the baseband, which can be easily eliminated by an electric filter. Assuming $\gamma = \pi/2$, the amplitude of the obtained signal is:

$$i = \begin{cases} 2J_1(m)\cos(\omega_{RF}t) & s(t)=1 \\ 0 & s(t)=0 \end{cases} \tag{4}$$

As can be seen, the amplitude of the carrier is "1" with bit "1", and "0" with bit "0". Therefore, two-level microwave ASK signal is generated.

Figure 26(a) shows the waveforms of the original 50-Mb/s baseband signal with a pattern of "110100101101001011". The original 1-GHz microwave carrier is shown in **Figure 26(b)**. **Figure 26(c)** shows the modulated microwave ASK signal.

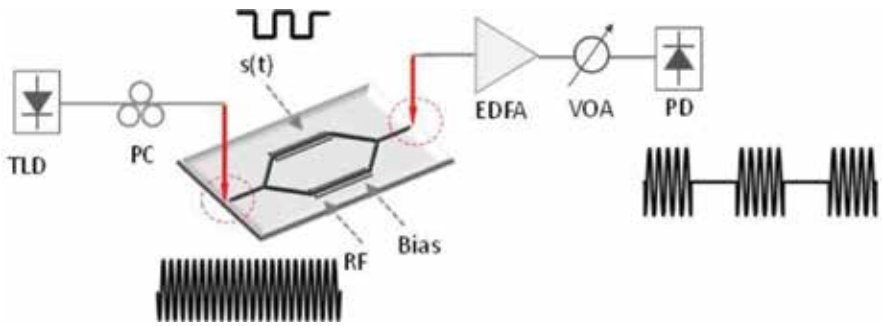

Figure 25. Schematic illustration of the proposed photonic microwave ASK signal generator.

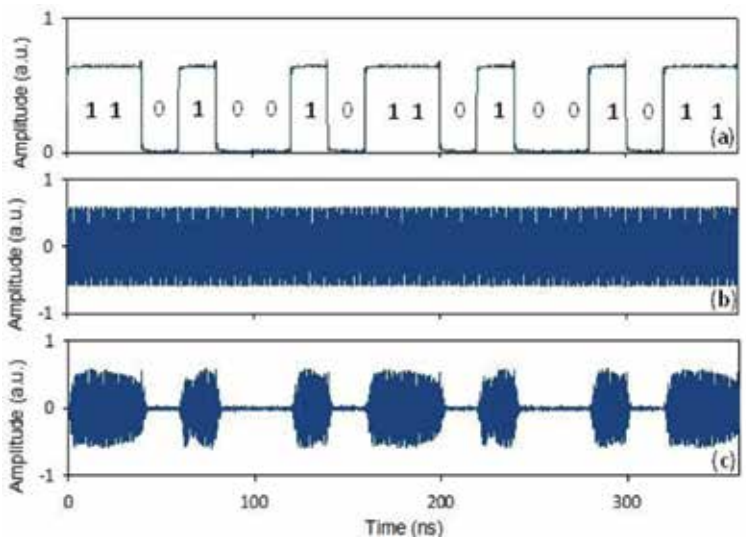

Figure 26. Waveforms of (a) the original 50-Mb/s baseband signal with a pattern of "110100101101001011", (b) original 1-GHz microwave carrier signal, and (c) the output microwave ASK signal.

5. Discussion

In summary, we review our recent works in chip-scale microwave photonic signal processing, including on-chip analog links, MWP filters, and photonic generation of microwave. As a new research topic, integrated MWP has just started to bloom and is set to have a bright future. After evaluating linearity performance of the on-chip analog links, future works may focus on increasing the linearities or decreasing nonlinearities of the on-chip analog links. As to MWP filters, more high performance silicon MWP filters will be demonstrated, involving resonators, photonic crystals, or other silicon photonic devices. In addition, more nonlinear optics can be used for MWP filters. For example, four-wave mixing (FWM) for MWP filtering has been realized [114, 115]. The demonstrated microwave signal multiplication and ASK modulation are still operated in low-frequency region. By optimizing the device design, the operation frequency can be improved and the power consumption can be further reduced. In addition to on-chip analog links, MWP filters, and photonic generation of microwave, silicon photonics can be also adopted to accelerate the success of versatile MWP signal processing functionalities, including arbitrary waveform generation, on-chip pulse shaping, delay line, beamformer, and more.

6. Conclusion

In this chapter, we have reviewed recent research efforts toward on-chip microwave photonic signal processing.

1. Using the fabricated silicon photonic devices, we evaluate the performance of on-chip analog signal transmission. The degradations level of SHD and THD are evaluated.
2. Various types of MWP filters are introduced, and the impact of optical nonlinearities to MWP filters is also discussed.
3. Photonic-assisted microwave signal multiplication/modulation: we propose a simple scheme to obtain frequency-multiplicated microwave signals or amplitude-coded microwave signals based on a single integrated silicon MZM. A 2-GHz frequency-doubled microwave signal is generated using a 1-GHz driving signal. A 50-Mb/s binary amplitude-coded 1-GHz microwave signal is also successfully generated in the experiment.

With future improvement, one would also expect to see more photonic-assisted microwave signal processing applications exploiting compact-integrated silicon photonic devices.

Acknowledgements

This work was supported by the National Program for Support of Top-Notch Young Professionals, the National Natural Science Foundation of China (NSFC) under grants 11574001, 11274131, and 61222502, the Program for New Century Excellent Talents in University under grant NCET-11-0182, the National Basic Research Program of China

(973 Program) under grant 2014CB340004, the Wuhan Science and Technology Plan Project under grant 2014070404010201, the Fundamental Research Funds for the Central Universities (HUST) under grants 2012YQ008 and 2013ZZGH003. The authors thank the Center of Micro-Fabrication and Characterization (CMFC) of WNLO for the support in the manufacturing process of silicon waveguides. The authors also thank to the facility support of the Center for Nanoscale Characterization and Devices of WNLO.

Author details

Jian Wang* and Yun Long

*Address all correspondence to: jwang@hust.edu.cn

Wuhan National Laboratory for Optoelectronics, School of Optical and Electronic Information, Huazhong University of Science and Technology, Wuhan, Hubei, China

References

[1] R. Soref, "The past, present, and future of silicon photonics," IEEE J. Sel. Top. Quantum Electron. 12, 1678–1687 (2006).

[2] B. Jalali, and S. Fathpour, "Silicon photonics," J. Lightwave Technol. 24, 4600–4615 (2006).

[3] M. Hochberg, and T. Baehr-Jones, "Towards fabless silicon photonics," Nat. Photonics. 4, 492–494 (2010).

[4] M. Asghari, and A. V. Krishnamoorthy, "Silicon photonics: Energy-efficient communication," Nat. Photonics. 5, 268–270 (2011).

[5] M. Soljačić, M. Ibanescu, S. G. Johnson, Y. Fink, and J. Joannopoulos, "Optimal bistable switching in nonlinear photonic crystals," Phys. Rev. E. 66, 055601 (2002).

[6] Y. Akahane, T. Asano, B.-S. Song, and S. Noda, "Fine-tuned high-Q photonic-crystal nanocavity," Opt. Express. 13, 1202–1214 (2005).

[7] P. Barclay, K. Srinivasan, and O. Painter, "Nonlinear response of silicon photonic crystal microresonators excited via an integrated waveguide and fiber taper," Opt. Express. 13, 801–820 (2005).

[8] M. Notomi, A. Shinya, S. Mitsugi, G. Kira, E. Kuramochi, and T. Tanabe, "Optical bistable switching action of Si high-Q photonic-crystal nanocavities," Opt. Express. 13, 2678–2687 (2005).

[9] Y. Zhang, D. Li, C. Zeng, Y. Shi, Z. Huang, J. Yu, and J. Xia, "Ultralow power nonlinear response in an Si photonic crystal nanocavity," IEEE Photon. J. 5, 6601409 (2013).

[10] Y. Zhang, D. Li, C. Zeng, Z. Huang, Y. Wang, Q. Huang, Y. Wu, J. Yu, and J. Xia, "Silicon optical diode based on cascaded photonic crystal cavities," Opt. Lett. 39, 1370–1373 (2014).

[11] W. Bogaerts, R. Baets, P. Dumon, V. Wiaux, S. Beckx, D. Taillaert, B. Luyssaert, J. Van Campenhout, P. Bienstman, and D. Van Thourhout, "Nanophotonic waveguides in silicon-on-insulator fabricated with CMOS technology," J. Lightwave Technol. 23, 401–412 (2005).

[12] B. E. Little, S. T. Chu, H. A. Haus, J. Foresi, and J. P. Laine, "Microring resonator channel dropping filters," J. Lightwave Technol. 15, 998–1005 (1997).

[13] B. E. Little, J. Foresi, G. Steinmeyer, E. Thoen, S. Chu, H. Haus, E. Ippen, L. Kimerling, and W. Greene, "Ultra-compact Si-SiO 2 microring resonator optical channel dropping filters," IEEE Photon. Technol. Lett. 10, 549–551 (1998).

[14] B. Little, S. Chu, W. Pan, and Y. Kokubun, "Microring resonator arrays for VLSI photonics," IEEE Photon. Technol. Lett. 12, 323–325 (2000).

[15] G. Priem, P. Dumon, W. Bogaerts, D. Van Thourhout, G. Morthier, and R. Baets, "Optical bistability and pulsating behaviour in Silicon-On-Insulator ring resonator structures," Opt. Express. 13, 9623–9628 (2005).

[16] W. Bogaerts, P. De Heyn, T. Van Vaerenbergh, K. De Vos, S. Kumar Selvaraja, T. Claes, P. Dumon, P. Bienstman, D. Van Thourhout, and R. Baets, "Silicon microring resonators," Laser & Photonics Rev. 6, 47–73 (2012).

[17] T. Barwicz, H. Byun, F. Gan, C. Holzwarth, M. Popovic, P. Rakich, M. Watts, E. Ippen, F. Kärtner, and H. Smith, "Silicon photonics for compact, energy-efficient interconnects [Invited]," J. Opt. Netw. 6, 63–73 (2007).

[18] J. S. Levy, A. Gondarenko, M. A. Foster, A. C. Turner-Foster, A. L. Gaeta, and M. Lipson, "CMOS-compatible multiple-wavelength oscillator for on-chip optical interconnects," Nat. Photonics. 4, 37–40 (2010).

[19] X. Xiao, H. Xu, X. Li, Z. Li, Y. Yu, and J. Yu, "High-speed on-chip photonic link based on ultralow-power microring modulator," in *Optical Fiber Communication Conference* (Optical Society of America, 2014), paper Tu2E. 6.

[20] J. K. Doylend, and A. P. Knights, "The evolution of silicon photonics as an enabling technology for optical interconnection," Laser & Photonics Rev. 6, 504–525 (2012).

[21] Y. Vlasov, "Silicon photonics for next generation computing systems," in *European Conference on Optical Communications*(2008), paper 1–2.

[22] L. Chen, K. Preston, S. Manipatruni, and M. Lipson, "Integrated GHz silicon photonic interconnect with micrometer-scale modulators and detectors," Opt. Express. 17, 15248–15256 (2009).

[23] C. Sun, M. T. Wade, Y. Lee, J. S. Orcutt, L. Alloatti, M. S. Georgas, A. S. Waterman, J. M. Shainline, R. R. Avizienis, and S. Lin, "Single-chip microprocessor that communicates directly using light," Nature. 528, 534–538 (2015).

[24] C. Sun, M. Georgas, J. Orcutt, B. Moss, Y.-H. Chen, J. Shainline, M. Wade, K. Mehta, K. Nammari, and E. Timurdogan, "A monolithically-integrated chip-to-chip optical link in bulk CMOS," IEEE J. Solid-St. Circ. 50, 828–844 (2015).

[25] Q. Li, Y. Liu, K. Padmaraju, R. Ding, D. F. Logan, J. J. Ackert, A. P. Knights, T. Baehr-Jones, M. Hochberg, and K. Bergman, "10-Gb/s BPSK link using silicon microring resonators for modulation and demodulation," in *Optical Fiber Communication Conference* (Optical Society of America, 2014), paper Tu2E. 5.

[26] D. Marris-Morini, L. Virot, C. Baudot, J.-M. Fédéli, G. Rasigade, D. Perez-Galacho, J.-M. Hartmann, S. Olivier, P. Brindel, and P. Crozat, "A 40 Gbit/s optical link on a 300-mm silicon platform," Opt. Express. 22, 6674–6679 (2014).

[27] A. Narasimha, B. Analui, Y. Liang, T. J. Sleboda, S. Abdalla, E. Balmater, S. Gloeckner, D. Guckenberger, M. Harrison, and R. G. Koumans, "A fully integrated 4× 10-Gb/s DWDM optoelectronic transceiver implemented in a standard 0.13 μm CMOS SOI technology," IEEE J. Solid-St. Circ. 42, 2736–2744 (2007).

[28] C. Doerr, L. Chen, L. Buhl, and Y.-K. Chen, "Eight-Channel SiO/Si N/Si/Ge CWDM Receiver," IEEE Photon. Technol. Lett. 23, 1201–1203 (2011).

[29] C. Doerr, and T. Taunay, "Silicon photonics core-, wavelength-, and polarization-diversity receiver," IEEE Photon. Technol. Lett. 9, 597–599 (2011).

[30] C. R. Doerr, N. K. Fontaine, and L. L. Buhl, "PDM-DQPSK silicon receiver with integrated monitor and minimum number of controls," IEEE Photon. Technol. Lett. 24, 697–699 (2012).

[31] J. Klamkin, F. Gambini, S. Faralli, A. Malacarne, G. Meloni, G. Berrettini, G. Contestabile, and L. Potì, "A 100-Gb/s noncoherent silicon receiver for PDM-DBPSK/DQPSK signals," Opt. Express. 22, 2150–2158 (2014).

[32] P. Dong, C. Xie, L. Chen, L. L. Buhl, and Y.-K. Chen, "112-Gb/s monolithic PDM-QPSK modulator in silicon," Opt. Express. 20, B624-B629 (2012).

[33] A. Shastri, M. Webster, G. Jeans, P. Metz, S. Sunder, B. Chattin, B. Dama, and K. Shastri, "Experimental demonstration of ultra-low-power single polarization 56 Gb/s QAM-16 generation without DAC using CMOS photonics," in *2014 The European Conference on Optical Communication (ECOC)* (2014).

[34] C. R. Doerr, L. Chen, D. Vermeulen, T. Nielsen, S. Azemati, S. Stulz, G. McBrien, X.-M. Xu, B. Mikkelsen, and M. Givehchi, "Single-chip silicon photonics 100-Gb/s coherent transceiver," in *Optical Fiber Communication Conference* (Optical Society of America, 2014), paper Th5C. 1.

[35] J. Yao, "Microwave photonics," J. Lightwave Technol. 27, 314–335 (2009).

[36] J. Capmany, J. Mora, I. Gasulla, J. Sancho, J. Lloret, and S. Sales, "Microwave photonic signal processing," J. Lightwave Technol. 31, 571–586 (2013).

[37] F. Liu, T. Wang, Z. Zhang, M. Qiu, and Y. Su, "On-chip photonic generation of ultra-wideband monocycle pulses," Electron. Lett. 45, 1 (2009).

[38] P. Cao, X. Hu, L. Zhang, J. Wu, X. Jiang, and Y. Su, "Photonic generation of microwave frequency shift keying signal using a single-drive Mach–Zehnder modulator," Opt. Express. 22, 14433–14440 (2014).

[39] Z. Tang, T. Zhang, F. Zhang, and S. Pan, "Photonic generation of a phase-coded microwave signal based on a single dual-drive Mach–Zehnder modulator," Opt. Lett. 38, 5365–5368 (2013).

[40] P. Xiang, X. Zheng, H. Zhang, Y. Li, and Y. Chen, "A novel approach to photonic generation of RF binary digital modulation signals," Opt. Express. 21, 631–639 (2013).

[41] D. Zhang, X. Feng, X. Li, K. Cui, F. Liu, and Y. Huang, "Tunable and reconfigurable bandstop microwave photonic filter based on integrated microrings and Mach–Zehnder interferometer," J. Lightwave Technol. 31, 3668–3675 (2013).

[42] Y. Long, and J. Wang, "All-optical tuning of a nonlinear silicon microring assisted microwave photonic filter: theory and experiment," Opt. Express. 23, 17758–17771 (2015).

[43] Y. Long, and J. Wang, "Ultra-high peak rejection notch microwave photonic filter using a single silicon microring resonator," Opt. Express 23, 17739–17750 (2015).

[44] D. Marpaung, B. Morrison, M. Pagani, R. Pant, D.-Y. Choi, B. Luther-Davies, S. J. Madden, and B. J. Eggleton, "Low-power, chip-based stimulated Brillouin scattering microwave photonic filter with ultrahigh selectivity," Optica. 2, 76–83 (2015).

[45] N. Ehteshami, W. Zhang, and J. Yao, "Optically tunable full 360° microwave photonic phase shifter using three cascaded silicon-on-insulator microring resonators," Opt. Commun. 373, 53–58 (2016).

[46] J. Wu, J. Peng, B. Liu, T. Pan, H. Zhou, J. Mao, Y. Yang, C. Qiu, and Y. Su, "Passive silicon photonic devices for microwave photonic signal processing," Opt. Commun. 373, 44–52 (2016).

[47] A. Casas-Bedoya, B. Morrison, M. Pagani, D. Marpaung, and B. J. Eggleton, "Tunable narrowband microwave photonic filter created by stimulated Brillouin scattering from a silicon nanowire," Opt. Lett. 40, 4154–4157 (2015).

[48] A. Zheng, J. Dong, L. Zhou, X. Xiao, Q. Yang, X. Zhang, and J. Chen, "Fractional-order photonic differentiator using an on-chip microring resonator," Opt. Lett. 39, 6355–6358 (2014).

[49] S. Yan, Y. Zhang, J. Dong, A. Zheng, S. Liao, H. Zhou, Z. Wu, J. Xia, and X. Zhang, "Operation bandwidth optimization of photonic differentiators," Opt. Express. 23, 18925–18936 (2015).

[50] Y. Yu, F. Jiang, H. Tang, L. Xu, X. Liu, J. Dong, and X. Zhang, "Reconfigurable photonic temporal differentiator based on a dual-drive Mach-Zehnder modulator," Opt. Express. 24, 11739–11748 (2016).

[51] H. Jiang, D. Marpaung, M. Pagani, K. Vu, D.-Y. Choi, S. J. Madden, L. Yan, and B. J. Eggleton, "Wide-range, high-precision multiple microwave frequency measurement using a chip-based photonic Brillouin filter," Optica. 3, 30–34 (2016).

[52] M. Pagani, B. Morrison, Y. Zhang, A. Casas-Bedoya, T. Aalto, M. Harjanne, M. Kapulainen, B. J. Eggleton, and D. Marpaung, "Low-error and broadband microwave frequency measurement in a silicon chip," Optica. 2, 751–756 (2015).

[53] J. Du, and J. Wang, "Experimental performance evaluation of analog signal transmission in a silicon microring resonator," Opt. Lett. 40, 1181–1184 (2015).

[54] C. Gui, Y. Zhang, J. Du, J. Xia, and J. Wang, "Experimental demonstration of analog signal transmission in a silicon photonic crystal L3 resonator," Opt. Express. 23, 13916–13923 (2015).

[55] W. Liu, M. Li, R. S. Guzzon, E. J. Norberg, J. S. Parker, L. A. Coldren, and J. Yao, "A photonic temporal integrator with an ultra-long integration time window based on an InP-InGaAsP integrated ring resonator," J. Lightwave Technol. 32, 3654–3659 (2014).

[56] J. Zhang, and J. Yao, "Microwave photonic integrator based on a multichannel fiber Bragg grating," Opt. Lett. 41, 273–276 (2016).

[57] H. P. Bazargani, M. Burla, and J. Azaña, "Experimental demonstration of sub-picosecond optical pulse shaping in silicon based on discrete space-to-time mapping," Opt. Lett. 40, 5423–5426 (2015).

[58] H. P. Bazargani, and J. Azaña, "Optical pulse shaping based on discrete space-to-time mapping in cascaded co-directional couplers," Opt. Express. 23, 23450–23461 (2015).

[59] T. Yang, J. Dong, L. Liu, S. Liao, S. Tan, L. Shi, D. Gao, and X. Zhang, "Experimental observation of optical differentiation and optical Hilbert transformation using a single SOI microdisk chip," Sci. Rep. 4, 3960 (2014).

[60] J. Wang, H. Shen, L. Fan, R. Wu, B. Niu, L. T. Varghese, Y. Xuan, D. E. Leaird, X. Wang, and F. Gan, "Reconfigurable radio-frequency arbitrary waveforms synthesized in a silicon photonic chip," Nat. Commun. 6, 5957 (2015).

[61] M. H. Khan, H. Shen, Y. Xuan, L. Zhao, S. Xiao, D. E. Leaird, A. M. Weiner, and M. Qi, "Ultrabroad-bandwidth arbitrary radiofrequency waveform generation with a silicon photonic chip-based spectral shaper," Nat. Photonics. 4, 117–122 (2010).

[62] J. McKinney, D. Leaird, and A. Weiner, "Millimeter-wave arbitrary waveform generation with a direct space-to-time pulse shaper," Opt. Lett. 27, 1345–1347 (2002).

[63] S. Liao, Y. Ding, J. Dong, T. Yang, X. Chen, D. Gao, and X. Zhang, "Arbitrary waveform generator and differentiator employing an integrated optical pulse shaper," Opt. Express. 23, 12161–12173 (2015).

[64] J. O'reilly, P. Lane, R. Heidemann, and R. Hofstetter, "Optical generation of very narrow linewidth millimetre wave signals," Electron. Lett. 28, 2309–2311 (1992).

[65] G. Qi, J. Yao, J. Seregelyi, S. Paquet, and C. Bélisle, "Generation and distribution of a wide-band continuously tunable millimeter-wave signal with an optical external modulation technique," IEEE Trans. Microwave Theory Tech. 53, 3090–3097 (2005).

[66] M. Burla, C. G. Roeloffzen, L. Zhuang, D. Marpaung, M. R. Khan, P. Maat, K. Dijkstra, A. Leinse, M. Hoekman, and R. Heideman, "System integration and radiation pattern measurements of a phased array antenna employing an integrated photonic beamformer for radio astronomy applications," Appl. Optics. 51, 789–802 (2012).

[67] H. Zmuda, R. A. Soref, P. Payson, S. Johns, and E. N. Toughlian, "Photonic beamformer for phased array antennas using a fiber grating prism," IEEE Photon. Technol. Lett. 9, 241–243 (1997).

[68] N.-N. Feng, P. Dong, D. Feng, W. Qian, H. Liang, D. C. Lee, J. B. Luff, A. Agarwal, T. Banwell, and R. Menendez, "Thermally-efficient reconfigurable narrowband RF-photonic filter," Opt. Express. 18, 24648–24653 (2010).

[69] Y. Yue, H. Huang, L. Zhang, J. Wang, J.-Y. Yang, O. F. Yilmaz, J. S. Levy, M. Lipson, and A. E. Willner, "UWB monocycle pulse generation using two-photon absorption in a silicon waveguide," Opt. Lett. 37, 551–553 (2012).

[70] X. Wang, W. Shi, H. Yun, S. Grist, N. A. Jaeger, and L. Chrostowski, "Narrow-band waveguide Bragg gratings on SOI wafers with CMOS-compatible fabrication process," Opt. Express. 20, 15547–15558 (2012).

[71] M. L. Farwell, W. S. Chang, and D. R. Huber, "Increased linear dynamic range by low biasing the Mach-Zehnder modulator," IEEE Photon. Technol. Lett. 5, 779–782 (1993).

[72] A. Khilo, C. M. Sorace, and F. X. Kärtner, "Broadband linearized silicon modulator," Opt. Express. 19, 4485–4500 (2011).

[73] M. Streshinsky, A. Ayazi, Z. Xuan, A. E.-J. Lim, G.-Q. Lo, T. Baehr-Jones, and M. Hochberg, "Highly linear silicon traveling wave Mach-Zehnder carrier depletion modulator based on differential drive," Opt. Express. 21, 3818–3825 (2013).

[74] J. Cardenas, P. A. Morton, J. B. Khurgin, A. Griffith, C. B. Poitras, K. Preston, and M. Lipson, "Linearized silicon modulator based on a ring assisted Mach Zehnder inteferometer," Opt. Express. 21, 22549–22557 (2013).

[75] M. LaGasse, W. Charczenko, M. Hamilton, and S. Thaniyavarn, "Optical carrier filtering for high dynamic range fibre optic links," Electron. Lett. 30, 2157–2158 (1994).

[76] P. Li, L. Yan, T. Zhou, W. Li, Z. Chen, W. Pan, and B. Luo, "Improvement of linearity in phase-modulated analog photonic link," Opt. Lett. 38, 2391–2393 (2013).

[77] H. Huang, Y. Yue, L. Zhang, C. Chase, D. Parekh, F. Sedgwick, M. Wu, C. Chang-Hasnain, M. Tur, and A. Willner, "Analog signal transmission in a high-contrast-gratings-based hollow-core-waveguide," J. Lightwave Technol. 30, 3640–3646 (2012).

[78] M. Song, L. Zhang, R. G. Beausoleil, and A. E. Willner, "Nonlinear distortion in a silicon microring-based electro-optic modulator for analog optical links," IEEE J. Sel. Top. Quantum Electron. 16, 185–191 (2010).

[79] A. Ayazi, T. Baehr-Jones, Y. Liu, A. E.-J. Lim, and M. Hochberg, "Linearity of silicon ring modulators for analog optical links," Opt. Express. 20, 13115–13122 (2012).

[80] S. J. Spector, S. Yegnanarayanan, R. Swint, T. M. Lyszczarz, and P. W. Juodawlkis, "Two-tone measurement of the nonlinear behavior of a silicon-on-insulator (SOI) ring resonator," in *CLEO: Applications and Technology* (Optical Society of America, 2012), paper JW4A. 74.

[81] X. Luo, X. Tu, J. Song, L. Ding, Q. Fang, T.-Y. Liow, M. Yu, and G.-Q. Lo, "Slope efficiency and spurious-free dynamic range of silicon Mach-Zehnder modulator upon carrier depletion and injection effects," Opt. Express. 21, 16570–16577 (2013).

[82] D. Marpaung, C. Roeloffzen, R. Heideman, A. Leinse, S. Sales, and J. Capmany, "Integrated microwave photonics," Laser & Photonics Rev. 7, 506–538 (2013).

[83] R. A. Minasian, "Photonic signal processing of microwave signals," IEEE Trans. Microwave Theory Tech. 54, 832–846 (2006).

[84] J. Capmany, B. Ortega, D. Pastor, and S. Sales, "Discrete-time optical processing of microwave signals," J. Lightwave Technol. 23, 702 (2005).

[85] J. Capmany, B. Ortega, and D. Pastor, "A tutorial on microwave photonic filters," J. Lightwave Technol. 24, 201–229 (2006).

[86] J. Mora, B. Ortega, A. Díez, J. L. Cruz, M. V. Andrés, J. Capmany, and D. Pastor, "Photonic microwave tunable single-bandpass filter based on a Mach-Zehnder interferometer," J. Lightwave Technol. 24, 2500–2509 (2006).

[87] B. Vidal, M. Piqueras, and J. Marti, "Tunable and reconfigurable photonic microwave filter based on stimulated Brillouin scattering," Opt. Lett. 32, 23–25 (2007).

[88] W. Zhang, and R. A. Minasian, "Widely tunable single-passband microwave photonic filter based on stimulated Brillouin scattering," IEEE Photon. Technol. Lett. 23, 1775–1777 (2011).

[89] L. Gao, X. Chen, and J. Yao, "Tunable microwave photonic filter with a narrow and flat-top passband," IEEE Microw. Wireless Compon. Lett. 23, 362–364 (2013).

[90] W. Li, and J. Yao, "A narrow-passband frequency-tunable microwave photonic filter with an improved dynamic range," in *Optical Fiber Communication Conference* (Optical Society of America, Anaheim, California, 2013), paper OTu2H. 3.

[91] P. K. Yu, "A novel digitally tunable microwave-photonic notch filter using differential group-delay module," IEEE Photon. Technol. Lett. 15 (2003).

[92] P. Alipour, A. A. Eftekhar, A. H. Atabaki, Q. Li, S. Yegnanarayanan, C. K. Madsen, and A. Adibi, "Fully reconfigurable compact RF photonic filters using high-Q silicon microdisk resonators," Opt. Express. 19, 15899–15907 (2011).

[93] D. Zhang, X. Feng, and Y. Huang, "Tunable and reconfigurable bandpass microwave photonic filters utilizing integrated optical processor on silicon-on-insulator substrate," IEEE Photon. Technol. Lett. 24, 1502–1505 (2012).

[94] J. Dong, L. Liu, D. Gao, Y. Yu, A. Zheng, T. Yang, and X. Zhang, "Compact notch microwave photonic filters using on-chip integrated microring resonators," IEEE Photon. J. 5, 5500307–5500307 (2013).

[95] M. S. Rasras, K.-Y. Tu, D. M. Gill, Y.-K. Chen, A. E. White, S. S. Patel, A. Pomerene, D. Carothers, J. Beattie, and M. Beals, "Demonstration of a tunable microwave-photonic

notch filter using low-loss silicon ring resonators," J. Lightwave Technol. 27, 2105–2110 (2009).

[96] J. Palací, G. E. Villanueva, J. V. Galán, J. Marti, and B. Vidal, "Single bandpass photonic microwave filter based on a notch ring resonator," IEEE Photon. Technol. Lett. 22, 1276–1278 (2010).

[97] D. Zhang, X. Feng, and Y. Huang, "Reconfigurable microwave photonic filter based on parallel-cascaded microrings assisted with a Mach–Zehnder interferometer," J. Opt. 14, 065502 (2012).

[98] D. Marpaung, B. Morrison, R. Pant, C. Roeloffzen, A. Leinse, M. Hoekman, R. Heideman, and B. J. Eggleton, "Si_3N_4 ring resonator-based microwave photonic notch filter with an ultrahigh peak rejection," Opt. Express 21, 23286–23294 (2013).

[99] D. Marpaung, B. Morrison, R. Pant, C. Roeloffzen, A. Leinse, M. Hoekman, R. Heideman, and B. J. Eggleton, "Ultrahigh suppression and reconfigurable RF photonic notch filter using a silicon nitride ring resonator," in *2014 Conference on Lasers and Electro-Optics (CLEO)*, (2014), paper 1–2.

[100] L. Goldberg, H. Taylor, J. Weller, and D. Bloom, "Microwave signal generation with injection-locked laser diodes," Electron. Lett. 19, 491–493 (1983).

[101] R. Ramos, and A. Seeds, "Fast heterodyne optical phase-lock loop using double quantum well laser diodes," Electron. Lett. 28, 82–83 (1992).

[102] J. O'Reilly, and P. Lane, "Remote delivery of video services using mm-waves and optics," J. Lightwave Technol. 12, 369–375 (1994).

[103] G. Qi, J. Yao, J. Seregelyi, S. Paquet, and C. Bélisle, "Optical generation and distribution of continuously tunable millimeter-wave signals using an optical phase modulator," J. Lightwave Technol. 23, 2687–2695 (2005).

[104] J. Yu, Z. Jia, L. Yi, Y. Su, G.-K. Chang, and T. Wang, "Optical millimeter-wave generation or up-conversion using external modulators," IEEE Photon. Technol. Lett. 18, 265–267 (2006).

[105] W. Li, and J. Yao, "Investigation of photonically assisted microwave frequency multiplication based on external modulation," IEEE Trans. Microwave Theory Tech. 58, 3259–3268 (2010).

[106] L. Gao, W. Liu, X. Chen, and J. Yao, "Photonic-assisted microwave frequency multiplication with a tunable multiplication factor," Opt. Lett. 38, 4487–4490 (2013).

[107] B. Chen, S. Zheng, H. Chi, X. Zhang, and X. Jin, "An optical millimeter-wave generation technique based on phase modulation and Brillouin-assisted notch-filtering," IEEE Photon. Technol. Lett. 20, 2057–2059 (2008).

[108] A. Wiberg, P. Pérez-Millán, M. V. Andrés, and P. O. Hedekvist, "Microwave-photonic frequency multiplication utilizing optical four-wave mixing and fiber Bragg gratings," J. Lightwave Technol. 24, 329 (2006).

[109] C. Zhang, L. Wang, and K. Qiu, "Proposal for all-optical generation of multiple-frequency millimeter-wave signals for RoF system with multiple base stations using FWM in SOA," Opt. Express. 19, 13957–13962 (2011).

[110] B. Vidal, "Photonic millimeter-wave frequency multiplication based on cascaded four-wave mixing and polarization pulling," Opt. Lett. 37, 5055–5057 (2012).

[111] J. Zheng, H. Wang, W. Li, L. Wang, T. Su, J. Liu, and N. Zhu, "Photonic-assisted microwave frequency multiplier based on nonlinear polarization rotation," Opt. Lett. 39, 1366–1369 (2014).

[112] J. Chou, H. Yan, and B. Jalali, "Adaptive RF-photonic arbitrary waveform generator," IEEE Photon. Technol. Lett. 15, 581–583 (2003).

[113] Y. Long, L. Zhou, and J. Wang, "Photonic-assisted microwave signal multiplication and modulation using a silicon Mach–Zehnder modulator," Sci. Rep. 6, 20215 (2016).

[114] V. R. Supradeepa, C. M. Long, R. Wu, F. Ferdous, E. Hamidi, D. E. Leaird, and A. M. Weiner, "Comb-based radiofrequency photonic filters with rapid tunability and high selectivity," Nat. Photonics 6, 186–194 (2012).

[115] B. Vidal Rodriguez, J. Palací López, and J. Capmany Francoy, "Reconfigurable photonic microwave filter based on four-wave mixing," in *IEEE Photonics Journal* (Institute of Electrical and Electronics Engineers (IEEE), 2012), paper 759–764.

Section 3

Antenna Design for Microwave Systems

Chapter 8

Microwave Antennas for Energy Harvesting Applications

Dalia M.N. Elsheakh

Additional information is available at the end of the chapter

http://dx.doi.org/10.5772/64918

Abstract

In the last few years, the demand for power has increased; therefore, the need for alternate energy sources has become essential. Sources of fossil fuels are finite, are costly, and causes environmental hazard. Sustainable, environmentally benign energy can be derived from nuclear fission or captured from ambient sources. Large-scale ambient energy is widely available and large-scale technologies are being developed to efficiently capture it. At the other end of the scale, there are small amounts of wasted energy that could be useful if captured. There are various types of external energy sources such as solar, thermal, wind, and RF energy. Energy has been harvested for different purposes in the last few recent years. Energy harvesting from inexhaustible sources with no adverse environmental effect can provide unlimited energy for harvesting in a way of powering an embedded system from the environment. It could be RF energy harvesting by using antennas that can be held on the car glass or building, or in any places. The abundant RF energy is harvested from surrounding sources. This chapter focuses on RF energy harvesting in which the abundant RF energy from surrounding sources, such as nearby mobile phones, wireless LANs (WLANs), Wi-Fi, FM/AM radio signals, and broadcast television signals or DTV, is captured by a receiving antenna and rectified into a usable DC voltage. A practical approach for RF energy harvesting design and management of the harvested and available energy for wireless sensor networks is to improve the energy efficiency and large accepted antenna gain. The emerging self-powered systems challenge and dictate the direction of research in energy harvesting (EH). There are a lot of applications of energy harvesting such as wireless weather stations, car tire pressure monitors, implantable medical devices, traffic alert signs, and mars rover. A lot of researches are done to create several designs of rectenna (antenna and rectifier) that meet various objectives for use in RF energy harvesting, whatever opaque or transparent. However, most of the designed antennas are opaque and prevent the sunlight to pass through, so it is hard to put it on the car glass or window. Thus, there should be a design for transparent antenna that allows the sunlight to pass through. Among various antennas, microstrip patch antennas are widely used because they are low profile, are lightweight, and have planar structure.

Microstrip patch-structured rectennas are evaluated and compared with an emphasis on the various methods adopted to obtain a rectenna with harmonic rejection functionality, frequency, and polarization selectivity. Multiple frequency bands are tapped for energy harvesting, and this aspect of the implementation is one of the main focus points. The bands targeted for harvesting in this chapter will be those that are the most readily available to the general population. These include Wi-Fi hotspots, as well as cellular (900/850 MHz band), personal communications services (1800/1900 MHz band), and sources of 2.4 GHz and WiMAX (2.3/3.5 GHz) network transmitters. On the other hand, at high frequency, advances in nanotechnology have led to the development of semiconductor-based solar cells, nanoscale antennas for power harvesting applications, and integration of antennas into solar cells to design low-cost light-weight systems. The role of nanoantenna system is transforming thermal energy provided by the sun to electricity. Nanoantennas target the mid-infrared wavelengths where conventional photo voltaic cells are inefficient. However, the concept of using optical rectenna for harvesting solar energy was first introduced four decades ago. Recently, it has invited a surge of interest, with different laboratories around the world working on various aspects of the technology. The result is a technology that can be efficient and inexpensive, requiring only low-cost materials. Unlike conventional solar cells that harvest energy in visible light frequency range. Since the UV frequency range is much greater than visible light, we consider the quantum mechanical behavior of a driven particle in nanoscale antennas for power harvesting applications.

Keywords: energy harvesting (EH), antenna, rectenna, rectifier, nantenna, microstrip patch antenna (MPA), radio frequency (RF), wireless communications

1. Introduction of energy harvesting

Energy harvesting (EH) is defined as the process of extracting energy from the surroundings of a system and converting it into usable electrical energy, and it is more suitable for situations where the ambient energy sources are well characterized. EH could be an alternative energy supply technology. Such systems scavenge power from human activity, ambient heat, light, radio frequency (RF), vibrations, etc. Operated battery systems are used in various applications including wireless mobile phones and hand-held devices. However, increasing lifetime and durability of the battery are a matter of interest. Hence, recently energy harvesting from ambient to charge the battery or even to empower the system without any battery has gained momentum [1–4]. Processing power doubles every 2 years, battery capacity doubles every 10 years, however, we need a more efficient way to enable longer life. The ever increasing use of wireless devices, such as mobile phones, wireless computing, and remote sensing has resulted in an increased demand and reliance on the use of batteries. But the amount of energy available in the batteries is not only finite but also low, which limits the lifetime of the systems. It also has more advantages in systems with limited accessibility, such as those used in monitoring a machine or an instrument in a manufacturing plant used to organize a chemical process in a hazardous environment.

Harvesting ambient Wi-Fi transmission power through the rectenna can be a possible solution to extend the battery life of the active radio-frequency identification (RFID) tag. Global market

http://dx.doi.org/10.5772/64918

showed unprecedented growth in Wi-Fi hotspot deployments with an estimated 350% rise by 2015. Due to use of active RFID tags operating on very low power consumption, harvested Wi-Fi power in the submicrowatt range would not be deemed useless. The developed prototype was capable of delivering 20 μW of continuous power with an output voltage of 2 V at low excitation levels of 0.06g peak. Upper and lower Wi-Fi frequencies had the highest average power densities while the average power densities of 3G (2100 MHz) and LTE (2600 MHz) were the lowest. The highest peaks recorded were in the submicrowatt per square centimeter range for both Wi-Fi frequencies as well as the GSM/4G LTE 900 band, which were around 600–700 nW/cm^2.

Design of antennas with high gain and wide bandwidth is crucial to maximize the received power. Various antenna topologies have been reported in the literature for RF energy harvesting transparent or opaque antennas [5–7]. Maximum gain of 11.98 dB is reported in [6] but for a bandwidth of only about 20 MHz. Efficiency of the overall system greatly depends upon the matching between the rectifier and antenna. Variable input impedance of the rectifier with frequency and input power further limits total system efficiency. With semiconductor and other technologies continually striving toward lower operating powers, batteries could be replaced by alternative sources, such as DC power generators employing energy harvesting techniques. However, to introduce low power devices, the situation has changed with the technique being a viable alternative to batteries in different applications. Especially for wireless devices located in sensitive and difficult access environments where battery-operated equipment might not been previously possible. **Figure 1** shows some devices that potentially could be exploited for RF energy harvesting applications. These might be, but not limited to, TV and radio broadcasts, mobile phone base stations, mobile phones, wireless LAN, and radar. The transducer is typically an antenna or an antenna array—harvesting ambient electromagnetic energy. The recovered DC then, either powers a low-powered device directly or stored in a super capacitor for higher power low-duty-cycle operation. The block diagram of a basic energy harvesting system is shown in **Figure 2** [10].

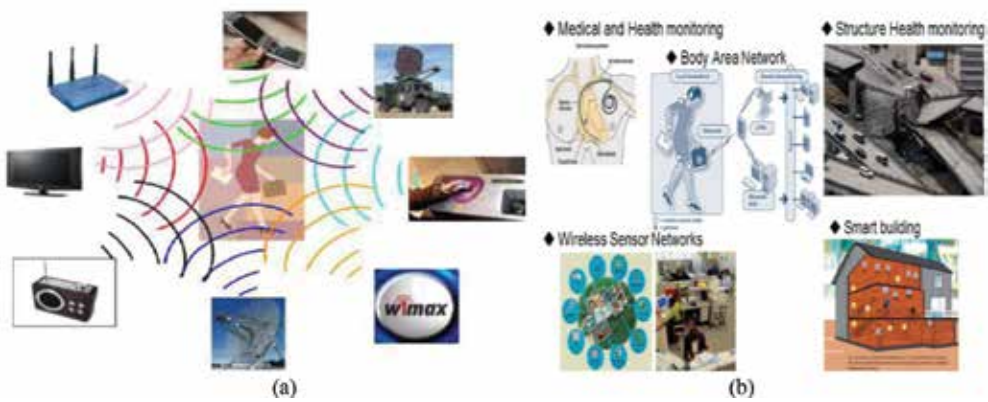

Figure 1. RF energy harvesting applications [8].

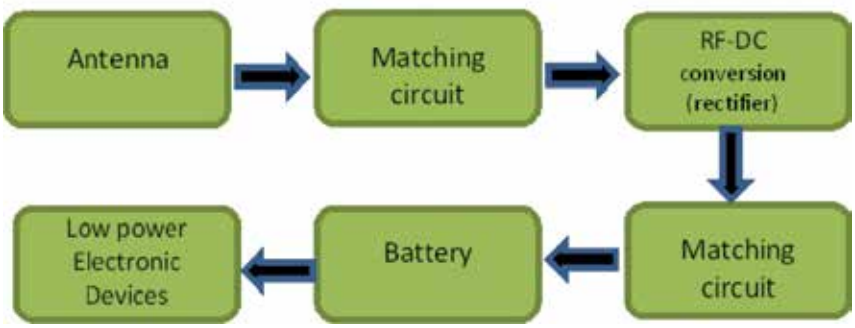

Figure 2. The block diagram of a basic energy RF harvesting system [9].

A nanoantenna (nantenna) is a nanoscopic rectifying antenna. It is an electromagnetic collector designed to absorb specific wavelengths that are proportional to the size of the nanoantenna. Nanoantennas may prove useful for converting solar radiation to electricity. Sufficient supplies of clean energy are intimately linked with global stability, economic prosperity, and quality of life. Finding energy sources to satisfy the world's growing demand is one of the society's challenges for the next half century. The world now uses energy at a rate of approximately 4.1 × 1020 J/yr, equivalent to continuous power consumption of 13 TW. The rapid technology development and economic growth worldwide are estimated to produce more than double the demand for energy to 30 TW by 2050 and more than triple the demand to 40 TW by the end of century. As a result of this, energy demands increased worldwide and as a consequence, the deleterious effects of hydrocarbon-based power such as global warming, air pollution, acid precipitation, ozone depletion, and forest destruction are increasingly apparent. The clean and renewable alternative energy resource is one of the most urgent challenges to the sustainable development of human civilization. About 120,000 TW of radiations from Sun reach Earth's surface far exceeding human needs [11–15].

2. Types of energy harvesting

The next few paragraphs provide an overview of some common energy harvesting schemes targeting devices in the list below. Solar energy, which involves converting the Sun's rays into useable electrical energy, is interesting but depends on the availability of daylight. The concept is certainly not foreign to the general population anymore. Solar-powered calculators and LED garden lights have been commonplaces for many years now. The efficiency of such conversion circuits has grown but the main detriment is the need for agreeable weather and timely use. Energy collection from natural sources at night is simply out of the question, limiting the user to daytime energy collection or requiring artificial sources of light with their own power supply needs. This method thus falls outside the scope of this work. Wind energy, for its part, requires bulky turbines for collection and necessitates the inclusion of mechanical components and brushings that are susceptible to wear and damage over time, if not properly maintained [11].

This is not an issue in traditional wind farm installations, where regular maintenance is expected to occur. The same expectation, however, cannot be placed on consumers and this energy source will thus not be further explored in this work. Kinetic energy harvesting aims to transform motional or inertial energy into a usable source of electrical charge via some type of transducer. In general, this requires some physical effort by the user, be it walking, running or otherwise shaking the device. Though this is not a problem for most able-bodied people, it could nonetheless be considered a hassle for a device intended for daily use, such as a personal cellular phone or a GPS unit. Radio-frequency energy, for its part, is readily available in all major industrialized centers and surrounding areas. Ambient energy harvesting, also known as energy scavenging or power harvesting, is the process where energy is obtained and converted from the environment and stored for use in electronics applications as shown in **Tables 1** and **2**. Usually this term is applied to energy harvesting for low power and small autonomous devices, such as wireless sensor networks, and portable electronic equipment. Some systems convert random motions including ocean waves into useful electrical energy that can be used by oceanographic monitoring wireless sensor nodes for autonomous surveillance. The literature shows that no single power source is sufficient for all applications, as energy sources must be considered according to the application characteristics [16–18] as shown in **Figure 3**, and **Figure 4** shows a diagram of a basic EH system.

Energy harvesting technique	Power density	Efficiency
Photovoltaic	Outdoors (direct Sun): 15 mW/cm^2 Outdoors (cloudiy): 0.15 mW/cm^2	Highest 32±1.5%
	Indoors: <10 μW/cm^2	Typical 25±1.5%
Thermoelectric	Human: 30 μW/cm^2/industrial: 1:10 mW/cm^2	±0.1% ±3.5%
Pyroelectric	8.64 μW/cm^2 at the temperature rate of 8.5°C/s	3.5%
Piezoelectric	250 μW/cm^2/330 μW/cm^2	
Electromagnetic	Human motion: 1–4 μW/cm^2	
Electrostatic	50–100 μW/cm^2	
RF	GSM900/1800 MHz: 0.1 μW/cm^2	50%
	Wi-Fi 2.4 GHz: 0.01 μW/cm^2	
Wind	380 μW/cm^2 at the speed of 5 m/s	5%
Acoustic noise	0.96 μW/cm^2 at 100 dB/0.003 μW/cm^2 at 75 dB	

Maximum power and efficiency are source dependent — excluding transmisssion efficiency.

Noise power densities are theoritical values.

Table 1. Power density and efficiency of energy harvesting techniques [11].

Energy source	Power density and performance
Acoustic noise	0.003 μW/cm²/0.96 μW/cm²
Temperature variation	10 μW/cm²
Ambient light	1 μW/cm²
Thermoelectric	30 μW/cm²
Vibration	200 μW/cm²
Vibration (piezoelectric)	300 μW/cm²
Air flow	50 μW/cm²
Push buttons	330 μW/cm²
Shoe inserts hand generators	30 W/kg
Heel strike	7 W/cm²

Table 2. Comparison of power density of energy harvesting methods [13].

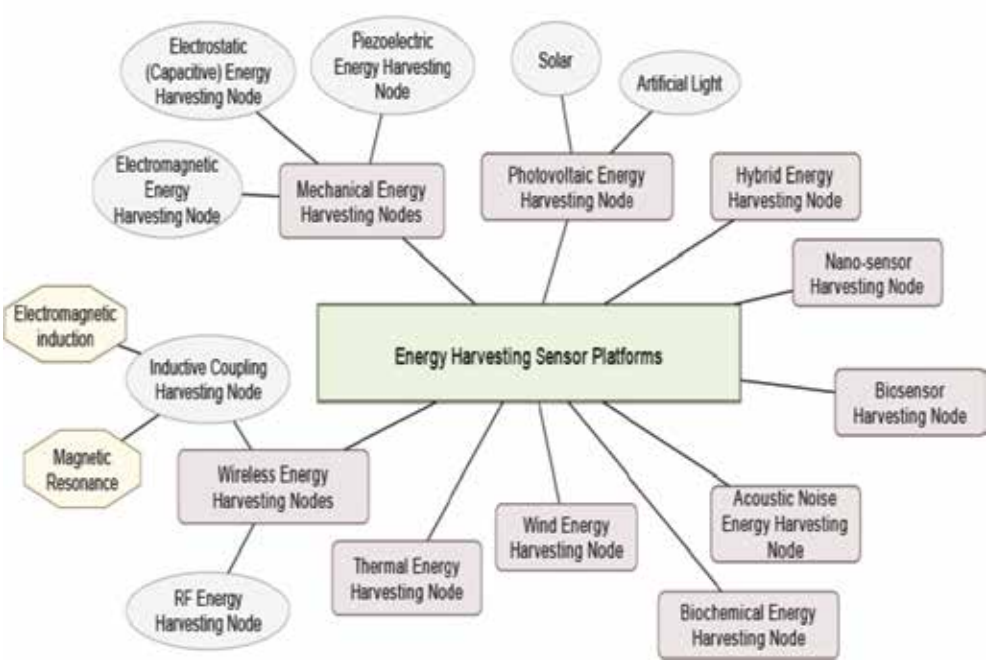

Figure 3. Different energy types (rectangles) and sources (ovals) [16].

http://dx.doi.org/10.5772/64918

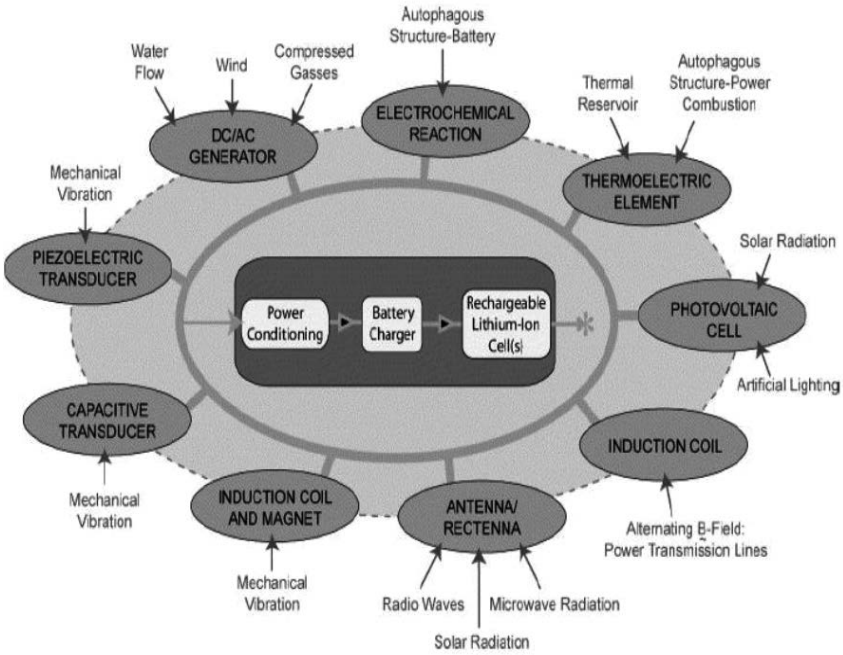

Figure 4. Example of the different radiating sources [19].

- Human body as mechanical and heat variations energy;
- Natural energy as wind, water flow or ocean waves, and solar energy;
- Mechanical energy as vibrations from machines from high-pressure motors, manufacturing machines, and waste rotations;
- Thermal energy as waste heat energy variations from heaters and friction sources;
- Light energy is divided into two categories of energy: indoor room light and outdoor sunlight energy. It can be captured via photo sensors, photo diodes, and solar photovoltaic panels;
- Electromagnetic energy as inductors, coils, and transformers is depending on how much energy is needed for the application. In addition, chemical, biological, and radiation can be considered ambient energy sources.

3. RF energy harvesting

The dramatic increase in demand for wireless devices has been met with a steady increase in infrastructure installations and thus an augmented source of radiated RF energy. This energy is in the air at virtually all times of the day and night, albeit at different power levels. A

study [2] of ambient global system for mobile communication (GSM) power in the Netherlands concluded that within a range of 25–100 m from a GSM base station, the summed average power present at all measured frequencies across the 935–960 MHz band varied between 0.1 and 3.0 mW/m^2 and depended greatly on the amount of GSM traffic at the time of measurement. This in itself poses a potential problem for energy harvesting devices: the small amount of energy available for harvesting is neither constant nor easily predictable. As such, one must ensure that any harvesting design remains useful over a wide dynamic range of available input power. Nonetheless, this form of ambient energy remains the most promising for use in consumer-oriented portable electronic devices, due to theoretical 24 h availability, lack of required physical effort to charge, and quasi-independence from weather conditions. Batteries have both effects as add extra size and add disposal to environmental pollution. A promising solution is available in capturing and storing the energy from external ambient sources for compact mobile and electronics devices; this technology is named as energy harvesting. Other names for this type of technology are power harvesting and free energy, which are derived from renewable energy [19]. Many research teams are working on reducing the consumption of the devices extending the battery life while the other teams have chosen to recycle ambient energy like in microelectromechanical systems (MEMS). The charging of mobile devices is easy because the user can do it but for other applications, the batteries remain a big problem as wireless sensor nodes that are located in difficult to access environments. This problem is due to the large number of devices and distribution in a wide area or located in inaccessible places. The rectification of microwave signals to DC power has been proposed for helicopter powering and solar power satellite [18–20].

DC power depends on the available RF power, the choice of antenna and frequency band, an energy harvesting technique using electromagnetic energy, specifically radio frequency. Communication devices generally have omnidirectional antennas that propagate RF energy in most directions to maximize connectivity for mobile applications [7]. The energy transmitted from the wireless sources for 10 GHz is much higher up to 30 W, however, only a small amount can be scavenged in the real environment. The rest of the power is dissipated as heat or absorbed by other materials. Radio-frequency identification (RFID) tags and implantable electronic devices are also used as RF power harvesting technique. This is because the wireless sensor nodes consume few μW in sleep mode and hundreds μW in active mode.

The electrical energy is then conditioned and used to charge a battery that stores and supplies the energy to a load, i.e., a WSN node. Each energy source has its own unique characteristics in terms of controllability, predictability, and magnitude; hence all these factors will need to be considered when choosing the most suitable source for a specific application. The number of consumer-oriented compact electronic devices (including, but not limited to, personal cellular phones, tablet PCs, and GPS units) has been growing at exponential rates for several years. Reliance on these devices for daily navigation, scheduling, and information-gathering activities has created an expectation of ever-longer battery life and less-frequent charging cycles with any new generation of product [21, 22].

This situation poses important questions to both the design engineers and the originating vendors of these devices. How can we power these circuits in a responsible manner? How can

engineers improve battery life and thus provide maximum "up" time for consumers? From the previous section, we are able to answer next question.

3.1. When does radio-frequency harvesting make sense?

Harvestable energy available can be installed and maintained in power devices that are difficult to reach. Harvestable energy is available for numerous devices, environmentally friendliness is required, and high uptime is demanded. Radio-frequency harvesting makes sense when used as remote patient monitoring, harmful agents detection, efficient office energy control, surveillance and security, detecting and tracking enemy troop movement, vineyard or other agricultural management, home automation, implantable sensors, long-range asset tracking and aircraft fatigue supervision.

The wireless devices are growing in many applications, such as mobile phones and sensor networks. Radio-frequency energy harvesting holds a promising future for generating a small amount of electrical power to drive partial circuits in wirelessly communicating electronics devices. As remote patient monitoring, harmful agents detection, efficient office energy control, surveillance and security, detecting and tracking enemy, troop movement, vineyard or other agricultural management, home automation, implantable sensors, long-range asset tracking, aircraft fatigue supervision, and reducing power consumption have become a major challenge in wireless sensor networks. As a vital factor affecting system cost and lifetime, energy consumption in wireless sensor networks is an emerging and active research area. RF energy is currently broadcasted from billions of radio transmitters around the world, including mobile telephones, hand-held radios, mobile base stations, and television/radio broadcast stations. **Figure 4** shows the huge amount of radio waves in air. From ambient sources enables the wireless charging of low power devices and has other benefits associated with product design, usability, and reliability. Battery-free devices can be designed to operate upon demand or when sufficient charge is accumulated. However, while many researchers have made an effort to increase the receiving RF power, the RF energy accumulated from air space is very limited, less than 1 W. However, several experiments were conducted using highly efficient receivers that were capable of receiving digital TV signals in the range of 40–20 dBm as in [23]. The system composed of a rectenna, which is a particular type of antenna that rectifies incoming electromagnetic waves into DC current. A typical rectenna consists of four main components: antenna, prerectification filter, rectifying circuit, and DC pass filter. A microwave antenna collects incoming RF power as shown in **Figure 5(a)**. An input low-pass filter (LPF; prerectification filter) suppresses the unwanted higher harmonics rejected by the rectifying circuit and also provides matching between the antenna and the rectifier [24]. A traditional rectenna system composed of a dipole element or a mesh of dipoles that capture microwave energy and Schottky diode for the rectification process. Different types of rectenna elements have been proposed recently. The antenna could be, for example, dipole, Yagi-Uda, microstrip, monopole, loop, coplanar patch, spiral, or even parabolic [25], whatever opaque or transparent antenna, as shown in **Figure 5(b)**. A half-wave parallel rectifier is used as a voltage doubler structure to theoretically double the output DC voltage or a dual-diode full-wave rectifier to increase the conversion efficiency [26].

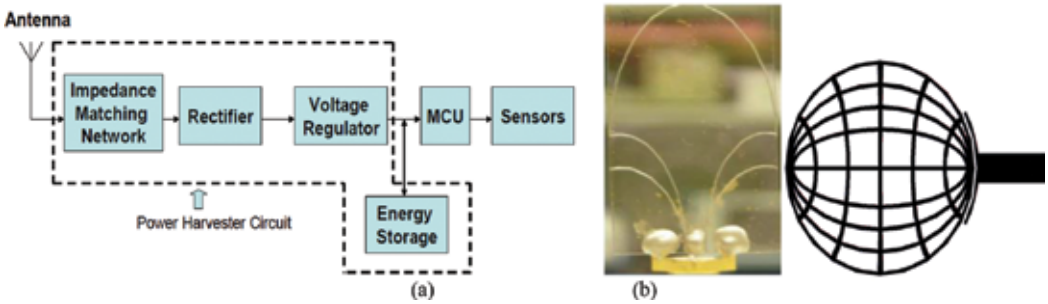

Figure 5. (a) Diagram of a typical power harvesting circuit and (b) different antenna shapes used.

4. Types of RF energy harvesting (EH)

RF signals used for wireless communication systems will be the most suitable energy source because heat, light, and vibration are not always available at every place. Electromagnetic energy exists in the form of alternating magnetic fields surrounding AC power lines or radio waves emitted by nearby transmitters. There are two types of EH application devices: near field and far field.

4.1. Far-field devices

The wearable rectenna well suited for energy harvesting for ultrahigh frequency (UHF) band and a tetra-band genetic-based rectenna designed to harvest from the global system for mobile communications, the Universal Mobile Telecommunications System (UMTS), and Wi-Fi RF sources [27].

4.2. Near-field devices

In this section, two examples of devices operating in the near-field region of the source are reported. The first one is a harvester optimized for power generation from spurious emissions of compact fluorescent lamps (CFLs). The second example of application is a near-field link optimized for powering IMDs. In both cases, a wireless power transfer is implemented by inductive coupling [28].

Choosing the frequency is an important consideration in RF energy harvesting systems and at the same time might be environment specific. Wavelengths up into the low GHz for indoor application would be a better choice, due to their ability to propagate well in these environments, rather than lower VHF/UHF transmissions for outdoor or remote location harvesting applications. Generally, in the modern built environment, GSM mobile phone signals are prevalent and propagate well both into and out of buildings, offering harvesting potential from both the GSM base stations and the user's handsets. This is a promising EH environment because of the tremendous growth of mobile phone usage in Egypt, one of the best growing countries with more than 97 million subscribers [29] (**Table 3**).

Energy source	Classification energy	Power density	Weakness	Strength
Solar power	Radiant	100 mW/cm^3	Require exposure to light, and low efficiency if device is in building	Can use without limit
RF waves	Radiant	0.02 μW/cm^2 at 5 km from AM radio	Low efficiency inside a building	Can use without limit
RF energy	Radiant	40 μW/cm^2 at 10 m	Low efficiency if out of line of sight	Can use without limit
Body heat	Thermal	60 μW/cm^2 at 5°C	Available only when temperature difference is high	Easy to build using thermocouple
External heat	Thermal	135 μW/cm^2 at 10°C	Available only when temperature difference is high	Easy to build using thermocouple
Motion body	Mechanical	800 μW/cm^3	Motion	High power density, not limited on interior and exterior
Flow blood	Mechanical	0.93 W at 100 mm	Low conversion efficiency	High power density, not limited on interior and exterior
Flow air	Mechanical	177 μW/cm^3	Low conversion efficiency inside a building	High power density
Vibrations	Mechanical	4 μW/cm^3	Has to exist at surrounding	HPD, not limited on interior and exterior
Piezoelectric	Mechanical	50 μW/cm^2	Has to exist at surrounding	HPD, not limited on interior and exterior

Table 3. Comparison of energy harvesting sources for WSNs [29].

5. Radio-frequency energy harvesting system description

During the daytime, various electronic devices are used, and hence, ambient RF energy in their bands is expected to be time dependent, with more energy available during the daytime than at nighttime. So in order to be able to make fair comparisons between locations, measurements were taken over the day on weekdays over a period of 1 month. Electric field strength was measured between 0.3 and 2.5 GHz/WLAN using an Agilent/Rohde & Schwarz, Field Fox RF analyzer with different types of antennas. It is important to note that the spectral measurements were undertaken during the analog-to-digital switches. Therefore, the measurements for wireless communications may represent an underestimate of present RF power levels when measured now. The effective isotropic-radiated power (EIRP) in different countries, which could be collected in the wireless frequency band, is shown in **Table 4** [30].

Country	Frequency band (MHz)	Power (EIRP)
The United States	902–928	4 W
The United Kingdom	865.6–867.6	2W ERP/3.28 W EIRP
Japan	952–954	4 W

Table 4. Frequency allocation and permitted radiated power for the selected UHF [30].

In order to achieve maximal energy collection by targeting several highly used frequency bands, a multifrequency antenna design with an omnidirectional radiation pattern will be targeted. Although a circular polarization would be ideal, it will not be used in this case, due the added implementation space required and tight design sizing constraints. **Table 5** [31] aims to compare the aforementioned antenna topologies. Here, the physical size is described in relation to wavelength; multiband behavior indicates the ability of the topology to cover more than one operational band at a time; and bandwidth describes the frequency range covered around the central operating frequency. Qualitative descriptions are also for the theoretical radiation pattern, the difficulty level of fabrication, the ability to quickly scale the design for new operating frequencies, and the level of difficulty relating to properly feeding/tapping the antenna.

Energy source harvesting power	Harvesting power	Energy source harvesting power	Harvesting power
Vibration/motion		RF/EM	
Human	4 $\mu W/cm^2$	GSM	0.1 $\mu W/cm^2$
Industry	100 $\mu W/cm^2$	Wi-Fi	0.001 mW/cm^2
Temperature difference		Solar	
Industry	1–10 mW/cm^2	Outdoor	10 mW/cm^2
Light		Indoor	<0.1 mW/cm^2
Indoor	10 $\mu W/cm^2$	Acoustic	
Outdoor	10 mW/cm^2	75–10 dB of noise	0.003–0.96 $\mu W/cm^2$
Human power source		Human power source	
Body heat	0.2–0.32 W (neck)	Walking	5–8.3 W

Table 5. Energy harvesting estimates [31].

5.1. Rectenna design

The approach of many papers (including [32]) has also explored the joint design of antenna and rectifier as one complete entity, commonly referred to as a "rectenna." This integrated design method aims to reduce the size of the final design, as well as streamline the design process, by eliminating unnecessary intermediate steps. For example, [33] shows the use of a source pull simulation on the rectifying diode, utilizing harmonic balance to determine the optimal source impedance that the antenna should present to the diode over a range of

http://dx.doi.org/10.5772/64918

expected input power levels. These results will allow the antenna designer to use this as a design goal while designing the antenna, eliminating the need for a separate matching network [34].

5.2. Input matching and detector

To assure maximum power delivery for good antenna, the impedance-matching network performs impedance transformation. **Figure 6** illustrates the impedance transformer role, where Vin and Zin are the induced voltage and the input impedance of the impedance transformer, respectively, and the YIC and VIC are the input admittance and input voltage of the rectifier, the transformer impedance is composed of reactive lossless components. When $V_{IC} = \left(\frac{\sqrt{Re(\{Yin}}{\sqrt{Re(\{Yic}}/2\right)V_{in,}$ the impedances are nearly matched and it turns out the impedance transformer to also work as a voltage booster [35]. When L-type matching network is used, the relationship of the input and output conductances can be derived as $Re(\{Yin = (1 + Q^2 Re(Y_{ic}))$, where Q is the quality factor of the matching network at resonate frequency. For a lossless L-type matching network consisted of L and C, Q = ω0 C/ Re{Yic}, where ω0 is the resonate frequency, as a result $= \sqrt{1 + \frac{Q^2}{2}}V_{in}$. A high Q is required in order to achieve a high voltage gain [36].

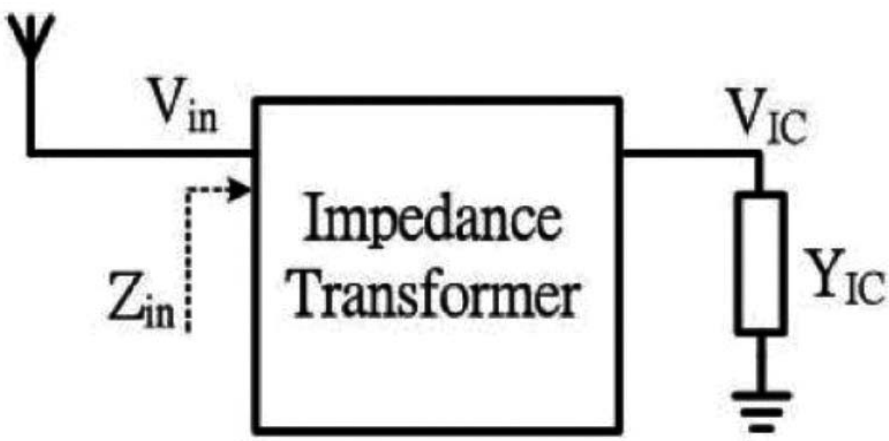

Figure 6. Impedance transfer.

5.3. Power combining

Power combining has been demonstrated in several ways in the literature, including RF combining of the received power from multiple antennas. The end goal is always to increase the amount of harvested RF energy. The author of [37] demonstrated a different configuration

by grouping antennas tuned to a handful of targeted frequencies, though not in an energy harvesting application. The configuration combined Koch fractal loops at 915 MHz with meandered structures aimed at the 2.45 GHz band (see **Figure 7**). It is shown that combining at the RF level allows more optimum power harvesting near the main receiving lobe, when speaking of directional antennas. Nonetheless, once the angle of reception is deviated more than ±25° from the main lobe, the DC combination proves to offer slightly superior performance.

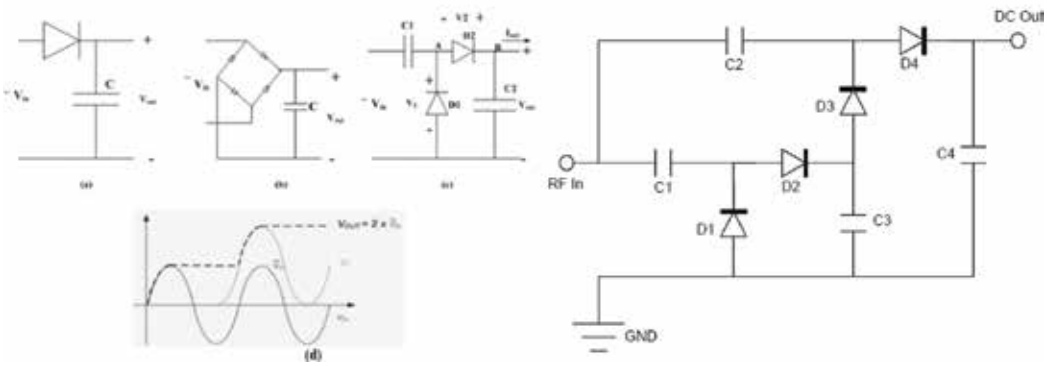

Figure 7. (a) Diode, (b) bridge of diodes, (c) a voltage multiplier rectifier, (d) its waveforms during the transient, and (d) three bridges of voltage multiplier.

5.4. Impedance matching

Impedance matching is another challenging concern, which stems primarily from the inconsistent impedance of the nonlinear rectifying elements (whether considering diodes or transistors). As varying potential is applied to the junction, junction capacitance changes slightly. Thus, the impedance varies with the amount of input power presented to it. Consequently, any static matching network is only truly effective over a finite input power range. This problem is clearly magnified when there are multiple antennas and/or multiple rectifiers. An increase of 100–150% in rectifier efficiency was noted through simulation [38, 39].

5.5. Rectification

Rectifier circuits provide a DC output voltage at the load. There are three main options for the rectifier. **Figure 9** shows that the bridge diode provides an output DC voltage to the load (VOUT) whose amplitude is lower than that of the incoming signal. The voltage rectifier is a multiplier, so it multiples the peak amplitude of the incoming signal. Due to long distances, the DC voltage level is not high enough to power an electronic circuit, so the voltage rectifier multiplier is used. Several attempts to enhance the efficiency of diode rectification have also been made in the literature. The use of PMOS transistors to replace diode-connected NMOS transistors as rectifying elements allows a reduction in threshold voltage and a 5% relative

increase in rectifier efficiency [41]. This is an interesting option for CMOS implementations (but outside the scope of this work). The idea of resistor emulation for the purpose of tracking the peak power point over a wide range of incident power levels is explored in [42]. This effectively increases the optimal input power range over which the rectifier remains efficient. Since the implementation at hand does not enjoy the luxury of predetermined input power levels, several papers have also proposed the notion of sacrificial biasing, a technique where DC bias is applied to the rectifying element's input in order to reduce the required threshold voltage needed to allow conduction. At the expense of some output current, the circuit's efficiency was shown to increase by 60% over the nonsacrificial equivalent NMOS circuit [43].

5.6. Energy storage

Most common energy storage device that used in a sensor node is a battery, either nonrechargeable or rechargeable. For example, a nonrechargeable battery (alkaline) is suitable for a microsensor with very low power consumption (50 μW). Other example, a rechargeable battery (lithium ion) is used widely in sensor nodes with energy harvesting technology. Various factors affect the quality of these batteries but the main factors are cost and price. Batteries are specified by a rated current capacity C, expressed in ampere-hour. It describes the rate at which a battery discharges without significantly affecting the prescribed supply voltage potential difference. However, the discharge rate increases when the rated capacity decreases [44, 45]. This means that a 1000 mAh battery produces 1000 mA for 1 h, if it is discharged at a rate of 1 C. 1 C is often referred to as a 1 h discharge. Likewise, a 0.5 C would be a 2 h and a 0.1 C, a 10 h discharge.

$$T = \frac{C}{I^n} \tag{1}$$

where C is the battery capacitance expressed in ampere-hours, I is the drawn current in ampere (A), T is the time of discharge in seconds, and n is the Peukert number, a constant that directly relates to the internal resistance of the battery. The Peukert number indicates how well a battery performs under continuous heavy current [45].

6. Antenna design used in RF energy harvesting

The antenna innovations in the aforementioned works involve explorations of new antenna variations, including, but not limited to, rectangular antennas and arrays thereof, slotted patch antennas, gap-coupled microstrip antennas, circular patch antennas, folded dipoles, circularly polarized spiral antennas, planar inverted-F antennas (PIFA), and fractal (particularly Koch) monopole, dipole and patch antennas. From the previous information, the antenna needs to offer [46]:

- Narrow band/multiband operation.

- CP polarization.
- Matching impedance for maximum power transfer to the following rectifier circuitry.

Antenna with different shapes and types has been employed in RFEH applications, from the simple dipole to more complex designs such as the bow tie or spiral antenna. It gives good performance in terms of polarization; however, it is generally limited to broadband designs with a few hundred MHz bandwidths. Multi narrow-band frequency designs are usually limited due to the need for a complex feed arrangement to each antenna element. Now there are many designs in [47], which provide three bands that based on close-coupled resonant elements [47].

CP has become one of the essential characteristics in designing rectennas [48]. CP prevents the variation of the output voltage due to the rotation of the transmitter or receiver. Dipoles or patch antennas are used in conventional rectenna design. The coplanar strip line is used to feed the dipole antennas. It can be used to combine several antenna elements for higher gain and also to form an antenna array more easily. Many CPS-fed rectennas have been recently in [49] and by using a high-gain antenna, reduces the number of rectenna elements needed. In most cases, an antenna with a higher gain will cover a larger effective area. So, there is a tradeoff between the antenna gain and the antenna area. However, even with circular polarization, the efficient power transmission still requires a precise main beam alignment between the transmitter antenna and the receiver rectenna array. The transmitter antenna usually has a quite narrow beam width at the broadside.

Despite the fact that a circularly polarized antenna can maintain a constant output voltage when the transmitter or the receiver rotates, it cannot prevent the output voltage variations due to improper main beam alignment. The array aperture of the nonuniform array can be designed to form a uniform amplitude antenna pattern on both the E-plane and H-plane and also widen the main-lobe beam width. The broadened main beam width rectenna keeps the output voltage invariant even if the rectenna has an improper beam alignment. This method indeed makes the main beam broadened, numerous antenna elements with various sizes are needed and the nonuniform array gain may be lower than that of the uniform array.

6.1. Opaque antenna

The rapid development of microstrip antenna technology began in the late 1970s. By the early 1980s, basic microstrip antenna elements and arrays were fairly well established in terms of design and modeling. The microstrip patch antenna (MPA) is recently used as a low-profile, flush-mounted antennas on rockets and missiles showed that this was a practical concept for use in many antenna system problems [49]. Different shapes of antennas were developed and their applications were extended to many other fields. A major contributing advance of MPA is the revolution in electronic circuit miniaturization brought about by developments in large-scale integration. Traditional MPA antennas are often bulky and costly part of an electronic system, and MPAs based on photolithographic technology are seen as an engineering breakthrough. The MPA structure consists of a radiating patch on one side of a dielectric substrate with a ground plane on the other side. The patch is generally made of a conducting material

such as copper or gold and can take any possible shape, such as square, rectangular, thin strip dipole, circular, elliptical, or triangular. Square, rectangular, dipole, and circular shapes are the most common because of ease of analysis and fabrication, and their attractive radiation characteristics, especially low cross-polarization radiation [50].

Several feed MPA configurations are used while the most popular ones are the microstrip line, coaxial probe, aperture coupling, and proximity coupling [51].

6.2. Compact and multiband microstrip antennas

Different other microstrip structures are successful candidates as microstrip planar inverted F-antenna with different geometrical radiator shapes. The main goal is to design antennas for wireless communication applications where the space value of the antenna is quite limited while it reserves the characteristics of multiband, lightweight, low cost, robustness, diversity, packaging capabilities and ability for RF PIN switches/MEMS integration for smart antenna systems. Several researches in literature concentrate on these antenna types and their developments. Famous techniques for antenna size reduction include dielectric loading to reduce the electrical size, top hat loading, and use of shorting PINs or plates [52]. Dielectric loading usually accompanied by bandwidth reduction and cost increase, so it is not a likely approach. The interesting choices are slot-coupled multiresonators, printed spiral antennas, planar inverted "F" antennas (PIFA), and a fractal implementation, such as the Koch. When simplicity of fabrication is considered, the PIFA and spiral antenna designs are more dependent on manufacturing tolerances [53, 54].

6.3. Transparent antenna

Transparent antenna was first presented by the National Aeronautics and Space Agency (NASA) when researchers Simmons and Lee demonstrated the use of AgHT-8 to produce single patch antennas to operate at 2.3 and 9.5 GHz. To design and produce workable antennas, different materials are used such as indium tin oxide (ITO) and aluminium-doped zinc oxide. Except for those produced using ITO or AgHT, most of the so-called transparent antennas are simply antennas constructed by coating transparent polymer substrates with nontransparent conductive traces of silver or other conductive ink [40, 55]. Some selected shapes of the transparent antennas as shown in **Figures 8** and **9** cannot be really categorized as fully transparent antennas since the traces are visible to the eye. The transparent antennas in this section are those that are fully transparent, in other words, even the conductive traces are transparent and discreet to the eye.

The main function of a transparent rectenna is to convert RF energy to DC power, the main design challenge is to obtain resonable conversion efficiency, and there are basically two methods to achieve this goal: First, transparent antennas being built on materials that are discreet, flexible, conformal, conductive, and having the ability to provide good antenna performance on glass to serve as the "last mile" link in subsequent generation communications after 4G have been the basis for this contention. Second, using transparent conductive oxide polymer (TCO), AgHT and its properties, and culminates in the development of a transparent

antenna that can be integrated with photovoltaic for window glass applications on homes and buildings. There are different applications such as on-body wireless communications in health care monitoring were also analyzed and presented [56, 57].

Figure 8. Transparent radiator of the monopole antenna.

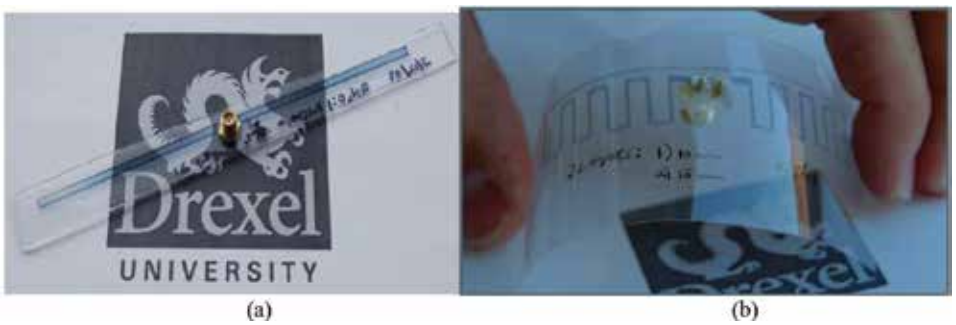

Figure 9. (a) RFID 1/2 dipole antenna and (b) RFID meandering dipole antenna [40].

Transparent conductive oxides have a variety of uses as shown in **Figure 10**; one common use is its ability to reflect thermal infrared heat. This characteristic is exploited to make energy-conserving windows. An example of which is AgHT, which is effectively a sun-shielding film manufactured by Solutia Inc. This low-emissivity window application is currently the largest area of use for TCOs. It is to collect the reasonable power and deliver it to the rectifying diode, and the second one is to suppress the harmonics generated by the diode that reradiate from the antenna as the power lost. For increasing the conversion efficiency by using several broadband antennas, large antenna arrays and circularly polarized antennas have been designed. This antenna receives relatively reasonable RF power from various sources, and antenna array increases incident power delivered to the diode for rectification. Antenna array is an effective means of increasing the receiving power but a tradeoff arises between the antenna size and the radiation gain. To increase the efficiency by second method, LPF is placed between transparent antennas and rectifying circuit or antenna with the property of harmonic

rejection is designed. Among various types of transparent antenna used in rectennas, meshing microstrip patch antennas are gaining popularity for use in wireless applications owing to their low profile, lightweight, low production cost, and being conformable to planar, simple, and inexpensive to manufacture using modern printed circuit technology [58].

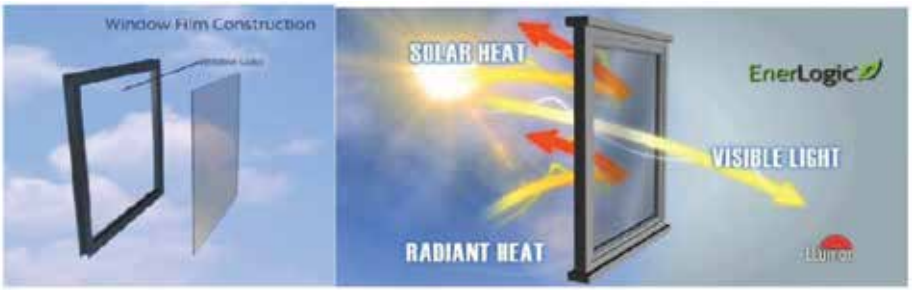

Figure 10. Transparent conductive oxide films used for sun shielding from harmful UV rays.

Figure 10 shows a typical structure of energy harvesting-enabled wireless sensor platform. A converter/a transducer convert the ambient energy forms to DC power and store the converted energy in energy storage devices as a battery or a super capacitor. A power management unit (PMU) maximizes the collected power level through matching and duty-cycle optimization in a power-efficient way. The lifetime of the power sources, such as a battery, can be increased by introducing energy harvesting systems that effectively recharge periodically the main power source or function as an additional source itself. Batteryless or battery-free autonomous operation when the main PMU can be also removed when there is a sufficient energy to drive the whole system for a truly standalone [58]. While for transparent antenna, the radiating element and ground plane are both designed using transparent conductive oxide polymer AgHT-4 while the substrate is made of glass. Recently, there has been increasing interests on the investigations of the new types of antenna designs using transparent materials. Other types also could be integrated with solar cells to reduce the surface area of small satellites [59].

6.4. Different antenna configurations in academia

Different published papers are presented in this section to describe different configuration of antenna used in RFEH. By using two orthogonal coupling slots, both as shown in **Figure 11**, linear polarizations are addressed [60]. This increased the applicability of the antenna to different incoming polarizations. The antenna was designed for an energy harvesting application at 2.45 GHz. Another more complex example of this approach is presented in [61], where a multilayer rectenna is designed using concentric annular rings (and a central circular patch), a slotted ground plane, and an integrated phase shifter/rectifier, all shown in **Figure 12**. Each of the resonator targets a separate frequency band, with the 900, 1760, and 2450 MHz bands being covered by the final design. The orthogonal slots in the ground plane, as in the last discussed design, ensure acceptance of additional signal polarizations. The phase shifter permits coherent signal combination for increased charge collection as shown in **Figure 12**.

Controlled metal spacing is also used in another fashion: parasitic gap-coupled antenna elements [62]. In this scenario, a center patch is the only radiating element fed, and two parasitic patches of differing dimensions are positioned near the main element in the same plane (see **Figure 13**). **Figure 14** shows the 3D radiation pattern for center-fed circular patch.

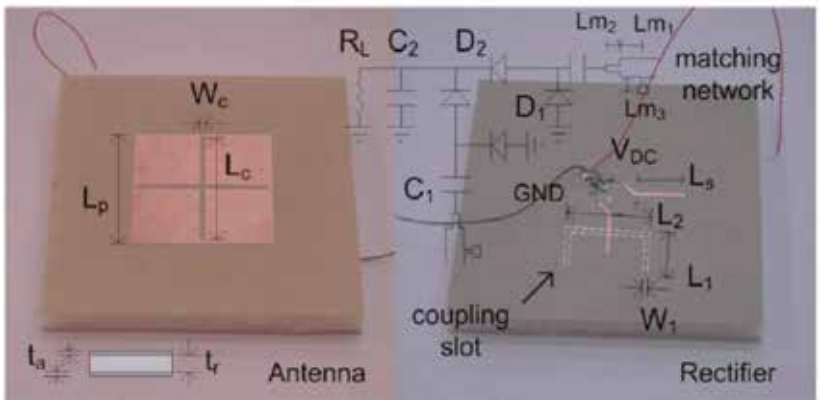

Figure 11. Cross-shaped slot-coupled rectenna.

Figure 12. Slot-coupled multiresonator (tri-band).

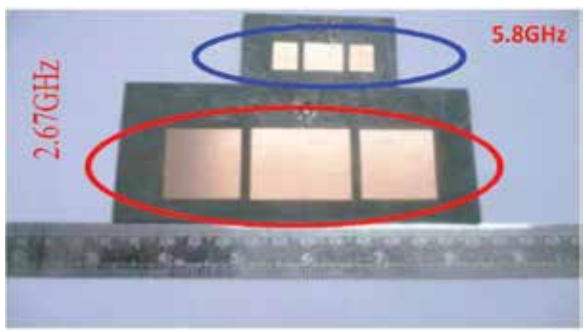

Figure 13. Two gap-coupled microstrip antennas.

http://dx.doi.org/10.5772/64918

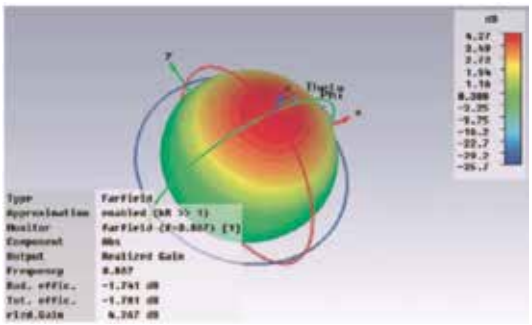

Figure 14. Radiation for center-fed circular patch.

The major advantage in this case is an increase in gain and thus an increase in harvested power level, if the orientation of the receiving antenna with respect to the energy can be maintained. Analogous to rectangular patch antennas, circular patch antennas cover a surface area dictated by the guide wavelength(s) of interest. The resonant frequency of a circular patch antenna is given in [63] as

$$f_{r,nm} = \frac{\alpha_{nm} C}{2\pi a_{eff} \sqrt{\varepsilon_{r,eff}}} \tag{2}$$

where αnm is the attenuation, aeff is the circular patch antenna radius, and $\varepsilon reff$ is the effective relative dielectric constant. Next, we take a look at folded dipoles as shown in **Figure 15**, which have been implemented in both free space [64] and printed forms. In the free space (nonprinted) version, the author of [64] fabricated a soldered folded dipole. This implementation showed a roughly 4% increase in rectification efficiency (to 15.43%) over an equivalent loop antenna. Another type of printed antenna that has seen increasing study in recent years is the spiral antenna (see **Figure 16**) [65]. In this implementation, a 64-element array of printed spiral antennas (shown in **Figure 17**) was constructed using series and parallel connections of array elements to achieve acceptance of both left-hand circularly polarized (LHCP) and right-hand circularly polarized (RHCP) signals.

Figure 15. Folded dipole implementation at 300MHz [64].

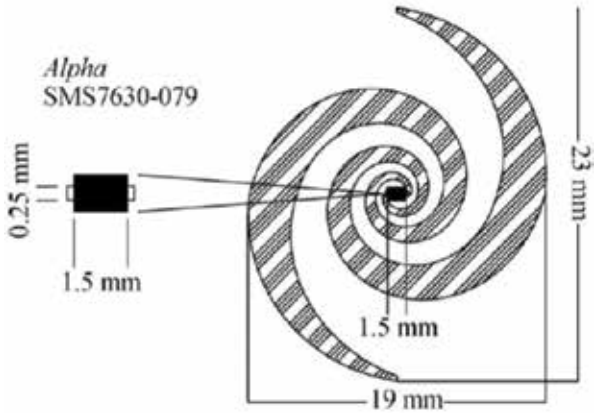

Figure 16. Single spiral antenna element.

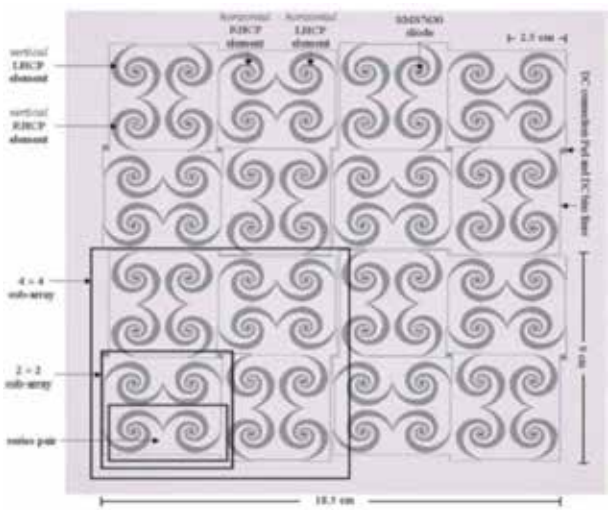

Figure 17. Array of 64 spiral antenna elements.

The authors also experimented with different DC combinations of the different rectifier outputs. The best rectification efficiency (20%) was achieved when all 4-element subarrays were connected in parallel. The total implementation was contained within a frame of 18.5 cm × 18.5 cm (34,225 mm^2). Relatively stable performance across 2–8 GHz was obtained, with test input power levels of -15.5dBm, −7.5,and 17.3 dBm. In this implementation, wideband frequency response was also shown (with minimum -10 dB return loss simulated from 1.6 to 4.0 GHz). Radiation patterns for the single element were also provided and varied with frequency but did not produce sharp gain peaks that would be nonideal for our implementation [66] as shown in **Figure 18**.

http://dx.doi.org/10.5772/64918

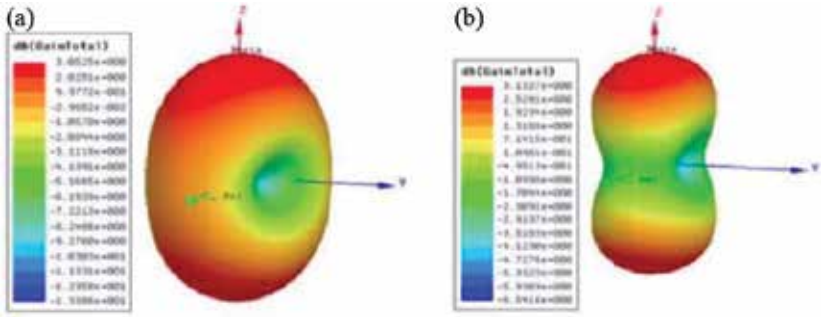

Figure 18. Spiral antenna radiation patterns at (a) 1.85 GHz and (b) 2.45 GHz.

Planar inverted-F antennas are also seeing widespread use on cellular handsets and other cellular and ISM band applications. A PIFA is in essence a raised patch antenna, shorted to the ground plane at one end (either by a pin or any width of perpendicular conductor) and fed through another pin or via at a predetermined location in the patch, based on target frequency. An example of one such antenna in an energy harvesting application can be found in [67], which targets the 2.45 GHz band. This example, illustrated in **Figure 19**, uses a full-width grounding wall (Wa = 12 mm) and contactless feeding mechanism via a feed line on the underside of the board and an aperture in the ground plane. This particular implementation was relatively narrowband, with 10 dB return loss being obtained across approximately 25 MHz, centered at 2.45 GHz. Sizing of the design was not optimized, with total dimensions of (90 cm × 40 cm × 2 cm). Evidently, construction of PIFA is more complex than a printed antenna and is susceptible to both physical variations in assembly and physical damage due to the potential fragility of both the grounding and feed point connections. Particular attention has been drawn to fractal antennas in recent years, as they see increasing use in modern designs [68]. **Figure 20** show an example of iteration common planar patch antennas based on fractal geometries. **Figure 21** shows the practical rectangular fractal patch antenna with matching network and its reflection coefficient [69].

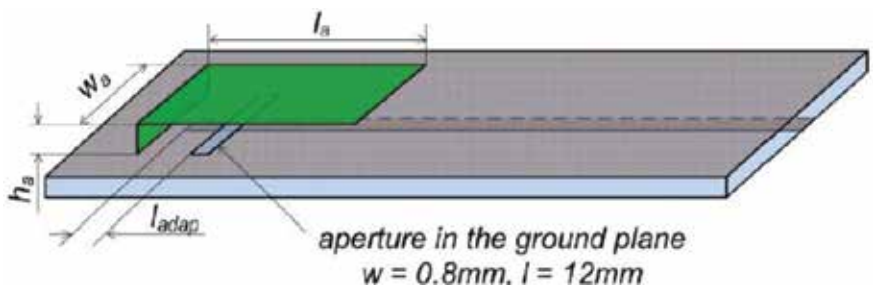

Figure 19. 2.45 GHz PIFA antenna [67].

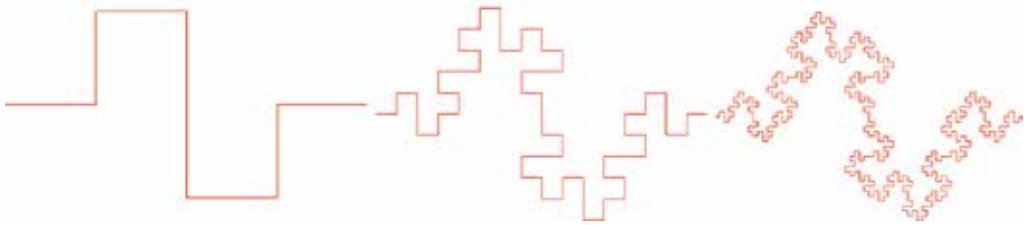

Figure 20. Minkowski sausage iterations.

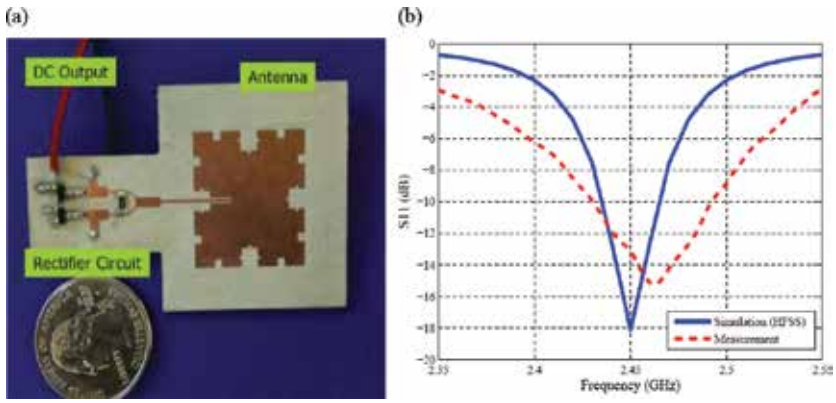

Figure 21. (a) Fabricated version of the proposed rectenna and (b) the reflection coefficient response [69].

6.5. Antenna miniaturization

Reduction of the size of the rectennas is essential these days with the rapid growth of wireless applications. Several methods have been suggested to reduce the microstrip antenna size. They include the use of thick or high dielectric constant of the substrates, modification of the basic patch shapes, short circuiting the patch to the ground plane, and other techniques that combine these three methods. The guided wavelength underneath the patch is reduced when high dielectric constant substrates are used; hence, the resonating patch size is also reduced. The reduction ratio is approximately related to $\sqrt{\varepsilon r}$. Employing high dielectric constant substrates is the simplest method of reducing antenna size but the resulting antenna exhibits narrow bandwidth, high loss, and poor efficiency due to surface wave excitation. Shorting posts have been used in different arrangements to reduce the overall dimensions of the MPA. These shorting posts were modeled and analyzed as short pieces of transmission line with a series inductance and shunt capacitance [70].

The techniques adopted to reduce the size of the antenna through geometry optimization is discussed in this section, slots with different shapes, or both of these techniques. Five miniaturized designs are shown in **Figure 22**. **Figure 22(a)** introduces a circular patch antenna with unbalance slots placed on the diameter line with 45° counter clockwise rotation of the vertical

http://dx.doi.org/10.5772/64918

diameter with different size and position relative to the center of the circular disk. The circular microstrip disk with introducing slots in antenna is resonate at 2.45 GHz, the antenna radius is reduced from the calculated result of 16.5–15.5 mm of the proposed one, yielding size reduction by 12% from original size [71]. **Figure 22(b)** shows a square-aperture-coupled patch antenna with a cross-shaped slot etched on its surface that achieved a patch size reduction of 32.5 %. The cross-shaped slot at the patch surface is etched to reduce the rectenna size due to the use of a [72]. A two-port, meandered, square patch antenna with 40 slits on the perimeter, 10 on each side, is investigated at **Figure 22(c)** to achieve 48% reduction in size. Each pair of slit is symmetrically placed with respect to the center of the side where it belongs. The current is disturbed due to the slits flowing on the surface, forcing them to meander, and thus increasing the electrical length of the patch antenna in both dimensions. So, the operating frequency decreases, whereas the physical size of the patch is unaffected. As well as, operation at a fixed frequency with reduced size is possible by increasing the slit length [73].

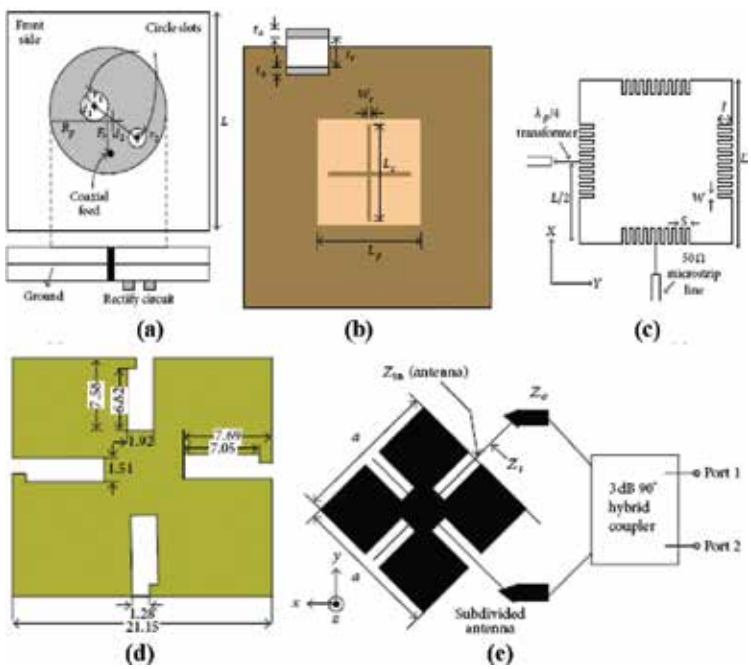

Figure 22. Various miniaturized antenna designs.

Two orthogonal pairs of irregular and unsymmetrical slits are etched on the square patch, shown in **Figure 22(d)**. The presence of slits in this antenna is a way to increase the surface current path length compared with that of the original square MPA and to reduce the size to 40% [74]. The antenna shown in **Figure 22(e)** consists of the interconnection of four corner patches sequential with four strips, and a fifth central patch representing a surface reduction of 60% [75]. The aforementioned designs were reduced by modifying the basic patch shapes and embedding suitable slots in the radiating patch. **Table 6** briefly does the comparison of

Figure 22 on the basis of changes done on their basic shape and their corresponding percentage of size reduction, whose detailed description is present in [76], respectively.

Figure 22	Shape	Frequency	Substrate	Conversion efficiency
(a)	Circular patch with slots placed on the diameter	2.45 GHz	FR-4 substrate (εr = 4.4)	12
(b)	Square patch with cross-shaped slot etched on its surface	2.45 GHz	Two Arlon A25N substrates separated by foam layer	32.5
(c)	Forty slits on the perimeter of a square patch	2.36 GHz	Taconic, TLY-5 laminate (εr = 2.21)	48
(d)	Square patch with two orthogonal pairs of irregular, unsymmetrical slits	GPS	RT/duroid 6010 LM substrate (εr = 10.2)	40
(e)	Patches alternating with four strips and a fifth central patch	5.85 GHz	RT/duroid 5870 substrate (εr = 2.33)	60

Table 6. Various antennas shapes and size reduction.

6.6. Harmonic rejections

The electronic circuits that used rectifier are used in rectennas to convert the AC current induced in the antenna by microwaves to DC current. The nonlinear components of rectifying circuits, such as diodes, generate harmonics of the fundamental frequency. These unwanted harmonics cause reradiation of the harmonic signal and electromagnetic interference with nearby circuits and antennas and reduce efficiency.

Therefore, to suppress these harmonics of microwave components, such an LPF must be added between the antenna and the diode so that the system performance is improved and prevented harmonic interference. For harmonic-rejecting antennas, different shapes of rectenna designs have been designed to reduce the MPA size and cost by removing the prerectification filter. In addition, the insertion loss at the fundamental frequency associated with it can be eliminated and increase the circuit efficiency. While the harmonic rejection antenna have also many advantages of low cost, simpler design, and conversion efficiency enhancement. Some of the designs having the behavior of harmonic rejection are shown in **Figure 23**. **Figure 23(a)** is similar to **Figure 22(a)**, where the unbalanced slot can achieve more harmonic rejection too by omitting the requirement of LPF. The diode of rectenna with square MP antenna operating at 2.4 GHz creates harmonics such as 4.8 and 7.2 GHz but a microstrip circular sector antenna with a circular sector angle of 240° and a feeding angle of 30° from the edge of the circular sector as shown in **Figure 23(b)** blocks these harmonics from reradiation [29].

http://dx.doi.org/10.5772/64918

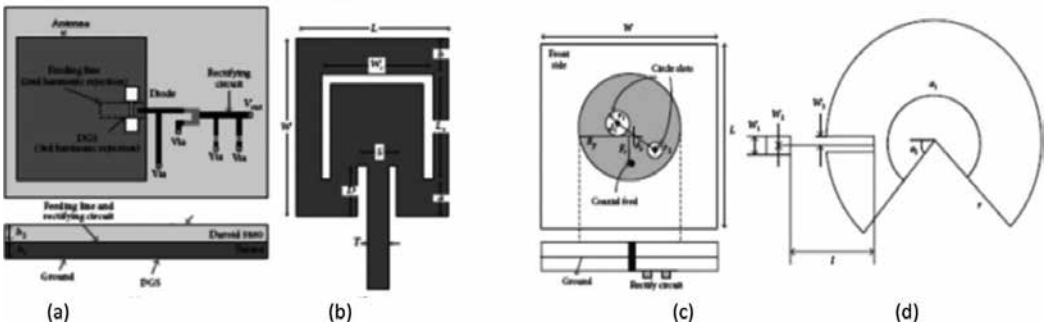

Figure 23. Various antenna designs for harmonic rejection.

Rectangular patch antenna with dumbbell-shaped slot as defected ground structure (DGS) on the ground plane resonating at 2.45 GHz as depicted in **Figure 23(c)** with reflection coefficient |S11| of −1.95 and −1.75 dB at the harmonic frequencies 4.9 and 7.35 GHz, respectively. **Figure 23(d)** is an inset-fed U-slot that resonates at 2.4 GHz, which exhibits high reflection coefficient at the second and third harmonics. The inset length not only causes deep resonance of the antenna in the desired frequency but also suppresses harmonics increasing the efficiency of the system [77]. It is also seen that along with rejecting harmonics, the antennas have higher gain than the conventional antennas in **Figure 23**. **Table 7** shows the comparison made between **Figure 23(a)–(d)** on the basis of the harmonic rejection, their corresponding gain, and conversion efficiency.

Figure 23	Shape	Frequency	Harmonic/rejection	Gain	Conversion efficiency
(a)	Circular patch with slots on the diameter	2.45 GHz	Unbalanced slots achieve second harmonic rejection	3.36 dBi CP gain	Efficiency would reach 53 and 75% with 1 K resistor load under ANSI/IEEE uncontrolled and controlled RF human exposure limit, respectively.
(b)	Microstrip circular sector antenna	2.4 GHz	Circular sector antenna with sector angle of 240° and inset feeding point at 30° from the edge avoids harmonic radiation	4.677 dBi	Maximum efficiency of 77.8% is achieved with a load resistor of 150 Ω and input power of 10 dBm
(c)	Rectangular patch antenna (RPA) with DGS	2.45 GHz	An optimized length of the feeding line and DGS are used to reject the second and third harmonics	6.4 dB	Conversion efficiency is 74% using a 1300 Ω load resistor at a power density of 0.3 mW/cm^2
(d)	U-shaped slot in middle surface of inset-fed RPA	2.4 GHz	U-slot antenna with inset feeding suppresses the harmonics	6.96 dBi	Not specified

Table 7. Various antenna shapes and the associated harmonic rejection [78].

6.7. Reconfigurable antennas

Design reconfigurable antennas have received much attention in RF energy harvesting models owing to their selectivity for operating frequency, tuning, and polarization. RF reconfigurability is basically achieved by dynamically switching the physical structure of the antenna by connecting and/or disconnecting different parts of the antenna structure, which interact with its radiation properties and thereby alter its RF response. The frequency diversity is the characteristic of having frequency selectivity and polarization selectivity can be termed as polarization diversity. Frequency diversity accommodates multiband or wideband frequency ranges and automatic frequency tuning. A reconfigurable MPA can achieve CP polarization among linear polarization (LP), right-hand circular polarization, and left-hand circular polarization. A multiband antenna is needed in order to avoid using two antennas and to allow transmission of video, voice, and data information. It can be realized by frequency diversity and simplifies installation.

Two different techniques are typically used to obtain wideband frequency ranges: using of stacked substrate patches and the activation of different staggered modes of the patch. The first approach incorporates a multilayered patch substrate that resonated at different frequencies. However, this approach has disadvantage as the height of the antenna increases. The second approach is achieved by using dual frequency operation by creating two modes under the patch, such as the TM10 and TM30 modes or the TM10 and TM01 modes. The MPA elements are primarily radiate LP waves; however, by using various arrangements of the feed with slight reshaped of the elements, circular and elliptical polarization can be obtained. CP can be achieved if two orthogonal modes are excited with a 90° time-phase difference between them. CP rectennas help in achieving DC voltage irrespective of rectenna rotation, thus avoiding polarization mismatch and loss. The diversity of the polarization reception is used for overcome of the effects of detrimental fading loss caused by multipath effects and for achieving a making polarization control in order to optimize the system performance.

The reconfigurable antenna is required for the inclusion of certain switching elements. These switches perform the job of connecting and disconnected different parts of the antenna. The switching job can be performed by passive and active elements as lumped elements (capacitors or inductors), RF microelectromechanical systems (MEMS), PIN diodes, or photoconductive switches. Several approaches have been explored, and various methods have been proposed for the methods of obtaining reconfigurable antennas. This section described various methods for the diversity in terms of frequency and polarization, MPA that have been used as reconfigurable rectennas. Seven different designs are introduced for either frequency or polarization diversity or both are shown in **Figure 24**. For polarization diversity, first three designs exhibit are introduced, for frequency diversity fourth and fifth designs demonstrate frequency diversity, and for both frequency and polarization diversities, the last two designs are introduced.

http://dx.doi.org/10.5772/64918

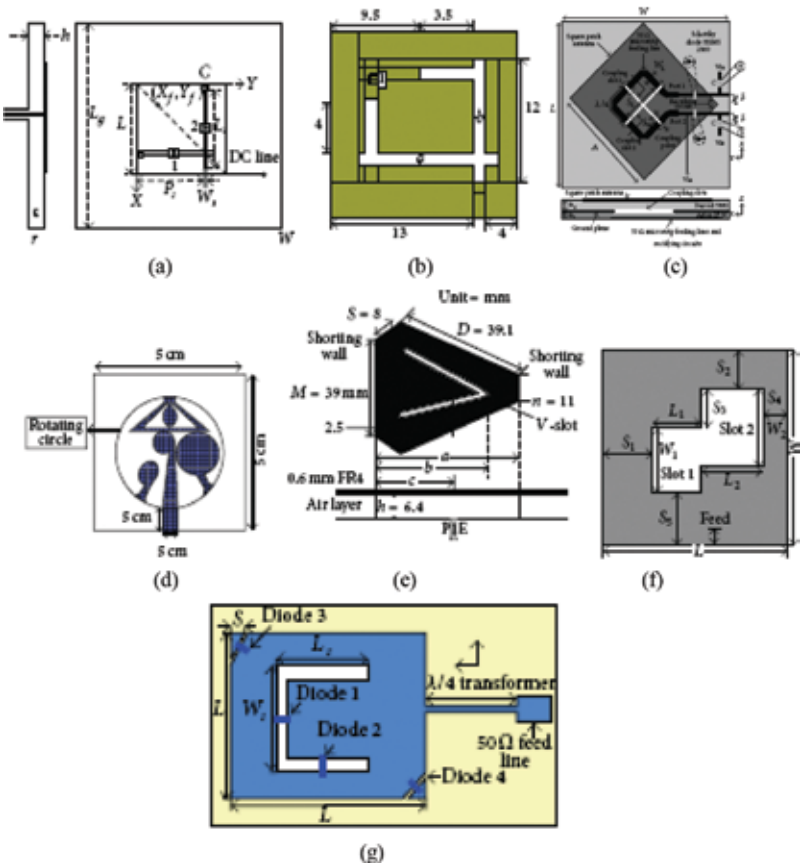

Figure 24. Various antennas design for reconfigurablility [78].

Two orthogonal slots and two PIN diodes at the center of the slot of the square MPA as shown in **Figure 24(a)** are created. The radiation fields of the TM10 and TM01 modes have the same magnitude and 90° out of phase at a midpoint frequency, generating RHCP pattern. When diode on the horizontal slot is ON and diode on vertical slot is OFF, **Figure 24(b)** shows two L-shaped slots having PIN diodes inserted in these slots of the square MPA. This design also adopts the similar way of obtaining polarization diversity, by making diodes "a" and "b" ON and OFF, respectively, for LHCP and vice versa for RHCP. The third design evaluated for polarization diversity is shown in **Figure 24(c)**. The microstrip feeding line is coupled to the square patch antenna through a cross-slot etched on the ground plane. When the excitation point is placed on port 2, the opposed coupling points on slot 2 have a peak of excitation current in phase while the opposed coupling points on slot 1 have a null of magnetic current. After a one-fourth period, the current excited is totally inverted and opposed coupling points have a null of magnetic current on slot 2 and maximum on slot 1. LHCP is then emitted, and RHCP is emitted when excitation is placed on port 1.

In **Figure 24(d)**, the diversity of resonant frequency is achieved through rotational motion of the circular patch that contains four different shapes corresponding to a different set of resonant frequencies. The different shapes are three circular patches and one slotted triangle. By the four different shapes, the four sets of frequencies are covered. For creating dual band operation (2.5–2.55 GHz), a triangular-shaped corner truncated short-circuited antenna with V-shaped slot and 3.4–3.7 GHz WiMAX bands as shown in **Figure 24(e)**. The two resonant modes are excited together by placing two shorting wall switch and a V-shaped slot in the MPA surface.

The patch antenna with both the feature of polarization and frequency diversity is introduced in the following designs. **Figure 24(f)** displays a CP MPA that can function as wireless battery charging at 5.5 GHz and data telemetry in the 5.15–5.35 GHz of wireless LAN (WLAN) band. This dual band and dual-polarized antenna is a square MPA containing two rectangular slots along its diagonal. The MPA generate RHCP by using two slots positioned along the left diagonal of and along the right diagonal to generate LHCP. The design of **Figure 24(g)** is also a MPA with frequency and polarization diversities. It consists of a corner truncated square patch incorporating U-slot and PIN diodes. Diversity of the frequency is achieved by controlling the electrical length through the PIN diode switching on the U-slot. When all diodes are OFF, it operates at resonant frequency of 2.41 GHz. It operates at 2.65 GHz in three cases: when all diodes are ON, when diodes 1, 3, and 4 are ON and diode 2 is OFF, and when diode 1 is ON and other diodes 2, 3, and 4 are OFF. Polarization diversity is achieved by switching PIN diodes ON the slot with truncated corners. If diode 2 is turned OFF and other diodes are ON, it exhibits LP characteristic. RHCP characteristic is exhibited when diode 1 is turned ON and other diodes 2–4 are turned OFF. If all diodes are ON, then LHCP is emitted [78].

6.8. Recent development (our proposed antennas)

The Electronics Research Institute has published many papers in International Periodical Journals regarding transparent or oblique antennas in RF harvesting energy. Following section describes different configurations of antennas. Multiband operations with reducing size are essential in cellular communication systems and other wireless communication applications such as WLANs, Bluetooth, and WiMAX. Among various possible antennas, planar inverted-F antennas (PIFAs) have the advantages of low profile, compact size, and very suitable for wireless communication applications in this day. The broadband characteristic of PIFA is achieved by using CPW feed, around 10% impedance bandwidth improvements over any other antenna feeding mechanism. The CPW offers several advantages over traditional microstrip line: it simplifies fabrication, it facilitates easy shunt as well as series surface mounting of active and passive devices, it reduces radiation loss, and a ground plane exists between any two adjacent lines, hence crosstalk effects between adjacent lines are very weak. Recently, meandered PIFA is widely used for creating resonant frequencies or with size reduction in mobile handset and wireless communication applications. The coupled slot is used within CPW-fed PIFA to create a new independent resonant frequency as shown in **Figure 25**.

http://dx.doi.org/10.5772/64918

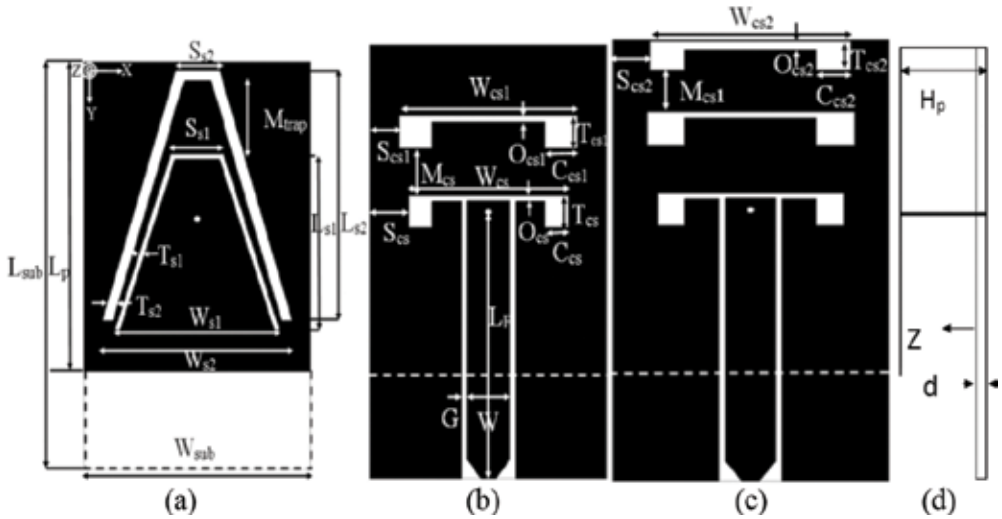

Figure 25. The geometry and configuration of (a) patch with two trapezoidal slots, (b) ground plane with dual coupled slots, (c) ground plane with three coupled slots, and (d) side view.

The functionality is not the only required demand in such antenna systems for wireless communication applications, and other characteristics should be satisfied such as small size, lightweight, omnidirectional radiation pattern, reasonable gain, acceptable impedance bandwidth, and frequency-independent operation. Usually when some parameters are adjusted to set a band to a particular frequency, the other resonances frequencies are affected, and so, the antenna has to be redesigned. However, it independently set the individual frequency bands, one by one, without affecting other bands, by applying varactor diodes with variable capacitors to electrically and independently tune the operating resonant frequencies over a wide frequency range as shown in **Figure 25** and the fabricated proposed antenna as shown in **Figure 26**, and it response is shown in **Figure 27** [79] (**Table 8**).

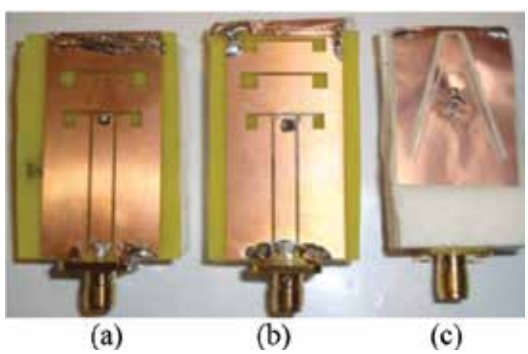

Figure 26. Photo of the fabricated antennas (a) two coupled slots, (b) three coupled slots ground plane, and (c) radiator plate.

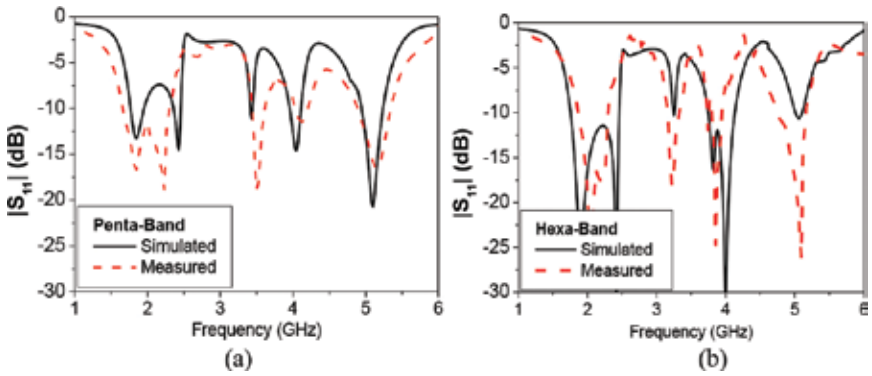

Figure 27. The simulated and measured |S11| of the proposed CPW-fed PIFA (a) pentaband and (b) hexaband.

Figure 24	Antenna shapes	Frequency GHz	Reconfigurable	Cause of reconfigurability	Application
(a)	Square patch orthogonal slots and two PIN diodes	2.64	Polarization diversity RHCP/ LHCP	By turning the diode ON/OFF. Either RHCP/LHCP can be obtained	WLANs satellite link and space robots
(b)	Square patch orthogonal L-shaped slots with two PIN diodes	4.44	Polarization diversity RHCP/ LHCP	Reconfigurability is achieved by switching two PIN diodes	Unlicensed and licensed WiMAX
(c)	Square patch coupled to microstrip line by aperture	2.45	Polarization diversity RHCP/ LHCP	Reconfigurability is obtained by selecting one of two excitation points	Not available
(d)	A circular patch to feed different shapes	Cover five 2–7	Frequency diversity	Reconfigurability is obtained by rotation motional of the part of the antenna	Cognitive radio system
(e)	Short circuited triangular patch antenna with truncated corner	2.5–2.55 and 3.4–3.7	Frequency diversity	By placing two shorting walls with a V-shaped slot patch	Covers 2.5–2.55 and 3.4–3.7 WiMAX
(f)	Two rectangular slots properly position	5.15–5.35 and 5.5	Frequency diversity and polarization	Positioning the slots along the left diagonals	Can function as a rectenna for wireless battery charging 5.5 and 5.15–5.35
(g)	Square patch with two PIN diodes on a U-shaped slot	2.415 and 2.65	Frequency diversity and polarization	The switching of the PIN diode on the U-slot realizes frequency diversity and polarization	WLAN digital multimedia broad casting

Table 8. Various antennas shapes and their reconfigurability.

http://dx.doi.org/10.5772/64918

Another sturcture is used for reconfigurable multiband PIFA as shown in **Figure 28**. The antenna is based on a combination of a CPW-fed PIFA, meander turn-shaped slot on the radiating plate [80] and coupled slot within the ground plane for multiband operation and size reduction characteristics. As the number of meander turn-shaped slots is increased, new resonant frequencies are excited. PIN diode is used to switch the fundamental resonant frequency from high to low frequency. This antenna operates over LTE band 11 (1.47–1.5 GHz), LTE band 8 (925–960 MHz), GSM1800 MHz/GSM1900 MHz/Bluetooth 2.4 GHz, WiMAX frequency range (3–4 GHz), and WLAN frequency range (5–6 GHz).

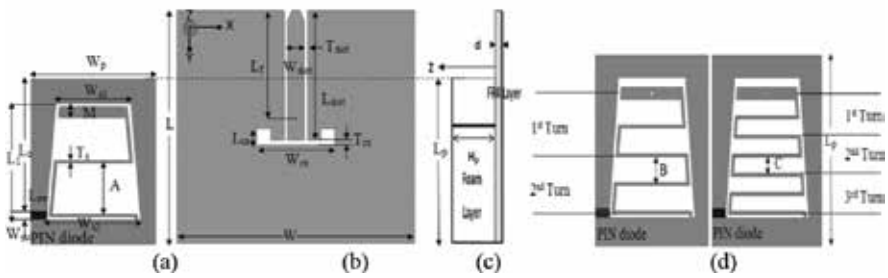

Figure 28. The geometry and configuration of CPW-fed PIFA with PIN diode switch (SW) (a) radiator with one meander turn, (b) ground plane, (c) antenna side view, (d) radiator with two meander turns, and (e) radiator with three meander turns.

The design is started by conventional CPW-fed PIFA (the meander turns shaped slot on the radiator and the coupled slot in the ground plane are removed) to operate at Bluetooth 2.4 GHz. **Figure 29** obtains the simulated |S11| of one meander turn-shaped slot with ON/OFF switch mode. First is used to show PIN diode switches with the open and close states to switch the antenna from LTE band 11 (1.47–1.5 GHz) to LTE band 8 (0.925–0.960 GHz) with total 63% size reduction as compared to the original PIFA size. The fabricated photo of the antennas are shown in **Figure 30**, the reflection coefficient for both PIN diode modes of the proposed antenna with three turns of meander slot are shown in **Figure 31(a–c)**, respectively. The concept is approved for the three designs.

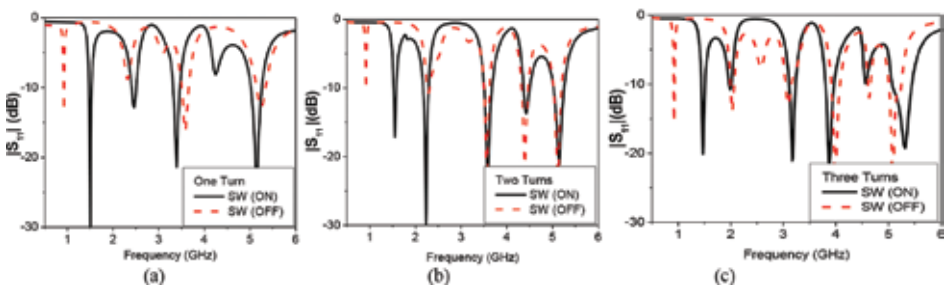

Figure 29. The simulated |S11 | of (a) one, (b) two, and (c) three meander turn-shaped slots with switch ON/OFF modes.

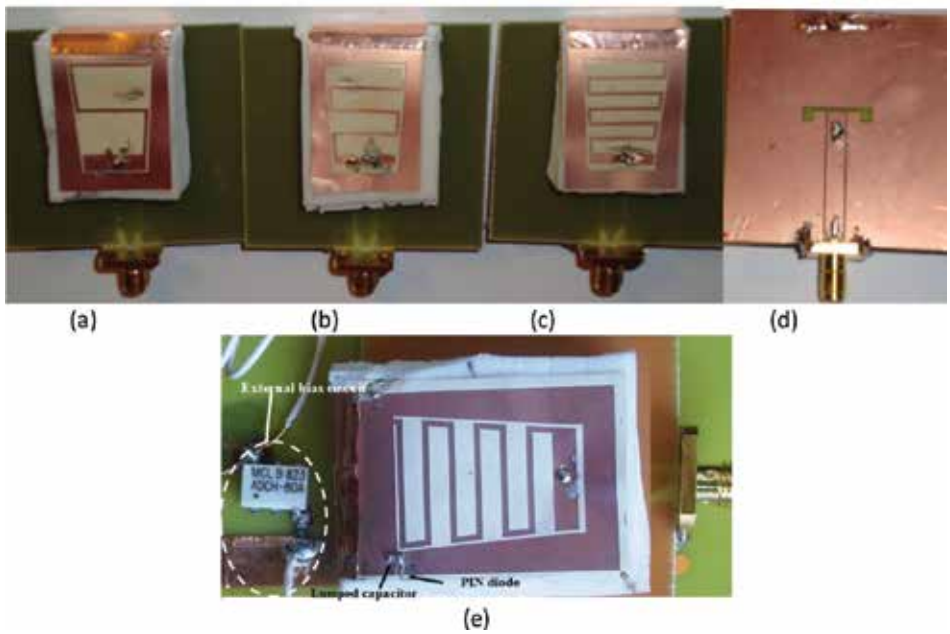

Figure 30. Photo of the fabricated proposed antennas (a) one turn, (b) two turns, (c) three turns, (d) ground plane with coupled slot, and (e) PIN diode and external biasing circuit.

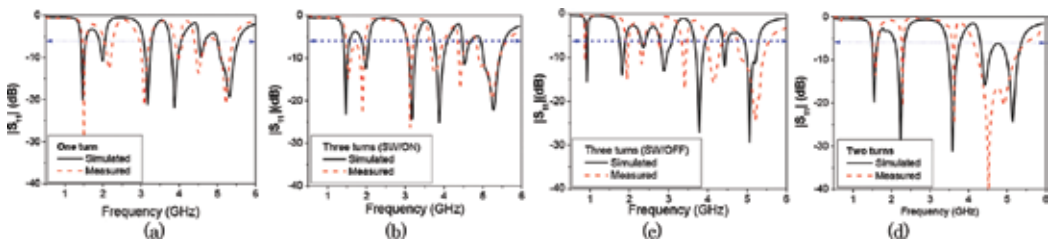

Figure 31. Comparison between simulated and measured |S11|of (a) one turn, (b) two turns, (c) three turns with SW/ON state, and (d) three turns with SW/OFF state.

The gains of antenna are in between 1.8 and 4.8 dBi at each resonant frequency with good impedance bandwidth (|S11|<-6 dB) that is suitable for standard channel bandwidth for wireless communication applications such as LTE band 8 (0.925–0.960 GHz), GSM1900, LTE band 2, LTE band 33, LTE band 11, Bluetooth, WiMAX, and WLAN. The radiation efficiency is larger than 70%, and it is decreased with switching the antenna on from high to low frequency due to ohmic losses of the PIN switches.

Another method used to achieve multiband with compact size is meta-material-inspired loading exploited to create a new resonance while maintaining the antenna's small form factor as shown in **Figure 32**.

http://dx.doi.org/10.5772/64918

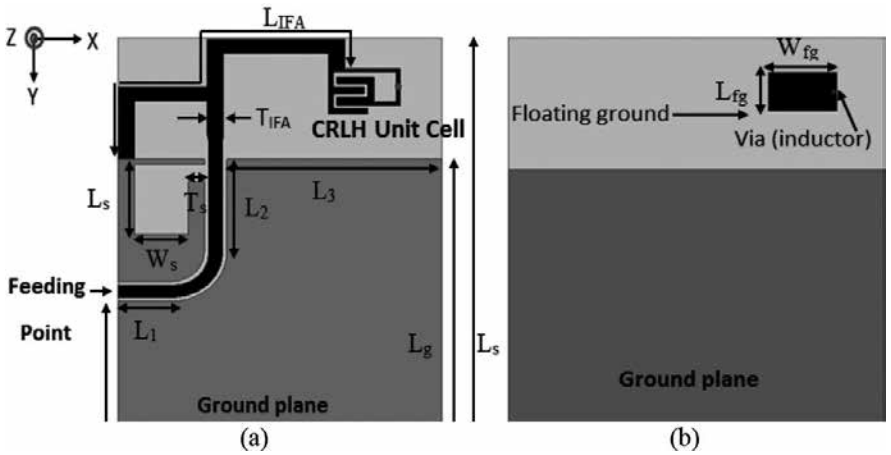

Figure 32. Geometry of triple-band MTM-inspired small USB antenna (a) top view and (b) bottom view.

This section presents two compact antenna designs using the meta-material techniques. The first design [81] consists of CPW printed IFAs loaded with CRLH unit cells to achieve new operating bands with the same antenna size beside the fundamental resonant frequencies of IFA arm itself.

A "defected" ground plane is formed by appropriately cutting a dumbbell-shaped slot out of the CPW ground plane to create extra resonant frequency. The proposed antenna design consists of two IFA arms loaded with two TL-MTM unit cells to create new two operating bands in addition to the operating frequencies of two IFA arms themselves for USB applications. The geometry with detailed design parameters of the proposed triple-band USB antenna is shown in **Figure 32**. The simulated S parameters of the design procedures are shown in **Figure 33**, starting with the single CPW-fed IFA that is designed to cover lower WLAN application and then used the CRLH meta-material-inspired cell to create the second resonant frequency to cover WI-MAX 3.5 GHz application. The antenna size reduced by around 22% from the fundamental resonant frequency of the printed F antenna. Finally, the slot is etched within the ground plane to cover the upper WLAN application (5.2–5.25 GHz).

The −10 dB antenna exhibits bandwidth of 200, 100 and 80 MHz for lower WLAN 2.4 GHz band, WiMAX 3.5GHz band, and upper WLAN 5.2 GHz band, respectively. These results agree well with simulation results as shown in **Figure 33**. The simulated gains are 2.3, 2.1, and 2 dBi at 2.4, 3.5,and 5.2 GHz, respectively with radiation efficiency more than 75%. The theory of loading two arms CPW-fed IFA with two CRLH unit cells was explained and verified using the RLC-lumped components of the simulators, advanced designing system (ADS), and high-frequency structure simulation (HFSS), and there is good agreement with the measured result, to be used for mobile and wireless data USB applications. The whole geometry with detailed design parameters of the proposed triple-band USB antenna is shown in **Figure 34** [82]. The photo of fabricated proposed antenna and measured results are shown in **Figure 35**. Measured impedance bandwidths (−6 dB) for each resonance are suitable for the channel bandwidth of

the LTE band 11 (1.42–1.47 GHz), GSM1800 (1780–1890 MHz), Bluetooth (2.4–2.45 GHz), WiMAX standards (3.4–3.5 GHz) and (3.7–4 GHz), and upper WLAN (5.2–5.25 GHz). The measured realized gains at four resonant frequencies are 2.8, 1.9, 3.1, and 2.1 dBi, respectively. The radiation efficiency was measured by using Wheeler cap method. The average radiation efficiency is more than 75% [83].

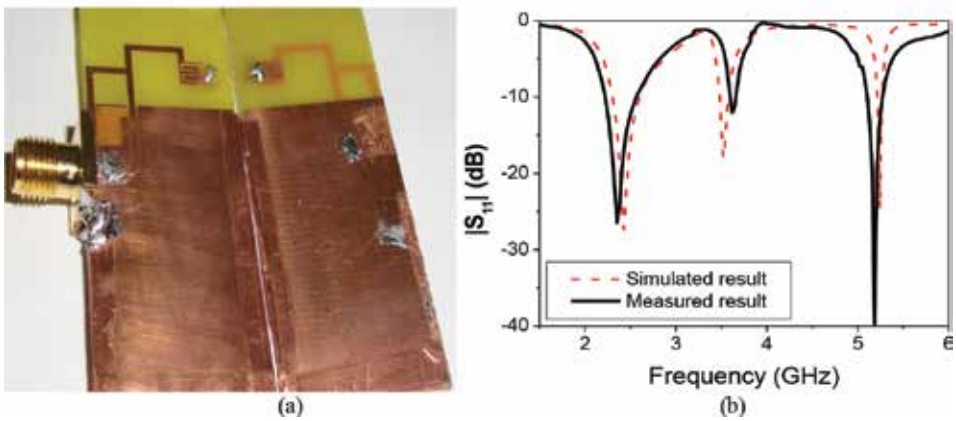

Figure 33. (a) Photo of the fabricated USB antenna and (b) the |S11 | comparison of the simulated and measured results.

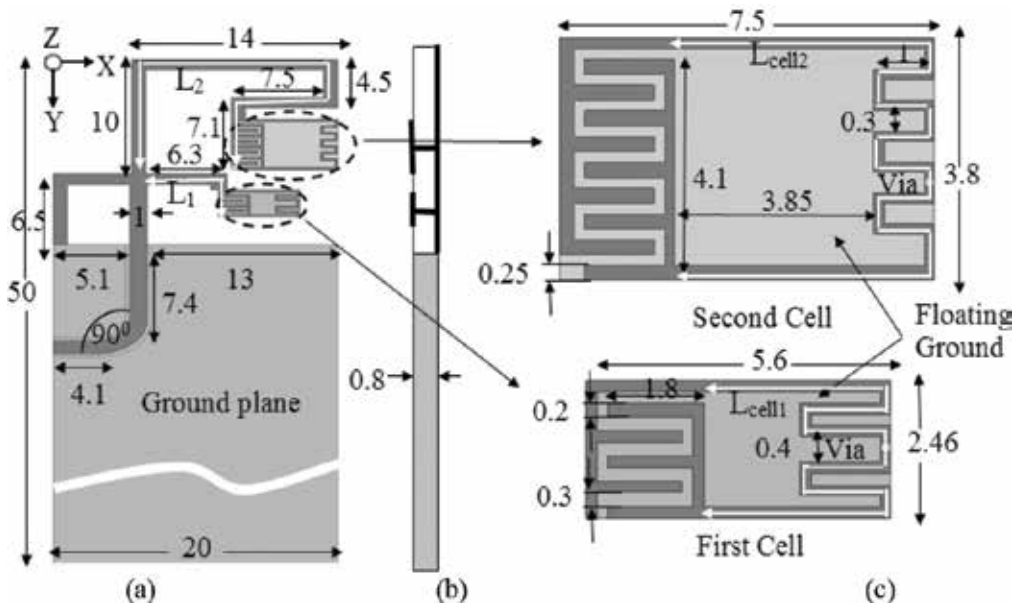

Figure 34. Quad band CPW-fed printed IFA antenna with two meta-material-inspired unit cells (all optimized dimensions are in mm) (a) top view, (b) side view and (c) two CRLH unit cells.

http://dx.doi.org/10.5772/64918

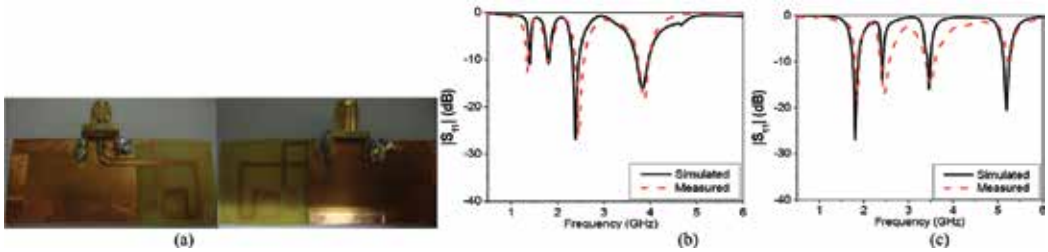

Figure 35. (a) The fabricated antenna, (b) simulated and measured |S11| of implemented antenna (1.4, 1.8, 2.4, and 3.8 GHz), and (c) optimized antenna (1.8, 2.4, 3.5, and 5.2 GHz).

6.9. Tunable design

The aim is to tune the operating frequency of the antenna and to have a single multifunctional antenna in a small terminal for many applications. Varactor diodes are the most commonly used technique to tune the operating frequencies in RF and front-end applications. A DC block capacitor, CDC = 100 nF, between the short and the ground is needed as shown in **Figure 36**. The capacitor CDC generates an open circuit for the DC voltage and a short circuit for the RF signal. An inductor of 1 μH is used to support complete path to the ground plane in the DC case [84, 85]. The comparisons between simulated and measured results are shown in **Figure 37**. The fabricated antenna with two different voltages V1 and V4 are shown in **Figure 38**.

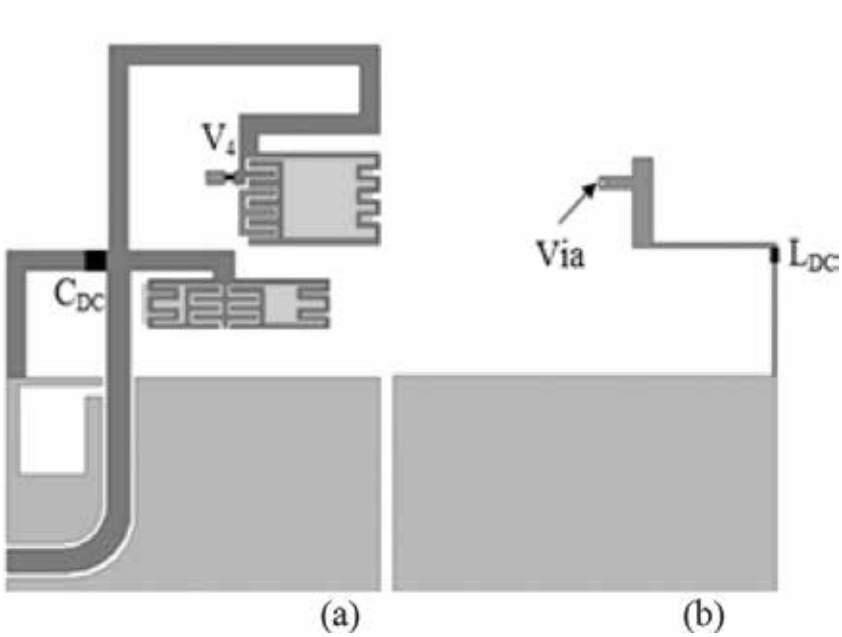

Figure 36. The proposed antenna with DC biasing network (a) top view and (b) back view.

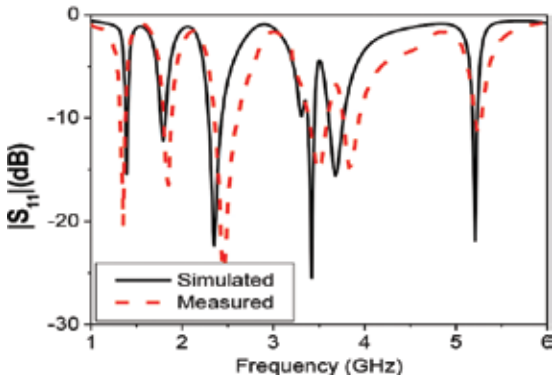

Figure 37. The simulated and measured |S11| of the proposed antenna with package of PVC casing material.

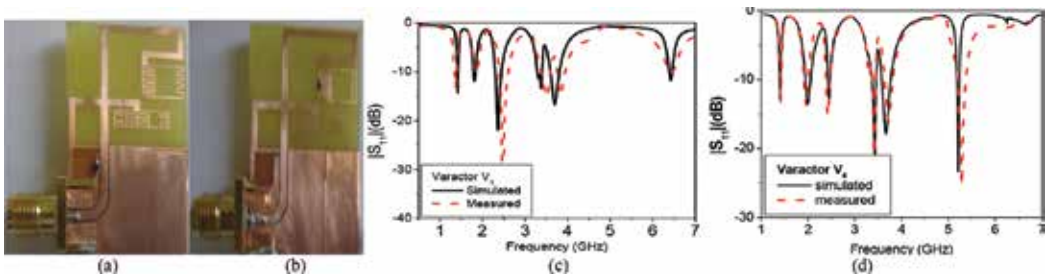

Figure 38. The photo of the fabricated USB antenna with 0.05 pF (a) varactor V1, (b) varactor V4 and the simulated and measured |S11| with varactors (c) V1 and (d) V4.

7. Nanoantennas

Approximately 30% of this incident Sun energy is reflected back to space from the atmosphere, atmospheric gases absorb 19% and reradiated to the Earth's surface in the mid-IR range from 7 to 14 μm and 51% is absorbed by the surface and reradiated at around 10 μm. The energy incident in both the visible and IR regions to the earth is reradiated IR energy underutilized by current technology.

Several approaches have been used to successfully harvest energy from the Sun and conversion of solar energy to electricity using photovoltaic cells. In addition to photovoltaics is the optical rectenna, which is a combination of a rectifier and a receiving antenna. The initial rectenna concept was demonstrated for microwave power transmission by Raytheon [86]. This illustrated the ability to capture electromagnetic energy and convert it to DC power at efficiencies approaching 84%. Most of the papers have been performed to extend the concept of rectennas to the infrared and visible regime for solar power conversion. While the progress have been made in the fabrication and characterization of metal-insulator-metal diodes for use in infrared

rectennas [87]. The optical antennas has been demonstrated, which can couple electromagnetic radiation in the visible regime in the same way as radio antennas do at their corresponding wavelengths [88]. The development of economical manufacturing methods for large-scale fabrication of nanoantenna-based solar collectors becomes the challenge. It needs to improve the efficiency of rectification of antenna-induced terahertz (THz) currents to a usable DC signal, and material properties and behavior of antennas/circuits in the THz solar regions need to be further characterized.

7.1. Photovoltaic limitations

To begin with the p-n junction solar cell is utilized for solar energy harvesting technologies. After this, the physics of energy absorption is used and carrier generation are the function of the material characteristics and corresponding electrical properties as photonic band gap. In order to excite an electron from the valence band into the conduction band, a photon needs only to have greater more than that of the band gap. However, the frequency solar spectrum approximates a black body spectrum at ~6000 K, and much of the solar radiation reaching the Earth is composed of photons with energies greater than the band gap of silicon. By the solar cell, these energy photons are absorbed but the difference in energy between these photons and the silicon band gap is converted into heat rather than into usable electrical energy. For a single-junction cell, this sets an upper efficiency of ~31% [89].

7.2. Alternative economical PV

Developing of another energy harvesting approach based on the use of nantennas to absorb incident solar radiation was founded. Moreover of PVs, which are quantum devices limited by material band gaps, antennas are resonated at natural resonance frequency and the bandwidth of operation is a function of physical antenna geometries. Nantenna electromagnetic collectors (NECs) can be formatted as frequency selective surfaces to efficiently absorb the entire solar spectrum. Contrastingly, by generating single electron-hole pairs, such as the PV case; a time-changing current in the antenna brought on by the incident of the electromagnetic field from the sun. Collection efficiency of the incident radiation is dependent upon proper design of resonance and impedance matching of the antenna [90].

7.3. Nanoantennas theory

The antennas theory is that the incident light on the antenna causes electrons in the antenna to move back and forth at the same frequency as the incident light. This is done by the electric field oscillating of the incoming electromagnetic wave. The movement of current electrons alternates in the antenna circuit and then converts itself into a direct current. The AC must be rectified, which is typically done with some kind of diode [91–96]. As shown in **Figure 39**, the obtained DC can then be used to power an external load. According to simple microwave antenna theory, the antenna resonant frequency (which results in lowest impedance and thus highest efficiency) scales linearly with the dimensions of the antenna. The solar spectrum wavelengths lie between approximately 0.3 to 2.0 μm. However, in order for a rectifying antenna to be an efficient electromagnetic collector in the solar spectrum, it needs to be on the

order of hundreds of nanometer in size. This can be achieved by shrinking the dimensions of the antenna to the scale of the wavelength. For this reason, nantennas are used as an alternative to scale the microwave theory down to the IR regions of the electromagnetic spectrum in **Figure 39** [97].

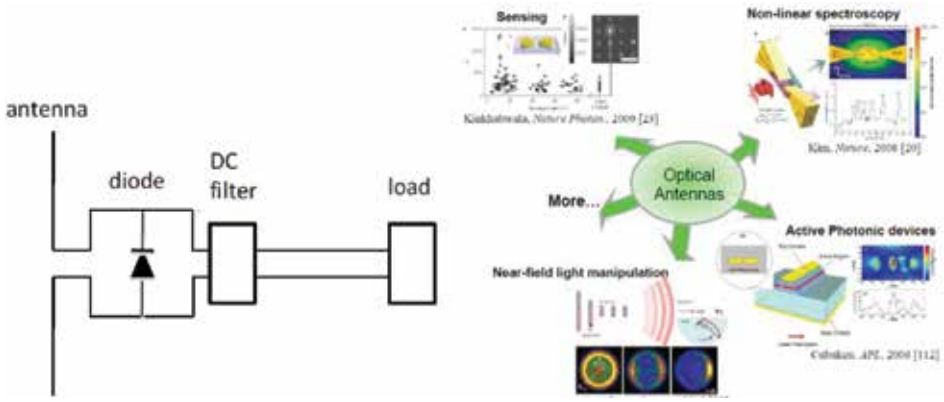

Figure 39. A wide range of applications are driving the research in optical antennas. The applications reported in recent years include biological and chemical sensing, nonlinear spectroscopy, high-harmonic generation, and solar energy harvesting.

Cyclic plasma induces when an antenna is excited into a resonance mode of free electrons that is movement from the metal antenna. The electrons freely flowing straight in to the antenna are oscillating current at the same frequency as the resonance. The current flow crossed the antenna feed point in a balanced antenna; the feed point is located at the point of lowest impedance as in **Figure 40**. The e-field is clearly concentrated at the center feed point, this provides a convenience point to collect energy and transport it to other circuitry for conversion. Nanoantenna structure incorporates an antenna layer, a dielectric standoff layer, and a ground plane as in **Figure 41**. It is found that in right shape, materials, and size, the simulated nantennas could harvest up to 92% of energy at infrared wavelength. The operation of optical frequencies, an ultrafast diode rectifies the optical frequency signal absorbed by the antenna, producing a DC voltage. The configuration shown is a clamping circuit that theoretically provided 100% conversion efficiency as a traditional rectifier. The way to use the rectified DC energy is to connect a load with a low-pass filter directly across the diode. The performing of a classical circuit analysis is the output: DC voltage, at the load can be high with the peak input AC voltage across the antenna [86]. The total efficiency of nanorectennas consists of two parts. The first part is the efficiency by which the light is captured by the nanoantenna and brought to its terminals. The second part is the efficiency by which the captured light is transformed into low-frequency electrical power by the rectifier. The radiation efficiency of IR for five different conducting materials silver, gold, aluminum, copper, and chromium, respectively, are reported in vacuum. Copper efficiencies reach to 60–70% but the bandwidth is rather limited. This is reflected in the total efficiency that reaches a maximal value of almost about 30% for a dipole length of 300 nm [97].

http://dx.doi.org/10.5772/64918

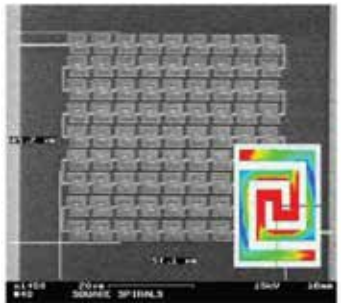

Figure 40. Array of loop nanoantennas, (inset) flow of T Hz current to feed point of antenna. Red represents highest concentrated e-field.

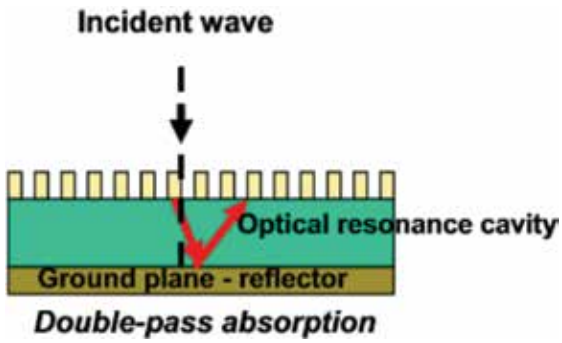

Figure 41. Side walls of nanoantenna showing path of incidence of wave.

The nantenna captured the electromagnetic energy from both solar radiation and thermal earth radiation. As shown in **Figure 42**, various self-complementary antennas used as dipoles, spirals, loops, etc. are the candidates due to their inherit wide bandwidth and feed point configurations for concentrating energy collection, and the antenna element size is related to the wavelength of light harvest.

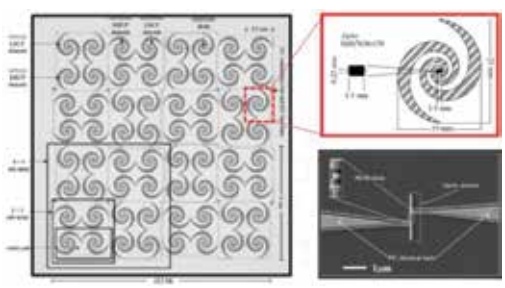

Figure 42. Array of square spiral nanoantennas.

The concept was performed using spiral antenna structures as shown in **Figure 43**. It shows that a modeled thermal energy profile indicating that the e-field is clearly concentrated at the center feed point.

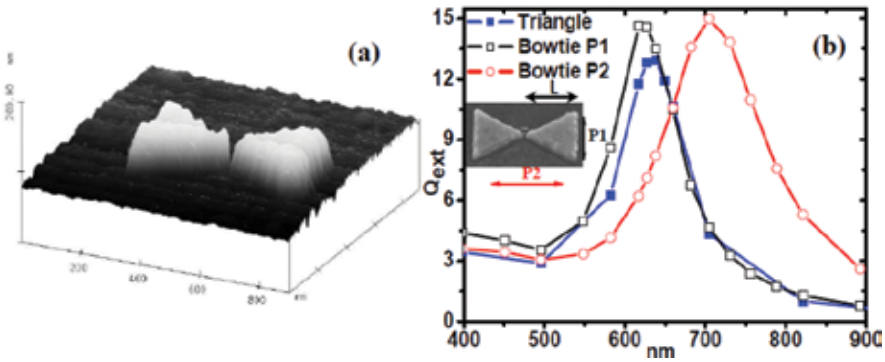

Figure 43. (a) Topographic image of a 120 nm Au bow tie antenna with 20 nm gap fabricated using electron-beam lithography and (b) DDA-simulated extinction efficiency showing polarization dependence and splitting of triangle resonance mode into two orthogonal modes for the bow tie dimer (L = 120 nm).

The nantenna radiation pattern displays the angular reception characteristics that result in a wider angle of incidence exposure to radiation than a typical PV device. The flux is collected from the Sun, which falls within the radial beam pattern of the antenna. It reduce the need of the mechanical solar tracking mechanisms that are a critical antenna characteristic that optimizes the energy collection from the Sun as it pass throughout the sky. There is another mechanism for increasing the efficiency of antenna arrays through the expansion of the radial field. Antennas do not provide a means of converting the collected energy, so this will need to be accomplished by associated circuitry, such as rectifiers. The virtual large surface area antenna focuses the electromagnetic energy onto the nano-sized energy conversion material fabricated at the antenna feed point. Theoretical efficiency is improved by the enhanced radiation capture area of the antenna. When efficiency compared to the theoretical of single junction solar cells (30%), nantennas appear to have a significant advantage. The advantage nantennas has over semiconductor photovoltaics is that nantenna arrays can be designed to absorb any frequency of light.

The nantenna resonant frequency is selected by varying its length. In order to absorb different wavelengths of light, different band gaps are needed. In order to vary the band gap, the semiconductor must be alloyed or a different semiconductor must be used altogether. Nantennas exhibit potential advantages in terms of polarization, tunability, and rapid time response. (i) they have very small area detection, (ii) their electromagnetic field allows localization beyond the diffraction limit, (iii) they very efficiently release radiation from localized sources into the far field, (iv) they make possible the tailoring of the interaction of electromagnetic field at the nanoscale, and (v) they could be tuned to a specific wavelength [89].

7.4. Applications

Large-scale economical fabrication is used for covering the roofs of buildings and supplementing the power grid. It collects different separate bands of electromagnetic energy. By using double-sided panels, a broad spectrum of energy from the sun during the day could absorbed while the other side might be designed to take in the narrow frequency of energy produced from the earth's radiated heat or residual heat from electronic devices as shown in **Figure 44**. This technology may also support several applications, including passive thermal management products, such as building insulation, window coatings, and heat dissipation in electronic consumer products, such as computers. These types of antennas are broadband collectors of energy with a spectral emission response. This generates a frequency-selective distribution of energy that potentially collected unwanted energy residual or incident heat and redistribute it at other innocuous wavelengths. Other applications are conceivable that nantenna collectors, combined with appropriate rectifying elements, could be integrated into the "skin" of consumer electronic devices to continuously charge their batteries.

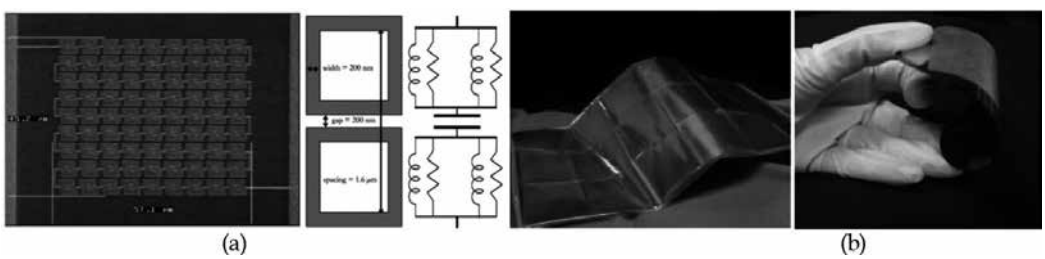

Figure 44. (a) SEM image of the square loop antenna array and (b) nanoantenna collector sheet.

Author details

Dalia M.N. Elsheakh

Address all correspondence to: daliaelsheakh@gmail.com

Electronics Research Institute, Giza, Egypt

References

[1] H.J. Visser, A.C.F. Reniers, and J.A.C. Theeuwes, "Ambient RF energy scavenging: GSM and WLAN power density measurements," IEEE 38th European Microwave Conference, Amsterdam, Netherlands. pp. 721–724, October 27–31, 2008.

[2] A. Doig, "Off-grid electricity for developing countries," IEE Review, vol. 45, Issue 1, pp 25–28, January 1999.

[3] L. Mateu and F. Moll, "Review of energy harvesting techniques and applications for microelectronics (Keynote Address)," in VLSI Circuits and Systems II, Sevilla, Spain, pp. 359–373, 2005.

[4] M. Arrawatia, M.S. Baghini, and G. Kumar, "RF energy harvesting system at 2.67 and 5.8GHz," IEEE Asia-Pacific Microwave Conference Proceedings, Yokohama, pp. 900–903, December 7–10, 2010.

[5] A. Boaventura, A. Collado, N.B. Carbalho, and A. Georgiadis, "Optimum behavior, wireless power transmission system design through behavioral models and efficient synthesis techniques," IEEE Microwave Magazine, vol. 14, no. 2, pp. 26–35, March 2013.

[6] T.T. Peter, T.A. Rahman, S.W. Cheung, R. Nilavalan, H.F. Abutarboush, and A. Vilches, "A novel transparent UWB antenna for photovoltaic solar panel integration and RF energy harvesting," IEEE Transactions on Antennas and Propagation, vol. 62, no. 4, pp. 1844–1853, April 2014.

[7] M. Arrawatia, M.S. Baghini, and G. Kumar, "RF energy harvesting from cell towers in 900MHz band," IEEE National Conference on Communications (NCC), Bangalore, pp. 1–5, January 28–30, 2011.

[8] D. Bouchouicha, F. Dupont, M. Latrach, and L. Ventura, "Ambient RF energy harvesting," International Conference on Renewable Energies and Power Quality, Spain, pp. 1–5, March 2010.

[9] J.A. Paradiso and T. Starner, "Energy scavenging for mobile and wireless electronics," IEEE Pervasive Computing, vol. 4, pp. 18–27, January–March 2005.

[10] K. Roth and J. Brodrick, "Energy harvesting for wireless sensors," ASHRAE Journal, May 2008.

[11] L. Mesica and A. Massaro, "New trends in energy harvaesting from Earth long- wave infrared emission," Advanced in Material Sciences and Engineering, vol. 2014, 2014.

[12] A. Arigliano, P. Caricato, A. Grieco, and E. Guerriero, "Producing, storing, using and selling renewable energy: the best mix for the small medium industry," Computers in Industry, vol. 65, no. 3, pp. 408–418, 2014.

[13] F. Manzano Agugliaro, A. Alcayde, F.G. Montoya, A. Zapata- Sierra, and C. Gil, "Scientific production of renewable energies worldwide: an overview," Renewable and Sustainable Energy Reviews, vol. 18, pp. 134–143, 2013.

[14] I. Kocakarin and K. Yegin, "Glass superstrate nanoantennas for infrared energy harvesting applications," International Journal of Antennas and Propagation, vol. 2013, Article ID 245960, 7 pp., 2013.

[15] R. Moghe, Y. Yang, and D.F. Divan, "A scoping study of electric and magnetic field energy harvesting for wireless sensor networks in power system applications," Energy Conversion Congress and Exposition, pp.3550–3557, 2009.

[16] Linear, 2014, Energy Harvesting Products, available at: http://www.linear.com/products/energyh arvesting

[17] Pavegen website, 2014, Technology Section, available at: http://www.pavegen.com/technology

[18] En Ocean website, 2014, Energy Harvesting Wireless Technology, available at: http://www.enocean.com /en/energy-harvesting-wireless/

[19] NikkoIA website, 2014, Applications, available at: http://www.nikkoia.com/en/biz-applications/security/

[20] Voltree Power website (2014), Bioenergy Harvester, available at: http://voltreepower.com/b ioHarvester.html

[21] A. Georgiadis, G. Andia, and A. Collado, "Rectenna design and optimization using reciprocity theory and harmonic balance analysis for electromagnetic (EM) energy harvesting," IEEE Antennas and Wireless Propagation Letters, vol.9, pp. 444–446, May 10, 2010.

[22] M. Zawadzki and J. Huang, "Integrated RF antenna and solar array for spacecraft application," in Proc. IEEE Int. Conf. Phased Array Syst. Technol., May 2000, pp. 239–242.

[23] Energy Harvesting Journal, 2010, An interview with Enocean by Raghu Das, available at: http://www.energyharvestingjournal.com/articles/an-interview-with-enocean-00002058.asp

[24] European Commission - Digital Agenda for Europe, 2014, Innovations in Energy Harvesting and Storage, Available at: http://ec.europa.eu/digital-agenda/futurium/en/content/innovations-energy-harvesting-and-storage

[25] Technology Strategy Board, 2011, Energy Harvesting: Watts Needed? Workshop, Royal Society, Carlton House Terrace London.

[26] A. Costanzo, F. Donzelli, D. Masotti, and V. Rizzoli, "Rigorous design of RF multi-resonator power harvesters," IEEE Proceedings of the Fourth European Conference on Antennas and Propagation, Barcelona, pp. 1–4, April 12–16, 2010.

[27] S.J. Orfanidis, "Electromagnetic waves and antennas," 2008, Rutgers University, Piscataway, New Jersey, USA, [Online], available at: http://www.ece.rutgers.edu/~orfanidi/ewa/ [Accessed April 2012]

[28] S. Rivière, A. Douyère, F. Alicalapa, and J.D. Lan Sun Luk, "Study of complete WPT system for WSN applications at low power level," Electronics Letters, Institution of Engineering and Technology, vol. 46, Issue 8, pp. 597–598, April 15, 2010.

[29] V. Rizzoli, D. Mascotti, N. Arbizzani, and A. Costanzo, "CAD procedure for predicting the energy received by wireless scavenging systems in the near-and far-field regions," IEEE Microwave Symposium Digest (MTT-S International), Bologna, pp.1, May 23–28, 2010.

[30] H. Jabbar, Y.S. Song, and T.T. Jeong, "RF energy harvesting system and circuits for charging of mobile devices," IEEE Transactions on Consumer Electronics, vol. 56, Issue 1, pp. 247–253, February 2010.

[31] M. Mi, M.H. Mickle, C. Capelli, and H. Swift, "RF energy harvesting with multiple antennas in the same space," IEEE Antennas and Propagation Magazine, vol. 47, no. 5, pp. 100–106, October 2005.

[32] T.S. Salter Jr., G. Metze, and N. Goldsman, "Improved RF power harvesting circuit design," International Semiconductor Research Symposium Proceedings, College Park, MD, USA, pp.1-2, December 12–14, 2007.

[33] D.G. Rowe, "Nokia developing phone that recharges itself without mains electricity," www.guardian.co.uk, Wed., June 10, 2009.

[34] W. Sun, N.P. Kherani, K.D. Hirschman, L.L. Gadeken, and P.M. Fauchet, "A three-dimensional porous silicon p-n diode for betavoltaics and photovoltaics,"Advanced Materials, 17, pp.1230–1233, 2005.

[35] V. Sakamuri and J. Frolik, "Design of a 2.4 GHz interrogator for a rectenna-based sensor system," IEEE 12th Annual Wireless and Microwave Technology Conference (WAMICON), pp.1–4, April 2011.

[36] J.W. Zhang, K.Y. See, and T. Svimonishvili, "Printed decoupled dual-antenna array on-package for small wirelessly powered battery-less device," IEEE Antennas and Wireless Propagation Letters, vol. 13, pp. 923–926, 2014.

[37] I.T. Nassar and T.M. Weller, "Development of novel 3-D cube antennas for compact wireless sensor nodes," IEEE Transactions on Antennas and Propagation, vol. 60, no. 2, pp. 1059–1066, February 2012.

[38] S.H. Nasab, M. Asefi, L. Albasha, N. Qaddoumi, "Investigation of RF signal energy harvesting," Active and Passive Electronic Components Journal (Hindawi Publishing Corporation), vol. 2010, Article ID 591640, pp.1–7, October 2010.

[39] T. Salter, K. Choi, M. Peckerar, G. Metze, and N. Goldsman, "RF energy scavenging system utilizing switched capacitor DC-DC converter," Electronics Letters (Institution of Engineering and Technology, Maryland, USA), vol. 45, Issue 7, pp. 374–376, March 26, 2009.

[40] J. Hautcoeur, L. Talbi, and K. Hettak, "Feasibility study of optically transparent CPW-fed monopole antenna at 60-GHz ISM bands," IEEE Transactions on Antennas and Propagation Magazine, vol. 61, pp. 1651–1657, 2013. T.W. Turpin and R. Baktur,

"Meshed patch antennas integrated on solar cells," IEEE Antennas and Wireless Propagation Letters, vol.8, pp. 693–696, 2009.

[41] Z. J. Wu, W.L. Biao, S.K. Yak, T.C. Ming, B.C. Chye, Y.K. Seng, and D.M. Anh, "Wireless energy harvesting using serially connected voltage doublers," Proceedings of the 2010 Asia-Pacific Microwave Conference, Yokohama, pp. 41–44, December 7–10, 2010.

[42] J. Ayers, K. Mayaram, and T.S. Fiez, "An ultralow-power receiver for wireless sensor networks," IEEE Journal of Solid-State Circuits, vol. 45, Issue. 9, pp. 1759–1769, August 23, 2010.

[43] P. Khoury, "A power-efficient radio frequency energy-harvesting circuit", Master thesis, Electrical Engineering Department, University of Ottawa, Ontario, Canada, January 2013.

[44] J.M. Ick and Y.B. Jung, "Novel energy harvesting antenna design using a parasitic radiator", Progress In Electromagnetics Research, vol. 142, pp. 545–557, 2013.

[45] N. Md. Din, C.K. Chakrabarty, A. Bin Ismail, K.K.A. Devi, and W.Y. Chen, "Design of RF energy harvesting system for energizing low power devices," Progress in Electromagnetics Research, vol. 132, pp. 49–69, 2012.

[46] A. Rahman, A. Alomainy, and Y. Hao, "Compact body-worn coplanar waveguide fed antenna for UWB body-centric wireless communications", European Conference on Antennas and Propagation, November 2007.

[47] Z.W. Sim, R. Shuttleworth, M.J. Alexander, and B.D. Grieve, "Compact patch antenna design for outdoor RF energy harvesting in wireless sensor networks," Progress In Electromagnetics Research, vol. 105, pp. 273–294, 2010.

[48] R.C. Hansen and R.E. Collin, Small Antenna Handbook, John Wiley and Sons Inc., IEEE Press, 2011.

[49] T. Szepesi and K. Shum (Analog Devices), "Cell phone power management requires small regulators with fast response," EE Times News and Analysis, February 2002. [Online] available at http://www.eetimes.com/electronics-news/4164128/Cell-phone-power-management-requires-small-regulators-with-fast-response [Retrieved April 2012].

[50] Rogers Corporation, "RT/duroid® 6006/6010LM High Frequency Laminates Data Sheet Rev 1.60000," Advanced Circuit Materials Division, Chandler, AZ. Publication: #92-105. Revised 03/2011. [Online], available at http://www.rogerscorp.com/documents/612/acm/RT-duroid-6006-6010-laminate-data-sheet, Retrieved June 2012.

[51] M. Arrawatia, M.S. Baghini, and G. Kumar, "RF energy harvesting system from cell towers in 900MHz band," Communications (NCC), 2011 National Conference, pp.1–5, January 28–30, 2011.

[52] J.P. Thomas, M.A. Qidwai, and J.C. Kellogg, "Energy scavenging for small-scale unmanned systems," Journal of Power Sources, vol. 159, pp. 1494–1509, 2006.

[53] W.C. Brown, "Status of the microwave power transmission components for the solar power satellite," IEEE Transactions on Microwave Theory and Techniques, vol. MTT-29, no. 12, pp.1319 –1327, 1981.

[54] M.A. Malek, S. Hakimi, S.K.A. Rahim, and A.K. Evizal, "Dual-band CPW fed transparent antenna for active RFID tags," IEEE Antennas and Wireless Propagation Letters, 2015.

[55] J.S. Hyok, Y.H. Tsung, D.F. Sievenpiper, P.H. Hui, J. Schaffner, and E. Yasan, "A method for improving the efficiency of transparent film antennas," IEEE Antennas and Wireless Propagation Letters, vol. 7, pp. 753–756, 2008.

[56] T. Paing, J. Shin, R. Zane, and Z. Popovic, "Resistor emulation approach to low-power RF energy harvesting," IEEE Transactions on Power Electronics, vol. 23. Issue 3, pp. 1494–1501, May 2008.

[57] D. Masotti, A.Constanzo, and S. Adam, "Design and realization of a wearable multi-frequency RF energy harvesting system," 5th European Conference on Antennas and Propagation (EUCAP) Proceedings, Rome, pp. 517–520, April 11–15, 2011.

[58] A.S. Weddell, G.V. Merrett, T.J. Kazmierski, and B.M. El-Hashimi, "Accurate supercapacitor modeling for energy harvesting Wireless Nodes," IEEE Transactions on Circuits and Systems-II: Express Briefs, vol. 58, no.12, pp. 911–915, December 2012.

[59] F. Raval and J. Makwana, "Optimization of resonance frequency of circular patch antennas at 5 GHz using practical swarm optimization", International Journal of Advances in Engineering and Technology, May 2011.

[60] A. Yu and X. Zhang, "A broadband patch antenna array for wireless LANs," IEEE Antennas and Propagation Society International Symposium, pp. 228–231, vol. 26–21, June 2002.

[61] M. Ali, G. Yang, and R. Dougal, "A new circularly polarized rectenna for wireless power transmission and data communication," IEEE Antennas and Wireless Propagation Letters, vol. 4, pp. 205–208, January 2005.

[62] K. Chung, Y. Nam, T. Yun, and J. Choi, "Reconfigurable microstrip patch antenna with switchable polarization," ETRI Journal, vol. 28, pp. 379–382, March 2006.

[63] H. Liu, S. Lin, and C. Yang, "Compact inverted-F antenna with meander shorting strip for laptop computer WLAN applications" IEEE Antenna and Wireless Propagation Letters, vol. 10, pp. 540–543, 2011.

[64] Z.W. Sim, R. Shuttleworth, and B. Grieve, "Investigation of PCB microstrip patch receiving antenna for outdoor rf energy harvesting in wireless sensor networks", 2009 IEEE Conference on Antennas and Propagation Proceedings, Loughborough, pp. 129–132, November 16-17, 2009.

[65] P. Borja and N. Romeu, "An iterative model for fractal antennas: application to the sierpinski gasket antenna," IEEE Transactions on Antennas and Propagation, vol. 48, no. 5, pp. 713–719, May 2000.

[66] S.B. Neetu and R.K. Bansal, "Design and Analysis of Fractal Antennas based on koch and sierpinski fractal geometries," International Journal of Advanced Research in Electrical, Electronics and Instrumentation Engineering, vol. 2, June 2013.

[67] T.Q.V. Hoang, A. Douyere, JL. Dubard, and JD. Lan Sun Lunk, "TLM design of a compact PIFA rectenna," 2011 International Conference on Electromagnetics in Advanced Applications (ICEAA), pp. 508–511, September 12–16, 2011.

[68] Y. Fujino, M. Fujita, N. Kaya, S. Kunimi, M. Ishii, N. Ogihata, N. Kusaka, and S. Ida, "A dual polarization microwave power transmission system for microwave propelled airship experiment," Proc. de ISAP'96, vol. 2, pp. 393–396, 1996.

[69] B. Strassner and K. Chang, "5.8-GHz circularly polarized rectifying antenna for wireless microwave power transmission," IEEE Transactions on Microwave Theory and Techniques, vol. 50, pp. 1870–1876, August 2002.

[70] C.K. Chin, Q. Xue, and C.H. Chan, "Design of a 5.8-GHz rectenna incorporating a new patch antenna," IEEE Antenna and Wireless Propagation Letters, vol. 4, pp. 175–178, 2005.

[71] G. Kumar and K.P. Ray, "Broadband microstrip antennas," Artech House, Inc., 2003.

[72] Jawad K. Ali, "A New Reduced Size Multiband Patch Antenna Structure Based on Minkowski prefractal Geometry," Journal of Engineering and Applied Sciences, vol. 2, no. 7, pp. 1120–1124, 2007.

[73] T.A. Milligan, "Modern antenna design," 2nd Edition, IEEE Press, 2005.

[74] S. Shrestha, S.K. Noh, and D.Y. Choi, "Comparative study of antenna designs for RF energy harvesting," 10 pp., 2013.

[75] S. Kim, "RF energy harvesting techniques for wirelessly powered devices," in Proceedings of the IEEE MTT-S International Microwave Workshop Series on Intelligent Radio for Future Personal Terminals (IMWS-IRFPT '11), Daejeon, Republic of Korea, 2011.

[76] R. Selvakumaran, W. Liu, B.H. Soong, L. Ming, and Y.L. Sum, "Design of low power rectenna for wireless power transfer," Tencon IEEE Region 10 Conference, Singapore, pp. 1–5, January 2009.

[77] A.M. Soliman, D.M. Elsheakh, E.A. Abdallah, and H.M. El-Hennawy, "Inspired metamaterial quad-band printed inverted-F (IFA) antenna for USB applications," The Applied Computational Electromagnetics Society (ACES) Journal, pp. 564–570, May, 2015.

[78] A.M. Soliman, D.N. Elsheakh, and E.A. Abdallah, "Low SAR multiband CPW fed PIFA with independent resonant frequency control for wireless communication applications," IET Microwaves, Antennas and Propagation, vol. 8, pp. 207–216, 2014.

[79] D. Elsheakh and A.M.E. Safwat, "Slow-wave quad-band printed inverted-F antenna (IFA)," IEEE Transactions on Antennas and Propagation, vol. 62, no. 8, pp. 4396–4401, 2014.

[80] A.M. Soliman, D.N. Elsheakh, E.A. Abdallah, and H. Elhenawy, "Reconfigurable independent multiband CPW-fed printed F-antenna for USB applications," Microwave and Optical Technology Letters, vol. 56, no.10, pp. 2237–2245, 2014.

[81] B.A. Munk, Frequency Selective Surfaces: Theory and Design, Wiley, New York, NY, 2000.

[82] A.M. Soliman, D. N. Elsheakh and Esmat A. Abdallah, Hadia Elhenawy, "Multi-Band Printed Metamaterial Inverted-F Antenna (IFA) for USB Applications", IEEE Antennas and Wireless Propagation Letters, vol. 15, pp. 297–300, 2015.

[83] D. Elsheakh, A. M. Soliman, and E. Abdallah, "Design of Planar Inverted F-Antenna over Uniplanar EBG Structure for Laptop MIMO Applications" IEEE international symposium on antenna and propagation AP-S, Memphis, Tennessee, 2014, USA.

[84] D. Elsheakh, A. M. Soliman, H. M. Elhennawy and E. Abdallah, "Compact Independent Tri-band Printed IFA loaded with Inspired Metamaterial for wireless Communication Applications", The 7th European Conference on Antennas and Propagation (EuCAP) 8-12 April in Gutenberg, Sweden, 2013.

[85] A.M. Soliman, D.N. Elsheakh, E.A. Abdallah, and H. Elhenawy, "Design of planarinverted F-antenna over uniplanar EBG structure for laptop MIMO applications," Microwave and Optical Technology Letter, vol. 57, pp. 277–285, February 2015.

[86] H. Laborat, "Microwave Power Transmission System Studies", vol. IV , Raytheon Company, Equipment Division, -7 - SUDBURY, MASS. 01776.

[87] Z. Zhang, A.W. Bargioni, S.W. Wu, S. Dhuey, S. Cabrini, and P. J. Schuck, "Manipulating nanoscale light fields with the asymmetric bowtie nano-colorsorter," vol. 12, pp. 4505–4509, 2009.

[88] R. Vogelgesang and A. Dmitriev, "Real-space imaging of nano-plasmonic resonances," Analyst 135, pp. 1175, 2010.

[89] T. Xu, Y.K. Wu, X. Luo, and L.J. Guo, "Plasmonic nano-resonators for higher solution colour filtering and spectral imaging," Nature Communications 1, vol. 59, 2010.

[90] J.J. Greffet, M. Laroche, and F. Marquier, "Impedance of a nano-antenna and a single quantum emitter," Physical Review Letters, vol. 105, 2010.

[91] W. C. Brown, "Status of the microwave power transmission components for the solar power satellite," IEEE Trans. Microw. Theory Tech., vol. 29, pp. 1319–1327, Dec. 1981.

[92] Y. K. Tan and S. K. Panda, "Energy harvesting from hybrid indoor ambient light and thermal energy sources for enhanced performance of wireless sensor nodes," IEEE Trans. Ind. Electron., vol. 58, no. 9, pp. 4424–4435, Sep. 2011.

[93] J. Colomer et al., "Novel autonomous low power VLSI system powered by ambient mechanical vibrations and solar cells for portable applications in a 0.13_ technology," in Proc. IEEE Power Electron. Specialists Conf., Jun. 17–21, 2007, pp. 2786–2791.

[94] K. Ko, A. Kumar, K.H. Fung, R. Ambekar, G.L. Liu, N.X. Fang, and K.C. Toussaint, Jr., "Nonlinear optical response from arrays of Au bowtie nanoantennas," Nano Letters, vol. 61, 2011.

[95] H. Matsumoto, "Research on solar power satellites and microwave power transmission in Japan," IEEE Microw. Mag., vol. 3, no. 4, pp. 36–45, Dec. 2002.

[96] A. Georgiadis and A. Collado, "Solar powered class-e active antenna oscillator for wireless power transmission," in Proc. IEEE Radio Wireless Symp., Jan. 20–23, 2013, pp. 40–42.

[97] C. Guclu, T.S. Luk, G.T.Wang, F. Capolino, "Radiative emission enhancement using nano-antennas made of hyperbolic metamaterial resonators," *Appl. Phys. Lett.* 2014, 105, 123101, doi:10.1063/1.4895816.

Chapter 9

Compact Planar Antennas for Beam Steering and RFID Tags

Mohammad Alibakhshi-Kenari,
Mohammad Naser-Moghadasi,
Ramazan Ali Sadeghzadeh, Bal Singh Virdee and
Ernesto Limiti

Additional information is available at the end of the chapter

http://dx.doi.org/10.5772/65918

Abstract

The chapter presents innovative planar antennas for beam steering and radio frequency identification (RFID) applications. Beam steering has become vital in commercial wireless communications, including mobile satellite communications where high data rate communication is required. The chapter describes a low-cost beam-steering antenna based on a leaky-wave antenna structure that is capable of steering the main radiation beam of the antenna over a large range from −30° to +15°. Interest in RFID systems operating in the ultrahigh frequency (UHF) is rapidly growing as it offers benefits of long read range and low cost, which make it an excellent system for use in distribution and logistics systems. This chapter presents a technique of overcoming the limitations of conventional HF coils in RFID tags where the total length of the spiral antenna is restricted inside the available area of the tag.

Keywords: leaky-wave antenna (LWA), broadside radiation, beam steering, RFID tag, Hilbert curve, HF/UHF dual-band antenna

1. Introduction

Sophisticated modern wireless systems have begun employing beam-scanning antennas to improve their coverage and hence increase system capacity. Antennas whose radiation beam can be steered by electronic means are therefore becoming highly desirable. Beam steering can be realized in antenna arrays by modifying the phase of the transmitted signal. The phase of the signal can be altered electronically with phase shifters.

Alternatively, this can be achieved using a leaky-wave antenna (LWA) in which the direction of the radiation beam is a function of the operating frequency [1–3]. In part 2, the design and experimental results are presented of a printed LWA. Features of the LWA include a simple structure, small size, low profile, large bandwidth (BW), high gain, and large beam steering from -30° to +15°. In part 3, an innovative dual-band card-type tag is presented that is based on a single-loop radiator. The card-tag design is implemented using Hilbert-curve for radio frequency identification (RFID)-positioning applications. The RFID tag radiator design is realized by combining the Hilbert curve and the square-loop radiator, where the Hilbert curve is designed to operate at HF band, and the square loop at ultrahigh-frequency (UHF) band.

2. Printed leaky-wave antenna design

The LWA, shown in **Figure 1**, can be considered a rectangular patch antenna with a rectangular dielectric slot. The bottom side of the antenna substrate is a ground plane. Within the slot are six radiating arms comprising E-shaped structures which are organized in three columns and two rows. The structure is excited through a subminiature version A (SMA) connector on one side, and the structure is terminated with a 50-Ω load on the opposite side. The bandwidth and radiation characteristics of the antenna can be controlled by simply modifying the number of E-shaped arms, their dimensions, and also the separation between them. The LWA antenna was analyzed by three full-wave EM simulators, that is, Agilent ADS, HFSS™, and CST-MWS. LWA prototype design presented was constructed on Rogers RT/Duroid5880 substrate with a thickness of 1.6 mm, a dielectric constant of 2.2, and tan δ of 9×10^{-4}. The optimized antenna design was fabricated and tested to validate its performance. The length, width, and height of the antenna are 19.2 ($59 \times 10^{-3}\lambda_o$), 15.2 ($47 \times 10^{-3}\lambda_o$), and 1.6 mm ($4 \times 10^{-3}\lambda_o$), respectively, where λ_o is free-space wavelengths at 930 MHz.

Figure 2 shows that the proposed LWA covers an impedance bandwidth (for S_{11} < -10 dB) of 2.81 GHz (0.90–3.71 GHz) with ADS; 2.95 GHz (0.93–3.88 GHz) with CST MWS; and 3.2 GHz (0.77–3.97 GHz) with HFSS™, which correspond to fractional bandwidth of 121.9, 122.6, and 135.0%, respectively. The measured impedance bandwidth is 2.72 GHz (0.93–3.65 GHz), which correspond to fractional bandwidth of 118.7%. There is generally good agreement between the simulated and measured results.

Besides the broadband bandwidth property of the antenna, another feature of this antenna is its ability to provide continuous scanning of its main beam over a large range from -30° to +15° with high gain across its entire operating range as shown in **Figure 3** and **Figure 4**. These results show that the antenna radiates at different angles at 1.2 and 1.88 GHz, and 2.65, and 3.4 GHz. As the frequency is increased, the scanned angle changes almost in a linear fashion, as shown in **Figure 5**. The measured antenna gain and radiation efficiency at various frequencies are given in **Table 1**. The gain and efficiency are larger than 6 dBi and 62% across the antenna's operating band.

http://dx.doi.org/10.5772/65918

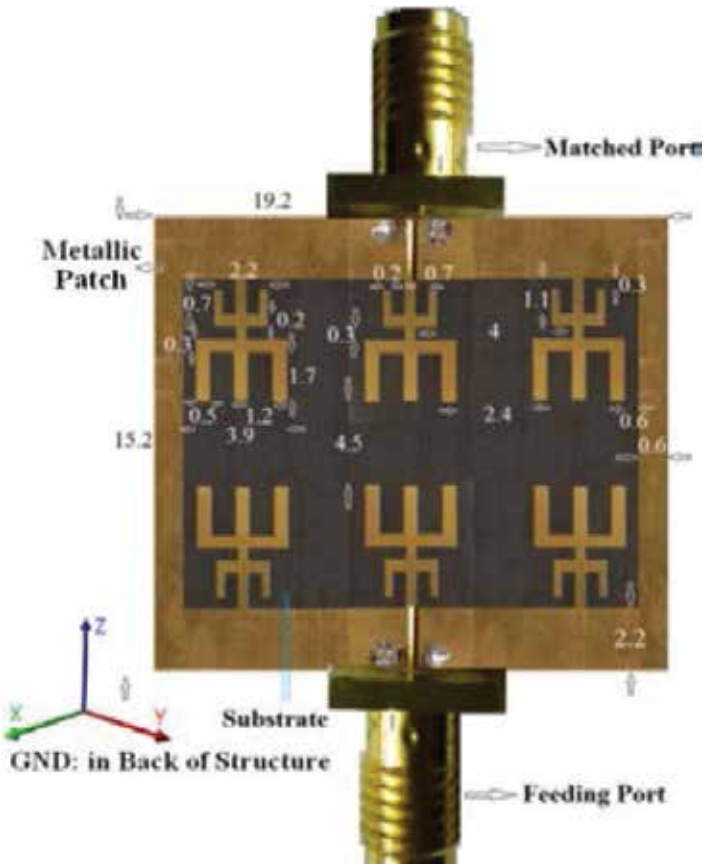

Figure 1. Fabricated prototype of the leaky-wave antenna (units in millimeters).

The maximum gain occurs at 2.65 GHz, that is, broadside radiation (**Figure 5**), and it remains between 8 and 6 dBi across the band, as shown in **Figure 6**. In addition to the scanning angle and gain curves versus frequency, the antenna gain curve as a function of scanning angle is given in **Figure 7**.

To summarize, the novel printed leaky-wave antenna structure presented above is capable of steering the main beam from -30° to +15°. The design of the antenna is based on several E-shaped-radiating arms implementing within the slot. The LWA is highly compact with dimensions of 19.2 × 15.2 × 1.6 mm^3, and has a large fractional bandwidth of 118.7% (0.93–3.65 GHz) with peak radiation gain and efficiency of 8 dBi and 90%, respectively, at 2.65 GHz. The proposed LWA can be flush-mounted on vehicles, laptops, cellular base-stations, and mobile phones. In addition, it can be easily integrated on different substrates for use in other circuits and devices. The broadside-radiating antenna is suitable for wireless communications systems.

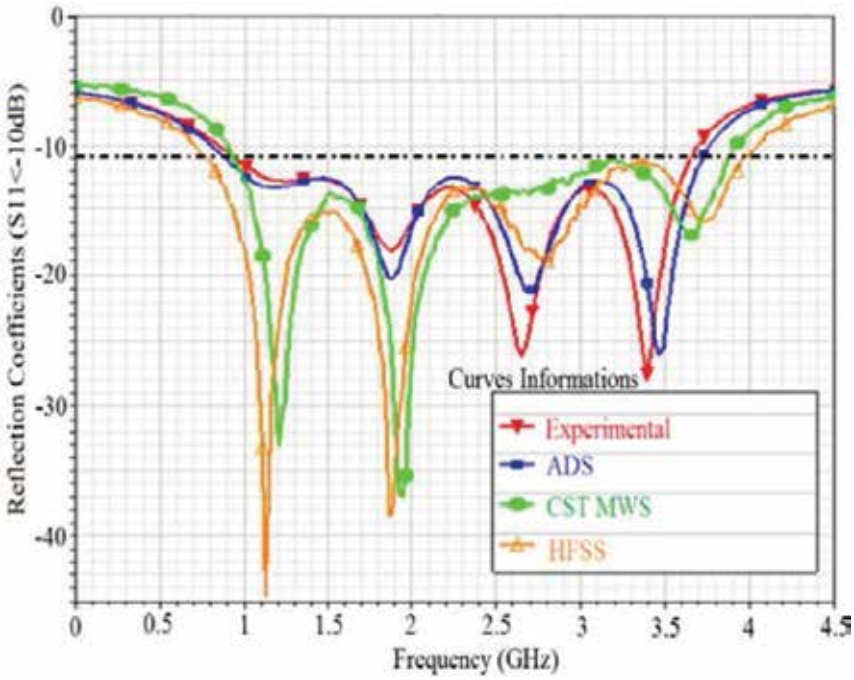

Figure 2. Simulated and measured reflection coefficients of the proposed LWA.

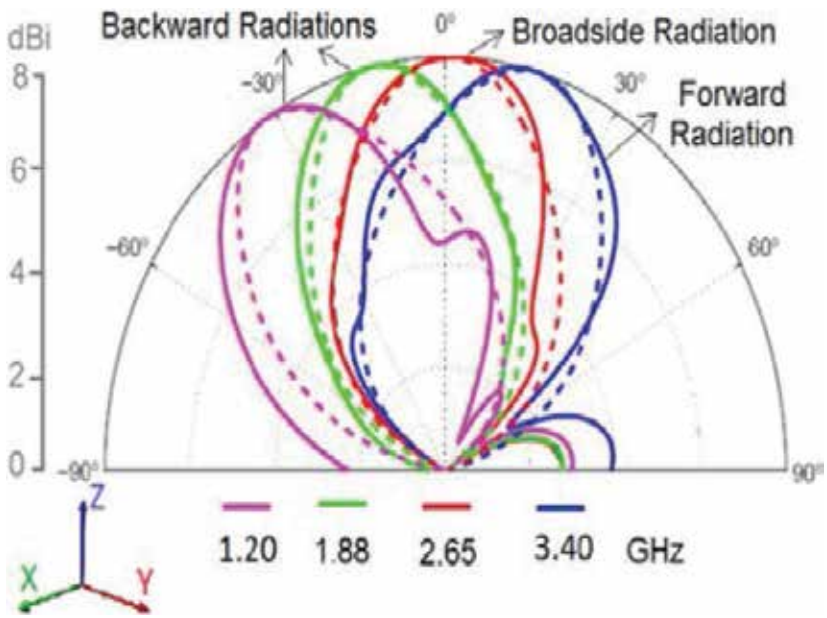

Figure 3. 2-D radiation patterns in dB scale at spot frequencies. Solid lines: measured results and dashed lines: simulated results.

http://dx.doi.org/10.5772/65918

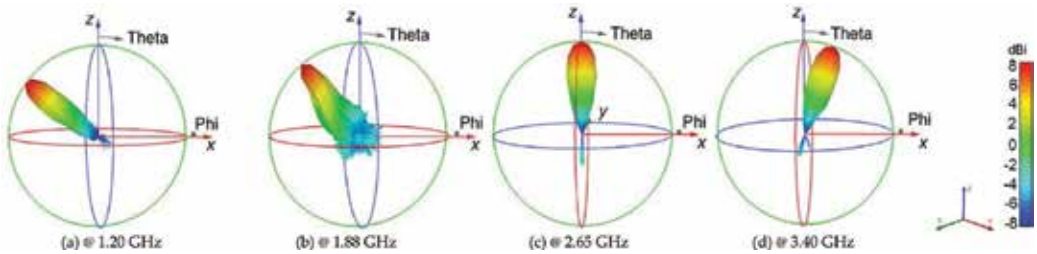

Figure 4. 3-D radiation patterns (decibel scale) at (a) 1.2 GHz, (b) 1.88 GHz, (c) 2.65, and (d) 3.40 GHz.

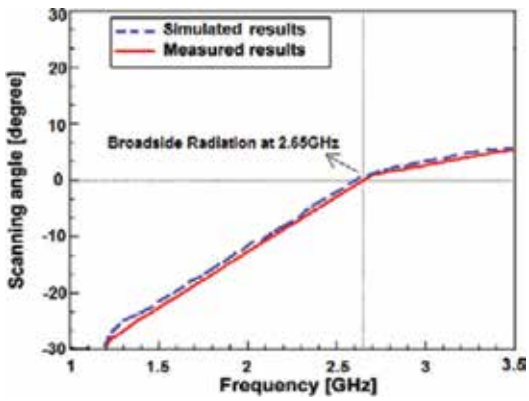

Figure 5. Scanning angle versus frequency. Broadside direction is 0°.

Frequency (GHz)	0.93	1.20	1.88	2.65	3.40	3.65
Gain (dBi)	6	7	7.7	8	7.8	7.2
Efficiency (%)	62	74	81	90	85	79

Table 1. Measured antenna radiation characteristics.

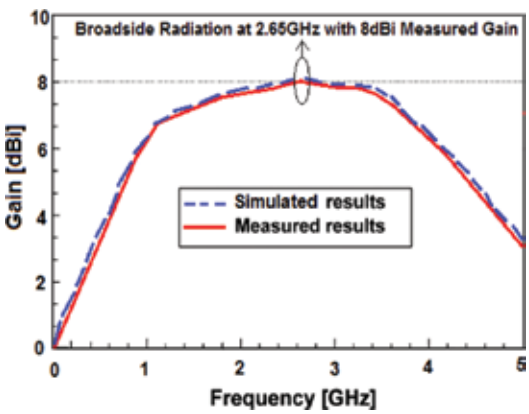

Figure 6. Gain as a function of frequency.

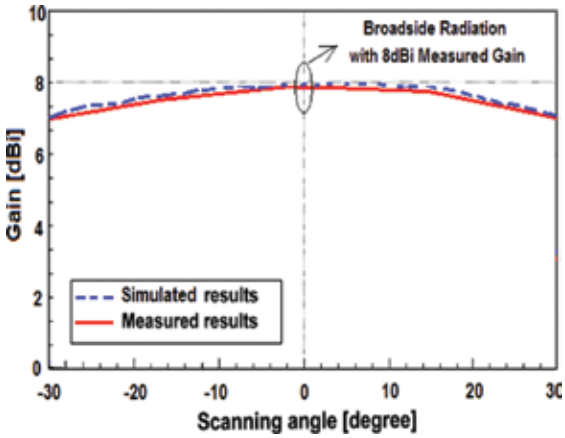

Figure 7. Gain curves versus scanning angle.

3. Dual-band RFID tag antenna

Based on the card-type dual-band tags [4–27], and the series Hilbert-curve tag, an alternative card-type dual-band RFID tag is proposed in this chapter. The proposed tag merges with the series Hilbert curve for HF coil antenna and square-loop patch for UHF antenna to form a single radiator that is compact and exhibits dual-band performance. The antenna's axial-ratio (AR) spectrum is shown to confirm its circular polarization characteristics.

The loop-tag antenna structure is based on the third-order Hilbert-fractal curve, and the antenna is impedance matched with a stub network, as shown in **Figure 8**. **Table 2** lists the parameters describing the antenna structure shown in **Figure 9**. The antenna was fabricated

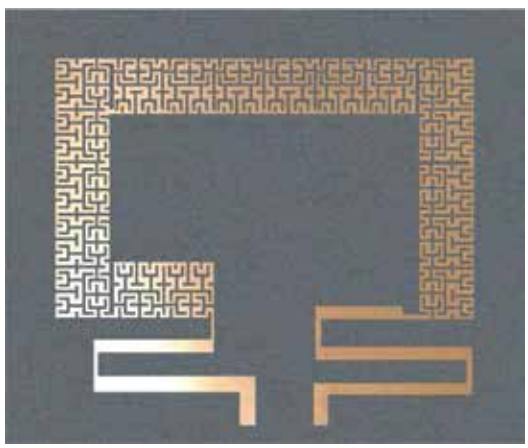

Figure 8. Fabricated Hilbert-curve loop RFID tag.

L_1	L_2	L_3	L_4	L_5	L_6	W_1	W_2	W_3	W_4	W_5	W_6	W_7	W_8	W_9	W_{10}
8	27.4	4	1.8	4.2	1.2	2.5	0.9	18.6	0.65	16.5	0.65	56	18	24	24.1

Table 2. Dimensions of Hilbert-curve loop RFID tag (units in millimeters).

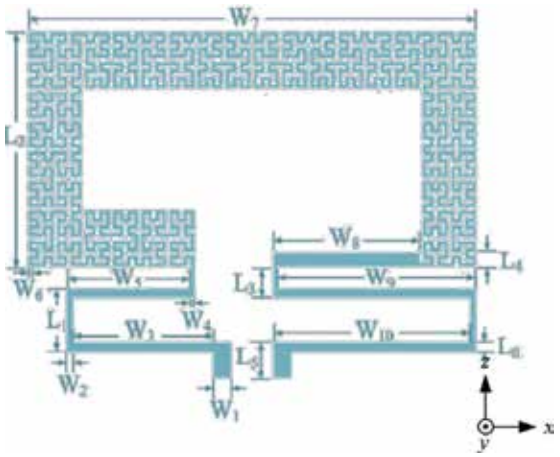

Figure 9. Parameters defining the RFID tag.

on Rogers/RT Duroid5880 dielectric substrate with a thickness (h) of 0.8 mm and a dielectric constant (ε_r) of 2.2.

The RFID tag, which is shown in **Figure 8**, operates over dual-band, in particular, the HF and UHF bands. Conventional RFID tags essentially comprise two distinct antennas [4–27], whereas the proposed dual-band structure employs one radiator that functions in the high frequency and ultrahigh-frequency bands.

3.1. High-frequency antenna

The series Hilbert-curve structure is used here as a HF coil antenna to implement the 25-MHz band RFID tag. When the plane of the coil is oriented perpendicular to the received magnetic field, it induces a voltage in the winding of the Hilbert-fractal curve. By increasing the area of the Hilbert curve, it will capture greater magnetic flux from the received signal; as a consequence greater voltage is induced in the coil. Hence, the space-filling fractal curve is recommended to occupy the RFID tag area as much as possible.

The total inductance and the resistive loss in the HF coil antenna determine its quality factor (Q_{HF}), which indicates energy loss relative to the amount of energy stored in the coil. The magnitude of Q_{HF} increases with a decrease in loss. The quality factor of the antenna can be easily measured as it is related to the antenna's center frequency (f_0) and 3-dB bandwidth (BW) by the relationship $Q_{HF} = f_0/\text{BW}$. Also, the resonant frequency of the HF coil is a function of the coil's inductance and the capacitance, and is represented by the relationship $f_0 = 1/2\sqrt{\text{LC}}$.

3.2. Ultra high-frequency antenna

The length of the loop resonator is the fundamental design parameter of the proposed Hilbert-curve UHF antenna as it determines the self-resonant frequency of the antenna. In the design, the length of the loop resonator is folded within a defined area. By stimulating the loop with an electric field, a standing wave is excited in the loop. The resulting electric current flowing through the conductive loop causes the tag to radiate. The current distributions over the tag reveal the characteristics of the HF/UHF dual-band antenna. To optimize power transfer to or from the tag, it is necessary to properly match it to the microchip. This can be accomplished by using a microstrip network instead of using discrete lumped inductances and capacitances because at UHF the lumped components perform poorly due to generation of parasitic reactance.

3.3. Simulation and measured results

The simulated and measured return-loss responses of the proposed RFID tag are shown in **Figure 10**. Commercial software (HFSS) by Ansys was used to simulate the return loss of the antenna [28]. It is evident that there is excellent agreement between the simulation and measurement results. Measurements confirm that the RFID tag can operate over the frequency ranges of 12.5–37.5 MHz and 0.4–1.4 GHz for return-loss performance better than -10 dB. The four resonant modes have a center frequency of f_c = 25 MHz, f_c= 785 MHz (760–815 MHz), 835 GHz (822–905 MHz), and 925 MHz (918–1000 MHz). These results show that the proposed RFID tag is suitable for dual-band applications in the HF and UHF bands. In addition, the band centered at 25 MHz shown in **Figure 10** is applicable for near-field communication (NFC).

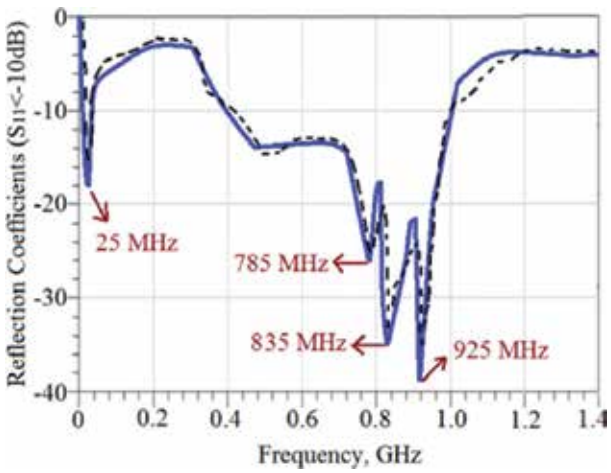

Figure 10. Simulated (solid-line) and measured (dashed-line) reflection-coefficient response.

The results of the impedance analysis, shown in **Figure 11**, reveal that the real-part of the impedance has a maximum magnitude of 49, 50, and 48Ω at 785, 835,and 925 MHz, respectively. The imaginary part of the impedance presents an inductive of magnitude 9, 8, and 11Ω

http://dx.doi.org/10.5772/65918

at 785, 835, and 925 MHz, respectively. Inductive impedance was used to impedance match the capacitive RFID microchip. At 25 MHz, the real part of the impedance is 2Ω, and the imaginary part is 40Ω, as shown in **Figure 11**. For the tag antenna impedance $Z_{A(HF)}$ = RA + jXA, the qualityfactor (Q_A) is expressed by

$$Q_A = X_A / R_A \tag{1}$$

The quality factor (Q_A) indicates that when the antenna is close to its resonance frequency, its impedance is almost real.

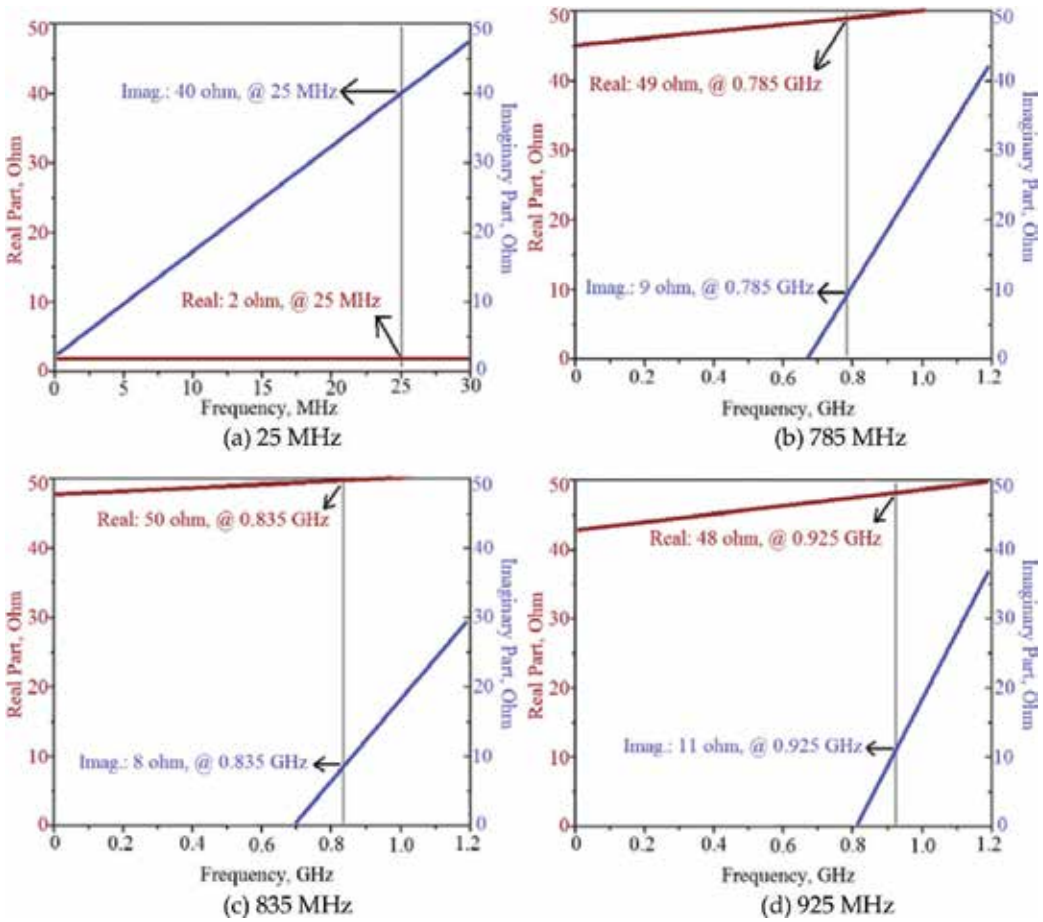

Figure 11. Measured results of impedance spectrum at (a) 25, (b) 785, (c) 835, and (d) 925 MHz.

The antenna is matched to the RFID microchip with an *LC* circuit to achieve a Q_A of 25.1 at 25 MHz. The quality factors (Q_A) from **Figure 11** are as follows: 0.15, 0.17, and 0.165 at 785, 835, and 925 MHz, respectively. Distribution of the current density over the planar antenna, shown in **Figure 12**, gives insight of how the proposed dual-band antenna affects the current at the various frequencies. In **Figure 12**, the total length of the series Hilbert-curve loop

is 1/20 λ_g, and the mean circumstance of the loop in **Figure 12** is λ_g. The antenna belongs to the small antenna category as the total length of series Hilbert curve is less than 1/10 λ_g.

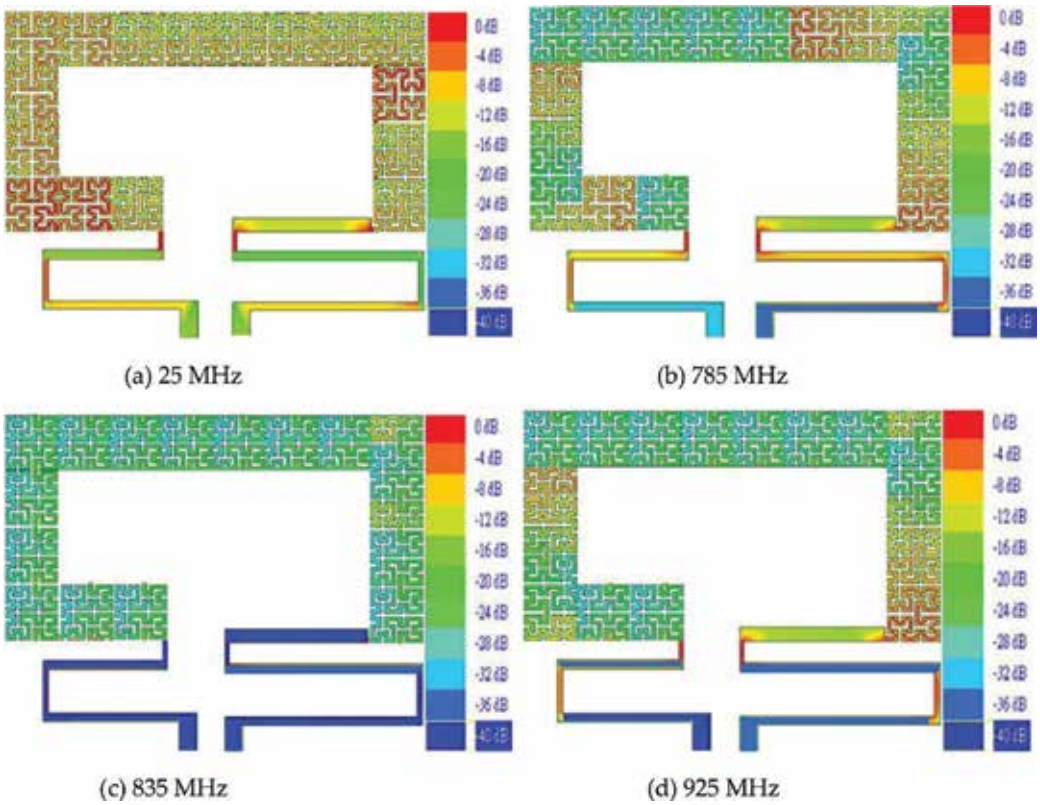

Figure 12. Current distributions at (a) 25, (b) 785, (c) 835, and (d) 925 MHz.

When the antenna was tested, it was aligned in the *zx*-plane as defined in **Figure 9** with the feed-line along the *x*-axis. Automatic measurement system in an anechoic chamber was used to measure the radiation pattern of the antenna. Radiation patterns of the RFID tag antenna were measured in the *xz*- and *yz*-planes. The radiation patterns at 25, 785, 835, and 925 MHz in the HF/UHF bands are depicted in **Figure 13**.

Simulated and measured radiation patterns of the RFID tag antenna in the *xz*- and *yz*-planes at 25, 785, 835, and 925 MHz over the HF/UHF bands are shown in **Figure 13**. Good agreement is obtained between the simulation and measured results. Measurements show that the radiation in the *xz*-plane is quasi omnidirectional at 25, 785, and 835 MHz; however, the radiation is bidirectional at 925 GHz. In the *yz*-plane, the radiation is omnidirectional at 25, 785, and 925 MHz, and is clearly bidirectional at 835 MHz. **Figure 14** shows that the directivity of the RFID tag antenna is 1.75 dBi at 25 MHz in the HF band, and 2.65, 2.82, and 2.75 dBi at 785, 835, and 925 MHz, respectively, in the UHF band.

http://dx.doi.org/10.5772/65918

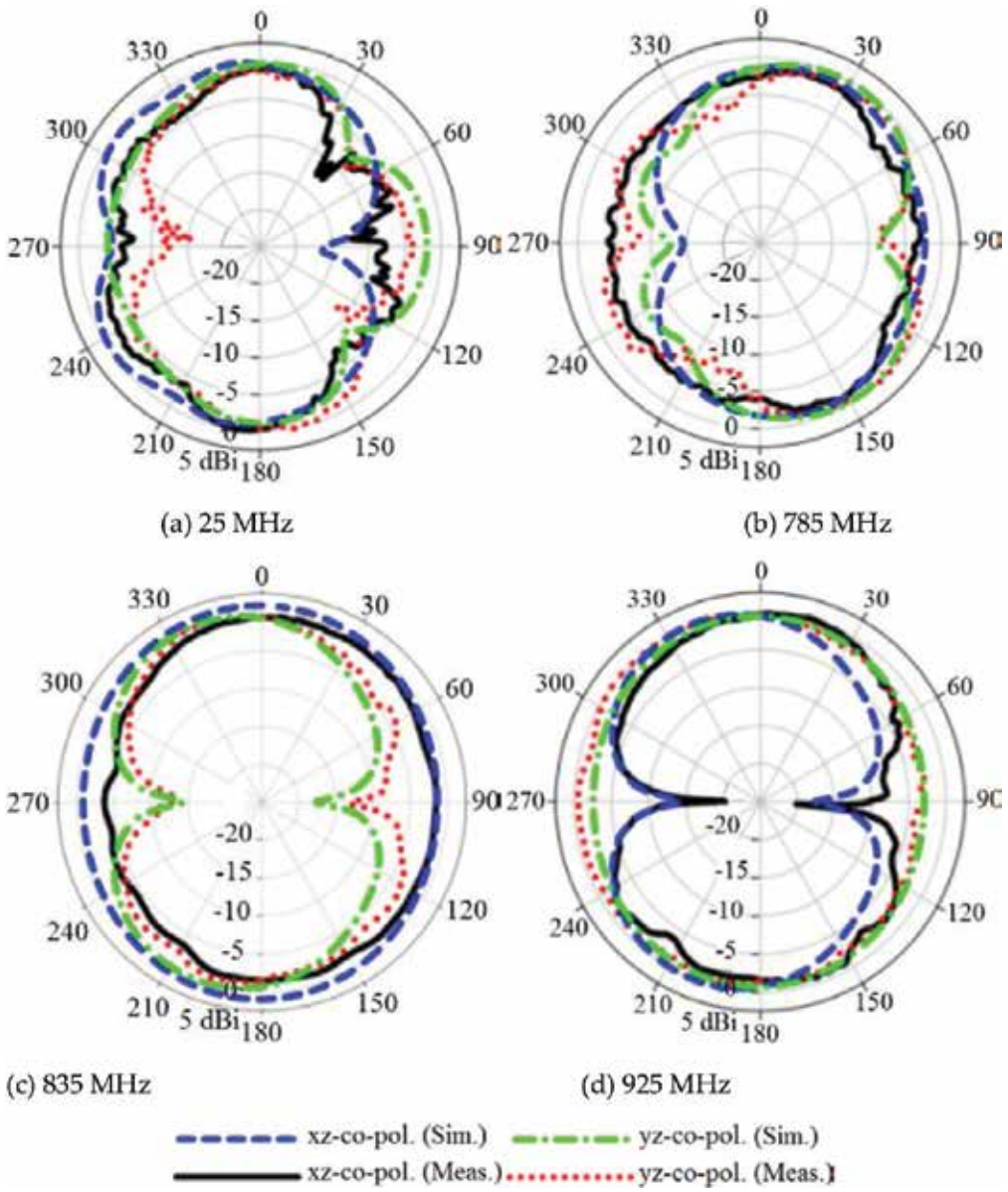

Figure 13. Radiation patterns of the RFID tag at: (a) 25, (b) 785, (c) 835, and (d) 925 MHz.

Circular polarization wave is generated by exciting two orthogonal modes in the RFID tag. This is achieved with the orthogonal arrangement of the Hilbert-curve tag. The axial-ratio spectrum of the polarization related to various angles (ϕ and θ) is presented in **Figure 15**. The minimum axial ratio is observed at 785, 835, and 925 MHz at $\phi = 0^{\circ}$, $\theta = 95^{\circ}$ with corresponding -3-dB AR

bandwidth of 480 (560–1040 MHz), 605 (515–1120 MHz), and 455 MHz (620–1075 MHz). The minimum AR is observed at 25 MHz at $\phi = 0^{\circ}$, $\theta = 92^{\circ}$ with corresponding -3-dB AR bandwidth of 14 MHz (18–32 MHz). Thus, the proposed antenna can be applied to diversity operation.

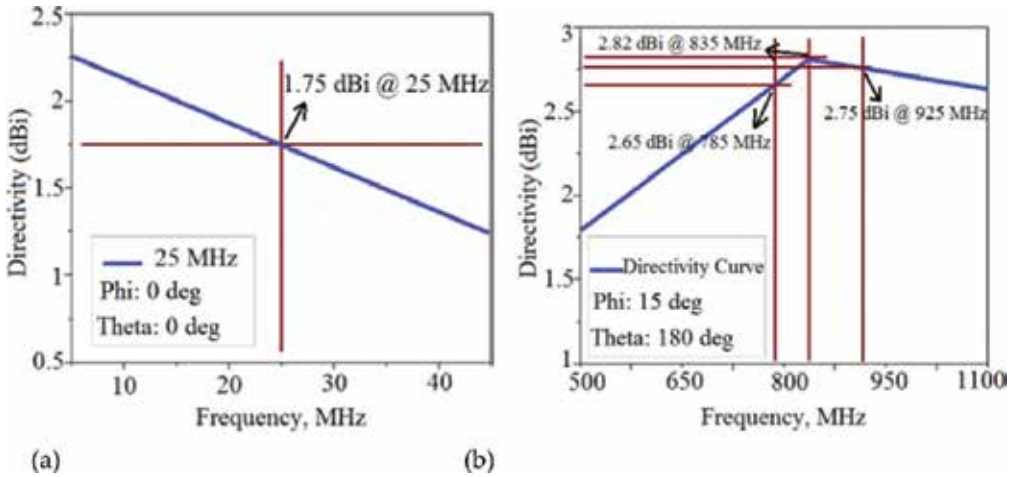

Figure 14. Directivity at (a) 25 MHz in the HF band, and (b) 785, 835, and 925 MHz in the UHF bands.

3.4. UHF-matching circuit

The maximum activation distance of the tag for the given frequency is given by [29, 30]

$$d_{\max} = \frac{c}{4\pi f}\sqrt{\frac{\mathrm{EIRP}_r}{P_{\mathrm{chip}}}\tau G} \tag{2}$$

where EIRP_r is the effective transmitted power of the reader, P_{chip} is the sensitivity of the tag microchip, $G$is the maximum tag antenna gain, and the power transmission factor τ is given by

$$\tau = \frac{4R_{\mathrm{tag}}R_A}{\left|X_{\mathrm{chip}} + X_A\right|^2} \le 1 \tag{3}$$

where the tag antenna impedance is $Z_{\mathrm{A(UHF)}} = R_{\mathrm{A}} + j\ X_{\mathrm{A}}$ and microchip impedance $Z_{\mathrm{chip}} = R_{\mathrm{chip}} + j\,X_{\mathrm{chip}}$.

The microchip NSC MM9647 can be applied to the tag in UHF band. Its impedance is $Z_{\mathrm{chip}} = 80 - j\ 120\ \Omega$ [31]. The effective isotropic radiated power ($EIRP_r$) of the reader is 1.2 W, the sensitivity P_{chip} of tag microchip is -10 dBm, the maximum tag antenna gain G = 3.35 dBi, and the activation distance $d$with is $d_{\max}$ = 5 m. Therefore, from Eq. (2), the power transmission factor τ is 0.95. The tag antenna impedance from **Figure 11** is $Z_{A(\mathrm{UHF})} = 49 + j9\ \Omega$ at 785 MHz, $Z_{\mathrm{A(UHF)}} = 50 + j\ 8\Omega$ at 835 MHz, and $Z_{\mathrm{A(UHF)}} = 48 + j\ 11\Omega$ at 925 MHz; hence from Eq. (3), the RFID's microchip impedance of $Z_{\mathrm{chip}} = 80 - j\Omega$ enables conjugate matching to be obtained.

http://dx.doi.org/10.5772/65918

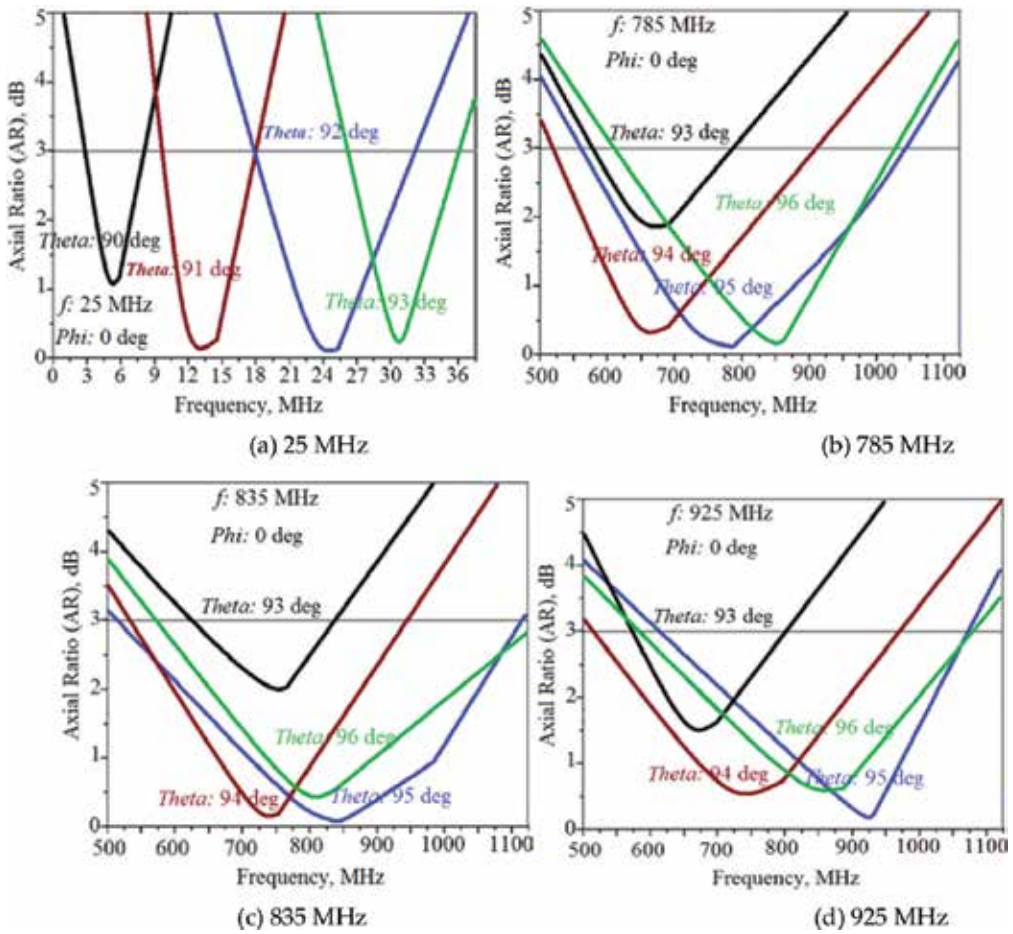

Figure 15. Axial-ratio spectrum centered at: (a) 25, (b) 785, (c) 835, and (d) 925 MHz.

3.5. HF-matching circuit

Another example of designing a matching network is presented using Tag-it$_{TM}$ HF-I standard transponder microchip which has capacitance C_{chip} = 2.85 pF at 25 MHz [32]. The tag antenna's impedance from **Figure 11 (a)** is$Z_{A(HF)} = 2 + j\,40\Omega$, where L_A = 0.45 μH and R_A = 2 Ω. The impedance-matching *LC* circuit is shown in **Figure 16**. The desired shunt capacitor C_{shunt} = 0.42 nF is obtained from Eq. (4) and Eq. (5). From Eq. (6), the total circuit factor Q_T is 25.1

$$L_A = \frac{jX_A}{j\omega} \tag{4}$$

$$C_{shunt} = \frac{1}{L_A\omega^2} \tag{5}$$

$$Q_T = \frac{1}{R_A}\sqrt{\frac{L_A}{C_{shunt}+C_{chip}}} \tag{6}$$

The response of impedance-matching *LC* circuit, shown in **Figure 17**, is designed at 25 MHz with 3-dB bandwidth of 35 MHz. This impedance-matching *LC* circuit can be used with the RFID tag.

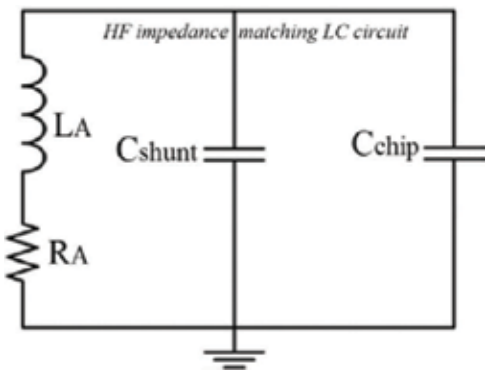

Figure 16. HF impedance-matching *LC* circuit.

To summarize in Section 3, the design of a novel single-radiator card-type tag antenna was presented. The tag antenna was implemented using series Hilbert-curve loop and matched stub. The design merges together the series Hilbert-curve HF coil with a square-loop UHF antenna to realize a singular radiator for an RFID tag that satisfies the commercial requirements of compact design and dual-band functionality. The tag exhibits good broadband and circular polarization response, and has a small physical footprint which can be easily manufactured. The antenna operates over the UHF band (400 MHz to 1 GHz) with a return loss better than -10 dB. The matching network was designed and integrated with the RFID chip with knowledge of the inductive impedance of the tag at various frequencies. The RFID tag predominately radiates quasi omnidirectionally in both the orthogonal *xy*- and *yz*-planes. The properties of the antenna make it suitable for various applications at HF and UHF bands.

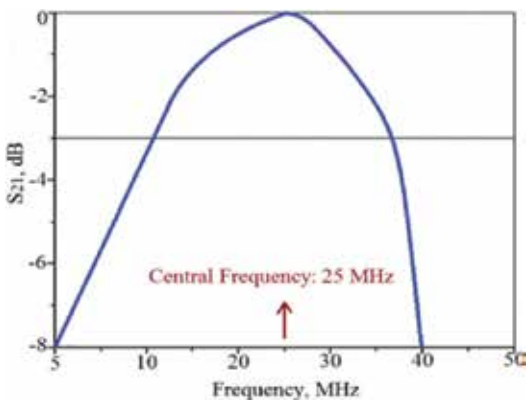

Figure 17. Impedance-matching *LC* circuit response.

Acknowledgements

The authors would like to give special thanks to faculty of Microelectronics for financial support.

Author details

Mohammad Alibakhshi-Kenari[1,*], Mohammad Naser Moghadasi[2], Ramazan Ali Sadeghzadeh[3], Bal Singh Virdee[4] and Ernesto Limiti[1]

*Address all correspondence to: naeem.alibakhshi@yahoo.com

1 Department of Electronic Engineering, University of Rome Tor Vergata, Rome, Italy

2 Faculty of Engineering, Science and Research Branch, Islamic Azad University, Tehran, Iran

3 Faculty of Electrical Engineering, K. N. Toosi University of Technology, Tehran, Iran

4 London Metropolitan University, Center for Communications Technology, London, UK

References

[1] S. Lim, C. Caloz, T. Itoh, "Metamaterial-Based Electronically Controlled Transmission-Line Structure as a Novel Leaky-Wave Antenna with Tunable Radiation Angle and Beamwidth," *IEEE Transactions on Microwave Theory and Techniques*, 2005; 53(1): 161–173. DOI: 10.1109/TMTT.2004.839927

[2] C. Caloz, T. Itoh, "Array Factor Approach of Leaky-Wave Antennas and Application to 1-D/2-D Composite Right/Left-Handed (CRLH) Structures," *IEEE Microwave and Wireless Components Letters,* 2004; 14(6): 274–276. DOI: 10.1109/LMWC.2004.828009

[3] A. Neto, S. Bruni, G. Gerini, M. Sabbadini, "The Leaky Lens: A Broad-Band Fixed-Beam Leaky-Wave Antenna," *IEEE Transactions on Antennas Propagation*, 2005; 53(10): 3240–3246. DOI: 10.1109/TAP.2005.856351

[4] A. Toccafondi, C.D. Giovampaola, F. Mariottini, A. Cucini, "UHF-HF RFID Integrated Tag for Moving Vehicle Identification," *IEEE Antennas Propagation International Symposium Digest*, 2009: 1–4. DOI: 10.1109/APS.2009.5171707

[5] L.W. Mayer, A.L. Scholtz, "A Dual-Band HF/UHF Antenna for RFID Tags," *Proceedings of IEEE 68th Vehicular Technology Conference,*2008: 1–5.

[6] P. Iliev, P.L. Thuc, C. Luxey, R. Staraj, "Dual-Band HF-UHF RFID Tag Antenna," *Electronics Letters*,2009; 45: 439–441.

[7] R.H. Zeng, Q.X. Chu, "A Compact Slot-Coupled Dual-Band RFID Tag Antenna," *Microwave and Optical Technology Letters*,2009; 51(9): 2046–2048.

[8] Y.C. Lee, J.S. Sun, "A Fractal Dipole Tag Antenna for RFID Dual-Band Application," *Microwave and Optical Technology Letters*,2008; 50(7); 1963–1966.

[9] A. Attaran, R. Rashidzadeh, R. Muscedere, "Chipless RFIDTag Using RF MEMS Switch,"*Electronics Letters*,2014; 50(23): 1720–1722. DOI: 10.1049/EL.2014.3075

[10] Y.B. Ouattara, C. Hamouda, B. Poussot, J.M. Laheurte, "Compact Diversity Antenna for UHF RFIDReaders," *Electronics Letters*, 2012; 48(16): 975–977. DOI: 10.1049/EL.2012.1805

[11] K.S. Leong, M.L. Ng, P.H. Cole, "Miniaturization of Dual Frequency RFID Antenna with High Frequency Ratio," *IEEE Antennas Propagation International Symposium Digest*, 2011: 5475–5478.

[12] J.S. Kuo, J.J. Wang, C.Y. Huang, "Dual-Frequency Antenna for RFID Tags with Complementary Characteristic," *Microwave and Optical Technology Letters*, 2007; 49(6): 1396–1398.

[13] F. Paredes, G.Z. Gonzàlez, J. Bonache, F. Martín, "Dual-Band Impedance-Matching Networks Based on Split-Ring Resonators for Applications in RF Identification (RFID)," *IEEE Transactions on Microwave Theory and Techniques*, 2010; 58(5): 1159–1166.

[14] Y. Nishioka, K. Hitomi, H. Okegawa, T. Mizuno, T. Fukasawa, H. Miyashita, Y. Konishi, "Novel Antenna Configuration for HF and UHF Band Hybrid Card-Type RFID Tags," *Antennas and Propagation (EuCAP)*, 2010: 1–5.

[15] Z.L. Ma, L.J. Jiang, J. Xi, T.T. Ye, "A Single-Layer Compact HF-UHF Dual-Band RFID Tag Antenna," *IEEE Antennas Wireless Propagation Letters*, 2012; 11: 1257–1260.

[16] T. Deleruyelle, P. Pannier, M. Egels, E. Bergeret, "Dual Band Mono-Chip HF-UHF Tag Antenna," *Antennas and Propagation Society International Symposium (APSURSI)*, 2010: 1–4.

[17] Y. Pan, L. Zheng, H.J. Liu, J.Y. Wang, R.L. Li, "Directly-Fed Single-Layer Wideband RFIDReader Antenna," *Electronics Letters*, 2012; 48(11): 607–608.

[18] G.H. Du, T. Tang, Y. Deng, "Dual-band metal skin UHF RFID tag antenna", *Electronics Letters*, 2013; 49(14): 858–860.

[19] J. Anguera, C. Puente, E. Martínez, E. Rozan, "The Fractal Hilbert Monopole: A Two-Dimensional Wire," *Microwave and Optical Technology Letters*, 2003; 36(2): 102–104.

[20] J. Zhu, A. Hoorfar, N. Engheta, "Feed-Point effects in Hilbert-Curve Antennas," *IEEE Antennas and Propagation Society International Symposium, URSI Digest*, 2002: 6623–6626.

[21] J. Anguera, C. Puente, C. Borja, J. Soler, "Fractal-Shaped Antennas: a Review," *Wiley Encyclopedia of RF and Microwave Engineering*, 2005; 2: 1620–1635.

[22] D. Gala, J. Soler, C. Puente, C. Borja, J. Anguera, "Miniature Microstrip Patch Antenna Loaded with a Space-Filling Line Based on the Fractal Hilbert Curve," *Microwave and Optical Technology Letters*, 2003; 38(4): 311–312.

[23] I. Sanz, J. Anguera, A. Andú,jar, C. Puente, C. Borja, "The Hilbert Monopole Revisited," *European Conference on Antennas and Propagation, EuCAP*, 2010.

[24] K.J. Vinoy, K.A. Jose, V.K. Varadan, V.V. Varadan, "Hilbert Curve Fractal Antenna: A Small Resonant Antenna for VHF/UHF applications," *Microwave and Optical Technology Letters*, 2001; 29(4): 215–1219.

[25] K.J. Vinoy, K.A. Jose, V.K. Varadan, V.V. Varadan, "Resonant Frequency of Hilbert Curve Fractal Antenna," *IEEE APS*, 2001; 3: 648–651.

[26] M.Z. Azad, M. Ali, "A Miniaturized Hilbert PIFA for Dual-Band Mobile Wireless Applications," *IEEE Antennas and Wireless Propagation Letters*, 2005; 4: 59–62.

[27] J.C. Liu, B.H. Zeng, I. Chen, C.C. Chang, D.C. Chang, "An Inductive Self-Complementary Hilbert-Curve Antenna for UHF RFID Broadband and Circular-Polarization Tags," *Progress in Electromagnetic Research B*, 2009; 16: 433–443.

[28] Ansoft HFSS, www.ansoft.com/products/hf/hfss.

[29] Y. Nishioka, K. Hitomi, H. Okegawa, T. Mizuno, T. Fukasawa, H. Miyashita, Y. Konishi, "Novel Antenna Configuration for HF and UHF Band Hybrid Card-Type RFID Tags," *Antennas and Propagation (EuCAP)*, 2010: 1–5.

[30] Z.L. Ma, L.J. Jiang, J. Xi, T.T. Ye, "A Single-Layer Compact HF-UHF Dual-Band RFID Tag Antenna," *IEEE Antennas Wireless Propagation Letters*,2012; 11: 1257–1260. DOI: 10.1109/LAWP.2012.2225821

[31] S. Basat, S. Bhattacharya, A. Rida, S. Johnston, L. Yang, M.M. Tentzeris, J. Laskar, "Fabrication and Assembly of a Novel High-Efficiency UHF RFID Tag on Flexible LCP substrate," *IEEE Electronic Components and Technology Conference*, 2006: 1352–1355.

[32] Specifications, ISO15693, ISO18000-3, Elastic RFID Tech Co.

Chapter 10

Multiband Planar Antennas for Broadband Wireless Systems

Mohammad Alibakhshi-Kenari,
Mohammad Naser-Moghadasi,
Ramazan Ali Sadeghzadeh, Bal Singh Virdee and
Ernesto Limiti

Additional information is available at the end of the chapter

http://dx.doi.org/10.5772/65802

Abstract

Next generation of wireless mobile systems calls for more compact and multiband antennas. This is because such systems need to be small and can operate over multiple wireless communication standards. The design and development of miniature antennas that function over a wideband are highly challenging. In this chapter, novel antenna designs are presented, which provide a solution to this deficiency. These antennas are based on composite right-/left-handed transmission line (CRLH-TL) metamaterials. Unlike traditional right-handed (RH) transmission materials, metamaterials based on left-handed (LH) transmission lines have unique features of antiparallel group and phase velocities. Pure LH transmission lines cannot be implemented due to the existence of RH parasitic effects that occur naturally in practical LH transmission lines. In this chapter, novel CRLH transmission line structures are presented, which include right-handed parasitic effects.

Keywords: compact antennas, composite right-/left-handed transmission lines, metamaterials, multiband antennas, VHF/UHF antennas

1. Introduction

The design and development of wideband antennas are highly challenging, especially for application in portable wireless communications systems [1]. Due to the limited space assigned

for the antenna in such systems, shrinking the size conventional antennas can lead to degradation in its performance and complicate mechanical assembly. An alternative solution is to employ metamaterial (MTM) technology in the design of antennas. MTM antennas have smaller dimensions because their size is independent of wavelength (λ), which does not compromise its performance [2, 3]. Various implementations of the MTM structures have been reported and demonstrated [4]. In this chapter, a number of identical MTM transmission line (TL) unit cell structures are cascaded together in series to realize a compact antenna with a small footprint. Equivalent model of the MTM-TL unit cell is composed of a series inductor (L_R) and capacitor (C_L), and shunt inductor (L_L) and capacitor (C_R). Components L_L and C_L determine the left-handed (LH) mode propagation properties of the structure, whereas L_R and C_R are parasitic effects resulting from the practical realization of the MTM-TL structure, which determine the right-handed (RH) mode propagation properties. Practical realization of the MTM-TL is commonly referred to as the composite right-/left-handed transmission line (CRLH-TL), which provides a conceptual route for implementing small-sized antennas. The CRLH-TL-based antennas can also be made wideband to support today's multiband wireless communication system needs. The electrical size of a conventional CRLH-TL is strongly related to its physical dimensions, and consequently by reducing its size, we can effectively increase its operational frequency. Physical size of a CRLH-TL is determined by the four aforementioned parameters (C_R, L_R, C_L, and L_L). This implies that if these four parameters are realized in a very compact form, the antenna size will be highly compact and small [5, 6]. A typical realization of CRLH-TL is found in a quasi-lumped transmission line with elementary cells consisting of a series capacitor and a shunt inductor. In practice, the right-handed parasitic effects (C_R and L_R) created by the gap between the microstrip line and ground plane cannot be avoided, which results in unwanted current flow on the radiating patch that can degrade the antenna performance [7–9].

In this chapter, an innovative wideband antenna is designed, fabricated, and tested using a unique metamaterial transmission line unit cell structure. The MTM-TL unit cell is based on distributed implementation of the series capacitor and shunt inductor realized with a slit (L- and F-shaped) and spiral configurations, respectively. The radiating unit cells benefit from miniaturized size, planar structure, low profile, ease of fabrication, light weight, and low cost. In addition, the proposed MTM-TL unit cell provides wideband operation with good radiation properties. The parametric study presented in the chapter shows that the number of unit cells and the slit dimensions can have a dramatic influence on the antenna's performance in terms of operational bandwidth and radiation characteristics. Two antennas are designed for RF applications with maximum size of 14×5 mm^2.

2. Antenna design procedure

2.1. Equivalent circuit model

Equivalent circuit model of the CRLH-TL unit cell, shown in **Figure 1**, consists of C_L, L_L, C_R, and L_R. The circuit model of the purely right-handed transmission line (PRH-TL) is shown

http://dx.doi.org/10.5772/65802

in **Figure 1b**, which is a dual of **Figure 1a** and is a purely left-handed transmission line (PLH-TL), where the series inductor is replaced with a capacitor, and the shunt capacitor is substituted with an inductor. PLH-TL represents an ideal model, which does not exist in practice. Such a structure will have associated parasitic series inductance (L_R) and shunt capacitance (C_R) as well as loss components represented by series conductance (G_L) and shunt conductance (G_R). A more realistic equivalent circuit model of PLH-TL, shown in **Figure 1c**, is a combination of left-handed and right-handed transmission line, which is referred to as composite right-/left-handed transmission. At low frequency, C_L and L_L are dominant, and hence the transmission line exhibits left-handed characteristics; however, at high frequency, L_R and C_R are dominant, which makes the transmission line exhibit right-handed characteristics.

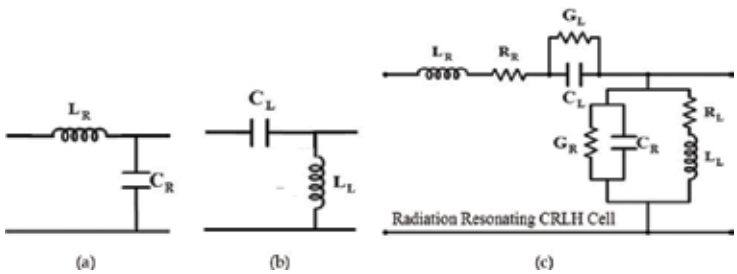

Figure 1. Equivalent circuit model of: (a) purely right-handed transmission line, (b) purely left-handed transmission line, and (c) CRLH-TL with loss.

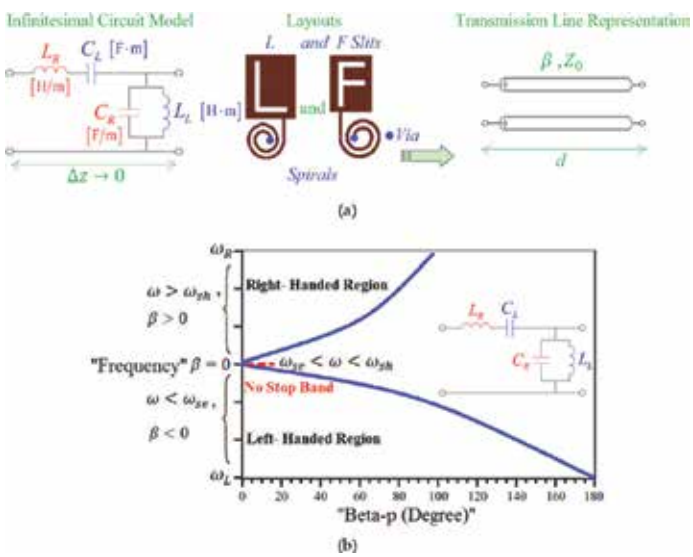

Figure 2. (a) Simplified loss-less equivalent circuit model of the CRLH-TL unit cells and its implementation with L- and F-shaped slit, and (b) dispersion diagram of the CRLH-TL unit cells.

The simplified circuit model and layouts of the proposed CRLH unit cell structures are shown in **Figure 2a**, where capacitance (C_L) is implemented with the either L-shaped or F-shaped slits in the microstrip patch, and inductance (L_L) is implemented with a spiral that is ground plane through via-hole. Capacitance (C_R) is associated with the gap between the microstrip section and the ground plane, and inductance (L_R) is associated with the microstrip patch. The unit cells are designed using conventional microwave integrated technology. The unit cell can be easily implemented and is a low-profile design. As shown below, wideband antennas can be designed by simply cascading together in series an appropriate number of unit cells for operation across VHF and UHF bands.

The CRLH-TL unit cell topologies in **Figure 2a** has a propagation constant (γ) given by:

$$\gamma = \alpha + j\beta = \sqrt{ZY} \tag{1}$$

where

$$\beta(\omega) = s(\omega)\sqrt{\omega^2 L_R C_R + \frac{1}{\omega^2 L_L C_L} - \left(\frac{L_R}{L_L} + \frac{C_R}{C_L}\right)} \tag{2}$$

$$s(\omega) = \begin{cases} -1 if \omega < \omega_{se} = min\left(\frac{1}{\sqrt{L_R C_L}}, \frac{1}{\sqrt{L_L C_R}}\right) \\ 0 if \omega_{se} < \omega < \omega_{sh} \\ +1 if \omega > \omega_{sh} = max\left(\frac{1}{\sqrt{L_R C_L}}, \frac{1}{\sqrt{L_L C_R}}\right) \end{cases} \tag{3}$$

and

$$Z(\omega) = j(\omega L_R - 1/\omega C_L) \tag{4}$$

$$Y(\omega) = j(\omega C_R - 1/\omega L_L) \tag{5}$$

Parameters $\beta(\omega)$, $s(\omega)$, $Z(\omega)$, and $Y(\omega)$ are a function of frequency and related to dispersion, sign function, impedance, and admittance of the antenna structure, respectively. The series and shunt resonance frequencies, respectively, are:

$$\omega_{se} = \frac{1}{\sqrt{L_R C_L}} \tag{6}$$

$$\omega_{sh} = \frac{1}{\sqrt{L_L C_R}} \tag{7}$$

The phase and group velocities, respectively, are defined by:

$$v_p = \frac{\omega}{\beta} = \omega^2 \sqrt{L_L C_L} \tag{8}$$

$$v_g = \left(\frac{\partial \beta}{\partial \omega}\right)^{-1} = \omega^2 \sqrt{L_L C_L} \tag{9}$$

The dispersion diagram of the proposed CRLH unit cells is shown in **Figure 2b**. Bandwidth of CRLH-TL unit cells is defined between the high-pass (left-handed) cutoff frequency (ω_L) and the low-pass (right-handed) cutoff frequency (ω_R). The cutoff frequencies ω_L and ω_R are given by:

$$\omega_L = \frac{1}{\sqrt{L_L C_L}} \tag{10}$$

$$\omega_R = \frac{1}{\sqrt{L_R C_R}} \tag{11}$$

The CRLH-TL unit cells were designed and constructed on Rogers RT/duroid® RO4003 substrate with dielectric constant of $\varepsilon_r = 3.38$, thicknesses of $h = 0.8$ and 1.6 mm, and tan $\delta = 0.0022$. The L- and F-shaped unit cells occupied a space of 2.3 × 4.9 × 0.8 mm^3 and 2.06 × 4.4 × 1.6 mm^3, respectively. Microstrip feed line is used to excite the unit cells from the right-hand side of the structure, which is terminated on the left-hand side with a 50 Ω load (i.e., SMD1206), which is 4.2 mm long. The antenna design was modeled and analyzed with a 3-D full-wave electromagnetic field simulator from Ansys called High Frequency Structure Simulator (HFSS™) [10]. The optimized antennas were fabricated and tested, and the results are presented below.

2.2. Metamaterial antenna with L-shaped slits

The CRLH-TL unit cell consists of a rectangular radiation patch on which is engraved an L-shaped slit, and the patch is inductively grounded with a high-impedance spiral stub. The L-shaped slit acts like a LH capacitance (C_L), and the inductive spiral whose end is connected to

the ground plane metallic via-holes acts like a LH inductance (L_L). In reality, the LH reactive components are accompanied with RH parasitic effects represented by series inductance (L_R) and shunt capacitance (C_R) resulting from current flow in the microstrip metallization and voltage gradient created between the metal pattern of the microstrip and the ground plane. Thus, the unit cell is more accurately represented by a composite right-/left-handed model with the inclusion of resistive and conductance loss components represented by R_R, R_L and G_R, G_L, respectively, which account for the ohmic and dielectric loss associated with the unit cell. Four CRLH-TL unit cells were cascaded together in series, as shown in **Figure 3**, to implement an antenna design for application in VHF band (30–300 MHz) and UHF band (300 MHz–3 GHz). The antenna structure was optimized using HFSS™.

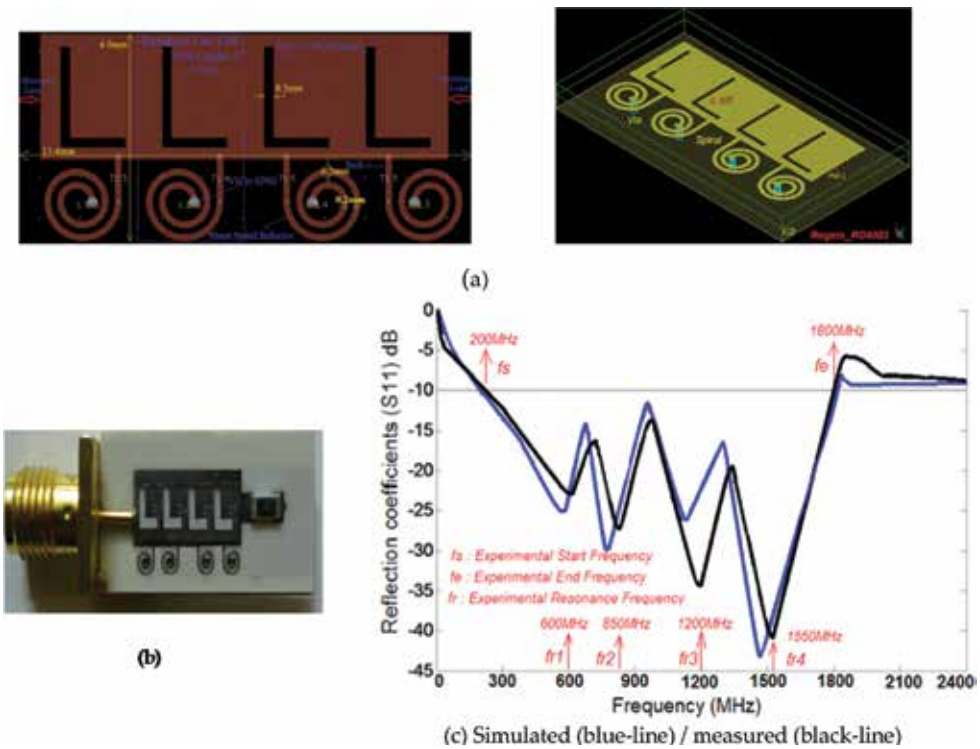

Figure 3. CRLH-TL antenna configuration with four L-shaped slits on the RT/duroid® RO4003 substrate with thickness of 0.8 mm, (a) distributed implementation (top isometric view), (b) fabricated prototype, and (c) reflection coefficient response of the antenna.

Besides the small dimensions, the bandwidth and good radiation properties are other main performance criteria in the antenna systems. With the proposed antenna design, the bandwidth can be increased by simply introducing more unit cells. Hence, there is a tradeoff between size of the antenna, bandwidth and radiation properties. Each cell occupies an area of 2.3 × 4.9 mm^2. Dimensions of the L-shaped slit antenna are 13.4 × 4.9 × 0.8 mm^3 or $0.0089\lambda_o \times 0.0032\lambda_o \times 0.00053\lambda_o$, where λ_o is free-space wavelength at 200 MHz.

http://dx.doi.org/10.5772/65802

For the L-shaped antenna, the simulated bandwidth is 1625 MHz (195 MHz–1.82 GHz) using HFSS™, and the measured bandwidth is 1600 MHz (200 MHz–1.8 GHz) for VSWR ≤ 2, which corresponds to a fractional bandwidth of 160%. The reflection coefficient response of the antenna, shown in **Figure 3**, clearly indicates its resonates at four distinct frequencies of 600, 850, 1200, and 1550 MHz. The measured gain and efficiency of the antenna are 1.2 dBi and 34% at 600 MHz, 1.7 dBi and 45% at 850 MHz, 2.1 dBi and 62% at 1200 MHz, and 3.4 dBi and 88% at 1550 MHz. The measured 2D and simulated 3D radiation patterns of the antenna are shown in **Figure 4** at the various resonance frequencies. The measured antenna gain and efficiency response are shown in **Figure 4c**.

The simulated and measured radiation patterns of the antenna at various frequencies in the two principle planes, the *x*-*z* and *x*-*y* planes, are shown in **Figure 4**. The antenna has approximately omnidirectional radiation patterns in the *x*-*z* plane. The *x*-*y* plane patterns show two nulls in the *y*-direction, which is similar to a typical monopole antenna.

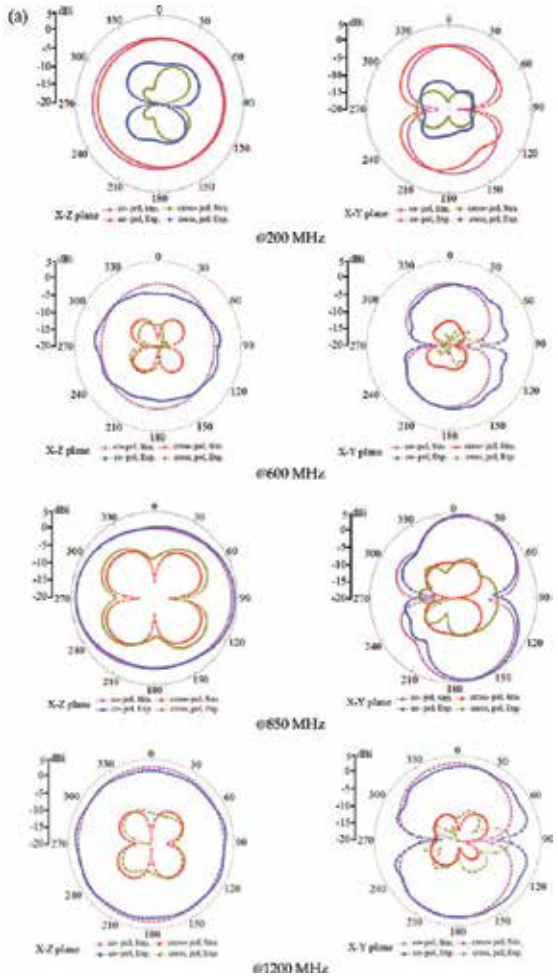

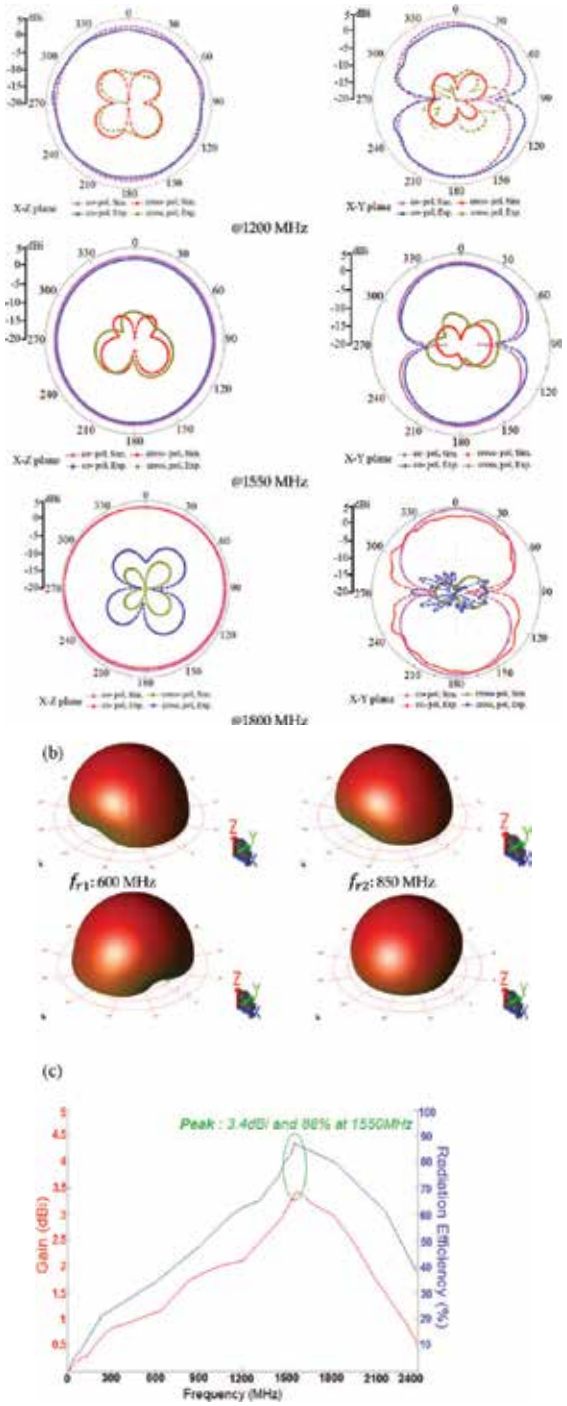

Figure 4. Radiation patterns of the L-shaped antenna, (a) measured 2D patterns, (b) simulated 3D patterns, and (c) measured gain and efficiency response.

2.3. Metamaterial antenna with F-shaped slits

In this section, the main goal is to design and implement an antenna with better performance than the above L-shaped antenna. This was achieved by modifying the L-shaped antenna by changing the slits to F-shaped. The equivalent circuit model of the unit cell is shown in **Figures 1** and **2**. In this case, the optimized antenna employed five CRLH-TL unit cells, as shown in **Figure 5a**. Each unit cell occupied an area of $2.06 \times 4.40\ mm^2$ ($0.00075\lambda_o \times 0.0016\lambda_o$) at 110 MHz. Dimensions of the antenna are $14.5 \times 4.4 \times 1.6\ mm^3$ or $0.0053\lambda_o \times 0.0016\lambda_o \times 0.00058\lambda_o$, where λ_o is free-space wavelength at 110 MHz. Each unit cell occupied an area of $2.06 \times 4.40\ mm^2$ ($0.00075\lambda_o \times 0.0016\lambda_o$) at 110 MHz.

The antenna was fabricated on RT/duroid® RO4003 substrate with thickness of 1.6 mm. The reflection coefficient response of the antenna in **Figure 5b** shows that the antenna has a measured impedance bandwidth of 1.99 GHz (110 MHz–2.10 GHz) for VSWR ≤ 2, which corresponds to a fractional bandwidth of 180.1%. The antenna resonates at 450, 725, 1150, 1670, and 1900 MHz.

The measured gain and efficiency of the F-shaped antenna, shown in **Figure 5c**, are 1.0 dBi and 31% at 450 MHz, 1.8 dBi and 47% at 725 MHz, 2.5 dBi and 70% at 1150 MHz, 3.8 dBi and 89% at 1670 MHz, and 4.5 dBi and 95% at 1900 MHz.

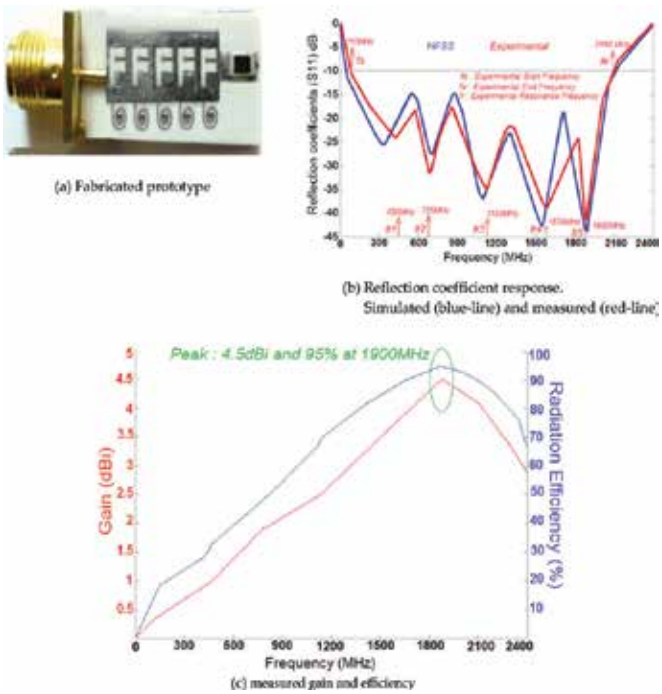

Figure 5. Five CRLH-TL unit cell antenna configuration with F-shaped slit designed on RT/duroid® RO4003 with thickness 1.6 mm, (a) fabricated photograph and (b) reflection coefficient as function of frequency (c) measured gain and efficiency versus frequency.

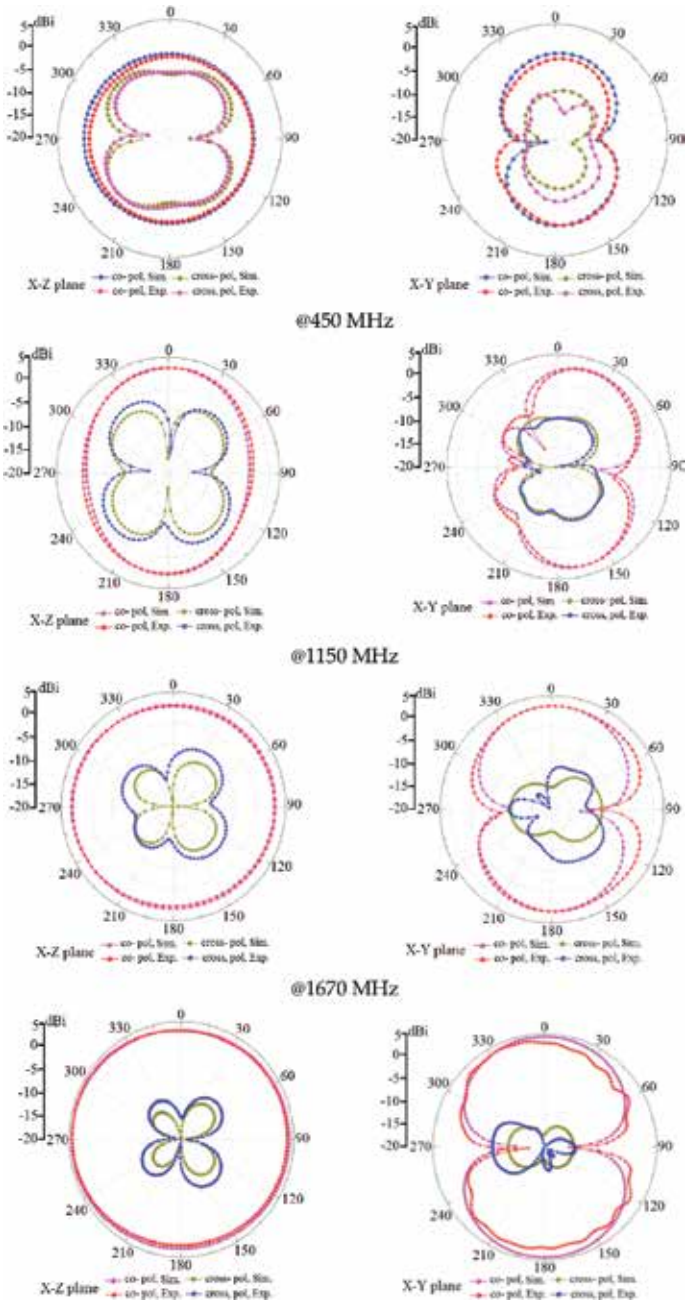

Figure 6. 2D radiation patterns of the F-shape slit CRLH-TL antenna.

The simulated and measured radiation patterns of the antenna in the *x-z* and *x-y* planes at various spot frequencies are shown in **Figure 6**. It is evident that the measured radiation patterns agree well with the simulation results. The results show that the radiation is omni-

http://dx.doi.org/10.5772/65802

directional in the *x*-*z* plane over a wideband frequency range. In the *x*-*y* plane, the radiation is null in the positive and negative *y* directions, which is typical for monopole antennas.

3. Analysis on antenna design parameters

To achieve the desired antenna performance, the number of unit cells (n), number of spiral turns (N_{SP}), spiral width (W_{SP}), and distances between spirals (S_{SP}) need to be optimized, which was done using Ansys HFSS™ EM Simulator. **Figures 7–12** show the effect of these parameters on the reflection coefficient response of the antenna. **Figure 7** shows that the bandwidth is improved from 43.47% for one unit cell to 180.1% for five unit cells. The increase in unit cells has also increased the number of resonance spikes.

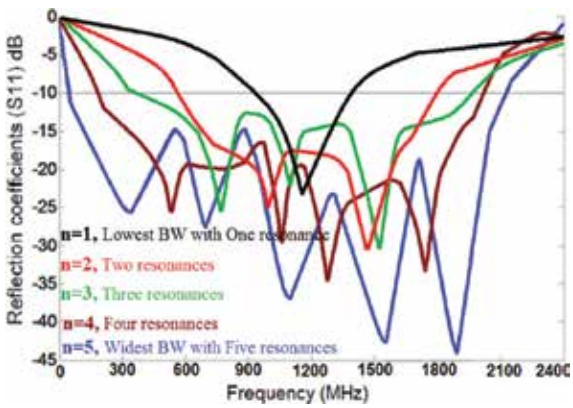

Figure 7. Reflection coefficient response of the proposed antenna as a function of number of unit cells.

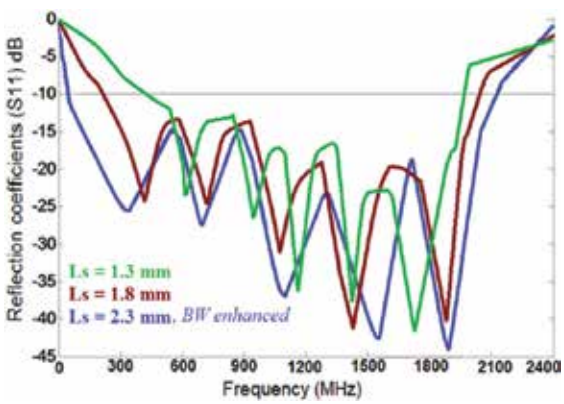

Figure 8. Reflection coefficient response of the antenna as a function of the vertical slit length. The slit width was kept fixed at 0.3 mm.

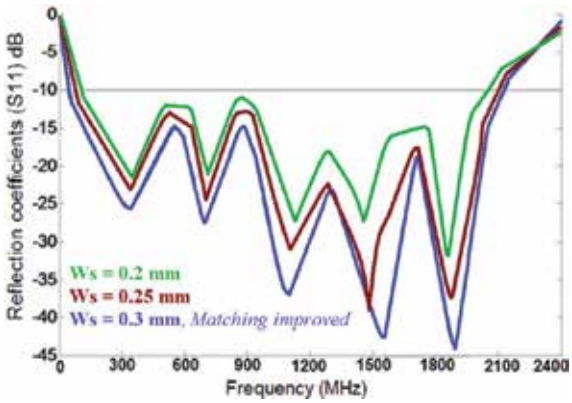

Figure 9. Reflection coefficient response of the antenna as a function of the slit width.

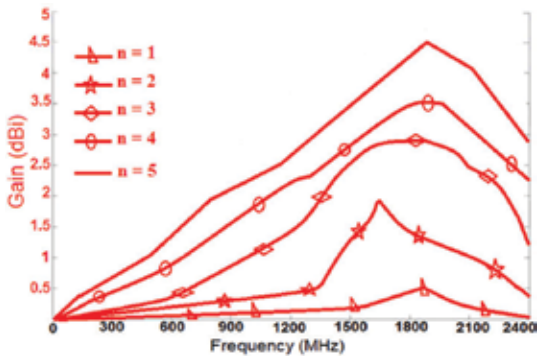

Figure 10. Antenna gain versus frequency with variation in number of unit cells ($n = 1$–4 for simulation and $n = 5$ is measured). Length was fixed at 2.3 mm.

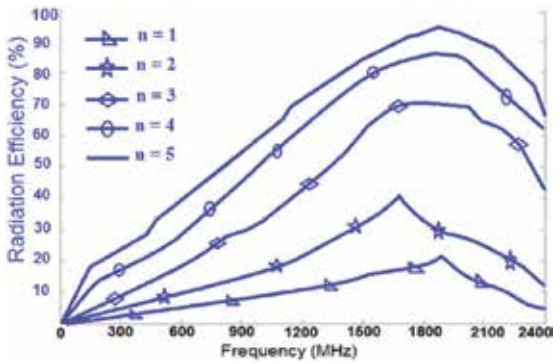

Figure 11. Antenna efficiency versus frequency with variation in number of unit cells ($n = 1$–4 for simulation and $n = 5$ is measured).

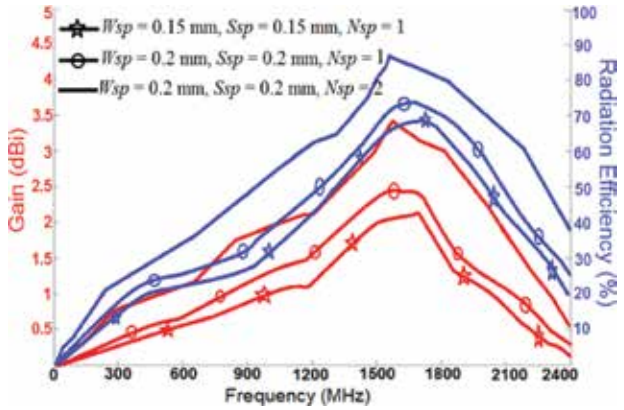

Figure 12. Gain and efficiency response as a function of spiral width (W_{SP}), distances between spirals (S_{SP}) and number of spiral turns (N_{SP}).

References (UC: unit cells)	Dimensions (ES: electrical size, PHS: physical size)	Fractional bandwidth	Gain (Max)	Eff. (Max)
[11] b-shaped antenna with 4×UC	ES: $0.047\lambda_o \times 0.021\lambda_o \times 0.002\lambda_o$ at 1 GHz, PHS: $14.2 \times 6.32 \times 0.8$ mm^3	104.76% (1–3.2 GHz)	2.3 dBi	62%
[11] b-shaped antenna with 6×UC	ES: $0.051\lambda_o \times 0.016\lambda_o \times 0.002\lambda_o$ at 0.8 GHz, PHS: $19.2 \times 6.32 \times 0.8$ mm^3	123.8% (0.8–3.4 GHz)	2.8 dBi	70%
[12] J-shaped antenna with 8×UC	ES: $0.564\lambda_o \times 0.175\lambda_o \times 0.02\lambda_o$ at 7.5 GHz, PHS: $22.6 \times 7 \times 0.8$ mm^3	84.23% (7.25–17.8 GHz)	2.3 dBi	48%
[12] I-shaped antenna with 7×UC	ES: $0.556\lambda_o \times 0.179\lambda_o \times 0.041\lambda_o$ at 7.7 GHz, PHS: $21.7 \times 7 \times 1.6$ mm^3	87.16% (7.8–19.85 GHz)	3.4 dBi	68.1%
[12] J-shaped antenna with 6×UC	ES: $0.45\lambda_o \times 0.175\lambda_o \times 0.02\lambda_o$ at 7.5 GHz, PHS: $18 \times 7 \times 0.8$ mm^3	74.4% (7.5–16.8 GHz)	2.1 dBi	44.3%
[12] I-shaped antenna with 5×UC	ES: $0.428\lambda_o \times 0.179\lambda_o \times 0.041\lambda_o$ at 7.7 GHz, PHS: $16.7 \times 7 \times 1.6$ mm^3	82.88% (7.7–18.6 GHz)	3.1 dBi	58.6%
[13]	ES: $0.134\lambda_o \times 0.035\lambda_o \times 0.002\lambda_o$ at 0.67 MHz, PHS: $60 \times 16 \times 1$ mm^3	116.7% (0.67–2.55 GHz)	4.7 dBi	62.9%
[14]	ES: $0.108\lambda_o \times 0.108\lambda_o \times 0.009\lambda_o$ at 1.8 GHz,PHS: $18 \times 18 \times 1.6$ mm^3	26.5% (1.8–2.35 GHz)	3.7 dBi	20%
[15]	ES: $0.164\times\lambda_o \times 0.013\ \lambda_o \times 0.013\lambda_o$ att 0.8 MHz, PHS: $60 \times 5 \times 5$ mm^3	103.03% (0.8–2.5 GHz)	0.4 dBi	53.6%
[16]	ES: $0.06\lambda_o \times 0.06\lambda_o \times 0.021$ aλ_o at 1 GHz, PHS: $18.2 \times 18.2 \times 6.5$ mm^3	66.66% (1–2 GHz)	0.6 dBi	26%
Proposed F-shaped slit antenna 5×UC	ES: $0.0053\lambda_o \times 0.0016\lambda_o \times 0.00058\lambda_o$ at 0.11 MHz, PHS: $14.5 \times 4.4 \times 1.6$ mm^3	180.1% (0.11–2.1 GHz)	4.5 dBi	95%

Table 1. Comparison of the antenna characteristics.

Figure 8 indicates that the larger the vertical length of the slit, the larger the bandwidth (for $S_{11} < -10$ dB). Increase in slit length from 1.3 to 2.3 mm increases the bandwidth by 36.5%.

Figure 9 shows that the increase in the width from 0.2 to 0.3 mm increases the bandwidth by 9.3%. The gain and the radiation efficiency of the antenna are greatly affected by the number of unit cells. The peak gain and radiation efficiency increase substantially with the number of unit cells as shown in **Figures 10** and **11**. The measured peak gain and peak radiation efficiency are 4.5 dBi and 94.8% for five unit cells at 1890 MHz. **Figure 12** shows that the spiral width, their separation and number of turns also affect the antenna's gain and radiation efficiency.

Features of the proposed two antennas are compared with other similar antennas in **Table 1**.

Acknowledgements

The authors would like to give special thanks to faculty of Microelectronics for financial support.

Author details

Mohammad Alibakhshi-Kenari[1*], Mohammad Naser-Moghadasi[2],
Ramazan Ali Sadeghzadeh[3], Bal Singh Virdee[4] and Ernesto Limiti[1]

*Address all correspondence to: naeem.alibakhshi@yahoo.com

1 Dipartimento di Ingegneria Elettronica, Università degli Studi di Roma Tor Vergata, Via del Politecnico, Roma, Italy

2 Faculty of Engineering, Science and Research Branch, Islamic Azad University, Tehran, Iran

3 Faculty of Electrical Engineering, K. N. Toosi University of Technology, Tehran, Iran

4 London Metropolitan University, Center for Communications Technology, London, UK

References

[1] J. Anguera, A. Andújar, M.C. Huynh, C. Orlenius, C. Picher, and C. Puente, "Advances in antenna technology for wireless handheld devices," *International Journal of Antennas and Propagation*, Volume 2013 (2013), Article ID 838364, 25 pages http://dx.doi.org/10.1155/2013/838364

[2] C. Caloz and T. Itoh. *Electromagnetic Metamaterials: Transmission Line Theory and Microwave Applications*, 2005, Wiley. ISBN: 978-0-471-66985-2 376 pages December 2005, Wiley-IEEE Press

[3] N. Engheta and R.W. Ziolkowski, *Metamaterials: Physics and Engineering Explorations*, 2006, Wiley. ISBN: ISBN: 978-0-471-66985-2 376 pages December 2005, Wiley-IEEE Press

[4] R.A. Shelby, D.R. Smith, and S. Schultz, "Experimental verification of a negative index of refraction," *Science*, 2001; 292(5514): 77–79. doi:10.1126/science.1058847

[5] C.J. Lee, M. Achour, and A. Gummalla, "Compact metamaterial high isolation MIMO antenna subsystem," *Asia Pacific Microwave Conference*, 2008: 1–4. doi:10.1109/APMC.2008.4957946

[6] C.J. Lee, K.M.H. Leong, T. Itoh, "Broadband small antenna for portable wireless application," *International Workshop on Antenna Technology: Small Antennas and Novel Metamaterials*," *iWAT* 2008: 10–l3.

[7] M. Alibakhshi-Kenari, M. Movahhedi and H. Naderian, "A new miniature ultra wide band planar microstrip antenna based on the metamaterial transmission line," *IEEE Asia-Pacific Conference on Applied Electromagnetics*, 2012: 293–297. doi:10.1109/APACE.2012.6457679

[8] M. Alibakhshi-Kenari, "A new compact UWB traveling-wave antenna based on CRLH-TLs for embedded electronic systems," *International Journal of Microwave and Wireless Technologies*, 2014: 1–4. doi:10.1017/S1759078714001020

[9] J.D. Jackson, *Classical Electromagnetics*, Wiley, New York, 3rd ed., 1999.

[10] Ansoft HFSS, www.ansoft.com/products/hf/hfss.

[11] M. Alibakhshi-Kenari, "Printed planar patch antennas based on metamaterial," *International Journal of Electronics Letters*, Volume 2, Issue 1, Jan. 2014, pp 37–42

[12] M. Alibakhshi-Kenari, "Introducing the new wide band small plate antennas with engraved voids to form new geometries based on CRLH MTM-TLs for wireless applications," *International Journal of Microwave and Wireless Technologies*, 2014; 6(06): 629–637. doi:10.1017/S1759078714000099

[13] J. Luo, S. Gong, P. Duan, C. Mou, and M. Long, "Small-size wideband monopole antenna with CRLH-TL for LTE mobile phone," *Progress in Electromagnetics Research C,* 2014; 50: 171–179.

[14] M.A. Abdalla, A.A. Awad, K.M. Hassan, "Wide band high selective compact metamaterial antenna for 2 GHz wireless applications," *Antennas and Propagation Conference (LAPC),* 2014: 350–354. doi:10.1109/LAPC.2014.6996395

[15] Y. Li, Z. Zhang, J. Zheng and Z. Feng, "Compact heptaband reconfigurable loop antenna for mobile handset," *IEEE Antennas and Wireless Propagation Letters*, 2011; 10: 1162–1165. doi:10.1109/LAWP.2011.2171311

[16] Lee, C.J., Leong, K.M.K.H., Itoh, T.: 'Composite right/left-handed transmission line based compact resonant antennas for RF module integration', IEEE Trans. Antennas Propag., 2006, 54, (8), pp. 2283–2291.

Chapter 11

Design of a Ku Band Planner Receive Array for DBS Reception Systems

Mustafa Murat Bilgic and Korkut Yegin

Additional information is available at the end of the chapter

http://dx.doi.org/10.5772/66374

Abstract

The main objective of this chapter is to present to the readers a step-by-step design approach when designing antenna array. Subsequently, the chapter will proceed following an example design of a passive Ku band planner receive array antenna for direct broadcast from satellite (DBS) reception for mobile systems. First, an appropriate antenna topology capable of reaching our target goals will be selected and optimized to be the base array element. During the design process of the base element, some figures-of-merit will be proposed in order to make a comparative study with the designed antenna and previously published antenna structures. Subarrays of microstrip line feed antennas will be combined by waveguides in order to build a low-loss feed network for the array antenna. The main question during the design of the feed network is: "How should one form the subarrays and their accompanying waveguide feed networks?" These sections will answer this question by formulating the subarray and array feed network loss as an optimization problem with constraints on the size and the weight of the array. In the concluding sections, measurements on realized antennas will show that the design exhibits a 16.5% relative bandwidth, covering the complete downlink band, and the designed antennas have a 28.4–31.3 dBi gain for both vertical and horizontal polarizations. Results of some field tests will be given and conclusions will be made in the final section.

Keywords: wideband antennas, antenna arrays, hybrid feed networks

1. Introduction

Antennas are crucial components needed during the design of systems in which information is transmitted via electromagnetic waves. Special attention must always be paid to the antenna design in order to build up an efficient system. Antenna engineering is the area in which

engineers are specialized in designing antennas for a wide range of applications. Each application may require a different approach during the design process; also in each approach, engineers will come across different challenges. Antenna engineering is a fascinating application of electromagnetic theory where theory and practice are collated to form a beautiful harmony.

One can find a vast number of fairly comprehensive books on antenna theory written by some of the greatest scholars. Each year an enormous number of academic papers are being published, expanding the area of antenna theory. However, very few resources on practical design procedures are available. The main objective of this chapter is to show a step-by-step design procedure for a large antenna array that will hopefully give valuable insight to young engineers who are at the beginning of their path to become an antenna engineer.

The text following this section will first define the antenna problem. The specifications that a planner Ku band receive antenna array must necessarily achieve for reception of direct broadcast from satellite (DBS) systems will be defined. Section 3 will cover the design of a high performance antenna array element. A suitable microstrip antenna topology will be selected based on some figures-of-merit that will be defined according to the given specifications. The selected structure will be optimized to supply the best performance and a comparative study between previously published examples will be executed. Section 4 will show the design of optimal subarrays and microstrip line feed networks. These subarrays will then be combined with waveguides to build up a larger array. Finally, measurement results of realized antennas will be discussed.

2. System level requirements for mobile satellite TV antennas

Information and entertainment systems for reception of direct broadcast from satellite (DBS) on mobile environments have been a great challenge for the automotive industry. Over the last two decades, there has been growing interest for developing low-cost, high performance systems working on mobile platforms. Such systems in automobiles now demand compact mobile antennas for reception of DBS from different service providers simultaneously.

Most of the existing commercial products were based on reflector-type antennas, which possess excellent bandwidth, gain, noise figure, and half power beam width (HPBW) characteristics. These aspects also make these antennas ideal candidates for control and tracking of satellites while the vehicle is on the move. Satellite tracking with reflector-type antennas is basically carried out by mechanically steering the antenna in both the elevation and the azimuth axes. However, the bulky size and high profile of reflector antennas cause aerodynamic problems on vehicles. Moreover, these structures are not suitable for smaller vehicles. A low profile structure such as microstrip antenna arrays with reduced size would be more advantageous. The primary specification is to build a planner structure using microstrip antennas which would hold the same properties of a reflector antenna. The low profile antenna would also be mechanically steered in both elevation and azimuth planes so that no active components such as phase shifters hence amplifiers would be necessary.

http://dx.doi.org/10.5772/66374

In the field of TV broadcasting, geostationary satellites are set apart 6° or more from each other: For azimuth tracking, the antenna's half power beam width is commonly preferred to be less than 5° whereas it is chosen to be more than 1.5° to optimize tracking the satellite on a moving vehicle. In order to successfully lock to the satellite over a 32 MHz IF bandwidth, which is the maximum bandwidth for TurkSat,[1] a minimum of 7 dB of carrier-to-noise ratio (CNR) is required.

It is possible to achieve high antenna gain throughout a maximum of 3° azimuth HPBW in a planar microstrip antenna array with appropriate number of elements. However, maintaining target antenna gain at low elevation angles is difficult with broadside antenna elements. The TM_{20} mode type radiation pattern may be more suitable, but achieving target bandwidth with such patch is extremely challenging. Besides, the antenna size would be much larger compared to TM_{01} mode broadside looking patch. Utilizing subarrays or panels, positioned on the same platform, which are capable of being mechanically tilted to certain elevation angles would be a compromise on height profile. Yet this still is a more expensive choice and it also complicates the control of the system. This solution is known to have been used in previous studies [1–5] and it is still broadly used in many satellite systems. Added complexity of this system outweighs the benefits of fulfilling electrical specifications.

At this point, it will be suggested to use two panels built from microstrip patch antennas for each polarization to minimize the added complexity of this implementation. The array will be formed in order to have a tilted beam. Since the array can be mechanically tilted, it would be easier to scan low elevation angles without exceeding the overall height limits. The system configuration of the proposed design is illustrated in **Figure 1**.

The directivity of a TM_{01} mode broadside patch is roughly:

$$D_P = \frac{4\pi}{\Omega_A} \approx \frac{4\pi}{\pi} = 4(6\ \text{dBi}) \tag{1}$$

where, Ω_A represents beam solid area. For K elements, the array directivity D_A becomes:

$$D_A \approx K D_P \tag{2}$$

If elevation scanning of ± 15° is assumed, $HPBW_\theta$ in elevation can be taken as 30°. $HPBW_\varnothing$ can be set to 3° for azimuth tracking. Then, the directivity of the array is roughly [6]:

$$D_A \approx \frac{40,000}{\text{HPBW}_\theta \text{HPBW}_\varnothing} \approx 444(26.47\ \text{dBi}) \tag{3}$$

Furthermore, if 55% total efficiency (due to feed network loss, mismatch loss) is assumed, the gain of the array should be 807 (29 dBi). Number of broadside patch elements required for this gain is 202. To preserve symmetry and to account for other losses (e.g. random, mutual coupling among array elements), we estimate that 256 elements per polarization is needed.

[1]The antenna in this design example is for the transponders fixed on TurkSat 2A and 3A satellite. It is positioned to an elevation angle of 42°E in Turkey.

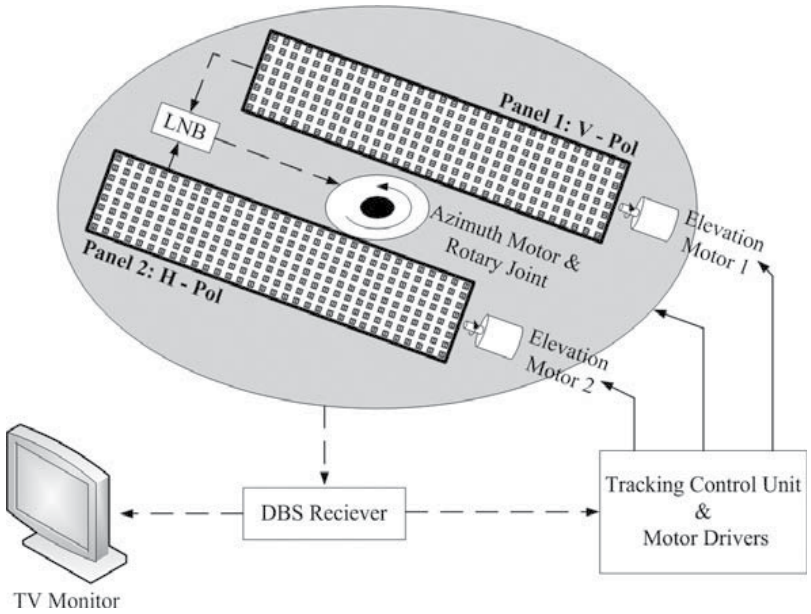

Figure 1. System configuration of the proposed array antenna.

Based on the simple calculations given above and a quick overview of some commercial products, the target system specifications are formed and summarized in **Table 1**.

Specification	Value
Frequency	10.8–12.8 GHz
Polarization	Dual linear (vertical and horizontal)
Antenna G/T (EIRP >54 dBW)	>5.5 dB/°K at 45° elevation
Antenna gain	29 dBi (per polarization)
Spatial coverage	35–75° elevation, 0–360° azimuth
Antenna height (w/max mechanical tilt)	<70 mm
System diameter	<75 cm
Weight (w/o electromechanical components)	<3 kg

Table 1. Target system specifications.

3. Wideband, high gain antenna element design

Based on the specifications given in Section 2, a high gain and wideband planar antenna is desired. When designing such antennas, the first step should be achieving the target bandwidth. Antenna gain becomes the next goal, because gain directly impacts signal-to-

http://dx.doi.org/10.5772/66374

noise ratio (SNR) of the system. Often, minimum gain in the target bandwidth is specified to fulfill SNR requirements. However, gain and bandwidth are usually complementary metrics where the improvement in one, results in the degradation of the other. Thus, one must optimize the design for gain-bandwidth product (GBWP) rather than bandwidth/gain only. An upper bound on gain-bandwidth product can be placed for electrically small antennas [7, 8], but this is rather difficult for multiple resonant or wideband antennas.

One of the most common planar antenna configurations is the aperture-coupled microstrip antenna (ACMSA) configuration [9]. Slot coupling is also suitable for high-frequency applications where structural dimensions are in millimeter or submillimeter range. Most of these applications need high directive gain; thus, utilize phased arrays where high gain and wideband antenna elements are required. To increase the bandwidth of an ACMSA, parasitic elements in the form of stacked patches or coplanar parasitic elements were proposed [10, 11]. Unlike coplanar parasitic elements, stacked patches do not increase the aperture area of the antenna, hence they do not require increased interelement spacing that may cause grating lobes. Either a nonresonant slot is coupled to stacked resonant patches or a resonant slot radiates with resonant stacked elements. Stacked patches coupled with a resonant slot exhibit fractional bandwidth (FBW) more than 50% with gain in excess of 5 dBi [12, 13]. For nonresonant slot coupling, various slot shapes ranging from rectangular slots to dog-bone shape slots have been proposed [9–15]. Hourglass shape nonresonant slot was identified as the best configuration in terms of fractional bandwidth [10]. However, none of these studies considered GBWP, and which configuration produces best gain-bandwidth performance is yet unknown. Also, it is still unclear whether resonant slot or nonresonant slot has better performance.

In any antenna design, bandwidth, gain, and HPBW are the most essential design characteristics along with other features such as cross polarization ratio, front-to-back ratio, in-band gain ripple, electrical height, and physical dimensions. Although it is difficult to define a common figure-of-merit (FOM) to combine all these metrics into one, several FOMs will be derived based on GBWP. Performance-wise comparisons of various nonresonant and resonant aperture coupled stacked patches will be defined for the best configuration in terms of these FOMs.

This design is particularly focused on Ku band applications for mobile satellite TV reception and satellite communications. A wideband equivalent circuit representation of the optimized ACMSA will be derived. Based on this study, a high gain, wideband antenna structure operating at Ku band with highest FOM compared to earlier studies will be proposed. Realized antenna and measurement results will also be provided.

3.1. Gain-bandwidth product of rectangular patch antenna

The bandwidth for a rectangular patch antenna with length L, width W and substrate height h is given as:

$$\mathrm{BW} = \frac{\mathrm{VSWR}-1}{Q\sqrt{\mathrm{VSWR}}} \tag{4}$$

where, Q represents the quality factor of the patch. Fractional bandwidth rather than absolute bandwidth is regarded as the bandwidth, thus, BW can also be expressed as:

$$\mathrm{BW} = \frac{f_u - f_l}{f_c} \tag{5}$$

where, f_u, f_l and f_c represent upper, lower, and center frequency of the impedance match frequency band.

For VSWR < 2, BW becomes:

$$\mathrm{BW} = \frac{1}{Q\sqrt{2}} \tag{6}$$

For electrically thin substrates ($h/\lambda \ll 1$), BW can be estimated as [16]:

$$\mathrm{BW} = \frac{16}{6\pi\sqrt{2}} \frac{c_1 p}{e_r} \frac{k_0 h}{\varepsilon_r} \frac{W}{L} \tag{7}$$

where, e_r is the efficiency, $k_0 = 2\pi/\lambda_0$ (free space wavenumber), ε_r is the permittivity of the substrate, c_1 and p are functions used in the approximation [17]. For $W/L < 2$, p becomes almost 1, and c_1 becomes 0.4 for air-dielectric and nearly 1 for high permittivity substrates. It is clear from Eq. (6) that the electrical height of the antenna is directly proportional to the bandwidth. For a given substrate height, the bandwidth is relatively wider at higher frequencies.

The gain of the patch antenna is approximated as [18]:

$$G = \frac{4(k_0 W)^2}{\pi\eta_0} e_r R_r \tag{8}$$

where, R_r represents radiation resistance. R_r given in Ref. [19] was not very accurate as stated by its authors so a more accurate representation given in [20] can be used. R_r given in [20] is approximated to its leading terms and is proportional to:

$$\frac{R_r = \varepsilon_r 1}{(k_0 h)^2 (k_0 w/2)^2 \left[-1 + \frac{14}{(k_0 w/2)^2}\right]} \tag{9}$$

The gain of the antenna is inversely proportional to $(k_0 h)^2$. Hence, neglecting the constants and assuming p equals to 1, GBWP for rectangular patch is proportional to:

$$\mathrm{GBWP} = \frac{1}{k_0 h} \frac{W}{L} \frac{1}{\left[-1 + \frac{14}{(k_0 w/2)^2}\right]} \tag{10}$$

Therefore, increasing $k_0 h$ for bandwidth improvement deteriorates attainable gain and limits GBWP. High aspect ratio (W/L) also improves GBWP if higher order modes are not excited. It

http://dx.doi.org/10.5772/66374

is interesting to see that substrate permittivity and antenna efficiency are not the factors of GBWP. Low permittivity substrates are good for bandwidth improvement but relatively worse for antenna gain. Aperture-coupled antennas mostly follow the same trend of rectangular antennas, however, approximate relations are quite difficult to obtain.

Although these approximate formulas have been widely accepted, they are only valid for electrically thin substrates. 3D simulations were performed on rectangular patch antenna with pin feed and defined GBWP as:

$$\text{GBWP} = \frac{\int_{f_l}^{f_u} G(f)df}{f_u - f_l}\left(\frac{f_u - f_l}{f_c}\right) \tag{11}$$

where, $f_l \le f_i \le f_u$, $i = 1, 2, \ldots, N$ and $G(f)$ represents gain (linear not decibel) as a function of frequency. Rectangular patch antenna is optimized for best GBWP for different k_0h and substrates of different relative permittivity ε_r. The results are shown in **Figure 2**. Unlike approximate formulas, simulations show that GBWP has a maximum at certain k_0h and it is maximum for air-dielectric substrate. A similar analysis for different patch aspect ratios has also been simulated for air-dielectric patch only (see **Figure 3**). Again, it appears that there exists an optimum electrical height where GBWP is optimal. All simulations were run around Ku-band downlink frequency band (10.8–12.8 GHz).

GBWP performance has also been compared between pin-feed rectangular patch antenna and nonresonant rectangular slot coupled patch antenna, and the results are displayed in **Figure 4**. It can be observed that slot-coupled geometry produces much better GBWP performance as the inductance of pin feed severely limits BW of rectangular patch antenna.

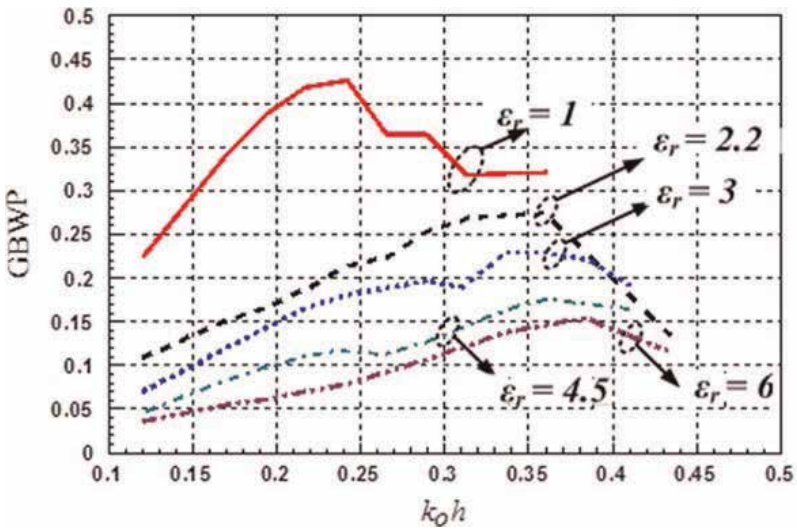

Figure 2. GBWP vs. k_0h. for different dielectric materials.

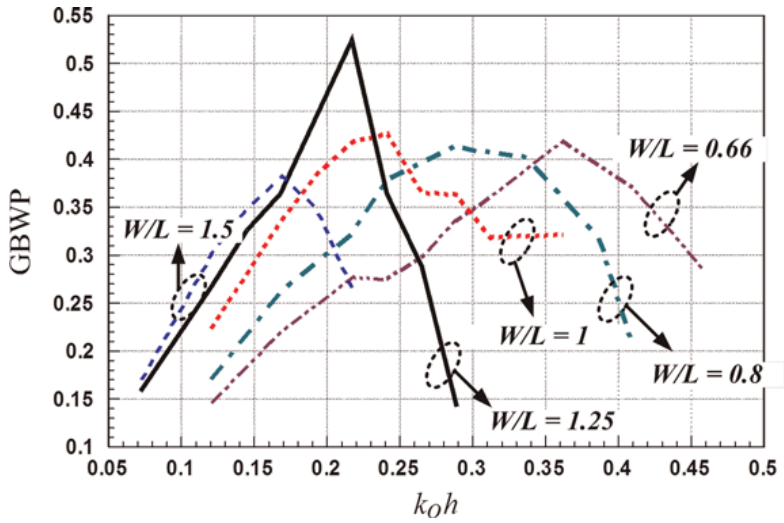

Figure 3. GBWP vs. k_0h for different aspect ratios.

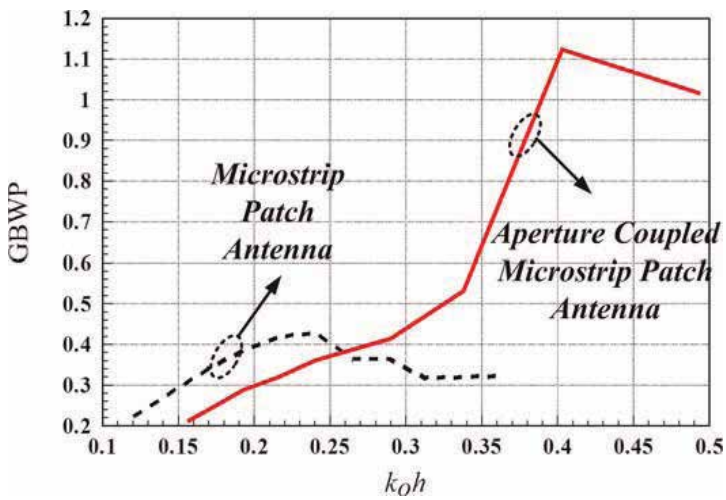

Figure 4. GBWP vs. k_0h comparison between aperture coupled (nonresonant slot) microstrip antenna and pin-feed microstrip antenna (antenna substrate is air and ε_r for feed substrate of aperture coupled antenna is 2.2).

3.2. Aperture coupled microstrip patch antenna

A typical aperture-coupled microstrip patch antenna is shown in **Figure 5**, with a slight difference. The structure shown below has a secondary patch named "the parasitic patch." This parasitic element is placed in order to give the structure a double resonant characteristic to enhance the bandwidth. The key analysis in this section is to decide what type of aperture structure is the optimum based on GBWP.

http://dx.doi.org/10.5772/66374

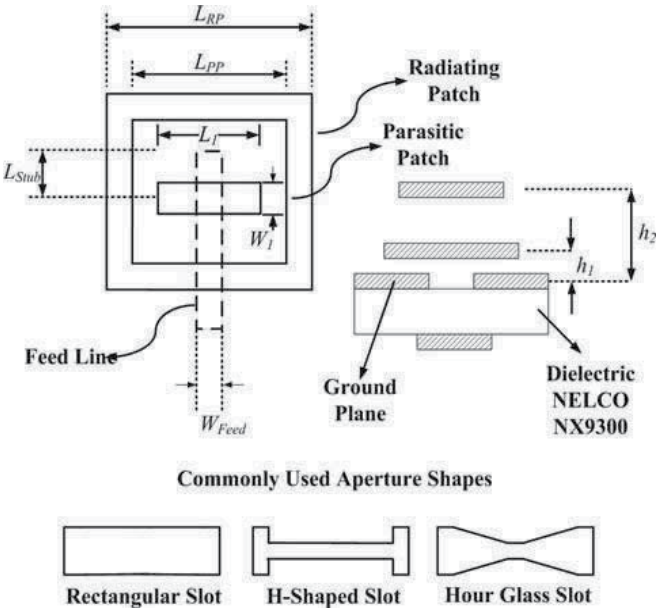

Figure 5. Aperture-coupled antenna and possible aperture shapes.

To compare the antenna performances, FOM_1 (figure-of-merit 1) is defined as GBWP (Eq. (11)) without considering the electrical height and half power beam width (HPBW) of the antenna. We also studied resonant slot coupled patch antenna, pin-feed microstrip antenna (MSA) and resonant slot with two stacked patches (three resonators), all optimized for performance. The results are shown in **Table 2**.

We observe that all nonresonant slot coupled antennas have very similar performance, but hourglass is slightly better than the others. A resonant slot with two stacked patches achieves almost 54% BW.

Antenna	Gain (dBi)	BW	k_0h	FOM_1
H-shaped slot	7.87–9.06	0.275	0.837	2.088
Hour glass slot	7.88–9.07	0.283	0.837	2.150
Rectangular slot	7.89–9.04	0.275	0.837	2.083
Resonant slot	3.51–9.19	0.350	0.736	2.142
Three resonators	5.14–8.88	0.539	0.431	1.314
Pin-fed MSA	9.2–9.3	0.047	0.277	0.401

Table 2. Comparative study based on FOM1.

3.3. Design of a Ku band antenna

Earlier sections have led us to a conclusion on the topology of the element antenna. The final results show that an aperture-coupled stacked patch antenna with an hour-glass shaped

nonresonant aperture would be the best solution for the element antenna. **Figure 6** shows the structure of the antenna to be designed.

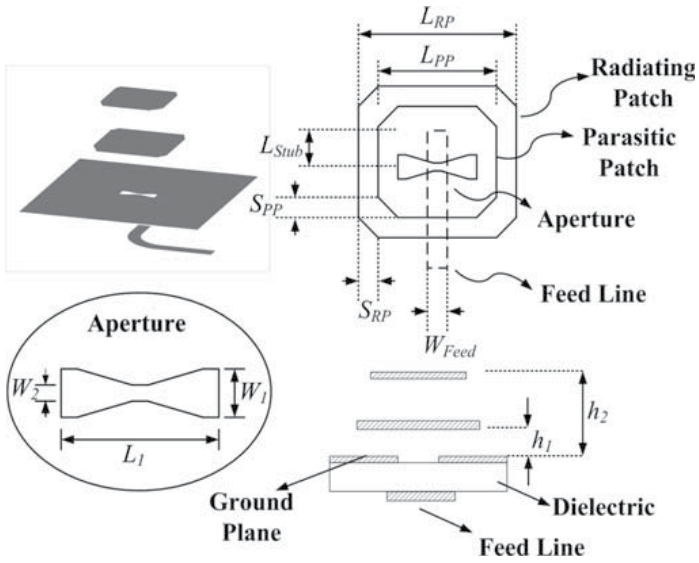

Figure 6. Aperture-coupled stacked microstrip patch antenna.

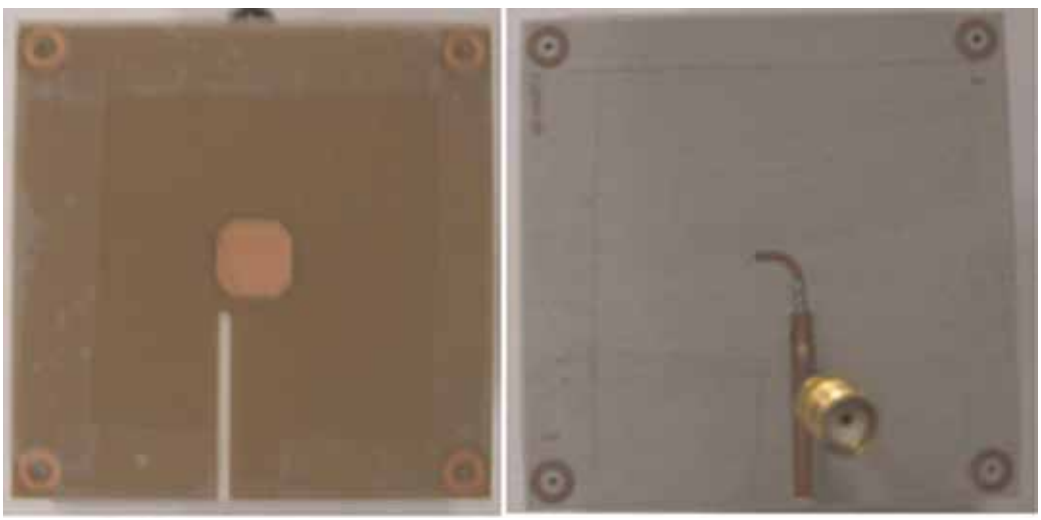

Figure 7. Antenna-prototype: top (patch) side and bottom (feedline) side.

The antenna was optimized through simulations in a commercial full-wave electromagnetic solver to give the best results possible, followed by this optimization the realized antenna is shown in **Figure 7**. Target band is the Ku band downlink frequencies. Radiating and parasitic

http://dx.doi.org/10.5772/66374

patches were formed on flexible PCBs with 75 μm thickness and were placed over the slots using Rohacell HF 31 foam (ε_r = 1.046, tanδ = 0.0017). Measurements were carried out in an anechoic chamber using R&S ZVA40 Network Analyzer, and measurement results are displayed in **Figure 8**. Impedance match bandwidth is defined as |S11| < -9.5 dB (VSWR < 2).

Simulations show that the antenna has 25% FBW with maximum broadside gain of 9.67 dBi at 11.24 GHz. Measured antenna has 29% FBW and maximum broadside gain of 9.5 dBi. In-band gain ripple is less than 0.5 dB, which is also desirable in phased array antenna applications. Broadside gain is greater than 9.3 dBi in 10.8–12.75 GHz frequency band. Vertical polarization principal plane (φ = 0°) radiation pattern at 11.9 GHz, center frequency of Ku band downlink, is shown in **Figure 9**. The HPBW is almost 80°. Due to its wide beamwidth, the antenna can be utilized in electronically beam-tilted phased array antennas. Measurements corroborate well with simulation results in terms of gain, impedance bandwidth, radiation patterns, and HPBW.

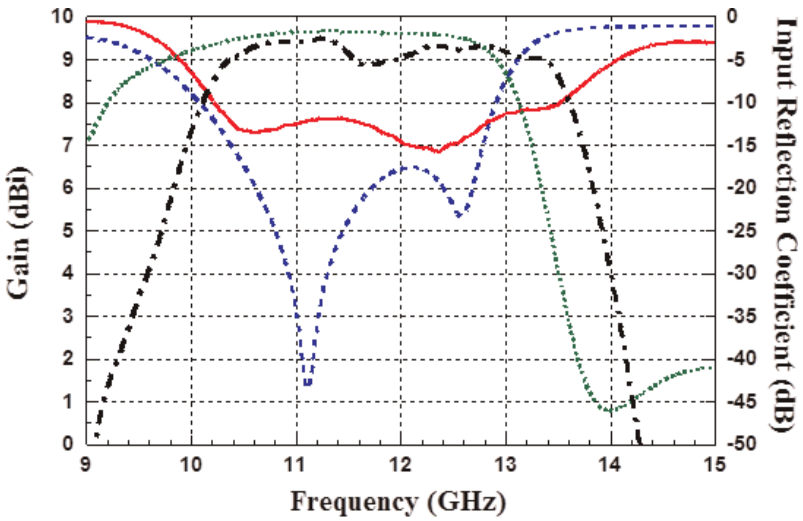

Figure 8. Simulated and measured, gain and input reflection coefficient vs. frequency graphs of aperture coupled antenna (Measured Input Reflection Coefficient, Measured Gain, Simulated Gain, Simulated Input Reflection Coefficient).

3.4. Other FOM definitions and a comparative study with previous antenna designs

In a typical system design, minimum in-band gain is more critical than average gain to satisfy minimum target SNR. Hence, we modified FOM_1 in terms of minimum gain and electrical height of the antenna as:

$$FOM_2 = G_{min} BW \frac{1}{k_0 h} \tag{12}$$

where G_{min} represents the minimum gain throughout the band and $k_0 h$ represents electrical height ($2\pi h/\lambda$) at f_c. Finally, we define a third FOM to include HPBW as:

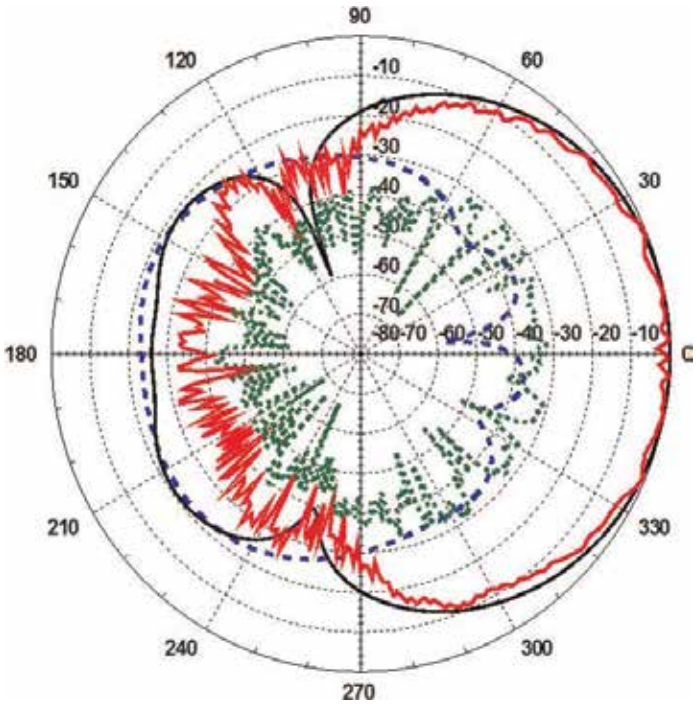

Figure 9. Simulated and measured, normalized gain patterns at 11.5 GHz (Measured Co-Pol pattern, Simulated Co-Pol pattern, Measured X-pol pattern, Simulated X-pol pattern).

$$\mathrm{FOM}_3 = G_{\min}\left(\frac{\mathrm{HPBW}}{\pi}\right)\mathrm{BW}\frac{1}{k_0 h} \tag{13}$$

Table 3 shows a comparative study between this work and some of the previously designed antennas based on the three figure-of-merit definitions, bolded numbers show the best design

Antenna	Gain (dBi)	BW (%)	HPBW/π	k_0h	FOM_1	FOM_2	FOM_3
This work	9–9.5	0.290	0.438	0.868	2.389	**2.118**	**0.929**
[12]	5–7	0.525	0.431	1.452	2.424	1.142	0.493
[14]	7–8.9	0.391	0.444	1.925	2.388	0.642	0.285
[15]	8.2–9.1	0.155	0.437	0.607	1.211	1.806	0.790
[21]	9–9.3	0.110	0.433	0.617	0.905	1.413	0.612
[21]	12–13.9	0.110	N/A	3.539	2.221	0.492	N/A
[22]	8–13.5	0.235	0.138	4.451	**3.485**	0.333	0.046
[23]	9.2–9.7	0.190	0.435	1.007	1.601	1.313	0.571
[24]	8.5–9.17	0.355	0.435	1.171	2.777	1.836	0.799
[25]	6.2 – 6.7	0.040	0.351	0.544	0.187	0.344	0.120

Table 3. Comparative study based on all three figure-of-merits.

based on defined FOM's. It is clear that values obtained in this work are very close to those from [14] in FOM_1 where electrical height is not taken into account. Also values obtained in [22] being the best solution, nearly all the other designs are better than this work. But when the physical dimensions, minimum gain, and half power beamwidths are taken into account; present work is better than all other antennas in FOM_2 and FOM_3. We believe FOM_2 and FOM_3 are critical in array applications as the height of the antenna can be further increased with suspended or inverted substrate etched structures to enhance gain at the expense of increased antenna profile.

4. Array and hybrid microstrip/waveguide feed network design

In third section and its sub-sections, the design of an aperture-coupled stacked microstrip patch antenna was accomplished and the antenna was compared with previous studies. It has proven its value accomplishing the figures-of-merit defined. This section will focus on the array synthesis and the feed network design.

4.1. Array synthesis

There are multiple methods and formations possible to develop an antenna array capable of satisfying the specifications given in **Table 1**. Yet the most important specifications were the maximum dimensions and weight, which were supplied according to the needs of the industry. The system diameter must not exceed 75 cm, the height must be less than 7 cm and the weight must be less than 5 kg. The antenna will have two panels, one for each polarization. Based on these facts, the array should cover an area with lengths less than 73cm × 20 cm. Using array theory, it is possible to synthesize an array of 256 elements with the area of given dimensions. **Figure 10** shows the layout of a two-dimensional array.

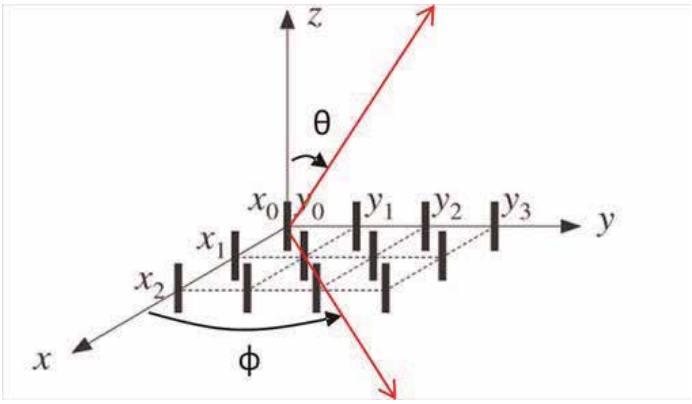

Figure 10. Two-dimensional array.

Let us say that, n and m are the number of elements in the x and y directions, respectively. The interelement spacing in the x and y directions are d_x and d_y, respectively. $xs_{n,m}$ and $ys_{n,m}$ are the

positions of the source antennas on the (x,y) coordinate system. θ_0 and φ_0 are the angles pointing the main beam direction of the antenna pattern. The current distribution of each element being $I_{a,b}$, the array factor of such an array can be written as follows:

$$AF(\theta,\varphi)=\sum_{b=1}^{m}\sum_{a=1}^{n}I_{a,b}e^{j\{\beta[xs_{n,m}(\sin\theta\cos\varphi-\sin\theta_0\cos\varphi_0)+ys_{n,m}(\sin\theta\cos\varphi-\sin\theta_0\cos\varphi_0)]\}} \tag{14}$$

The array antenna in this application should have the highest gain possible. Since the array is a receive-only structure, side lobe levels are not of utmost importance. HPBW in both elevation and azimuth axes are very important for the design due to the physical limits given in the specifications. A trade-off between azimuthal HPBW and gain has been made. For maximum gain, elements in the azimuth axis have been placed 0.82λ (d_y) apart. On the other hand, elements in the elevation axis have been placed 0.73λ (d_x) apart. Spacing in the elevation axis was set in that magnitude so that the phasing of each row would have an electrical phase shift of 90° for a beam pointing at the desired beam angle (θ_0 = 20°, φ_0 = 0°). The array factor given in Eq. (14) would become:

$$AF(\theta,\varphi)=\sum_{b=1}^{32}\sum_{a=1}^{8}A_{a,b}e^{j\{2\pi[0.82(b-16.5)\left(\sin\theta\cos\varphi-\sin(20)\right)+0.73(a-4.5)(\sin\theta\cos\varphi)]\}+\vartheta_{a,b}} \tag{15}$$

where $A_{a,b}$ is the magnitude of current at each element (which is 1, for uniform excitation) and $\vartheta_{a,b}$ is the electrical phasing of each element (90° between each row, uniform in the azimuth axis). **Figure 11** shows the elevation pattern of the synthesized array of 256 which consists of 8 rows and 32 columns.

4.2. Hybrid microstrip and waveguide feed network

Ohmic and dielectric losses tremendously increase in high frequencies, therefore a dramatic loss is perceived by the feed network for large arrays. We must also put the surface wave excitation and radiation losses into account concerning the feed network. The reason that corporate microstrip feed network becomes immensely difficult when combining 256 elements is thus the electrically long microstrip lines. To overcome feed network loss, series feed, parallel feed, series-parallel feed, all waveguide feed and waveguide-microstrip hybrid feed, various techniques were proposed in the past. Waveguide-only feed, i.e., each antenna element being fed into the waveguide, is not attractive due to cost and weight of the die-cast structure. Series, parallel, and their combinations exhibit poor bandwidth performance and only work well for narrowband systems. Most suitable choice would be hybrid microstrip and waveguide feed system, but the size of the corporate feed for the subarray must be carefully determined. Dominant mode waveguides are known for their low loss properties. The crucial aspect of design of such a hybrid structure would be microstrip-to-waveguide transition. For this design, the waveguide must be 6 mm below the feedline, on the other side of a reflecting ground. In the following parts of this section; the design of a low loss microstrip-to-waveguide transition, a detailed analysis on microstrip line and waveguide losses will be discussed and finally the optimum solution for the feed network structure will be calculated.

http://dx.doi.org/10.5772/66374

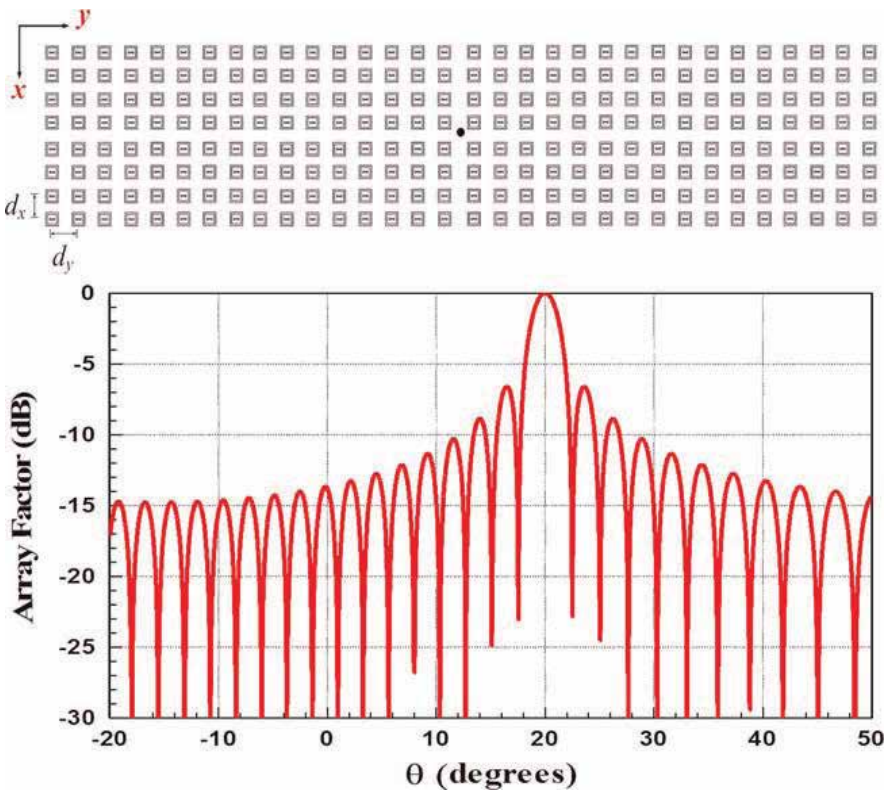

Figure 11. Array factor elevation pattern of synthesized array.

4.2.1. Microstrip feed network losses

The well-known reasons for loss in microstrip lines are conductor losses, dielectric losses, radiation losses, and surface wave losses. Regarding the fields within two guided-wave media, TEM waves do not propagate in microstrip lines. When the longitudinal components of the fields are significantly diminished compared to transverse components, the quasi-TEM approximation is applicable. Equations given below can be found in almost every book about antennas and microwave theory. Although the accuracy of these equations is not that liable for the Ku band, it will provide a fairly satisfying approximation for determining the dimensions of the subarray feed network. Dielectric properties of the substrate that will be used are; dielectric constant (ε_r) 3, loss tangent ($\tan\delta$) 0.0023, thickness (h) 0.5 mm, and copper thickness (t) 35 μm.

The frequency for which the effects of dispersion that can be neglected is calculated from (for h given in mm, f_{dis} is in GHz):

$$f_{\text{dis}} = 0.03\sqrt{\frac{Z_0}{h\sqrt{\varepsilon_r - 1}}} \tag{16}$$

f_{dis} is calculated to be nearly 8 GHz. For a Ku band application, the dispersion effects cannot be neglected. The effects of dispersion mostly affect the relative dielectric constant. Calculations can be modified to include these effects with varying frequencies.

Let W be the width of the feedline and t the copper thickness, the effective feedline width to dielectric thickness ratio can be calculated as:

$$\frac{W_{\text{eff}}}{h} = \frac{W}{h} + \frac{t}{\pi h}\left(1 + \ln\frac{2h}{t}\right) \quad for\ {}^{W}/_{h} \geq {}^{1}/_{2}\ \pi \tag{17}$$

$$\frac{W_{\text{eff}}}{h} = \frac{W}{h} + \frac{t}{\pi h}\left(1 + \ln\frac{4\pi W}{t}\right) \quad for\ {}^{W}/_{h} \leq {}^{1}/_{2}\ \pi \tag{18}$$

Effective dielectric constant can be calculated as:

$$\varepsilon_{\text{eff}} = \frac{\varepsilon_r + 1}{2} + \frac{\varepsilon_r - 1}{2}\left(1 + 12\frac{h}{W_{\text{eff}}}\right)^{-{}^{1}/_{2}} \quad for\ {}^{W_{\text{eff}}}/_{h} \geq 1 \tag{19}$$

$$\varepsilon_{\text{eff}} = \frac{\varepsilon_r + 1}{2} + \frac{\varepsilon_r - 1}{2}\left[\left(1 + 12\frac{h}{W_{\text{eff}}}\right)^{-{}^{1}/_{2}} + 0.04\left(1 - \frac{W_{\text{eff}}}{h}\right)^{2}\right] \quad for\ {}^{W_{\text{eff}}}/_{h} \leq 1 \tag{20}$$

Effects of frequency variations on ε_{eff}:

$$\varepsilon_{\text{eff}}(f) = \frac{\varepsilon_r - \varepsilon_{\text{eff}}}{1 + (0.6 + 0.009Z_0)\left(\frac{8f\pi h}{Z_0}\right)^{2}} \tag{21}$$

Characteristic impedance Z_0 can be calculated by:

$$Z_0 = \frac{60}{\sqrt{\varepsilon_{\text{eff}}(f)}}\ \ln\left(8\frac{h}{W_{\text{eff}}} + 0.25\frac{W_{\text{eff}}}{h}\right) \quad for\ {}^{W_{\text{eff}}}/_{h} \geq 1 \tag{22}$$

$$Z_0 = \frac{{}^{120\pi}/_{\sqrt{\varepsilon_{\text{eff}}(f)}}}{\frac{W_{\text{eff}}}{h} + 1.393 + 0.667\ln\left(\frac{W_{\text{eff}}}{h} + 1.44\right)} \quad for\ {}^{W_{\text{eff}}}/_{h} \leq 1 \tag{23}$$

Wavelength:

$$\lambda = \frac{\lambda_0}{\sqrt{\varepsilon_{\text{eff}}(f)}}\left[\frac{\varepsilon_{\text{eff}}(f)}{1 + 0.63\left(\varepsilon_{\text{eff}}(f) - 1\right)\left(\frac{W_{\text{eff}}}{h}\right)^{0.1255}}\right]^{{}^{1}/_{2}} for\ {}^{W_{\text{eff}}}/_{h} \geq 0.6 \tag{24}$$

$$\lambda = \frac{\lambda_0}{\sqrt{\varepsilon_{\text{eff}}(f)}}\left[\frac{\varepsilon_{\text{eff}}(f)}{1 + 0.6\left(\varepsilon_{\text{eff}}(f) - 1\right)\left(\frac{W_{\text{eff}}}{h}\right)^{0.0297}}\right]^{{}^{1}/_{2}} for\ {}^{W_{\text{eff}}}/_{h} \leq 0.6 \tag{25}$$

From these equations, one can easily calculate the width (W) for 50 Ω line at the Ku band mid frequency, to be 1.055 mm. The total loss in a feedline can be calculated from the sum of the attenuation constants for α_c (conductor loss), α_d (dielectric loss), α_{surf} (surface loss) and α_{rad} (radiation loss). Since we are trying to practically calculate the losses of a microstrip feed network for an antenna array, the length of the feedline will be found to be greater than 5λ.

http://dx.doi.org/10.5772/66374

For this reason, the effects of radiation and surface wave losses can be neglected since their effects are small compared to the conductor and dielectric losses.

Conductor losses can be calculated by:

$$\alpha_c = 20\log e^{\frac{1}{Z_0 W_{\text{eff}}}\sqrt{\frac{\pi f \mu_0}{\sigma_c}}} \tag{26}$$

Dielectric losses can be calculated by:

$$\alpha_d = 20\log e^{\frac{2\pi\varepsilon_r\left(\varepsilon_{\text{eff}}(f)-1\right)\tan\delta}{\lambda(\varepsilon_r-1)\sqrt{\varepsilon_{\text{eff}}(f)}}} \tag{27}$$

4.2.2. Microstrip to waveguide transition losses

The transition geometry involves copper disk and dielectric loaded pin for wideband match and low loss. The geometry of the transition is illustrated in **Figure 12**. In order to register all ohmic losses of this design, the transition was modeled using a full-wave electromagnetics solver where waveguide is aluminum and the probe is copper. Simulated results for insertion loss and transmission loss are shown in **Figure 12**. Prototype of the disk-loaded transition was manufactured and measurements were carried out. Input reflection coefficient was below 15 dB and the loss for this transition was measured to be 0.78 ± 0.02 dB in the desired frequency band.

4.2.3. Waveguide combiner losses

In hybrid system, one must take the loss in the waveguide combiner into account as well for quantification. Instead of a typical E-type combiner, an H-type waveguide was chosen. The major reason to prefer this design was to decrease the height of the WR75 waveguide. Because the electric field lines are set parallel to longitudinal axis of the guide. Unlike the E-plane combiner, the output ports are in phase with each other as well resulting in no need for phase compensation. Moreover, it is easier to realize this waveguide since one is able to cut into one of the longer sections of waveguide in order to machine its remaining part from die-cast as well. Summary of all losses are presented in **Table 4**. Given these parameters, the size and form of the subarrays and waveguide sections can be designed.

4.2.4. Optimizing the hybrid feed network

An optimization problem for minimum feed network loss can be formulated and solved for subarray size. Layout of a general array is illustrated in **Figure 13**. Number of elements in x- and y-directions is denoted as N and M, respectively. Let N_S and M_S represent the number of elements in the subarray.

The number of levels for single output can be expressed as:

$$\log_2 NM = \log_2 N_s M_s + \left(\log_2 \frac{N}{N_s} + \log_2 \frac{M}{M_s}\right) \tag{28}$$

where $\log_2 N_S M_S$ and ($\log_2 N/N_S + \log_2 M/M_S$) represent number of levels in the subarray and in the waveguide, respectively. Loss in the hybrid combiner can be stated as:

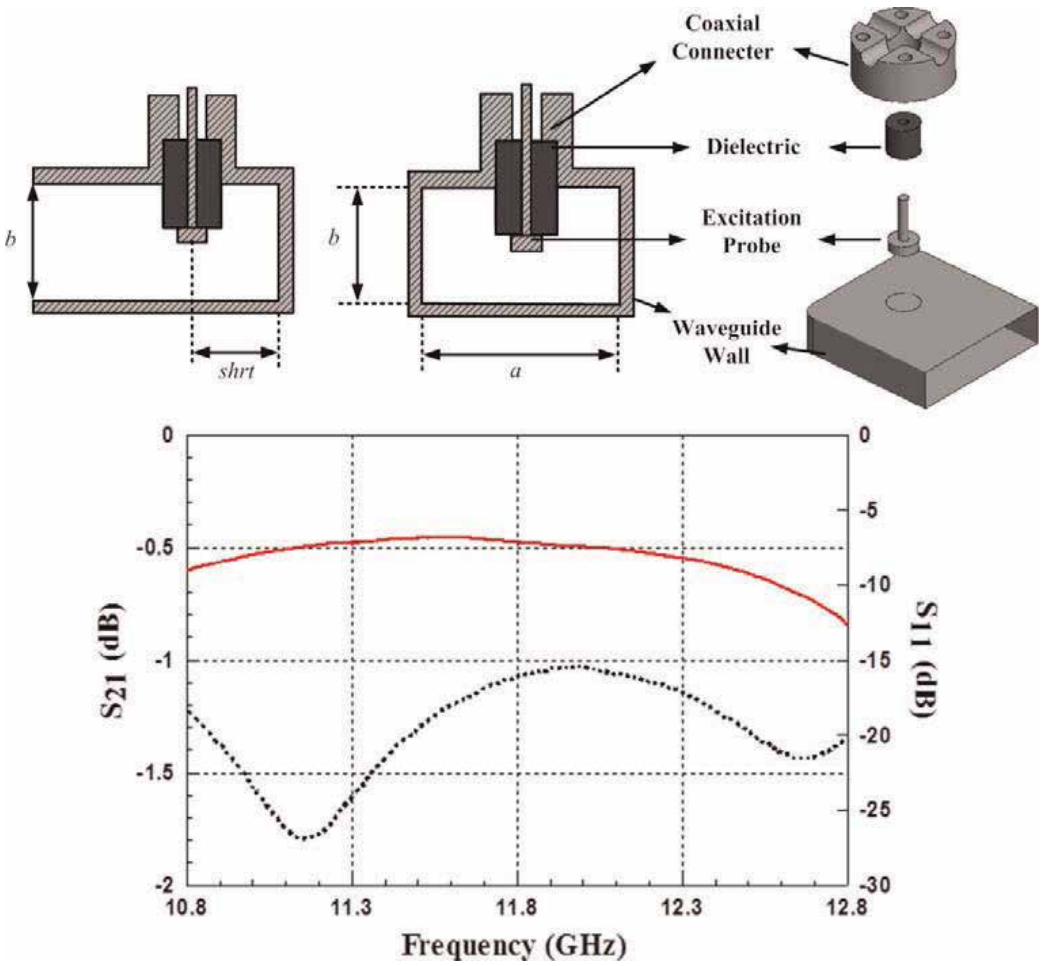

Figure 12. Microstrip line to waveguide transition and simulation results.

$$\left(\log_2 \frac{N}{N_s} + \log_2 \frac{M}{M_s}\right) L_{T,WG} + L_{\text{TRANS}} = L_1 \tag{29}$$

where $L_{T,WG}$ and L_{TRANS} are waveguide T-junction losses and microstrip to waveguide transition losses. A single transition is found to be effective while calculating the corporate feed

Component	Value
Microstrip line	0.072 dB/cm
Microstrip T-junction	0.11 dB
Microstrip-to-waveguide transition	0.78 dB
Waveguide T-junction	0.12 dB

Table 4. Summary of losses.

http://dx.doi.org/10.5772/66374

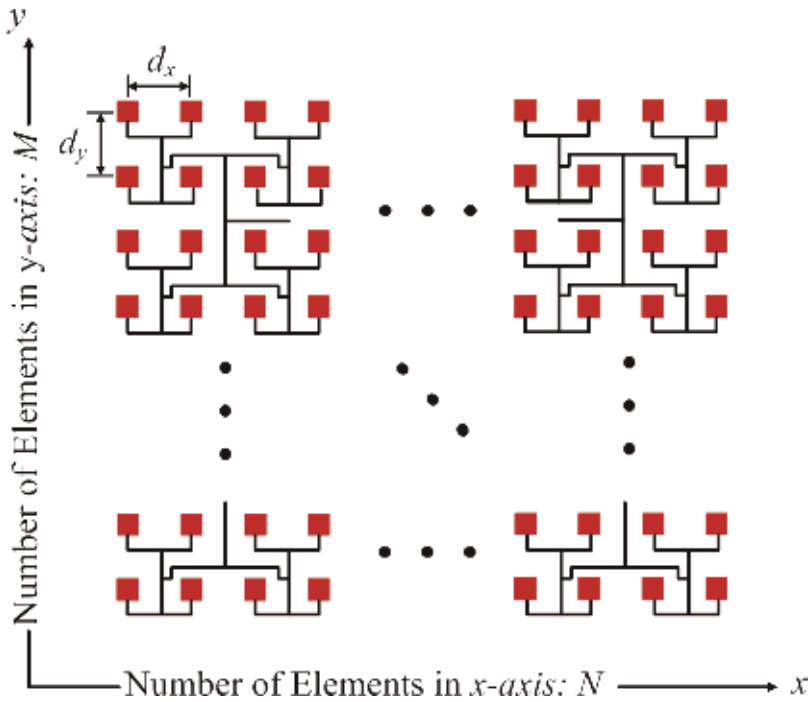

Figure 13. Layout of the feed network.

network loss in spite of the various (NM/N_SM_S) transitions in the waveguide. Loss in microstrip lines could be written as follows:

$$\left(\frac{d_x + d_y}{2} + \left(\frac{N_s}{2} - 1\right)d_x + \left(\frac{M_s}{2} - 1\right)d_y\right)L_{MS} + (\log_2 N_s + \log_2 M_s)L_{T,MS} = L_2 \tag{30}$$

where d_x, d_y represent interelement spacing in x and y directions, and denote microstrip T-junction loss and microstrip line loss, respectively. Microstrip line loss includes ohmic and dielectric losses and it is calculated for a 50 Ω straight line section. Then, total loss becomes:

$$L_{tot} = L_1 + L_2 \tag{31}$$

Furthermore, for corporate feed N, M, N_S and M_S must be multiples of 2, i.e., $N = 2^n$, $M = 2^m$, $N_s = 2^{n_s}$, and $M_s = 2^{m_s}$. Total loss can be restated as:

$$(n - n_s + m - m_s)L_{T,WG} + (n_s + m_s)L_{T,MS} + L_{TRANS} + (2^{n_s - 1}d_x + 2^{m_s - 1}d_y + l)L_{MS} = L_{tot} \tag{32}$$

where l represents $-(d_x + d_y)/2$. Optimization function for minimization of loss for subarray size n_s and m_s can be formulated as follows:

$$\begin{gathered} minimize\ L_{tot}(n_s, m_s)\forall \quad n_s, m_s \in Z^+ \\ Subject\ to \\ 1 \le n_s \le \min(n, m) \\ 1 \le m_s \le \min(n, m) \\ w(n_s, m_s) \le 3\text{kg} \end{gathered} \tag{33}$$

where $w(n_s, m_s)$ is the weight of the waveguide combiner, and dimensions of the subarray cannot is determined to be smaller than the full array size in all directions. The waveguide feed network consists most of the weight. Differing structures in the range of 4:1 to 64:1 gave way to the design of different waveguide feed networks (commercial full-wave electromagnetic solver) and models (CAD program for mechanical design). The weights of waveguide combiners were calculated according to aluminum alloy 6068 used in die-cast machines. Consequently, it was found that the required weight condition could only be reached for equal to 8:1 or smaller combiner structures. For instance, a 16:1 waveguide combiner (in which the elements in the subarray are 16) weighs 4.3 kg. Hence, the constraint on weight is replaced with $(n_s + m_s) > 5$. At a minimum of 32 elements is required in x-direction to obtain 3° HPBW in azimuth because a sum of 256 elements ($n + m = 8$) is utilized in the full array. Hence, m and n are set to 3 and 5, respectively (8 and 32 elements). It is now possible to have a solution for the optimization issue for subarray dimensions (n_s, m_s). Constrained nonlinear optimization was utilized to find (n_s, m_s) as (3, 2), and the optimal solution was found to have total loss of 2.16 dB. Since waveguide and microstrip T-junctions were overestimated, the realized loss will probably be lower than the calculated value.

The size of the subarray is set to 4 × 8 (32 elements total) and the subarrays are combined as 8:1 in the waveguide. We also observed that if we were able to use an alternative material such as electro-form-plated dielectric material, it was possible to reduce weight, which would enable a larger combiner that had less total loss.

5. Realization of the Ku band antenna and measurement results

The previous sections have led to the conclusion that the 256-element array antenna would consist of 8 rows and 32 columns. Further analysis on losses in the feed network components has shown that four row, eight column (32 elements) subarrays, where antenna elements are combined by microstrip feedline networks would give optimal performance and have an acceptable loss. Eight subarrays will then be combined by a reduced height waveguide combiner. This section will conclude with the design of each component and build both the vertical and horizontal polarization arrays.

5.1. Design of 4 × 8 (32-element) arrays

The Ku band array antenna is divided into eight subarrays for each polarization. Within each subarray, corporate feed network is used. Although corporate feed network has more loss than parallel feed network, it has much wider impedance bandwidth when tapered microstrip lines and tapered T-junctions are used. Each antenna input was defined as a 50

Ω port and *S*-parameters of 33-port network (32 for antennas and 1 for output port) were optimized for match, uniform power distribution, bandwidth, and minimum port-to-port coupling. Following that, as terminating loads in the feed network, simulated input impedance values of 32 antenna elements were placed. Finally, the layout was driven for the best match at the combined output. Vertical and horizontal subarrays for a fixed 20° elevation tilt are shown in **Figure 14**. Antiphase feeding between upper and lower parts of the vertical polarization subarray is used to reduce microstrip line lengths for required phasing (90°) between the rows of the array. The same technique was not possible to implement in the horizontal polarization subarray due to perpendicular orientation of coupling slots underneath feedlines. Element spacing along longer axis (azimuth tilt direction) and along shorter axis (elevation tilt direction) of the subarray is 0.82λ and 0.73λ, respectively.

Figures 15–17 show the realized antennas and their measurement results. The results show that the realized antennas have a minimum of 19 dBi gain throughout the desired bandwidth. A good matching lower than -10 dB is also achieved throughout the desired bandwidth.

5.2. Design of 8-to-1 waveguide power combiner

The optimum value for the waveguide combiner was calculated to be an 8-to-1 combiner, with reduced height. **Figure 18** shows a sketch drawing of the waveguide combiner.

Most of the losses and the power division take place in the bends and T-junctions. **Figure 19** shows a closer view of the waveguide junctions and bends. The parameters in **Figure 19** are the main optimization parameters. Optimizer goals were to minimize losses and have better impedance match less than -15 dB throughout the desired bandwidth. The most crucial component in the design of such divider is the position of the shorting probe. **Figure 20** shows the surface current of optimized combiner section. Optimized results are given in **Figure 21**. **Figure 21** (bottom graphic) shows the transition characteristic at all ports; simulations estimate the worst case, a loss of 0.5 dB.

5.3. Complete array realization and measurement results

The prototype antenna with all subarrays is built and the prototype is displayed in **Figure 22**. The performance of a dish antenna was taken as a reference for comparison. A parabolic reflector with corrugated circular feed horn (an existing commercial antenna) was also modeled for this purpose to be named "the reference antenna." This reference antenna exhibits similar performance to that of a 40 cm diameter dish antenna except that it has a lower profile. The simulation model with a great number of unknowns made it impossible to simulate full array with waveguide feed network. This resulted in the separate simulations of the planner array and the waveguide feed network to calculate both their S-parameters which led to the combination of these two results to get the final array performance. Measurements and simulations of planar array for input impedance match and gain at 20° tilt are displayed in **Figures 23** and **24**. Both the planar array and reference antenna showed in their gain simulations that they quantify similarly. Whereas

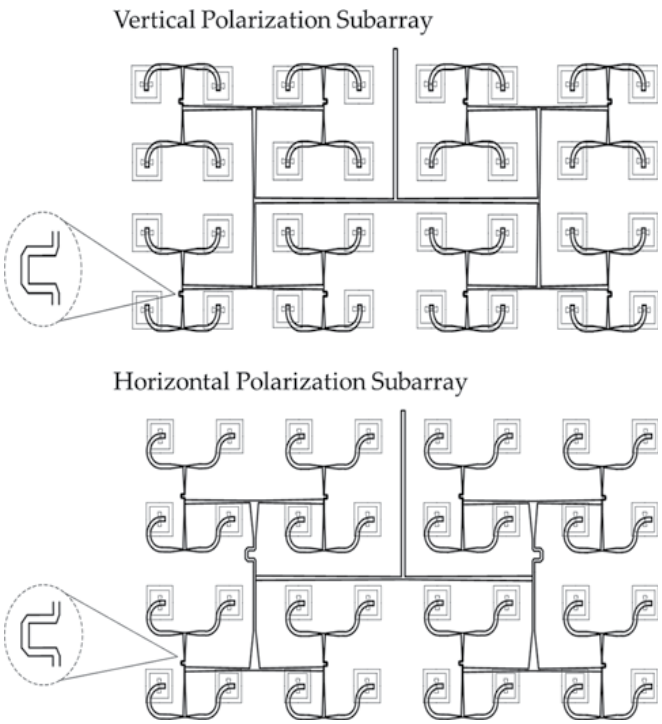

Figure 14. 32 element subarray configurations for vertical polarization and horizontal polarization.

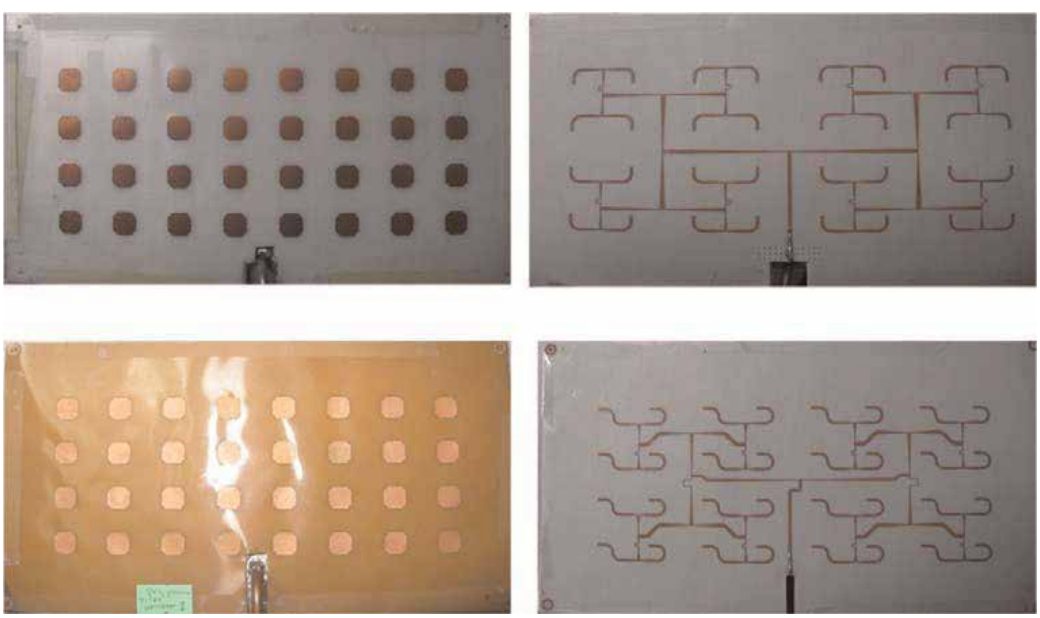

Figure 15. Realized vertical (top two pictures) and horizontal (bottom two pictures) subarray antennas.

http://dx.doi.org/10.5772/66374

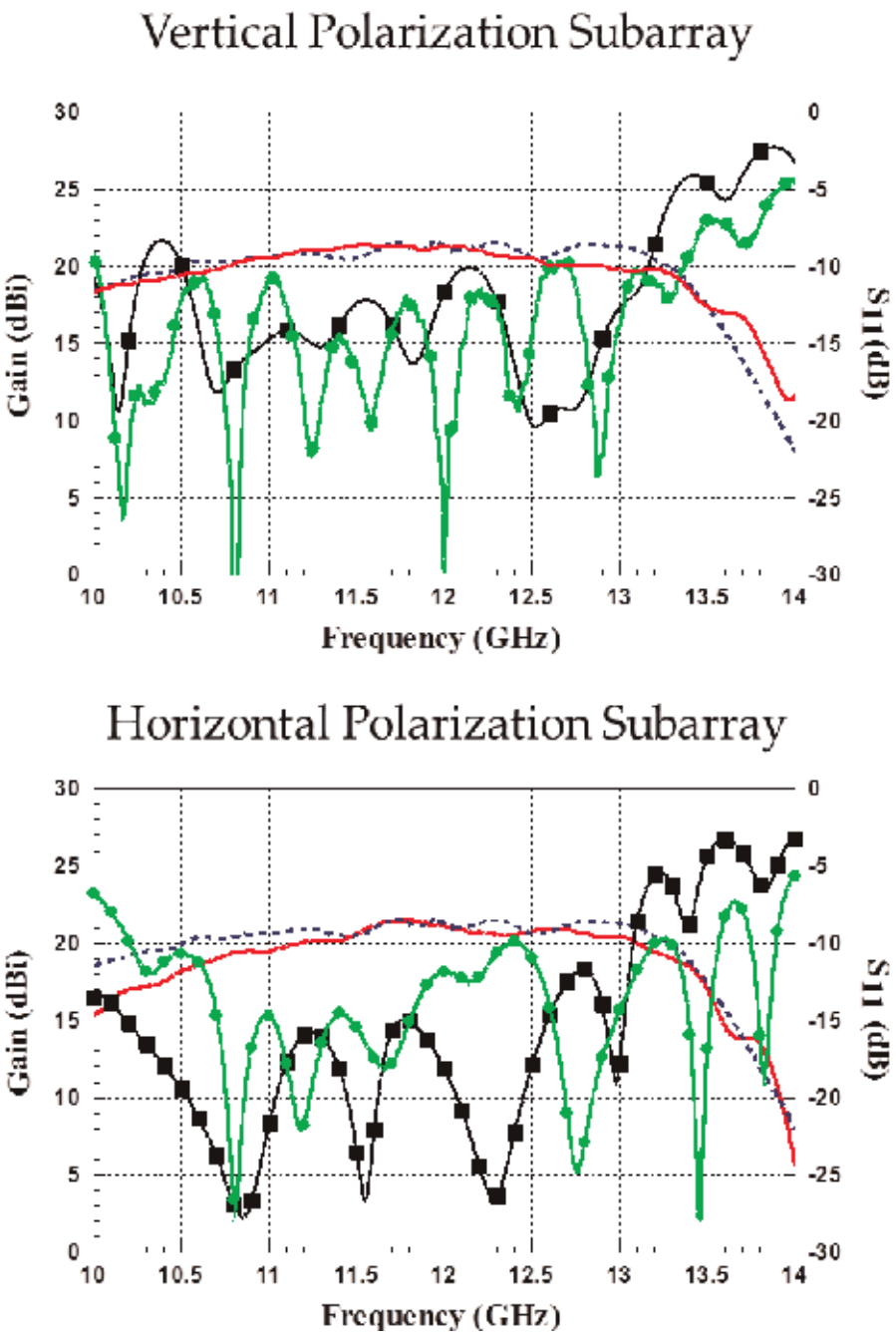

Figure 16. Input reflection coefficient and gain of 32 element subarrays (Measured Gain, Simulated Gain, Measured S11, Simulated S11).

when comes to measured gain, it was lower than the simulated gain because of the waveguide-to-coax adapter that was utilized in the measurements and for the nonideal

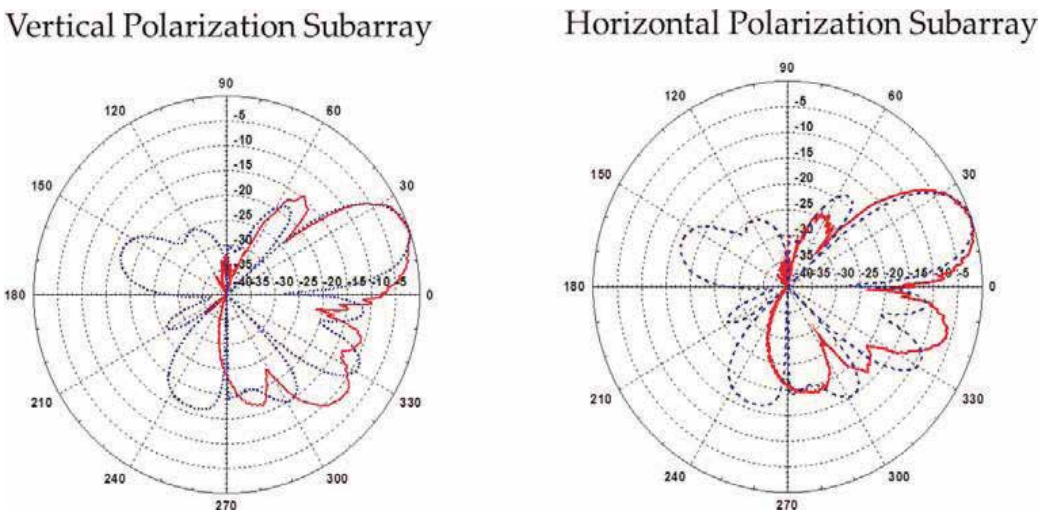

Figure 17. Normalized radiation pattern of 32-element subarray at 11.9 GHz (φ = 0°, elevation patterns) (Measured Gain, Simulated Gain).

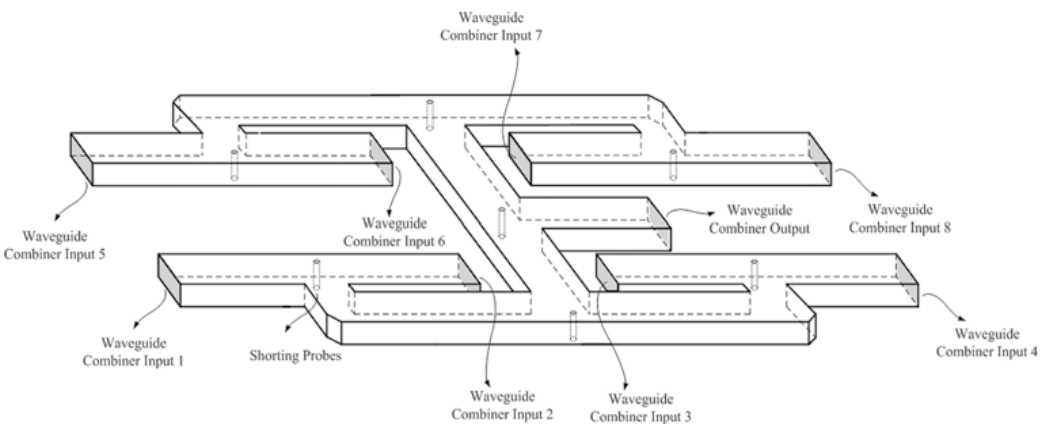

Figure 18. 8-to-1 power combiner.

simulation set-up. However, over entire target frequency band, the measured gain at desired tilt angle was found to be greater than 28.4 dBi. Planar array gain is 1.2 dB lower than the expected value from array theory. The radiation patterns of planar array at 20° tilt angle for azimuth and zenith cuts are shown in **Figure 25** and **Figure 26**. Measured $HPBW_\theta$ and $HPBW_\varphi$ are 8 and 2.5°, respectively. If the antenna was designed for broadside reception, its gain would have been definitely higher. The aperture efficiency of the planar array is between 57 and 67% over the target frequency band (**Figures 25–27**).

http://dx.doi.org/10.5772/66374

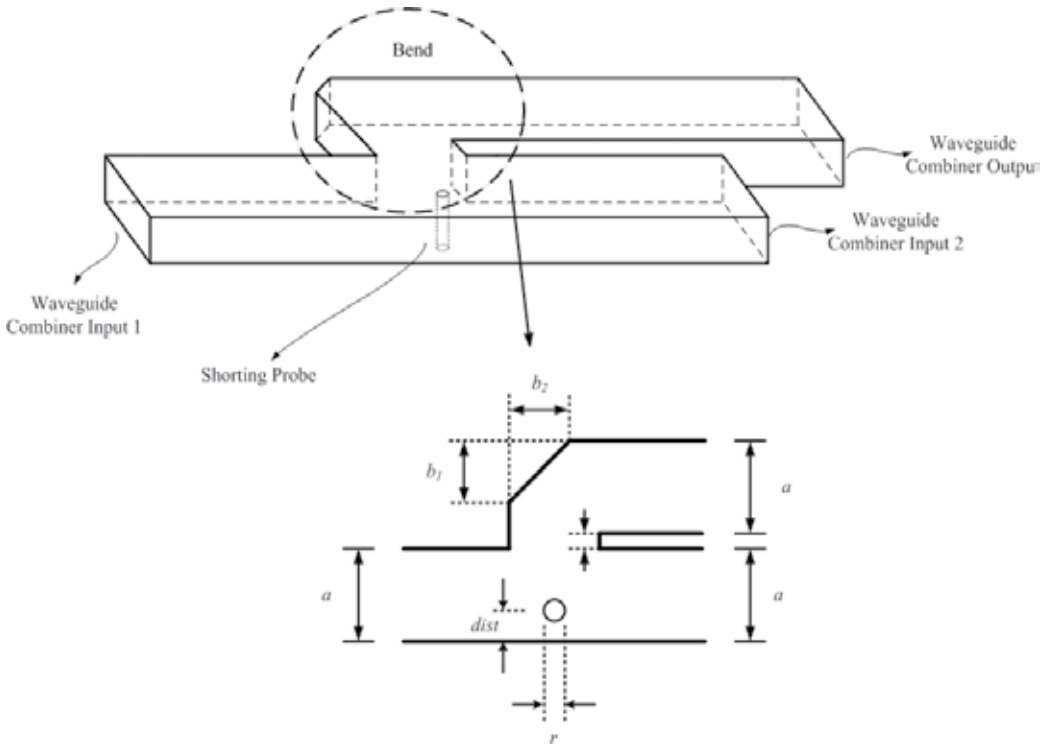

Figure 19. Waveguide bends and junctions.

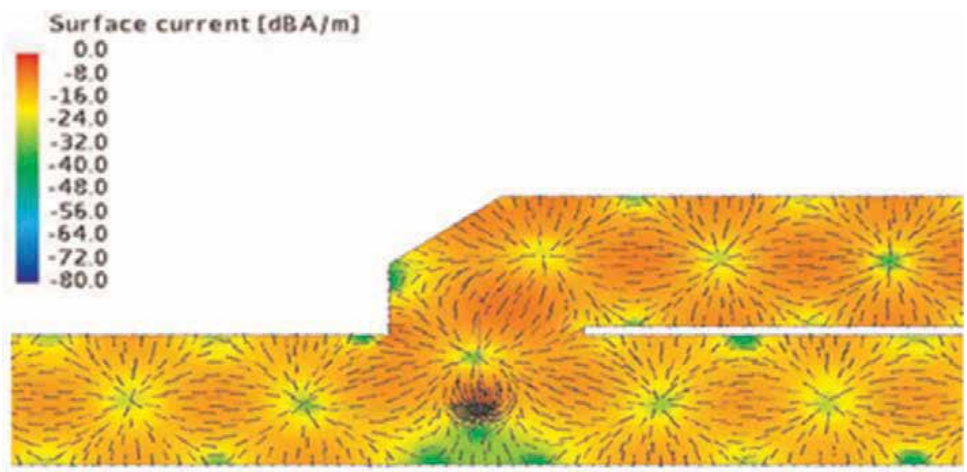

Figure 20. Simulation of surface currents on the waveguide combiner.

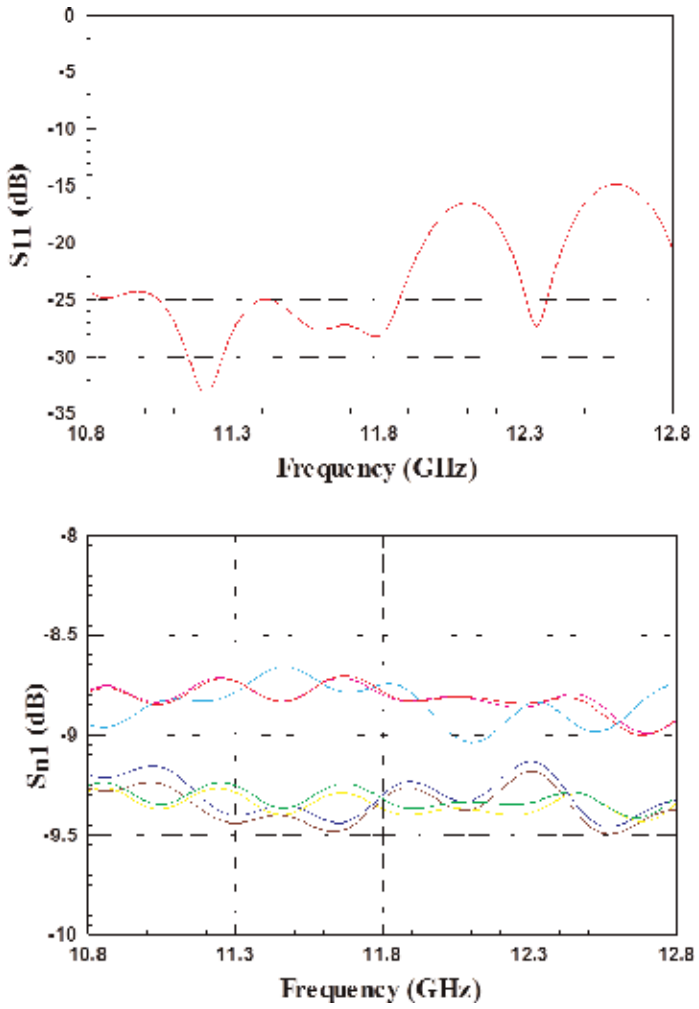

Figure 21. Simulated input reflection coefficient at combiner output (top), simulated transmission coefficients of 8-to-1 power combiner (bottom).

The designed array antenna has also been field-tested for signal quality and satellite reception with an LNB and a receiver. The IF loop output of the receiver was connected to the Rohde & Schwarz FSH-8 GHz spectrum analyzer. Signal from transponders was observed to have an average CNR of 9.5 dB. In **Figure 28**, the measurement results are given. Reception quality retrieved from the receiver digital outputs was above 65%, which is slightly lower than that of the reference antenna (71%).

http://dx.doi.org/10.5772/66374

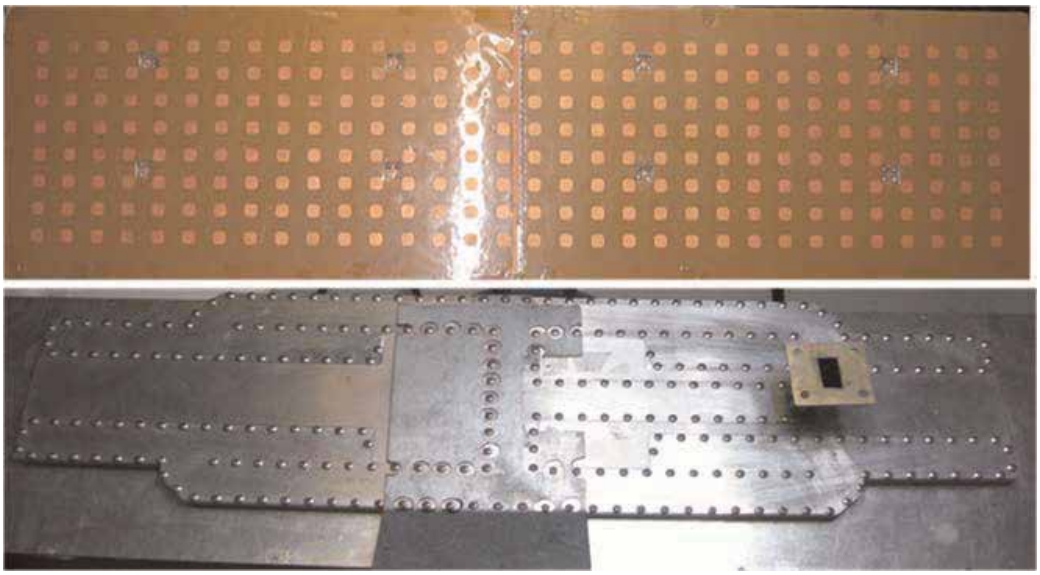

Figure 22. Prototype of vertical polarization 256-element array (dimensions: 70.73 cm × 18.23 cm × 2.43 cm, the height of the waveguide adapter is excluded from dimension).

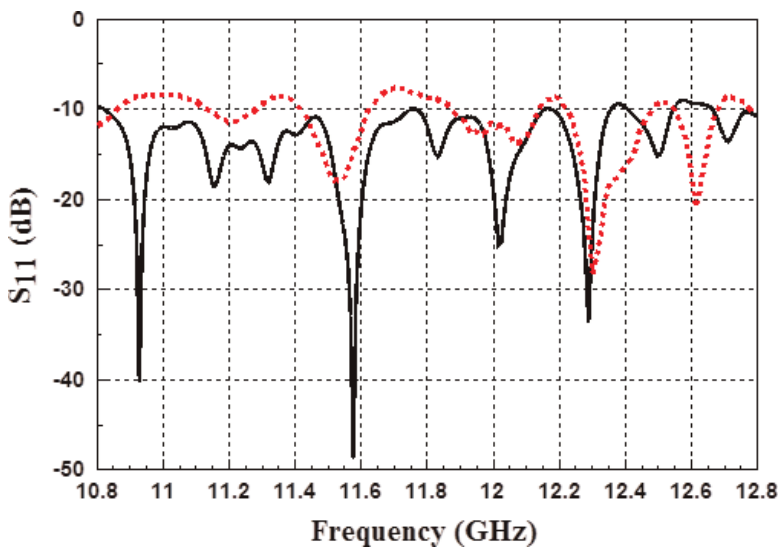

Figure 23. S11 of array antenna. (Measured, Simulated).

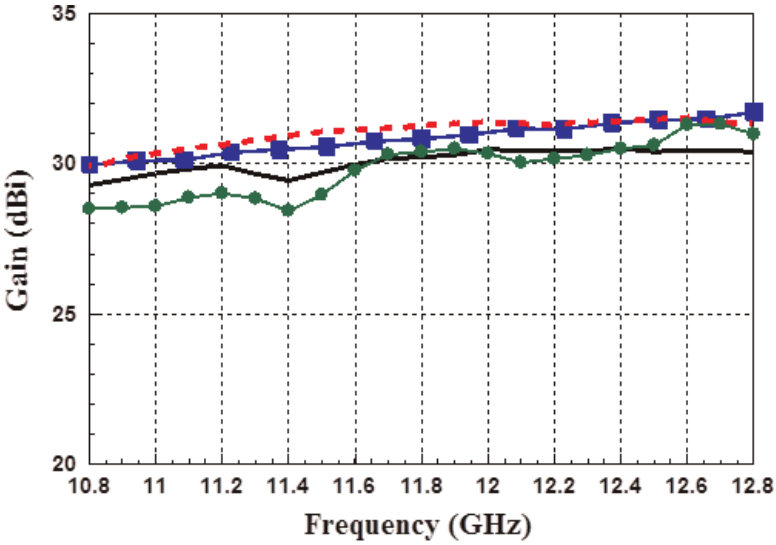

Figure 24. Gain of array antenna (θ = 20°cut) (Measured Vertical Polarization, Measured Horizontal Polarization, Simulated 256 Element Array, Simulated Reference).

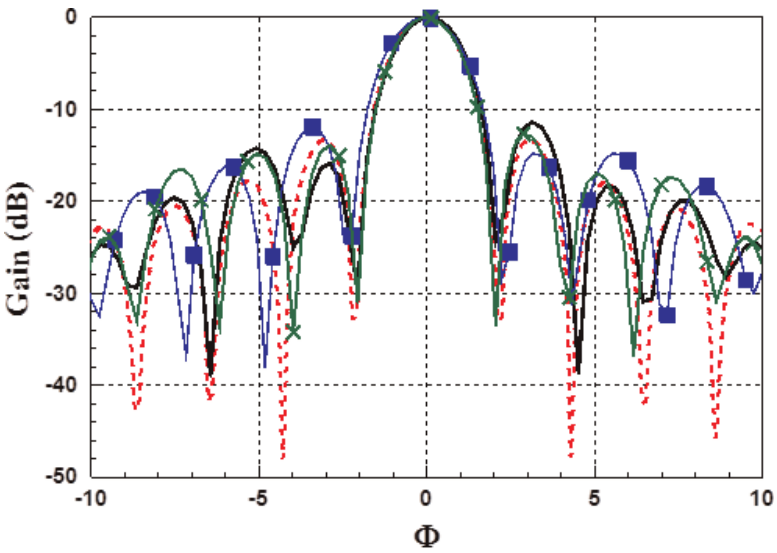

Figure 25. Radiation pattern of vertical polarized full array in azimuth plane (θ = 20°cut). (Measured @ 11.9 GHz, Simulated @ 11.9 GHz, Measured @ 10.8 GHz, Measured @ 12.8 GHz).

http://dx.doi.org/10.5772/66374

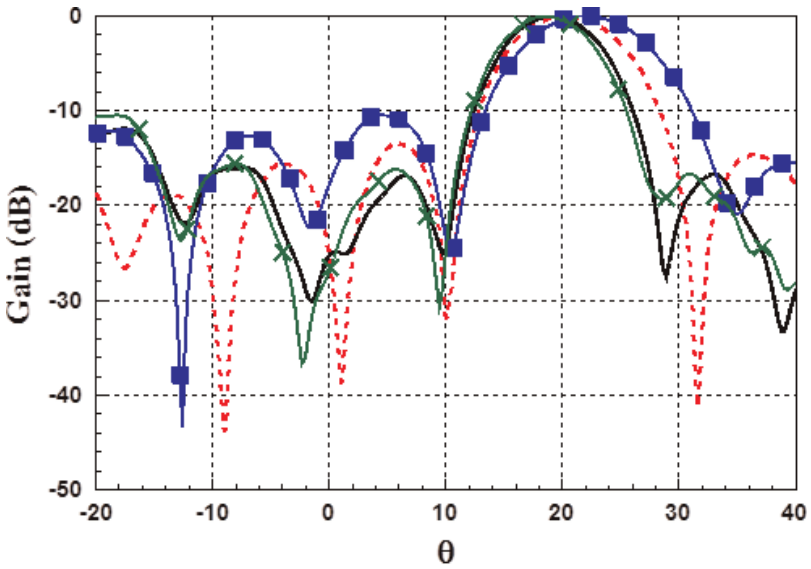

Figure 26. Radiation pattern of vertically polarized full array in φ-plane (φ=0° cut) (Measured @ 11.9 GHz, Simulated @ 11.9 GHz, Measured @ 10.8 GHz, Measured @ 12.8 GHz).

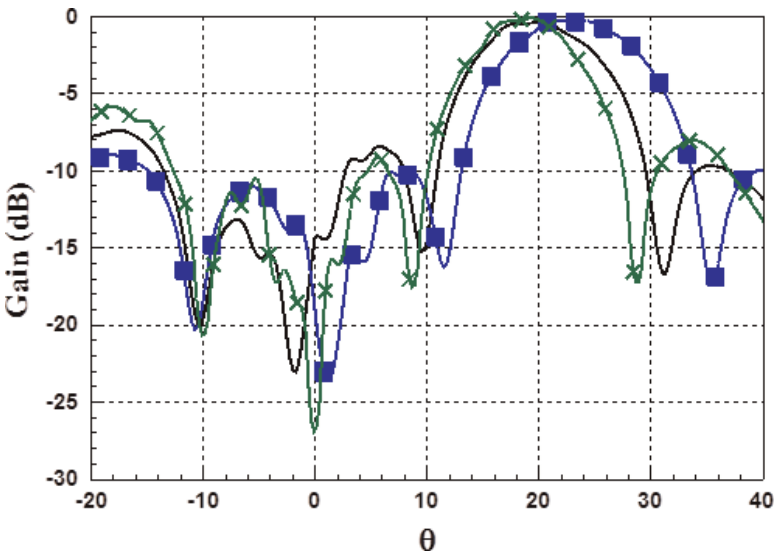

Figure 27. Radiation pattern of horizontally polarized full array in φ-plane (φ=0° cut) (Measured @ 11.9 GHz, Measured @ 10.8 GHz, Measured @ 12.8 GHz).

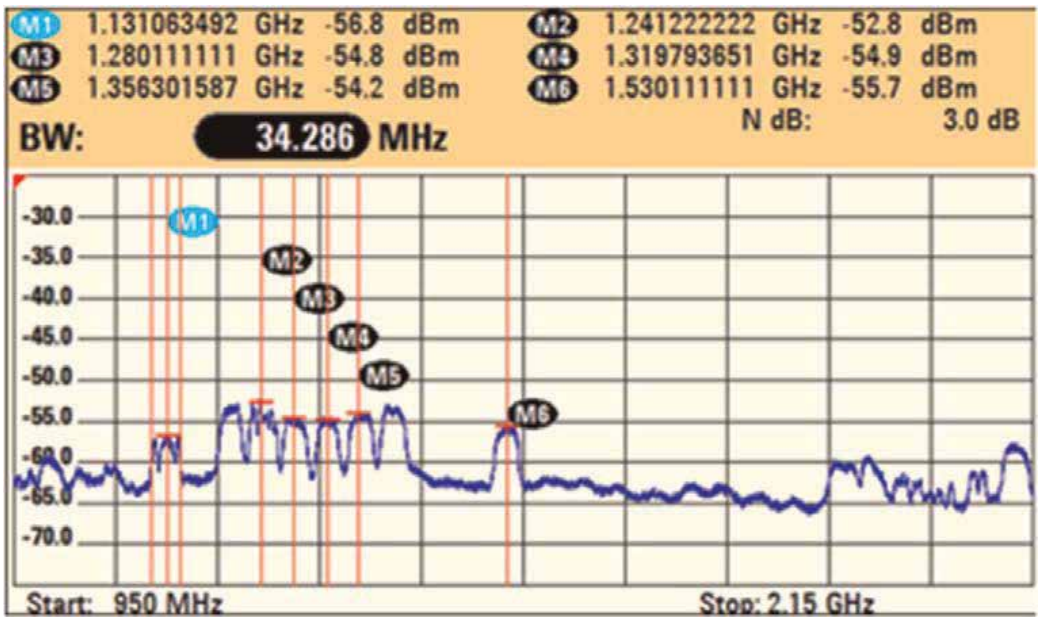

Figure 28. Spectrum analyser measurement of DBS signal.

Author details

Mustafa Murat Bilgic[1]* and Korkut Yegin[2]

*Address all correspondence to: proje@unitest.com.tr

1 Unitest Test and Calibration Services, Istanbul, Turkey

2 Electrical and Electronics Engineering Department, Ege University, Izmir, Turkey

References

[1] Watanabe T., Ogawa M., Nishikawa K., Harada T., Teramoto E., Morita M. Mobile antenna system for direct broadcasting satellite. In: Antennas and Propagation Society International Symposium; 21–26 July 1996; Baltimore, MD, USA. IEEE; 1996. pp. 70–73, vol.1. DOI: 10.1109/APS.1996.549544

[2] Vaccaro S., Tiezzi F., Rúa M., De Oro C. Ku-band low-profile Rx-only and Tx-Rx antennas for mobile satellite communications. In: 2010 IEEE International Symposium on Phased Array Systems and Technology (Array); 12–15 Oct. 2010; Waltham, MA. IEEE; 2010. pp. 536–542. DOI: 10.1109/ARRAY.2010.5613316

[3] Xiang H., Jiang X., Li S. Design of a high gain low sidelobe microstrip antenna array at Ku-band. In: CMC '09 WRI International Conference on Communications and Mobile Computing; 6–8 Jan. 2009; Yunnan. IEEE; 2009. pp. 29–32. DOI: 10.1109/CMC.2009.204

[4] Azdegan R. A Ku-band planar antenna array for mobile satellite TV reception with linear polarization. IEEE Transactions on Antennas and Propagation. 2010; **58** (6):2097–2101. DOI: 10.1109/TAP.2010.2046836

[5] Shahabadi M., Busuioc D., Borji A., Safavi-Naeini S. Low-cost, high-efficiency quasi-planar array of waveguide-fed circularly polarized microstrip antennas. IEEE Transactions on Antennas and Propagation. 2005; **53**(6):2036–2043. DOI: 10.1109/TAP.2005.848510

[6] Kraus J. D., Marhefka R. J. Antennas. 3rd ed. Chapter 2-Basic Antenna Concepts Singapore: McGraw-Hill Education; 2001. 938 p.

[7] McLean J. A re-examination of the fundamental limits on the radiation Q of electrically small antennas. IEEE Transactions on Antennas and Propagation. May 1996; **44**(5). DOI: 10.1109/8.496253

[8] Yaghjian A., Best S. Impedance, bandwidth and Q of antennas. IEEE Transactions on Antennas and Propagation. 2005; **53**(4):1298–1324. DOI: 10.1109/TAP.2005.844443

[9] Pozar D. Microstrip antenna aperture-coupled to a microstripline. Electronics Letters. 1985; **21**(2):49–50. DOI: 10.1049/el:19850034

[10] Kumar G., Ray K. P. Broadband microstrip patch antennas. Chapter 4-Multilayer Broadband MSAs, Artech House; London,United Kindom, 2003. 424 p.

[11] James J. R., Hall P. S. Handbook of Microstrip Antennas: IET; London, United Kindom, 1989. 1312 p.

[12] Targonski S., Waterhouse R., Pozar D. Wideband aperture coupled stacked patch antenna using thick substrates. Electronics Letters. 1996;**32**(21):1941–1942. DOI: 10.1049/el:19961306

[13] Pozar D., Targonski S. Improved coupling for aperture coupled microstrip antennas. Electronics Letters. 1991; **27**(13):1129–1131. DOI: 10.1049/el:19910705

[14] Serra A., Nepa P., Manara G., Tribellini G., Cioci S. A wide-band dual-polarized stacked patch antenna. IEEE Antennas and Wireless Propagation Letters. 2007; **6**:141–143. DOI: 10.1109/LAWP.2007.893101

[15] Rostan F., Gottwald G., Heidrich E. Wideband aperture-coupled microstrip patch array for satellite TV reception. In: Eighth International Conference on Antennas and Propagation; 1993; Edinburgh. IET; pp. 190–193, vol. 1.

[16] Jackson D. R., Alexopoulos N. G. Simple approximate formulas for input resistance, bandwidth, and efficiency of a resonant rectangular patch. IEEE Transactions on Antennas and Propagation. 1991; **39**(3):407–410. DOI: 10.1109/8.76341

[17] Gera A. The radiation resistance of a microstrip element. IEEE Transactions on Antennas and Propagation. 1990; **38**(4):568–570. DOI: 10.1109/8.52277

[18] Pues H., Van de Capelle A. Accurate transmission-line model for the rectangular microstrip antenna. IEE Proceedings in Microwaves, Optics and Antennas. December 1984; **131**(6):334–340. DOI: 10.1049/ip-h-1.1984.0071

[19] Das B., Joshi K. Impedance of a radiating slot in the ground plane of a microstripline. IEEE Transactions on Antennas and Propagation. 1985; **30**(5):922–926. DOI: 10.1109/TAP.1982.1142922

[20] Edimo M., Mahdjoubi K., Sharaiha A., Terret T. Simple circuit model for coax-fed stacked rectangular microstrip patch antenna. IEE Proceedings—Microwaves, Antennas and Propagation. 1998; **145**(3):268–272. DOI: 10.1049/ip-map:19981853

[21] Choi W., Cho Y. H., Pyo C., Choi J. A high-gain microstrip patch array antenna using a superstrate layer. ETRI Journal. 2003; **25**(5):407–411.

[22] Pirhadi A., Bahrami H., Nasri J. Wideband high directive aperture coupled microstrip antenna design by using a FSS superstrate layer. IEEE Transactions on Antennas and Propagation. 2012; **60**(4):2101–2106. DOI: 10.1109/TAP.2012.2186230

[23] Choi W., Kim J. M., Bae J. H., Pyo C. High gain and broadband microstrip array antenna using combined structure of corporate and series feeding. In: Antennas and Propagation Society International Symposium; 20–25 June 2004; IEEE; 2004. pp. 2484–2487, vol. 3. DOI: 10.1109/APS.2004.1331877

[24] Lee J., Ahn C., Chang K. Broadband circularly polarized aperture-coupled microstrip antenna with dual-offset feedlines. In: IEEE International Symposium on Antennas and Propagation (APSURSI); 3–8 July 2011; Spokane, WA. IEEE; 2011. pp. 1127–1130. DOI: 10.1109/APS.2011.5996481

[25] Mousavi P., et al. A Low-cost ultra low profile phased array system for mobile satellite reception using zero-knowledge beam forming algorithm. IEEE Transactions on Antennas and Propagation. 2008; **56** (12):3667–3679. DOI: 10.1109/TAP.2008.2005928

Section 4

Applications of Microwave Systems

Chapter 12

Noninvasive Electromagnetic Biological Microwave Testing

Dalia M.N. Elsheakh, Esmat A. Abdallah and
Hala A. Elsadek

Additional information is available at the end of the chapter

http://dx.doi.org/10.5772/64773

Abstract

Blood glucose monitoring is a primary tool for the care of diabetic patients. At present, there is no noninvasive monitoring technique of blood glucose concentration that is widely accepted in the medical industry. New noninvasive measurement techniques are being investigated. This work focuses on the possibility of a monitor that noninvasively measures blood glucose levels using electromagnetic waves. The technique is based on relating a monitoring antenna's resonant frequency to the permittivity, and conductivity of skin, which in turn, is related to the glucose levels. This becomes a hot researched field in recent years. Different types of antennas (wideband and narrowband) have been designed, constructed, and tested in free space. An analytical model for the antenna has been developed, which has been validated with simulations. Microstrip antenna is one of the most common planar antenna structures used. Extensive research development aimed at exploiting its advantages such as lightweight, low cost, conformal configurations, and compatibility with integrated circuits have been carried out. Rectangular and circular patches are the basic shapes that are the most commonly used in microstrip antennas. Ideally, the dielectric constant ε_r, however, and other performance requirements may dictate the use of substrate whose dielectric constant can be greater. As in our prototype blood sensor, the miniaturized size is one of the main challenges.

Keywords: microstrip patch antenna (MPA), microstrip cavity resonator biosensor (MCRB), blood glucose monitoring (BGM), diabetic patients (DP), specific absorption rate (SAR), Federal Communications Commission (FCC), radio frequency (RF), Federal Drug Association (FDA), ground penetrating radar (GPR)

1. Introduction

Electromagnetic radiation consists of waves of electric and magnetic energy moving together (i.e., radiating) through space at the speed of light. Biological hazardous effects can results from the exposure to electromagnetic (radio frequency, RF). The main effect is the thermal effects that raise the temperature of the tissues exposed to the electromagnetic waves radiation. The electromagnetic energy effect could be harmful in normal routines. FCC's policies and rules regulate the exposure and absorption of RF energy by certain healthy thresholds. The SAR (specific absorption rate) is the federal standard term used to determine safety limits for usage of wireless handheld devices as mobile phones. The standard FCC limit for such devices is 1.6 W/kg of tissues (average over one gram of tissue). The FCC does not normally investigate problems of transmitting/receiving interference with medical devices such as in hospitals. However, the FDA's center for devices and radiological health has primary check for medical usage regulations.

The used blood glucose monitors nowadays require an amount of blood (its volume about 2–10 μL) and can be taken from fingertips or any other site in the human body. It is a painful measurement. Although blood glucose measurements fluctuate much more than HbA1c measurements (where HbA1c = mmol/mol), there is a strong correlation between HbA1c measurements and average glucose measurements taken over the same time period. While it has been shown that continuous monitoring systems are more effective in adjusting blood glucose to recommended levels, adolescents and young adults often have difficulty adhering to this intensive invasive treatment. For this reason, noninvasive monitoring systems would be preferred. GMS can cost several thousand dollars, and while blood monitors are relatively inexpensive, the disposable electrodes become costly over time. The noninvasive glucose monitoring techniques have been divided into the following categories: interstitial fluid chemical analysis, breath chemical analysis, infrared spectroscopy, optical coherence tomography, temperature-modulated localized reflectance, Raman spectroscopy, polarity changes, ultrasound, fluorescence, thermal spectroscopy, ocular spectroscopy, and impedance spectroscopy. Currently, monitoring blood glucose concentration is the most frequently measured through invasive techniques. The most popular noninvasive method are interstitial fluid chemical analysis, breath chemical analysis, fluorescence, ocular spectroscopy, and RF transmission.

Each type of wave has a different wavelength and corresponds to a different frequency range in the electromagnetic spectrum. This means that these wavelengths are between 1 mm and 1 m. Because of these longer wavelengths range, microwaves are more capable of penetrating through various materials [when the electric field passes through the dielectric medium, the medium has an effect on the electric field called permittivity (ε)]. Different tissues in the human body have different contents of water and hence have different permittivities since permittivity depends on water molecules, which is due to the polarization of water molecules when it exposed to an electromagnetic field. When the frequency increased the water molecules line up very slowly, which causing energy storing in the tissues.

http://dx.doi.org/10.5772/64773

The real part of the material complex permittivity indicates the energy storage of that material, while the imaginarily part is the loss tangent factor that indicates the amount of electric field energy lost when passing through the material. Fortunately, most biological materials have permeability close to that of the free space; hence, the permeability is not a concern during text involving blood glucose levels, hence allowing the tests to concentrate on measuring the change in dielectric (permittivity) properties of the material. Measuring dialectic properties can indicate indirect measures of other properties that have a relation to the molecular structure of the material.

Different tissues in the human body have different contents of water and hence have different permittivities since permittivity depends on water molecules, which is due to the polarization of water molecules when exposed to an electromagnetic field. When the frequency increased, the water molecules line up very slowly, which causing energy storing in the tissues. While the real part of relative permittivity drops off in distinct steps as the frequency increases; therefore, it experiences something called dispersion. Each dispersion region occurs at different frequency ranges and presents different effects of electromagnetic waves on the body. The interaction of the blood glucose and any dielectric material surrounding the antenna will cause a change in the antenna characteristics. This is due to the fact that all bodies have complex relative permittivities which will interact with the antenna. As one parameters of the antenna performance is the resonance frequency which can be correlated to be blood glucose concentration. It should be noted that the range of changing the glucose level is narrow in the nondiabetic as compared to the range of changing the glucose level in diabetic patients.

An antenna is a structure, usually made from a good conducing material that has been designed to have a shape and size such that it will act as an electromagnetic sensor that radiates/receives power in an efficient manner. It is a well-established fact that time-varying currents will radiate electromagnetic waves. Thus, an antenna is a structure on which time-varying currents can be excited with relatively large amplitude when the antenna is connected to a suitable source, usually by means of a transmission line or waveguide. There is an endless variety of structural shapes that can be used for an antenna. However, from a practical point of view, those structures that are simple and economical to fabricate are the most commonly used.

For many applications, the advantages of microstrip antennas outweigh their limitations. Initially, microstrip antennas found widespread applications in military systems such as missiles, rockets, aircrafts, and satellites. Currently, these antennas are being increasingly used in the commercial sector at different applications due to the reduced cost of the dielectric substrate material and mature fabrication technologies. With continued research and development and increased usage, microstrip antennas are ultimately expected to replace conventional antennas for most applications such as mobile and satellite applications, radar antennas, Wi-Fi applications, and biomedical application.

There are many researches done on how the electrical properties of the human blood and cells that human body composed of are various due to biological effects. Microwaves are appearing in biomedical engineering applications with ever-increasing frequency. They are being used for different applications as brain imaging, breast cancer detection, and blood virus detection.

A good understanding of the electromagnetic characteristics in biological materials is required to have effective models.

One of these researches for noninvasive test is to design a micro-immunosensing diagnostic assay called "microstrip cavity resonator biosensor (MCRB)," which was used for the diagnosis of enterovirus; however, the technology can then be modified for rapid, sensitive diagnosis of other viral diseases. The diagnostic method is based on the classical antigen antibody reaction; the complex antigen antibody can be diagnosed through the use of reflection coefficient, input impedance, and resonance frequency of the microstrip cavity resonator biosensor. The values of these parameters change according to changing of the electrical properties of the tested samples, such as dielectric constant, electrical conductivity, and resistivity, from case of normal sample layer to infected sample layer with antigen/antibodies embedded. Software can be developed for automatic reading, classifying, and determining the sample infection. The use of microwave biosensor for rapid detection of the viruses limits the need for sophisticated laboratory diagnostic methods that needs long time and expert scientist to perform the test. Clearly, these blood or any clinical samples diagnostic systems are required to be developed to reach small, lightweight, robust, unobtrusive design that can be mobilized in any place. It should maintain high performance in terms of reliability and efficiency. The printed antenna presents a significant miniaturization solution for such mobile systems. The antenna acts as microstrip cavity resonator biosensor (MCRB) with performance that is directly related to the biological material super imposed layer's physical properties. The antenna design for such measurement system has a tradeoff between design parameters as efficiency, bandwidth, and radiation characteristics from one side and the accuracy and sensitivity of the measurements from the other side. It is widely accepted that antenna performance is significantly affected by close proximity to the human body. One can conclude that there is a lot of nondestructive testing concerning the noninvasive electromagnetic biological testing. What have been introduced are just two examples of using nondestructive testing in biology.

Ground penetrating radar (GPR) is used for searching on the biological material underground as mummies, excavations, and water. Ground penetrating radar (GPR) is a noninvasive or nondestructive, sub-surface imaging method that has showed a lot of success in a wide range of fields regarding geological, geotechnical, hydrological, environmental, and archaeological applications. As aforementioned, GPR technique uses an antenna pair to send EM energy into the ground and then record the returning signals. Therefore, this antenna pair has a crucial importance in affecting the overall system performance. Ground penetrating radar systems need antennas that radiate efficiently over a broad range of frequencies.

This chapter is organized as follows: Section 1 introduces nondestructive tests and it includes three examples, namely noninvasive glucose monitoring technique, the microwave biosensor for rapid detection of the viruses, and the ground penetrating radar. Section 2 introduces a background about the invasive glucose monitoring techniques and some statics about the number of diabetic people all over the world and also some economic view. It also gives a glance about the noninvasive glucose monitoring techniques that have been heavily researched over the past several decades. The problem definition is presented in Section 3 and differentiating between Type 1 and Type 2 diabetics. Section 4 introduces the methodology which the

http://dx.doi.org/10.5772/64773

relation between the permittivity and biological modeling, some measurements on simulating sugar water as well as the design of wide band and narrow band antenna analysis. Section 5 gives a study about the microstrip cavity resonator biosensor (MCRB), and it gives a clear idea about the mobile virus diagnosis system. The ground penetrating radar system is given in Section 6 together with the design and simulation of two antennas that are used with GPR, namely the quasi-Yagi antenna and the miniaturized log-periodic dipole antenna. Simulation and measurements are given in this section. Conclusions are given in Section 7, followed by acknowledgments.

2. Background

Diabetes mellitus often refer to as diabetes is a group of metabolic diseases in which a person has high blood sugar. This high blood sugar will often cause symptoms of frequent urination, increased hunger, and increased thirst. The two types that affect the general population are known as Type 1 and Type 2 diabetes. Blood glucose concentration represents the amount of sugar in the blood of the human being, and it is measured in mg/dl. Diabetic patients suffer from the body inability to control insulin production and hence have danger sugar level. This will cause danger health problems on the future of the patient. There are two types of blood sugar level, namely hypoglycemic (concentration less than 72 mg/dl) and hyperglycemic (concentration greater than 200 mg/dl) [1, 2]. The diabetic patient should measure the glucose level in blood every day.

Once on at least from economic view in 2003, the cost of treating diabetes was estimated to be $132 billion. By 2020, it is estimated that the number of people diagnosed with diabetes could rise to over 17 million, costing an estimated $192 billion [3]. While there is no cure for diabetes, symptoms are controlled through the regulation of blood glucose levels. There are several types of measurements that can be used to monitor glucose regulation. Once in the blood stream, glucose combines with hemoglobin found in red blood cells (erythrocytes) to create glycated hemoglobin. The hemoglobin will remain glycated for the life of the erythrocyte, typically 90–120 days [4]. This makes concentration measurement the best indication of average blood glucose concentration. While measurements are the best method of long-term control, self-monitoring of blood glucose levels is fundamental to diabetes care. Frequent monitoring avoids hypoglycemia, and aids in determining dietary choices, physical activity, and insulin doses. Nowadays blood glucose measurements require an amount of blood ranging from 2 to 10 μL from fingertips or any place in the patient body, and this is considered a painful measurements. While current blood glucose monitors require small amounts of blood (2–10 μL) and can be used at sites other than the fingertips, it is still a painful and tedious measurement. Although blood glucose measurements fluctuate much more than HbA1c measurements (where HbA1c = mmols/mol), there is a strong correlation between HbA1c measurements and average glucose measurements taken over the same time period [5]. In order to reduce the blood glucose level of a patient to the recommended level, continuous monitoring system should be done. This intensive treatment is very difficult to patient, which is the reason for searching about a noninvasive monitoring technique. On the other hand, the

mummy's container (cartonnage, coffin, or sarcophagus) or on linen wrappings and included papyrus scrolls in sometimes contain biological bodies.

2.1. Invasive glucose monitoring techniques

Current glucose monitoring devices are extremely similar to the devices originally created in the 1960s. Aside from the miniaturization, ease of use, and the ability to log data, the measurements fundamentally are the same as the first laboratory sensors. There are several downsides to the current offerings of glucose meters. The blood meters require a blood sample, which is a painful procedure. CGMS can cost several thousand dollars, and while blood monitors are relatively inexpensive, the electrodes are disposable and become costly over time. A single-use blood electrode strip costs about 2$, and a CGMS 3–7 day sensor can cost 30–35$ as shown in **Figures 1** and **2**.

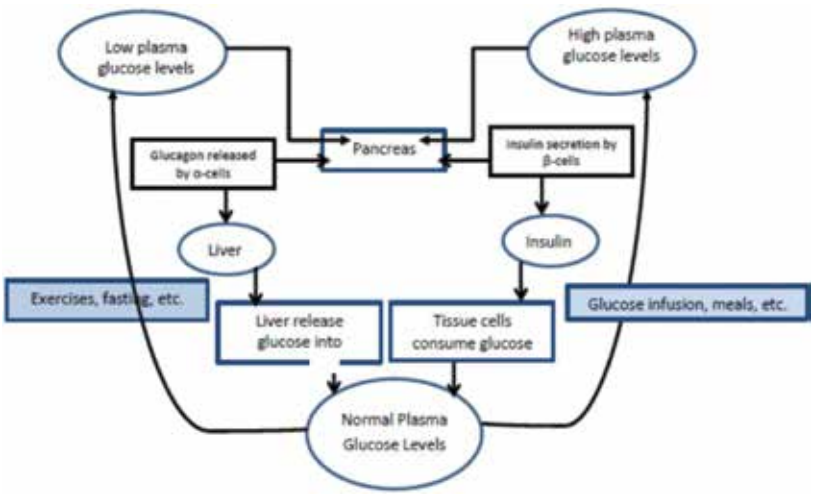

Figure 1. Typical blood glucose control system and simplified glucose measurement method.

Figure 2. Life scan OneTouch Ultra glucose meter (left), and Medtronics CGMS (right).

http://dx.doi.org/10.5772/64773

2.2. Noninvasive glucose monitoring techniques

Noninvasive glucose monitoring techniques have been heavily researched over the past several decades. They have been divided into the following categories: interstitial fluid chemical analysis, breath chemical analysis, infrared spectroscopy, optical coherence tomography, temperature-modulated localized reflectance, Raman spectroscopy, polarity changes, ultrasound, fluorescence, thermal spectroscopy, ocular spectroscopy, and impedance spectroscopy. Currently, monitoring blood glucose concentration is the most frequently measured through invasive techniques. Noninvasive blood glucose monitors offer a solution to measure proper blood glucose levels without puncturing the skin.

The following have been noninvasive; non-RF techniques have been tried [5–8]:

2.2.1. Interstitial fluid chemical analysis [9]

This technique is similar to the traditional monitoring methods since it needs the patient to switch out disposal pads for each measurement. It depends on the interaction between the enzyme and the fluids excreted from the skin. A product appeared in the market in the form of a watch using the interstitial fluid chemical analysis.

2.2.2. Breath chemical analysis [10]

It measures the level of acetone from a breath. Higher levels of acetone have been correlated to higher levels of blood glucose concentration. This method is, however, not as accurate as traditional blood glucose meters.

2.2.3. Fluorescence [11]

It is radiating from the skin and can track the level of blood glucose. The skin tissue is excited using an ultraviolet laser, and fluorescence is emitted at 380 nm. The intensity of the fluorescence can be correlated to a glucose level.

2.2.4. Ocular spectroscopy [12]

The contact lens interacts with the tears from an eye as the contact lens is illuminated by a light source; the color of the reflected light can be correlated with a blood glucose concentration. It shows promising returns.

2.2.5. RF transmission [13]

It uses two antennas to monitor blood glucose concentration noninvasively. Two matched antennas transmit and receive in a two port measurement. The transmission occurs between 5.3–5.5 GHz. The test was performed on a water-glucose solution to mimic testing on a human.

3. Problem definition

Healthcare expenditures whether by the health system or the patents reached 11% of the total healthcare in the word in 2011 (141 billion US$). Most of the countries spend between 5% and 18% of their total healthcare expenditures on diabetes. As regard Egypt, the mean healthcare expenditures was 175 US $/diabetic patient. Because of the seriousness and variability of the disease, regular testing for diabetics is required where number of tests per person vary from one to four times each day. Test strips used in daily testing are relatively expensive, costing around $1.00 per strip [4]. Over a year of testing at average twice per day, the patient will spend $730 on test strips alone and in 2020 an estimated 17.4 million people will be diagnosed with costs near $192 billion [4]. Due to the increase in the population with diabetes and the increase in the costs in treating diabetes, it is fast becoming necessary to develop new ways to test diabetes that are noninvasive, less expensive, and easy to use at home. Diabetes mellitus, more commonly known only as diabetes, is "a disease in which the body does not produce or properly use insulin" [5]. About 90–95% of the diabetes patients are of Type2 diabetes. This is characterized from the hyperglycemia which is due to impaired insulin utilization together with the body's inability to compensate increased insulin production. About 5–10% of diabetes patients are of Type 1 diabetes, which is the most dangerous type. It occurs during childhood and adolescence. It happens due to a severe deficiency of insulin secretion resolution resulting from atrophy of the islets of langerhans [5–6].

Developments for noninvasive techniques to measure blood glucose level come from the fact that Type 1 diabetics should test two times daily, and even four to six times may be required for proper monitoring in order not to result in life threatening due to misusage to insulin.

All invasive blood glucose monitors require the user to prick a finger, palm, or forearm with a lancet so that a small droplet of blood can be collected. These devices use electrochemistry of the testing strip to determine glucose levels. Each strip contains 10 layers of spacers and chemicals, including glucose oxidase and microcrystalline potassium ferricyanide. The ranges vary between meters, and the readings are not linear over the entire range; therefore, readings that are either very high or very low are open for interpretation and need to be confirmed by repeated measurements or measurements taken by a different meter [14]. According to the FDA, the goal of all future self-monitoring blood glucose systems should be able to achieve a variability of 10% at glucose concentrations of 30–400 mg/dL 100% of the time. With current systems, measurements should be within 15% of a minimally invasive method which is one that does not use subcutaneous sampling or sensors in fatty tissue to collect blood. Instead it uses percutaneous needles or sensors in the dermal layer where there are less nerve endings at sites other than the fingers to collect or react with interstitial fluid or blood. However, there are no FDA approved minimally invasive devices with sensors or sampling probes for continuous monitoring [15]. Noninvasive methods require no puncturing of the skin for testing purposes.

http://dx.doi.org/10.5772/64773

4. Approach and methodology

Microwaves occupy the frequencies in the electromagnetic spectrum ranging from 300 MHz to 300 GHz, which represents different types of waves. Some of the most common types of waves encountered are radio waves, UHF waves, microwaves, infrared rays, visible light, and X-rays. Each type of wave has a different wavelength and corresponds to a different frequency range in the electromagnetic spectrum [15]. The wavelengths of microwaves can be determined by the equation.

$$\lambda = \frac{C}{f} \tag{1}$$

where C is the light velocity in free space = 3×10^8 m/s.

This means these wavelengths are between 1 mm and 1 m length. Because of these longer wavelengths, microwaves are more capable of penetrating through various materials. Most measurement tools used today tend to only be able to measure wavelengths up to 50 GHz.

4.1. Material's parameters

All materials molecules have charged particles when applications of electric or magnetic field on the material, secondary field are produced which results in conduction, polarization, or magnetization of the particles. Polarization of particles results in the material acting as a dielectric which can be characterized by dielectric constant. The material relative permittivity is the ratio between the material permittivity and the permittivity of the free space. It is experimentally measurable parameters.

$$\varepsilon_r = \frac{\varepsilon}{\varepsilon_o} \tag{2}$$

When an electric field is applied across a conducting medium, an equation for complex permittivity has to be used.

$$\varepsilon = \varepsilon' - j\varepsilon'' \tag{3}$$

The real part of the complex permittivity is the dielectric constant (relative permittivity) of a material, or the energy storage of that material. The imaginary part is the loss factor, or the amount electric field energy lost when passing through a material [16]. Most biological materials have permeability close to that of free space, so permeability is not a concern during tests involving blood glucose levels, allowing the tests to focus on the frequency variations of the relative permittivity [17, 18]. Measuring the dielectric properties of a material can indirectly measure other properties that have a correlation to the molecular structure of the material [19].

Because the dielectric properties of a material are dependent upon its molecular structure, a change in the molecular structure will cause the dielectric properties of the material to change. Measuring the dielectric properties of a material can indirectly measure other properties that have a correlation to the molecular structure of the material. This can be important when the property of interest is difficult to measure directly. Most measurements involving microwaves and permittivity are taken using a vector network analyzer, or VNA. A VNA is a device that is used to measure the S-parameters of a microwave circuit over a specified frequency range and is pictured in **Figure 3**.

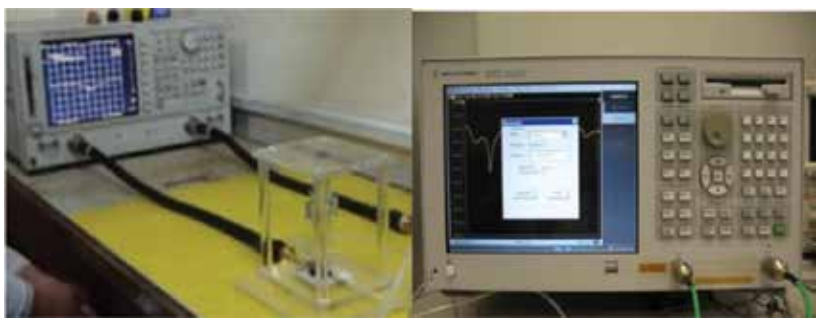

Figure 3. Vector network analyzer.

When an electric field is applied along conducting medium, the complex permittivity equation has to be used. Where the real part is indicates the material permittivity. In biological field, as mentioned earlier, permeability is near free space which means that the dielectric constant would be the parameter that has direct effect on frequency variation hence material properties that could be important for biological analysis.

S-Parameters: well known as scattering parameters that are used to describe completely reflection and transmission properties of a traveling wave that is scattered or reflected when a network under test is inserted into a transmission line with certain characteristic impedance.

DAK: dielectric assistive kit that is used to measure the dielectric properties of material, conductivity, permittivity, and loss tangent with high precision. **Figure 4** shows the dielectric problem designed for fast precise and nondestructive measurements of solids liquids and semisolids properties over wide frequency range, and the probe can be moved to the media under test to directly measure the dielectric parameters, thus eliminating phase distributions due to cable movements.

This open-ended coaxial probe uses advanced algorithms and novel hardware to measure the dielectric properties of liquids, solids, and semi-solids over a broad range of parameters. The measurement method is fast and nondestructive to the material under test.

Microwaves in medical applications have been making large steps in recent years since microwave technology, such as ultrasounds, allows doctors to see inside of the body without the ionizing radiation found in x-rays. To better understand how microwaves can be used in

http://dx.doi.org/10.5772/64773

medical applications, it is important to understand how microwaves affect and interact with the body.

Figure 4. DAK.

4.2. Permittivity and biological modeling

The effects of RF on biological tissues depend on the exposed field strength or the power deposited on the unit mass of these tissues. **Figure 5** shows the change in the permittivity of the human tissues due to change in the applied frequency. This effect is clear on water molecules (which are the most abundant molecules in the human body) as shown in **Figure 5**, hence, the applying field cause the water molecules to be stored in the tissues.

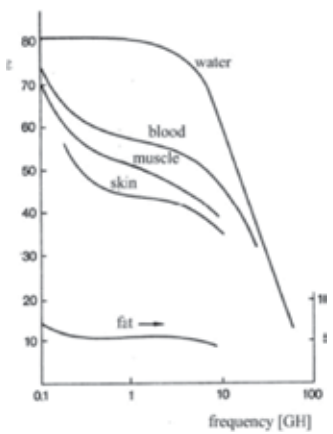

Figure 5. Dielectric constant versus frequency for different biological tissues.

Thus, the tissues do not allow energy to pass through and permittivity decrease with frequency increase.

The real part of relative permittivity drops off in distinct steps as the frequency increases; therefore, it experiences something called dispersion, which is reflected in **Figure 6** [19]. Each

dispersion region occurs at different frequencies and represents different effects of electromagnetic waves on the body.

$$\hat{\varepsilon}(\omega) = \varepsilon_{\infty} + j\frac{\Delta\varepsilon}{1 + j\omega\tau} \tag{4}$$

Since biological tissues are complex in both structure and composition, and distribution parameters have to be taken into account. As a result, the second-order Debye equation is formed [11].

$$\hat{\varepsilon}(\omega) = \varepsilon_{\infty} + \sum_{n}^{2} j\frac{\Delta\varepsilon}{1 + j\omega\tau} \tag{5}$$

where ε_{∞}, $\Delta\varepsilon$, τ are the optical permittivity, pole amplitude, and the relaxation time, respectively.

The interaction between antenna and any biological material effects on the antenna electrical properties; this effect occurs due to the complex permittivity of the biological material surround the antenna; blood is biological dielectric that subject to complex permittivity equation that depends on operating frequency range.

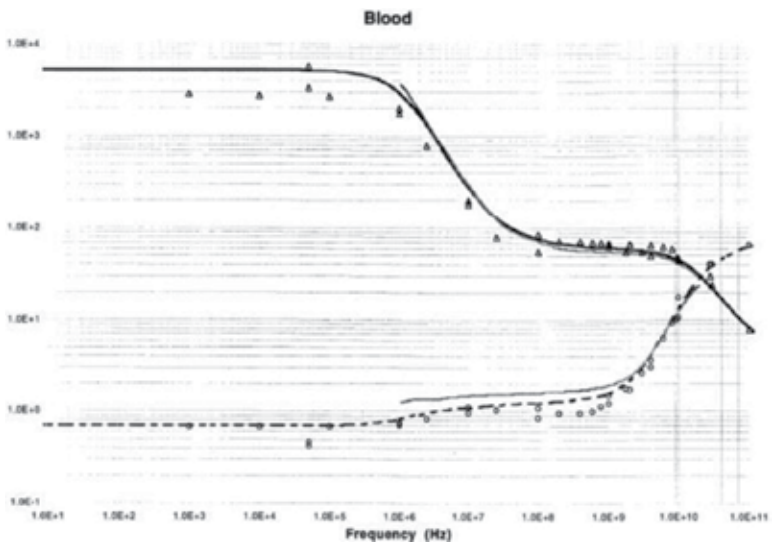

Figure 6. Permittivity and conductivity versus frequency.

Gobriel and et al [23] have analyzed the blood properties and discussed how its permittivity and conductivity changes with frequency. It is important to keep permittivity constant or semi

http://dx.doi.org/10.5772/64773

constant in the test region; hence, we target to monitor the changes in blood permittivity due to glucose level changes.

Certain regions of dielectrics are subject to Debye and more refined Cole-Cole models. The Debye is often used for dispersions because it can contain multiple terms to describe the differing sections of the model [12], Eqs. (5) and (6).

$$\text{Debye mode}: \varepsilon(\omega) = \varepsilon_{\infty} + \sum_{m=1}^{n} j \frac{\Delta\varepsilon_m}{1 + j\omega\tau_m} + \frac{\delta_i}{j\omega\varepsilon_o} \tag{6}$$

$$\text{Cole-Cole model}: \hat{\varepsilon}(\omega) = \varepsilon_{\infty} + \sum_{n}^{2} j \frac{\Delta\varepsilon_m}{(1 + j\omega\tau_m)(1 - \alpha_m)} + \frac{\delta_i}{j\omega\varepsilon_o} \tag{7}$$

In [13], it has been determined that Cole-Cole analysis model is the best that describes the complex permittivity change of blood with frequency range. Proper curve fitting technique can be added to the Cole-Cole model to illustrate the relation between change of the blood sample permittivity with frequency and glucose level in it by [12], and the glucose factor was added by researchers [13]. An inverse relationship between dielectric permittivity and blood glucose concentration has been determined [14] as shown in **Figure 7**. The investigation was completed used an aqueous glucose solution and measured a changing glucose level and changing permittivity level over time. The change in blood glucose concentration is narrow because the patient is nondiabetic and does not experience the range of blood glucose levels that a diabetic patient experiences. It is a well–established fact that time-varying currents will radiate electromagnetic waves. Thus, an antenna is a structure on which time-varying currents can be excited with relatively large amplitude when the antenna is connected to a suitable source, usually by means of a transmission line or waveguide. There is an endless variety of structural shapes that can be used for an antenna. However, from a practical point of view, those structures that are simple and economical to fabricate are the most commonly used. In order to make antenna work adequately efficiently, the minimum size of the antenna must be comparable to wavelength [15].

Microstrip antenna is one of the most common planar antenna structures used. It has advantages such as lightweight, low cost, conformal configurations, and compatibility with integrated circuits. For many applications, the advantages of microstrip antennas outweigh their limitations. Initially, microstrip antennas found widespread applications in military systems such as missiles, rockets, aircrafts, and satellites. Currently, these antennas are being increasingly used in the commercial sector at different applications due to the reduced cost of the dielectric substrate material and mature fabrication technologies. With continued research and development and increased usage, microstrip antennas are ultimately expected to replace conventional antennas for most applications such as mobile and satellite communications, radar antennas, Wi-Fi applications, and biomedical application [20, 21].

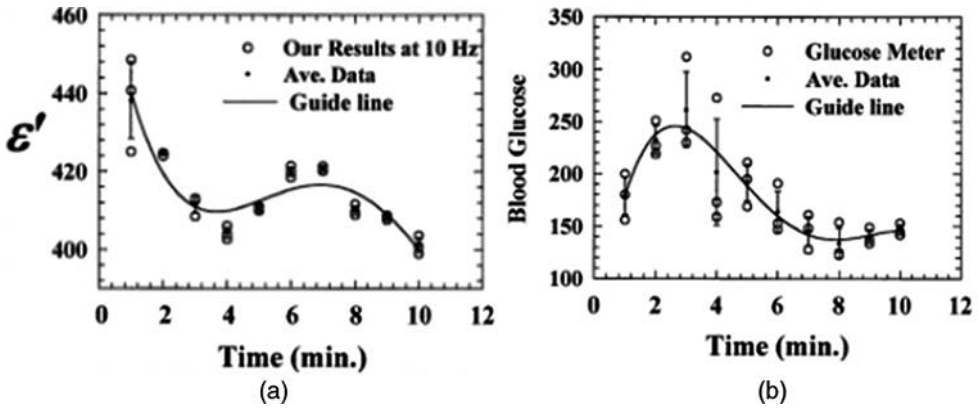

Figure 7. (a) Changes in dielectric versus (b) changes in blood glucose concentration.

This research will represent a revolution in the field of designing tests for the screening of substances of human origin with three main achievements over the available methods:

a. The instant results of screening tests on time.

b. No need for well-trained personnel or sophisticated laboratory equipment.

c. The test can be done anywhere as the device will be a portable system.

As discussed earlier, when a biological material is introduced into a resonant cavity, the cavity field distribution changes; hence, consequently, the input impedance and resonant frequencies are changed. This may depend also on the properties of electromagnetic wave input signal to the cavity as amplitude, shape, and phase. Dielectric material interacts only with electric field in the cavity. According to the theory of cavity perturbation, the complex frequency shift is as follows [3]:

$$\frac{-\partial\Omega}{\Omega} = \frac{\left(\varepsilon_r' - 1\right)\int_{v_s} E.E_o^* dV}{2\int_{v_c} \left\lfloor E \right\rfloor^2 dV} \tag{8}$$

$$\frac{\partial\Omega}{\Omega} \approx \frac{d\omega}{\omega} + \frac{j}{2}\left[\frac{1}{Q_s} - \frac{1}{Q_o}\right] \tag{9}$$

In the above equations (Eqs. (8) and (9)), ε'_r is the real part of the relative complex permittivity associated with the dielectric loss of the material. V_s and V_c are corresponding volumes of the sample and the cavity resonator, respectively. The conductivity can be related to the imaginary

part of the complex dielectric constant by separating real and imaginary parts results in Eqs. (10) and (11).

$$\varepsilon_r' - 1 = \frac{f_o - f_s}{2f_s}\left(\frac{V_c}{V_s}\right) \tag{10}$$

$$\varepsilon_r'' - 1 = \frac{Q_o - Q_s}{Q_o Q_s}\left(\frac{V_c}{4V_s}\right) \tag{11}$$

$$\sigma_e = \omega\varepsilon'' = 2\pi f \varepsilon_o \varepsilon_r'' \tag{12}$$

where f_o, Q_o, and ε''_r are operating frequency, and quality factor Q_o are corresponding to values at empty sample holder, while f_s and Q_s are same values but with filled sample holder and imaginary parts of the relative complex permittivity. The low profile, lightweight, and low manufacturing cost of microstrip patch antennas (MPA) have made them attractive candidate for this application.

4.3. Measurements on a glucose simulating sugar water

Early testing and analysis focused on looking for a shift in resonant frequency of the antenna. Modeling the shift of blood glucose concentration in the human body model using Computer simulation technology (CST) or high-frequency structure simulation (HFSS) simulators showed that the resonant frequency of the antenna would shift. Modeling the blood permittivity change with the change in its glucose level can easily lead to the change in the antenna resonance frequency. The simulation in **Figure 8** shows how the resonant frequency of the dipole antenna changes with increasing the concentration of glucoses in blood sample. As the glucose concentration increases, the antenna input impedance (real and imaginary) parts shifts. However, the real part maximum point does not lay with the imaginary part zero value; that is, these two points should lie together according to ideal theory. In such case, the resonance frequency is considered as the frequency at which the input impedance imaginary part equals zero. **Figure 9** presents how the resonance frequency increases with the increase in blood glucose concentration. On the other hand, same **Figure 9** shows that the magnitude of the antenna return loss does not show a correlation between the resonant frequency and the glucose concentration level.

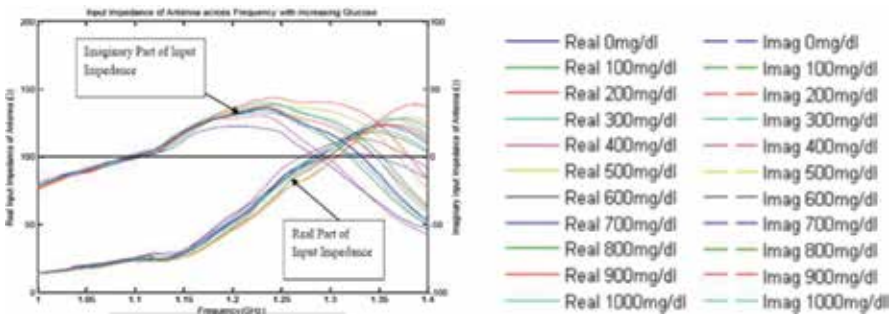

Figure 8. Simulated real and imaginary input impedance of antenna versus frequency for different glucose levels.

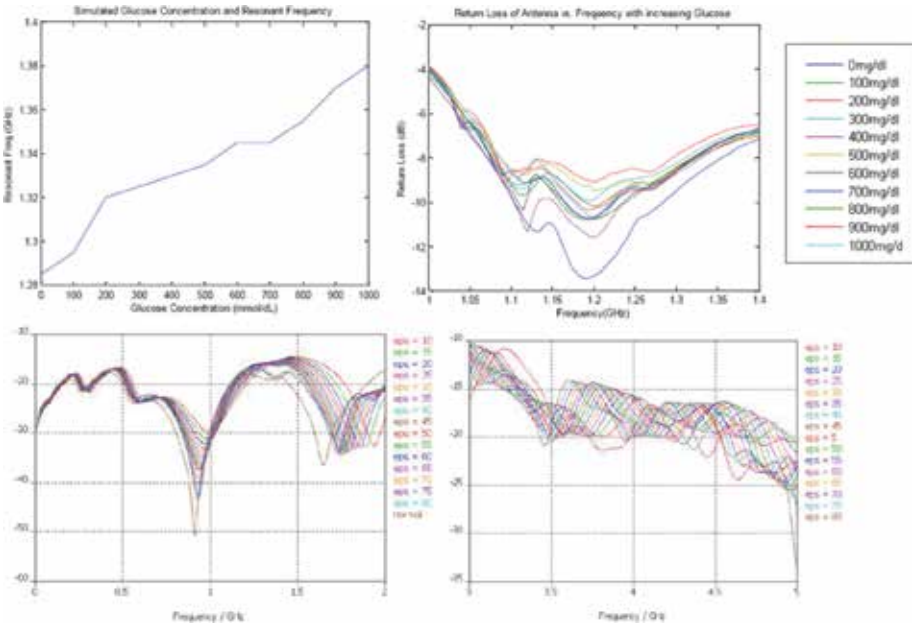

Figure 9. Resonate frequency of antenna versus glucose concentration of aqueous solution and return loss of antenna versus frequency for different glucose levels.

4.4. Design of a wideband antenna

Our proposed method would involve an antenna which would change resonant frequency based on the dielectric properties of the tissues present in its fringing fields (**Figure 10**). A similar method has been used previously by this research group to effectively characterize tissue dielectric properties [12–14]. **Figure 11** shows the measured resonant frequency of antenna vs. blood glucose levels. Modified UWB antenna return loss for varying glucose concentrations is shown in **Figure 12**. Where g is blood glucose from 70 to 150 mg/dL, and the model is defined by **Table 1**.

http://dx.doi.org/10.5772/64773

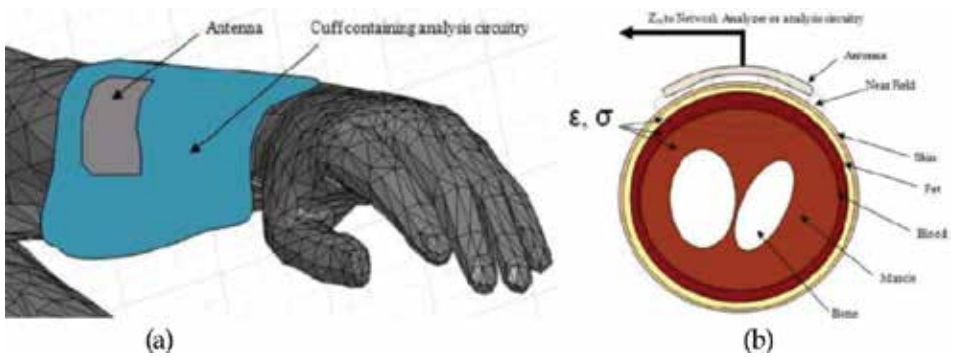

Figure 10. (a) Conceptual blood glucose measurement form factor and (b) detection of tissue properties through antenna fringing field.

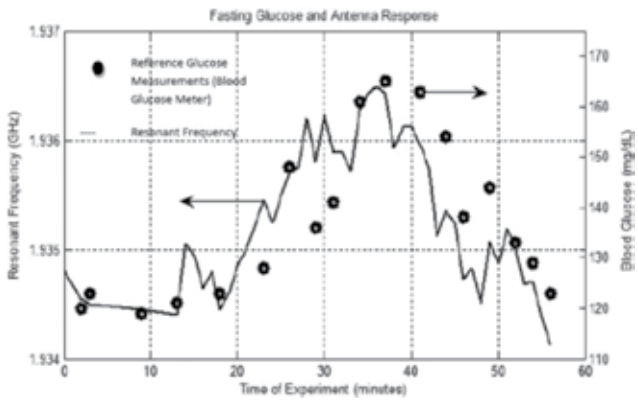

Figure 11. Measured resonant frequency of antenna vs. blood glucose levels.

Tissue Type	Original Blood Model [32]	Modified Blood Model
ε_∞	4	2.8
$\Delta\varepsilon_1$	56	56.5
$\Delta\varepsilon_2$	5200	5500
$\Delta\varepsilon_3$	0	0
$\Delta\varepsilon_4$	0	0
τ_1	8.377e-12	8.377e-12
τ_2	132.629e-9	132.629e-9
τ_3	-	-
τ_4	-	-
α_1	0.1	0.057
α_2	0.1	0.1
α_3	-	-
α_4	-	-
σ	0.7	0.5

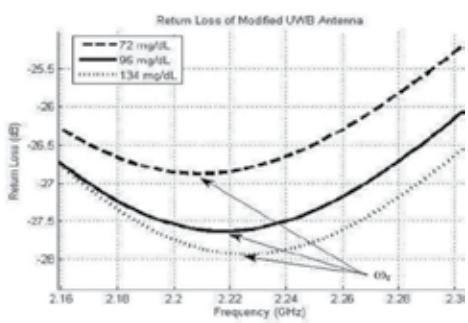

Figure 12. Tissue layers used for simplified human body model and modified UWB antenna return loss for varying glucose concentrations.

Tissue type	Original blood model [32]	Modified blood model
ε_∞	4	2.8
$\Delta\varepsilon_1$	56	56.5
$\Delta\varepsilon_2$	5200	5500
$\Delta\varepsilon_3$	0	0
$\Delta\varepsilon_4$	0	0
τ_1	8.377e−12	8.377e−12
τ_2	132.629e−9	132.629e−9
τ_3	–	–
τ_4	–	–
α_1	0.1	0.057
α_2	0.1	0.1
α_3	–	–
α_4	–	–
σ	0.7	0.5

Table 1. Parameters of original and modified blood Cole-Cole models.

4.5. Analytical model of narrowband antenna

A method to determine a lumped element equivalent circuit has been applied successfully for dipole antennas [22]. This method has been applied to this planar antenna, with some minor additions (**Figure 13**). The feed network can be modeled as a transmission line between the radiator and the port. **Figure 14** shows the real and imaginary impedance of the simulated antenna and the equivalent circuit model. Good agreement can be seen between the model and the simulated data. The values of this model that match the free space resonance at 1.8 GHz can be found in **Table 2**.

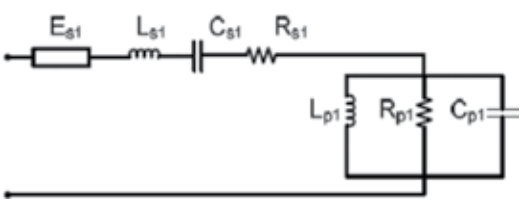

Figure 13. Analytical model accounting for antenna orientation used to validate model.

http://dx.doi.org/10.5772/64773

The presence of tissue near the antenna will act as an additional capacitor C_{p2} present in the parallel resonant RLC network that is a function of the tissue dielectric properties and position (**Figure 15**). The C_{p2} capacitor values have then been determined in the equivalent circuit to match the antenna reactance from the HFSS simulations. The various C_{p2} values determined are plotted in **Figure 16** as a function of the dielectric permittivity and distance from the antenna. It can be seen that for all distances, the changes in C_{p2} are nearly a linear function of permittivity, which would be expected for a capacitor behavior.

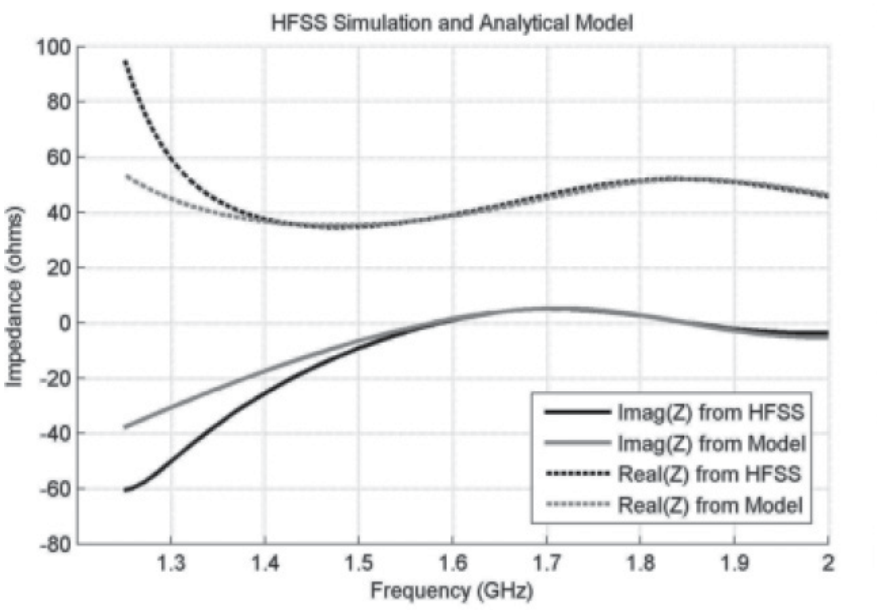

Figure 14. HFSS simulation and analytical model.

E_{S1}	L_{S1} (nH)	C_{s1} (pF)	R_{s1} (Ω)	L_{p1} (nH)	R_{p1} (Ω)	C_{p1} (nF)
50 Ω transition line 230 degree delay at 1.8 GHz	1.5	2.25	29	1.32	36.5	3.5

Table 2. Lumped element values of analytical model.

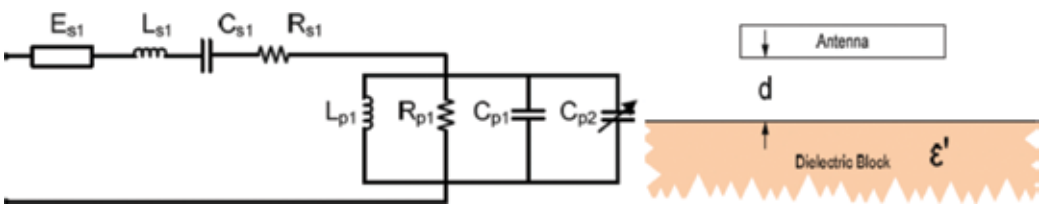

Figure 15. Analytical model accounting for tissue layers and antenna orientation used to validate model.

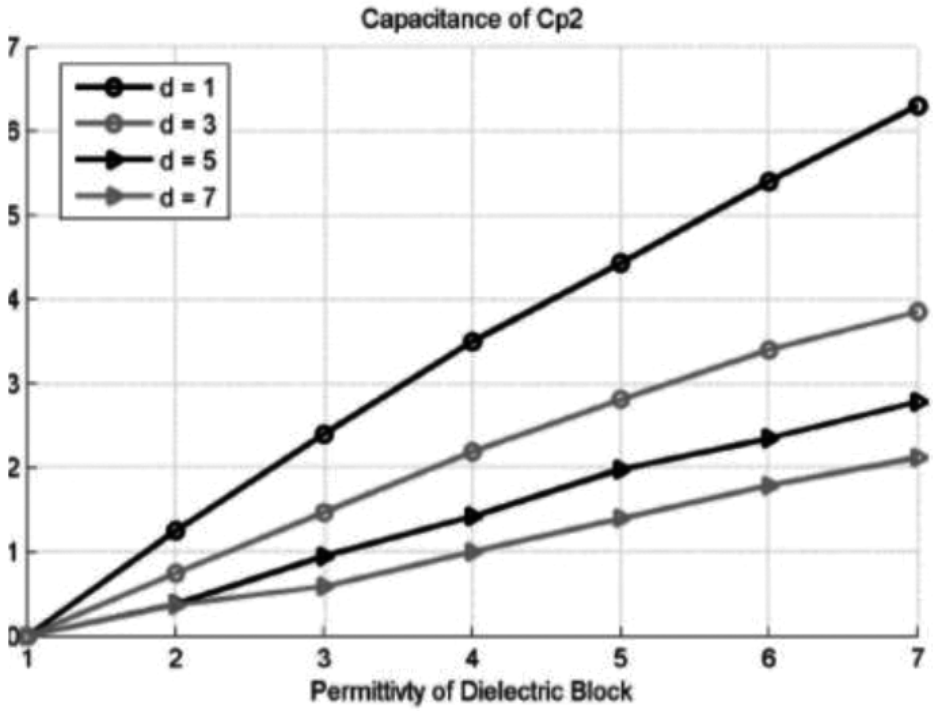

Figure 16. Capacitance of Cp_2 for various dielectrics.

5. Microstrip cavity resonator biosensor (MCRB)

Microwave applications have assumed considerable importance in medicine because they are effective in the reduction on the mental and physical burden borne by patients with non-invasive way. Such applications are of three types [23]:

a. Thermal treatments which use microwave energy as a source of heat. Antennas used to elevate the temperature of cancer tissues are located inside or outside of the patient's body, and the shapes of the antennas used depend on their locations.

b. Diagnosis and information gathering inside the human body (e. g., by computerized tomography and magnetic resonance imaging) and noninvasive temperature measurement inside the human body. Telecommunications illustrates the importance of functions of implantable medical devices which need to transmit diagnostic information.

c. Gathering of medical information on the human body from outside the body (bio-sensors), techniques in this category are considered to be an exertion of communication technologies.

http://dx.doi.org/10.5772/64773

The challenges may be summarized as follows:

1. **Application–driven challenges**

   *Data fusion (aggregate and filter)

   *Support of multiple data rates

   *Robustness, zero maintenance

   *Security and privacy at low energy cost

2. **Technology challenges**

   *Low complexity/low–power designs

   *Smart personal networks and sensors

   *Integration of heterogeneous networks considering BWCS.

Antennas and propagation are the most basic points for integrating wireless body area network (WBANs), wireless sensor network (WSNs), and personal area network (WPANs) into future wireless heterogeneous networks which is a necessary step to shape the 4G landscape. Body–centric communications is a research topic combining WBANs, WSNs, and WPANs. These communication techniques are built basically on biosensors that antenna are acting as the vital component in their structures [23].

An antenna is a structure, usually made from a good conducing material that has been designed to have a shape and size such that it will act as an electromagnetic sensor that radiates/receives power in an efficient manner. It is a well-established fact that time-varying currents will radiate electromagnetic waves. Thus, an antenna is a structure on which time-varying currents can be excited with relatively large amplitude when the antenna is connected to a suitable source, usually by means of a transmission line or waveguide. There is an endless variety of structural shapes that can be used for an antenna. However, from a practical point of view, those structures that are simple and economical to fabricate are the most commonly used. In order to make antenna work adequately efficiently, the minimum size of the antenna must be comparable to wavelength.

5.1. Microstrip patch antenna

Microstrip antenna is one of the most common planar antenna structures used. Extensive research development aimed at exploiting its advantages such as lightweight, low cost, conformal configurations, and compatibility with integrated circuits have been carried out. For many applications, the advantages of microstrip antennas outweigh their limitations. Initially, microstrip antennas found widespread applications in military systems such as missiles, rockets, aircrafts, and satellites. Currently, these antennas are being increasingly used in the commercial sector at different applications due to the reduced cost of the dielectric substrate material and mature fabrication technologies. With continued research and development and increased usage, microstrip antennas are ultimately expected to replace conven-

tional antennas for most applications such as mobile and satellite applications, radar antennas Wi-Fi applications, biomedical application [24–26].

One of the most important requirements in wireless biosensors is the mobility of the device; its size can be reducing with keeping same performance. As shown in **Figure 17**, the simplest configuration of microstrip antenna path is dielectric substrates with metal patch forms one side and ground plane on the other side. Regular patch shapes are always preferred for easy analysis and performance predications. Rectangular and circular patches are the basic shapes that most commonly used in microstrip antennas. Ideally, the dielectric constant ε_r, of the substrate should be low ($\varepsilon_r < 2.5$), to enhance the fringing fields that account for radiation. However, other performance requirements may dictate the use of substrate whose dielectric constant can be greater. As in our prototype blood sensor, the miniaturized size is one of the main challenges; hence, higher dielectric constants are desired ($\varepsilon_r < 10.2$).

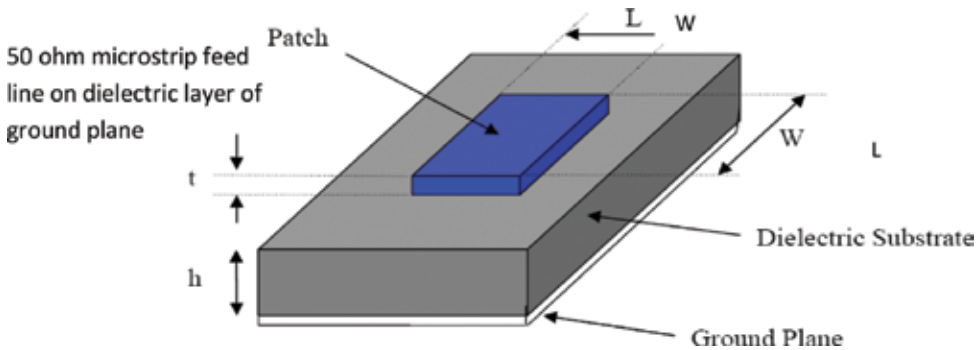

Figure 17. Proximity-coupled feed microstrip patch antenna.

Recently, a big attention is devoted towards compact microstrip antenna design with multi-function as multi-frequency bands, dual polarization, broadband, and high gain. Several open literatures introduce inherent solution for narrow bandwidth of the microstrip antenna as proximity-coupled feed, capacitive-coupled feed, and 3D transmission line feed.

In our prototype system, proximity-coupled feed antenna is used as shown in **Figure 17** to ensure continuous clear surface of the antenna patch metal; hence, it acts as the blood sample holder [25].

One of the most famous blood diagnosis methods is the surface plasmon resonance (SPR) in thin metal layers. It is one of the most sensitive label-free methods for the measurement of the reaction dynamic of biological molecules on gold surfaces. The application of modern powerful CCD cameras provides the possibility of SPR Imaging. In this case, the incident laser light is fixed at an angle which is slightly shifted away from the minimum of the SPR resonance curve to the middle of one wing. Variations of the intensity of the reflected laser light are proportional to the shift of the resonance minimum caused by surface reactions. This enables simultaneous monitoring of many reactions at identical conditions. However, providing high throughput,

the imaging methods usually possess a degraded detection power compared with single-spot measurements wireless communication that can be used. The cost and time consuming of such systems create the need of other fact, cheap, and mobile diagnostic systems.

5.2. Resonator biosensor

A typical application of the field of biosensors is the detection of biological substances by measuring changes in electrical properties of the materials. Biosensors are now being employed in medicine, biotechnology, and environmental monitoring. The use of biosensor for rapid detection of the enteroviruses will limit the need for sophisticated laboratory diagnostic methods that needs long time and expert scientists to perform the test. Usually, it takes at least 12 h of laboratory work to make sure that a clinical sample is safe. The physician in the field normally do fast and simple tests like physical examination of the clinical sample, performing some preliminary tests, and then gives a fast decision regarded as potentially safe or not.

All these tools are available today; however, until now there exists no fast and sensitive method to know whether the clinical sample is infected with enteroviruses or not. Thus, the risk is still very high that the physician comes to a wrong decision on the health status of the clinical tested sample. If the clinical sample is infected, it means that there is a great possibility for the enteroviruses outbreaks which initiates danger risk.

Nowadays used methods for diagnostic screening have reached a high degree of accuracy, sensitivity, and reliability. Most methods achieve an accuracy of more than 99.9%. The drawback of these methods is that they are time consuming. The accuracy is mainly based on very complicated enzymatic activity (ELISA) or radioimmunoassay (RIA) or nucleic acid-based reactions (PCR, hybridization) that lead to visual changes that can be measured. The accuracy of these biological methods depends on highly sophisticated reactions that need to be done in well-equipped laboratories with well-trained personnel. Within the project, a fast and sensitive testing method for biological sample will be developed. This method has the potential to detect the existence of pathogens. The transducer principle is based on microwave cavities resonator biosensor (MCRB), which is known to be a sensitive label-free method that allows detecting receptor-legend binding. Using homogenous distributed spots allows reaching high accuracy compared to the state of the art. Therefore, we meet the request for "*new screening techniques*," which are "*sensitive enough to avoid false negatives*." The **MCRB** system is also capable to detect multiple pathogens simultaneously if antibodies of all these pathogens are immobilized on the transducer chips. Only true/false indicator will be detected. **Figure 18** shows some of our antenna simulation results of reflected scattering parameters change due to the immobilization of sample layer upon the microstrip antenna surface. **Figure 18** illustrates that there is a detectable shift in resonating frequency and reflection coefficient due to the change in the tested sample characteristics, hence verifying the proposed research idea, that depends on measuring this change due to the presence of enterovirus infection in the tested sample as will be described later in next section. This allows a very rapid testing for pathogens in one single procedure. Thus, this method is fast and cheap, and therefore, meets the requirements for "*development of more cost-effective approaches*." The developed system will finally by clinically show its abilities in detecting

pathogens in any biological sample. To be able to carry out statistically relevant tests, numerous test runs will be necessary per pathogen [26, 27].

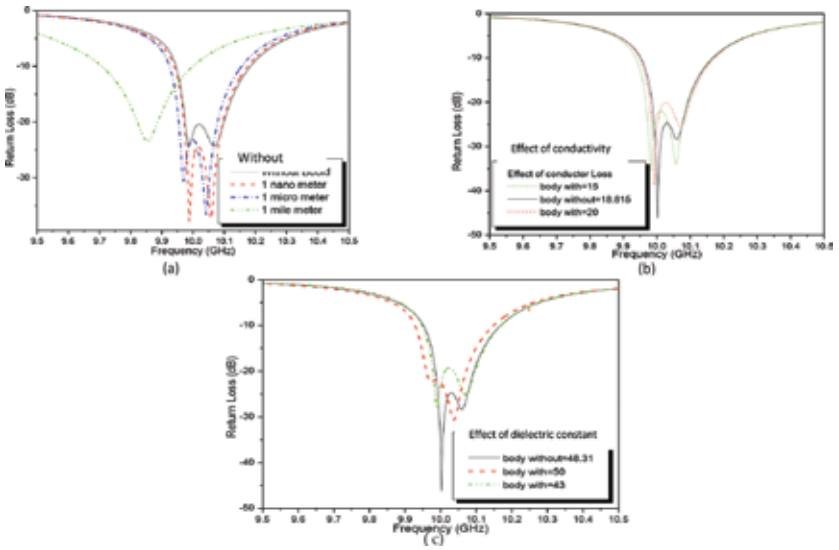

Figure 18. Simulation results of proximity-coupling microstrip antenna reflection coefficients with changing characteristics of sample deposited layer on antenna surface. Effect of changing (a) layer thickness, (b) layer conductor loss, and (c) layer dielectric constant.

The effect of sample characteristics is shown in **Figure 18** that shows in part (a) the effect of deposited sample layer thickness on antenna reflection coefficient. Part (b) shows the effect of sample layer deposition on the measured conductor loss, while part (c) shows same effect on changing the dielectric constant. These simulations are done using electromagnetic readymade software package of (high-frequency structure simulation, HFSS) for proximity coupling fed microstrip antenna at operating frequency of 10 GHz. The results of **Figure 18** verify our proposed idea of MCRB. Many studies have been devoted to the absorption of proteins onto solid surfaces and the immunological reaction between antibody and antigen.

The proposing of a micro-immunosensing diagnostic assay is based on the very specific immune reaction between antigen and antibody. The assay can be manufactured by first absorbing a layer of antibodies that has multiple specificities to enteroviruses and then immobilized on an-active gold-coated dielectric slide (low-profile microstrip antenna surface), which forms one wall of a thin flow-cell, while the other interacting in an aqueous buffer solution that is induced to flow across this surface.

When the biological sample, containing the antigen the antibodies are directed, is brought in contact with the coated solid phase, the specific immune reaction occurs and the marker antigen will bind to the antibody. This binding, resulting in a layer growth that can be detected, for example, when electromagnetic wave is incident on the antenna surface coated with gold, reflection coefficient S_{11}, and input impedance (real and imaginary) can be measured by (vector

network analyzers) VNA. The reflection coefficient amplitude in dB, input impedance in ohms, and frequency resonance value in GHz are expected to be changed from case of normal clinical sample layer to infected clinical sample layer or to infected sample layer with antigen/antibodies embedded. Recording this change and classifying it, after reading of large number of samples, one can detect in fast way the infection of enteroviruses in clinical sample. Software code is developed for automatic reading, classifying, and determining the sample infection afterwards. This procedure depends on small miniaturized size of microstirp antenna to act as sample plate. Coating the antenna surface with gold will be used to isolate its surface from outside environment and exclude any unwanted surrounding parameters that may effect on the accuracy or sensitivity of readings. Proper thickness of sample layer deposited on antenna surface would be determined through simulations first and then through pre-experimental tests. The expected frequency range of operation will be in C-band (2–3 GHz), Bluetooth, and ISM band (industrial, scientific, and medical) and/or in X band (from 8 to 12 GHz). This will be decided according to the system sub-components purchase availability in local market or abroad [28].

Also, the system size allows for mobile applications. No need for connection to host computer as in SPR system. The whole test will be done in the field with no need to return or connect to the laboratory since a comparison with the calibration levels will be done automatically through the developed control software. The other advantages are the low cost of electromagnetic system and the reduced hazardous effects than other sources as lasers, IR, etc.

First, clean sample layer will be deposited with normal buffer electrical properties. The output signal level and frequency will be measured accurately to determine the standard references.

Second, the same measurements will be done for the samples collected from tested area layered onto the chip; various samples showing different stages of different titer of viruses will be used to standardize the test. The antenna chip prototype is as shown in **Figure 19**. It consists of a planner antenna with metal surface, coated with gold (to prevent oxidation), a measuring facility for power level and frequency, electromagnetic source, mechanical micro-pump, etc. The whole system hardware block diagram is as shown in **Figure 20**. Third, a thin-film sample under test will be deposited on the surface with micro-fluid injection procedure.

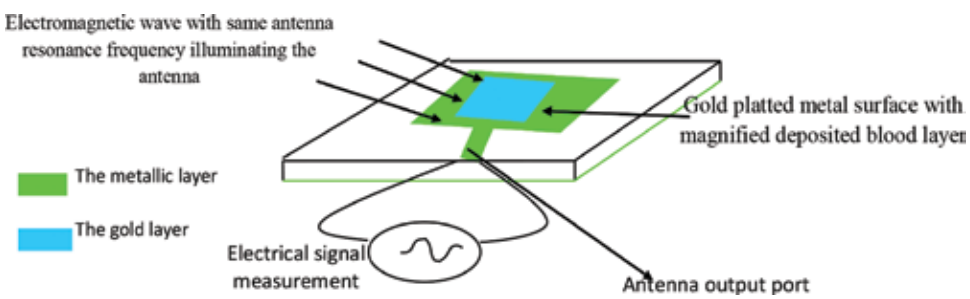

Figure 19. Microwave cavity resonator bio-electromagnetic sensor system verification idea.

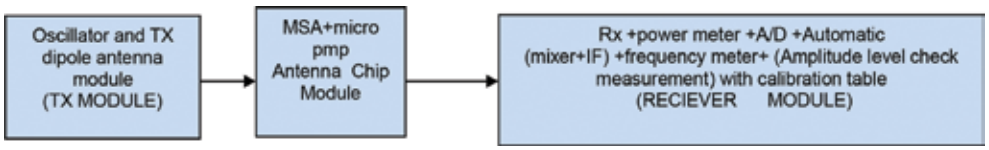

Figure 20. Block diagram of mobile virus diagnosis system.

The output signal level which depends on the electrical properties of the deposited layer will be measured accurately. Comparison with calibration table will be done automatically. From the signal level reading, a decision of infection existence will be automatically taken. The knowledge of the used antigen gives information about viruses that need to be detected. The frequency of operation is in the range of 2–3 GHz in C-band and/or 8–12 GHz in X-band; so the antenna chip size will be in the range of few square mms. The novelty in this idea, as mentioned earlier, is the measurement of the change of the electrical properties which makes the idea free from the molecular size limitation that exists in other systems as optical biosensors. Same idea but with different experimental procedures, as microwave waveguide resonator or microwave probe insertion, is verified in the literature [24–29].

Improving the screening tests in terms of speed and costs for biological samples will cut the costs and will thus give a direct economic value. Better screening methods decrease the risk of infection, and most importantly will provide a perfect tool to screen more enteroviruses. Nowadays, screenings include a limited number of pathogens due to cost and/or scientific reasons. The conceived system consists mainly of (MCRB) cavity resonator chips. The instrument is primarily designed for detecting multiple pathogens in sample. Due to the limited resources of this project, we concentrate on the relevant enteroviruses. Otherwise, the need of resources for performing relevant tests would by far exceed the budget. But it has to be emphasized that this system has the potential to detect more than one pathogen, simultaneously if the corresponding receptors are immobilized on the transducer chip [29].

The MCRB system could become a standard system for screening donor blood. Depending on the application, the system can be designed for different levels of complexity. The result of the screening can give quantitative figures for each pathogen. The high specificity, accuracy, and sensitivity of the new method help to reach the goal of avoiding false positives as well as false negatives. Despite the accuracy of the method, it is very rapid and can give results in few minutes. This ability together with the potential to screen for numerous pathogens makes the MCRB system well suited for screening donors prior to organ transplantations.

A low-profile microstrip disc antenna with micorstrip line proximity coupling feed is proposed in order to keep the antenna surface clean for imposing the blood sample layer. The patch is placed alongside a small rectangular ground plane co-planar to it as shown in **Figure 21a**. Antenna prototype is designed to operate at 2.4 GHz. **Figure 21** illustrates the fabricated antenna. The resonating antenna with deposited layer of normal blood serum is considered the reference of the measurements from which the changes due to the viral layer deposition are measured. The Agilent E8719A vector network analyzer is used for preliminary prototype

http://dx.doi.org/10.5772/64773

measurements. This is replaced by portable transceiver Ettus N210 with open source control software in the final prototype design.

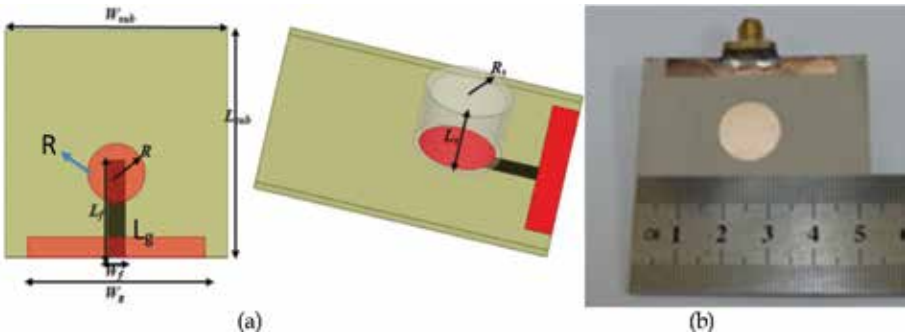

Figure 21. (a) Geometry antenna configuration and (b) proposed microstrip antenna with gold platted surface.

Figure 22 illustrates the results for different concentrations of attenuated G1P(8) Rota virus. The scattering parameter $|S_{11}|$ for antenna in installation steps of the chamber/housing over antenna shifts the resonating frequency down to 1.88 GHz with $|S_{11}| = -15$ dB as in **Figure 22a**. This can be attributed due to resistive loading effects of glass chamber and rubber gasket. Starting viral immobilization on the sensor surface shifts the cavity resonating frequency down to 1.865 GHz with $|S_{11}|$ equal to −13 dB at the fourth viral concentration of 1×10^6 virus particles. These preliminary results verify the sensor idea practically; however, more investigations are still running.

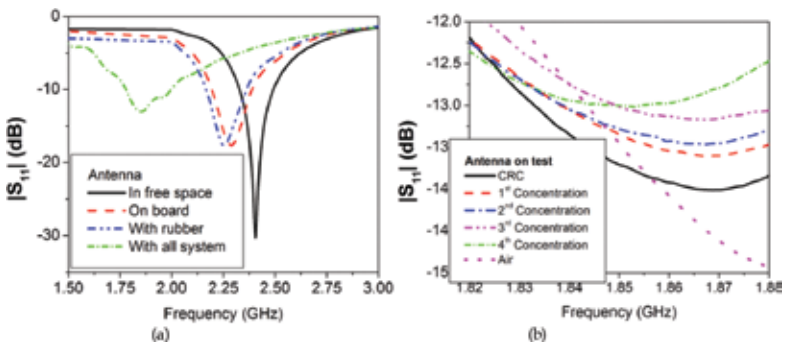

Figure 22. Measurements of reflection coefficients $|S_{11}|$ at 2.4 GHz of micro-immunosensor for different installation steps in part (a) and for different viral concentrations in part (b).

The antenna was simulated using 3D full-wave electromagnetic simulator, high-frequency structure simulator (HFSS) version 13. The dielectric constant change was measured using blank buffer solution used to dilute Rota virus stock solution using DAK (dielectric assistive kit). The system measures liquids, solids, and semi-solids dielectric constant over a broad range of frequency from 10 MHz to 20 GHz. The measurement method is fast and nondestructive

for the material under test. **Figure 23** shows the changes due to different concentrations of Polio virus.

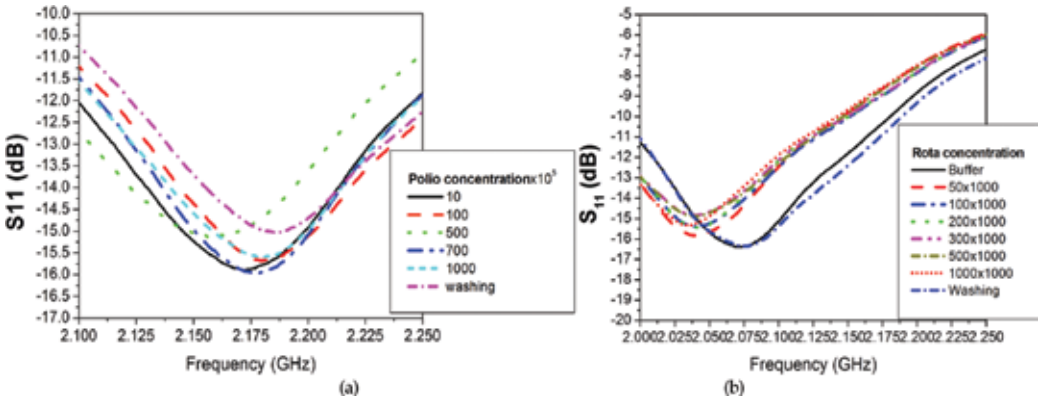

Figure 23. The effect of type A antenna S_{11} change due to insertion of different virus concentrations: (a) Polio and (b) Rota.

6. Ground penetrating radar (GPR)

For searching on underground mummies or any biological bodies as well as water the ground penetrating radar (GPR) is used. GPR is a nondestructive technique. To enhance the performance parameters of the GPR antennas, different parameters should be considered. As mentioned earlier, when the transmitting and/or the receiving antennas are placed close to the ground, they suffer from significant changes in their input impedance. This change is a function of the antenna elevation angle and the soil type. Different techniques have been proposed to maintain the input impedance matching conditions. It has been shown in [30] that the input impedance of a bow-tie antenna changes with the flare angle variation, giving the possibility of adaptive antenna matching. In bowtie antenna, the input impedance is affected by the ground plane; however, one can modify it by adjusting the design flare angle to keep the reflections in the minimum level at the antenna terminals.

Other techniques have also been reported regarding the implementation of impedance matching networks for different antenna systems to achieve maximum matching condition, such as, radio frequency-microelectromechanical systems (RF-MEMS)-based matching module for adaptive antennas where RF-MEMS devices are used for the implementation of variable capacitors at the antenna input for better transfer of power to the antenna, or the use of a pi-network matching circuit adaptively controls by two varactors, reducing the refection between the matching circuit and the RF front end of a transceiver.

Another critical parameter for the GPR antenna system is system directivity. High directive antennas for GPR systems are needed to avoid the loss of power. Recently, several antennas

http://dx.doi.org/10.5772/64773

have been reported where the use of electromagnetic bandgap (EBG) and frequency selective surface (FSS) shows highly directional radiation properties. Another technique to increase the antenna system directivity is to use an antenna array rather than one single radiating element. To keep the system low profile, planar antennas are recommended for such application. On the other hand, mutual coupling between the different radiating elements might take place. Some structures have been proposed to reduce the mutual coupling between the radiating elements of microstrip antenna arrays such as cavity backed and substrate removal microstrip antennas. The other approach is using metamaterials insulator between the antenna arrays elements to reduce the mutual coupling. These metamaterials are designed to operate at certain frequency band gap or insulating region where the effective permittivity and permeability have opposite signs. However, this insulating/band gap frequency range is usually narrow bandwidth which resembles the main limitation with this approach.

GPR technique uses transmitting and receiving antennas separated by a small fixed distance, to send electromagnetic (EM) energy into the ground and then record the returning signals. Depending on the application, different antennas are used where low-frequency antennas provide greater penetration, but lower resolution and high-frequency antennas have limited penetration but higher resolution as shown in **Figure 24**.

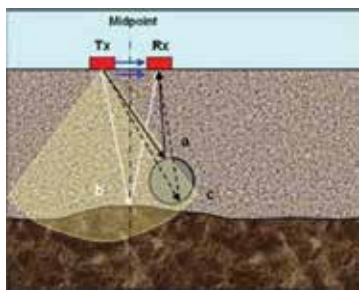

Figure 24. EM wave sent into the ground by TX antenna and the reflected EM wave received by RX antenna received wave discontinuity should be at the top and bottom of a buried object.

As mentioned earlier, ground penetrating radar consists of a transmitting antenna which is used to transmit a signal to the ground. Depending on the received signal scattered from the buried body in the ground, identification of the underground target may take place. This is based on the fact that the velocity of propagation of electromagnetic (EM) waves, given by v (m/s), depends on the complex dielectric permittivity of the medium of propagation, where the complex dielectric permittivity of the medium is given by $\varepsilon^*(f) = \varepsilon'(f) - j\varepsilon''(f)$. It should be noted that the imaginary part of the complex dielectric permittivity $\varepsilon''(f)$ expresses the energy dissipated in the medium, while the real part $\varepsilon'(f)$ is associated with the capability to store energy when an alternating electric field is applied.

An important parameter that should be considered in GPR operation is that the complex dielectric permittivity of the soil under test varies considerably with the frequency of the applied electromagnetic signal. This frequency dependence of permittivity is a function of the

polarization arising from the orientation with the imposed electric field of molecules that have permanent dipole moments. The mathematical formulation of Debye describes this process for pure polar material by [31]:

$$\varepsilon^*(f) = \varepsilon_\infty + \frac{\varepsilon_s - \varepsilon_\infty}{1 + \left(\frac{jf}{f_{rel}}\right)} - \frac{j\sigma_{dc}}{2\pi f \varepsilon_o} \tag{13}$$

where ε_∞ represents the permittivity at frequencies so high that molecular orientation does not have time to contribute to the polarization, ε_s represents the static permittivity (i.e., the value at zero frequency) and f_{rel} (Hz) is the relaxation frequency, defined at which the permittivity equals $(\varepsilon_s + \varepsilon_\infty)/2$. The separation of Eq. (13) into real and imaginary parts is shown in **Figure 25**, for a material of $\varepsilon_s = 20$, $\varepsilon_\infty = 15$ and $f_{rel} = 10^{8.47}$ Hz (300 MHz). **Figure 25** shows the real part and imaginary part values analyzed by Debye model. From the figure, the permittivity has constant values with zero losses at low and high frequencies, while losses appear at intermediate frequency.

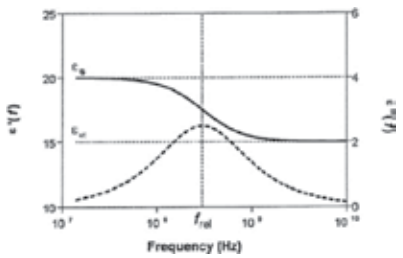

Figure 25. Example of the Debye model for the real part (solid line) and imaginary part (dashed line) of the permittivity.

The Debye parameters of water are $\varepsilon_s = 80.1$, $\varepsilon_\infty = 4.2$, and $f_{rel} = 10^{10.2}$ Hz (17.1 GHz) at 25°C. In sandy soils, most water is effectively in its free liquid state. In the case of GPR measurements, $\varepsilon''(f)$ is often small compared with $\varepsilon'(f)$. The real part of the permittivity of water within the megahertz to gigahertz bandwidth is given by **Table 3**:

Temperature (°K)	279	297	303	337
Relative dielectric	86	79	75	66

Table 3. Dielectric permittivity measurement of drinkable water [18].

For reliable measurements, the multi-offset reflection method will be used where multiple measurements with different antennas separations (radar transmitting and receiving antennas) are performed. More precisely, the wide angle reflection and refraction (WARR) configuration will be adopted in the design architecture and measurement setup [32]. As shown in

http://dx.doi.org/10.5772/64773

Figure 26 (a), the WARR setup consists of a transmitting antenna at a fixed location, while the distance between the receiving antennas is increased stepwise.

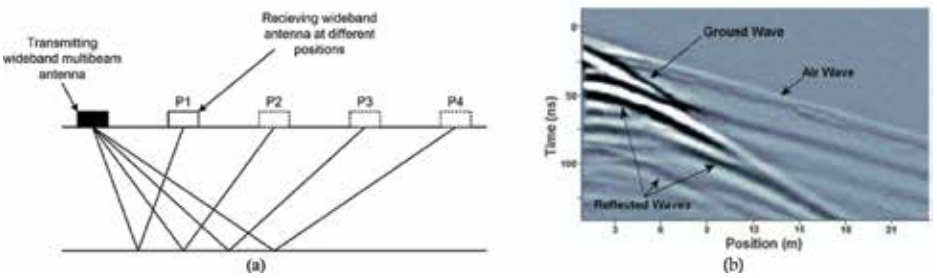

Figure 26. (a) Wide angle reflection and refraction (WARR) acquisition, (b) common-midpoint (CMP) measurement made with a 100 MHz antenna at the Cambridge Research Station, University of Guelph, ON, Canada.

To collect the reflected data, only one antenna will be used. This antenna will be displaced continuously along the survey line with a fine spatial interval between two receiving positions and continuous-wave radar (CW) modulation scheme will be adopted. Continuous bottom layers with different soil water content or more generally with sufficient permittivity contrast can be easily identified as this result in consistent reflected waves data that can fit the following condition (see illustrative examples of **Figure 26 (b)**)

$$v_{soil} = \frac{2\sqrt{d^2 + 0.5a^2}}{t_{rw(a)}} \tag{14}$$

where $t_{rw(x)}$ is the zero time corrected arrival times of the reflected waves, a is the antenna separations, d is the depth of the reflecting layer, and v_{soil} is the root mean square (RMS) velocity down to the bottom of that layer. The RMS velocity and the depth d can be calculated by solving Eq. (14) for different antenna separations [33]. Naturally, the soil beneath the surface till the water level (within the penetration range allowed by the GPR) consists of multiple horizontal layers (reflectors). Eq. (15) is used together with the Dix formula [34] in order to estimate the dielectric constant of each layer as formulated by Eq. (16).

$$v_{\int,n} = \sqrt{\frac{t_{rw,n}v^2_{soil,n} - t_{rw,n-1}v^2_{soil,n-1}}{t_{rw,n} - t_{rw,n-1}}} \tag{15}$$

where $v_{soil,n}$ and $v_{soil,n-1}$ are the average interval velocities from the surface down to the bottom of layers n and $n–1$, respectively. $t_{rw,n}$ and $t_{rw,n-1}$ are the two-way travel time down to the bottom

of layers n and $n-1$, respectively, the upper layer of the soil being denoted by $n=1$. The thickness of layer n is thus given by Eq. (16) as follows:

$$d = \frac{v_{i,n}\left(t_{rw,n} - t_{rw,n-1}\right)}{2} \tag{16}$$

Upon determining the velocity profiles with the depths of the corresponding layers, the corresponding permittivity profile curves can be extracted using the relationship between the interval velocity v_i and the dielectric constant. The imaginary part of the water permittivity becomes negligible with respect to the real part and the former relationship simplifies to the following:

$$v(f) = \frac{c}{\sqrt{\varepsilon'}} \tag{17}$$

Upon determining the measured water permittivity, water content-permittivity relationships can be used to estimate the volumetric water content. Different relationships can be then used as reported in [33–36].

6.1. Quasi-Yagi antenna with size reduction for water detection

Figure 27 shows the geometric structure of planar Yagi-uda antenna printed on commercial FR4 substrate with thickness of 9.5 mm. The antenna shape consists of T-shaped dipole driver and two parasitic meander shapes. The feeding system is printed on the bottom layer of the substrate with length L_f and S_D. The circular resonator is used to match the input impedance of the antenna to a 50 Ω feeding line. The dimension of the substrate width and the length is 72 × 70 cm^2. A $\lambda/4$ slot line ended with a circular slot of diameter L_D is used for matching the antenna [37, 38].

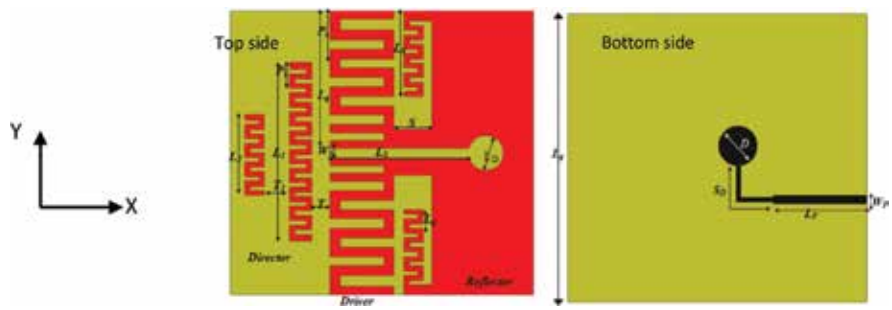

Figure 27. The quasi-Yagi antenna configuration.

http://dx.doi.org/10.5772/64773

Figure 28 shows the Yagi antenna reflection coefficient at frequency range from 50 to 150 MHz with negligible change in the bandwidth due to coupling effect between the antenna driver and director. The coupling effect can be controlled by adjusting the distance between driver and director. **Figure 29** illustrates the reflection coefficient as a function of the balun diameter and its distance from the feeding.

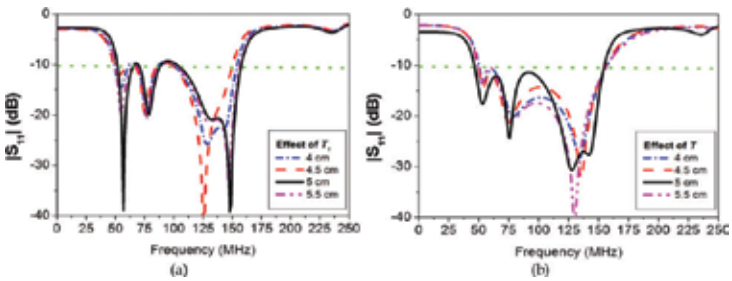

Figure 28. Effect of the length (a) T_1 and (b) Ton the simulated reflection coefficient.

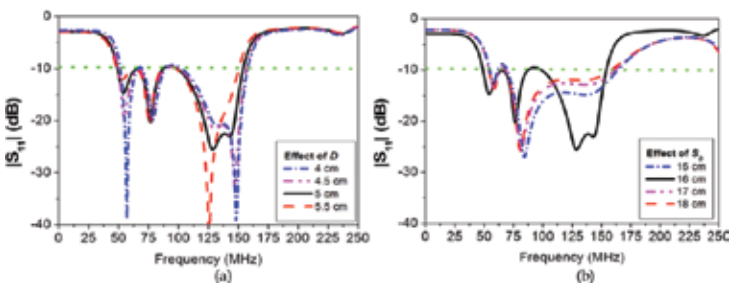

Figure 29. Effect of the length (a) D and (b) S_D on the simulated reflection coefficient.

6.1.1. Ground penetrating radar antenna system

Ground penetrating radar system is used for underground water detection. The operating frequency band extends from 50 to 150 MHz for frequency-modulated continuous-wave (FMCW) radar. The electrical properties of the sand and fresh water layers are investigated using laboratory measurement and EM simulation. The simulated parameters are obtained from Debye dispersive model in the high-frequency structure simulator (HFSS). The radar system as shown in **Figure 30 (a)** requires a high antenna gain to achieve an acceptable scanning resolution. **Figure 30b** illustrates the values of scattering parameters S11 due to projection on the ground surface where the distance between the radiating surface and the ground changes from 0 to 100 cm. The sand layer volume is 300 × 200 × 200 cm^3 as shown in **Figure 30a**. The proposed antenna performance is investigated with and without sand layer as shown in **Figure 30**. The sufficient distance that keeps the antenna reflection coefficient near from free space is almost about 50 cm as shown in **Figure 31a**.

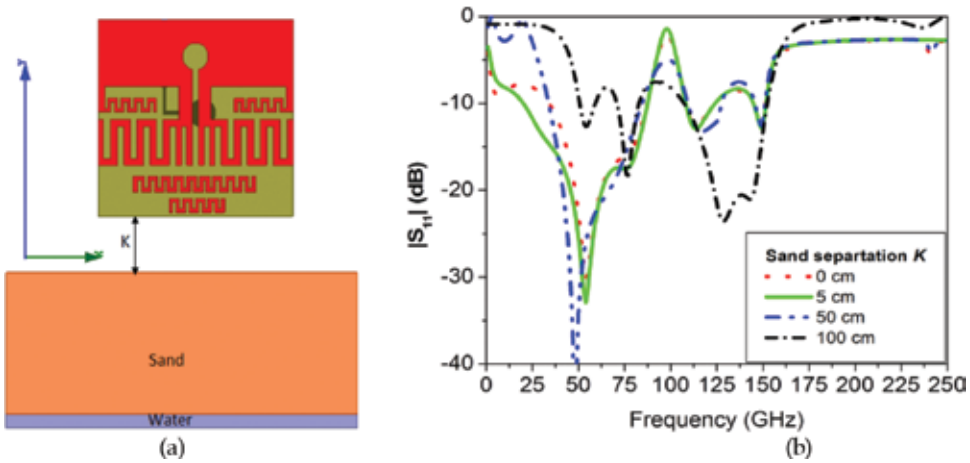

Figure 30. (a) The GPR antenna system for water detection and (b) the effect of K on proposed antenna reflection coefficient.

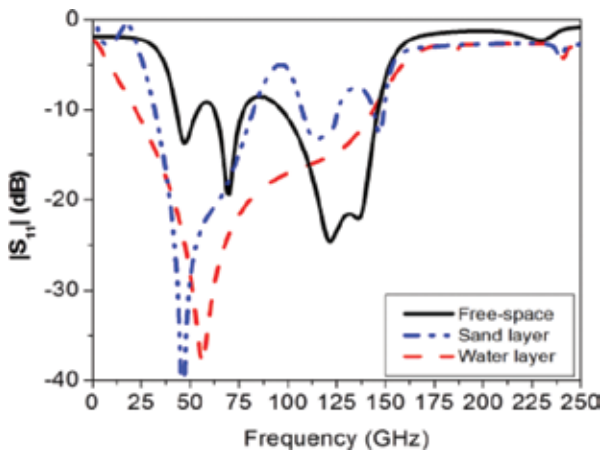

Figure 31. $|S_{11}|$ of the receiver antenna in different cases at K = 50 cm.

6.1.2. Measured results and discussion

The antenna was fabricated as shown in **Figure 32a** using a standard photolithographic etching technology on FR4 substrate with a 100 micrometers copper thickness. **Figure 32b** shows the comparison of the $|S_{11}|$ between measured and simulated results of the optimized antenna which are in fairly good agreement. The antenna measured bandwidth is from 56 to 140 MHz for −6dB threshold in reflection coefficient which covers the required application requirements. The slight difference between the measured and simulated reflection coefficient could be attributed to a misalignment between curved microstrip-line and the circular slot of the balun and effect of the SMA connector.

http://dx.doi.org/10.5772/64773

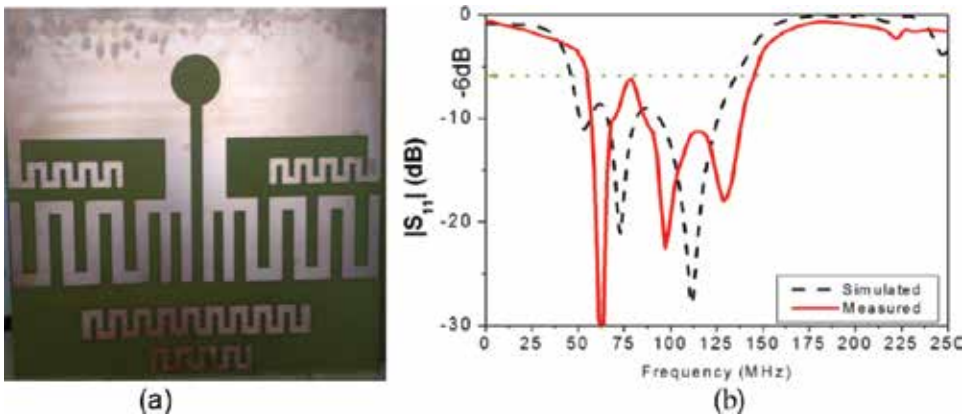

Figure 32. $|S_{11}|$ comparison between measured and simulated reflection coefficient of the proposed antenna.

6.2. Miniaturized log-periodic dipole antenna

The printed log-periodic dipole antenna has many advantages such as lightweight, low costs, and simple to manufacture. **Figure 33** shows the miniaturized printed log periodic antenna (PLPA) which is first order fractal shape. This approach decreases the antenna size with approximately no effect on its bandwidth performance. The proposed antenna printed on thin commercial substrate FR4, 1.6 mm thickness with dielectric constant 4.7 and loss tangent 0.02. The proposed antenna dimensions are shown in **Table 4**. There are seven pairs of array element with scaling factor Ω equal to 0.75 and spacing factor Ψ equal to 0.6. **Figure 34** shows the reflection coefficient response for both conventional, modified LPDA, and FLPDA. The optimized full antenna dimensions are shown in **Table 4**.

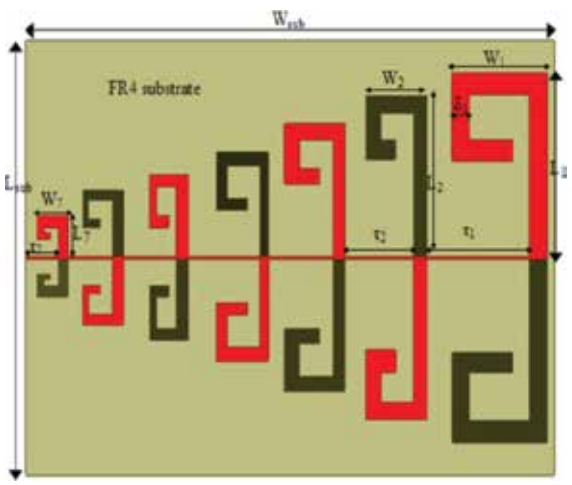

Figure 33. Proposed GPR antenna with first fractal geometry.

L_{SUB}	W_{SUB}	L_1	L_2	L_7	W_F
110	75	32	23.2	7.2	0.32
W_1	W_2	W_7	τ_1	τ_2	τ_7
19.8	12.7	6.5	21.2	14.2	6.8

Table 4. The antenna dimensions in (cm).

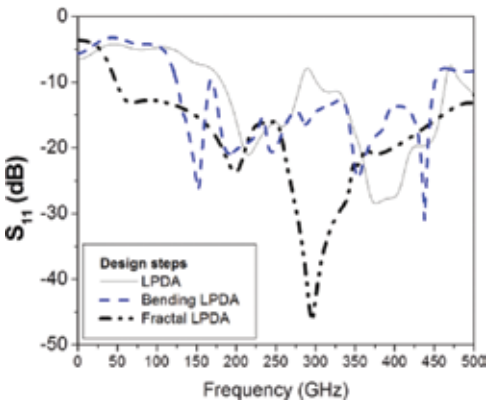

Figure 34. The $|S_{11}|$ design procedures of the proposed antenna.

6.2.1. Ground penetrating radar antenna system

Usually, GPR antennas are placed either on the ground or in a location near the ground with respect to the operating wavelength; hence, each single antenna must satisfy the requirements of radiation and coupling effects. The electrical properties of the sand and fresh water layers are investigated using laboratory measurement and EM simulator. The measurement is done using DAK (coaxial sensor probe and R&S®ZVA vector network analyzers (10 MHz–14 GHz), while the simulated parameters are obtained using Debye dispersive model in the high-frequency structure simulator (HFSS). Both results are very quiet similar as shown in **Figure 35(a, b)**. Debye model is a lossy dielectric dispersive model with a lower frequency near DC, use the loss model material input dialog box to specify the material's conductivity at DC or, its HFSS simulator which has a material specify box in which the conductivity and loss tangent of the material should be defined at DC and low frequency, respectively.

$$\varepsilon_{r_{complex}} = \varepsilon_{r_{optical}} + \left(\frac{\varepsilon_{r_{static}} - \varepsilon_{r_{optical}}}{1 + j\omega\tau} \right) \tag{18}$$

where τ = the relaxation time, $\varepsilon_{rstatic}$ = the static permittivity, and $\varepsilon_{roptical}$ = the high-frequency/optical permittivity. Debye's model is valid for most microwave applications.

http://dx.doi.org/10.5772/64773

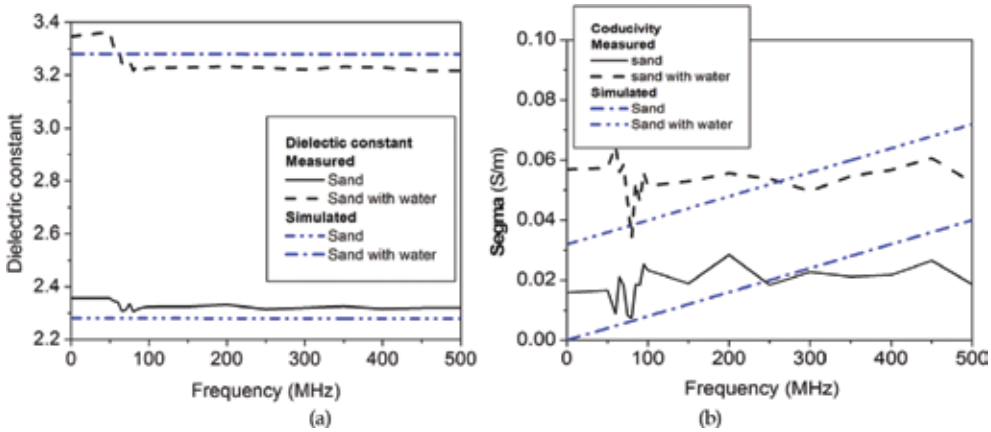

Figure 35. Comparison between measured and simulated electrical properties of sand and sand with water.

In radar system, SAR techniques require high antenna gain to achieve acceptable measurement resolutions. This necessitates that a sufficient large aperture at the lowest frequency to be transmitted. **Figure 36** shows the effect of antenna height on the ground surface (S). It is clear that as distance ***S*** increases, the reflection coefficient becomes closer to the case of free space. The ground volume is 300 × 200 × 200 cm^3, and it can be seen that the width of the 3-dB footprint increases considerably as the source is raised from the ground.

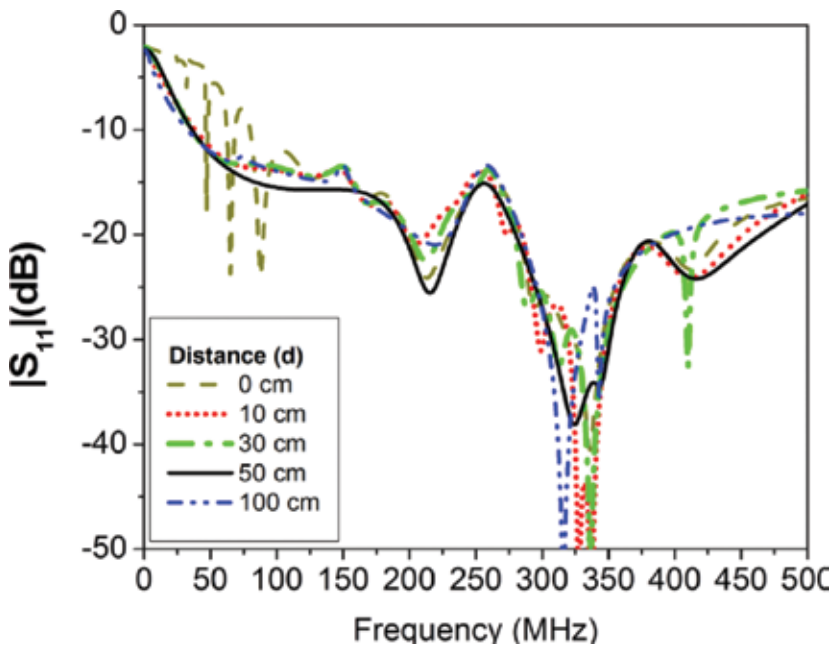

Figure 36. The effect of S on proposed antenna reflection coefficient.

To determine the sufficient distance between both antennas, Snell's law is applied as shown in **Figure 37a**

$$\theta i = \theta r \tag{19}$$

$$tan\theta i \approx \frac{S/2}{q+H} \tag{20}$$

where θi and θr are the incident and reflected angles.

The proposed antenna performance is investigated with and without sand layer. It shows that the antenna directivity is highly increased by about 2dBi as shown in **Table 5**. However, the resonant frequency reduced by about 5% as shown in **Figure 37c**.

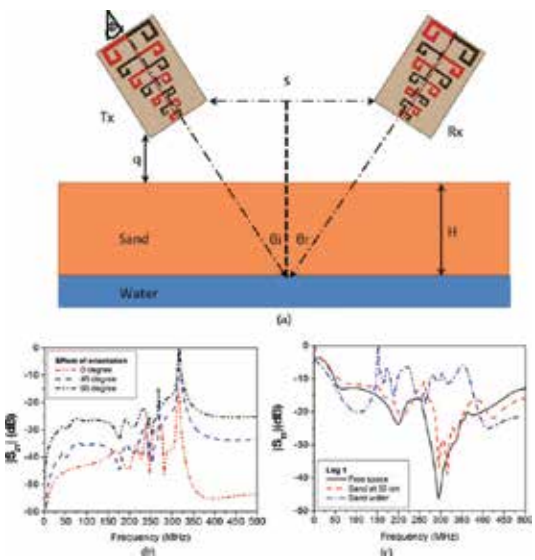

Figure 37. (a) The GPR system for water detection, (b) the $|S_{21}|$ mutual coupling between Tx and Rx, and (c) the receiver antenna in different cases.

Freq (MHz)	Free space	Sand layer	Sand and water layer
Average efficiency%	87	88	86
Average direction (dBi)	3	5	4.8
Average BW (%)	440	400	150
Average beamwidth (degrees)	150	100	100
Average (F/B) (ratio)	1.5	2	1.95

Table 5. The antenna parameters.

6.2.2. Experimental results and discussion

To verify the simulated results, the proposed fractal log-periodic dipole antenna was fabricated using photolithographic techniques and measured using m network analyzer. **Figure 38 (a)** shows a photograph of the fabricated antenna, and **Figure 38b** shows the comparison between measured and simulated reflection coefficient against frequency. It can be observed that measured results reasonably agree with the simulated ones for the proposed antenna and the bandwidth is about 225% (50–500 MHz) centered at 150 MHz. These frequencies are chosen at lower and higher frequencies in the pass band of this antenna, that is, at 50 and 500 MHz.

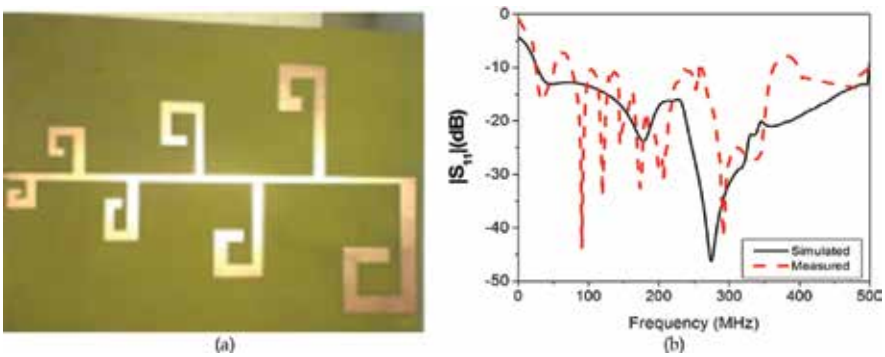

Figure 38. (a) Photograph of the fabricated antenna and (b) comparison between measured and simulated, reflection coefficient.

7. Conclusion

Three examples are given for nondestructive tests, namely noninvasive glucose monitory techniques for dielectrics, microwave bio-sensor for rapid detection of the viruses in biological, and the ground penetrating radar. The first example focuses on the possibilities of a monitor that noninvasively measures blood glucose levels using electromagnetic waves. The technique is based on relating a monitory antenna's resonant frequency to the permittivity and conductivity of skin which in turn is related to the glucose levels. The second applications is the use of biosensor for rapid detection of the enteroviruses which limits the need for sophisticated laboratory diagnostic methods that needs long time and expert scientists to perform the best. The physician in the field normally does fast and simple tests and then gives a fast decision regarded as potentially safe or not. The proposing micro-immunosensing diagnostic assay is based on the very specific immune reflection between antigen and its antibody. The third application is using the ground penetrating radar as a nondestructive test for identifying the underground targets. It consists of a transmitting antenna, which is used to transmit a signal to the ground depending on the received signal scattered from the buried body in the ground, identification of the underground target may take place. In our case, this technique was used for detecting underground water, which is very vital application for many countries nowadays.

Acknowledgements

Some results are done under the support of Egypt Science and Technology Development Fund, STDF, Egypt with contract number: 4149 and contact no. 3137.

Author details

Dalia M.N. Elsheakh*, Esmat A. Abdallah and Hala A. Elsadek

*Address all correspondence to: daliaelsheakh@gmail.com

Electronics Research Institute, Giza, Egypt

References

[1] D. Daneman, "Type 1 Diabetes." The Lancet, vol. 367, no. 9513, pp. 846–858, 2006.

[2] C. Ogden, C. Engelga, A. A. Hedley, M S Eberhardt, and S H Saydah. "Prevalence of Overweight and Obesity Among Adults with Diagnosed Diabetes – United States, 1988–1994 and 1999–2002." Morbidity and Mortality Weekly Report, November 19, pp. 1066–1068, 2004.

[3] H. Paul, T. Dall, and P. Nikolov. "Economic Costs of Diabetes in the U.S." Diabetes Care (American Diabetes Association), vol. 26, pp. 917–932, 2003.

[4] "Executive Summary: Standards of Medical Care in Diabetes—2010." Diabetes Care (American Diabetes Association), vol. 33, pp. S4–S10, 2010.

[5] M. David, J. Kuenen, B. Rikke, H. Zeng, D. Schoenfeld, and R. J Heine. "Translating the A1C Assay Into Estimated." Diabetes Care (American Diabetes Association), no. 31, pp.1–6, 2008.

[6] R. Francine, L. C Gibson, M. Halvorson, S. Carpenter, L. K Fisher, and P. Pitukcheewanont. "A Pilot Study of the Continuous Glucose Monitoring System." Diabetes Care (American Diabetes Association), no. 24, pp. 2030–2034, 2001.

[7] C. Leland, and C. Lyons. "Electrode Systems for Continuous Monitoring in Cardio vascular Surgery." Annals of the New York Academy of Sciences, vol. 102, pp. 29–45, 1962.

[8] D. Jeffrey, and A. P F Turner. "Home Blood Glucose Biosensors: A Commercial." Biosensors and Bioelectronics, vol. 20, no. 12, pp.2435–2453, 2005.

[9] T. Andrea, A. Maran, and G. Pacini. "Non-invasive Glucose Monitoring: Assessment of Technologies and Devices According to quantitative criteria." Diabetes Research and Clinical Practice, no. 77 pp. 16–40, 2007.

[10] G. Dongman, D. Zhang. "Monitor Blood Glucose Levels via Breath Analysis System and Sparse Representation Approach." IEEE Sensors Conference, Nov. pp.1238–1241, Kona, HI 2010.

[11] M.Yuki, T. Horiguchi, H. Ishizawa, S.Tezuka, H.Hara. "Basis Examination for Development of Noninvasive Blood Glucose Measuring Instrument by Near-Infrared Confocal Optical System." SICE Annual Conference, Taipei, Taiwan, 2010.

[12] L.Kirill, M. Eledrisi, M. Motamedi, R. Esenaliev, "Noninvasive Blood Glucose Monitoring with Optical Coherence tomography: a pilot study in human subjects." Diabetes Care (American Diabetes Association), 25, no. 12, pp. 2263–2267, 2002.

[13] Yeh, Shu-Jen, Chrales Hanna, Omar Khalil, "Monitoring Blood Glucose Changes in Cutaneous Tissue by Temperature-Modulated Localized Reflectance Measurements." Clinical Chemistry, vol. 49, no. 6, pp.924–934, 2003.

[14] C. Green, and R. Jean, "Design of a Microwave Sensor for Non-Invasive Determination of Blood-Glucose Concentration." Master's Thesis, Engineering and Computer Science, Baylor University, 2005.

[15] B. Randall, E. C Green, and M. J McClung. "A Microwave Frequency Sensor for Non-Invasive Blood-Glucose." IEEE Sensors Applications Symposium, Atlanta, GA, 2008.

[16] M. Yvanoff and J Venkataraman. "A Feasibility Study of Tissue Characterization Using LC Sensors." IEEE Transactions on Antennas and Propagation, vol. 57, no. 4, pp. 885–893, 2009.

[17] J. Jung, W. Choi ; J. Choi, "A Small Wideband Microstrip Fed Monopole Antenna." IEEE Microwave and Wireless Components Letters , vol.15, pp. 703–705, Oct., 2005.

[18] J. Yves, N. Le Prieur, L. Campion, I. Guilhem, H. Allannic, and D. Maugendre. "Clinical and Statistical Evaluation of Self-Monitoring Blood Glucose Meters." Diabetes Care(American Diabetes Association), vol. 21, no. 11, pp.1919–1924, 1998.

[19] G.L. Dai and M.Y. Xia, "Design of Compact Dual-Band Switchable Bandpass Filter", Electron Letters, vol. 45, pp. 506–507, 2009.20. "ADF4350 Data Sheet Rev. 0." Analog Devices. 2008. http://www.analog.com/static/ imported-files/data_sheets/ ADF4350.pdf.

[20] D.Elsheakh and E.Abdallah, "Novel Rapid Detection of Different Viruses in blood Using Microimmuno-Sensor", The 7th European Conference on Antennas and Propagation (EuCAP) 8–12 April in Gutenberg, Sweden, 2013.

[21] "Agilent 85070E Dielectric Probe Kit: Technical Overview." Agilent Technologies. March 28, 2008. http://cp.literature.agilent.com/litweb/pdf/5989-0222EN.pdf

[22] D. Pozar, "Microwave Engineering", 4th ed. John Wiley & Sons, Inc, 2012

[23] S. Gabriel, et al. "The Dielectric Properties of Biological Tissues: II. Measurements in the Frequency Range 10 Hz to 20 GHz." Physics in Medicine and Biology, pp. 2231–2250, vol. 41, no.11.

[24] D. Elsheakh, H. A. Elsadek, E. A.Abdallah, S. Atteya, and W. N. ELmazny, " Rapid Detection of Blood Entero-Viruses Using Microstrip Antenna Bio Sensor", The 16th European Microwave Week, Germany, 2013.

[25] K.S. Cole and R.H. Cole, "Dispersion and Absorption in Dielectrics – I Alternating Current Characteristics". The Journal of Chemical Physics, vol. 9, pp. 341–352. Bibcode 1941JChPh…9..341C.doi:10.1063/1.1750906.

[26] J.H. Park, et al., "The Correlation of the Complex Dielectric Constant and Blood Glucose at Low Frequency." Biosensors and Bioelectronics, vol. 19, no. 4, pp. 321–324, 2003.

[27] Y. Rahmat-Samii, "Wearable and Implantable Antennas in Body-Centric Communications," Antennas and Propagation, 2007. EuCAP 2007. The Second European Conference, pp.1–5, 11–16, Nov. 2007.

[28] T. Chen, D. Dubuc, K.Grenier, "Resonant-Based Microwave Biosensor for Physiological Liquid Identification," 42nd European Microwave Conference (EuMC), pp. 448,450, 2012.

[29] D. Elsheakh and E. Abdallah, "Novel Rapid Detection of Different Viruses in blood Using Microimmuno-Sensor", The 7th European Conference on Antennas and Propagation (EuCAP), 8–12 April in Gutenberg, Sweden, 2013.

[30] D.Elsheakh, H. A. Elsadek, E. A. Abdallah, S. Atteya, and W. N. ELmazny, " Rapid Detection of Blood Entero-Viruses Using Microstrip Antenna Bio Sensor", The 16th European Microwave Week, Germany, 2013.

[31] P. Debye, "Polar Molecules," Dover Publications, Mineola, NY, 1929.

[32] M. Pieraccini, A. Bicci, D. Mecatti, G. Macaluso, C. Atzeni, "Propagation of Large Bandwidth Microwave Signals in Water," IEEE Antennas and Propagation Society, vol. 57, no. 11, pp. 3612–3618, 2009.

[33] D. N. Elsheakh and E. A. Abdallah, "Ultra Wide Band Planar Printed Quasi-Yagi Antenna with Size Reduction for Water Detection in the Egyptian Desert", Microwave and Optical Technology Letters, vol. 57, no. 1, pp.226–233, 2015.

[34] D. N. Elsheakh and E.A. Abdallah, "Compact Shape of Vivaldi Antenna for Water Detection by Using Ground Penetrating Radar (GPR)", Microwave and Optical Technology Letters, vol. 56, no.8, pp. 1801–1809, 2014.

[35] D. Elsheakh and E. A. Abdallah, "Compact Printed Log-Periodic Dipole Antenna for Water Detection by Using Ground Penetrating Radar (GPR)", Microwave and Optical Technology Letters, vol. 56, no. 6, pp. 1225–1232, 2014.

http://dx.doi.org/10.5772/64773

[36] X. X. Yin et al., "A Resistive Loaded Tapered Slot antenna for Ground Penetrating radar", Modern Radar, vol. 28, pp. 58–68, 2006.

[37] K., Tutku, A. Hood, and E. Topsakal. "Design of a Dual-Band Implantable Antenna and Development of Skin Mimicking Gels for Continuous Glucose Monitoring." IEEE Transactions on Microwave Theory and Techniques vol. 56, no. 4, pp. 1001–1008, 2008.

[38] K. Buell, H. Mosallaei, and K. Sarabandi, "Metamaterial Insulator Enabled Superdirective Array," IEEE Antennas and Propagation Society, vol. 55, no. 4, pp. 1074–1085, 2007.

Chapter 13

LTCC-Based System-in-Package (SiP) Technology for Microwave System Applications

Young Chul Lee

Additional information is available at the end of the chapter

http://dx.doi.org/10.5772/66327

Abstract

Monolithic low-temperature co-fired ceramic (LTCC) SiP modules have been presented for microwave applications. In order to integrate almost passive circuits of a radio system into the LTCC substrate, key technologies such as suppressing parasitic resonant modes, low-loss transitions and compact passive devices have been investigated. Well analyzed mechanisms on the parasitic resonant modes and their suppressing methods have been applied to high-isolation SiP structures. A strip line (SL) to CPW vertical transition using a stepped via structure embedding air cavities has been devised and has been used to design a SL BPF. A surface mount technology (SMT) pad transition has been developed by utilizing a modified coaxial line. A LPF composed of vertical plate capacitors and helical inductors and a 2 × 2 array antenna have been developed. A 61 GHz heterodyne transmitter LTCC SiP module has been implemented by monolithically embedding all passive circuits such as a SL BPF, 2 × 2 array antenna, SMT pads and feeding lines into it. A 60 GHz amplitude shift-keying (ASK) transceiver LTCC SiP module has been implemented as small as 17.8 × 17.9 × 0.6 mm^3 by integrating a high-isolation via fence and a LPF. They have been characterized in terms of an output power, spectrum and link test.

Keywords: LTCC, SiP, transition, BPF, antenna

1. Introduction

In general, the final stage for implementation of microwave systems is system integration. It could be either integrated circuit (IC) die-level integration or package level one. And also, how to integrate microwave systems should be considered at the first stage of its development. Roughly, there are two categories for an integration technology of microwave systems: on-chip

technology and in-package one. The progress in these integration technologies has been formidable over the past decade for microwave applications. In these technologies, the main key issue is antenna integration on the chip or in the package, because its integration can provide several advantages such as low cost, compact size, high reliability and high reproducibility.

In the case of on-chip integration technologies based on complementary metal-oxide-semiconductor (CMOS), bipolar CMOS (BiCMOS) and silicon germanium (SiGe) BiCMOS, various researches have been explored up to recently. However, due to high permittivity (~11.7) and low resistivity (~10 Ω cm) [1, 2] of the Si-based substrate, integrated antennas have been suffered from low radiation efficiency and matching bandwidth. In order to modify properties of the substrate, although several novel techniques such as air cavity [3], artificial magnetic conductor [4], suspended membrane [5], ion implantation [6] and meta-surface [7] have been investigated; high-gain and broadband requirements are still below expectations, compared to those of package-based integration technologies [1, 8, 9].

In the package-based integration technologies, aside from highly integrated radio dies, almost passive components such as antenna, BPF and others are monolithically realized in the package substrate, thanks to three-dimensional (3D) stacking capability using via, multilayer and cavity. Very compact and high-performance microwave modules have been recently presented by using multilayer ceramic or printed circuit board (PCB) [10] technologies. Low-temperature co-fired ceramic (LTCC) [11–13] is a representative multilayer ceramic technology. For the past two decades, several LTCC modules involving antennas and other passive circuits with microwave radio chips have been developed and also it is possible to integrate high-gain antennas because of its properties of low-loss substrate and metallization (Ag).

In this chapter, highly integrated monolithic SiP modules have been presented for microwave system applications. In order to integrate radio systems in the single LTCC package module, key technologies such as suppressing parasitic resonant modes, low-loss transitions and compact and high-performance passive devices have been investigated after definition of monolithic SiP module. Finally, a 61 GHz transmitter (Tx) LTCC SiP module and a 60 GHz ASK transceiver one have been implemented in a size of 36 × 12 × 0.9 and 17.8 × 17.9 × 0.6 mm^3, respectively and they have been characterized in terms of an output power, spectrum and link test.

2. Monolithic SiP module

Figure 1 shows a three-dimensional (3D) schematic concept of the monolithic LTCC SiP module integrating a whole radio system consisting of active ICs and passive components in the single LTCC substrate. The filter and antenna are monolithically integrated in the LTCC dielectric and on its top layer, respectively. Active ICs are also mounted on the top of the LTCC multilayers. For miniaturization of the SiP module, passive circuits such as filters, antenna, surface mounted technology (SMT) pads, DC bias feedings and transmission lines are vertically or horizontally deployed by using vertical via interconnections, internal ground

http://dx.doi.org/10.5772/66327

plane (I-GND) and signal line transitions in the substrate. Several transmission lines such as a strip line (SL), conductor-backed coplanar waveguide (CB-CPW), or microstrip line (MSL) are utilized within the LTCC block or on its top layer. By considering device and interconnection structures to be integrated in the SiP module, suitable transmission line is designed.

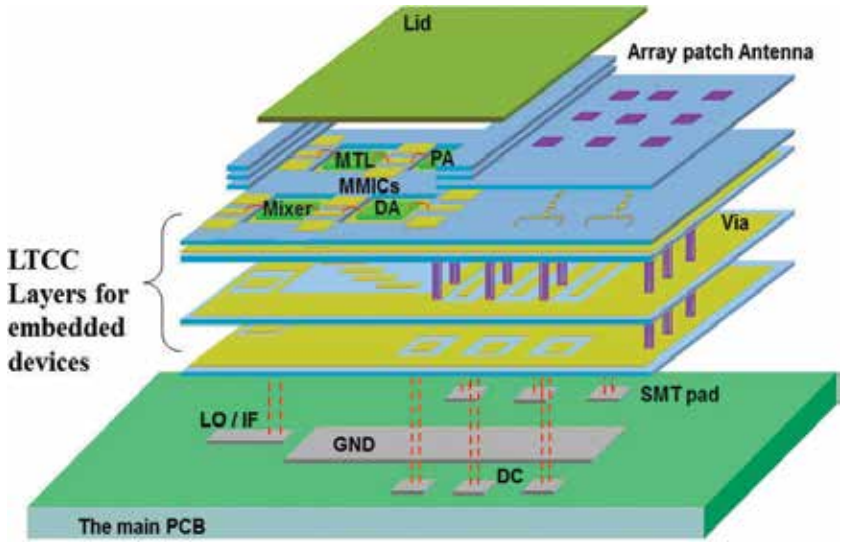

Figure 1. Three-dimensional (3D) schematic concept of a monolithic SiP module.

However, because various integrated transmission lines, passive devices and transitions are compactly integrated in the small area of the monolithic LTCC SiP module, they can make parasitic propagating structures and lead to unwanted cross talk issue. So, suppression of the parasitic resonant modes is one of the key issues in the design of SiP module. In addition, attenuation in interconnections between different signal lines or inter layers should be minimized for power efficiency and noise performance of the SiP module. And also, high-performance and compact passive devices should be designed.

3. Suppression of parasitic resonant modes

A CB-CPW and SL are in general used as signal lines of a SiP module because of their low dispersion and radiation. The CB-CPW consists of a lower and upper ground plane, embedded vias and a signal line (W) and the SL as shown in **Figure 2A**. However, these ground planes and vias can make parasitic resonant circuits such as rectangular waveguide (R-W/G), a parallel-plate waveguide and a patch antenna [14, 15] and they cause undesired resonant modes. An input signal is coupled by the gap of the CB-CPW, propagates through the parallel plate and finally radiates due to a parasitic patch resonator. In the case of the SL as shown in **Figure 2B**, it is basically a buried device and its structure is also composed of a lower and upper

ground plane, vias and a strip. The ground planes and vias generate the parasitic R-W/G, which is analogous to that of the CB-CPW.

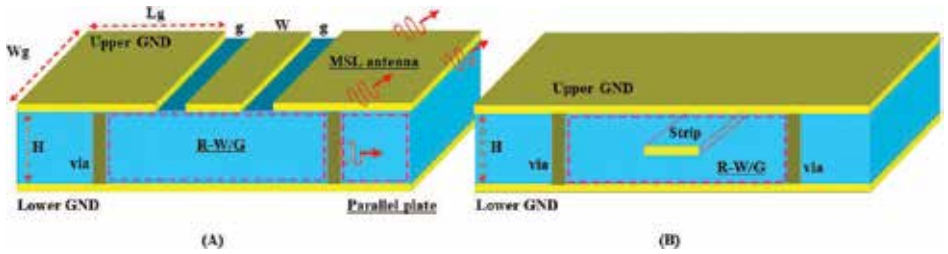

Figure 2. Structure of a CB-CPW (A) and SL (B) involving parasitic resonant circuits.

The resonant frequency (f_{WG}) due to the R-W/G is given by Pozar [16],

$$c_{p\ sample} = \frac{Q_{sample}}{Q_{ref}} \frac{m_{ref}}{m_{sample}} C_{p\ ref} \tag{1}$$

where D is the spacing between vias and it is the same as a horizontal dimension of a rectangular waveguide, ε_o is the permittivity of free space, μ_o is the permeability of free space and ε_r is the relative dielectric constant of the substrate.

The resonant frequency (f_{pr}) due to the surface ground planes is similar to that of the simple patch antenna [14, 15],

$$f_{pr} = \frac{c}{2W_g} \left(\frac{\epsilon\_r + 1}{2} \right)^{-1/2} \left[\text{GHz} \right] \tag{2}$$

where W_g is a width of a rectangular patch and c is the speed of light.

Figure 3 shows measured insertion loss characteristics of a 50 Ω CB-CPW line (A) and a SL BPF (B) fabricated in the LTCC substrate. Unwanted resonant modes are distinctly observed in the CB-CPW and SL BPF. In the case of the CB-CPW as shown in **Figure 3A**, its width, gap and length are 300, 150 and 3260 μm, respectively and its substrate height is 400 μm. Vias in order to short the lower and upper ground planes are placed at the both sides with a distance (D) of 1620 μm. The parasitic R-W/G is generated in the CB-CPW due to the ground planes and vias. In these dimensions of the CB-CPW, a propagation mode of the parasitic R-W/G is generated at 34 GHz. Resonances at 19.5 and 39 GHz are due to a parasitic patch antenna mode and its harmonic, respectively. Some input signal in the CB-CPW propagates to the parasitic R-W/G by coupling through its gap, passes through a parallel-plate W/G and finally radiates from the parasitic patch antenna. **Figure 3B** presents tested insertion losses of the 40 GHz SL BPF. The BPF was realized with six-stacked LTCC layers. Among the six-stacked layers, the SL filter was placed on the third layer and the CPW pads are on the top layer for on-wafer probing.

http://dx.doi.org/10.5772/66327

Both top and bottom ground planes were connected to each other through ground vias to equalize the electric potential. The inset of **Figure 3B** shows the critical two dimensions (D_{CPW} and D_{SL}), which cause resonant phenomena. D_{CPW} of 1.15 mm is the distance between embedded vias. The lower and upper ground planes of the SL are shorted by using via blocks. The distance of D_{SL} is 2.32 mm. Two parasitic R-W/Gs with the lengths of D_{CPW} and D_{SL} are created in this SL BPF. Therefore, its performances are degraded due to spurious responses at 36 and 47.6 GHz, which are the parasitic R-W/G modes of TE20 generated by D_{SL} of 2.32 mm and D_{CPW} of 1.15 mm, respectively.

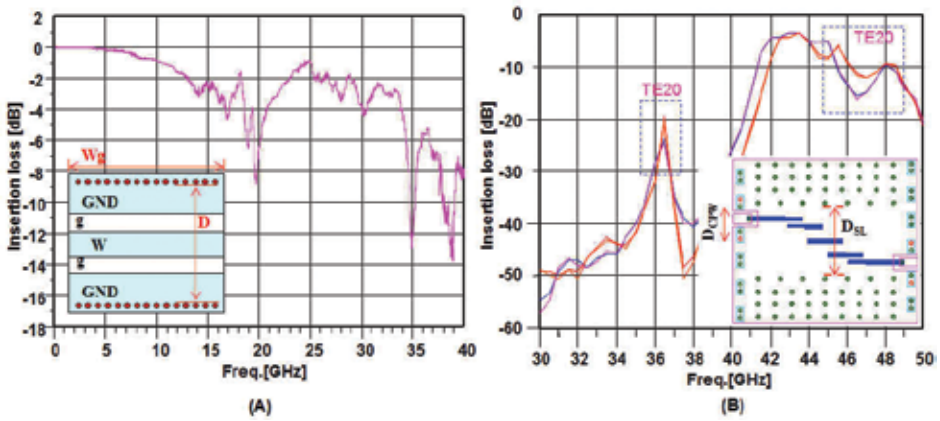

Figure 3. Unwanted resonance modes due to parasitic structures in the fabricated CB-CPW (A) [an inset: the top view of the CB-CPW] and the fabricated SL BPF (B) [the inset: the layout of the BPF].

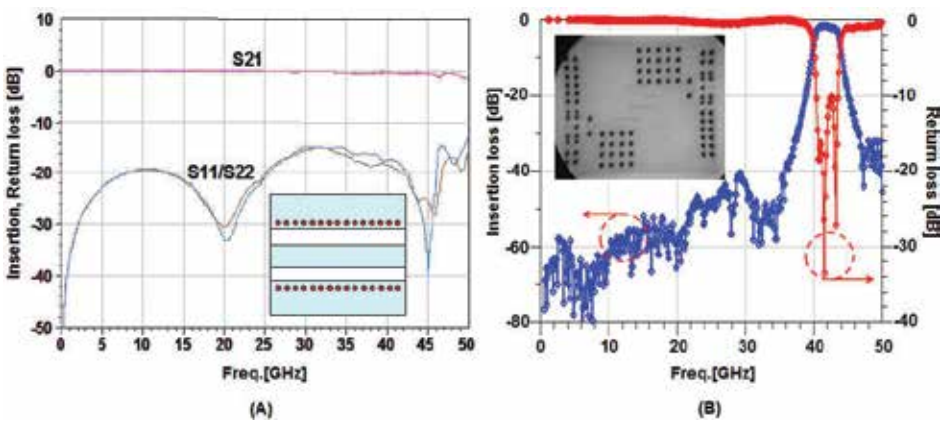

Figure 4. Resonance-free CB-CPW (the inset: the top view of the CB-CPW) (A) and SL BPF (the inset: X-ray photo of the fabricated SL BPF) (B).

The parasitic R-W/G modes (f_{WG}) in operating frequency band can be successfully suppressed by placing the vias within shorter distance than the calculated value from Eq. (1), because

parasitic propagating modes are generated in the higher frequency than that of an interesting band. By using this method, the CB-CPW and SL BPF were modified and fabricated. Their measured characteristics are indicated in **Figure 4**. The modified via placement for the CB-CPW and the SL BPF is presented in each inset of **Figure 4A** and **B**, respectively. The parasitic resonant modes are clearly suppressed in the operation frequency region [17]. In the CB-CPW, the distance (D) of 1620 μm is shortened to 700 μm and its layout and measured results are shown in **Figure 4A**. For the SL BPF, D_{CPW} of 1.15 mm is modified to 760 μm, which corresponds to the parasitic rectangular WG mode of TE10 at 76 GHz. One of the two GND-via blocks facing each other is deleted in order not to make the parasitic R-W/G in the SL structure. The X-ray photo of the fabricated SL BPF and the measured loss characteristics are presented in **Figure 4B**.

4. Low-loss transitions for 3D integration

For the 3D integration of microwave radio systems, several vertical transitions such as CPW-to-SL transition [18, 19], MSL-to-SL transition [20, 21], CPW-to-CPW transition [18, 22] and coaxial-like surface mount technology (SMT) pad transition [23] have been developed. These transitions allow the integration of passive and active circuits to be placed in inner layers or mounted on the top layer. The main issue for **3D** interconnection using transitions is to reduce attenuation and discontinuity. In particular, radiation due to structural discontinuity causes cross talk issue. Therefore, several attempts have been tried in order to remedy problems due to discontinuities. In order to improve impedance matching or compensate parasitics, the coaxial-like transition and intermediate ground planes have been utilized [18–23].

4.1. Strip line (SL)-to-CPW vertical via transition

In the vertical via transitions, the total physical height of the directly stacked vias has a decisive effect on their RF performance besides capacitive or inductive effects in the transition region. In the case of its height over one tenth of the wavelength (>0.1 λ) in the mm-wave frequencies, input signals can be significantly radiated or reflected.

Figure 5 shows proposed SL-to-CPW transition and its simulated performances [24]. A cross-sectional structure of the proposed SL-to-CPW via transition is shown in **Figure 5A**. Each LTCC layer is 100 μm high. The CPW on the top layer is connected with the embedded SL on the 4th layer (L4) by using vertical vias, which are subdivided into three-stepped one. Because of the proposed three-stepped via structure, the critical dimension, which mainly causes the physical discontinuity, is decreased from 300 to 100 μm. The wavelength (λ) on the LTCC CPW with relative dielectric constant of 7.0 is 2.56 mm at 60 GH. Its rate of the critical dimension to λ is decreased from 11 to 3.9%, respectively. However, it leads to the increase in the shunt capacitance between the vias and SL ground planes. For reduction in the increased shunt capacitance, the embedded air cavities are inserted below the stepped vias. In order to evaluate the proposed vertical via transition, the SL-to-CPW vertical transition is designed in back-to-back type as shown in **Figure 5B**. The ground planes of the CPWs and SL are connected by shielding vias. In order to design the 50 Ω CPW and SL, the CPW with the width of 250 μm and gap of

http://dx.doi.org/10.5772/66327

99 μm is designed and the width of the SL is 135 μm. For comparison purposes, the conventional transition using the directly stacked vias is also designed. For the conventional transition, two 526 μm-long CPW lines are connected with the 2650 μm-long SL. In the proposed one, two 526 μm-long CPW lines and 2050 μm-long SL are used. The air cavities are embedded through the 2nd to 5th layer below the 7th layer via and through the 2nd to 3rd layer below the 5th layer via. By using a 3-D finite integration technique (FIT) simulator [25], all transitions have been designed and analyzed. Calculated results of the proposed transition in comparison with the conventional one are presented in **Figure 5C** and **D**. The proposed transition shows better performance in terms of return and insertion loss than that of the conventional one because of reduced via discontinuities. For quantitative analysis of improved performance, radiation losses ($1-|S_{11}|^2-|S_{21}|^2$) of the SL-to-CPW vertical transitions are calculated by using the simulated insertion and return loss and are illustrated in **Figure 5D**. At 60 GHz, radiation of the proposed transition is reduced by 23 and 62% by using the three-stepped via structure and embedded air cavities, respectively, compared to the conventional one.

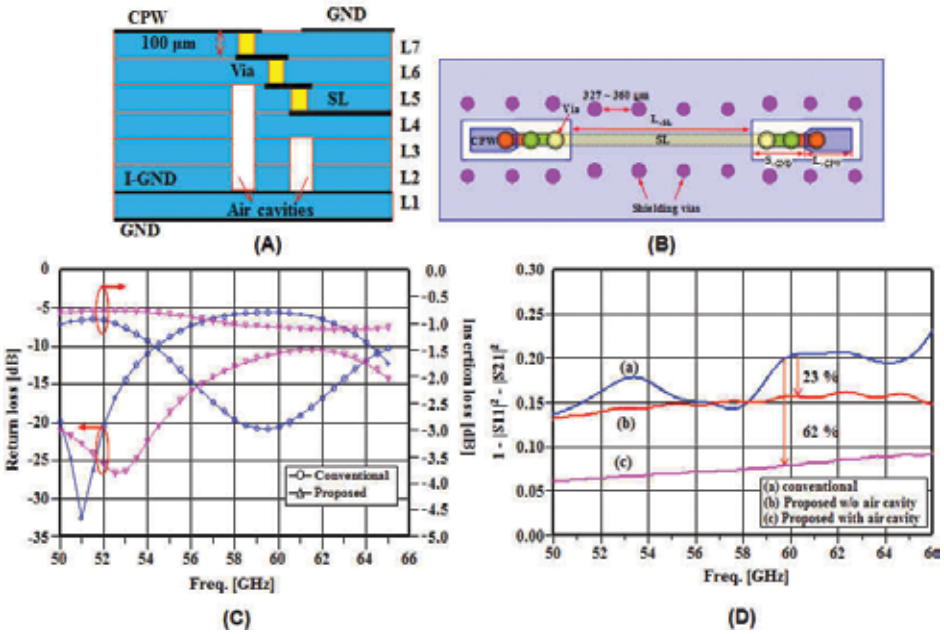

Figure 5. Proposed SL-to-CPW via transition and its simulated performances [(A): its cross-sectional view (Lx: the number of LTCC layers), (B): its layout in a back-to-back structure, (C): return and insertion loss characteristics and (D): radiation loss ones].

The designed transitions in the back-to-back structure were fabricated using seven-layered LTCC substrate and the fabricated ones were characterized by using a probing method as shown in **Figure 6**. For the proposed transition, embedded air cavities are clearly formed below the 5th and 7th layer via as shown in an inset of **Figure 6B** and also its S_{11} and S_{21} characteristics are improved compared to the conventional one. The measured S_{11} and S_{21} of the CPW-SL-

CPW are less than −10 dB and −2.0 dB, respectively, from 50 to 65 GHz. In particular, its low S_{21} of −1.6 dB is achieved at 60 GHz. These values represent all losses along the three-segment transmission lines and the two vertical via transitions. Considering the total loss of transmission lines with −0.19 dB, which is calculated by using a conventional line calculator, the transition loss per a ST transition is 0.7 dB at 60 GHz.

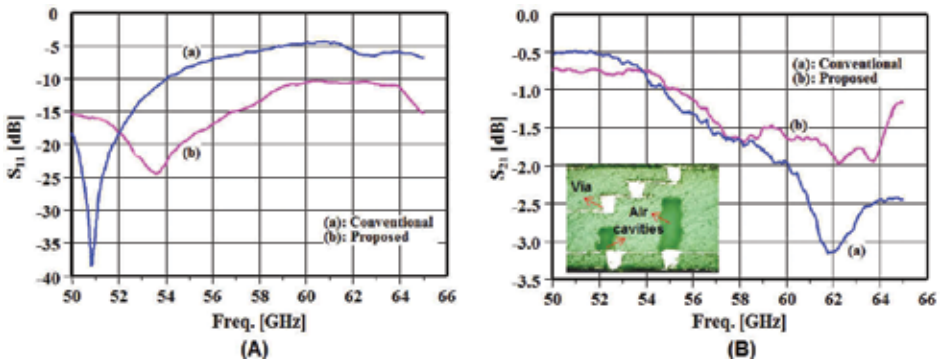

Figure 6. Measured return losses (A) and insertion ones (B) of the fabricated vertical via transitions in the back-to-back type using the proposed transition and the conventional one (an inset: cross-sectional views of the fabricated proposed one).

4.2. SMT pad using a coaxial-line transition

In general, LTCC SiP modules have been developed in type of SMT package because of low cost and easy assembly. In order to mount LTCC SiP modules on the main board, the low-loss transition between the signal port and SMT pad is required. In addition, the excitation of package modes [26] should be investigated for millimeter-wave applications. Typical transitions from I/O (input and output) port to the SMT pad in the SiP module have been designed by using vertical via structures [18–24]. In the case of long transition with several stacked vias over seven layers (>0.7 mm), it is difficult to control discontinuities and radiation. Therefore, by using a coaxial-line structure, the SMT pad has been implemented for the SMT LTCC SiP applications.

In order to suppress radiation in the long transition with several stacked vias, a SMT pad transition using a coaxial-line structure is proposed. By using a commercial tool [25], a CPW-to-coaxial line-to-SMT pad transition in a nine-layer LTCC substrate has been designed and its structure and designed results are presented in **Figure 7A**, **B** and **C**, respectively. The relative dielectric constant of the LTCC substrate is 7.8 at 20 GHz. Each layer is 100 μm thick. The total height of the vertical vias in the transition region is 700 μm. Because of a bulky structure of a 50 Ω coaxial line, an inner and outer diameter is optimized in terms of its transition loss and size. Considering losses in the transition, the impedance of the coaxial line of 37 Ω is determined. The diameter of the inner conductor (via) is fixed in 135 μm. The diameter and width of the outer conductor are 695 and 235 μm, respectively. The CPW line is designed in the cavity on L7 for interconnection with other devices or measurement. An embedded CPW (ECPW)

http://dx.doi.org/10.5772/66327

between the coaxial line and CPW is designed on the same layer for their interconnection. The CPW line is with a 144 μm wide strip and a gap of 83 μm. The width and gap of the ECPW are 90 and 95 μm, respectively. Because of the overlapped part between the outer conductors of the coaxial line and the CPW line on the PCB board, E-fields are concentrated and consequently, a significant amount of reflection can be generated. The overlapped part, which is coaxial-line outer conductor to the left of the SMT pad, is cut off. In addition, in order to suppress the radiation at the bending part of interconnection between the coaxial line and CPW, a semicircular cap on the 9th layer (L9) of the LTCC substrate is designed. It radius is 928 μm. The modified SMT pad transition is shown in **Figure 7A**. Its E-field distribution at its cross section and its designed characteristics, comparing the effect of the cap are illustrated in **Figure 7B** and **C**, respectively. E-fields of the pad transition with a cap (WC) are confined between the cap and coaxial cable in the LTCC substrate in **Figure 7B**. From 8 to 20 GHz, the return losses (S_{11} and S_{22}) and insertion losses (S_{21} and S_{12}) of the pad transition with the cap (WC) are clearly improved compared with the pad transition without the cap (WOC).

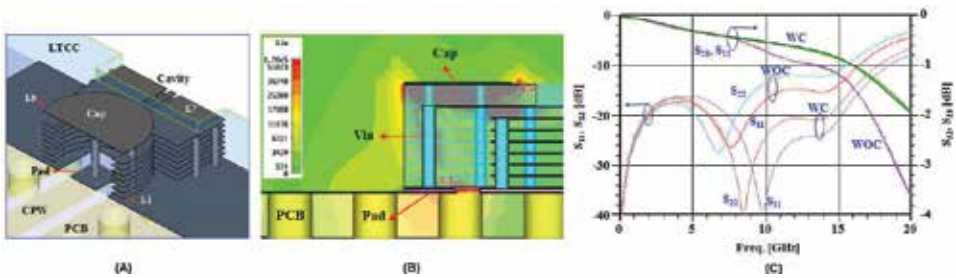

Figure 7. Perspective view (A) of the SMT pad transition using a modified coaxial-line structure, E-field distribution at its cross section (B) and its designed characteristics, comparing the effect of the cap on the top layer (C).

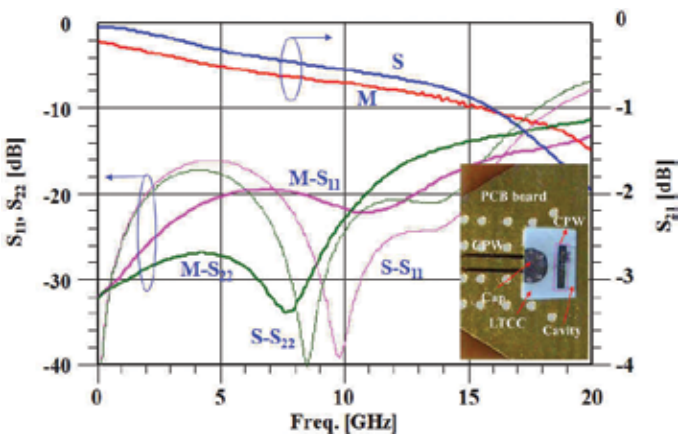

Figure 8. Measured results of the fabricated SMT pad transition, compared to the simulated ones (the inset: the fabricated SMT pad transition on the PCB board, M: measurement and S: simulation).

The modified SMT pad transition was fabricated by using LTCC standard fabrication process. Its measured characteristics are presented in **Figure 8**, compared with simulated ones. Poles of both return (S_{11} and S_{22}) and insertion loss (S_{21}) make a difference between the simulated and measured results. This difference comes from parasitic components due to soldering works. The measured insertion loss of 0.9 dB is achieved at 15 GHz. The return losses of S_{11} and S_{22} are below −14 dB at the same frequency. This SMT pad can be used for X- or Ku-band applications or LO-frequency ports for millimeter-wave SiP applications.

5. Compact LTCC passive devices—SL BPF, LPF and 2 × 2 array antenna

For compact radio system SiP module applications, the key components are the band-pass filter (BPF) and antenna, because they cover significant space and are difficult to be integrated in the RF ICs by using semiconductor technology. In general, they have been implemented in types of planar structures. However, planar structured circuits are usually bulky and are prone to unwanted radiation. Therefore, compact size, shielded electromagnetic cross talk and low-loss **3D** interconnection have been considered as the most important issues for passive device integration in the RF system SiP module.

5.1. A dual-mode four-pole 60 GHz LTCC SL BPF

A SL structured BPF using a dual-mode patch resonator can satisfy key issues for filter integration such as miniaturization and suppressed cross talk, because the dual-mode patch resonator offers a very compact structure [27] and radiation of the SL structure buried between upper and lower ground planes is negligible. However, in order to interconnect it with other circuits on the surface, the low-loss vertical via transition is required.

Figure 9A, **B** and **C** shows a fully embedded SL dual-mode BPF, its perspective view and a layout of two CPW-to-CPW planar transitions, respectively. The BPF is designed on seven-layer LTCC substrate with a relative dielectric constant of 7.0. The dual mode can be generated by adding a perturbation (cut) at a point that is 45° from the axes of coupling to the patch resonator (P-R). Two resonators are used on the 3rd and 5th layer for wide bandwidth characteristics and two P-R blocks are 684 μm away. The feed lines, external coupling between the resonators on the 3rd and 5th layers and internal coupling between their two blocks are on the 4th layer. Its center frequency (fc) and bandwidth (BW) are 61 GHz and 4.5%, respectively. The side length of the resonator is about half a wavelength (613 μm). The widths of the feed lines are 135 μm. By changing the depth of the cut, the coupling coefficients can be controlled and the calculated optimum cut length is 150 μm. The external coupling distances on the 4th layer are 140 μm and the internal coupling is realized by an overlap of 40 μm between two resonators on the 3rd and 5th layer. By using the low-loss CPW-to-SL transitions described in Section 4.1, the 600 μm-thick SL BPF is interconnected with 100 μm-thick RFICs mounted in the SiP module. However, the steep height difference between their GND planes can cause radiation problems. Therefore, by using CPW planar transition, GND planes are gradually transited from the 1st layer to the 3rd and 5th layers as shown in **Figure 9B**. This CPW planar

transition consists of three CPW lines and two transitions (TR1 and TR2). Their width and the gap for 50 Ω impedance CPW lines are designed. The width of a CPW1 (=CPW2) and CPW3 is 244 and 100 μm, respectively. Its corresponding gap is 90, 140 and 90 μm, respectively. The transition length of TR1 and TR2 is 40 and 144 μm, respectively. LCPW1, LCPW2 and LCPW3 for each CPW length are 500, 430 and 500 μm, respectively.

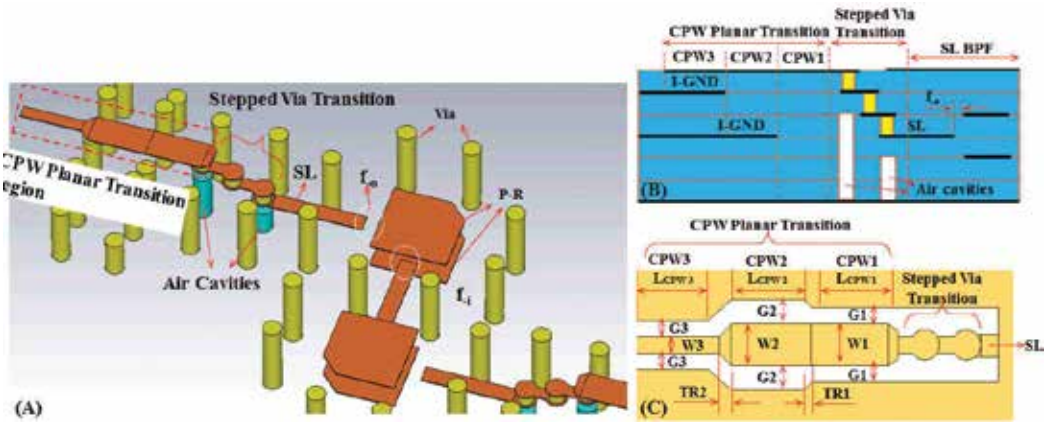

Figure 9. Perspective view (A) of a 60 GHz SL LTCC BPF involving CPW-to-SL stepped via transitions embedding air cavities, its cross-sectional view (B) and CPW-to-CPW planar transitions (C) [P-R: a patch resonator, f_o: an input and output feed line, f_i: an inter coupling feed line, I-GND: an internal ground plane].

The SL 60 GHz BPF fabricated in seven LTCC dielectric layers and its measured results are presented in **Figure 10**. Its total size including the entire transitions is 3.2 × 6.5 × 0.7 mm^3. By using the on-wafer probing method, the implemented BPF was tested. The comparison of the simulated and measured results is presented. While the measurement shows a lower center frequency and narrower BW than the simulation results, two results coincide rather well in the pass band from 60.075 to 61.925 GHz. The misalignment among feed lines and resonators results in different coupling coefficients, compared to the designed ones. Therefore, its frequency characteristics are a little different from the simulated results. The measured fc and fractional BW are 60.8 GHz and 4.1%, respectively. The return loss is less than −10.0 dB at the pass band. Its insertion loss including two vertical and four planar transitions is 4.98 dB. Considering the insertion loss of the transitions, its insertion loss is 3.74 dB.

5.2. A 5th order low-pass filter (LPF)

In order to eliminate harmonics or analog components among output signals, in general, a LPF has been used. The LPF based on the Chebyshev LPF prototype [16] as shown in **Figure 11** is designed in order to fully embed in this LTCC SiP module [28]. It has a cutoff frequency of 1.5 GHz, ripple of 0.05 dB and order of 5. In order to improve its return loss characteristics, values of capacitance (C1–C3) and inductance (L1, L2) in the designed basic LPF circuit are optimized.

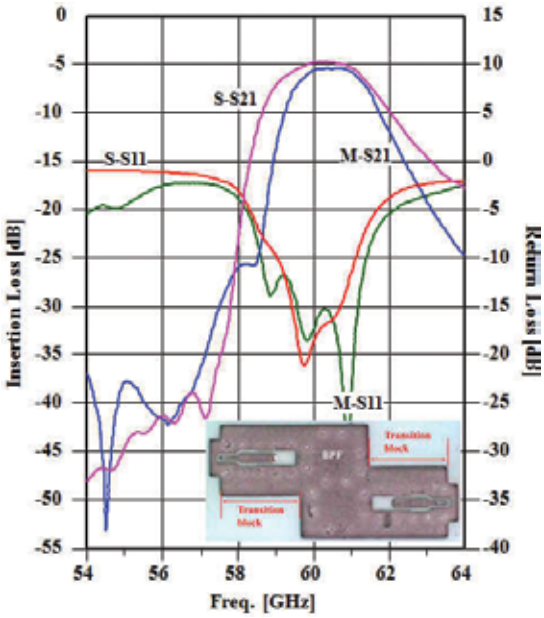

Figure 10. Measured performance of the fabricated SL BPF, compared to the simulated one (the inset: the photo of the fabricated BPF, S: simulation and M: measurement).

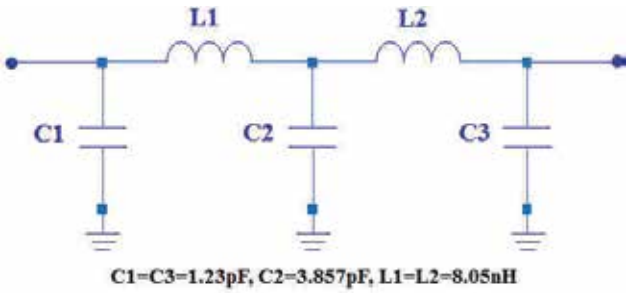

Figure 11. A prototype circuit of the 5th order Chebyshev LPF.

These capacitors and inductors are vertically designed within the six-layered LTCC dielectric whose permittivity is 7.2 at 2 GHz. In the case of the capacitor, three parallel-plate capacitors are interconnected in parallel by using vertical vias. Its capacitance value (C1 and C2) is controlled by an overlapped area among plates. The overlapped area of the C1 (=C3) and C2 is 400 × 500 and 600 × 1100 μm^2, respectively. In the case of the inductor, a 10,175 um-long line is coiled in the six-layer LTCC dielectric. The number of turn is 4.5. Its width of a metal strip is 170 μm. The number of turn and inner opening area of the helical inductor is 4.5 and 600 × 330 μm^2, respectively. The 5th order LPF is designed by integrating these elements in the size of 4.0 × 3.2 × 0.68 mm^3. It was fabricated using a LTCC commercial foundry. In **Figure 12A**, **B** and **C**, **3D** structures of the LPF elements (C1, C2 and L1), the designed LPF and measured

http://dx.doi.org/10.5772/66327

results of the fabricated LPF are presented. The measured insertion loss (S_{21}) and return losses (S_{11}, S_{22}) are less than −0.46 and −11 dB, respectively. They are similar to simulated results.

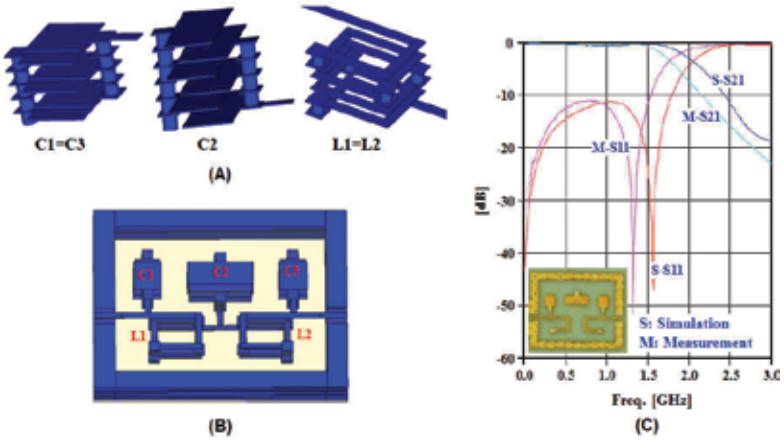

Figure 12. Perspective views of the elements (A) and LPF integrating them (B) and measured results compared to the simulated ones (C) [the inset: the fabricated LPF].

5.3. A compact 2 × 2 array patch antenna

The 2 × 2 patch array antenna is designed with a LTCC MSL structure. **Figure 13A** and **B** shows the **3-D** structure of the LTCC antenna and an embedded MSL (EMSL) power divider, respectively. Three layers from L6 to L8 are for the antenna and additional layers from L1 to L5 are used for internal and outer ground planes. The radiating patches are placed on the 8th layer (L8) and their size is the same as 645 × 1299 μm^2. The EMSL structured feeding network is designed on the 7th layer (L7) using a T-divider (power divider). In this structure, 70.7 Ω-quarter-wavelength ($\lambda_g/4$) transformers are required. However, it is impossible to implement them because limitation of the line width is 90 μm in the LTCC design rule. Therefore, the additional $\lambda_g/4$ transformers with low impedance (Z) are designed at the common port as shown in **Figure 16B**. The width of high-Z lines is 90 μm and their impedance is 47 Ω. For the low-Z lines, their width and length are optimized considering overall characteristics. The optimized width and its impedance are 130 μm and 40 Ω, respectively. The GND plane is on the 5th layer. The antenna size is as small as 10 × 10 × 0.3 mm^3.

Figure 14A and **B** shows the measured return loss characteristic and beam patterns of the fabricated antenna, respectively. Its X-ray photo is in the left inset of **Figure 14A**. In order to test a return loss and beam patterns, a WR15 waveguide (WG)-to-MSL transition was used as shown in the right insets of (A). A −10 dB bandwidth is 6.3 GHz from 56.5 to 62.8 GHz. At 61 GHz, the measured E- and H-plane radiation patterns are presented in **Figure 14B**. A gain of 7 dBi and a 3-dB beam width of 36° in H-plane pattern are obtained. The E-plane pattern is wider because of spurious generated in the E-plane direction of the feeding network.

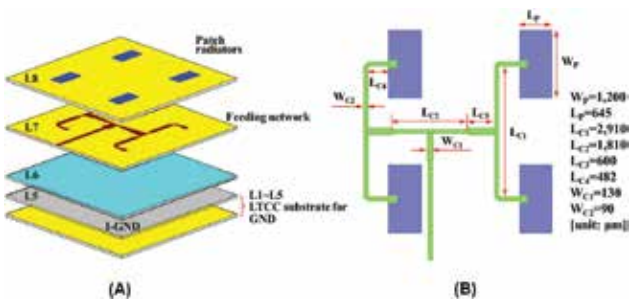

Figure 13. Layer structure of the 2 × 2 array LTCC antenna (A) and its feeding network and radiating patches (B).

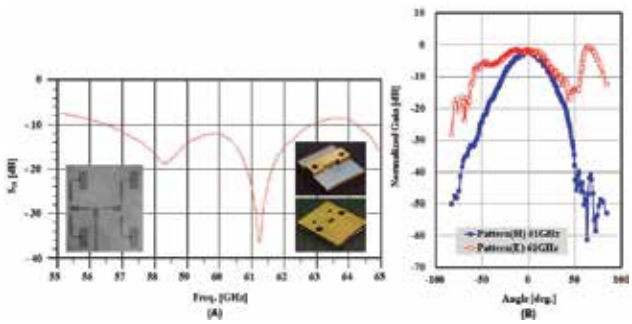

Figure 14. Measured return loss characteristic of the fabricated 2 × 2 array LTCC antenna (the left and right inset: its X-ray photo and the antenna assembled with a WR15 WG-to-MSL transition, respectively) (A) and its measured beam patterns (B).

6. Compact LTCC SiP modules for V-band applications

In this chapter, a typical heterodyne 61 GHz transmitter (Tx) and a highly integrated 60 GHz amplitude shift-keying (ASK) transceiver (TRx) SiP module are presented in detail [29–31]. They have been designed and implemented by using the key technologies such as suppression unwanted resonant modes, low-loss vertical transitions and compact passive devices presented in the previous chapters.

6.1. Monolithic 61 GHz transmitter LTCC SiP module

A block diagram of a typical heterodyne 61 GHz transmitter (Tx) is shown in **Figure 15**. This Tx is comprised of a BPF, a antenna, a up-converting mixer, two frequency multipliers (MTLs), a drive amplifier (DA) and a power amplifier (PA). The local oscillation (LO) signal (59.15 GHz) of the mixer is supplied by multiplying the external LO source of 14.79 GHz by 4.

The 61 GHz Tx is monolithically integrated into the single SiP module as shown in **Figure 16**. This SiP module consists of a nine-layer LTCC dielectric. The BPF, which is implemented in

http://dx.doi.org/10.5772/66327

the previous subchapter 5.1, is fully embedded through L2 to L7 by using the CPW-to-SL vertical transition and the CPW-to-CPW planar transition. The BPF is connected with a driver amplifier and mixer IC. The 2 × 2 array MSL patch antenna is integrated in L6 through L8. In order to mount the 61 GHz Tx LTCC SiP module on a printed circuit board (PCB), a SMT package is adopted. Therefore, using SMT pads, all the ports of the module are designed on its bottom side. In particular, the SMT pad for a LO port is integrated by using the transition implemented in Section 4.2. Pad dimensions for DC ports, IF ports of 1.85 GHz and LO ports of 14.79 GHz are 700 × 700, 320 × 550, 560 × 560 μm^2, respectively. Five active chips mounted in the cavity of the L7 are isolated from each other using isolation cavities structure, which consists of L8 and L9. The DC bias lines and long IF feed lines are shielded using isolating ground planes and vias.

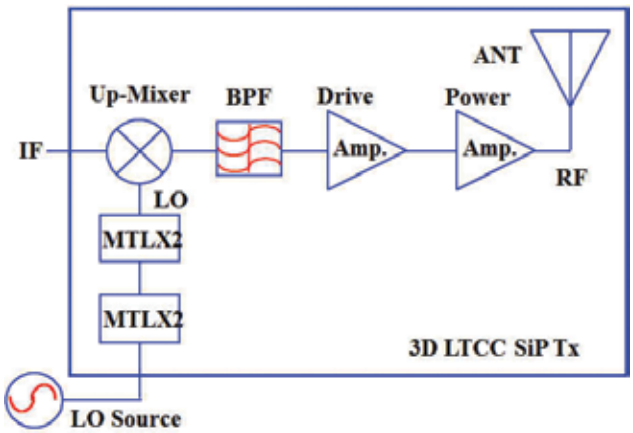

Figure 15. Block diagram of the 61 GHz heterodyne transmitter.

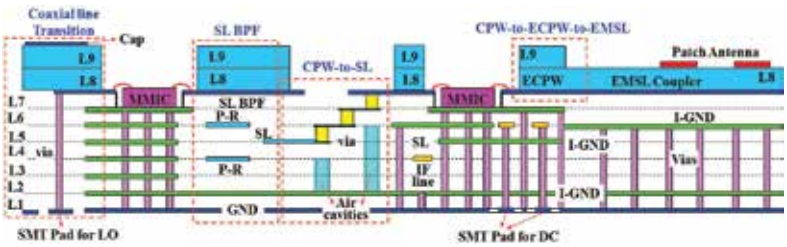

Figure 16. A cross-sectional view of the monolithic 61 GHz Tx LTCC SiP module integrating a BPF, an antenna, MMICs and DC bias circuits (ECPW: the embedded CPW, EMSL: the embedded MSL, P_R: the patch resonator and Lx: the layer number of the LTCC multilayer).

Designed SiP module was implemented in nine-LTCC multilayers using the standard LTCC process. **Figure 17A** shows the fabricated monolithic LTCC SiP module of the 61 GHz Tx. The whole size of the transmitter is as small as 36 × 12 × 0.9 mm^3. **Figure 17B** shows its bottom side with SMT pads.

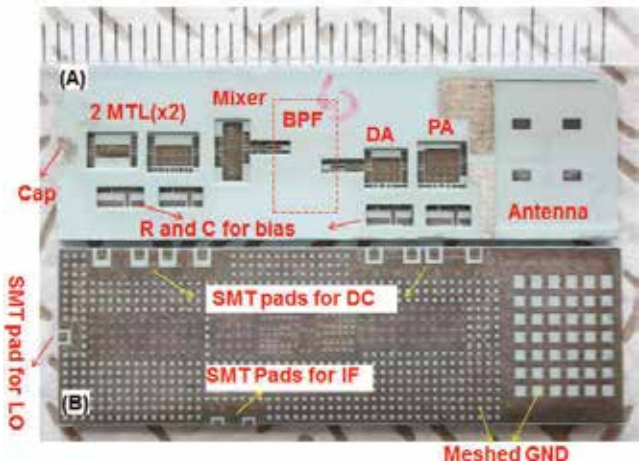

Figure 17. Implemented monolithic 61 GHz Tx LTCC SiP module [36 × 12 × 0.9 mm^3, (A) and (B): top and bottom side].

The fabricated LTCC Tx module was mounted on the PCB. At the output port of the power amplifier of the module, the output power and frequency spectrum were measured using on-wafer probing. **Figure 18A** plots the RF output power and the power gain as a function of the IF input power of 1.85 GHz. A measured output power at a 1-dB gain compression point (P1dB) and up-conversion gain is 10.2 dBm and 7.3 dB, respectively, at 61 GHz. Output spectrums such as a LO, RF and spurious signals are shown in **Figure 18B**. The isolation level between the LO and RF and the spurious one are less than 26.4 and 22.4 dBc, respectively. The measured output performance demonstrates that the integrated BPF suppresses effectively the LO and spurious signal.

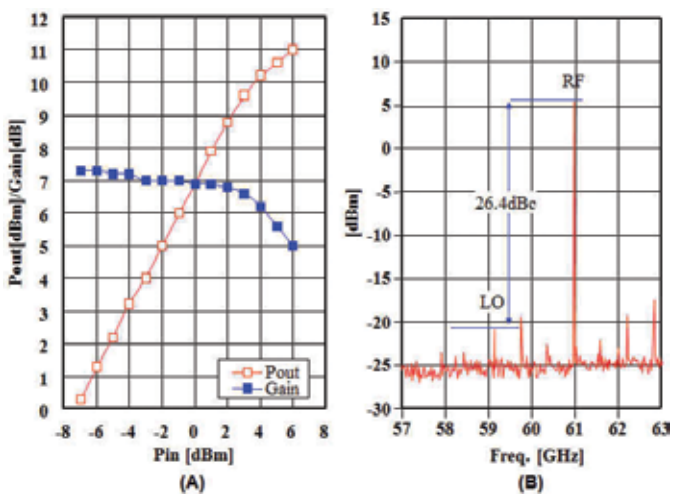

Figure 18. Measured output performance of the fabricated module (A) output power and conversion gain and (B) output frequency spectrum.

http://dx.doi.org/10.5772/66327

6.2. Compact 60 GHz ASK transceiver LTCC SiP module

The amplitude shift-keying (ASK) modulation has been utilized in various microwave systems [32]. In particular, several millimeter-wave systems have adopted it for high-speed applications, because of circuit simplicity and high power efficiency. In addition, an analog-digital converter (ADC) is hard to be implemented and it is easy to demodulate ASK noncoherently by using an envelope detector.

In this work, the 60-GHz ASK transceiver (TRx) is designed and implemented. **Figure 19A**, **B** and **C** shows its block diagram, its layout for a LTCC SiP module and its cross-sectional structure, respectively. The Rx part consists of a high-gain and low-noise amplifier (LNA) block, detector, low-pass filter (LPF) and attenuator (ATT), which is inserted for the impedance buffering in the high-gain budget. The Tx part is composed of an up-converting mixer, two frequency multipliers (MTLs) and a power amplifier. The LO signal of the Tx is supplied to the mixer by multiplying the external LO source of 7.78 GHz by eight times. The carrier frequencies of the Tx and Rx link are 62.24 and 58.75 GHz, respectively. The whole 60-GHz ASK TRx is integrated into the six-layered LTCC SiP module in the size of 17.8 × 17.9 × 0.6 mm^3 as shown **Figure 19B**. In the conceptual vertical structure in **Figure 19C**, a LPF, isolation via fence and DC bias components are embedded. RFICs are mounted on cavities in L6. Each LTCC layer is 84 μm high. A via diameter is 120 μm before co-firing process. The main signal line is a 50 Ω CPW line, whose width and gap are 123 and 100 μm, respectively. The five-order Chebyshev LPF with a cutoff frequency of 1.5 GHz inserted in the ASK de-modulator (Rx part) in order to eliminate harmonics and analog components at its output. The previously implemented LPF in Section 5.2 was utilized. The ground plane in the bottom side of the Tx and Rx part is also separated for eliminating return path.

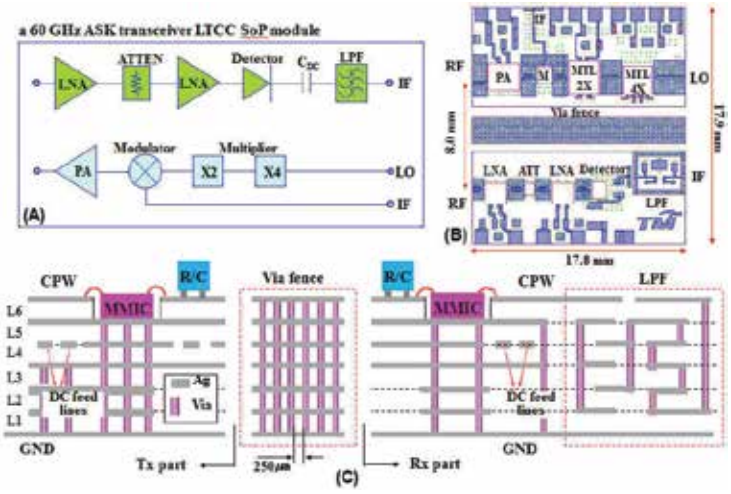

Figure 19. A block diagram of a 60 GHz ASK transceiver (TRx) (A), the layout of the ASK TRx LTCC SiP module (B) and its conceptual vertical structure (C) embedding a LPF, via fence, RFICs and DC bias components in the 6-layer LTCC dielectrics [Lx: the number of the LTCC dielectric layer].

The high-isolation via fence between Tx and Rx part is investigated by using a 3-D electromagnetic (EM) tool [25] as shown in **Figure 20A**. In general, the isolation of over 80 dBc is required between the ASK modulator and demodulator. In order to confine the EM-fields within each Tx or Rx area, the via fence is designed between 50 Ω CPW lines, which can be assumed as the signal path of the Tx (P1–P2) and Rx (P3–P4) part. The spacing between them is 8 mm, which is the same that between the Tx and Rx port in the diplexer of the main system. The diameter of vias and spacing between their edges are 120 and 250 μm, respectively. The E-field distribution of the designed model at 60 GHz is presented in **Figure 20A**. This result shows that E-fields inputted from a port 1 (P1) can be effectively confined within one path (Tx) due to the via fence. Simulated isolation characteristics between two lines from DC to 100 GHz are presented in **Figure 20B**. It clearly shows that the isolation better than 80 dBc is obtained.

The designed ASK TRx LTCC SiP module was fabricated using a six-layer LTCC substrate in the commercial Foundry [33]. The implemented ASK TRx LTCC SiP module is as small as 17.8 × 17.9 × 0.6 mm^3 as shown in the inset of **Figure 21A** and it was assembled into a metal housing with DC bias boards. **Figure 21B** and C shows the measured RF and IF spectrum in the Tx and Rx part, respectively, of the ASK TRx LTCC SiP module. In **Figure 21B**, the measured output power (Pout) is 12.8 dBm at the LO of 62.24 GHz and IF frequency swept from 10 MHz to 1.5 GHz. By inserting a 20 dB attenuator between the Tx and Rx parts considering the free space path loss, the IF spectrum of the Rx part was tested. By changing the IF signal from 10 MHz to 1.5 GHz at the Tx part with the LO signal of 58.752 GHz, the flat IF output signal less than −2 dBm is obtained up to 1.25 GHz as shown in **Figure 21C**. The conversion gain is 38 dB at the IF output of 1.25 GHz.

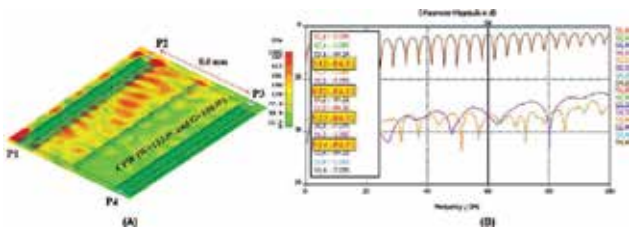

Figure 20. An assumed model for evaluation of isolation between the Tx and Rx and its E-field distribution (A) and simulated results (B).

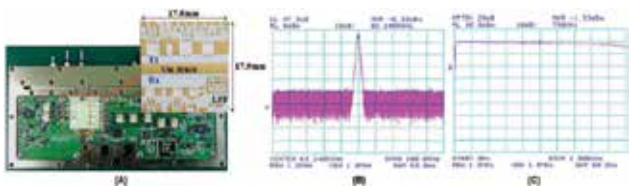

Figure 21. Fabricated ASK TRx LTCC SiP module (A), its measured spectrum at the output port of the Tx part (B) and the IF port of the Rx one (C).

http://dx.doi.org/10.5772/66327

7. Conclusion

In this chapter, highly integrated monolithic LTCC SiP modules have been presented for microwave applications. Almost passive circuits of the whole radio system have been monolithically embedded in the LTCC multilayer dielectric substrate. The main key technologies for the monolithic SiP module are suppressing parasitic resonant modes, low-loss transitions and compact and high-performance passive devices. In general, the parasitic rectangular waveguide consisting of via, upper ground plane and lower one is easily and frequently formed in the SiP module and also effectively suppressed by reducing its horizontal dimension, spacing between vias. The low-loss SL-to-CPW vertical via transition using the stepped via structure and embedded air cavity achieves −0.7 dB transition loss at 60 GHz. By using the modified coaxial line, the SMT pad transition is developed and demonstrates 0.9 dB loss at 15 GHz. By using the developed SL-to-CPW transition, the dual-mode four-pole 60 GHz SL BF is fully embedded in the LTCC substrate in the size of 3.2 × 6.5 × 0.7 mm^3 and the insertion loss of 3.74 dB and the BW of 4.1% are obtained. The fully embedded 5th order LPF composed of vertical plate capacitors and helical inductors is implemented as small as 4.0 × 3.2 × 0.6 mm^3. Its measured insertion and return losses are −0.46 dB and less than −11 dB, respectively. The 2 × 2 array patch antenna with the gain of 7 dBi and beam width of 36° has been developed. By utilizing the well analyzed and developed key technologies, 61 GHz transmitter and 60 GHz ASK transceiver LTCC SiP modules have been implemented. The 61 GHz Tx LTCC SiP module achieves an output power of 10.2 dBm at 61 GHz and the conversion gain of 7.3 dB. Because of the integrated SL BPF, the LO and spurious signals are suppressed below 26.4 dBc and 22.4 dBc, respectively. Using the off-shelf receiver, the wireless link is verified. In the case of the 60 GHz ASK LTCC SiP module, in order to achieve 80 dBc isolation between the Tx and Rx part, the high isolated substrate using the via fence is proposed and used in the SiP design. The 60 GHz ASK TRx LTCC SiP module is fabricated as small as 17.8 × 17.9 × 0.6 mm^3 and it achieves the output power of 12.8 dBm at LO of 62.24 GHz and the flat IF output signal less than −2 dBm up to 1.25 GHz.

Acknowledgements

These works were financially supported by the Ministry of Science and Technology of Korea and KISTEP from 2002 to 2006 and by Telecom Malaysia Research & Development (TMRND) from 2008 to 2009.

Author details

Young Chul Lee

Address all correspondence to: leeyc@mmu.ac.kr

Department of electronic engineering, Mokpo National Maritime University (MMU), Mokpo, South Korea

References

[1] Bouayadi O.E., Lamy Y., Dussopt L. and Simon G. 3D integration and packaging of mmWave circuits and antennas: opportunities and challenges. Microwave Journal. 2016;59:22–28.

[2] Zhang Y. P. and Liu D. Antenna-on-chip and antenna-in-package solutions to highly integrated millimeter-wave devices for wireless communications. IEEE Transactions on Antennas and Propagation. 2009;57:2830–2841. doi:10.1109/TAP.2009.2029295

[3] Papapolymerou I., Franklin Drayton R. and Katehi L.P.B. Micromachined patch antennas. IEEE Transactions on Antennas and Propagation. 1998;46:275–283. doi:10.1109/8.660973

[4] Kuo H.-C., Yue H.-L., Ou Y.-W., Lin C.-C. and Chuang H.-R. A 60-GHz CMOS subharmonic RF receiver with integrated on-chip artificial-magnetic-conductor Yagi antenna and balun bandpass filter for very-short-range gigabit communications. IEEE Transactions on Microwave Theory and Techniques. 2013;61:1681–1691. doi:10.1109/TMTT.2013.2247622

[5] Muller A., Saadaoui M., Pons P., Neculoiu D., Bary L., Dubuc D., Grenier K., Vasilache D., Buiculescu C., Petrini I. and Plana R. Membrane supported endfire antennas manufactured using silicon micromachining. IEEE International Workshop on Antenna Technology: Small Antennas and Novel Metamaterials. 2005;113–116. doi:10.1109/IWAT.2005.1461017

[6] Chan K.T., Chin A., Lin Y.D., Chang C.Y., Zhu C.X., Li M.F., Kwong D.L., McAlister S., Duh D.S. and Lin W.J. Integrated antennas on Si with over 100 GHz performance, fabricated using an optimized proton implantation process. IEEE Microwave and Wireless Components Letters. 2003;13:487–489. doi:10.1109/LMWC.2003.817146

[7] Pan S., Caster F., Heydari P. and Capolino F. A 94-GHz extremely thin metasurface-based BiCMOS on-chip antenna. IEEE Transactions on Antennas and Propagation. 2014;62:4439–4451. doi:10.1109/TAP.2014.2330575

[8] Swaminathan M., Bavisi A., Yun W., Sundaram V., Govind V. and Monajemi P. Design and fabrication of integrated RF modules in liquid crystalline polymer (LCP) substrates. 31st Annual Conference of IEEE Industrial Electronics Society. 2005;2346–2351. doi:10.1109/IECON.2005.1569270

[9] Li R., DeJean G., Maeng M., Lim K., Pinel S., Tentzeris M. M. and Laskar J. Design of compact stacked-patch antennas in LTCC multilayer packaging modules for wireless applications. IEEE Transactions on Advanced Packaging. 2004;27(4):581–589. doi:10.1109/TADVP.2004.831866

[10] Pilard R., et al. HDI organic technology integrating built-in antennas dedicated to 60 GHz SiP solution. Proceedings of the 2012 IEEE International Symposium on Antennas and Propagation. 2012. doi:10.1109/APS.2012.6348633

[11] Lamminen A. E., Saily J. and Vimpari A. R. 60-GHz patch antennas and arrays on LTCC with embedded-cavity substrates. IEEE Transactions on Antennas and Propagation. 2008;56(9):2865–2874. doi:10.1109/TAP.2008.927560

[12] Ohata K., et al. 1.25 Gbps wireless gigabit ethernet link at 60GHz-band. 2003 IEEE MTT-S International Microwave Symposium Digest. 2003. doi:10.1109/MWSYM.2003.1210955

[13] Kuo J.-L., et al. 60-GHz four-element phased-array transmit/receive system-in-package using phase compensation techniques in 65-nm flip-chip CMOS process. IEEE Transactions on Microwave Theory and Techniques. 2012;60(3):743–756. doi:10.1109/TMTT.2011.2176508

[14] Haydl W. H. Resonance phenomena and power loss in conductor-backed coplanar structures. IEEE Microwave and Guided Wave Letter. 2000;20(12):514–516. doi:10.1109/75.895086

[15] Das N. K. Methods of suppression or avoidance of parallel-plate power leakage from conductor-backed transmission lines. IEEE Transactions on Microwave Theory and Techniques. 1996;44(2):169–181. doi:10.1109/22.481565

[16] Pozar D. M.. Microwave Engineering. John Wiley & Sons, Inc: 1998.

[17] Lee Y. C., Cho Y. H. and Park C. S. BPF integrated amplifier module using LTCC technology for millimeter-wave applications. Microwave and Optical Technology Letters. 2015;57(8):1821–1825. doi:10.1002/mop.29206

[18] Panther C. G., Stubbs M. G. and Wight J. S. Vertical transitions in low temperature co-fired ceramics for LMDS applications. IEEE MTT-S International Microwave Symposium Digest. 2001;3:1907–1910. doi:10.1109/MWSYM.2001.967281

[19] Lei S., Guo Y. X. and Ong L. C. CPW to stripline transitions in LTCC for millimeter-wave applications. IEEE Asia Pacific Microwave Conference (APMC) Proceedings. 2005. doi:10.1109/APMC.2005.1606430

[20] Schmuckle F. J., Jentzch A., Heinrich W., Butz J. and Spinnler M. LTCC as MCM substrate: design of strip-line structures and flip-chip interconnections. IEEE MTT-S International Microwave Symposium Digest. 2001;3:1093–1096. doi:10.1109/MWSYM.2001.967280

[21] Yang T.-H., Chen C.-F., Huang T.-Y., Wang C.-L. and Wu R.-B. A 60GHz LTCC transition between microstrip line and substrate integrated waveguide. IEEE Asia Pacific Microwave Conference (APMC) Proceedings. 2005. doi:10.1109/APMC.2005.1606294

[22] Heyen J., Gordiyenko A., Heide P. and Jacob A.F. Vertical feedthroughs for millimeter-wave LTCC modules. 33rd European Microwave Conference Proceedings. 2003;411–414. doi:10.1109/EUMC.2003.1262309

[23] Lee Y. C. SMT pad using a coaxial line structure for LTCC SoP applications. Microwave and Optical Technology Letters. 2009;51(7):1769–1772. doi:10.1002/mop.24447

[24] Lee Y. C. CPW-to-stripline vertical via transitions for 60GHz LTCC SOP applications. Progress In Electromagnetics Research Letters. 2008;2:37–44. doi:10.2528/PIERL07122805

[25] CST MICROWAVE STUDIO, CST Inc., [Internet] Available: http://www.cst.com

[26] Ziroff A., Nalezinski M., Menzel, Wolfgang A. Novel approach for LTCC packaging using a PBG structure for shielding and package mode suppression. European Microwave Conference. 2003;419–422. doi:10.1109/EUMC.2003.1262311

[27] Lee Y. C. and Park C. S. A fully embedded 60-GHz novel BPF for LTCC system-in-package applications. IEEE Transactions on Advanced Packaging. 2006;29(4):804–809. doi:10.1109/TADVP.2006.884807

[28] Lee Y. C., Kim T. W., Ariffin A. B. and Myoung N. G. 60-GHz amplitude shift-keying receiver LTCC system-on-package module. Microwave and Optical Technology Letters. 2011;53(4):758–761. doi:10.1002/mop.25824

[29] Lee Y. C., Chang W.-I. and Park C. S. Monolithic LTCC SiP transmitter for 60GHz wireless communication terminals. IEEE MTT-S International Microwave Symposium Digest. 2005. doi:10.1109/MWSYM.2005.1516839

[30] Lee Y. C. and Park C. S. LTCC-based monolithic system-in-package (SiP) module for millimeter-wave applications. International Journal of RF and Microwave Computer-Aided Engineering. 2016; 26(9): 803–811. dio:10.1002/mmce.21032

[31] Lee Y. C. 60-GHz amplitude shift-keying transceiver LTCC system-on-package module. Microwave and Optical Technology Letters. 2013;55(1):48–51. doi:10.1002/mop.27264

[32] Tarusawa Y., Ogawa H. and Hirota T. A new constant resistance ASK modulator using double-sided MIC. IEEE Transactions on Microwave Theory and Techniques. 1987;35:819–822. doi:10.1109/TMTT.1987.1133758

[33] RN2-LTCC [Internet]. Available: http://WWW.rn2-ltcc.com

Chapter 14

Materials Characterization Using Microwave Waveguide Systems

Kok Yeow You

Additional information is available at the end of the chapter

http://dx.doi.org/10.5772/66230

Abstract

This chapter reviews the application and characterization of material that uses the microwave waveguide systems. For macroscopic characterization, three properties of the material are often tested: complex permittivity, complex permeability and conductivity. Based on the experimental setup and sub-principle of measurements, microwave measurement techniques can be categorized into either resonant technique or nonresonant technique. In this chapter, calibration procedures for non-resonant technique are described. The aperture of open-ended coaxial waveguide has been calibrated using Open-Short-Load procedures. On the other hand, the apertures of rectangular waveguides have been calibrated by using Short-Offset-Offset Short procedures and Through-Reflect-Line calibration kits. Besides, the extraction process of complex permittivity and complex permeability of the material which use the waveguide systems is discussed. For one-port measurement, direct and inverse solutions have been utilized to derive complex permittivity and complex permeability from measured reflection coefficient. For two-port measurement, in general, the material filled in the waveguide has been conventional practice to measure the reflection coefficient and the transmission coefficient by using Nicholson-Ross-Weir (NRW) routines and convert these measurements to relative permittivity, ε_r and relative permeability, μ_r. In addition, this chapter also presents the calculation of dielectric properties based on the difference in the phase shifts for the measured transmission coefficients between the air and the material.

Keywords: microwave waveguides, relative permittivity, relative permeability, conductivity, resonant methods, nonresonant methods, materials characterization

1. Introduction

For macroscopic material characteristic investigations, three properties of the material are often measured: relative permittivity ε_r, relative permeability μ_r and conductivity σ. Normally, many microwave measurements only focus on the properties of relative permittivity, ε_r rather

than the permeability μ_r and the conductivity σ. Recently, there has been an increased interest in the determination of dielectric properties of materials at microwave frequencies range. This is because those properties were played the important roles in the construction of high-frequency electronic components, the superconducting material properties, the quality of printed circuit board (PCB) substrate, the efficiency of microwave absorption materials, metamaterial characterizations and the performance of dielectric antenna design. Based on the setup and sub-principle of measurements, measurement techniques can be categorized into either resonant methods or nonresonant methods. In practice, the prime considerations in measuring the dielectric properties of the materials are the thickness required of the material, the size of the waveguide, limitations of the operating frequency and the accuracy of the measurements.

For material characterizing using resonant methods, a resonator is filled with a material or sample as shown in **Figure 1** [1, 2]. This produces a resonance frequency shift and also a broadening of the resonance curve compared to the resonator without filled with any sample. From measurements of shifting resonance frequency, the properties of the sample can then be characterized. The particular resonance frequency for the resonator without filled with the sample is depends on its shape and dimensions. The resonance measurement techniques are good choices for determining low-loss tangent, tanδ values for the low-loss sample, but such techniques cannot be used for the measurement of swept frequency.

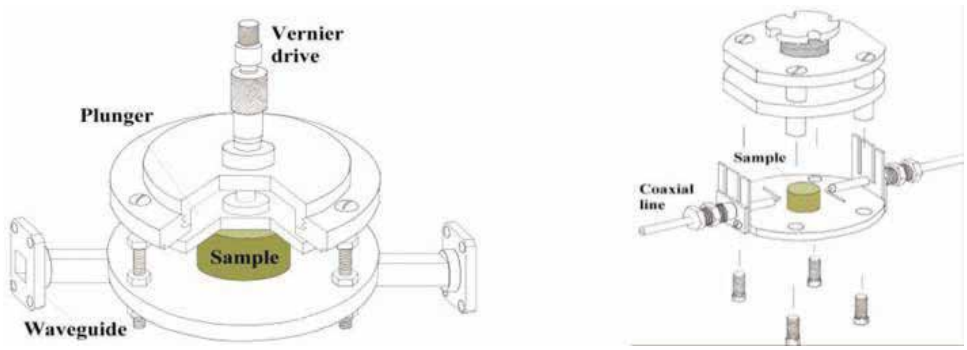

Figure 1. The resonator cavity filled with sample under test [1, 2].

A free-space and transmission/reflection measurement techniques are grouped in the category of nonresonant methods. The free-space technique is a far-field measurement, and a horn antenna is used as the radiator as shown in **Figure 2** [3–5]. The free-space method is suitable for the measurement for thin film sample with high temperature because horn radiators do not come into direct contact with the sample, and thus, the RF circuits of the instrument are safer from heat damage. However, this method provides a less precise measurement because the sensing field is highly dispersed. Furthermore, the distance between the sample surface and the horn aperture is difficult to gauge precisely. The coaxial, circular or rectangular waveguides are implemented in transmission/reflection measurement techniques which are directly

http://dx.doi.org/10.5772/66230

in contact with the sample. Although various measurement techniques are available to be used, when choosing the appropriate technique, some other factors are required to be considered in the selection of technique, such as accuracy, cost, samples shape and operating frequency. This chapter is focused only on coaxial and rectangular waveguides.

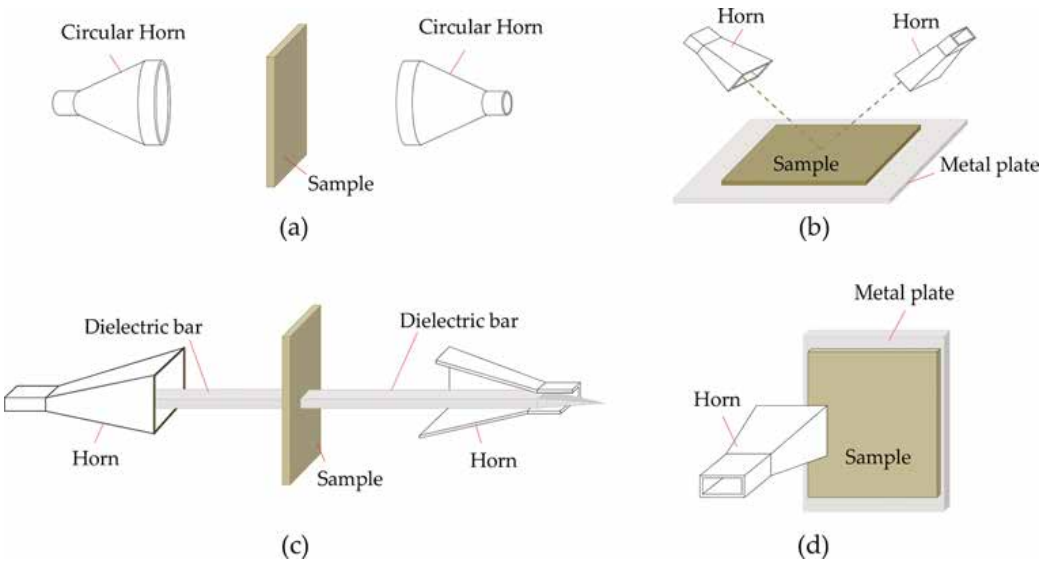

Figure 2. Free-space measurement setup for dielectric measurement of the thin sample [3–5].

2. Microwave measurement using coaxial and rectangular waveguides

2.1. Coaxial and rectangular waveguides

There are various sizes of the coaxial probes and rectangular waveguides, which are dependent on the operating frequency and its application. The coaxial probe is a waveguide consisting of inner and outer conductors, with radii a and b, respectively, as shown in **Figure 3**. On the other hand, the rectangular waveguide is a rectangular metal pipe with width, b and height, a, which guides high-frequency electromagnetic waves from one place to another without significant loss in intensity. There are several commercial rectangular waveguides, such as WR510, WR90, WR75 and WR62 waveguides, which covering a broad measurement range for L-band, X-band and Ku-band, respectively, as shown in **Figure 4**. Generally, the material characterization using waveguide discontinuity methods can be categorized into one-port and two-port measurements. The measurements assume that only the dominant transverse electric, TE_{10} mode propagates in the rectangular waveguide. On the other hand, only transverse electromagnetic mode (TEM) is assumed to be propagated in the coaxial line waveguide.

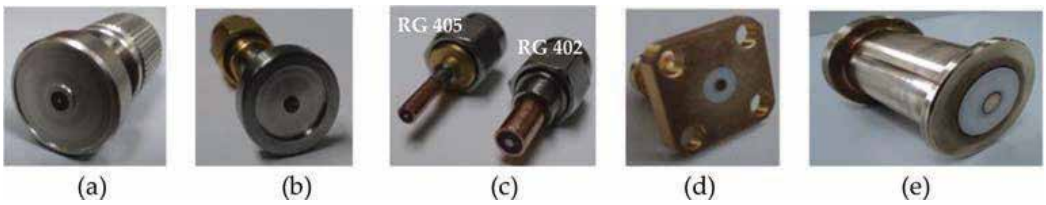

Figure 3. (a) Keysight dielectric probe kit with inner radius of outer conductor, b = 1.5 mm and radius of inner, a = 0.33 mm. (b) Customized small coaxial probe with b = 0.33 mm and a = 0.1 mm [6]. (c) RG402 and RG 405 semi-rigid coaxial probe [7]. (d) SMA stub coaxial probe with b = 2.05 mm and a = 0.65 mm [8]. (e) Customized large coaxial probe with b = 24 mm and a = 7.5 mm.

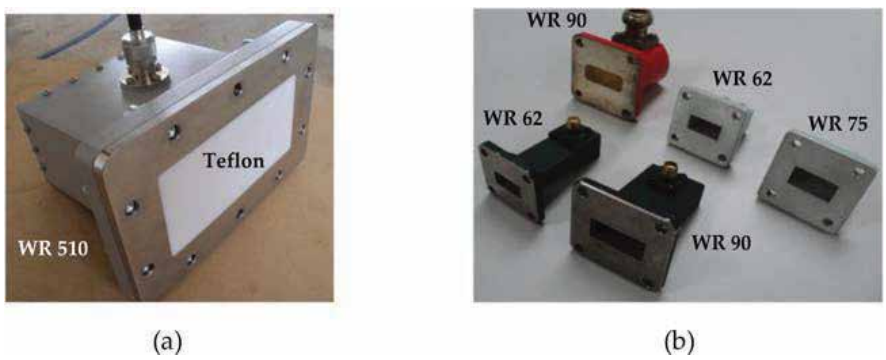

Figure 4. (a) WR510 waveguide-to-coaxial adapter and (b) WR 90, WR 75 and WR 62 waveguide-to-coaxial adapters [9].

2.2. Measurements principles

The one-port measurement is based on the principle that a reflected signal (reflection coefficient, S_{11}) through the waveguide, which end aperture is contacting firmly with the material under test (sample), will obtain the desired information about the material as shown in **Figure 5**. The main advantage of using one-port reflection technique is that the method is the simplest, broadband, nondestructive way to measure the dielectric properties of a material. However, one-port measurement is suitable only for measuring the relative permittivity, ε_r, of the dielectric material (nonmagnetic material, $\mu_r = 1$). This is due to insufficient information to predict the permeability, μ_r, if only obtained the measured reflection coefficient, S_{11} without transmission coefficient, S_{21}.

For **Figure 5a** and **c** measurements, the sample is considered infinite, as long as the sample thickness d is greater than the radius of the outer conductor b. However, the radiation, or sensing area, for an aperture rectangular waveguide is much greater than that of a coaxial probe. For instance, the WR90 waveguide has a radiation distance up to 20 cm in the air from the aperture waveguide. Hence, the sample under test must be much thicker when the rectangular waveguide is utilized in the measurement. Besides, the coaxial probe and rectangular waveguide are also capable of testing the thin film sample as shown in **Figure 5b** and **d**. The measurements required that the thin sample is backed by a metallic plate.

http://dx.doi.org/10.5772/66230

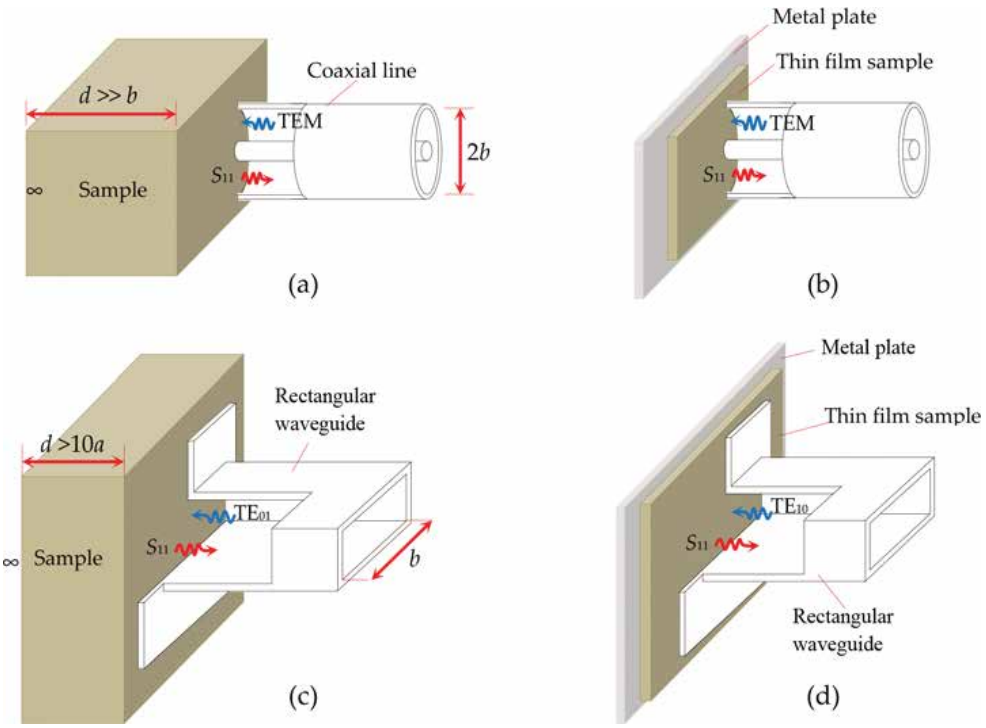

Figure 5. Open-port measurements using the (a), (b) coaxial probe and the (c), (d) rectangular waveguide.

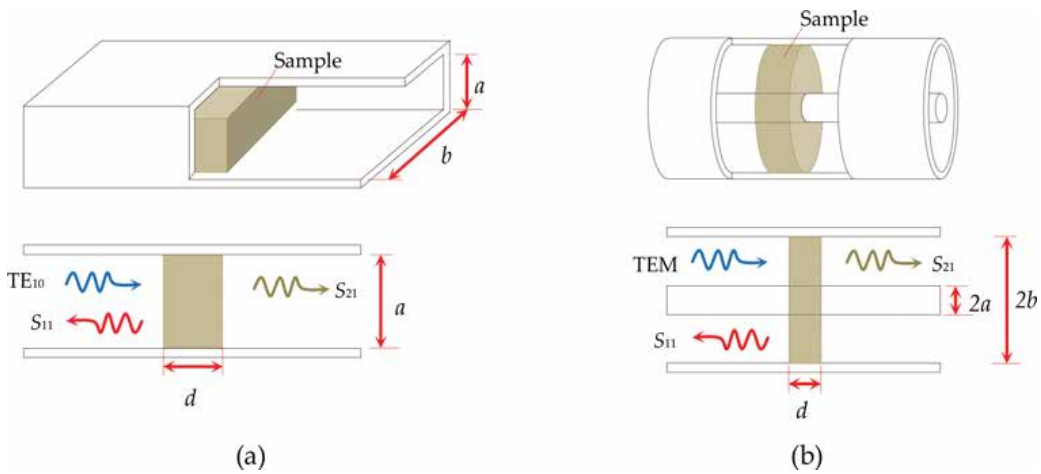

Figure 6. Two-port measurements using the (a) rectangular waveguide and the (b) coaxial transmission line.

The two-port measurement uses both reflection and transmission methods. Here, the material under test is placed between waveguide transmission lines or segments of the coaxial line as shown in **Figure 6**. The two-port measurement using coaxial or rectangular waveguides became popular due to the convenient formulations derived by Nicholson and Ross [10] in

1970, who introduced a broadband determination of the complex relative permittivity, ε_r and permeability, μ_r of materials from reflection and transmission coefficients (S_{11} and S_{21}). For measurements in **Figure 6**, the sample must be solid and carefully machined with parallel interfaces, and must perfectly fill in the whole cross section of the coaxial line or waveguide transmission line. The main advantage of using two-port Nicholson-Ross-Weir (NRW) technique [10, 11] is that the both relative permittivity, ε_r and relative permeability, μ_r of the sample can be predicted simultaneously. When using NRW method for thin samples, the thickness of the sample must be less than $\lambda/4$.

2.3. Measurements setup

In this chapter, the dimensions of the used coaxial probe and the rectangular waveguide as examples of the one-port measurement are shown in **Figure 7a** and **b**, respectively. The coaxial probe is capable of measuring the reflection coefficients covered the frequency range between 0.5 and 7 GHz. On the other hand, the rectangular waveguide adapter covers frequency from 8.2 to 12.4 GHz. For two-port measurement, a 5 cm length of the coaxial and the rectangular transmission lines is implemented. The experiment setup of the waveguides with an Agilent E5071C vector network analyzer (VNA) is shown in **Figure 8**.

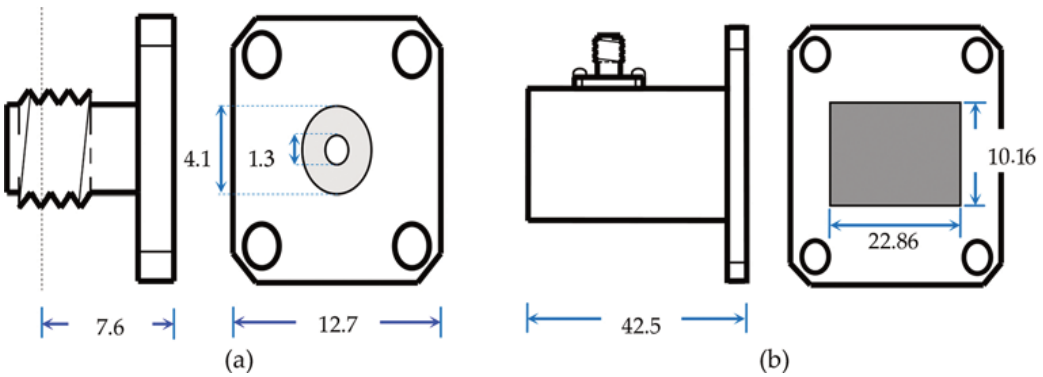

Figure 7. Cross-sectional and front views for the dimensions (in millimeter) of the (a) coaxial probe and the (b) rectangular waveguide.

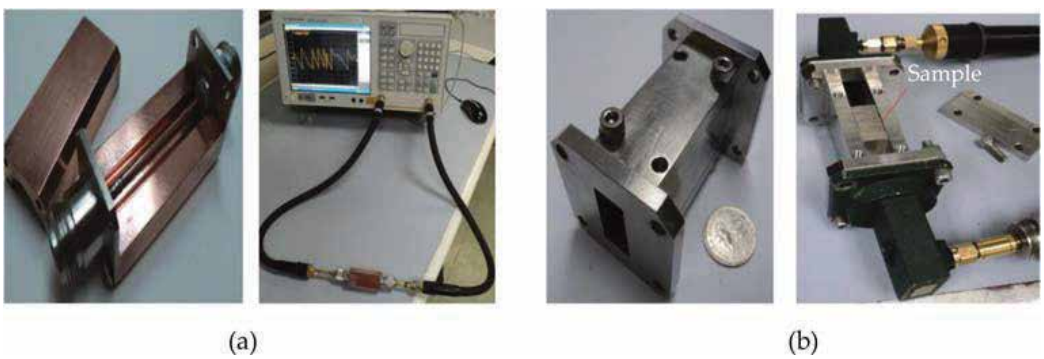

Figure 8. The experiment setup for the (a) coaxial cavity and the (b) rectangular waveguide cavity.

3. Waveguide calibrations

3.1. One-port calibrations

3.1.1. Open standard calibration

The reflection coefficient S_{11a_sample} of the sample at the probe aperture (at the BB' plane) should be measured as shown in **Figure 9b** [8]. However, during the measurement process, only the reflection coefficient S_{11m_sample} at the end of the coaxial line (at the AA' plane) is measured. The measured S_{11m_sample} must be calibrated due to the reflection at the AA' plane, which is separated from the sample (at the BB' plane) by a coaxial line. Thus, a de-embedding process should be done to remove the effects of the coaxial line.

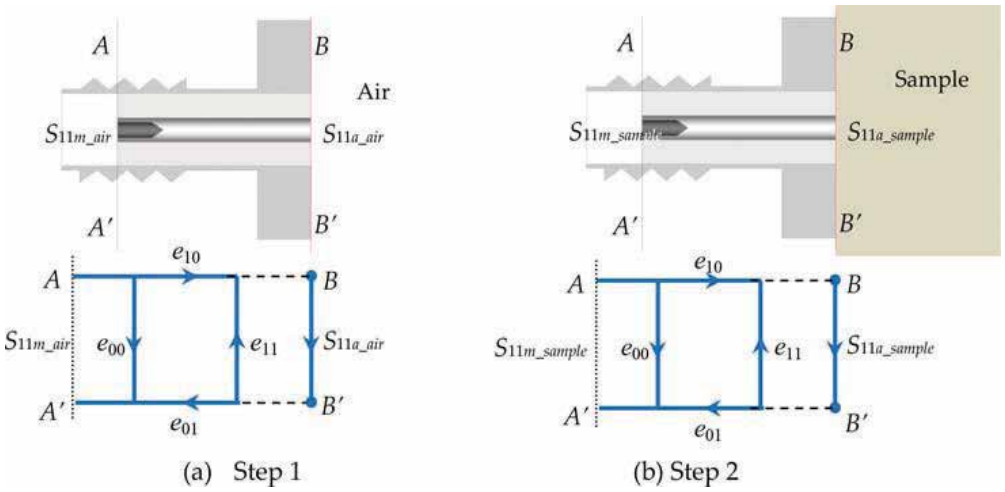

Figure 9. Error network and finite coaxial line: (a) terminated by air; (b) terminated by a sample under test.

In this subsection, a simple open standard calibration is introduced which requires the probe aperture open to the air as shown in **Figure 9a**. Firstly, the S_{11m_air} for the air is measured. Later, the probe aperture is contacted with the sample under test, and its S_{11m_sample} is measured as shown in **Figure 9b**. The relationship between the S_{11m_air} at the plane AA' and S_{11a_air} at the probe aperture BB' is expressed in a bilinear equation as:

$$S_{11a\_air} = \frac{S_{11m\_air} - e_{00}}{e_{11}S_{11m\_air} + e_{10}e_{01} - e_{00}e_{11}} \tag{1}$$

Similarly, the relationship between measured S_{11m_sample} and S_{11a_sample} is given as:

$$S_{11a\_sample} = \frac{S_{11m\_sample} - e_{00}}{e_{11}S_{11m\_sample} + e_{10}e_{01} - e_{00}e_{11}} \tag{2}$$

The e_{00}, e_{11} and $e_{10}e_{01}$ are the unknown scattering parameters of the error network for the coaxial line.

The e_{00} is the directivity error that causes the failure to receive the measured reflection signal completely from the sample being tested at plane *BB'*. The e_{11} is the source matching error due to the fact that the impedance of the aperture probe at plane *BB'* is not exactly the characteristic impedance (Z_o = 50 Ω). The $e_{10}e_{01}$ is the frequency tracking imperfections (or phase shift) between plane *AA'* and sample test plane *BB'*. For this calibration, the e_{00} and e_{11} terms in Eqs. (1) and (2) are assumed to be vanished ($e_{00} = e_{11} = 0$). By dividing Eq. (2) into Eq. (1), yields

$$\frac{S_{11a\_sample}}{S_{11a\_air}} = \frac{S_{11m\_sample}}{S_{11m\_air}} \tag{3}$$

Once the $S_{11\boldsymbol{m\_air}}$ and $S_{11\boldsymbol{m\_sample}}$ are obtained, the actual reflection coefficient, S_{11a_sample}, of the sample at the probe aperture, *BB'* can be found as:

$$S_{11a\_sample} = \frac{S_{11a\_air}}{S_{11m\_air}} \times S_{11m\_sample} \tag{4}$$

The standard values of the reflection coefficient, S_{11a_air} in (4), can be calculated from Eq. (5) that satisfying conditions: (DC < f < 24) GHz.

$$S_{11a\_air} = \frac{1 - j(\omega/Y_o)(C_o f^{-1} + C_1 + C_2 f + C_3 f^2)}{1 + j(\omega/Y_o)(C_o f^{-1} + C_1 + C_2 f + C_3 f^2)} \tag{5}$$

Symbol $\omega = 2\pi f$ and $Y_o = [(2\pi)/\ln(b/a)]\sqrt{(\varepsilon_o \varepsilon_c/\mu_o \mu_r)}$ are the angular frequency (in rad/s) and characteristic admittance (in siemens), respectively. For instance, the complex values of the C_o, C_1, C_2 and C_3 in (5) for Teflon-filled coaxial probe with $2a$ = 1.3 mm, $2b$ = 4.1 mm and ε_c = 2.06 are given as [12]:

$$C_o = 5.368082994761808 \times 10^{-7} + j\, 2.320071598550666 \times 10^{-7} \quad (\mathrm{F \times Hz})$$

$$C_1 = 3.002820660256831 \times 10^{-14} - j\, 2.988971515445163 \times 10^{-16} \quad (\mathrm{F})$$

$$C_2 = 1.112989441958266 \times 10^{-25} + j\, 7.730261500907114 \times 10^{-26} \quad (\mathrm{F/Hz})$$

$$C_3 = 3.140652268416283 \times 10^{-36} - j\, 6.786433840933426 \times 10^{-36} \quad (\mathrm{F/Hz^2})$$

It should be noted that this simple calibration technique will not eliminate the standing wave effects in the coaxial line.

3.1.2. Open-short-load (OSL) standard calibrations

In this subsection, the three-standard calibration is reviewed in which open, short and load standards are used in the de-embedding process [13]. Let S_{11a_a}, S_{11a_s} and S_{11a_w} represent the known reflection coefficients for the open, short and load (water) standards which are terminated at the aperture plane *BB'*, while S_{11m_a}, S_{11m_s} and S_{11m_w} are the measured reflection coefficients for open, short and load standards at plane *AA'*. The S_{11m_a} is measured by leaving

the open end of the probe in the air as shown in **Figure 10a**. Later, the measurement is repeated to obtain the S_{11m_s} by terminating the probe aperture with a metal plate as shown in **Figure 10b**. Finally, the S_{11m_w} is obtained by immersing the probe in water as shown in **Figure 10c**.

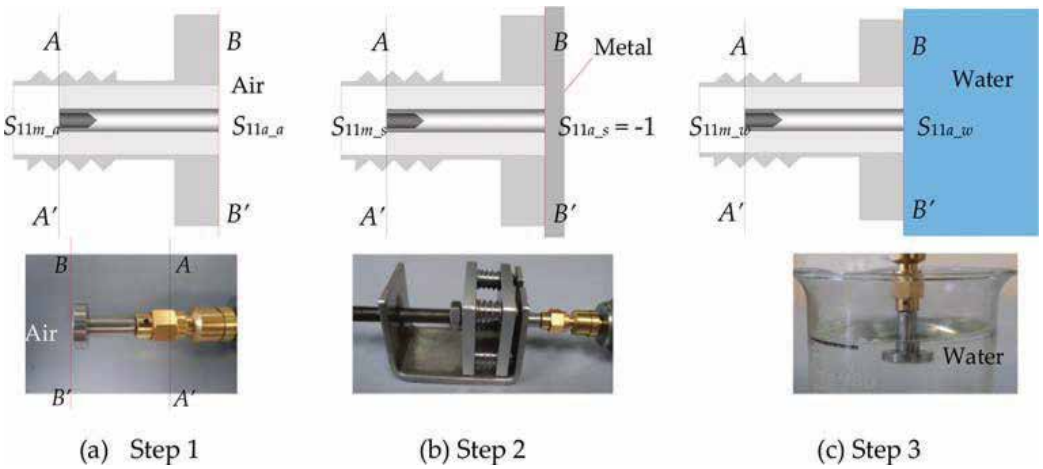

Figure 10. Finite coaxial line: (a) terminated by free space; (b) shorted by a metal plate; (c) immersed in water.

Once the complex values of S_{11a_air}, S_{11a_short}, S_{11a_water}, S_{11m_a}, S_{11m_s} and S_{11m_w} are known, the three unknown complex coefficients (e_{00}, e_{11}, and $e_{10}e_{01}$) values in Eq. (2) can be found as:

$$e_{00} = \frac{S_{11a\_s}S_{11a\_w}S_{11m\_a}\Delta_{w\_s} + S_{11a\_o}S_{11a\_s}S_{11m\_w}\Delta_{s\_a} + S_{11a\_a}S_{11a\_w}S_{11m\_s}\Delta_{a\_w}}{S_{11a\_w}S_{11a\_s}\Delta_{w\_s} + S_{11a\_a}S_{11a\_s}\Delta_{s\_a} + S_{11a\_w}S_{11a\_a}\Delta_{a\_w}} \tag{6a}$$

$$e_{11} = \frac{-(S_{11a\_a}\Delta_{w\_s} + S_{11a\_w}\Delta_{s\_a} + S_{11a\_s}\Delta_{a\_w})}{S_{11a\_w}S_{11a\_s}\Delta_{w\_s} + S_{11a\_a}S_{11a\_s}\Delta_{s\_a} + S_{11a\_w}S_{11a\_a}\Delta_{a\_w}} \tag{6b}$$

$$e_{10}e_{01} = (e_{00}\times e_{11}) + \frac{S_{11a\_a}S_{11m\_a}\Delta_{w\_s} + S_{11a\_w}S_{11m\_w}\Delta_{s\_a} + S_{11a\_s}S_{11m\_s}\Delta_{a\_w}}{S_{11a\_w}S_{11a\_s}\Delta_{w\_s} + S_{11a\_a}S_{11a\_s}\Delta_{s\_a} + S_{11a\_w}S_{11a\_a}\Delta_{a\_w}} \tag{6c}$$

where

$\Delta_{a\_w} = S_{11m\_a} - S_{11m\_w}$, $\Delta_{s\_a} = S_{11m\_s} - S_{11m\_a}$, and $\Delta_{w\_s} = S_{11m\_w} - S_{11m\_s}$

3.1.3. Short-offset-offset short (SOO) standard calibrations

The open-short-load (OSL) technique is rarely used in the one-port rectangular waveguide calibration due to unavailable commercial open kit for the rectangular waveguide. In this subsection, the short-offset-offset short (SOO) calibration [14, 15] is introduced for waveguide calibration by using waveguide adjustable sliding shorts as shown in **Figure 11**. The calibration procedures are shown in **Figure 12**.

In this calibration method, the measured reflection coefficients for one shorted aperture and two different lengths, l of offset short are required. Let S_{11m_1}, S_{11m_2} and S_{11m_3} represent the known measured reflection coefficients at plane AA' for the shorted aperture and the two offset shorts at location l_1 and l_2 from the waveguide aperture, respectively. Before calibration, the selection of the appropriate offset short length, l_1 and l_2 will be an issue. The lengths of the offset shorts can be determined by conditions:

1. The three phase shift between the S_{11m_1}, S_{11m_2} and S_{11m_3} must not be equal:

$$\angle(S_{11m\_2})-\angle(S_{11m\_1})\neq\angle(S_{11m\_3})-\angle(S_{11m\_1})\neq\angle(S_{11m\_3})-\angle(S_{11m\_2})$$

2. The resolution degree between any three phase shift must be significant large (>100°) as shown in **Figure 13**. In this work, the distance l_1 and l_2 for the offset shorts from the X-band waveguide aperture are equal to 0.007 m and 0.013 m, respectively.

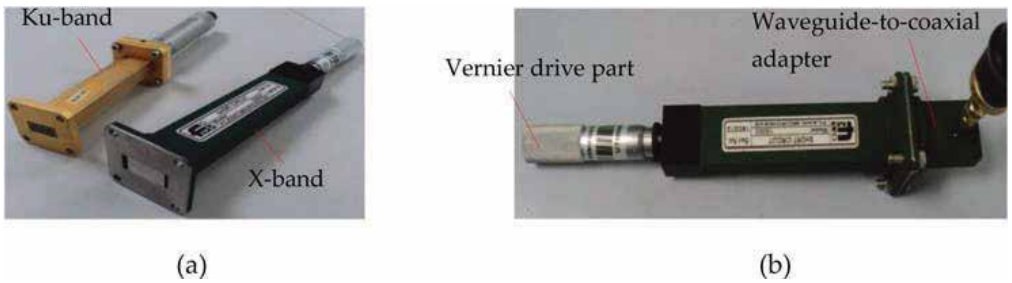

Figure 11. (a) Ku-band and X-band waveguide adjustable sliding shorter. (b) Connection between sliding short with waveguide-to-coaxial adapter.

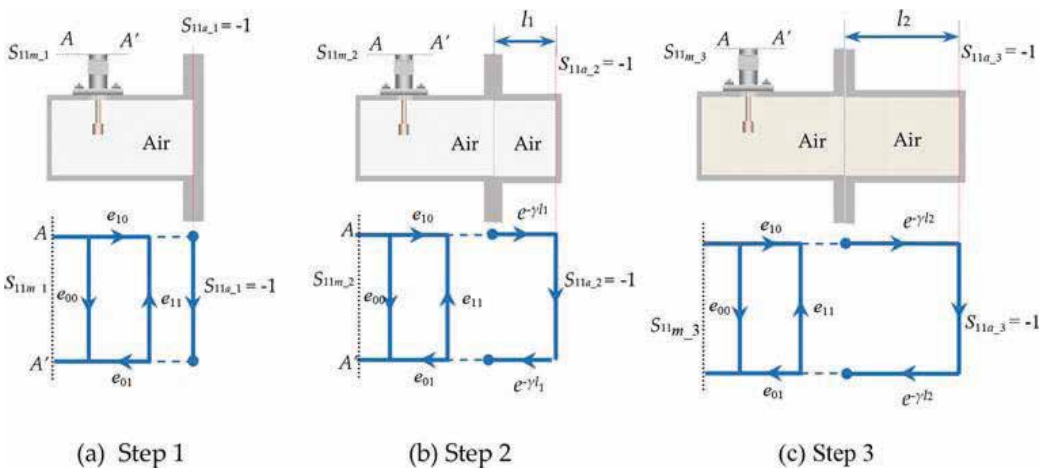

Figure 12. Calibration procedures of the aperture rectangular waveguide using an adjustable shorter. (a) Step 1; (b) Step 2; (c) Step 3

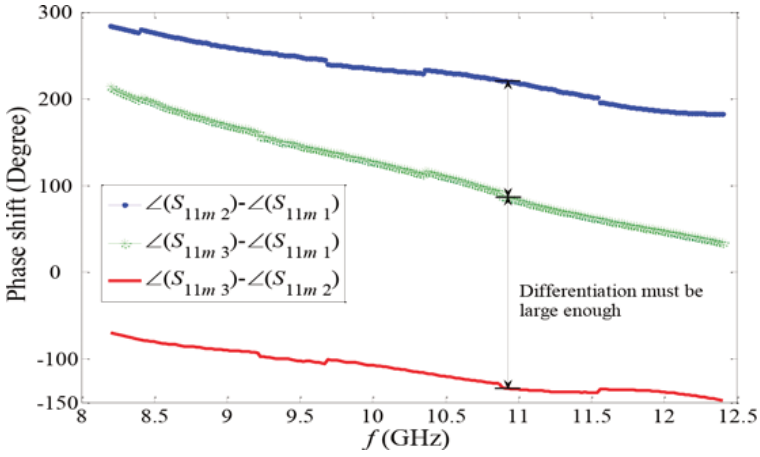

Figure 13. The three phase shift of the measured reflection coefficients for the shorted aperture and two offset shorts with l_1 = 0.7 cm and l_2 = 1.3 cm, respectively.

Once the S_{11m_1}, S_{11m_2}, S_{11m_3}, l_1 and l_2 are obtained, the three unknown complex coefficients (e_{00}, e_{11}, and $e_{10}e_{01}$) values in Eq. (2) can be found as:

$$e_{00} = \frac{S_{11m\_1}S_{11m\_2}(e^{-2\gamma l_1}-1)-S_{11m\_2}S_{11m\_3}\left(e^{2\gamma(l_2-l_1)}-1\right)-S_{11m\_1}S_{11m\_3}\left(e^{-2\gamma l_1}-e^{2\gamma(l_2-l_1)}\right)}{(e^{-2\gamma l_1}-1)(S_{11m\_2}-S_{11m\_3})-\left(e^{2\gamma(l_2-l_1)}-1\right)(S_{11m\_2}-S_{11m\_1})} \tag{7a}$$

$$e_{11} = \frac{e^{2\gamma l_1}(S_{11m\_2}-e_{00})+e_{00}-S_{11m\_1}}{S_{11m\_1}-S_{11m\_2}} \tag{7b}$$

$$e_{10}e_{01} = (e_{00}-S_{11m\_1})(1+e_{11}) \tag{7c}$$

The complex reflection coefficient, S_{11a_sample}, at the waveguide aperture which is open to the air was measured. Then, the measured S_{11a_sample} was converted to normalized admittance, Y/Y_o parameter by a formula: $Y/Y_o = (1 - S_{11a\_sample})/(1 + S_{11a\_sample})$. The SOO calibration techniques were validated by comparing normalized admittance, Y/Y_o with the literature data [15–22] as shown in **Figure 14**. The real part, $\mathrm{Re}(Y/Y_o)$, and the imaginary part, $\mathrm{Im}(Y/Y_o)$, of admittance results were found to be in good agreement with literature data over the operational range of frequencies.

3.2. Two-port calibrations [through-reflect-line (TRL)]

The through-short-line (TRL) calibration model [23] is used for two-port rectangular waveguide measurement. The TRL technique requires three standards, which are *through, short* and *line* measurements at the *CC'* and *DD'* planes so-called reference planes (at the front surface of the sample under test) as shown in **Figure 15**.

The error coefficients (e_{00}, e_{11}, $e_{10}e_{01}$, e_{33}, e_{22}, e_{32}, and e_{23}) in **Figure 15** can be obtained by solving the matrix equation of Eq. (8).

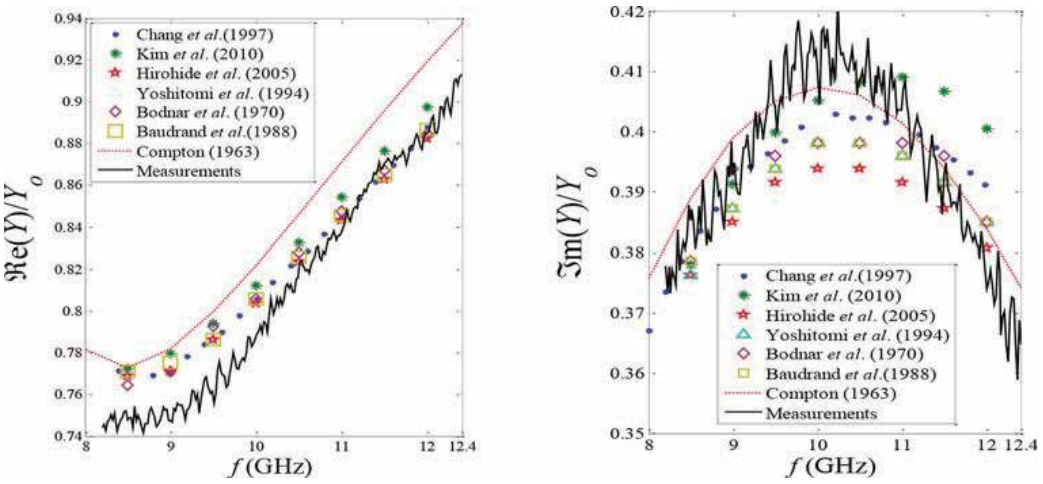

Figure 14. Comparison of real part, $\mathrm{Re}(Y/Y_o)$, and imaginary part, $\mathrm{Im}(Y/Y_o)$, of the normalized admittance for air.

$$\begin{bmatrix} 1 & 0 & 0 & 0 & S_{12m\_Thru} & 0 & 0 & 0 & 0 & 0 & 0 & 0 \\ 0 & S_{11m\_Thru} & -1 & 0 & 0 & 0 & -S_{12m\_Thru} & 0 & 0 & 0 & 0 & 0 \\ 0 & 0 & 0 & 0 & S_{22m\_Thru} & -1 & 0 & 0 & 0 & 0 & 0 & 0 \\ 0 & S_{21m\_Thru} & 0 & 1 & 0 & 0 & -S_{22m\_Thru} & 0 & 0 & 0 & 0 & 0 \\ 1 & -S_{11m\_Short} & 1 & 0 & 0 & 0 & 0 & 0 & 0 & 0 & 0 & 0 \\ 0 & 0 & 0 & 0 & -S_{12m\_Short} & 0 & -S_{12m\_Short} & 0 & 0 & 0 & 0 & 0 \\ 0 & -S_{21m\_Short} & 0 & 0 & 0 & 0 & 0 & 0 & 0 & 0 & 0 & 0 \\ 0 & 0 & 0 & 1 & -S_{22m\_Short} & 1 & -S_{22m\_Short} & 0 & 0 & 0 & 0 & 0 \\ 1 & 0 & 0 & 0 & e^{-j\beta l}S_{12m\_Line} & 0 & 0 & 0 & 0 & 0 & 0 & 0 \\ 0 & e^{j\beta l}S_{11m\_Line} & e^{j\beta l} & 0 & 0 & 0 & -S_{12m\_Line} & 0 & 0 & 0 & 0 & 0 \\ 0 & 0 & 0 & 0 & e^{-j\beta l}S_{22m\_Line} & -e^{-j\beta l} & 0 & 0 & 0 & 0 & 0 & 0 \\ 0 & e^{j\beta l}S_{21m\_Line} & 0 & 1 & 0 & 0 & -S_{22m\_Line} & 0 & 0 & 0 & 0 & 0 \end{bmatrix} \begin{bmatrix} e_{00} \\ e_{11} \\ \Delta_x \\ ke_{33} \\ ke_{22} \\ k\Delta_y \\ k \\ 0 \\ 0 \\ 0 \\ 0 \\ 0 \end{bmatrix} = \begin{bmatrix} S_{11m\_Thru} \\ 0 \\ S_{21m\_Thru} \\ 0 \\ S_{11m\_Short} \\ 0 \\ S_{21m\_Short} \\ 0 \\ S_{11m\_Line} \\ 0 \\ S_{21m\_Line} \\ 0 \end{bmatrix} \tag{8}$$

where $k = e_{10}/e_{23}$, $\Delta_x = e_{00}e_{11} - e_{10}e_{01}$ and $\Delta_y = e_{22}e_{33} - e_{32}e_{23}$. Once the S_{11m_sample}, S_{21m_sample}, S_{12m_sample} and S_{22m_sample} at plane AA' and BB' for the sample under test are measured, the calibrated reflection coefficient, S_{11a_sample} at plane CC' and transmission coefficient, S_{21a_sample} at plane DD' can be calculated as:

$$S_{11a\_sample} = \frac{\left\{ \begin{array}{l} \left(\dfrac{S_{11m\_sample} - e_{00}}{e_{10}e_{01}}\right)\left[1 + \left(\dfrac{S_{22m\_sample} - e_{33}}{e_{23}e_{32}}\right)e_{22}\right] \\ -e_{22}\left(\dfrac{S_{21m\_sample} - S_{21m\_Thru}}{e_{10}e_{32}}\right)\left(\dfrac{S_{12m\_sample} - S_{12m\_Thru}}{e_{23}e_{01}}\right) \end{array} \right\}}{D} \tag{9a}$$

$$S_{21a\_sample} \cong \frac{\left(\dfrac{S_{21m\_sample} - S_{21m\_Thru}}{e_{10}e_{32}}\right)}{D} \tag{9b}$$

The denominator, D in (9a) and (9b) is given as:

http://dx.doi.org/10.5772/66230

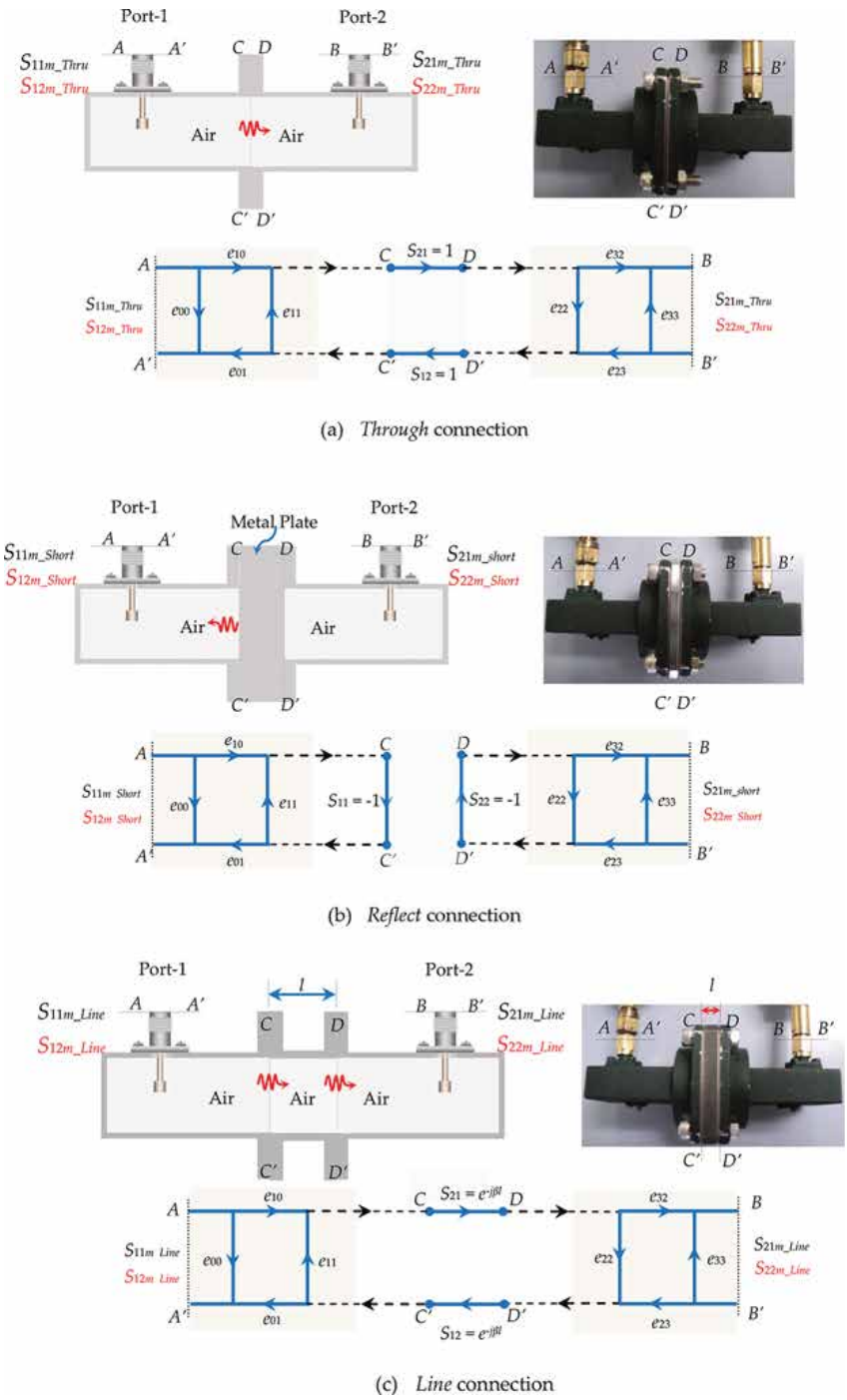

Figure 15. through-short-line (TRL) calibration procedures and its network errors. *(a) Through* connection; *(b) Reflect* connection; *(c) Line* connection.

$$D = \left\{ \begin{array}{l} \left[1 + \left(\frac{S_{11m\_sample} - e_{00}}{e_{10}e_{01}}\right)e_{11}\right]\left[1 + \left(\frac{S_{22m\_sample} - e_{33}}{e_{23}e_{32}}\right)e_{22}\right] \\ -\left(\frac{S_{21m\_sample} - S_{21m\_Thru}}{e_{10}e_{32}}\right)\left(\frac{S_{12m\_sample} - S_{12m\_Thru}}{e_{23}e_{01}}\right)e_{22}e_{11} \end{array} \right\}$$

4. Material parameters extraction

4.1. Reflection measurements (one-port measurements)

There are two methods of determining sample parameters (ε_r, μ_r or σ), which are the direct method and the inverse method. The direct method involves the explicit model to predict the sample under test based on the measured reflection coefficient, S_{11a_sample}, while the inverse method is implemented rigorous integral admittance model to estimate the sample parameters (ε_r, μ_r or σ) using optimization procedures. For coaxial probe measurement cases, the explicit relationship between ε_r and S_{11a_sample} [8] is tabulated in **Table 1**. For rectangular waveguide cases, the measured S_{11a_sample} is transferred to normalized admittance, $\tilde{Y}_{a\_sample}$ through equation: $\tilde{Y}_{a\_sample} = (1 - S_{11a\_sample})/(1 + S_{11a\_sample})$. The predicted value of ε_r is obtained by minimizing the difference between the measured normalized admittance, $\tilde{Y}_{a\_sample}$ and the quasi-static integral model, $\tilde{Y}$ (in **Table 2**) [9, 17] by referring to particular objective function. The procedures of direct method are more straightforward than the inverse method. The detail descriptions of the parameters (Y_o, C and γ_o) and the coefficients (a_1, a_2 and a_3) in Eqs. (10)–(13) can be found in [8, 9, 17].

4.2. Reflection/transmission measurements (two-port measurements)

Conventionally, the complex $\varepsilon_r = \varepsilon_r' - j\varepsilon_r''$ and the $\mu_r = \mu_r' - j\mu_r''$ of the sample filled in the coaxial or rectangular waveguide are obtained by converting the calibrated reflection coefficient, S_{11a_sample} and the transmission coefficient, S_{21a_sample} by using Nicholson-Ross-Weir (NRW) routines [10, 11]. In this section, another alternative method, namely transmission phase shift (TPS) method [24], is reviewed. The TPS method is a calibration-independent and material position-invariant technique, which can reduce the complexity of the de-embedding procedures. The important formulations of the NRW and the TPS methods are tabulated in **Table 3**.

Sample cases	Open-ended coaxial probe
Semi-infinite space sample (**Figure 5a**)	$\varepsilon_r = \left(\frac{Y_o}{j\omega C}\right)\left(\frac{1 - S_{11a\_sample}}{1 + S_{11a\_sample}}\right)$ (10)
Thin sample backed by metal plate (**Figure 5b**)	$\varepsilon_r = \left(\frac{Y_o}{j\omega C}\right)\left(\frac{1 - S_{11a\_sample}}{1 + S_{11a\_sample}}\right)(a_1 + a_2 e^{-d/M} + a_3 e^{-2d/M})$ (11)

Table 1. Explicit formulations for open-ended coaxial probe.

Sample cases	Open-ended rectangular waveguide
Semi-infinite space sample (**Figure 5c**)	$\tilde{Y} = \frac{j8b}{a\gamma_o}\int_0^a\int_0^b \left\{(a-x)\left\{D_1(b-y)\cos\frac{\pi y}{b} + D_2\sin\frac{\pi y}{b}\right\} \times \frac{\exp\left(-jk_1\sqrt{x^2+y^2}\right)}{\sqrt{x^2+y^2}}\right\}dxdy$ (12)
	where $D_1 = \frac{1}{b^2}\left(\frac{k_1^2}{4\pi} - \frac{\pi}{4b^2}\right)$, $D_2 = \frac{1}{\pi b}\left(\frac{k_1^2}{4\pi} + \frac{\pi}{4b^2}\right)$, and $k_1 = \frac{2\pi f}{c}\sqrt{\varepsilon_r}$
Thin sample backed by metal plate (**Figure 5d**)	$\tilde{Y} = \frac{j8b}{a\gamma_o}\int_0^a\int_0^b \chi\frac{\exp\left(-jk_1\sqrt{x^2+y^2}\right)}{\sqrt{x^2+y^2}}dxdy$
	$+\frac{j16b}{a\gamma_o}\sum_{n=1}^{\infty}\int_0^a\int_0^b \chi\frac{\exp\left(-jk_1\sqrt{x^2+y^2+4n^2d^2}\right)}{\sqrt{x^2+y^2+4n^2d^2}}dxdy$ (13)
	where $\chi = (a-x)\left\{D_1(b-y)\cos\frac{\pi y}{b} + D_2\sin\frac{\pi y}{b}\right\}$

Table 2. Integral admittance formulations for open-ended rectangular waveguide.

	Waveguide factors	Explicit equations	
NRW method [10–11]	Coaxial: $\zeta = 1$ Waveguide: $\zeta = \sqrt{k_o^2 - \left(\frac{\pi}{b}\right)^2}$	$\varepsilon_r = j\zeta\left(\frac{1-\Gamma}{1+\Gamma}\right)\left(\frac{c}{2\pi fd}\right)\ln\left(\frac{1}{T}\right)$	(14a)
		$\mu_r = j\frac{1}{\zeta}\left(\frac{1+\Gamma}{1-\Gamma}\right)\left\{\frac{c}{2\pi fd}\ln\left(\frac{1}{T}\right)\right\}$	(14b)
TPS method [24]	Coaxial: $\xi = 0$ and $\gamma_o = k_o$	$\varepsilon'_r = \frac{1}{k_o^2}\left\{\left(\gamma_o + \frac{\phi_{21\_air} - \phi_{21\_sample}}{d}\right)^2 + \xi - \alpha^2\right\}$	(15a)
	Waveguide: $\xi = \left(\frac{\pi}{b}\right)^2\gamma_o = \sqrt{k_o^2 - \left(\frac{\pi}{b}\right)^2}$	$\varepsilon''_r = \frac{2\alpha}{k_o^2}\left(\gamma_o + \frac{\phi_{21\_air} - \phi_{21\_sample}}{d}\right)$	(15b)

Table 3. Explicit formulations for reflection/transmission measurements.

where $k_o = 2\pi f/c$ is the propagation constant of free space ($c = 2.99792458\ \text{ms}^{-1}$); b (in meter) are the width of the aperture of the waveguide, respectively; d(in meter) is the thickness of the sample. The expressions for parameters Γ and T in Eqs. (14a, b) can be found in [10, 24]. The ϕ_{21_air} and ϕ_{21_sample} in Eqs. (15a, b) are the measured phase shift of the transmission coefficient

in the air (without sample) and the sample, respectively. On the other hand, symbol α (in nepers/meter) is the dielectric attenuation constant for the sample.

You et al. [24] have been mentioned that the uncertainty of the permittivity measurement is high for the low-loss thin sample by using TPS method due to the decreasing of the sensitivity for the transmitted wave through the thin sample, especially for transmitted waves that have longer wavelengths. However, the literature [24] did not discuss how the thickness of the thin sample may affect the uncertainty of measurement using TPS technique in quantitative. From this reasons, the TPS method is reexamined in this section. Various thicknesses of acrylic, FR4 and RT/duroid 5880 substrate samples were placed in the X-band rectangular waveguide and measured for validation. **Figure 16a–c** shows the predicted dielectric constant, ε_r' of the samples using Eq. (15a) at 8.494, 10.006 and 11.497 GHz, respectively. Clearly, the TPS method is capable of providing a stable and accurate measurement for operating frequency in X-band range when the thicknesses of the samples have exceeded 2 cm [25].

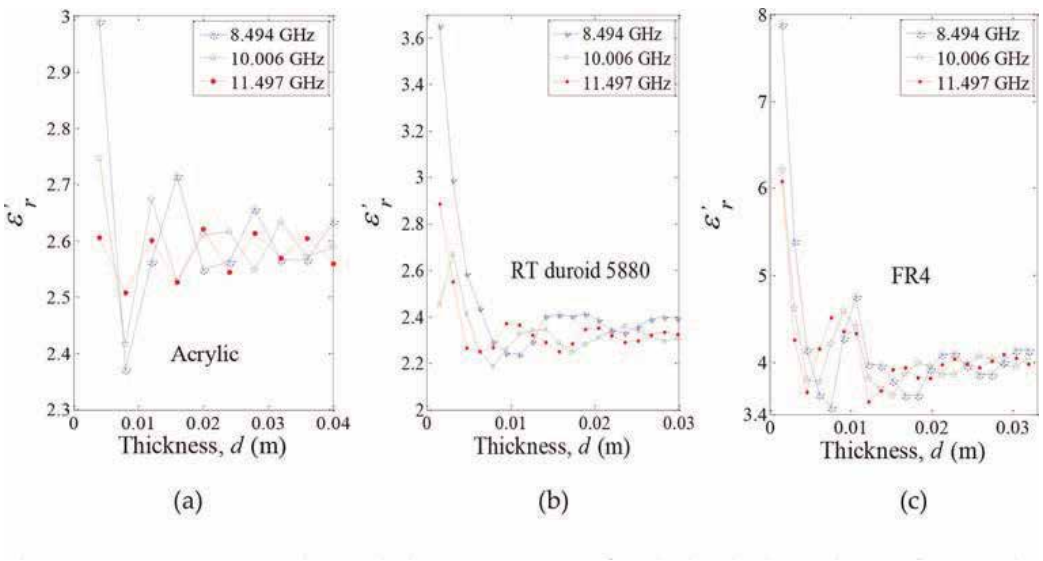

Figure 16. Variations in relative dielectric constant, ε_r with the thickness layer of (a) acrylic, (b) RT/duroid 5880 substrate and (c) FR4, respectively.

5. Conclusion

The brief background of the microwave waveguide techniques for materials characterization is reviewed and summarized. Not only that the measurement methods play an important role, the calibration process is crucial as well. However, most of the literatures have ignored the description of calibration. Measurement without calibration certainly cannot predict the properties of materials accurately. Thus, in this chapter, some of the waveguide calibrations are described in detail.

Author details

Kok Yeow You

Address all correspondence to: kyyou@fke.utm.my

Department of Communication Engineering, Faculty of Electrical Engineering, Universiti Teknologi Malaysia, Johor, Malaysia

References

[1] Hakki B W, Coleman P D: A dielectric resonator method of measuring inductive capacities in the millimeter range. IRE Transactions on Microwave Theory and Techniques. 1960; **8(7)**: 402–410.

[2] Courtney W E: Analysis and evaluation of a method of measuring the complex permittivity and permeability of microwave insulators. IEEE Transactions on Microwave Theory and Techniques. 1970; **18(8)**: 476–485.

[3] Tosaka T, Fujii K, Fukunaga K, Kasamatsu A: Development of complex relative permittivity measurement system based on free-space in 220–330 GHz range. IEEE Transaction on Terahertz Science and Technology. 2015; **5(1)**: 102–109.

[4] Abbas Z, Pollard R D, Kelsall R W: Complex permittivity measurements at Ka-Band using rectangular dielectric waveguide. IEEE Transactions on Instrumentation and Measurement. 2001; **50(5)**: 1334–1342.

[5] Kemptner E, Thurner S: Free space material characterization for microwave frequencies. 6th European Conference on Antennas and Propagation (EUCAP). 2011: 3513–3515.

[6] You K Y, Mun H K, You L L, Jamaliah S, Abbas Z: Small and slim coaxial probe for single rice grain moisture sensing. Sensors. 2013;**13(3)**: 3652–3663.

[7] You K Y, Jamaliah S, Abbas Z: Effects of length and diameter of open-ended coaxial sensor on its reflection coefficient. RadioEngineering. 2012; **21(1)**: 496–503.

[8] You K Y, Then Y L: Simple calibration and dielectric measurement technique for thin material using coaxial probe. IEEE Sensors Journal. 2015; **15(10)**: 5393–5397.

[9] You K Y, Abbas Z, Malek M F A, Cheng E M: Non-destructive dielectric measurements and calibration for thin materials using waveguide-coaxial adaptors. Measurement Science Review. 2014; **14(1)**: 16–24.

[10] Nicolson A M, Ross G F: Measurement of the intrinsic properties of materials by time-domain techniques. IEEE Transactions on Instrumentation and Measurement. 1970; **19(4)**: 377–382.

[11] Weir W B: Automatic measurement of complex dielectric constant and permeability at microwave frequencies. Proceedings of the IEEE. 1974; **62(1)**: 33–36.

[12] You K Y. RF Coaxial Slot Radiators: Modeling, Measurements, and Applications. USA: Artech House; 2015. ISBN: 978-1-60807-822-6.

[13] Kraszewski A, Stuchly M A, Stuchly S S: ANA calibration method for measurements of dielectric properties. IEEE Transactions on Instrumentation and Measurement. 1983; **32 (2)**: 385–386.

[14] Da Silva E F, McPhun M K: Calibration techniques for one-port measurement. Microwave Journal. 1978; **21(6)**: 97–100.

[15] Chang C W, Chen K M, Qian J: Nondestructive determination of electromagnetic parameters of dielectric materials at X-band frequencies using a waveguide probe system. IEEE Transactions on Instrumentation and Measurement. 1997; **46(5)**: 1084–1092.

[16] Kim J H, Enkhbayar B, Bang J H, Ahn B C:New formulas for the reflection coefficient of an open-ended rectangular waveguide radiating into air including the effect of wall thickness or flange. Progress in Electromagnetics Research M. 2010; **12**: 143–153.

[17] Compton R T Jr. The Aperture Admittance of a Rectangular Waveguide Radiating into a Lossy Half-Space. Technical Report, 1691-1, Columbus, Ohio: Ohio State University; 1963.

[18] Ganchev S I, Bakhtiari S, Zoughi R: A novel numerical technique for dielectric measurement of generally lossy dielectrics. IEEE Transactions on Instrumentation and Measurement. 1992; **41(3)**: 361–365.

[19] Yoshitomi K, Sharobim H R: Radiation from a rectangular waveguide with a lossy flange. IEEE Transactions on Antennas and Propagation.1994; **42(10)**: 1398–1403.

[20] Hirohide, Serizawa, Hongo K: Radiation for a flanged rectangular waveguide. IEEE Transactions on Antennas and Propagation.2005; **53(12)**: 3953–3962.

[21] Bodnar D G, Paris D T: New variational principle in electromagnetic. IEEE Transactions on Antennas and Propagation.1970; **18(2)**: 216–223.

[22] Baudrand H, Tao J, Atechian J: Study of radiation properties of open-ended rectangular waveguides. IEEE Transactions on Antennas and Propagation. 1988; **36(8)**: 1071–1077.

[23] Engen G F, Hoer C A: Thru-reflect-line: an improved technique for calibrating the dual six-port automatic network analyzer. IEEE Transactions on Microwave Theory and Techniques. 1979; **27(12)**: 987–993.

[24] You K Y, Lee Y S, Zahid L, Malek M F A, Lee K Y, Cheng E M: Dielectric measurements for low-loss materials using transmission phase-shift method. JurnalTeknologi. 2015; **77 (10)**: 69–77.

[25] You K Y: Effects of sample thickness for dielectric measurements using transmission phase-shift method. International Journal of Advances in Microwave Technology. 2016; **1(3)**: 64–67.

Chapter 15

Review on Microwave Metamaterial Structures for Near-Field Imaging

Hatem El Matbouly

Additional information is available at the end of the chapter

http://dx.doi.org/10.5772/66831

Abstract

In the past decade, metamaterials have attracted a lot of attention because of their abilities to exhibit unusual electromagnetic properties. These properties are exploited in designing functional components and devices for many potential applications. In this chapter, we review the theory and design of metamaterial structures for microwave near-field imaging/microscopy. The chapter highlights metamaterial microwave components to obtain super-resolution and manipulating subwavelength images. Moreover, a review on surface plasmons manipulation at microwave frequencies is presented as a technique to enhance the transmission for near-field microscopy. The chapter presents as well a survey on the near-field imaging instrumentation and its advances mainly for microwave and THz regimes.

Keywords: metamaterials, microscopy, near-field, microwave, novel electromagnetic structures, subwavelength imaging, surface plasmons

1. Introduction

The technique of microwave near-field microscopy is used to characterize materials by measuring the microwave electromagnetic response of materials on length scales shorter than the wavelength of the incident electromagnetic wave. With this technique one can achieve a spatial resolution at a submicrometer level compared to conventional far-field imaging technique, which has a resolution limitation [1]. This technique may facilitate new measurements on systems that cannot be studied directly with scanned probes, such as buried features or single molecule detection [2] as well as in biomedical applications [3].

New advances in metamaterials research are making unnatural electromagnetic phenomena become realizable [4]. The purpose of this chapter is to focus on using metamaterial and its exciting properties for the enhancement of near-field microscopy and imaging.

This chapter starts with a general overview on the near-field imaging/microscopy and its applications including a description of the microwave near-field imaging system and its components. Metamaterial design technique will be discussed as a step to design novel structures that allow further improvements in spatial resolution.

The chapter concludes with a review on another possibility to enhance microwave near-field microscopy that is the manipulation of surface plasmons at microwave and millimeter-wave frequencies. This can enhance the transmission through subwavelength near-field apertures.

2. Overview on microwave near-field imaging/microscopy

2.1. Backgrounds

The conventional far-field optical imaging system suffers from resolution limitations, this is due to Abbe's theory that restrains the spatial resolution to a diffraction limit [5]. In case of far-field imaging, forming an image is subjected to the Rayleigh criterion, which is the condition to resolve the diffraction pattern of two points separated by a distance of Δy. This condition is given by $\Delta y = 0.61\ \lambda/\mathrm{NA}$, where λ is the wavelength and (NA) is the numerical aperture of the microscope [6]. On the contrary, subwavelength spatial resolution imaging can only be achieved by using near-field technique suggested first by E.A Synge in early 1928 (see the next section for a survey on near-field technique). The near-field results in the excitation of an electric dipole moment within a sample, the idea is to probe the dipole radiation in the near-field region, $\vec{E}_{rad}$ is the radiated electric field and $\vec{B}_{rad}$ is the radiated magnetic field of the dipole radiation which are given by [7]

$$\vec{E}_{\mathrm{rad}} = \frac{1}{4\pi\varepsilon_0}\left\{k^2(\hat{r}\times\vec{p})\times\hat{r}\frac{e^{ikr-\omega t}}{r} + (3r(\hat{r}\cdot\vec{p})-\vec{p})\left(\frac{1}{r^3}-\frac{ik}{r^2}\right)e^{ikr-\omega t}\right\} \quad (1)$$

$$\vec{B}_{\mathrm{rad}} = \frac{1}{4\pi}\left\{k^2(\hat{r}\times\vec{p})\left(\frac{1}{r^3}-\frac{ik}{r^2}\right)e^{ikr-\omega t}\right\} \quad (2)$$

where $\vec{p}$ is the dipole moment, $\vec{k}$ is the wave number and $\vec{r}$ is the distance between the source and the observation point. The first part of Eq. (1) is the propagating far field of the dipole radiation that cannot be used for subwavelength imaging because the diffraction limits the image resolution. However, the second part is the near field of the dipole radiation and there is no diffraction problem associated with using it since it has a nonpropagating nature. In this case the spatial resolution will not be limited by the wavelength if the nonpropagating near field is used [7, 8].

2.2. Description of a microwave near-field imaging microscope

A schematic diagram of the near-field microwave microscope is shown in **Figure 1**. The near-field microscope consists of a microwave source, a transmission line resonator coupled to the

http://dx.doi.org/10.5772/66831

microwave generator, a near-field probe connected to the transmission line, a detector to measure the reflected signal from the resonator and a feedback circuit [9].

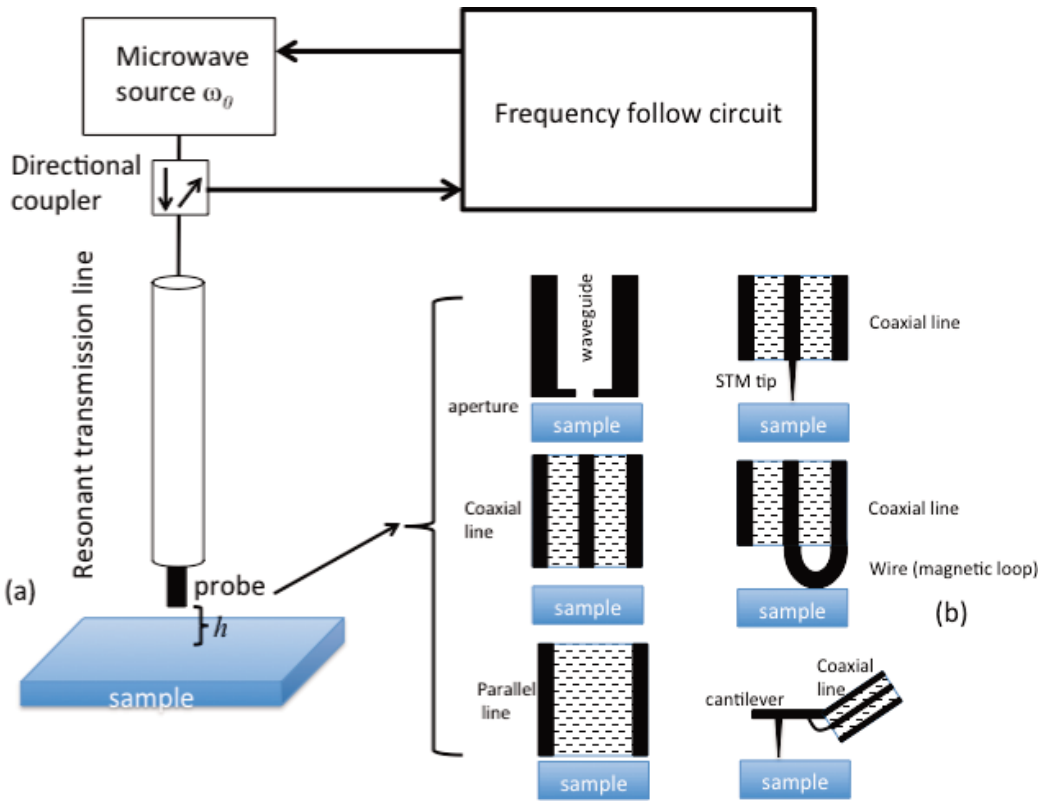

Figure 1. The schematic diagram of the near field microscope (a) the structure of the microscope and (b) different near field probe structures.

The probe is an antenna-like structure operating at the subwavelength, which is used to scan in close proximity of the sample's surface. As shown in **Figure 1(a)**, the probe can take different forms for instance it can be an aperture in an opaque screen, an electric wire formed by a sharpened rod or scanning tunneling microscopy (STM) tip, an atomic force microscopy (AFM) tip, an electrically open flush end of a transmission line, a magnetic loop, or a variety of other geometries [10]. The electromagnetic response of the surface is measured as the probe is scanned over the sample [11]. The probe can be either in contact or at a separation h from the sample surface, which is usually much less than the probe characteristic length-scale D, this ensures a good signal level from the sample surface [11, 12]. In the near zone of an antenna, the structure of electric and magnetic fields is more complicated as their distribution is strongly dependent on the antenna geometry as well as electrodynamics properties of the surrounding region [13–15].

The design of near-field probes can be divided into two main categories, aperture-based probes and apertureless probes [16]. For aperture-based probes, a subwavelength aperture is

used to limit the illuminating source, or to collect the local near-field response. It can be a subwavelength hole in a metallic film, a metallic coated pipette, or a tapered optical fiber as illustrated in **Figure 1(b)**.

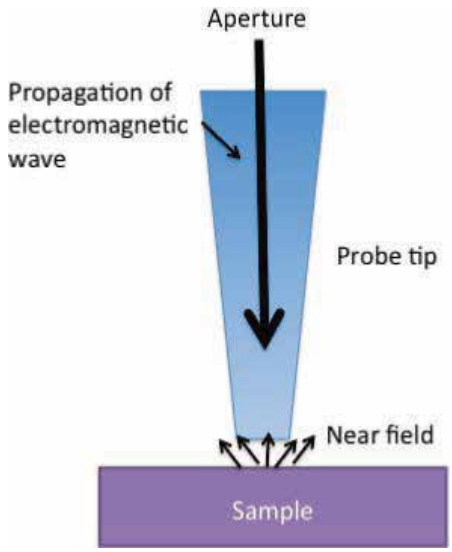

Figure 1 (b). Near-field imaging using aperture type probe.

By positioning the aperture in the close proximity of the sample, the transmitted wave through the aperture only represents the local properties of the sample. Thus, in principle, subwavelength spatial resolution becomes possible by reducing the aperture size and raster scanning the sample surface [17]. The concept was first experimentally demonstrated by Ash and Nicholls [26] (see the next section for a survey on near-field technique), who resolved a $\lambda/60$ grating structure by using λ = 3 cm microwave (10 GHz). In optical frequencies, the spatial resolutions are typically tens of nanometers when using a tapered single mode optical fiber probe. However, the aperture probes suffer from strong signal attenuation. For a hole in a metallic film, the electric field transmission is proportional to $(D/\lambda)^3$, where D is the diameter of the hole [11, 13]. For an optical fiber probe, the image contrast suffers from a strong decrease when the aperture diameter exceeds a critical value. So the signal intensity will be far too small to be detected when the aperture size is further reduced to achieve a better spatial resolution. On the other hand, for the long wavelength of THz radiation, according to the wavelength dependence, the transmission efficiency is extremely low and makes the THz aperture near-field imaging impractical.

An alternative approach is to allow a propagating wave to irradiate some large portion of the sample, but to employ a field-concentrating feature, such as a tip, is to enhance the probe-sample interaction locally. **Figure 2** shows the probing using apertureless near-field probe.

Using a metallic probing tip, the incident wave is scattered by the tip-surface system. Usually, the scattering wave is modulated by a dithering tip and measured in nonspecular directions due to reduced background noise. The wave scattering depends on the local surface

properties. By measuring the scattering wave when scanning over a sample, the surface properties can be mapped. In principle, the spatial resolution for an apertureless probe is only limited by the size of the probing tip. Resolution as small as 10 angstrom has been reported with this technique at optical frequencies and a subwavelength factor of 10^{-6} was achieved at the microwave region [18].

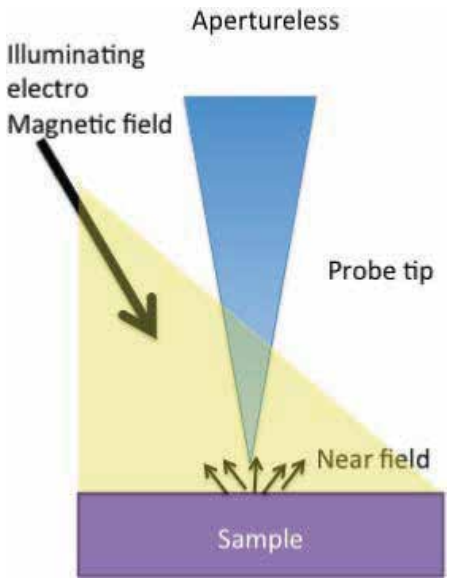

Figure 2. Near-field imaging using apertureless type probe.

3. Survey on near-field imaging from microwave to terahertz frequencies

The idea of near-field microscopy was first demonstrated theoretically by Synge in 1928 [19]. He used an opaque screen with a small subwavelength diameter hole (10 nm in diameter) at 10 nm above the surface of an optically transparent flat sample. The transmitted light is collected by raster scanning the surface. Detailed calculations of the near-field distribution of an aperture were conducted later by Bethe [20] and Bouwkamp [21, 22]. A large fraction of high-spatial frequency evanescent waves is contained in the near field, which can lead to subwavelength spatial resolution [23, 24].

In the 1960s, when the idea of near-field imaging transferred to practice, ferromagnetic resonance microwave microscopy has been developed to characterize ferromagnetic material thin films, for example, Soohoo developed a microwave magnetic probe capable of measuring the spatial variation of the magnetic properties of materials [25] using a cavity made of superconducting material.

A detection system using quasi-optical hemispherical resonator was used at microwave frequencies by Ash and Nicholls [26]. In this experiment, a small aperture (1.5 mm diameter) similar to Synge geometry is used. The aperture is scanned over a sample with a microwave

signal at 10 GHz. The sample was harmonically distance modulated at a fixed frequency and the reflected signal was phase-sensitively detected at this modulation frequency to improve sensitivity to sample contrast. This microscope demonstrated contrast sensitivity to metal films on dielectric substrates, as well as bulk dielectrics with dielectric constant differing by only about 10%.

Nonresonant scanned aperture probes were also developed in the 1960s. In the case of nonresonant probe, a transmission line (coaxial or waveguide) delivers a microwave signal to the probe aperture where the fringe electric and magnetic fields from the aperture interact with the sample. Some part of the signal is stored locally in evanescent and near-zone waves, some is absorbed by the sample, some is reflected back up the transmission line and some is scattered away as far-field radiation. By monitoring the scattered or reflected signals as a function of probe height and position, an image of the sample response can be constructed. An example of this type of probe was developed by Bryant and Gunn [27]. They measured the reflected signal from a tapered open-ended coaxial probe with an inner conductor diameter of 1 mm. The probe was used for quantitative measurements of semiconductor resistivities between 0.1 and 100 Ω cm^{-1}.

The development of near-field optical microscopes using optical waveguides beyond cutoff [28, 29] affected the development of new microwave microscopes. The first of these microwave systems operating at 2.5 GHz was developed by Fee et al. to measure the reflected signal from a nonresonant open-ended coaxial probe [30]. A 500-μm in diameter conductor coaxial probe is used and the central conductor was sharpened to a tip of 30 μm in radius. An image of copper grid lines showed a spatial resolution of about 30 μm (or λ/4000). Other waveguide structure microscopes based on a scanned aperture were developed by Golosovsky et al. [31, 32] and Bae et al. [33–35].

The first THz near-field microscopy was demonstrated in [36]. In this work, a tapered metallic waveguide was used as the aperture to limit the size of the incident ultrashort THz pulses. The probe aperture is similar to the tapered optical fiber tips used in most of scanning near-field optical microscopy. With the aperture diameter ~λ/3 (100 μm), a spatial resolution better than λ/4 was demonstrated for a gold pattern on silicon substrate. A collection mode THz scanning near-field microscopy was developed by Mitrofanov et al. [37–39]. It uses an aperture-type probe to collect the near field instead to filter the illuminating light. He showed improvements in sensitivity and resolution by integrating the probe and a photo-conducting antenna THz detector in the near-field region of the aperture. THz near-field imaging with a dynamic aperture was demonstrated by Wynne et al. and Chen et al. [40, 41]. In his work, the dynamic aperture was formed by a transient photo-carrier layer induced by a THz near-field imaging. In case that the optical pulse arrives earlier than the THz pulse, the THz transmission is modulated by the induced photo-carrier layer, whose size is determined only by the optical beam focus. This approach has the potential to improve spatial resolution and image contrast, while it is limited to semiconductor surface.

Apertureless THz near-field imaging has been also investigated [42, 43]. In their work, van and Planken used a metallic probing tip with THz waves to image down to 18 μm in size. Moreover, a scattering type apertureless THz scanning near-field microscope has been

demonstrated by Wang et al. [44]. THz radiation is scattered and modulated by the dithering metallic probing tip in the tip-surface system, the THz signal is detected in nonspecular directions [45].

4. Metamaterial for near-field imaging manipulation

Conventional imaging devices or lenses suffer from diffraction limit which constrain the image resolution. In addition, conventional imaging cannot propagate the evanescent waves which carry the subwavelength information due to the exponential decay exhibited in natural materials. These issues can be overcome using metamaterials. For instance, image focusing, rotation, lateral shift and image magnification are achievable with subwavelength resolutions using a two- or three-dimensional metamaterials structures, usually with negative refraction properties, to achieve resolution beyond the diffraction limit (ideally, infinite resolution). Such behavior is enabled by the capability of double-negative materials to yield negative phase velocity.

4.1. Metamaterial design by electromagnetic field transformation

Electromagnetic metamaterials are periodic structures than can artificially manipulate the electromagnetic properties of media. They can be engineered for the radio-frequency (RF) and microwave range as well as for terahertz and optical frequencies. Metamaterials allow the possibility of attaining mediums with properties, which have not been considered before, such as, negative or close to zero refractive index since they are inaccessible in nature. In addition, they can mix the electric and magnetic response of a material (chirality) [46, 47]. The first step to design a metamaterial medium is using the electromagnetic transformation to get the new medium properties (i.e., transformed permittivity and permeability). Transformation electromagnetics are based on the invariance of Maxwell's equations with respect to coordinate transformations; this enables a user-defined coordinate transformation to be translated into electric and magnetic material parameters. **Figure 3** shows the relations between the different coordinates [48, 49].

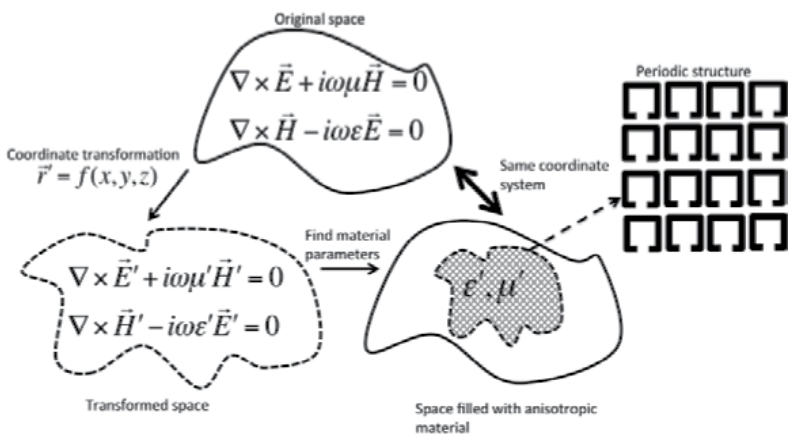

Figure 3. Transformation electromagnetic for metamaterial medium.

Once the transformed permittivity and permeability and their spatial distribution are obtained, the structure of unit cell (or particle) is designed by optimizing its geometric parameters. The most common unit cell structure is the split ring resonator (SRR). The unit cell can be a resonant or nonresonant. In case of the resonant unit cell, the losses are high at the resonance frequency; however, they have a large dynamic rang. The nonresonant unit cell has the advantage of small losses but with low dynamic rang [49].

4.2. Metamaterials medium types

The electromagnetic mediums are categorized as isotropic or anisotropic. In the isotropic electromagnetic medium the permittivity, ε and permeability, μ, of the medium are uniform in all directions of the medium. The dispersion relation in that medium is $k = \omega\sqrt{\mu\varepsilon}$. One simple example of an isotropic electromagnetic medium is the free space. However, the medium is called anisotropic when the permittivity, ε and permeability, μ, of a medium depend upon the directions of field vectors and hence, they are in tensor form. Based on Maxwell equations in an anisotropic medium the dispersion relation can be obtained by solving the matrix equation [49, 50]:

$$det\left[\overline{\overline{k}} \cdot \overline{\overline{\varepsilon}}^{-1} \cdot \overline{\overline{k}} + k^2{}_0\overline{\overline{\mu}}\right] = 0 \tag{3}$$

where $\overline{\overline{\mu}}, \overline{\overline{\varepsilon}}$ and $\overline{\overline{k}}$ are all matrices and $k^2{}_0 = \omega^2\mu_0\varepsilon_0$ (μ_0, ε_0 are the permeability and permittivity of free space, respectively). Metamaterials are composite structures in which the electromagnetic wave propagation depends on the orientation of structured metallic unit cells. Usually, these unit cells are designed to have a certain permittivity and permeability responses by optimizing its geometric parameters. One common example of unit cell structure is the split ring resonator (SRR) (see Section 4.1) [51]. The anisotropic metamaterial is defined with its permittivity and permeability tensor as follows

$$\overline{\overline{\varepsilon}} = \begin{pmatrix} \varepsilon_x & 0 & 0 \\ 0 & \varepsilon_y & 0 \\ 0 & 0 & \varepsilon_z \end{pmatrix} \text{ and } \overline{\overline{\mu}} = \begin{pmatrix} \mu_x & 0 & 0 \\ 0 & \mu_y & 0 \\ 0 & 0 & \mu_z \end{pmatrix} \tag{4}$$

where the diagonal elements of $\overline{\overline{\varepsilon}}$ and $\overline{\overline{\mu}}$ could have positive or negative values. To understand the propagation properties of a wave in such medium a TE plane wave is considered. Using Eqs. (3) and (4), one can get the anisotropic dispersion relation of the medium

$$\frac{k_y^2}{\varepsilon_z\mu_x} + \frac{k_x^2}{\varepsilon_z\mu_y} = \frac{\omega^2}{c^2} \tag{5}$$

where c is the speed of light in free space and k is the wave vector of the propagating wave. For losses material, the plane wave solution in the anisotropic medium can be either a propagating wave or evanescent wave depending on the sign of the wave number k_x and hence, the medium can be classified as in **Table 1** [49].

Medium type	Material parameters	Wave property	Cut off conditions
Cutoff media	$\varepsilon_z\mu_y > 0,\ \frac{\mu_y}{\mu_x} > 0$	Propagating	$k_y < k_c$
		Evanescent	$k_y \geq k_c$
Anti-cutoff media	$\varepsilon_z\mu_y < 0,\ \frac{\mu_y}{\mu_x} < 0$	Evanescent	$k_y < k_c$
		Propagating	$k_y \geq k_c$
Never-cutoff media	$\varepsilon_z\mu_y > 0,\ \frac{\mu_y}{\mu_x} < 0$	Propagating	All real k_y
Always-cutoff media	$\varepsilon_z\mu_y < 0,\ \frac{\mu_y}{\mu_x} < 0$	Evanescent	No real k_y

Table 1. Anisotropic media for a z-polarized TE plane wave.

4.3. Construction of compensated bilayer of anisotropic metamaterials for imaging

Veselago introduced the bilayer compensation to illustrate the ability to focus on the electromagnetic wave from a point source by a flat slab of composite material with a negative refraction. The proposed structure was a bilayer of vacuum and a left-hand material (with permittivity and permeability equal to –1) where the left-hand material compensates for the propagation effect associated with an equal length of vacuum. This bilayer structure is called Veselago lens (or the perfect lens) [52]. The same idea can be implemented using positive and negative refracting layers of anisotropic metamaterials to implement near-field focusing in the same way as Veselago lens. **Figure 4** shows the bilayer of anisotropic metamaterials in two dimensions.

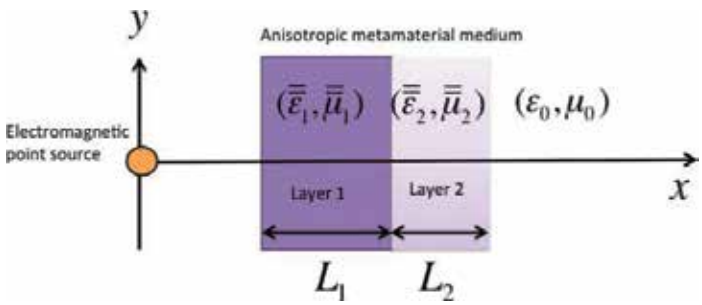

Figure 4. Compensated anisotropic metamaterial medium structure.

Depending on the sign of the permittivity and permeability of the two layers, one can get different material types for the compensated bilayers. For instance, compensated bilayer can be made of combination of positive and negative refracting layers of never-cut off medium (NCM) or anticutoff medium (ACM). **Table 2** shows examples of metamaterials that could make up the compensated bilayer [49].

Bilayer type	Layer	ε_x	ε_y	ε_z	μ_x	μ_y	μ_z	Material
Veselago lens	L1	1	1	1	1	1	1	Free space
	L2	-1	-1	-1	-1	-1	-1	Left hand material
NCM compensated bilayer	L1	-1	1	1	-1	1	1	Positive refractive NCM
	L2	1	-1	-1	1	-1	-1	Negative refractive NCM
ACM compensated bilayer	L1	1	-1	-1	-1	1	1	Positive refractive ACM
	L2	-1	-1	1	1	-1	-1	Negative refractive ACM

Table 2. Compensated bilayer anisotropic metamaterial types.

5. Near-field subwavelength image manipulating through compensated anisotropic metamaterial

5.1. Superlens

As mentioned earlier, the performance limitation of conventional lenses is due to the diffraction limit. In conventional imaging the field emitting from an object is a superposition of plane waves with dispersion relation given by [53]

$$k_z = \sqrt{\frac{\omega^2}{c^2} - (k_x^2 + k_y^2)} \tag{6}$$

In case of energy propagation in the +z-direction, the only real values are the ones allowed for and hence all the components of k_z contains the spectrum of the image which are transmitted and refocused by an ordinary lens. On the other hand, if k_z is imaginary, i.e., $\frac{\omega^2}{c^2} < (k_x^2 + k_y^2)$, the wave is an evanescent wave whose amplitude decays as the wave propagates along the z-axis. This leads to a loss of the high-frequency components of the wave, which contain information about subwavelength features of the object being imaged. The super lens with negative-index materials can overcome this problem. Since in such materials transporting the electromagnetic energy in the +z-direction requires negative wave vector. This amplifies the evanescent wave and all components of the angular spectrum can be transmitted without distortion [53].

Super lensing can be achieved with bilayer of anisotropic metamaterial, i.e., (NCM) and (ACM) bilayers. However, the mechanism of constructing perfect image with subdiffraction resolution in the case of (NCM) and (ACM) bilayers is different than the mechanism of super lens with single-negative index layer (Veselago lens). As discussed in the previous section, the subwavelenght resolution, in case of perfect lens, is achieved thought the amplification of the evanescent wave which by consequence recovers the subwavelength features. In the case of NCM or ACM bilayers lens, the evanescent components of the wave are converted to a propagating mode in the bilayer region and then back to evanescent component at the back surface of the bilayer which creates and image beyond the

diffraction limit. A comparison between the evanescent wave propagation in different bilayers is shown in **Figure 5** [49, 54].

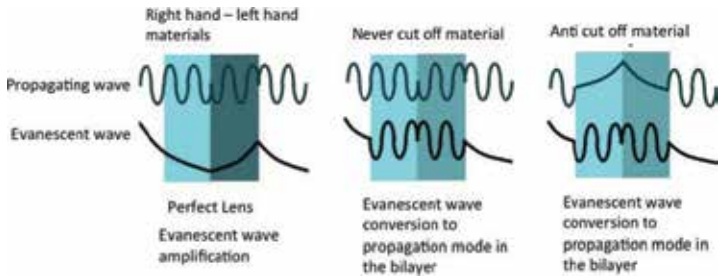

Figure 5. Different evanescent wave propagation in three types of metamaterial bilayer structures.

It is important to mention that the electric or magnetic loss is considered a major problem in the implementation of metamaterials in the imaging structures. The reason is that these losses can limit the resolution of the perfect lens. These losses are due to the imaginary part of the permittivity and permeability tensors. In general, the beamwidth of the electric field is degraded at the back surface due to losses compared to the source plane. The effect of degradation is different depending on the type of the bilayer used for the super lens. In case of the left-hand material lens the electric field degradation is about $\lambda/5$ while for NCM or ACM is $\lambda/10$. This indicates that the NCM and ACM lenses are less sensitive to material parameters losses than the left-hand material lens [49, 55, 56].

Another issue with the bilayer structures is the retardation effect. This effect is due to the difficulty to realize a completely compensated bilayer in practical cases. As with the losses, the retardation effect degrades the electric field beamwidth and the NCM or ACM are less sensitive to that degradation than the left-hand material. This is why anisotropic metamaterial medium is considered advantageous since it can approximate the ideal situation [49, 57].

5.2. Bilayer lens using transmission line metamaterial

The bilayer of anisotropic metamaterial for imaging can be realized using L-C transmission line network. Different types of anisotropic metamaterials such as ACM and NCM can be constructed by L-C loaded microstrip line grids operating at certain frequency bandwidth. The planner microstrips are periodically loaded by serial capacitance in z- or y-direction with or without shunting inductance loaded at the center of the node. The unit cell of the planner transmission line metamaterial is illustrated in **Figure 6** [47, 49, 58].

For z-polarized electromagnetic wave the dispersion relation is dependent on ε_z, μ_x and μ_y as indicated in Eq. (5). Dispersion relation of a transmission line metamaterial can be obtained using periodic transmission line theory [59, 60]. For example, under the effective medium approximation, the dispersion relation of the unit cell, shown in **Figure 6(a)**, is

$$\frac{k^2{}_y}{2\beta^2(1-2\omega_0/\omega\beta d)}+\frac{k^2{}_x}{2\beta^2}=1 \tag{7}$$

where $\omega_0 = 1/2C_yZ_0$, Z_0, β and d are the characteristic impedance, the propagation constant and the length of the transmission line section.

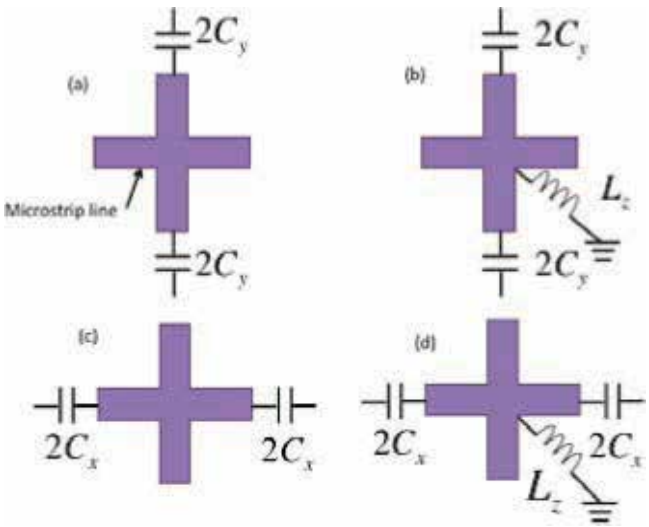

Figure 6. Different unit cells of loaded transmission line grid for implementing different anisotropic metamaterials. (a) positive refraction NCM (b) positive refraction ACM (d) negative refraction ACM (d) negative refraction NCM.

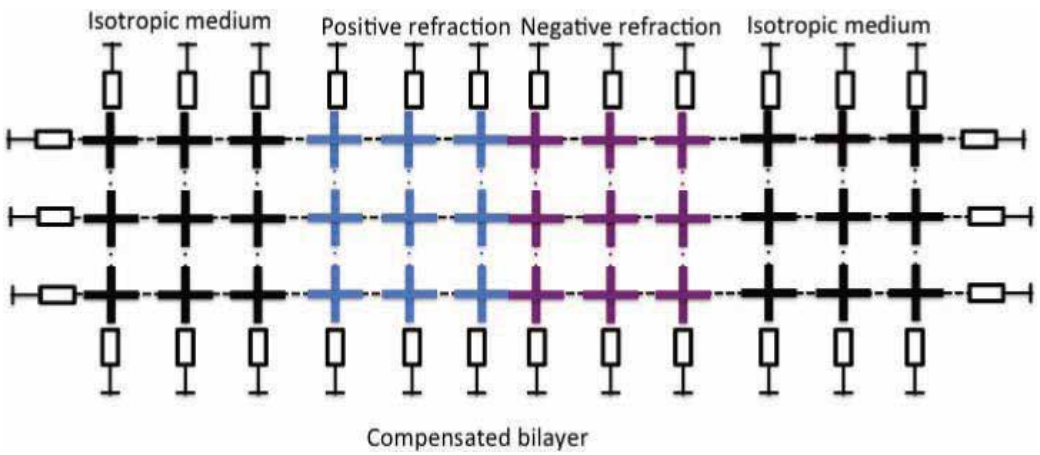

Figure 7. The schematic diagram of a 2D compensated bilayer using loaded L-C metamaterial transmission line.

Using these four unit cells in a network, one can construct a 2D compensated bilayer lens composed of positive NCM/negative NCM or positive ACM/negative ACM. **Figure 7** shows

the schematic diagram of the bilayer medium. The loaded capacitances and inductances need to be chosen to satisfy the requirement of the bilayer medium see **Table 2**.

The imaging properties of the compensated bilayer structure are investigated experimentally in the microwave range [61]. The results show that the electromagnetic wave from a point source has been focused on the image plane with beamwidth of $0.1\ \lambda$ which is below the diffraction limit. This focusing result is well below the left-hand material planer lens, which is $0.21\ \lambda$ [49, 61]. The NCM bilayer lens has better subwavelength resolution because it is less sensitive to material losses.

6. Plasmonic and field enhancement metamaterials

The structures presented in the previous section such as bilayers and superlens can be integrated in the system of a near-field microwave microscope [62]. This can improve image measurements by improving spatial resolution, this helps in studying surfaces that cannot be imaged directly with a scanned probes. Moreover, the technique of manipulation of surface plasmons for enhancing electromagnetic propagation can be used in imaging system at microwave frequencies. Surface plasmons are known in optical frequency [63]. They can be excited on a metal by an external plane-wave beam. This can enhance the electric field at the surface compared with that in the incident beam and it has been suggested that this effect is an important aspect of surface-enhanced Raman scattering [64]. Surface plasmons have been investigated for extraordinary optical transmission through subwavelength hole arrays [65]. This overcomes the constraint of low transmittivity of subwavelength apertures. Ebbesen et al. observed that the maxima the transmission efficiency could exceed unity (when normalized to the area of the holes), which are orders of magnitude greater than predicted by standard aperture theory [65]. A review that summarizes the basic principles and achievements in the field of plasmonic for subwavelength guiding has been presented [66]. This review chapter discusses as well the potential future developments and applications of nanophotonic devices and circuits and near-field microscopy with nanoscale resolution [67].

Manipulating surface plasmons at microwave and millimeter-wave frequencies is possible due to the field of metamaterials [68]. This can be achieved using composite dielectric where the property of having negative permittivity below the plasma frequency has been investigated [69]. This investigation showed that thin wires structure reduces the plasma frequency having longer wavelength to be diffracted and the system can be described by an effective dielectric constant of the plasma form. This achievement opens new possibilities for microwave structures to produce enhanced transmission through subwavelength apertures as in the case of photonic structures.

7. Conclusion

This chapter introduced a review on metamaterial structures for near-field microscopy. A general overview on the near-field imaging/microscopy instrumentation is first presented

followed by a survey on the research done on this topic. The metamaterial design based on transformation electromagnetic as well as a summary on metamaterial media was introduced. The bilayer metamaterial medium is discussed for super-resolution structures that can manipulate subwavelength images and evanescent waves. Finally, the manipulation of surface plasmons is presented as a technique to enhance the transmission for near-field microscopy.

Author details

Hatem El Matbouly

Address all correspondence to: hatem.el-matbouly@lcis.grenoble-inp.fr

LCIS, Grenoble-INP, Grenoble Alpes University, Valence, France

References

[1] Eric B, Jay KT, "Near-field optics: microscopy, spectroscopy and surface modi cation beyond the diraction limit", Science, Vol. 257, No. 5067, pp. 189–195, 1992.

[2] Xiaoliang SX, Robert CD, "Probing single molecule dynamics", Science, New Series, Vol. 265, No. 5170, pp. 361–364, 1994.

[3] Chen H, Ma S, Wu X, Yang W, Zhao T, "Diagnose human colonic tissues by terahertz near-field imaging", Journal of Biomedical Optics, Vol. 20, No. 3, art. no. 036017, 2015.

[4] Yuandan D, Tatsuo I, "Promising future of metamaterials", IEEE Microwave Magazine, March, 2012.

[5] Born M, Wolf E, "Principles of optics", Cambridge University Press, Cambridge, 6th edition, 1998.

[6] http://hyperphysics.phy-astr.gsu.edu/hbase/phyopt/raylei.html

[7] Jackson J, "Classical Electrodynamics", John Wiley, New York, 3rd edition, 1998.

[8] Alexander NR, Nadezhda VY, "Electrodynamics of microwave near-field probing: Applicationto medical diagnostics", Journal of Applied Physics, Vol. 98, arct. no. 114701, 2005.

[9] Steven MA, Steinhauer DE, Feenstra BJ, Vlahacos CP, Wellstood FC, "Near Field Microwave Microscopy of Materials Properties", H. Weinstock and M. Niseno (eds), Microwave Superconductivity, Kluwer Academic Publishers. Printed in the Netherlands, 2001.

[10] https://www.photonics.ethz.ch/fileadmin/user_upload/Courses/NanoOptics/nfoprobes_rev-1.pdf

[11] Steven MA, Vladimir VT, Andrew RS, "Principles of Near-Field Microwave Microscopy", July 17, 2006. http://citeseerx.ist.psu.edu/viewdoc/download?doi=10.1.1.569.1377&rep=rep1&type=pdf

[12] Schelkuno S, "Antennas, Theory and Practice". Wiley and Sons, Inc., New York, 1952.

[13] Osofsky SS, Schwarz SE, "Design and performance of a noncontacting probe for measurements on high-frequency planar circuits", IEEE Transactions on Microwave Theory and Techniques, Vol. 40, No. 8, pp. 1701–1708, 1992.

[14] Jean JB, Rémi C, "Image formation in near-field optics", Progress in Surface Science, Vol. 56, No. 3, pp. 133–237, 1997.

[15] Alexander NR, "Quasistatics and electrodynamics of near-field microwave microscope", Journal of Applied Physics, Vol. 115, arct. no. 084501, 2014.

[16] Björn TR, "High-frequency near-field microscopy", Review of Scientific Instruments, Vol. 73, No. 7, 2002.

[17] Steinhauer DE, Vlahacos CP, Dutta SK, Wellstood FC, Steven MA, "Surface Resistance Imaging with a Scanning Near-Field Microwave Microscope", Applied Physics Letters, Vol. 71, pp. 1736,1997. http://arxiv.org/abs/cond-mat/9712142v1

[18] Lewis G, et al, "Apertureless scanning near-field optical microscopy: A comparison between homodyne and heterodyne approaches", Journal of Optical Society B, Vol. 23, May 2006.

[19] Synge EH, "A suggested method for extending the microscopic resolution into the ultramicroscopic region". Philosophical Magazine, Vol. 6, pp. 356, 1928.

[20] Bethe HA, "Theory of diffraction by small holes", Physical Review, Vol. 66, No. 7–8, pp. 163–182, 1944.

[21] Bouwkamp CJ, "On the freely vibrating circular disk and the diffraction by circular disks and apertures", Physica, Vol. 16, No. 1, pp. 1–16, 1950.

[22] Bouwkamp CJ, "Diffraction Theory", Reports on Progress in Physics, Vol. 17, 1954.

[23] Massey GA, Davis JA, Katnik SM, Omon E, "Subwavelength resolution far-infrared microscopy", Applied Optics, Vol. 24, No. 10, pp. 1498–1501, 1985.

[24] Grober RD, Rutherford T, Harris TD, "Modal approximation for the electromagnetic field of a near-field optical probe", Applied Optics, Vol. 35, No. 19, pp. 3488–3495, 1996.

[25] Soohoo RF, "A microwave magnetic microscope", Journal of Applied Physics, Vol. 33, No. 3, pp. 1276–1277, 1962.

[26] Ash EA, Nicholls G, "Super-resolution aperture scanning microscope", Nature, Vol. 237, No. 5357, pp. 510–512, 1972.

[27] Bryant CA, Gunn JB, "Noncontact technique for the local measurement of semiconductor resistivity", Review of Scientific Instruments, Vol. 36, No. 11, pp. 1614–1617, 1965.

[28] Pohl DW, Denk W, Lanz M, "Optical stethoscopy: Image recording with resolution lambda/20". Applied Physics Letters, Vol. 44, No. 7, pp. 651–653, 1984.

[29] Betzig E, Isaacson M, Lewis A, "Collection mode near-field scanning optical microscopy", Applied Physics Letters, Vol. 51, No. 25, pp. 2088–2090, 1987.

[30] Fee M, Steven C, Hänsch TW, "Scanning electromagnetic transmission line microscope with sub-wavelength resolution", Optics Communications, Vol. 69, No. 3–4, pp. 219–224, 1989.

[31] Golosovsky M, Dan D, "Novel millimeter-wave near-field resistivity microscope", Applied Physics Letters, Vol. 68, No. 11, pp. 1579–1581, 1996.

[32] Copty A, Golosovsky M, Davidov D, Frenkel A, "Localized heating of biological media using a 1-W microwave near-field probe", IEEE Transactions on Microwave Theory and Techniques, Vol. 52, No. 8 II, pp. 1957–1963, 2004.

[33] Bae J, Okamoto T, Fujii T, Mizuno K, Nozokido T, "Experimental demonstration for scanning near-field optical microscopy using a metal micro-slit probe at millimetre wavelengths", Applied Physics Letters, Vol. 71, No. 24, pp. 3581–3583, 1997.

[34] Nozokido T, Iibuchi R, Bae J, Mizuno K, Kudo H, "Millimeter-wave scanning near-field anisotropy microscopy", Review of Scientific Instruments, Vol. 76, No. 3, art. no. 033702, 2005.

[35] Nozokido T, Bae J, Koji M, "Scanning near-field millimeter-wave microscopy using a metal slit as a scanning probe", IEEE Transactions on Microwave Theory and Techniques, Vol. 49, No. 3, pp. 491–499, 2001.

[36] Hunsche S, Koch M, Brener I, Nuss M, "THz near-field imaging", Optical Communications, Vol. 150, No. 22, 1998.

[37] Mitrofanov O, et al. "Collection mode near field imaging with 0.5 THz pulses", IEEE Journal of Selected Topics in Quantum Electronics, Vol. 7, No. 4, pp. 630–640, 2001.

[38] Mitrofanov O, et al. "Near field microscope probe for far infrared time domain measurements", Applied Physics Letters, Vol. 77, pp. 591–593, 2000.

[39] Mitrofanov O et al. "Terahertz near field microscopy based on a collection mode detector", Applied Physics Letters, Vo. 77, pp. 3496–3498, 2000.

[40] Wynne K, Carey J, Zawadzka J, Jaroszynski D, "Tunneling of single cycle terahertz pulses through waveguide", Optical Communications, Vo. 176, pp. 429–435, 2000.

[41] Chen Q, Jiang Z, Xu G, Zhang XC, "Near field terhertz imaging with a dynamic aperture", Optical Letters, Vol. 25, p. 11222, 2000.

[42] van der VN, Planken P, "Electro optic detection of sub wavelength terahertz sport sizes in the near field of a metal tip", Applied Physics Letters, Vol. 81, p. 1558, 2002.

[43] Planken P, van der VN, "Spot size reduction in terahertz apertureless near field imaging", Optical Letters, Vol. 29, p. 2306, 2004.

[44] Wang K, Barkan A, Mittleman B, "Propagation effects in aperture less near field optical antennas", Applied Physics Letters, Vol. 84, p. 305, 2004.

[45] Chen HT, Kersting R, Cho G, "Terahertz imaging with nanometer resolution", Applied Physics Letter, Vol. 83, p. 3009, 2003.

[46] George VE, Michael S, "Transforming Electromagnetics using Metamaterials", IEEE magazine, April, 2012.

[47] Yuandan D, Tatsuo I, "Promising Future of Metamaterials", IEEE magazine, April, 2012.

[48] Nathan BK, David RS, John BP, "Electromagnetic design with transformation optics", Proceedings of the IEEE, Vol. 99, No. 10, 2010.

[49] Tie JC, David R, Smith RL, "Metamaterials Theory, Design and Applications", Springer, 2010.

[50] Eroglu A, "Wave Propagation and Radiation in Gyrotropic and Anisotropic Media", DOI 10.1007/978-1-4419-6024-5_2, Springer Science+Business Media, LLC, 2010.

[51] Guven K, Ozbay E, "Near field imaging in microwave regime using double layer split-ring resonator based metamaterial", Opto-Electronics Review, Vol. 14, No. 3, pp. 213–216, 2006.

[52] Viktor GV, "The electrodynamics of substances with simultaneously negative values of ε and μ", Reviews of Topical Problems, Soviet Physics Uspekhi, 1968.

[53] Penday J, "Manipulating the near field with metamaterials", Optics & Photonics News, Sep. 2004.

[54] Smith DR, Willie JP, Vier DC, Nemat-Nasser SC, Schultz S, "Composite medium with simultaneously negative permeability and permittivity", Physical Review Letters, Vol. 84, No. 18, 2000.

[55] David RS, David S, Jack JM, Pavel K, Patrick R," Partial focusing of radiation by a slab of indefinite media", Applied Physics Letters, Vol. 84, p. 2244, 2004.

[56] Shen JT, Platzman PM, "Near field imaging with negative dielectric constant lenses", Applied Physics Letters, Vol. 80, p. 3286, 2002.

[57] David RS, David S, Marshall R, Sheldon S, Ramakrishna SA, John BP, "Limitations on subdiffraction imaging with a negative refractive index slab", Applied Physics Letters, Vol. 82, p. 1506, 2003.

[58] Lai A, Itoh T, Caloz C, "Composite right/left-handed transmission line metamaterials", IEEE Microwave Magazine, Vol. 5, No. 3, 2004.

[59] David MP, "Microwave Engineering", 4th Edition, Wiley & Sons, 2012.

[60] Yijun F, Xiaohua T, Yan C, Tian J, "Electromagnetic wave propagation in anisotropic metamaterials created by a set of periodic inductor-capacitor circuit networks", Physics Review B, Vol. 72, art. no. 245107, 2005.

[61] Anthony G, George VE, "Overcoming the diffraction limit with a planar left-handed transmission-line lens", Physics Review Letter, Vol. 92, art. no. 117403, 18 March 2004.

[62] Muhammed SB, Omar MR, "Experimental and numerical study of sensitivity improvement in near-field probes using single-negative media", IEEE Transactions on Microwave Theory and Techniques, Vol. 57, No. 12, pp. 3427–3433, 2009.

[63] Stefan AM, Harry AA, "Plasmonics: Localization and guiding of electromagnetic energy in metal/dielectric structures", Journal of Applied Physics, Vol. 98, art. no. 011101,2005.

[64] Andrey KS, Vladimir MS, "Electrodynamics of Metamaterials", World Scientific Publishing Co. Pte. Ltd. 2007.

[65] Ebbesen TW, Lezec HJ, Ghaemi HF, Thio T, Wolff PA, "Extraordinary optical transmission through sub-wavelength hole arrays", Nature, Vol. 391, pp. 667–669, 1998.

[66] Dmitri KG, Sergey IB, "Plasmonics beyond the diffraction limit", Nature Photonics, Vol. 4, pp. 83–91, 2010.

[67] Nicholas F, Hyesog L, Cheng S, Xiang Z, "Sub-diffraction-limited optical imaging with a silver superlens", Science, Vol. 308, p. 22, April 2005.

[68] Megel et al. "Enhanced milimeter wave transmission through quasioptical subwaveleght perforated plate", IEEE Transaction on Microwave and Propagation, Vol. 53, No. 6, pp. 2146–2154, 2006.

[69] Pendry JB, Holden AJ, Robbins DJ, Stewart WJ, "Low frequency plasmons in thin-wire structures", Journal of Physics: Condensed Matter, Vol. 10, pp. 371–3821998.

Chapter 16

Nonlinear Channel Equalization Approach for Microwave Communication Systems

Modar Shbat, Francisco C. Ordaz-Salazar and
Javier S. González-Salas

Additional information is available at the end of the chapter

http://dx.doi.org/10.5772/65969

Abstract

The theoretical principles of intersymbol interference (ISI) and channel equalization in wireless communication systems are addressed. Several conventional and well-known equalization techniques are discussed and compared such as zero forcing (ZF) and maximum likelihood (ML). The main section in this chapter is devoted to an abstract concept of equalization approach, namely, dual channel equalization (DCE). The proposed approach is flexible and can be employed and integrated with other linear and nonlinear equalization approaches. Closed expressions for the achieved signal-to-noise ratio (SNR) and bit error rate (BER) in the case of ZF-DCE and ML-DCE are derived. According to the obtained outcomes, the DCE demonstrates promising improvements in the equalization performance (BER reduction) in comparison with the conventional techniques.

Keywords: channel equalization, intersymbol interference (ISI), zero forcing (ZF) equalization, maximum likelihood (ML) equalization, bit error rate (BER), dual channel equalization (DCE)

1. Introduction

All types of microwave wireless communication systems under different digital modulation schemes and antennas configuration suffer from the channel effects and related problems such as attenuation, signal amplitude and phase distortions, time-varying fading (Doppler shift), multipath fading, and intersymbol interference (ISI). A common and well-known wireless channel modeling method is based on the representation of the channel as a band-limited digital filter, i.e., linear time-invariant (LTI) filter with specific transfer function (impulse response). Thus, to alleviate and reduce the channel effects, especially for multipath fading and ISI, it is possible to design a digital filter with transfer function that is inverse to the transfer function of the associated wireless channel. This digital filter is called the equalizer

[1, Chapter 10]. Additionally, the employment of multiple antennas can also help to mitigate the multipath fading consequences (transmit/receive diversity) and increase the data rate (spatial multiplexing).

In practice, the wireless transmission system sends a sequence of messages (one-shot transmission) where these successive transmissions should not interfere even if they are closely spaced to increase the data rate. This interference between the successive transmissions is referred as intersymbol interference (ISI) that is able to complicate and reduce the detection performance [2, Chapter 4]. The simple symbol-by-symbol (SBS) detector (optimal in the case of additive white Gaussian noise AWGN channel) cannot be the maximum likelihood estimator for a sequence of message under ISI problem. A receiver for succession messages detection is shown in **Figure 1**, where the matched filter outputs are processed by the receiver and SBS detector to generate the estimate $\hat{X}_k$ of the input symbol X_k at time k.

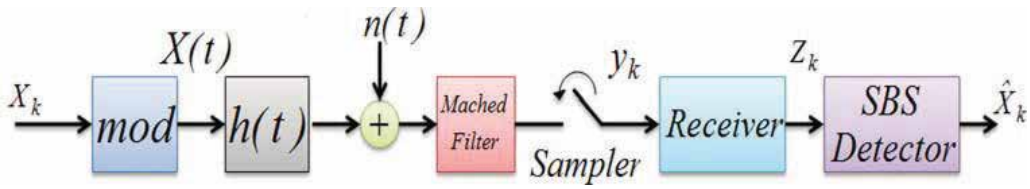

Figure 1. The band-limited channel with receiver and SBS detector.

An equalizer or equalization method can be essentially embedded in the contents of the receiver block presented in **Figure 1**. Different equalization techniques lead to different receiver structures that are not always optimal for detection, but rather are widely implemented as suboptimal cost-effective solutions that alleviate the ISI. Any equalization approach converts the band-limited channel with ISI into memory less appearing channel (AWGN-like) at the receiver output. The wireless channel equalization forms a major challenge in current and future communication networks.

In Section 2 of this chapter, the ISI between successive transmissions is modeled to prove that the distortion caused by this overlapping is unacceptable and some corrective actions should be applied. Some targeted and desired wireless channel responses that exhibit no ISI are discussed in Section 3 with the corresponding Nyquist criterion for the ISI-free channels. In fact, the signal-to-noise ratio (SNR) parameter used to quantify the receiver performance can be consistently considered for equalization techniques evaluation as well. Several conventional and well-known equalization approaches are presented in Section 4 such as zero-forcing equalizer (ZFE), minimum mean square error (MMSE) equalizer, and decision feedback equalizer (DFE). In the last section (Section 5), the proposed equalization approach and its performance are discussed and compared to other equalization techniques under the same initial conditions.

2. Successive message transmission and ISI

The frequency or wireless channel reuse is a common technique to transmit several succession messages separated by the symbol period (T units in time where $1/T$ is the symbol rate). For

http://dx.doi.org/10.5772/65969

sending one of M possible messages every T time units, the data rate of the communication system is defined as:

$$R = \frac{log_2(M)}{T}. \tag{1}$$

Increasing the data rate R can be achieved by decreasing T which reduces or narrows the time between message transmissions and as a consequence increases ISI on the band-limited channel. The transmitted signal of K successive transmissions (conveying one of M^K possible messages) is given by

$$x(t) = \sum_{k=0}^{K-1} x_k(t-kT). \tag{2}$$

The detection of M^K messages approach has a complexity that grows exponentially with the block message length K (especially when $K \to \infty$). The SBS detection can be considered as an alternative suboptimal solution that detects independently each of the successive K messages. The ISI problem is the main limitation of the SBS detection approach when the performance degradation increases as T decreases (or R increases). The ISI can be analyzed by rewriting Eq. (2) using the following form:

$$x(t) = \sum_{k=0}^{K-1} \sum_{n=1}^{N} x_{kn}\varphi_n(t-kT), \tag{3}$$

where the original transmissions $x_k(t)$ are decomposed using a standard orthogonal basis set $\{\varphi_n(t)\}$. For instance, in the case of quadrature amplitude modulation (QAM), the baseband basis:

$$\varphi(t) = \frac{1}{\sqrt{T}} sinc\left(\frac{t}{T}\right) \tag{4}$$

produces orthogonal functions for all integer-multiple of T time translations and the successive transmissions sampled at time instants kT are ISI free. Owing to the channel filtering alterations, the filtered basis functions at the channel output are no longer orthogonal and the ISI is introduced.

The band-limited noise-free channel output used for successive transmission of data symbol can be presented as

$$x_p(t) = \sum_{k=0}^{K-1} \sum_{n=1}^{N} x_{kn}\varphi_n(t-kT) * h(t) = \sum_{k=0}^{K-1} \sum_{n=1}^{N} x_{kn}p_n(t-kT), \tag{5}$$

where $p_n(t) = \varphi_n(t) * h(t)$ and when $h(t) \neq \delta(t)$, the functions $p_n(t-kT)$ do not form orthogonal basis (see **Figure 2**). The equalization techniques try to convert the functions $p_n(t-kT)$ to an orthogonal set of functions, thus the SBS detection approach can be applied at the equalized channel output.

The Nyquist criterion [3, Chapter 1] can specify the conditions for ISI-free channel on which SBS detector is optimal. This criterion helps to construct band-limited functions to reduce the

ISI negative effects. Another way to explain the ISI problem is to relate it with the channel frequency response. When consecutive symbols are transmitted using linear modulation over a wireless channel, the frequency response (impulse response) of the channel makes a transmitted symbol to be spread in the time domain. Thus, the ISI is generated because the previously transmitted and currently received symbols are overlapped. The Nyquist theorem could relate the time domain conditions to its equivalent frequency domain ones. Simply, considering the channel impulse response $h(t)$ and the symbol period $h(t)$, the condition of ISI-free response can be expressed as:

$$h(nT) = \begin{cases} 1; & n = 0 \\ 0; & n \neq 0 \end{cases} \text{ for all integers } n. \tag{6}$$

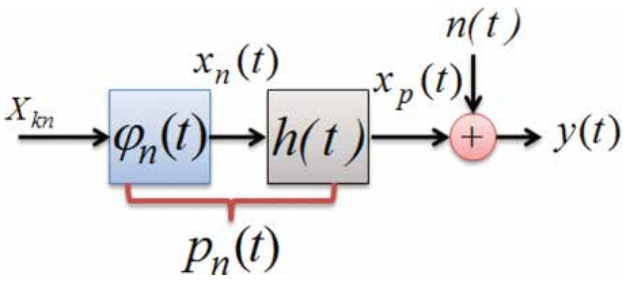

Figure 2. The band-limited channel equivalent impulse response representation.

The last condition can be represented in another form as follows (the Nyquist ISI criterion):

$$\frac{1}{T}\sum_{k=-\infty}^{+\infty} H\left(f-\frac{k}{T}\right) = 1;\ \forall f, \tag{7}$$

where $H(f)$ is the channel frequency response (Fourier transform of $h(t)$). Hence, the $\sin c$ pulse shape allows eliminating the ISI at sampling instants and any filter with excess bandwidth and odd-symmetry around Nyquist frequency can satisfy and meet the ISI-free requirements such as raised cosine filter (RCF).The raised cosine filter with bandwidth equal to $(\frac{1}{2T})(1+\alpha)$ can be presented using the following form [3]:

$$P_{RC}(t) = \frac{\sin\left(\frac{\pi t}{T}\right)}{\frac{\pi t}{T}} \frac{\cos\left(\frac{\alpha \pi t}{T}\right)}{1-\left(\frac{2\alpha t}{T}\right)^2};\ 0 \leq \alpha \leq 1, \tag{8}$$

where α is the roll-off factor. The RCF impulse and frequency responses are shown in **Figure 3** for different roll-off factor α values.

The eye diagram is a widely used convenient method to observe the effects of ISI and noise introduced by the channel where the quality of the received signal (the ability to correctly recover the symbols and timing) can be illustrated (oscilloscope presentation). The interpretation of the eye diagram gives important information such as:

http://dx.doi.org/10.5772/65969

- sensitivity to timing error or jitter (smaller is better);
- wasted power;
- amount of distortion at sampling instants;
- amount of noise tolerance (larger is better);
- best time for sampling;
- the matching degree between the transmitter and receiver filters;
- the presence of ISI; and
- measurement of eye opening is performed to estimate the achievable BER.

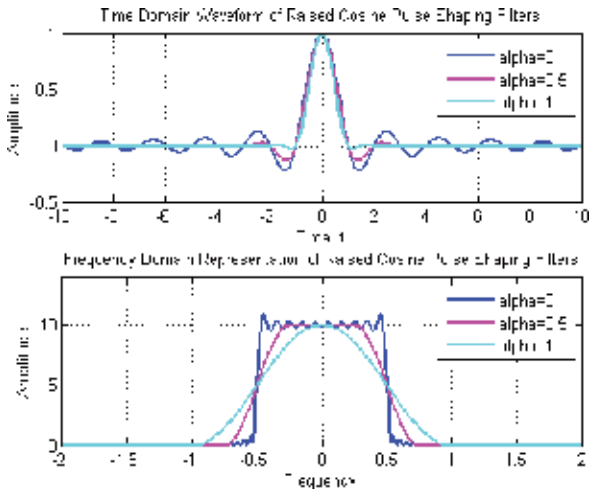

Figure 3. RCF impulse and frequency responses.

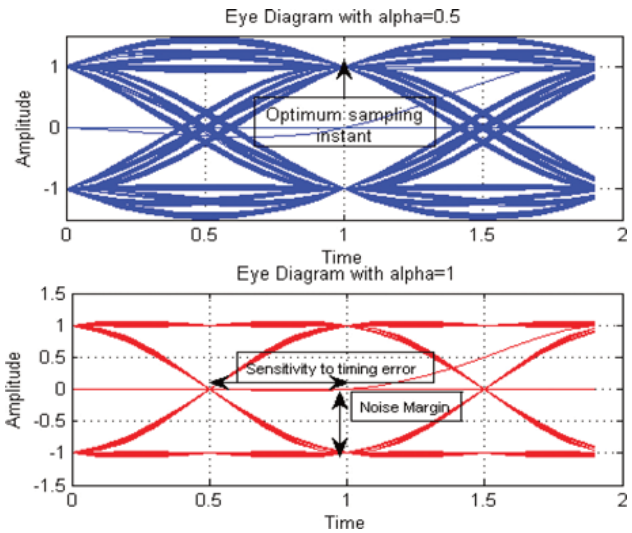

Figure 4. Raised cosine eye diagram for BPSK-modulated symbols.

The eye diagram using raised cosine filtering is presented in **Figure 4** for binary phase shift keying (BPSK)-modulated symbols at two roll-off factor values $\alpha = 0.5; 1$. In general, the ideal sampling instant is at the point where the vertical eye opening is maximum. Under the presence of ISI, the vertical eye opening reduces which leads to higher probability of error (BER). More sensitivity to timing error is presented by smaller horizontal eye opening. From **Figure 4**, it can be observed that the horizontal eye opening is smaller at roll-off factor $\alpha = 0.5$ in comparison with the case when $\alpha = 1$ owing to that the tails of the RCF are stripped down faster. It is important to mention here that higher values of roll-off factor require more transmission bandwidth. Smaller values of roll-off factor α lead to larger errors if the best sampling time (the center of the eye) is not achieved.

3. The equalization main concept

As mentioned before, the equalization technique is the design of a digital filter with inverse or counter transfer function in accordance with the transfer function of the associated wireless channel. This concept is shown in **Figure 5** where the frequency responses of the wireless channel and the equalizer are compared.

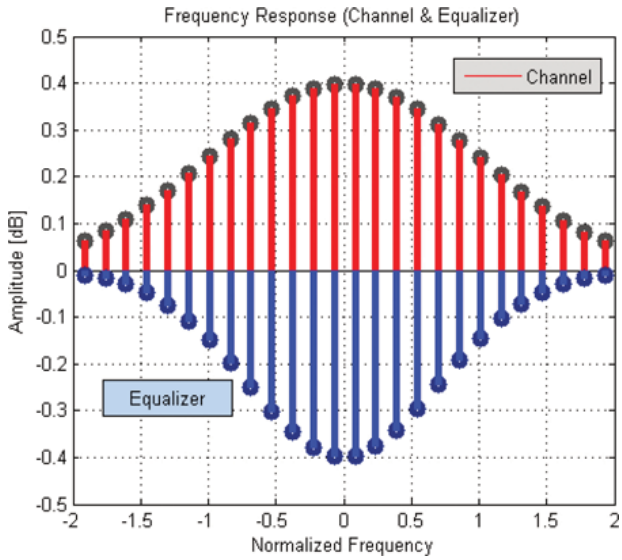

Figure 5. The wireless channel and equalizer frequency responses.

The equalizer design concept is presented in **Figure 6** (a simple block diagram for the channel effect and the equalizer transfer function). The discrete time model that should be considered under the equalization technique designing process is presented using the following form:

http://dx.doi.org/10.5772/65969

$$\hat{C}_k = \sum_{i=0}^{L-1} E_i u_k, \tag{9}$$

where $\hat{C}_k$ is the data sequence at the equalizer output, L is the number of symbols, E_i represents the coefficients of the causal impulse response of the equalizer $H_{EQ}(f)$, and u_k is the input of the equalizer given by

$$u_k = \sum_{j=0}^{L-1} h_j C_k + n_k, \tag{10}$$

where C_k is the transmitted data sequence, the coefficients h_j represents the equivalent causal impulse response (transfer function) of the wireless channel, and n_k is the discrete time additive noise. The channel transfer function $H_{ch}(f)$ can be presented as:

$$H_{ch}(f) = |H_{ch}(f)| \exp[j\theta_{ch}(f)], \tag{11}$$

where $|H_{ch}(f)|$ is the amplitude response, and $\theta_{ch}(f)$ is the phase response. The bit error rate (BER) reduction is achieved when the value of the error given by

$$e_k = C_k - \hat{C}_k \tag{12}$$

is reduced using equalization.

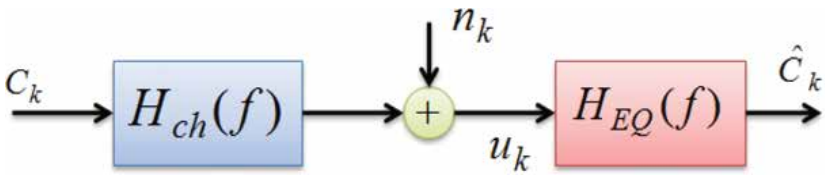

Figure 6. The equalizer main design model.

It is useful at this point to demonstrate the effects of the equalization on the detection performance or quality at the receiver side by presenting the difference between the received symbols with and without applying equalization. This comparison is given in **Figure 7** for the quadrature phase shift keying (QPSK)-modulated symbols. When the equalization is not applied, the uncertainty on the received signal constellation is very high (caused by the channel effect) and as a consequence the detection quality is low (detection performance degradation). Applying the equalization technique, the uncertainty level is lower and the detection performance is improved.

As a last word in this section, the ISI can produce a bias in the SNR value at the receiver. The error e_k presented by Eq. (12) is identical to the additive noise n_k in the case of unbiased detection rule. However, in the case of biased receiver, the probability density function (PDF)

of the error e_k is a scaled and shifted version of the noise n_k PDF (the mean value depends on the actual data symbol C_k). The last condition can be formulated as follows:

$$E[\hat{C}_k|C_k] = C_k, \text{Unbiased Receiver} \tag{13}$$

For a given unbiased receiver [4] for a detection decision rule on a general signal constellation C_k, the maximum unconstrained SNR corresponding to the same receiver under any biased decision rule is given by

$$SNR_b = SNR_u + 1, \tag{14}$$

where SNR_b and SNR_u are the SNR for biased and unbiased receivers, respectively. The previous apparent discrepancy is more understandable recalling that the error rate is a monotone function of the SNR only. Thus, from Eq. (14), the negative effect of ISI on the SNR at the receiver is observed.

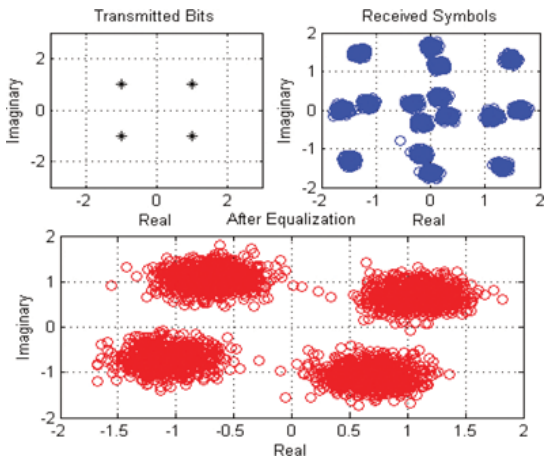

Figure 7. QPSK received symbols with and without equalization.

4. Equalization techniques

In general, the channel equalization techniques are classified to linear and nonlinear algorithms or to blind (without training sequence) and nonblind based on the degree of knowledge. The earliest mentions of digital equalization techniques are made under different design criterions, for example, zero forcing (ZF) equalization [5], minimum mean square error (MMSE) equalization [6], maximum likelihood (ML) equalization [7], decision feedback equalization (DFE) [8], and maximum *a posteriori* (MAP) equalization [9]. In this chapter, a new nonlinear equalization approach is proposed based on the dual channel equalization (DCE) idea with the purpose to improve the equalization performance, namely, the BER reduction, in comparison with the other widely used equalizers under multiple input multiple output (MIMO) wireless channel. The simulation results demonstrate considerable and promising performance improvements applying the suggested equalization approach in comparison

with the conventional techniques. In order to help the reader to acquire the basics of equalization concepts, a few well-known and conventional equalization techniques will be reviewed and discussed in the next subsections.

4.1. System model

The complex baseband MIMO wireless channel model is considered with number of transmit antennas equal to N and number of receive antennas equal to M.

The received signal at the input of the receiver (the I/O relation of the MIMO channel) can be presented in the following form:

$$\mathbf{y} = \mathbf{H}\mathbf{x} + \mathbf{z}, \tag{15}$$

where $\mathbf{y} \in C^{M1}$ is the vector form of the received signal, $\mathbf{H} \in C^{MN}$ is the matrix form of the Rayleigh fading channel with independent and identically distributed (i.i.d) coefficients obeying the circularly symmetric complex Gaussian distribution at zero mean and variance $\sigma_h^2 = 1$, denoted as $h_{ij} \sim CN(0,1)$ for $1 \le i \le M, 1 \le j \le N$, $\mathbf{x} \in C^{N1}$ is the vector form of the transmitted signal, and $\mathbf{z}$ is the circularly symmetric complex white Gaussian noise with zero mean and variance σ_n^2, i.e., $\mathbf{z} \sim CN(0, \sigma_n^2 \mathbf{I})$. It is assumed that the N data substreams have uniform power which means $\mathbf{x} \in C^{N1}$ has a covariance matrix given by

$$E[\mathbf{x}\mathbf{x}^*] = \sigma_x^2 \mathbf{I}_N, \tag{16}$$

where $E[.]$ represents the mathematical expectation, $(.)^*$ is the conjugate transpose, and $\mathbf{I}_N$ is NN identity matrix. The signal-to-noise ratio (SNR) at the receiver input is expressed as:

$$SNR = \frac{\sigma_x^2}{\sigma_n^2}. \tag{17}$$

The channel matrix $\mathbf{H} \in C^{MN}$ is equalized or inverted by the weight matrix (the equalizer matrix) $\mathbf{W} \in C^{MN}$. Thus, the obtained signal $\hat{\mathbf{x}}$ at the equalizer output is defined as follows:

$$\hat{\mathbf{x}} = \mathbf{W}\mathbf{y}. \tag{18}$$

4.2. ZF equalization

ZF is a linear equalization that applies the inverse of the wireless channel frequency response to alleviate the channel effects on the received signal and restore the transmitted symbols. The name is assigned based on the reduction of ISI down to zero in the noise-free channel case (forcing the residual ISI to zero). The ZF equalizer can be designed using finite of infinite impulse response filters (FIR or IIR filters).

Employing ZF equalization technique with matrix $\mathbf{W}_{\mathrm{ZF}}$, the equalizer directly applies the inverse of the channel response to the received signal $\mathbf{y}$. Thus, the ZF equalizer satisfies the following condition:

$$\mathbf{W}_{\mathrm{ZF}}\mathbf{H} = \mathbf{I}_{\mathrm{MN}}. \tag{19}$$

The general form of the ZF equalizer matrix $\mathbf{W}_{\mathrm{ZF}}$ is defined as:

$$\mathbf{W}_{\mathrm{ZF}} = (\mathbf{H}^H\mathbf{H})^{-1}\mathbf{H}^H, \tag{20}$$

where $(.)^H$ represents Hermitian transpose operation. The BER in the case of ZF equalization technique and BPSK modulation can be defined using the following form [10]:

$$BER_{\mathrm{ZF}} = \left[\frac{1}{2}\left(1-\sqrt{\frac{SNR}{1+SNR}}\right)\right]^{M-N+1} \sum_{m=0}^{M-N+1}\binom{M-N+m}{m}\left(\frac{1+\sqrt{SNR/1+SNR}}{2}\right), \tag{21}$$

where m is the index of the received signal substream. The last equation is derived considering the Neyman-Pearson (NP) detection criteria. Thus, the SNR of the obtained M decoupled substreams is defined as [10]:

$$SNR_{\mathrm{ZF},m} = \frac{SNR}{[(\mathbf{H}^H\mathbf{H})^{-1}]_{mm}};\ 1{\le}m{\le}M, \tag{22}$$

where $[.]_{mm}$ corresponds to the mth diagonal element. The denominator of the achieved partial SNR given in Eq. (22) can be presented in terms of the mth column $\mathbf{h}_m$ of $\mathbf{H}$ as follows:

$$[(\mathbf{H}^H\mathbf{H})^{-1}]_{mm} = \frac{1}{\mathbf{h}_m^H\mathbf{h}_m - \mathbf{h}_m^H\mathbf{H}_m(\mathbf{H}_m^H\mathbf{H}_m)^{-1}\mathbf{H}_m^H\mathbf{h}_m}. \tag{23}$$

The ZF equalizer tries to null and cancel out all the interfering terms that are sometimes accompanied with noise amplification, for this reason, ZF is not optimal under very noisy channels. In the case of FIR filter use (to deal with noncausal components a decision delay is applied), a complete elimination of ISI problem is not possible owing to the finite filter length. Alternative criterion called peak-distortion criterion can be applied to minimize the maximum possible signal distortion due to ISI at the equalizer output.

4.3. MMSE equalization

The main objective of MMSE equalizer is to minimize the variance of the error signal e_k in Eq. (12). The MMSE equalizer ensures the trade-off between residual ISI and noise enhancement (reduce the total noise power). Under conditions more close to practice, MMSE equalizer can achieve lower BER compared to ZF equalizer at low-to-moderate SNRs. Thus, the MMSE equalization is applied to minimize the value of the mean given by

$$E[(\mathbf{W}_{\mathrm{MMSE}}\mathbf{y}-\mathbf{x})(\mathbf{W}_{\mathrm{MMSE}}\mathbf{y}-\mathbf{x})^H], \tag{24}$$

where $\mathbf{W}_{\mathrm{MMSE}}$ is the MMSE equalizer matrix that is presented by the following expression [11]:

$$\mathbf{W}_{\mathrm{MMSE}} = \left[\mathbf{H}^H\mathbf{H} + \frac{1}{SNR}\mathbf{I}\right]^{-1}\mathbf{H}^H. \tag{25}$$

The MMSE matrix $\mathbf{W}_{\mathrm{MMSE}}$ is multiplied by the received signal vector $\mathbf{y}$ to obtain M decoupled substreams with SNR equal to [11]:

http://dx.doi.org/10.5772/65969

$$SNR_{\mathrm{MMSE},m} = \frac{SNR}{\left[\left(\mathbf{H}^H\mathbf{H} + \frac{1}{SNR}\mathbf{I}\right)^{-1}\right]_{mm}} - 1; 1 \le m \le M, \tag{26}$$

The BER for this equalizer considering the NP criterion and BPSK modulation can be approximated using the following form [11]:

$$BER_{\mathrm{MMSE}} = E[Q\sqrt{2SNR_{\mathrm{MMSE},m}}], \tag{27}$$

where $Q(x) = \frac{1}{\sqrt{2\pi}}\int_x^\infty \exp(-t^2/2)dt$ is the standard Gaussian Q-function. The output SNRs of the M decoupled substreams using ZF and MMSE equalizers are related as follows:

$$SNR_{\mathrm{MMSE},m} = SNR_{\mathrm{ZF},m} + \delta_{\mathrm{SNR}.m}; 1 \le m \le M, \tag{28}$$

where $\delta_{\mathrm{SNR},m}$ is nondecreasing function of SNR ($SNR_{\mathrm{ZF},m}$ and $\delta_{\mathrm{SNR},m}$ are statistically independent). Moreover, the ratio of the output SNR gains for these two equalizers for any full rank channel realization goes to unity (in dB) [11]:

$$10\log_{10}\left(\frac{SNR_{\mathrm{MMSE},m}}{SNR_{\mathrm{ZF},m}}\right) = 10\log_{10}\left(1 + \frac{\delta_{\mathrm{SNR},m}}{SNR_{\mathrm{ZF},m}}\right) \to 0;\ as\ \mathrm{SNR} \to \infty \tag{29}$$

Again the MMSE equalizer can be implemented with FIR and IIR filters and in both cases the error signal e_k in Eq. (12) depends on the estimated symbols $\hat{C}_k$. According to the orthogonality principle of MMSE optimization, the error e_k and the input of the MMSE equalizer must be orthogonal. The achieved SNR can be defined based on the error variance σ_e^2. For instance, in the case of MMSE-IIR equalizer, the SNR is given by

$$SNR_{\mathrm{MMSE,IIR}} = \frac{1-\sigma_e^2}{\sigma_e^2} \tag{30}$$

which is more general form of SNR in comparison with the form in Eq. (26).

4.4. ML equalization

The ML equalization technique tests all the possible data symbols and chooses the one that has the maximum probability of correctness at the output (optimal in the sense of minimizing the probability of error $P_e = P(\mathbf{x} \neq \hat{\mathbf{x}})$, where $\hat{\mathbf{x}}$ is the estimated or chosen signal at the equalizer output). The Euclidian distance between the received signal vector and the products of all possible transmitted signal vectors is calculated, and the signal with minimum distance is considered. The ML estimation of $\mathbf{x}$ takes the following form [12]:

$$\hat{\mathbf{x}}_{\mathrm{ML}} = \arg\min_{\hat{\mathbf{x}}\in\mathbf{x}} \underbrace{\|\mathbf{y} - \mathbf{H}\hat{\mathbf{x}}\|^2}_{\mathbf{J}} \tag{31}$$

As follows, the ML-based equalizer selects the data sequence $\hat{\mathbf{x}}$ that yields the smallest distance $\mathbf{J}_{\min}$ between the received signal vector $\mathbf{y}$ and the estimated or hypothesized message $\mathbf{H}\hat{\mathbf{x}}$. For NP-based receiver, the obtained SNR at ML equalizer output is related to $\mathbf{J}_{\min}$ and given by

$$SNR_{\mathrm{ML}} = \frac{\mathbf{J}_{\min}}{4\sigma_n^2}. \tag{32}$$

The achieved BER of ML equalizer is based on $\mathbf{J}_{\min}$ as well as defined as [12]:

$$BER_{\mathrm{ML}} = Q\left(\sqrt{\frac{\mathbf{J}_{\min}}{4\sigma_n^2}}\right). \tag{33}$$

In **Figure 8**, a comparison between the ZF, MMSE, and ML equalizer performances in terms of BER as a function of energy per bit E_b to the noise power spectral density N_0 ratio $(\frac{E_b}{N_0})$ is presented in the case of BPSK modulation and for MIMO antenna configuration with $N = M = 2$ and Rayleigh fading channel. As shown in **Figure 8**, the ML equalizer has the best performance and ZF equalizer has the worst one.

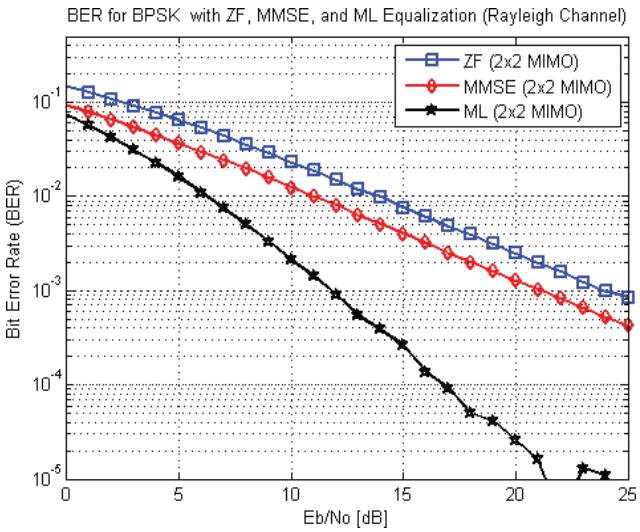

Figure 8. ZF, MMSE, and ML equalizer performances comparison.

4.5. Other equalization techniques

The main linear equalization drawback is that the equalizer filter enhances the noise at the output (increases the noise variance), and additionally, the noise is colored (especially for severely distorted channels). Employing noise prediction technique helps to avoid the described problem. The last short discussion leads to the basic idea about decision feedback equalization (DFE). The DFE structure consists of two filters: a feed forward-filter whose input is the channel output signal and a feedback-filter that feeds back the previous decisions for noise prediction process. This can be achieved by combining linear equalization technique like ZF or MMSE with noise variance prediction (ZF-DFE and MMSE-DFE). A simple block diagram for DFE is presented in **Figure 9**.

The maximum *a posteriori* (MAP) equalizer [13] estimates the transmitted symbol $x[n]$ at discrete-time index n that maximize the *a posteriori* probability $P(x[n] = x|\mathbf{y})$ as follows:

http://dx.doi.org/10.5772/65969

$$\hat{x}[n] = \arg\max P(x[n] = x|\mathbf{y}). \tag{34}$$

The MAP equalizer can be used as SBS detector with maximum-likelihood sequence estimation (MLSE) for transmission over rapidly time-varying (TV) wireless channel as shown in Ref. [13].

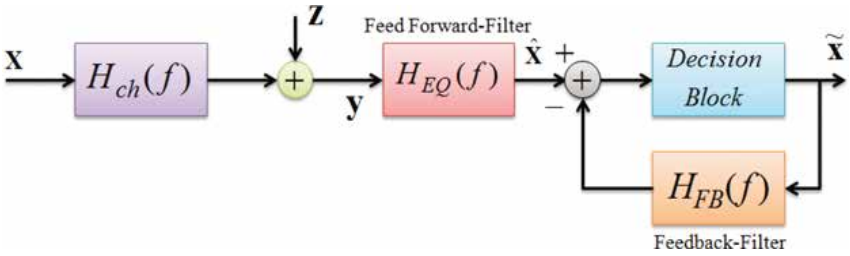

Figure 9. Basic DFE structure.

When some signal properties are used for the determination of the instantaneous error which updates the adaptive filter coefficients or weights, the fractionally spaced equalization (FSE) is an effective approach under the absence of the training sequences (blind equalization) [14]. The FSE receives number of input samples equal to N_{FSE} before it produces one output sample. The adaptive filter weights are updated employing a special algorithm such as constant modulus algorithm (CMA) which uses the constant modularity as the desired signal property. Thus, if the output rate is $1/T$, the input sample rate is N_{FSE}/T. Thus, the tap spacing of the FSE is a fraction of the baud spacing or the transmitted period. The FSE can be modeled as a parallel combination of several baud spaced equalizers known as multichannel model of FSE where the oversampling factor defines the tap spacing as follows:

$$\text{Tap Spacing} = \frac{T}{\text{Oversampling Factor}}. \tag{35}$$

In Ref. [15], a brief discussion about the recent equalization requirements and approaches is presented along with some important related references.

In optical communication field, a novel and efficient multiplier-less finite impulse response filter (FIR) based on chromatic dispersion equalization (CDE) is proposed for coherent receivers [16]. An iterative receiver is designed [17] for joint phase noise estimation, equalization, and decoding in a coded communication system with combined belief propagation, mean field, and expectation propagation (BP-MF-EP). In the frequency domain-based equalization, many important contributions are made recently, for example, in Ref. [18] and for single carrier frequency domain equalization (SC-FDE) in broadband wireless communication systems, a robust design under imperfect channel knowledge is considered based on a statistical channel estimation model where the equalization coefficients are defined under mean square error minimization criterion.

Another work deals with frequency domain equalization for faster-than-Nyquist (FTN) signaling is presented in Ref. [19] for doubly selective channels (DSCs) based on low complexity receivers with variational methods implemented in order to handle the interference of frequency domain symbols instead of using MMSE equalizer that involves high complexity in DSCs.

The frequency domain equalization is also proposed to be employed for broadband power line communications (PLC) as in Ref. [20]. PLC performance can benefit from frequency domain equalization techniques in the context of a cyclic-prefix single carrier modulation schemes. The study in Ref. [20] presents an equalization algorithm based on the properties of complementary sequences (CSs) to reduce the complexity by performing all the operations in the frequency domain without the necessity of noise variance estimator.

5. The new nonlinear equalization approach

5.1. Channel equalization with DCE

The proposed new nonlinear equalization approach applying dual channel equalization (DCE) is presented in this section. The DCE idea can be implemented and coupled with any standard channel equalizers such as ZF or ML equalizers. **Figure 10** shows a simple flow chart for the DCE idea presented as a coupling process between two digital filters. These filters can have the same or different transfer functions and for simplicity of analysis, the similarity case is considered. The topology in **Figure 10** is flexible and able to work with various equalization techniques. The squaring device block $(.)^2$ and the transfer function of the equalization filter $H_{\mathrm{EQ}}(f)$ are the sources of the nonlinearity in this approach. The band-stop filter $H_{\mathrm{EQ}}(f)$ main function is to filter out the received signal in order to obtain the reference colored noise ψ at the output of the second equalization filter. In fact, the squaring device and the equalization filter form a familiar preliminary design for square-law demodulation or square-law envelop detector.

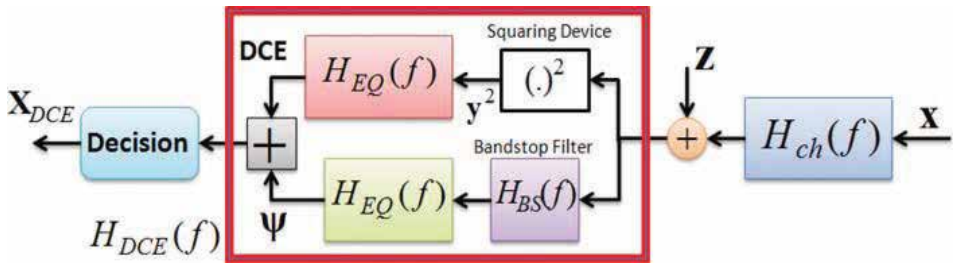

Figure 10. The DCE flow chart.

5.2. ZF equalization with DCE

The system model presented in Section 4.1 is valid in the analysis of ZF-DCE. The signal matrix $\mathbf{X}_{\mathrm{DCE}}$ at the output can be presented using the following form:

http://dx.doi.org/10.5772/65969

$$\mathbf{X}_{\mathrm{DCE}} = \mathbf{W}_{\mathrm{DCE\text{–}ZF}}\mathbf{y}^2 + \psi = \hat{\mathbf{X}}^2 + \psi, \tag{36}$$

where $\mathbf{W}_{\mathrm{DCE\text{–}ZF}}$ is the DCE matrix that takes the following form:

$$\mathbf{W}_{\mathrm{DCE\text{–}ZF}} = (\mathbf{H}^H\mathbf{H})^{-2}(\mathbf{H}^H)^2. \tag{37}$$

Taking into consideration Eq. (37), the given form in Eq. (36) can be rewritten as:

$$\mathbf{X}_{\mathrm{DCE}} = \hat{\mathbf{X}}^2 + \psi = \hat{\mathbf{X}}^2 + (\mathbf{H}^H\mathbf{H})^{-2}(\mathbf{H}^H)^2\mathbf{Z}_{\mathrm{BS}}, \tag{38}$$

where $\mathbf{Z}_{\mathrm{BS}}$ is the matrix form of the noise at the stopband filter. To derive the closed expressions for the achieved SNR and BER under the use of ZF-DCE, a complete description for the noise component ψ forming at the output is required (the error performance is strongly related to the power of ψ). Using the standard complex matrix decomposition (singular value decomposition SVD), the complex channel matrix ψ can be decomposed as follows:

$$\begin{cases} \mathbf{H} = \mathbf{U}\mathbf{T}\mathbf{V}^H \\ \mathbf{H}^H\mathbf{H} = \mathbf{U}\mathbf{T}\mathbf{T}^H\mathbf{U}^H = \mathbf{U}\Lambda\mathbf{U}^H, \end{cases} \tag{39}$$

where $\mathbf{U}$ is MM complex unitary matrix that contains the $\mathbf{H}\mathbf{H}^H$ eigenvectors ($\mathbf{U}^H\mathbf{U} = \mathbf{I}_M$, $\mathbf{U}^H = \mathbf{U}^{-1}$), $\mathbf{V}$ is NN complex unitary matrix that contains the $\mathbf{H}^H\mathbf{H}$ eigenvectors, $\mathbf{T} = diag(\lambda_1, ..., \lambda_N)$ is MN real diagonal matrix of the positive square roots of the corresponding eigenvalues, and Λ is MM diagonal matrix. The diagonal elements of $\mathbf{T}$ and Λ are defined by the following form:

$$\lambda_i = \begin{cases} \mathrm{d_i^2}, \mathrm{i} = 1, 2, ..., \min(N, M) \\ 0, \mathrm{i} = \min(N, M) + 1, ..., \mathrm{M} \end{cases} \tag{40}$$

where the squared singular values $\{d_i^2\}$ are the channel matrix $\mathbf{H}$ eigenvalues. The squared Euclidian norm $\|.\|$ of the channel matrix $\mathbf{H}$ is given by

$$\|\mathbf{H}\|^2 = tr(\Lambda) = \sum_{i=1}^{\min(N,M)} \lambda_i = \sum_{i=1}^{\min(N,M)} d_i^2, \tag{41}$$

where $tr(.)$ is the matrix trace. Based on Eqs. (39) and (41), the power of the noise ψ at the ZF-DCE output can be presented using the expression:

$$\begin{aligned} \|\psi\|^2 &= \|(\mathbf{H}^H\mathbf{H})^{-2}(\mathbf{H}^H)^2\mathbf{Z}_{\mathrm{BS}}\|^2 = \|(\mathbf{V}\mathbf{T}^2\mathbf{V}^H)^{-2}(\mathbf{V}\mathbf{T}\mathbf{U}^H)^2\mathbf{Z}_{\mathrm{BS}}\|^2 \\ &= \|\mathbf{V}^{-2}\mathbf{T}^{-4}(\mathbf{V}^H)^{-2}\mathbf{V}^2\mathbf{T}^2(\mathbf{U}^H)^2\mathbf{Z}_{\mathrm{BS}}\|^2 = \|\mathbf{V}^{-2}\mathbf{T}^{-2}(\mathbf{U}^H)^2\mathbf{Z}_{\mathrm{BS}}\|^2 \\ &= \|(\mathbf{V}^{-1}\mathbf{T}^{-1}\mathbf{U}^H)^2\mathbf{Z}_{\mathrm{BS}}\|^2. \end{aligned} \tag{42}$$

The mathematical expectation of the noise power given by Eq. (42) is defined as follows:

$$E\{\|\psi\|^2\} = E\{\|(\mathbf{V}^{-1}\mathbf{T}^{-1}\mathbf{U}^H)^2\mathbf{Z}_{\mathrm{BS}}\|^2\} = E\{\|(\mathbf{V}\mathbf{T}\mathbf{U})^{-2}\mathbf{Z}_{\mathrm{BS}}\|^2\} \tag{43}$$

The unitary matrix lemma states that the multiplication with a unitary matrix will not change the vector norm. Thus, owing to the fact that is $\mathbf{V}$ a unitary matrix, the presented form in Eq. (43) can be simplified:

$$\begin{aligned} E\{\|\psi\|^2\} &= E\{\|(\mathbf{VTU})^{-2}\mathbf{Z}_{\mathrm{BS}}\|^2\} = E\{\|\mathbf{T}^{-2}\mathbf{U}^{-2}\mathbf{Z}_{\mathrm{BS}}\|^2\} \\ &= E\{tr[(\mathbf{T}^{-2}\mathbf{U}^{-2})\mathbf{Z}_{\mathrm{BS}}\mathbf{Z}_{\mathrm{BS}}^H(\mathbf{U}^2\mathbf{T}^{-2})]\} = tr[(\mathbf{T}^{-2}\mathbf{U}^{-2})E\{\mathbf{Z}_{\mathrm{BS}}\mathbf{Z}_{\mathrm{BS}}^H\}(\mathbf{U}^2\mathbf{T}^{-2})] \\ &= tr[\sigma_z^2(\mathbf{T}^{-2}\mathbf{U}^{-2})(\mathbf{U}^2\mathbf{T}^{-2})] = \sigma_z^2 tr[(\mathbf{T}^{-2}\mathbf{U}^{-2})(\mathbf{U}^2\mathbf{T}^{-2})] = \sigma_z^2 tr[\mathbf{T}^{-4}] \\ &= \sigma_n^2 \sum_{i=1}^{N} \lambda_i^{-2}. \end{aligned} \tag{44}$$

where σ_z^2 is the variance of the noise $\mathbf{Z}_{\mathrm{BS}}$ at the bandstop filter output. The last form is obtained considering that $\sigma_z^2 = \sigma_n^2$ (in the frequency band of interest, the noise power spectral density is constant). The SNR at the ZF-DCE output can be defined based on Eq. (44) as follows:

$$SNR_{\mathrm{ZF\text{–}DCE}} = \frac{\sigma_x^2}{\sigma_n^2 \sum_{i=1}^{N} \lambda_i^{-2}}. \tag{45}$$

The general form used to determine the BER in the case of ZF equalization technique under BPSK modulation can be defined as [10]:

$$BER_{\mathrm{ZF}} = \int_0^{\infty} Q(\sqrt{2SNR_{\mathrm{ZF}}x}) \frac{1}{(M\text{–}N)!} x^{M\text{–}N} e^{-x} dx \tag{46}$$

The BER form in Eq. (21) [10] is the solution of the last integral in Eq. (46) and together with Eq. (45) can present the final BER closed expression of ZF-DCE as follows:

$$BER_{\mathrm{ZF}} = \left[\frac{1}{2}\left(1 - \sqrt{\frac{\sigma_x^2}{\sigma_x^2 + \sigma_n^2 \sum_{i=1}^{N} \lambda_i^{-2}}}\right)\right]^{M\text{–}N+1} \sum_{m=0}^{M\text{–}N+1} \binom{M\text{–}N+m}{m} \left(\frac{1}{2} + \frac{1}{2}\sqrt{\frac{\sigma_x^2}{\sigma_x^2 + \sigma_n^2 \sum_{i=1}^{N} \lambda_i^{-2}}}\right). \tag{47}$$

As noticed in Eqs. (45) and (47), the derived forms are based on λ_i that also considered as the ith eigenvalue of the sample covariance matrix $\mathbf{R_y}$ given by

$$\mathbf{R_y} = \frac{1}{N_s}\mathbf{y}\mathbf{y}^H. \tag{48}$$

where N_s is the number of samples received by each antenna. The direct relation between λ_i and $\mathbf{y}$ can be illustrated using the following form:

$$\frac{1}{2\sigma_n^2} \sum_{k=0}^{N_s-1} y(k)^H y(k) = \frac{N_s}{2\sigma_n^2} \sum_{i=1}^{M} \lambda_i \tag{49}$$

5.3. ML equalization with DCE

For this case, the DCE flow chart presented in **Figure 10** can be considered for ML-DCE design excluding the squaring device. The corresponding equalizer or channel matrix takes the following format:

$$\mathbf{W}_{\text{ML–DCE}} = \mathbf{H} = (\hat{\mathbf{x}}^H\hat{\mathbf{x}})^{-1}\hat{\mathbf{x}}^H\mathbf{y} \tag{50}$$

Based on Eq. (31), the ML-DCE estimation is defined as:

$$\hat{\mathbf{x}}_{\text{ML–DCE}} = \arg\min_{\hat{\mathbf{x}}\in\mathbf{x}} \|\mathbf{y}–\hat{\mathbf{x}}(\hat{\mathbf{x}}^H\hat{\mathbf{x}})^{-1}\hat{\mathbf{x}}^H\mathbf{y}\|^2 \tag{51}$$

The presented form in Eq. (51) can be simplified by the following operations:

$$\begin{aligned}
\hat{\mathbf{x}}_{\text{ML–DCE}} &= \arg\min_{\hat{\mathbf{x}}\in\mathbf{x}} [\mathbf{y}–\hat{\mathbf{x}}(\hat{\mathbf{x}}^H\hat{\mathbf{x}})^{-1}\hat{\mathbf{x}}^H\mathbf{y}]^H[\mathbf{y}–\hat{\mathbf{x}}(\hat{\mathbf{x}}^H\hat{\mathbf{x}})^{-1}\hat{\mathbf{x}}^H\mathbf{y}] \\
&= \arg\min_{\hat{\mathbf{x}}\in\mathbf{x}} [\mathbf{y}^H–\mathbf{y}^H\hat{\mathbf{x}}(\hat{\mathbf{x}}^H\hat{\mathbf{x}})^{-1}\hat{\mathbf{x}}^H][\mathbf{y}–\hat{\mathbf{x}}(\hat{\mathbf{x}}^H\hat{\mathbf{x}})^{-1}\hat{\mathbf{x}}^H\mathbf{y}] \\
&= \arg\min_{\hat{\mathbf{x}}\in\mathbf{x}} [\mathbf{y}^H\mathbf{y}–\mathbf{y}^H\hat{\mathbf{x}}(\hat{\mathbf{x}}^H\hat{\mathbf{x}})^{-1}\hat{\mathbf{x}}^H\mathbf{y}–\mathbf{y}^H\hat{\mathbf{x}}(\hat{\mathbf{x}}^H\hat{\mathbf{x}})^{-1}\hat{\mathbf{x}}^H\mathbf{y} + \mathbf{y}^H\hat{\mathbf{x}}(\hat{\mathbf{x}}^H\hat{\mathbf{x}})^{-1}\hat{\mathbf{x}}^H\hat{\mathbf{x}}(\hat{\mathbf{x}}^H\hat{\mathbf{x}})^{-1}\hat{\mathbf{x}}^H\mathbf{y}] \\
&= \arg\min_{\hat{\mathbf{x}}\in\mathbf{x}} [\mathbf{y}^H\mathbf{y}–2\mathbf{y}^H\hat{\mathbf{x}}(\hat{\mathbf{x}}^H\hat{\mathbf{x}})^{-1}\hat{\mathbf{x}}^H\mathbf{y} + \mathbf{y}^H\hat{\mathbf{x}}(\hat{\mathbf{x}}^H\hat{\mathbf{x}})^{-1}\hat{\mathbf{x}}^H\mathbf{y}] \\
&= \arg\min_{\hat{\mathbf{x}}\in\mathbf{x}} \underbrace{[\mathbf{y}^H\mathbf{y}–\mathbf{y}^H\hat{\mathbf{x}}(\hat{\mathbf{x}}^H\hat{\mathbf{x}})^{-1}\hat{\mathbf{x}}^H\mathbf{y}]}_{\mathbf{J}_{\text{DCE}}}.
\end{aligned} \tag{52}$$

It is obvious that to minimize the form in Eq. (52), the term $\left(\mathbf{y}^H\hat{\mathbf{x}}(\hat{\mathbf{x}}^H\hat{\mathbf{x}})^{-1}\hat{\mathbf{x}}^H\mathbf{y}\right)$ should be maximized as follows:

$$\begin{aligned}
\mathbf{J}_{\text{ML}} &= \arg\max_{\hat{\mathbf{x}}\in\mathbf{x}} \left(\mathbf{y}^H\hat{\mathbf{x}}(\hat{\mathbf{x}}^H\hat{\mathbf{x}})^{-1}\hat{\mathbf{x}}^H\mathbf{y}\right) = \arg\max_{\hat{\mathbf{x}}\in\mathbf{x}} [\mathbf{y}^H\hat{\mathbf{x}}(\hat{\mathbf{x}}^H\hat{\mathbf{x}})^{-1}\hat{\mathbf{x}}^H\hat{\mathbf{x}}(\hat{\mathbf{x}}^H\hat{\mathbf{x}})^{-1}\hat{\mathbf{x}}^H\mathbf{y}] \\
&= \arg\max_{\hat{\mathbf{x}}\in\mathbf{x}} [\left(\hat{\mathbf{x}}(\hat{\mathbf{x}}^H\hat{\mathbf{x}})^{-1}\hat{\mathbf{x}}^H\mathbf{y}\right)^H\left(\hat{\mathbf{x}}(\hat{\mathbf{x}}^H\hat{\mathbf{x}})^{-1}\hat{\mathbf{x}}^H\mathbf{y}\right)] = \arg\max_{\hat{\mathbf{x}}\in\mathbf{x}} \|\hat{\mathbf{x}}(\hat{\mathbf{x}}^H\hat{\mathbf{x}})^{-1}\hat{\mathbf{x}}^H\mathbf{y}\|^2.
\end{aligned} \tag{53}$$

The related SNR at the ML-DCE output is determined using $\mathbf{J}_{\min,\text{DCE}}$ as in the presented form Eq. (32) and the covariance matrix of the reference noise $\mathbf{Z}_{\text{BS}}$ forming at the bandstop filter given by

$$C_{Z_{\text{BS}}} = E[Z_{\text{BS}}^H Z_{\text{BS}}] = \sigma_z^2 I = \sigma_n^2 I \tag{54}$$

Defining the achieved SNR for ML-DCE, it is possible to calculate the BER using the same form in Eq. (**33**). Taking into account the sample covariance matrix $\mathbf{R}_y$ in Eq. (**48**), Eq. (**52**) can be represented as:

$$\hat{\mathbf{x}}_{ML–DCE} = \arg\min_{\hat{\mathbf{x}}\in\mathbf{x}} [N_s\mathbf{R}_{\mathbf{y}}–\mathbf{y}^H\hat{\mathbf{x}}(\hat{\mathbf{x}}^H\hat{\mathbf{x}})^{-1}\hat{\mathbf{x}}^H\mathbf{y}] \tag{55}$$

The use of two equalization filters and the bandstop filter (the main DCE idea) helps us to construct new equalization matrices and convert linear equalizers such as ZF equalizer to nonlinear one. Additionally, the reference noise forming at the second equalizer output contributes in the definitions of achieved BER and SNR and can be employed to estimate the noise variance (power) at the equalizer input. In this section, two equalizers are introduced, namely,

ZF-DCE and ML-DCE. The DCE concept can be implemented with other equalization techniques like MMSE and DFE as well. The proposed DCE performance is evaluated in the following subsection.

5.4. Simulation process and results

In this section, *NM* MIMO channel is considered where the number of transmit antennas N= 2 and the number of receive antennas M= 2 under Rayleigh fading channel and for BPSK modulation. The overall simulation process for this system employing the conventional and DCE types of equalization techniques are presented in **Figure 11**. The evolution and comparison criterion is based on the BER (probability of error) as a function of energy per bit E_b to the noise power spectral density N_0 ratio ($\frac{E_b}{N_0}$). The relation between $\frac{E_b}{N_0}$ and the SNR can be simply presented as:

$$SNR = \frac{E_b}{N_0}\frac{D_R}{BW}, \tag{56}$$

where D_R is the data rate and BW is the bandwidth.

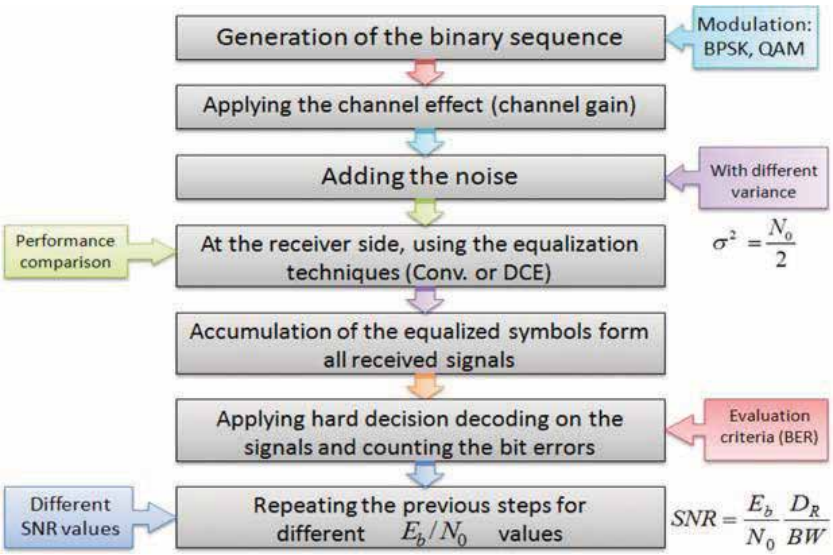

Figure 11. The simulation and evaluation processes.

In **Figure 12**, a comparison between the conventional ZF equalization technique and the modified ZF using dual channel equalization (DCE) is presented. The ZF-DCE approach demonstrates better performance (lower BER) comparing with the conventional ZF at the same $\frac{E_b}{N_0}$ (or SNR) range. The two equalizers have the same performance under relatively lower SNR ($\frac{E_b}{N_0} \leq 5[dB]$).

The ML-DCE and the conventional ML equalizer performances are compared in **Figure 13** under the same initial conditions but for different SNR ($\frac{E_b}{N_0}$) range with the purpose of demonstrating the

http://dx.doi.org/10.5772/65969

effective and efficient SNR values for DCE employment. Once again the ML-DCE outperforms the conventional ML in performance and for lower SNR compared with the case of ZF equalization where the two equalizers present asymptotic performance for SNR less than 0 dB or $\frac{E_b}{N_0} \leq 0[dB]$ (roughly speaking, the ML-DCE performance is slightly better at $\frac{E_b}{N_0} \leq 0[dB]$).

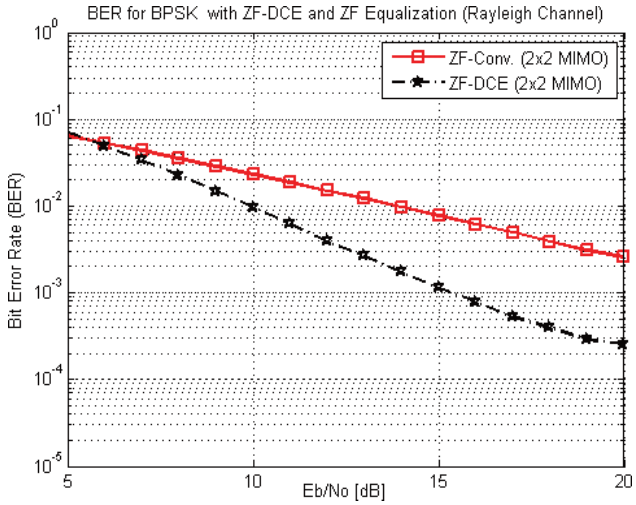

Figure 12. The comparison between conventional ZF and the ZF-DCE.

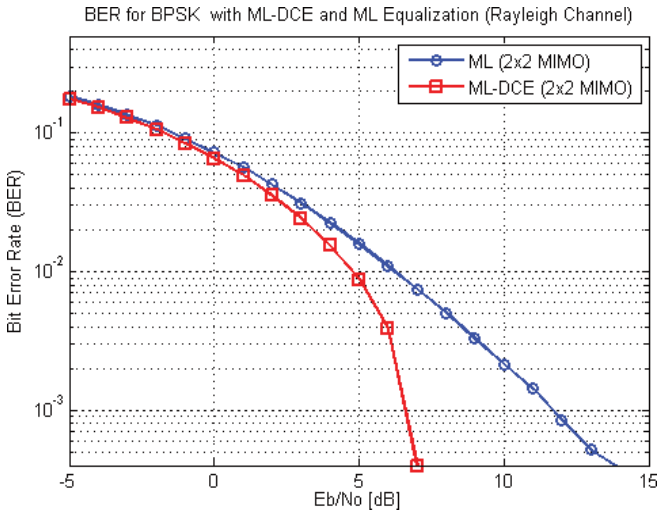

Figure 13. The comparison between conventional ML and the ML-DCE.

6. Conclusion remarks

The discussion of this chapter can be ended by making several remarks. The new equalization approach (DCE) shows promising outcomes in terms of improving the equalization performance

by reducing the BER (sequence error probability).The obtained results can be simply generalized for other equalization techniques and for frequency domain equalization as well. Additionally, it is easy to prove that the DCE symbol error performance can be better than that of the conventional equalizers. The type of filters used to design the DCE equalizer is not mentioned or discussed but both FIR and IIR filters are possible and reasonable candidates.

Although the design and implementation complexity issues (the computational cost to design the equalizer and to equalize the channel, respectively) for the proposed above equalization structure are not discussed in this chapter, an ostensible comments can be made. The DCE design relies on other equalization approaches and does not exhibit significant overhead complexity. Thus, the complexity increases employing DCE but not with overwhelming degree. Finally, a complete analysis based on practical conditions and for time-invariant (TIV) and time-varying (TV) channel models under specific scenarios is required before addressing the feasibility of the presented DCE approach.

Acknowledgements

This work is performed by Radio Physics Research Group (RPRG) at Polytechnic University of San Luis Potosi (UPSLP), San Luis Potosi, Mexico.

Author details

Modar Shbat[1]*, Francisco C. Ordaz-Salazar[1] and Javier S. González-Salas[2]

*Address all correspondence to: modar.shbat@upslp.edu.mx

1 Telematics Engineering Department, Polytechnic University of San Luis Potosí, San Luis Potosí, México

2 Mathematical Department, Polytechnic University of San Luis Potosi, San Luis Potosí, México

References

[1] Proakis J, Salehi M: Digital Communications. 5th ed: Chapter 10. McGraw-Hill, 2008.

[2] Wong T F, Lok T M: Theory of Digital Communication: Chapter 4. University of Florida, 2004.

[3] Orfanidis S J: Introduction to Signal Processing. Rutgers University, New Jersey, 2010.

[4] Rainfield Y: Unbiased MMSE vs. biased MMSE equalizers. Tamkang Journal of Science and Engineering, 2009; Vol.12, No.1: 45 –56.

[5] Klein A, Kaleh G K, Baier P W: Zero forcing and minimum mean-square-error equalization for multiuser detection in code-division multiple-access channels. IEEE Transaction on Vehicular Technology, 2002; Vol. 45, No. 2: 276–287.

[6] Gersho A: Adaptive equalization in highly dispersive channels for data transmission. Bell System Technical Journal. 1969; Vol. 48: 55–70.

[7] Bottomley G E: Channel Equalization for Wireless Communications: From Concepts to Detailed Mathematics: Chapters 5, 6. Wiley-IEEE Press, 2011.

[8] George D, Bowen R, Storey J: An adaptive decision feedback equalizer. IEEE Transactions on Communication Technology, 1971; Vol. 19, No. 3: 281–293.

[9] Bjerke B A, Proakis J G: Equalization and decoding for multiple-input multiple-output wireless channels. EURASIP Journal on Applied Signal Processing. 2002; No. 3: 249–266.

[10] Ding Y, et al.: Minimum BER block precoders for zero-forcing equalization. IEEE Transactions on Signal Process. 2003; Vol. 51, No. 9: 2410–2423.

[11] Jiang Y, Varanasi M K, Jian L: Performance analysis of ZF and MMSE equalizers for MIMO systems: An in-depth study of the high SNR regime. IEEE Transactions on Information Theory, 2011; Vol. 57, No. 4: 2008–2026.

[12] Forney G: Maximum likelihood sequence estimation of digital sequences in the presence of intersymbol interference. IEEE Transactions on Information Theory. 1972; Vol. 18, No. 3: 363–378.

[13] Barhumi I, Moonen M: MLSE and MAP equalization for transmission over doubly selective channels. IEEE Transactions on Vehicular Technology. 2009; Vol. 58, No. 8: 4120–4128.

[14] Gitlin R D, Weinstein S B: Fractionally-spaced equalization: an improved digital transversal equalizer. The Bell System Technical Journal. 1981; Vol. 60, No. 2: 275–296.

[15] Ma X, Davidson T, Gershman A, Swami A, Tepedelenlioglu C: Advanced equalization techniques for wireless communications. EURASIP Journal on Advances in Signal Processing. 2010; Vol. 2010, Article ID 623540, 2 pages, doi:10.1155/2010/623540.

[16] Martins C, Guiomar F, Amado S, Ferreira R, Ziaie S, Shahpari A, Teixeira A, Pinto A: Distributive FIR-based chromatic dispersion equalization for coherent receivers. Journal of Lightwave Technology, 2016; Vol. PP, No. 99: 1–1. [CE2] doi:10.1109/JLT.2016.2604741.

[17] Wang W, Wang Z, Zhang C, Guo Q, Sun P, Wang X: A BP–MF–EP based iterative receiver for joint phase noise estimation, equalization, and decoding. IEEE Signal Processing Letters. 2016; Vol. 23, No. 10: 1349–1353.

[18] Zhu Y, Zhe P, Zhou H, Huang D: Robust single carrier frequency domain equalization with imperfect channel knowledge. IEEE Transactions on Wireless Communications. 2016; Vol. 15, No. 9: 6091–6103.

[19] Yuan W, Wu N, Wang H, Kuang J: Variational inference-based frequency-domain equalization for faster-than-Nyquist signaling in doubly selective channels. IEEE Signal Processing Letters.2016; Vol. 23, No. 9: 1270–1274.

[20] Moya S, Hadad M, Funes M, Danato P, Carrica D: Broadband PLC-channel equalisation in the frequency domain based on complementary sequences.IET Communications. 2016; Vol. 10, No. 13: 1605–1613.

Chapter 17

Multiple Person Localization Based on their Vital Sign Detection Using UWB Sensor

Dušan Kocur, Daniel Novák and Mária Švecová

Additional information is available at the end of the chapter

http://dx.doi.org/10.5772/66361

Abstract

In the past period, great efforts have been made to develop methods for through an obstacle detection of human vital signs such as breathing or heart beating. For that purpose, ultra-wideband (UWB) radars operating in the frequency band DC-5 GHz can be used as a proper tool. The basic principle of respiratory motion detection consists in the identification of radar signal components possessing a significant power in the frequency band 0.2–0.7 Hz (frequency band of human respiratory rate) corresponding to a constant bistatic range between the target and radar. To tackle the task of detecting respiratory motion, a variety of methods have been developed. However, the problem of person localization based on his or her respiratory motion detection has not been studied deeply. In order to fill this gap, an approach for multiple person localization based on the detection of their respiratory motion will be introduced in this chapter.

Keywords: emergency events, person localization, respiratory motion, signal processing, ultra-wideband (UWB) sensor/radar, vital signs detection of persons

1. Introduction

At the beginning of the twenty-first century, the human society faced quite a number of specific social trends. The increasing density of population of towns and town agglomerations, criminality growing and political tensions producing terrorism, and growth of the percentage of elder people can be ranked among them.

A high density of the population at emergency events such as earthquakes or building collapses results in a high number of injured and trapped persons. At these disasters, many persons can survive the most critical moments. However, they have often limited capability of the motion or they are unconscious, what makes more difficult to save them. There is,

however, necessary to emphasize that the capability and rapidity of the victim localization is the most critical for their lifesaving.

People localization is very important not only for post-disaster rescue but also for military and security operations [1]. Here, reservoirs, power plants, and other critical infrastructures are extremely vulnerable to terrorist attack. Therefore, the request for monitoring of the mentioned critical areas and for the detection of unauthorized intrusion is still needed. The information about the number of persons and their positions can be very useful for security troops to take the right decisions. In the case of the mentioned disasters and law enforcement operations, people to be detected and localized are often situated behind nonmetallic obstacles (e.g. walls). That is the reason why conventional sensors (e.g. cameras) cannot be applied for person monitoring for such scenarios.

It is expected that the number of seniors will increase in the future. It will result in dramatic challenges to the society since elder people need additional care and assistance. It is well known that many people aged above 65 years fall down in their dwelling every year and above 3% of them are not able to rise again without external help. They have to stay in their uncomfortable situation over hours or even days before they get help. As a result, a number of people are dying in consequence of such accidents [2]. In order to save life of the seniors, they can be monitored, for example, by conventional cameras. However, this simple solution represents a serious invasion to their private life, and hence it is not well accepted. On the other hand, a solution enabling to localize seniors at their home taking into account their privacy and at the same time detection of emergency events is really very needful. It has been shown in Ref. [2] that ultra-wide frequency band radars (UWB sensors) can provide solutions of the outlined problem.

The analyses of the requirements for person localization according to above outlined scenarios have shown that short-range high-resolution radars emitting electromagnetic waves with ultra-wide frequency band (UWB radars) using relatively low frequencies can be used with advantage for such applications. The exploitation of the ultra-wide frequency band provides the high resolution of the radar. On the other hand, the electromagnetic waves emitted in the frequency band DC-5GHz can penetrate through standard building materials (e.g. wood, concrete, bricks, etc.) with acceptable attenuation. Therefore, UWB sensors employing this frequency band are capable to detect a target situated not only for line-of-sight but also for a target located behind a nonmetallic obstacle. Moreover, UWB radar systems can be constructed to be lightweight and small.

UWB radars could be available as handheld sensor systems consisting of antenna system, radio frequency (RF) block, analog-to-digital (AD) convertors, and digital circuitry including a computer and software. On the other hand, UWB sensors provide also privacy requested at people monitoring at their home, and hence they can be implemented as a part of complex sensor networks applied for senior monitoring in ambient-assisted living (AAL) programs as well.

The key part of the UWB sensor system software consists in the implementation of UWB radar signal processing procedure intent on human being detection, localization, and tracking. The

http://dx.doi.org/10.5772/66361

deeper analyses of person detection using UWB sensors have shown that it is necessary to distinguish between the detection of moving and static persons. In this context, a person moving within the monitored area in such a way that their coordinates are changing is referred to as a moving person. On the other hand, a living person is considered as static person, if he or she is situated but not moving within the monitored area in such a way that their coordinates are changing. Then, while a typical form of moving person movement is, for example, his or her walking or running, typical forms of static person movement are his or her respiration motions or heart beating, which is commonly referred to as person's vital signs. As examples of static persons, unconscious person located beneath the rubble of the building or avalanche, bound people (prisoners of terrorists) and sleeping persons, and so on can be given.

In this chapter, we focus on UWB radar signal processing procedure for localization of static persons situated behind a nonmetallic obstacle. First, we state the basic principle of the static person detection based on the detection of his or her respiratory motions. Then, the the state-of-the of UWB radar signal processing concerning static person detection and localization will be presented in Section 3. The core of the chapter will be presented in Section 4. Here, a Welch periodogram method for multiple static person localization based on their vital sign detection will be given. As the vital signs, person respiratory motions (breathing) will be considered. The particular phases of this method will be illustrated by corresponding experimental results. Finally, some conclusions will be summarized in Section 5.

2. Respiratory motion detection: problem statement and its fundamental solution

Figure 1 symbolizes the generic measurement arrangement illustrating the basic principle of respiratory motion detection [2]. A transmitting antenna Tx converts the signal $p(t,\tau)$ into an electromagnetic wave, which propagates toward the body of the person. There, it will be partially reflected and travels back to the receiving antenna Rx, which converts the wave back into signal $r(t,\tau)$ that has to be captured by appropriate radar electronics. Then, the radar device converts the received signals by a proper pulse compression method into impulse responses $h(t,\tau)$ of the environment through which the signal emitted by the radar is

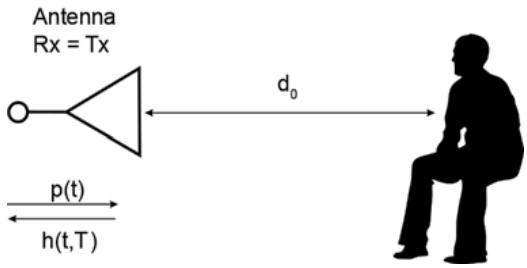

Figure 1. Basic measurement arrangement.

propagated. The variables t and τ, and the set of $h(t,\tau)$ represent fast-time (propagation time), slow-time (observation time), and raw radar data usually referred to as radargram, respectively.

Let us assume for this moment that the same antenna is used for the signal transmission and reception, and a static person is located in front of this antenna in the distance d_0. Under such conditions, signal $h(t,\tau)$ can be expressed as follows [2, 3]:

$$h(t,\tau) = \sum_{i=1}^{N} A_i p(t-t_i) + A_0 p\Big(t-t_d(\tau)\Big) = h_b(t,\tau) + h_0(t,\tau). \tag{1}$$

In this expression, the constant term A_i stands for the path gain (or loss) of the ith signal path. The signal components $A_i p(t-t_i)$ for $i \neq 0$ represent the reflections of the transmitted signal from static objects (i.e. not reflections due to static person). Then,

$$h_b(t,\tau) = \sum_{i=1}^{N} A_i p(t-t_i) \tag{2}$$

is the component of $h(t,\tau)$ representing static clutter and noise (e.g. noise due to antenna and other electronic components of radar device, etc.). On the other hand, signal

$$h_0(t,\tau) = A_0 p\Big(t-t_d(\tau)\Big) \tag{3}$$

expresses the component of $h(t,\tau)$ due to static persons. The time delay $t_d(\tau)$ (associated with vital signs) represents the time of arrival (TOA) of the static person. It covers the time signal required to travel across *Tx-target-Rx* trajectory. The time delay $t_d(\tau)$ varies depending on the distance of the target from the antenna system. Slight but periodic changes of TOA are caused by a movement of the target chest due to periodical chest movement caused by breathing process (with a frequency f_b) and heartbeats (with frequency f_h) [2, 3]. Then, $t_d(\tau)$ can be approximately expressed as

$$t_d(\tau) = 2d(t_0,\tau)/c \tag{4}$$

where $c = 3\text{x}10^8 \text{ms}^{-1}$ is the speed of light and

$$d(t_0,\tau) = d_0 + m_b(\tau) + m_h(\tau) = d_0 + m_b \sin(2\pi f_b \tau) + m_h \sin(2\pi f_h \tau) \tag{5}$$

$$m_b(\tau) = m_b \sin(2\pi f_b \tau) \tag{6}$$

$$m_h(\tau) = m_h \sin(2\pi f_h \tau) \tag{7}$$

The term $d_0(t_0,\tau)$ is a component expressing the reflection from static object situated in distance d_0 from the radar antenna, and m_b and m_h are the breathing and heart amplitude, respectively. The peak-to-peak thorax motion due to breathing of an adult person ranges from 4 to 12 mm, while the peak-to-peak motion due to the heartbeat is about 0.5 mm. Then, $m_b >> m_h$ and the signals $d(t_0,\tau)$ and $t_d(\tau)$ can be expressed as

http://dx.doi.org/10.5772/66361

$$d(t_0, \tau) \approx d_o + m_b \sin(2\pi f_b \tau) \tag{8}$$

$$t_d(\tau) = 2d(t_0)/c + (2m_b/c) \cdot \sin(2\pi f_b \tau). \tag{9}$$

Within a long-term observation, breathing can be qualified as a periodic process with its own frequency f_b. According to [4], this frequency can take values from 0.2 Hz caused by slow, calm breathing up to 0.7 Hz caused by fast, stressful breathing. Then, taking this knowledge and Eqs. (1), (3), and (8) as well into account, it can be concluded that the impulse response $h(t, \tau)$ consists of the clutter and noise Eq. (2) and a periodical signal $h_0(t, \tau)$. The signal $h_0(t, \tau)$ due to the respiratory motion of a person has a DC component (depending on d_0) and period $T_b = 1/f_b$. The frequency of its fundamental harmonic component is $f_b \in B$, where $B = \langle 0.2Hz,\ 0.7\ Hz \rangle$.

The abovementioned comments summarizing the detailed analyses presented in Refs. [2, 3] indicate that a static person can be detected based on the detection of a periodical signal components of the radargram $h(t, \tau)$ corresponding to a periodical motion with frequency $f_b \in B$ with regard to the slow-time variable (τ) for a constant fast-time instant (t_0). If such a component is detected for $t = t_0$, then the bistatic range of the target (i.e. the length of the trajectory distance *Tx-target-Rx*) is ct_0. And finally, if a proper number of bistatic ranges of the target for the properly defined positions of *Tx* and *Rx* are estimated, then the target coordinates can be estimated, for example, by a trilateration or multilateration method.

As it follows from the previous paragraph, the key element of the static person detection consists in the detection of the periodical components of the radargram with the frequency form the interval $B = \langle 0.2Hz,\ 0.7\ Hz \rangle$. Here, it should be stressed that the target echo to-noise- and clutter ratio (SNCR) and is usually low. The target detection and then its localization can be onward complicated by a complex environment where the target is situated (strong attenuation due to obstacle, multipath electromagnetic wave propagation, shadowing effect, narrowband interference due to wireless communication systems, etc.). Therefore, there are no simple solutions to be applied for static person detection and localization. The published solutions differ in their approach to clutter and noise suppression, to power spectrum estimation, and to target detection methods. Moreover, there are only a few papers dealing not only with the person detection but also with person localization. The state-of-the art in this field is shortly outlined in the next section.

3. Static person detection and localization: state-of-the art

During the last decade, a variety of the papers intent on human being detection by UWB sensors have been published. These contributions were initially focused mainly on UWB sensor system construction and on basic principle of human being detection (e.g. [5, 6]). Then, the research in the field of UWB sensor systems was devoted also to the development of UWB radar signal processing methods to be applied for moving and static person detection and localization. As we have shown in the previous section, the basic principle of the static person detection consists in the spectrum analyses of the radargram. This fact allows modifying the

methods originally designed for static person detection for estimation of the breathing and heart-beating rate (e.g. [3, 7]). In the next section, we deal with the problem of radar signal processing for the detection and localization of static person only.

This section briefly highlights the approaches and the outcomes of the research in the detection and localization of the static persons but also points out their respective deficiencies, which altogether give ground for motivation of the research presented herein.

Deep analyses of the problem of the human beings detection based on the detection of their respiratory motions have been provided in Refs. [2, 8]. In these works, a very useful model of raw radar data has been introduced. It has been shown that the raw radar data can be modeled as an additive mixture of signal of interest (target echo), stationary and nonstationary clutter, jamming and random noise. What is important, the components of the target echo along the slow-time axis are represented by periodical signals with the fundamental harmonic located in the frequency interval $B = \langle 0.2Hz, 0.7\ Hz \rangle$. The further analyses of the raw radar data have shown that target echo to-noise and clutter ratio SNCR is usually very small. Therefore, the process of the static person detection can be decomposed at least into two phases, which include clutter and noise suppression and spectrum analyses of the radargrams with the suppressed clutter and noise.

The approach chosen for respiratory motion detection proposed in Refs. [8, 9] is divided into three stages: stationary-clutter removal (range-profile subtraction, mean subtraction, linear-trend subtraction), SNCR improvement (filtering in range dimension, slow-time frequency-domain windowing, and nonstationary-clutter suppression by singular value decomposition (SVD)), and threshold-based decision- and range-estimation stage (results of SVD decomposition processing). For the power spectrum estimation, discrete Fourier transform (DFT) is applied. The proposed approach has been successfully demonstrated for the detection of a single person located under rubble.

On the other hand, a bit simpler approach for a static person detection has been introduced in Refs. [2, 5]. In these papers, an exponential averaging and DFT or Welch periodogram has been proposed for background subtraction and power-spectrum estimation, respectively. The obtained results have shown that also this alternative approach can be successfully used for the static person detection under some scenarios.

The analyses of some several other contributions (e.g. [2, 4, 10, 11]) have shown that moving target indicator method (MTI), SVD, combination of correlation analyses and a Curvelet transformation, and CLEAN algorithm can be used for the SNCR improvement. Besides conventional methods of spectrum analyses (e.g. DFT or Welch periodogram), the application of some new methods for the detection of the periodical components of radargram has been proposed. The methods such as Hilbert-Huang transformation (e.g. [11, 12]), S-transform (e.g. [13]), MUSIC algorithm (e.g. [7]) and wavelet transformation and wavelet entropy (e.g. [14]) can be rated among them. The fundamentals of Hilbert-Huang transformation, S-transform, and MUSIC methods can be found in Refs. [15–17], respectively.

The results of the detection phase are represented usually by two-dimensional (2D) figures expressing a propagation rate (fast-time) versus a frequency axis (respiration rate), where high-

http://dx.doi.org/10.5772/66361

level components (so-called "hot spots") of these figures indicate a presence of the targets. It means that the output of these methods cannot provide any information about target coordinates. In order to localize the static person, their bistatic range or TOA has to be estimated and associated and only then the target can be localized using a proper localization method.

The mentioned approach has been applied in Refs. [18, 19]. In this papers, a sensor network of bistatic UWB radars for multiple person localization was described. The signal processing procedure described in these studies consists of SNCR improvement (using a simple variant of MTI), detection (a power-spectrum estimator application), initial screening (it is conducted via frequency analysis of the detected signals), data association and parameter estimation (maximum likelihood observation-target association technique) and target localization (including determination of number of the target). The sensor network presented in Ref. [18] provides not only very good localization of a set of static persons for a line-of-sight scenario, but it provides the estimation of the frequency of their breathing, too.

The present short but comprehensive review of some papers devoted to the static person detection and localization indicate that there are only a few papers (e.g. [18, 19].) dealing with the problem of multiple static person localization. In order to fill this gap, an approach for multiple person localization based on the detection of their respiratory motion and employing a single UWB sensor only will be introduced in the next section.

4. WP-STAPELOC method

Taking into account the model of raw radar signal $h(t, \tau)$, the basic principle of static person detection introduced in Section 2, and the findings summarized in the previous section as well, the static persons can be localized using the following procedure of UWB sensor signal processing. The procedure consists of a set of phases of signal processing such as background subtraction, target echo enhancement, target detection, TOA estimation and TOA association, and target localization, where each phase is implemented by proper methods of signal processing. As it will be shown later, the detection of persons' respiratory motions is the key phase of the procedure. The input signal of the detectors employed in this phase will be formed using power spectrum of the radargram components. Because Welch periodogram will be used for the estimation of the mentioned power spectrum, the signal processing procedure for static person localization introduced in this section will be referred as WP-STAPELOC method (a method for STAtic PErson LOCalization based on power-spectrum estimation using Welch Periodogram).

In the next paragraphs of this section, the importance and implementation of the particular phases of WP-STAPELOC method will be presented. With the intention to provide a bit deeper insight into the procedure, the importance of its particular phases, the performance of the signal processing methods applied within these phases and the performance of the WP-STAPELOC method as a whole will be illustrated using the experimental data obtained by measurements intent on through-the-wall localization of three static persons using UWB sensor system (the so-called illustrative scenario). Following the outlined concept of this

section, the illustrative scenario will be first described, and then the particular phases of WP-STAPELOC method will be introduced.

4.1. Illustrative scenario

The illustrative scenario was intent on through-the-wall localization of three static persons using an UWB sensor. The measurement scheme for the illustrative scenario is outlined in **Figure 2**. The monitored area was represented by the basement room. The UWB sensor (radar) was situated behind the structural concrete wall of thickness 0.5 m (**Figure 2**). Three persons to be localized stood in the positions P1, P2, and P3. The only observable movements of the persons to be localized were their respiratory motions.

The raw radar data analyzed in this contribution were acquired by means of M-sequence UWB radar systems equipped with one transmitting and two receiving horn antennas (**Figure 3**). The radar antenna positions are outlined in **Figure 2**. The distance between *Tx* and *Rxi* for $i = 1, 2$ was set to 0.45 m. The system clock frequency and operational bandwidth of the applied UWB sensor were 4.5 GHz and DC-2.25 GHz, respectively. The order of the M-sequence emitted by the radar was nine, that is, the impulse response covers 511 samples regularly spread over 114 ns. Then, the unambiguous range of the UWB radar was about 17 m.

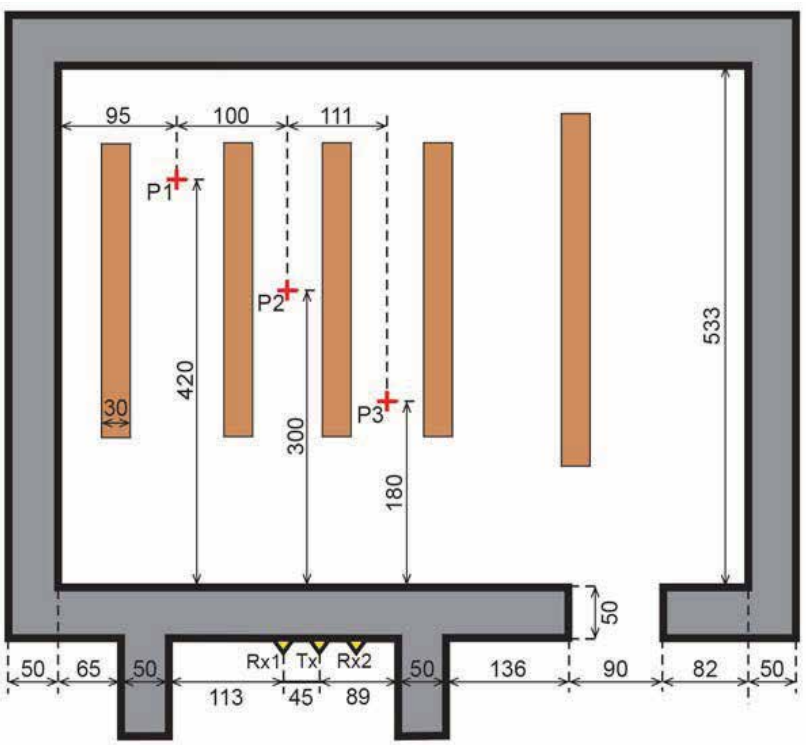

Figure 2. Measurement setup.

http://dx.doi.org/10.5772/66361

Figure 3. UWB radar system.

The radar measurement rate was approximately 13.5 impulse responses per second. The total length of the measurement was 74 s, which corresponds to 1000 impulse responses. The total power transmitted by the particular radar was about 1 mW.

The raw radar data obtained for the illustrative scenario are given in **Figures 4** and **5**. The strongest components identified in these figures correspond to the direct waves between *Tx* and *Rxi* (the so-called antenna coupling) and the reflections due to the wall. Unfortunately, the target-echo levels are too small, and hence no reflections due to persons are visible in **Figures 4** and **5**. These figures demonstrate very clearly that a further processing of the radargram is necessary to detect and localize the persons. In the next paragraph of this section, we describe WP-STAPELOC method, which can be applied for that purpose.

4.2. Phases of WP-STAPELOC method

As has been stated at the beginning of this section, the WP-STAPELOC method is UWB radar signal processing procedure consisting of the set of the five signal processing phases such as background subtraction, target-echo enhancement, target detection, TOA estimation and TOA association, and target localization, where each phase is implemented by proper methods of signal processing. Now, the particular phases will be presented in the next paragraphs of this section.

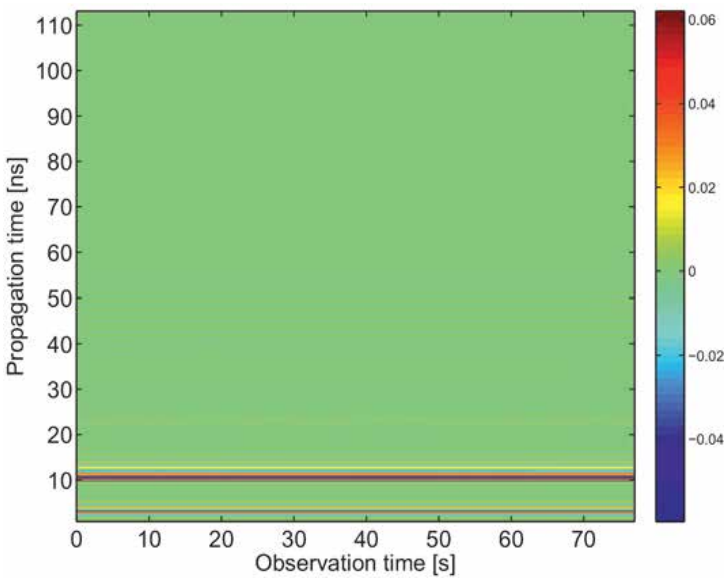

Figure 4. Raw radar data. Receiving channel Rx1.

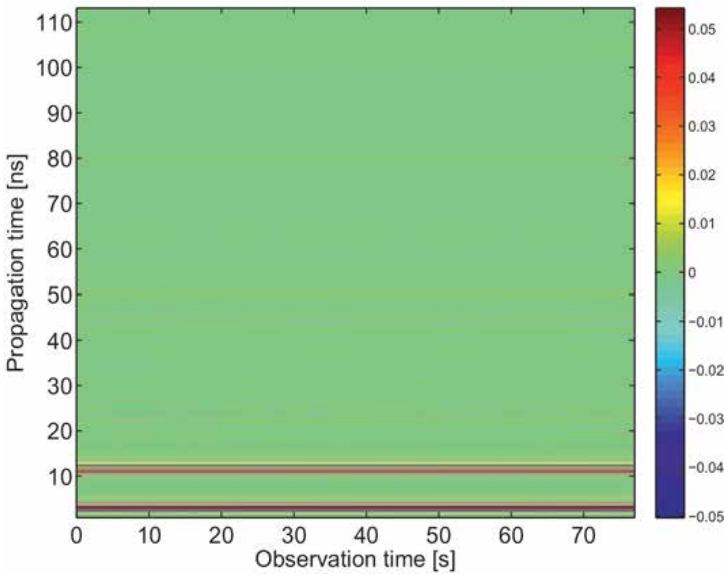

Figure 5. Raw radar data. Receiving channel Rx2.

4.2.1. Phase 1: background subtraction

The analysis of raw radar data has shown that it is impossible to directly identify any static persons in the obtained radargrams. This effect is due to the very small ratio of the

signals reflected by a target (nonstationary components of the radargram) to noise and clutter (stationary components of radargram mainly due to reflections of electromagnetic waves from static objects). In order to detect a target, this ratio has to be increased. For that purpose, background subtraction methods can be used. In Ref. [20], a variety of methods of the background estimation and subtraction have been described. The mentioned methods differ in relation to assumptions concerning the clutter properties, as well as by their computational complexity and convenience for online signal processing. Because of a good performance, high robustness, and low computational complexity, the method of exponential averaging belongs to the most popular and often used methods of background subtraction [20]. According to this method, the background estimate $\hat{b}(t,\tau)$ is obtained by

$$\hat{b}(t,\tau) = \alpha\hat{b}(t,\tau{-}1) + (\alpha{-}1)h(t,\tau), \quad 0 < \alpha < 1 \tag{10}$$

where α is a constant weighting factor setting the length of background estimator memory. Then, the radargram with a subtracted background can be obtained by the expression

$$h_b(t,\tau) = h(t,\tau){-}\hat{b}(t,\tau) \tag{11}$$

The radargrams with the subtracted background for the illustrative scenario considered in this chapter are given in **Figures 6** and **7**, respectively. Three high-level artifacts similar to lines parallel to the slow-time axis are located in the interval $\langle 20\text{ ns},\ 40\text{ ns}\rangle$ of fast-time axis. These high-level signals represent the components of the radargram due to static persons.

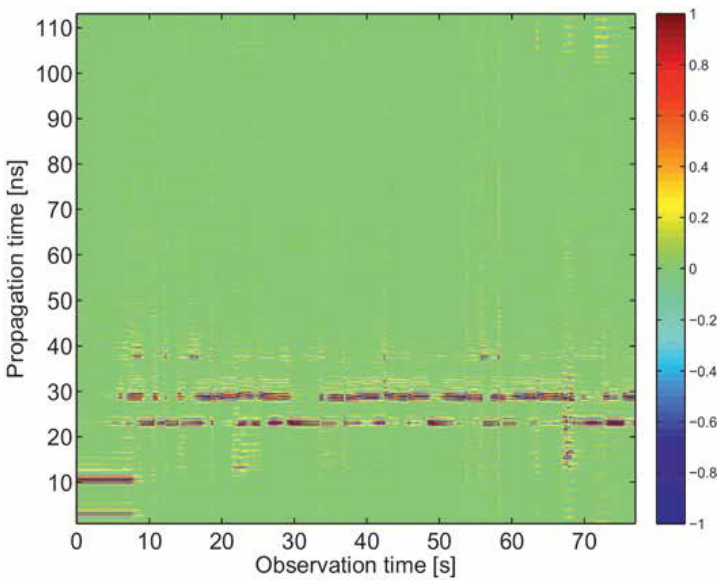

Figure 6. Radargram with subtracted background. Receiving channel Rx1.

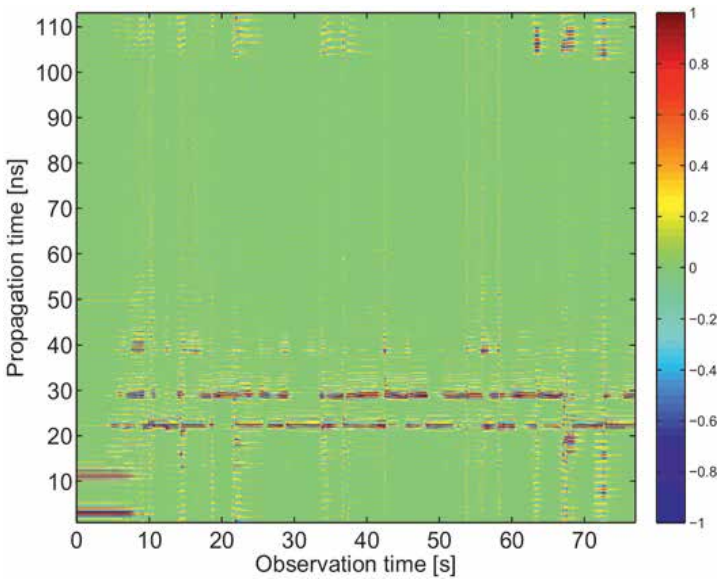

Figure 7. Radargram with subtracted background. Receiving channel Rx2.

4.2.2. Phase 2: target echo enhancement

SNCR can be improved using not only a background subtraction method but also a proper method of the target echo enhancement. An interesting approach for the improvement of SNCR with the special stress for the static person detection has been presented in, for example [8]. Here, the analyses of the impulse responses obtained at monitoring of a static person have shown that the target echo is located within frequency band 0.4–1.4 GHz. Then, filtering in the range dimension (i.e. along fast-time axis) by a proper pass-band filter can be used for low-level echo enhancement. The filter of that kind is sometimes also referred to as a range filter.

As we mentioned above, the key part of the WP-STAPELOC method consists in the power-spectrum estimation of the radargram components $h(t, \tau)$ for the constant values of t (i.e. for $t = t_k$). This condition expresses the fact that the power spectrum will be estimated only for those radargram components due to objects that have the same bistatic range with regard to Tx and Rx (i.e. *the distance Tx-target-Rxi*). It is well known from the spectrum estimation theory that in the case of the estimation of spectral components, which we like to detect (in our case, spectral components from the frequency band $B = \langle 0.2Hz,\ 0.7\ Hz \rangle$), the spectrum estimator performance depends usually on useful signal-to-noise ratio. Therefore, it would be helpful to increase this ratio before the spectrum estimator application. Following this idea, we propose to filter the signal $h(t_k, \tau)$ by a bandpass filter along the slow-time axis. The passband of this filter should be properly selected taking into account the frequency band $B = \langle 0.2Hz,\ 0.7\ Hz \rangle$ (signal components due to static persons) and the rate of measurement (i.e. frequency sampling of $h(t, \tau)$ along slow-time axis). In the next, a filter applied for this purpose will be referred to as a slow-time filter. The response of this filter will be denoted as $h_2(t, \tau)$.

http://dx.doi.org/10.5772/66361

In the case of the illustrative scenario, the low cutoff frequency of the *Tx* and *Rxi* antennas was 750 MHz and the operational bandwidth of UWB sensor was about DC-2.25 GHz. Because the practical operational bandwidth of UWB sensor system (radar device and antennas) used in the illustrative scenario was comparable with the frequency band 0.4–1.4 GHz reported in Ref. [8], no range filtering was applied for low-level echo enhancement. As the slow-time filter, the Cauer filter of the second order with the cutoff frequencies 0.1 and 0.8 Hz was applied. The obtained results are presented in **Figures 8** and **9**. If we compare the radargrams with the subtracted background and the corresponding slow-time filter outputs $h_2(t, \tau)$, we can see that the useful signal components (three high-level artifacts similar to lines parallel to slow-time axis located in the interval $\langle 20\text{ ns}, 40\text{ ns}\rangle$of fast-time axis) were enhanced, while some unwanted signal components were suppressed [21].

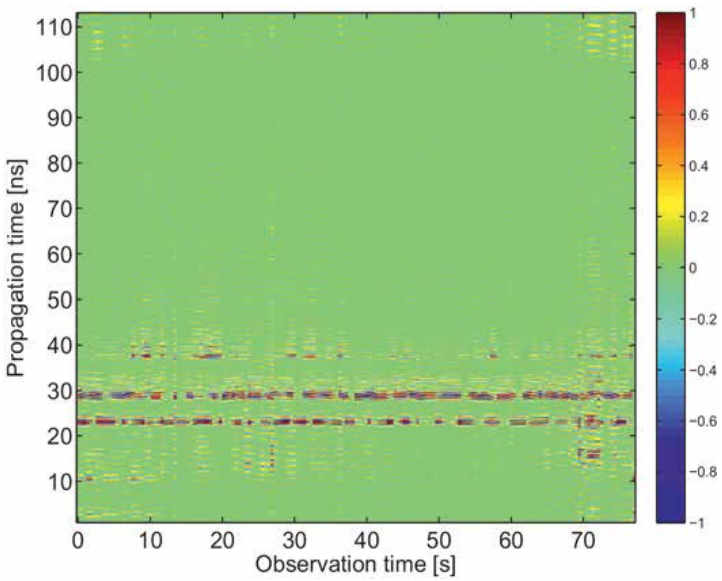

Figure 8. Slow-time filter output. Receiving channel Rx1.

4.2.3. Phase 3: target detection

Detection is the next phase of the radar signal processing procedure, which comes after the background subtraction and the target echo enhancement. Detection methods analyze the radargram with the subtracted background processed by range- and slow-time filters to reach the decision whether a signal scattered by a static person is present or absent in the analyzed radargram. Let the output of Phase 2 be denoted as $h_2(t, \tau)$. According to the conclusion of Section 2, the static person detection can be based on the detection of periodical components of signal $h_2(t_k, \tau)$ (i.e. a constant fast-time instant is considered). For those components, it is necessary to be located in the frequency band $B = \langle 0.2Hz,\ 0.7\ Hz\rangle$ and to have a sufficient level of their power as well. The former condition follows from the fact that the frequency band $B = \langle 0.2Hz,\ 0.7\ Hz\rangle$ covers the frequencies of human being respiration,

while the latter condition is essential to ensure that we can distinguish between the level of background noise and signal components caused by a static person. Moreover, we have to consider the fact that a person is the so-called distributed target, that is, not the only one but usually several reflections can be received by the sensor from the same person. Then taking into account this knowledge, static persons can be detected by the detector consisting of power-spectrum estimator employing Welch periodogram [17], order statistic constant false alarm rate detector (OS-CFAR) [22] and a simple threshold detector (TD). In the next, this kind of the detector will be referred to as a two-stage detector [23]. Its operation can be described as follows.

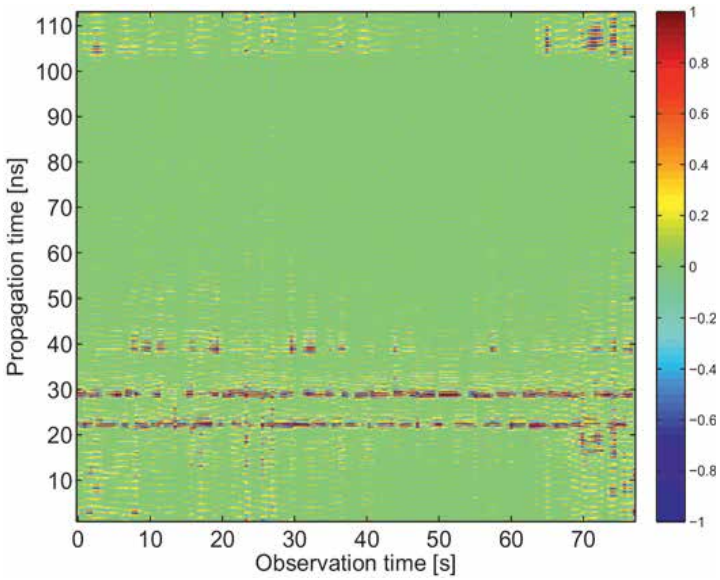

Figure 9. Slow-time filter output. Receiving channel Rx2.

First, the power spectra of the sequences $h_2(t_k, \tau)$ for $\tau \in \langle \tau_1, \tau_2 \rangle$ and for each time instant t_k are estimated using Welch periodogram [17]. Here, we would like to stress that the interval $\langle \tau_1, \tau_2 \rangle$ should be large enough to get a good power-spectrum estimation of the frequency components covering the frequency interval $B = \langle 0.2Hz,\ 0.7\ Hz \rangle$. In the next step, the total power of $h_2(t_k, \tau)$ contained in the frequency band $B = \langle 0.2Hz,\ 0.7\ Hz \rangle$ denoted as $X_1(t)$ is computed by the integration (summation) of the periodogram components located in this frequency band. Then, the variable $X_1(t_k)$ expresses a measure of the total power of $h_2(t_k, \tau)$ allocated in the frequency interval B including the power of signals reflected by all objects having the bistatic range $d(t_k) = ct_k$ (i.e. the distance *Tx-object-Rx*) with regard to the UWB sensor. As we stated before, a significant level of $X_1(t_k)$ indicates that in the bistatic range $d(t_k) = ct_k$ a static person can be located.

With the intention to decide if the level of $X_1(t_k)$ is significant to indicate the presence of a static person, OS-CFAR detector is employed with advantage as the first stage of the two-stage detector. The description of the OS-CFAR is beyond this paper. A reader interested in this topic

can find the detailed description of OS-CFAR detector, for example, in Ref. [22]. The input-output relation of the OS-CFAR can be described by the expression

$$h_1(t) = \begin{cases} 0 & \text{if } X_1(t) \leq \gamma_1(t) \\ 1 & \text{if } X_1(t) > \gamma_1(t) \end{cases} \tag{12}$$

where the level of the threshold $\gamma_1(t)$ is controlled by the OS-CFAR algorithm. The detector output $h_1(t)$ is a binary signal, where "1" ("0") indicates the presence (absence) of the target in the bistatic range $d(t) = ct$.

In the case of person detection by a high-resolution radar, the radar-range resolution is much finer than the size of the target. Then, a human target has to be considered as a distributed target. It means that several reflections due to the same target can be detected. In order to avoid a multiple detection of the same target, the second detection stage is applied within the detection phase. The input signal of this detector denoted as $X_2(t)$ is formed by the sequential summation of $X_1(t_k)$ over the interval with the length V, where V represents approximately the maximum number samples of $h(t, \tau)$ containing the reflections from the same target. Then, the signal $X_2(t)$ can be expressed as follows:

$$X_2(t) = \sum_{l=k}^{k+V-1} h_1(t_l) \tag{13}$$

Now, the operation of the second stage of the detector (TD) can be described by the expression

$$h_2(t) = \begin{cases} 0 & \text{if } X_2(t) \leq \gamma_2 \\ 1 & \text{if } X_2(t) > \gamma_2 \end{cases} \tag{14}$$

where γ_2 is a constant threshold. The TD output $h_2(t)$ is a binary signal, where "1" ("0") indicates the presence (absence) of a static person in the bistatic range $d(t) = ct$. The signal $h_2(t)$ represents also the output of the detection phase.

Now, the performance of the above-described two-stage detector can be illustrated using the data obtained at our illustrative scenario. First, the power spectra of slow-time filter outputs are given in **Figures 10** and **11**. Here, the frequency components due to the static persons located in the frequency band $B = \langle 0.2Hz,\ 0.7\ Hz \rangle$ and within the fast-time interval $\langle 20\text{ ns},\ 40\text{ ns} \rangle$ can be identified. The performance of OS-CFAR detector is outlined in **Figures 12–15**. These figures indicate that OS-CFAR detector is able to detect the static persons (three target detected in the fast-time interval $\langle 20\text{ ns},\ 40\text{ ns} \rangle$). We can observe also in these figures that several isolated reflections from the same person were detected by OS-CFAR detector. After the application of TD, the number of the detected targets is decreased. Targets are mostly detected in the fast-time interval $\langle 20\text{ ns},\ 40\text{ ns} \rangle$ (**Figures 16–19**).

As it might be expected, some false alarms can be observed in the OS-CFAR and TD outputs. The total number of the false alarms produced by TD is smaller than that created by OS-CFAR detector. Hence, we can see that TD application decreases the total number of false alarms observed at the output of the detection phase. We will show in the following paragraphs that

these false alarms will be eliminated by the TD output processing within TOA estimation and TOA association phase.

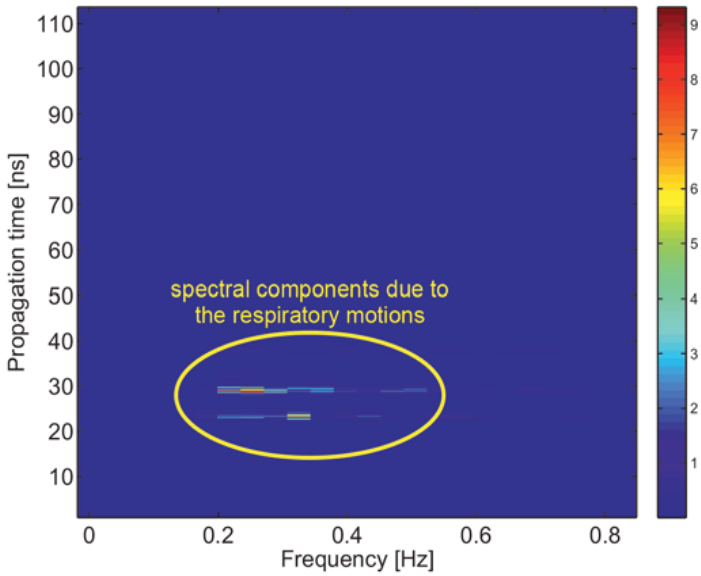

Figure 10. Power spectrum of slow-time filter output. Receiving channel Rx1.

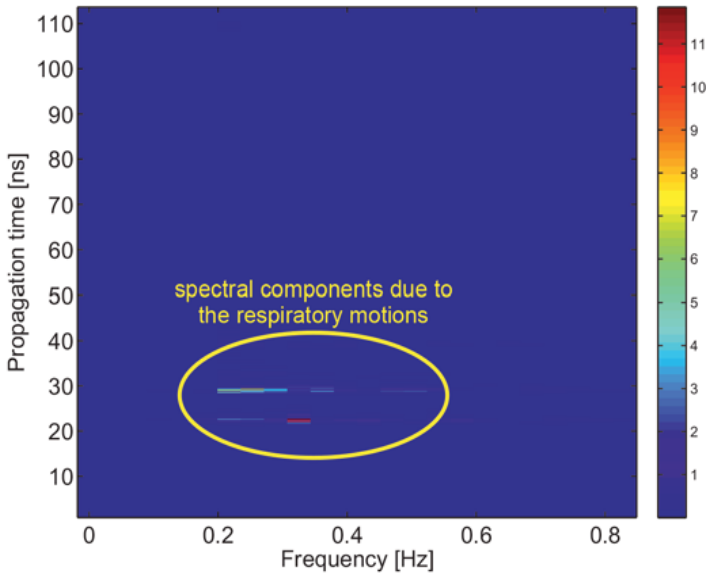

Figure 11. Power spectrum of slow-time filter output. Receiving channel Rx2.

http://dx.doi.org/10.5772/66361

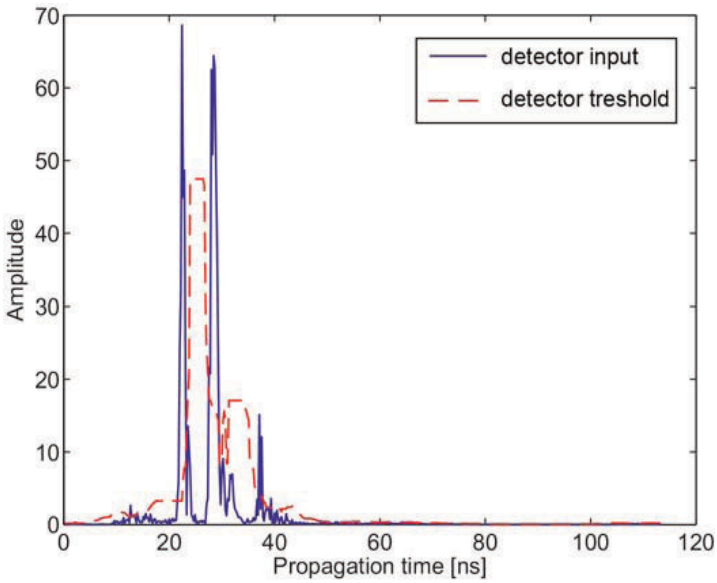

Figure 12. Total power of the signal $h_2(t_k, \tau)$ allocated in the frequency band B ($X_1(t)$, blue color) and OS-CFAR detector threshold ($\gamma_1(t)$, red color). Receiving channel Rx1.

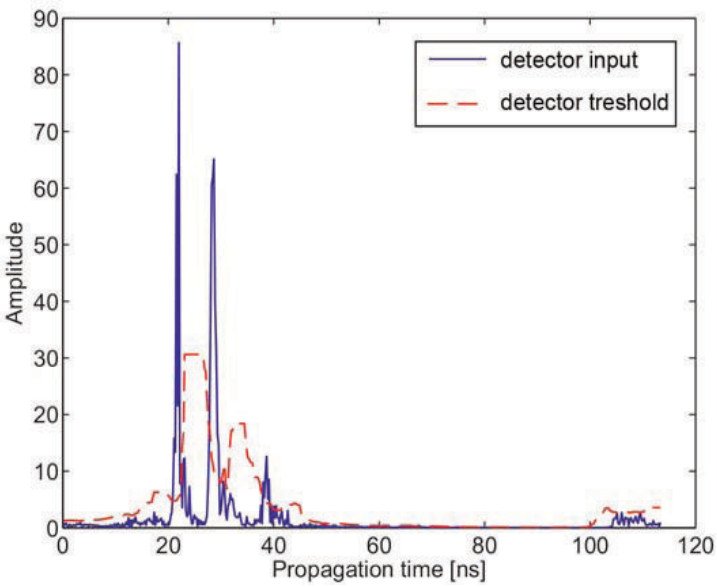

Figure 13. Total power of the signal $h_2(t_k, \tau)$ allocated in the frequency band B ($X_1(t)$, blue color) and OS-CFAR detector threshold ($\gamma_1(t)$, red color). Receiving channel Rx2.

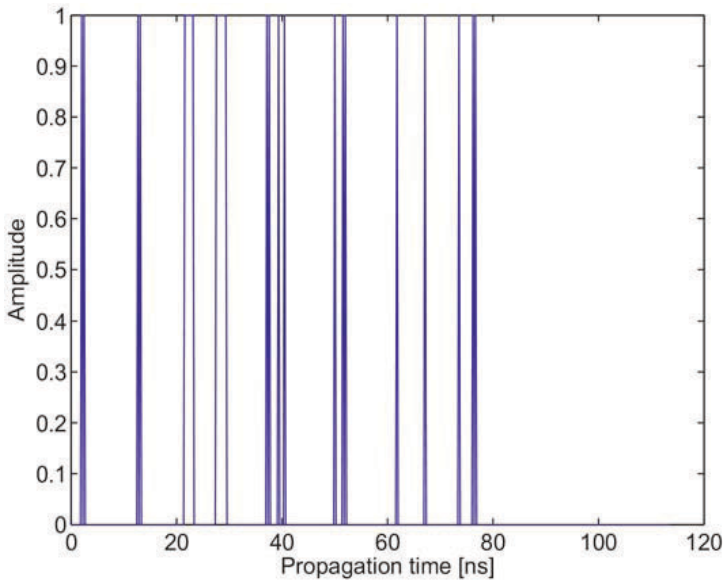

Figure 14. OS-CFAR detector output. Receiving channel Rx1.

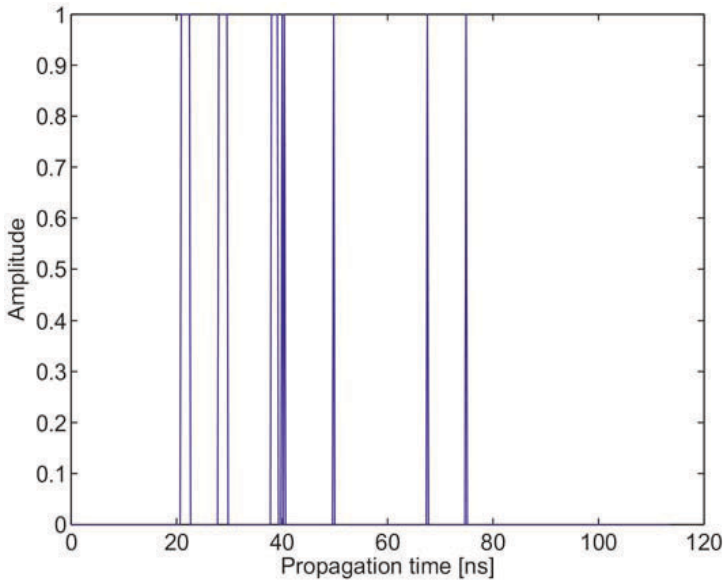

Figure 15. OS-CFAR detector output. Receiving channel Rx2.

4.2.4. Phase 4: TOA estimation and TOA association

The very efficient algorithm for TOA estimation can be found, for example, in Ref. [24]. This algorithm referred to as the trace connection method provides not only TOA estimation but

http://dx.doi.org/10.5772/66361

also the association of the data received from two receiving channels and deghosting operation essential for multiple target detection. The trace connection method is quite complex, and hence it is beyond this paper. The details concerning this method can be found, for example, in Ref. [24]. The output of this phase consists in the pairs of TOA associated with the same target obtained for the first (Rx1) and second (Rx2) receiving channel of the radar.

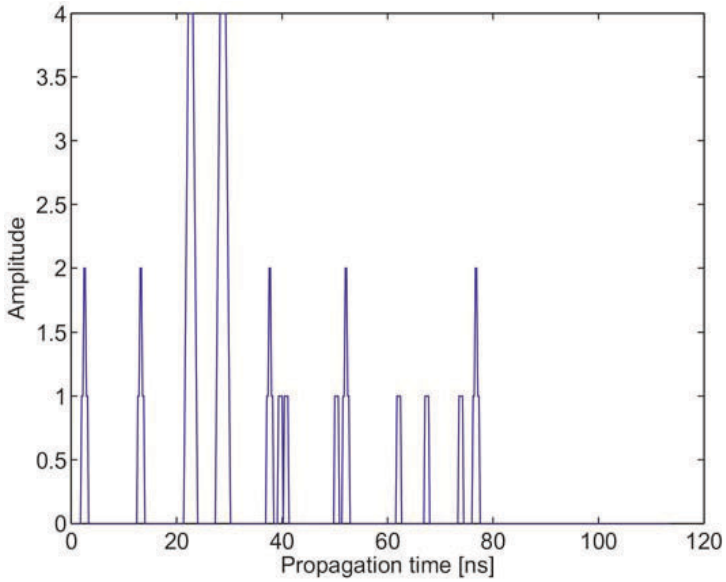

Figure 16. TD input. Receiving channel Rx1.

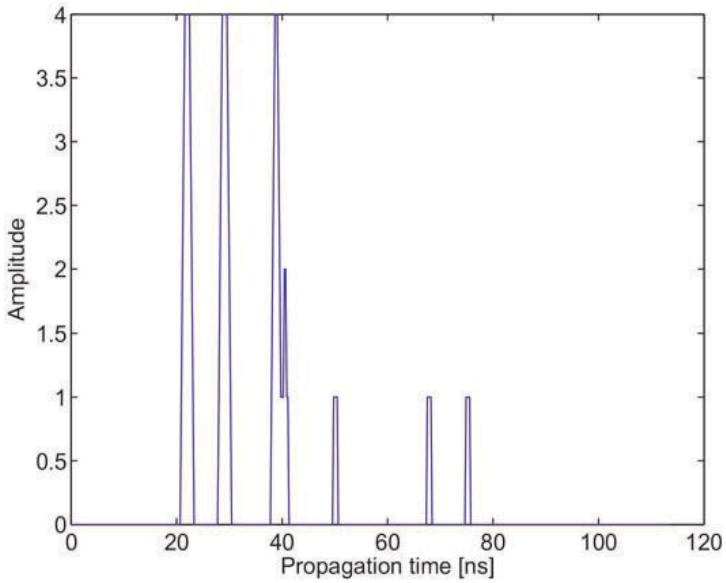

Figure 17. TD input. Receiving channel Rx2.

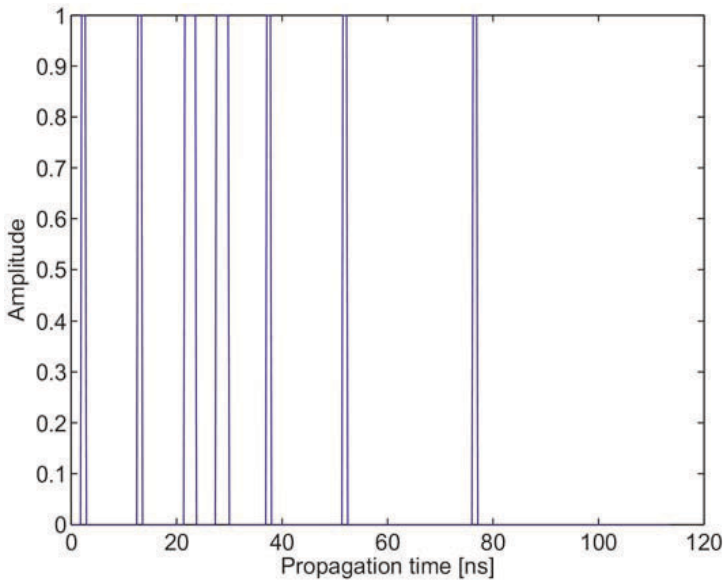

Figure 18. TD output. Receiving channel Rx1.

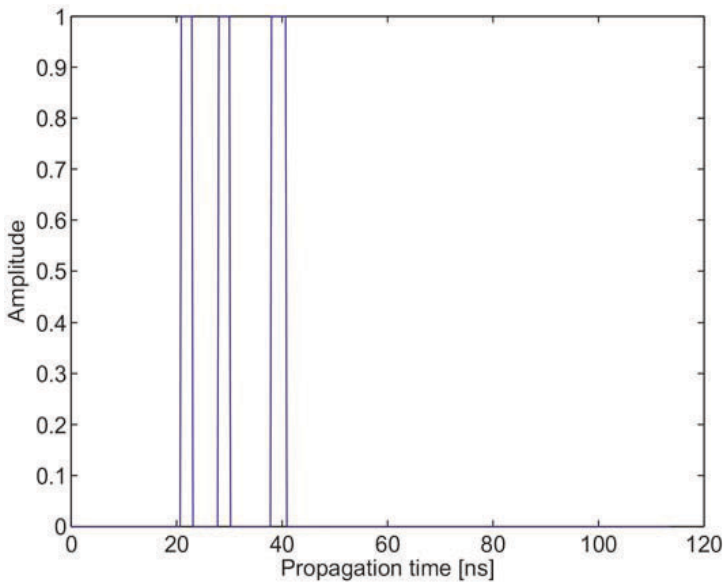

Figure 19. TD output. Receiving channel Rx2.

4.2.5. Phase 5: target localization

The estimations of the target coordinates represent the output of the target localization phase and at the same time the final result of WP-STAPELOC method. The results provided by the trace connection method (Phase 4) and by direct computation method (Phase 5) for the

illustrative scenario discussed throughout this paper are given in **Figure 20**. Here, the true and estimated positions of the static persons are expressed by green and red marks, respectively. Moreover, tolerance areas represented by the circles with the center in the true position of the target and with the diameter 30 cm are also sketched in **Figure 20**. The tolerance areas are used to demonstrate that the person is not a pointed but distributed target with a certain non-zero size. The results depictured in **Figure 20** confirm that WP-STAPELOC method performs very well for the illustrative scenario. In spite of the complex scenario (three-person localization through the thick concrete wall), all static persons were localized with the good accuracy (all persons were localized in corresponding tolerance area).

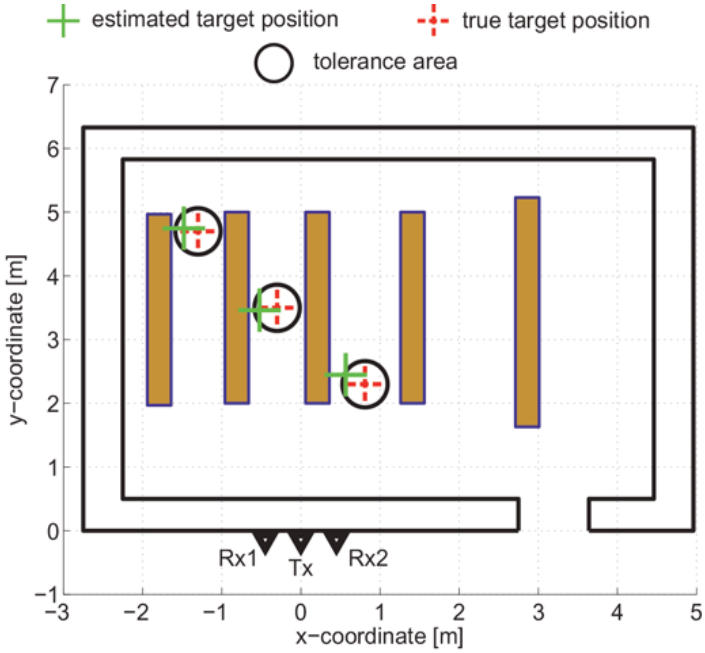

Figure 20. True (green mark) and estimated (red mark) positions of the static persons.

5. Conclusion

In this chapter, we have dealt with a problem of multiple static person localization using a single M-sequence UWB radar. For that purpose, we have introduced the novel radar signal processing procedure focused on the static person detection and localization. The key novelty of this method consists of the application of a two-stage detector based on the combination of power-spectrum estimator, OS-CFAR detector, and a simple TD. The performance of the proposed procedure has been evaluated for through-the-wall scenario of localization of three static persons. The obtained results have confirmed that the procedure described in this paper can provide a good performance also for challenging scenarios.

Unfortunately, the illustrated good performance of the WP-STAPELOC method does not mean that this method is able to provide a perfect and robust performance almost for all possible

scenarios. Nevertheless, the presented approach addresses the core problems of multiple static person localization and suggests their fundamental solutions. This fact is considered of the highest importance and benefits of the proposed methods. In order to obtain a really robust system for the localization of static persons by UWB sensors, a modified version of WP-STAPELOC method has to be developed. The new modified version based on the presented principles should take into account shadowing effect, wall effect and its compensation, multipath electromagnetic wave propagation, a presence of strong reflectors in monitored area, narrowband interference, and so on. Moreover, the static person localization method should be optimized with regard to its computational complexity. We believe that the solution of this challenging and complex task will be available in the near future.

Acknowledgements

This work was supported by the Slovak Research and Development Agency under the contract No. APVV-0404-12.

Author details

Dušan Kocur*, Daniel Novák and Mária Švecová

*Address all correspondence to: dusan.kocur@tuke.sk

Department of Electronics and Multimedia Communications, Technical University of Košice, Košice, Slovakia

References

[1] Huffmann C., Ericson L. Through-the-wall sensors for law enforcement. market Survey. [Internet]. 10/2012 [Updated: 04/2014]. Available from: https://www.ncjrs.gov/pdffiles1/nij/grants/245944.pdf [Accessed: 25.8.2016]

[2] Sachs J., Helbig M., Herrmann R., Kmec M., Schilling K., Zaikov E. Remote vital sign detection for rescue, security, and medical care by ultra-wideband pseudo-noise radar. Ad Hoc Networks. 2014;13:42–53. DOI: 10.1016/j.adhoc.2012.07.002

[3] Lazaro A., Girbau D., Villarino R. Techniques for clutter suppression in the presence of body movements during the detection of respiratory activity through UWB radars. Sensors. 2014;14(2):2595–2618. DOI: 10.3390/s140202595

[4] Singh S., Liang Q., Chen D., Sheng L. Sense through wall human detection using UWB radar. EURASIP Journal on Wireless Communications and Networking. 2011;20:1–11. DOI: 10.1186/1687-1499-2011-20

[5] Zaikov E., Sachs J., Aftanas M., Rovňáková J. Detection of trapped people by UWB radar. In: Microwave Conference (GeMIC), 2008 German; 10–12 March 2008; VDE VERLAG GmbH; 2008. pp. 1–4.

[6] Yarovoy A. G., Ligthart L. P., Matuzas J., Levitas B. UWB radar for human being detection. IEEE Aerospace and Electronic Systems Magazine. 2006;21(3):10–14. DOI: 10.1109/MAES.2006.1624185

[7] Rivera N. V., Venkatesh S., Anderson Ch., Buehrer R. M. Multi-target estimation of heart and respiration rates using ultra wideband sensors. In: Signal Processing Conference, 2006 14th European; 4–8 September 2006; Florence, Italy; IEEE; 2006. pp. 1–6.

[8] Nezirović A. Trapped-Victim Detection in Post-Disaster Scenarios using Ultra-Wideband Radar [dissertation]. Delft: Delft University of Technology; 210. 165 p. Available from: http://repository.tudelft.nl/islandora/object/uuid:4416dd48-9829-4af0-b678-8fcd8e87788a/?collection=research

[9] Nezirović A., Yarovoy A. G., Ligthart L. P. Signal processing for improved detection of trapped victims using UWB radar. IEEE Transactions on Geoscience and Remote Sensing. 2010;48(4):2005–2014. DOI: 10.1109/TGRS.2009.2036840

[10] Li X., Liang Q., Lau F. Sense-through-wall human detection using the UWB radar with sparse SVD. Physical Communication. 2014;13:260–266. DOI: 10.1016/j.phycom.2013.12.002

[11] Li J., Liu L., Zeng Z., Liu F. Simulation and signal processing of UWB radar for human detection in complex environment. In: Ground Penetrating Radar (GPR), 2012 14th International Conference; 4–8 June 2014; Shanghai,China; IEEE; 2012. pp. 209–213. DOI: 10.1109/ICGPR.2012. 6254862

[12] Liu Z., Liu L., Barrowes B. The application of the Hilbert-Huang transform in through-wall life detection with UWB impulse radar. PIERS Online. 2010;6(7):695–699. DOI: 10.2529/PIERS100217122115

[13] Li J., Zeng Z., Sun J., Liu F. Through-wall detection of human being's movement by UWB radar. IEEE Geoscience and Remote Sensing Letters. 2012;9(6):1079–1083. DOI: 10.1109/LGRS.2012.2190707

[14] Wang Y., Yu X., Zhang Y., Lv H., Jiao T., Lu G., et al. Using wavelet entropy to distinguish between humans and dogs detected by UWB radar. Progress in Electromagnetics Research. 2013;139:335–352. DOI: 10.2528/PIER13032508

[15] Huang N., Shen Z., Long S., Wu M., Shih H., Zheng Q. The empirical mode decomposition and the Hilbert spectrum for nonlinear and non-stationary time series analysis. Proceedings of the Royal Society of London A: Mathematical, Physical and Engineering Sciences. 1998;454(1971):903–995. DOI: 10.1098/rspa.1998.0193

[16] Stockwell R. G., Mansinha L., Lowe R. P. Localization of the complex spectrum: The S-transform. IEEE Transactions on Signal Processing. 1996;44(4):998–1001. DOI: 10.1109/78.492555

[17] Proakis J. G., Manolakis D. G. Digital Signal Processing. 4th ed. Michigan University: Pearson Prentice Hall; 2007. 1084 p.

[18] Kim Ch., Lee J. ToA-based multi-target localization and respiration detection using UWB radars. EURASIP Journal on Wireless Communications and Networking. 2014;2014(1):1–15. DOI: 10.1186/1687-1499-2014-145

[19] Kim C., Lee J., Cho T., Ki D., Cho B. H., Yoon J. Multi-target localization of breathing humans. In: Proceedings of the 2013 IEEE International Conference on Ultra-Wideband (ICUWB 2013); Sydney, Australia; 2013. pp. 49–54.

[20] Rovňáková J., Švecová M., Kocur D., Nguyen T. T., Sachs J. Signal processing for through wall moving target tracking by M-sequence UWB radar. In: Radioelektronika, 2008 18th International Conference; 24–25 April 2008; Prague, Czech Republic.; IEEE; 2008. p. 1–4. DOI: 10.1109 RADIOELEK.2008.4542694

[21] Kocur D., Švecová M., Rovňáková J. Through-the-wall localization of a moving target by two independent ultra wideband (UWB) radar systems. Sensors. 2013;13(9):11969–11997. DOI: 10.3390/s130911969

[22] Rohling H. Some radar topics: waveform design, range CFAR and target recognition. In: Byrnes J., Ostheimer G., editors. Advances in Sensing with Security Applications. 2nd ed. Springer, Netherlands; 2006. pp. 293–322. DOI: 10.1007/1-4020-4295-7_13

[23] Novák D., Kocur D. Multiple static person localization based on respiratory motion detection by UWB radar. In: 2016 26th International Conference Radioelektronika (RADIOELEKTRONIKA); 19–20 April 2016; Košice. IEEE; 2016. pp. 252–257. DOI: 10.1109/RADIOELEK.2016.7477386

[24] Rovňáková J., Kocur D. TOA estimation and data association for through-wall tracking of moving targets. EURASIP Journal on Wireless Communications and Networking. 2010;2010(1):1–11. DOI: 10.1155/2010/420767

Edited by Sotirios K. Goudos

Microwave systems are key components of every modern wireless communication system. The main objective of this book was to collect as many different state-of-the-art studies as possible in order to cover in a single volume the main aspects of microwave systems and applications. This book contains 17 chapters written by acknowledged experts, researchers, academics, and microwave engineers, providing comprehensive information and covering a wide range of topics on all aspects of microwave systems and applications. This book is divided into four parts. The first part is devoted to microwave components. The second part deals with microwave ICs and innovative techniques for on-chip antenna design. The third part presents antenna design cases for microwave systems. Finally, the last part covers different applications of microwave systems.

ISBN 978-953-51-4125-9

Photo by ktsimage / iStock

IntechOpen